Characterization of Lower Eocene Reservoirs in the LL-652 Area, Lagunillas Field

Final Report to

Lagoven, S.A., Caracas, Venezuela

by

Noel Tyler, William A. Ambrose,
Shirley P. Dutton, Fred Wang, and Joseph S. Yeh
Bureau of Economic Geology

Eulise Ferrer, Antonio Padron, and Williams Carrasquel
Lagoven, S.A.

QAe7819

CONTENTS

by William A. Ambrose and Eulise Ferrer

A.   Structural, Stratigraphic, and Dipmeter Data
B.   Petrographic Data
C.   Petrophysical Data
D.   Core Descriptions
E.   Maps
F.   Cross Sections
G.   Petrophysical Evaluation of Key Wells
H.   Discs with Data

Figures

Tables

Plates

I. EXECUTIVE SUMMARY

Lower Eocene reservoirs (C members) in the LL-652 area will contain substantial volumes of remaining oil (923 million barrels [MMbbl]) after primary development. This resource exists in poorly drained or undrained reservoir compartments defined by a combination of complex structure and heterogeneous tide-dominated deltaic facies geometry. The product of this combined structural and depositional complexity is reservoirs that have a high degree of geologic heterogeneity, considerable variation in reservoir quality, and, therefore, a low recovery efficiency.

The tide-dominated deltaic depositional model of the C members in the LL-652 area captures a system of dip-elongate, distributary-channel sandstones that merge northeastward with extensive, dip-parallel delta-front sandstones. These two facies compose most of the reservoir sandstones and therefore contain most of the remaining oil. Permeability range and average are similar for the major facies. However, there are significant permeability contrasts (up to three orders of magnitude) locally between distributary-channel and tidal-flat, fluvial-estuarine channel and distal delta-front, and distributary-channel and delta-front facies where clay clasts at the base of the distributary-channel facies may retard vertical fluid flow.

The structure of the LL-652 area is a north-northeast-trending, elongate anticline with a steeply dipping (25-45°) western and northwestern limb and a relatively gently dipping (5-10°) east and southeast limb. Multiple tectonic events generated three trends of normal faults and one trend of younger reverse faults, representing the local scale of five major structural trends in the Maracaibo Basin (Lugo, 1991). The LL-652 area is divided into five main and two minor structural compartments. The principal reservoir areas (C-4-X.01, C-5-X.02, and C-6-X.01) are separated from the C-4-X.03, C-5-X.08, and C-6-X.16 reservoir areas by a major northwest-trending normal fault in the northeast part of the LL-652 area. Other northwest-trending normal faults bound the reservoirs. A north-northeast-trending zone of partly sealing reverse faults with repeat section ranging from 60 to 150 ft (18 to 45.7 m) internally divides the principal reservoirs and provides additional compartments for remaining oil.

Cumulative production, apportioned by kh, varies greatly across the LL-652 area for each C submember. Reasons for this variability include (1) differences in age of producing well, (2) greater-than-average production in areas of repeat section and inferred great fracture permeability in zones of reverse faults, and (3) differences in net thickness of intervals perforated in each submember. However, net-sandstone thickness of each submember is controlled by the tide-dominated deltaic depositional fabric.

Cumulative production to March 1993 in 130 active wells in the LL-652 area was 165.5 MMbbl of oil, mainly 37° API, and 8.3 MMbbl of water. Eighty-two percent (135.8 MMbbl) of the oil production comes from the C-3-X and C-4-X Members, whereas the C-5-X Member accounts for only 12 percent (20.5 MMbbl). The C-6-X Member has 5 percent (8.4 MMbbl) of cumulative oil production, and the C-2-X Member has only 1 percent (0.8 MMbbl). The central structural compartment is the largest production area in the field and includes 76 wells with a cumulative production of 85.8 MMbbl. Seventy-seven percent (66.1 MMbbl) of this production comes from the C-4-X.01 reservoir compartment.

Diagenesis, not depositional environment, is the main control on porosity and permeability distribution in the C members. Porosity and permeability in the C members decrease with increasing depth. In particular, volume of quartz cement is the main influence on reservoir quality, and because volume of quartz cement increases significantly with depth, reservoir quality decreases with depth.

The original-oil-in-place (OOIP) resource base of the C members in the LL-652 area has been increased by 867 MMSTB (867 million stock tank barrels) (60 percent) to 2,318.2 MMSTB. This increase is mainly in the C-3-X and C-4-X Members through documenting additional reservoir areas and through improved quantification of porosity and other petrophysical parameters. Extended development through continued pattern infill with 97 new wells will increase reserves from 127 to 302 MMSTB. However, 116 MMSTB, in addition to the 302 MMSTB, can be produced from 102 geologically based infill wells strategically targeted to tap areas of high remaining oil saturation by contacting narrow sandbodies that pinch out

1

over distances less than the current 80-acre (1,968 ft [600 m]) well spacing. Horizontal and inclined wells in the C-3-X and C-4-X Members can capture additional volumes of poorly contacted mobile oil, particularly in steeply dipping strata in the northern part of the field.

A pilot waterflood in the Upper C-4-X Submember in the eastern part of the LL-652 area can recover an additional 10 to 20 MMSTB of oil, which is projected to be approximately 70 MMSTB throughout the LL-652 area for the Upper C-4-X Submember. Expansion of waterflood operations to the entire field could increase recovery by as much as 20 percent of the OOIP, representing a secondary-recovery resource of approximately 460 MMSTB.

II. INTRODUCTION

Many oil reservoirs contain substantial volumes of unrecovered mobile oil trapped in poorly drained compartments after primary and secondary development. For example, of the nearly 500 billion barrels (Bbbl) of oil that have been discovered in the United States, approximately 300 Bbbl in existing fields will remain unproduced after primary and secondary recovery with existing technology (Fisher, 1987; Tyler, 1988). Of this 330 Bbbl, 80 to 100 Bbbl is mobile oil that can be recovered at low cost through conventional infield exploration and development strategies that target untapped compartments and optimize existing waterfloods (fig. 1). Three-dimensional facies architecture and structural complexity exert a strong control over the distribution and continuity of reservoir compartments and paths of fluid flow and, therefore, the areas of the reservoir that have been swept. Reservoirs with complex internal architecture contain large volumes of remaining mobile oil, whereas those with simple internal architecture are efficiently drained.

Although oil reservoirs are internally complex and commonly contain undrained or partially drained compartments, traditional infill strategies, based on the assumption that all reservoirs are homogeneous and almost perfectly continuous, have simply maintained geometric grid patterns of well spacing. These infill strategies have missed numerous untapped or ineffectively swept compartments and have resulted in many nonproductive or poorly productive wells that increase the average cost per infill well.

A more efficient means of recovering mobile oil is through a geologically based infill-development strategy that targets compartments defined by large-scale, depositional-facies geometry and structure. Tyler (1988) demonstrated a relationship between original depositional environment, drive mechanism, and recovery efficiency (fig. 2). This relationship is based on a review of 450 major Texas oil reservoirs that together account for almost 75 percent of Texas production and provide examples of oil production from a wide variety of depositional environments (Galloway and others, 1983).

The recovery efficiency of reservoirs varies tremendously according to depositional type (fig. 2). Homogeneous barrier-island and wave-dominated deltaic reservoirs typically have strong water drives and have high mobile-oil recovery, whereas internally complex fluvial-deltaic reservoirs have moderate drive energies and exhibit recovery efficiencies ranging from approximately 20 to 50 percent. By comparison, lower Eocene tidally influenced deltaic reservoirs in the C members of the Misoa Formation in Lagunillas field, which are the focus of this study, are expected to have an ultimate recovery of only 20 percent at the end of primary recovery operations. Thus, a resource of 923 million barrels (MMbbl) of unrecovered mobile oil will remain in the field following recovery of remaining reserves at current levels of development and well spacing of approximately 80 acres. This report demonstrates that the structural complexity and depositional heterogeneity of these reservoirs have resulted in enormous potential for reserve growth from the remaining recoverable mobile oil. For example, the complex, multistage tectonic history of Lake Maracaibo has created many structural compartments between intersecting faults of different age. Additionally, sandbody trends, as a result of the tidally influenced deltaic depositional system of the reservoirs in the C members, are strongly linear and are consistently oriented northeastward. These sandstone trends impart a preferred pathway for fluid flow in the reservoir. Importantly, the sandstone bodies are narrow, typically less than the distance between well (2,000 ft [600 m]), and are bounded laterally by low-permeability siltstones and mudstones resulting in laterally discontinuous, or compartmentalized, reservoirs. This report documents the volume of oil remaining in the C reservoirs and will identify, on a between-well scale, the location of the remaining oil so that cost-effective, geologically targeted recovery strategies can be implemented to recover a large part of this resource. Specifically, this report targets selected reservoir zones for infill drilling, strategic recompletions, and waterflooding to maximize oil recovery.

Objective

The primary objective of this study was the geological characterization of the C members in the Eocene in the LL-652 area of Lake Maracaibo in order to better estimate hydrocarbon reserves, identify potential
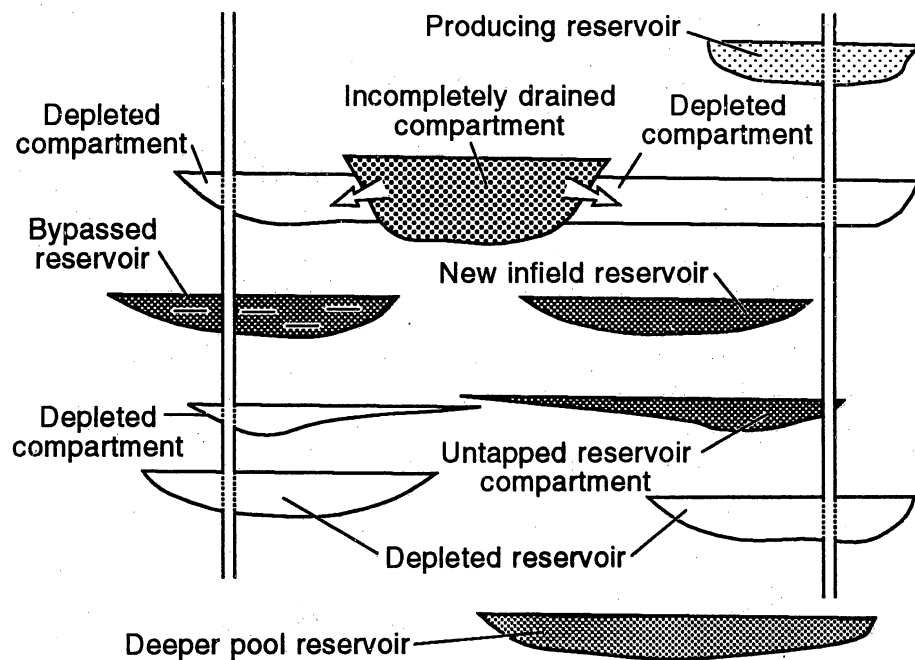
Figure 1. Types of reservoir compartments.
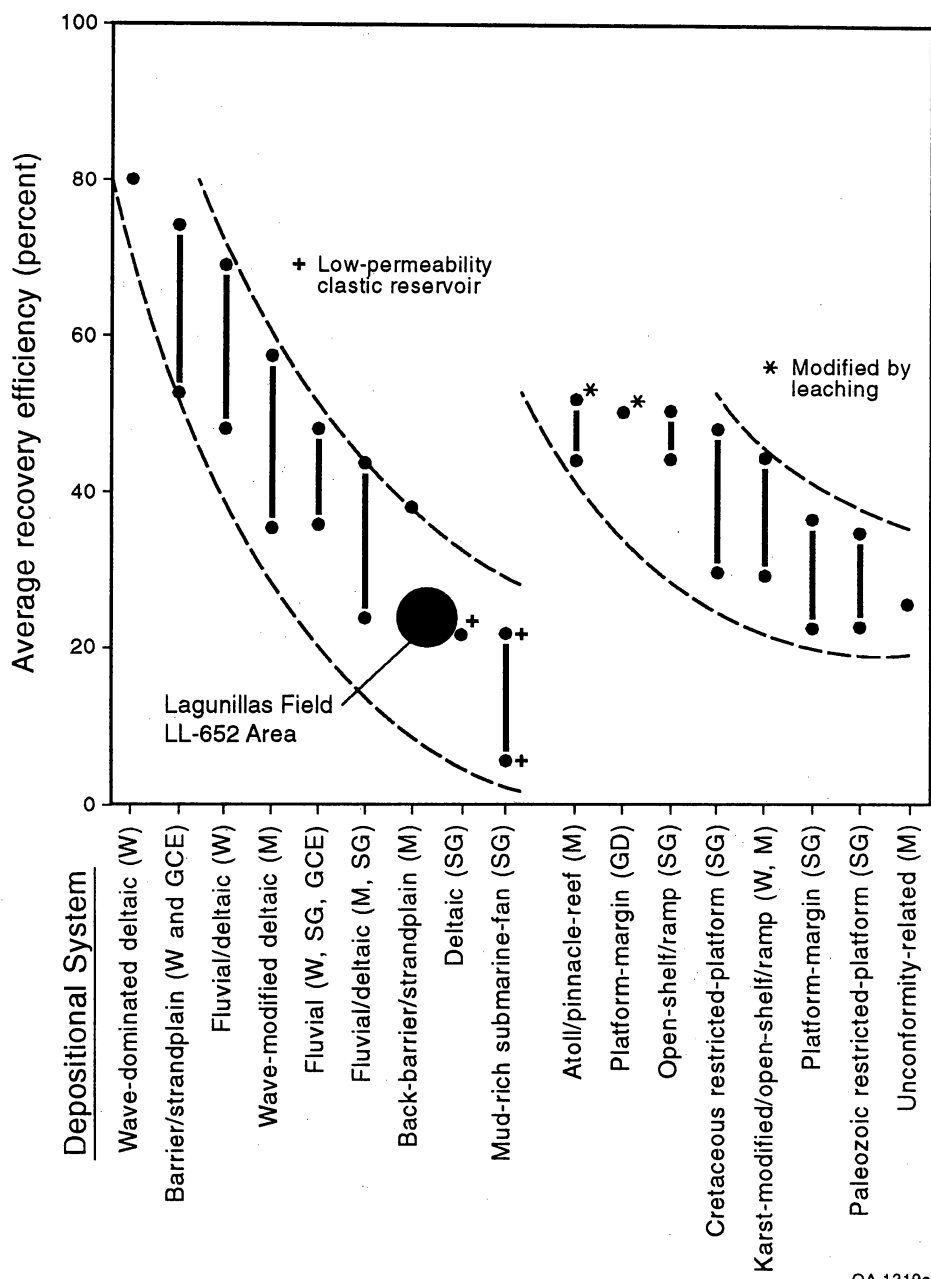
Figure 2. Average recovery efficiency of oil reservoirs versus depositional system in the Lower Misoa Formation (C members).

areas for secondary recovery projects, and to establish a field-depletion plan to evaluate advanced recovery opportunities and extended development. This objective was met by conducting an integrated study that included a structural, stratigraphic, petrophysical, and production-engineering analysis from well logs, cores, seismic data, thin sections, and petroleum engineering data. Thirteen specific tasks were designed to complete the study:

(1) Correlating and subdividing the major depositional cycles (stratigraphic sequences) of the C members.

(2) Determining the geometry (lateral and vertical continuity) of sandstone bodies in depositional cycles.

(3) Describing and analyzing whole cores in order to interpret depositional environments, to calibrate log responses, and to construct a depositional model.

(4) Determining original and current fluid contacts from log analysis, production data, and petrophysical analyses.

(5) Establishing reservoir limits from structural and stratigraphic maps.

(6) Producing a structural model by analyzing sealing and non-sealing faults and preparing structural maps of marker tops and fault planes.

(7) Extending the geological interpretation into the Maraven block for a better evaluation of the structurally complicated western part of the LL-652 area.

(8) Conducting a petrophysical study for each reservoir based on core information, well logs, production data, and petrophysical parameters (porosity, permeability, V_{cl}, m, n, a, capillary pressure, S_{wirr}, and grain density), supporting the calculation of original oil in place (OOIP) and recoverable reserves through primary development methods, and estimating the rock-quality characteristics.

(9) Producing isopach maps of net oil sandstone, porosity, permeability, water saturation, and porous hydrocarbon volume.

(10) Estimating OOIP and remaining mobile oil and delineating reservoir boundaries.

(11) Identifying potential areas for extended development, infill wells, recompletions, and secondary recovery projects.

(12) Evaluating diagenetic processes and type and distribution of clay that may affect the production performance of reservoirs in areas or potential intervals for secondary recovery projects.

(13) Creating a data bank with information gathered from the study for incorporation into existing data bases.

Study Area, Methods, and Database

The LL-652 area in Lagunillas field, located in the Maracaibo Basin in northwestern Venezuela, is considered to be one of the most important oil-producing basins in the world. The LL-652 area covers an area of about 54 mi^2 (140 km^2) and is bounded on the north by the western Tia Juana area, and on the west by the Maraven Block 1 concession (figs. 3 and 4). The LL-652 area was discovered in 1953. It is one of the most prolific hydrocarbon producers in the Misoa Formation in the C-1-X to C-6-X Members (fig. 5). With an official OOIP of 1.5 Bbbl, the LL-652 area has produced more than 170 MMbbl of mainly light oil from the B and C members during the last 40 years. Production comes from 10 reservoirs contacted by a total of 150 Lagoven wells. The main production and development problems in the LL-652 area include (1) undefined variations in reservoir quality throughout the area, particularly in the low-permeability C-5-X, C-6-X, and C-7-X Members, (2) high water production in high-resistivity zones in the C-6-X and C-7-X Members, (3) structural complexity in the northern, west-central, and southwestern parts

Gulf of Venezuela

COLOMBIA

VENEZUELA

Maracaibo

Tia Juana field

Maraven block I

Lagunillas field

MARACAIBO BASIN

LL-652 area

Sediment source

N

0   50 mi

0   80 km

Caribbean Sea

Venezuela

Colombia   Brazil

Fluvial   Deltaic   Open marine
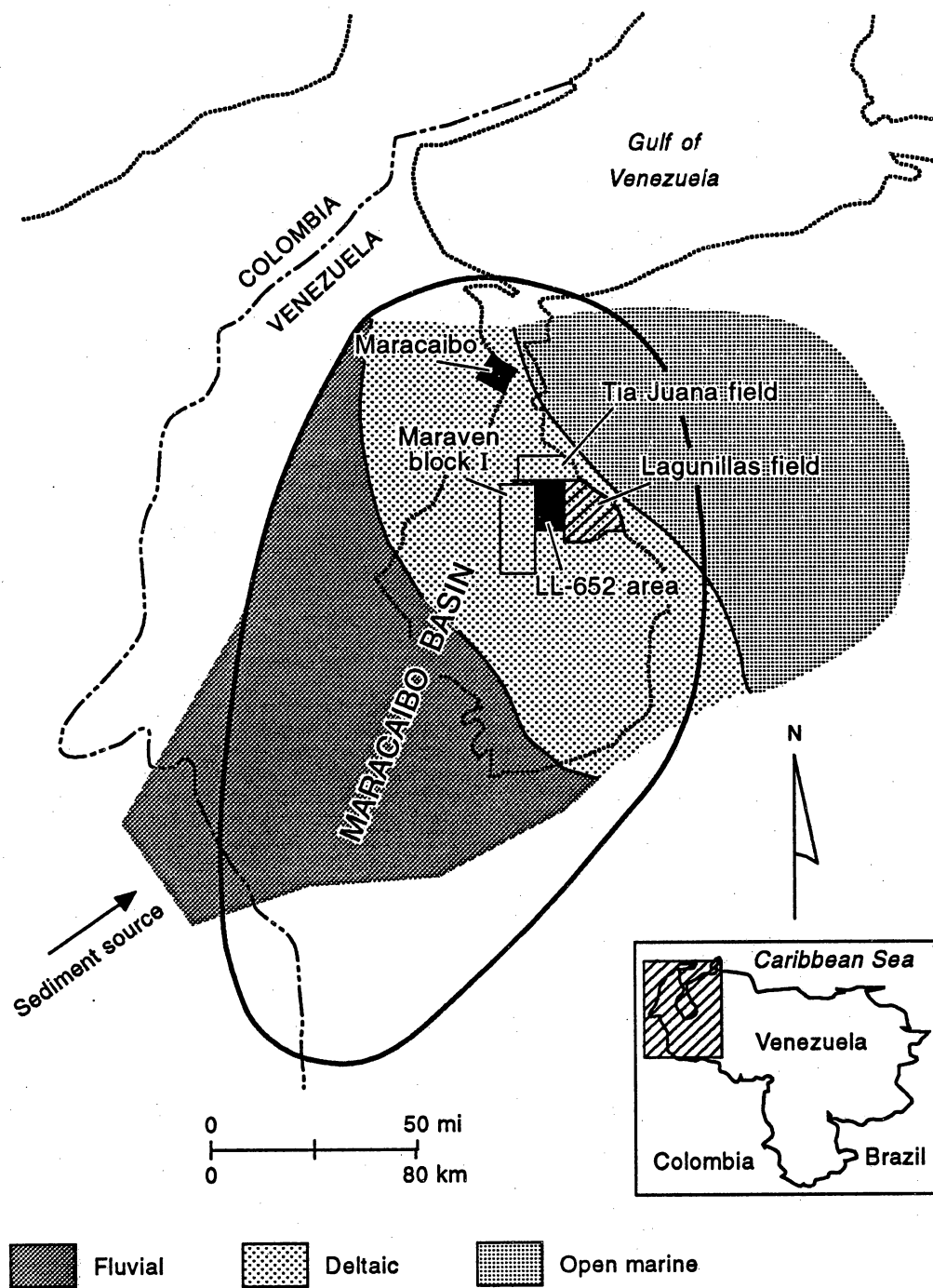
From Maguregui and Tyler (1991)

QAa4418c

Figure 3. Location of the LL-652 area and Lagunillas field in the Maracaibo Basin.

7

Figure 4. Well control and well names in the LL-652 area and western part of Maraven Block 1.

Figure 5. Type log (LL-2942) in the LL-652 area.

of the field, (4) poorly documented net-sandstone thickness trends and their influence on reservoir drainage, (5) unknown or poorly understood reservoir boundaries in the northern, western (Maraven boundary), and southern parts of the field, and (6) discrepancies between or poor information on oil-water contacts in the C-3-X through C-6-X Members.

The research was systematically conducted in phases or steps, briefly summarized here. Detailed descriptions of methods preface certain individual chapters of the report, including structural interpretation, petrography petrophysics, volumetrics, and infield development. In phase 1, a detailed study plan was made for all the stages of the project to determine research activities, priorities, critical phases, objectives, and limitations and to estimate manpower required to finish the project.

Phase 2 consisted of data collection and review. The collection and preparation of data were important steps and required as much effort as possible to select good-quality data, ensuring the timely development of all the stages of the project. A new base map was updated to assure the accuracy and completeness of all well locations. Geological, engineering, and geophysical data were collected from Lagoven S.A. and Maraven S.A. and cataloged and organized into files. Data were updated and new files generated as needed. Digitized tapes of well log data were transferred into the computer system. Previous studies of Lagunillas field and the Maracaibo Basin were obtained from Lagoven and Maraven company reports and published articles from general literature. Official and operational maps were reviewed in order to better define the limits of the study area and to incorporate production data in the reservoir models.

Phase 3 included log correlations. Initial log correlations were made with wells with the most complete and thickest stratigraphic sections. Major shale marker beds, which subdivide members and submembers, were identified as regional markers across the area. The LL-2942 well, which shows divisions of the members and submembers, (fig. 5) was selected as the type log because it contacts a complete unfaulted interval in the entire lower Eocene. An initial study area in the east-central part of Lagunillas field (fig. 6) was selected for initial correlations because it is structurally less complex and is located in an area where most of the cored wells are present and where the well control is greater. Detailed correlations with 10 major shale and 25 other, less-continuous shale marker beds in the B and C members were made in the initial area and extended away to the 150 wells in the LL-652 area and 40 wells of Maraven Block 1 (fig. 6). Correlations of each well were made with a minimum of three other wells within a loop beginning and ending with the same log, reducing correlation errors to a minimum. Correlations were extended across the study area in a grid of 27 stratigraphic cross sections (14 dip and 13 strike) to verify the correlations and faults and to identify wells with unresolved discontinuities and thickness changes in stratigraphic units (app. F). All well logs were included in at least one of the 27 cross sections. The general structural framework, initially established by well-log correlations, was checked and revised through structural maps of tops of each C member as well as on the Eocene unconformity. Additionally, 12 structural cross sections (fig. 7) were constructed to check and verify the existence of faults, structural dip, and folds. Twelve seismic cross sections (six dip and six strike, also located in fig. 7) were interpreted to further verify the structural framework and to demonstrate the stratal geometry of major stratigraphic sequences.

In phase 4, sedimentology and stratigraphy, whole cores from eight wells (LL-846, LL-2425, LL-2850, LL-3074, LL-3075, LL-3080, LL-3140, and LL-3282) (fig. 6), which together contain a total of 3,266 ft (995.7 m) of section, were described in detail to interpret depositional environments, calibrate log responses, develop a depositional model, and provide a framework for thin-section sampling. Cores were described graphically on a form that depicts grain-size trends, nature of contacts, sedimentary structures, rock type, degree of calcite cement, as well as other important features such as clay clasts, burrows, and organic fragments (see app. D for examples). In addition, relative percentages of stratification types and accessory features (degree of induration [consolidation], shells, burrows, organics, clay clasts, graded beds, sorting, roundness, fractures, visual porosity, and soft-sediment deformation) were indicated by relative width of filled-in columns. Close-up photographs were taken of important features in the core to document these features.
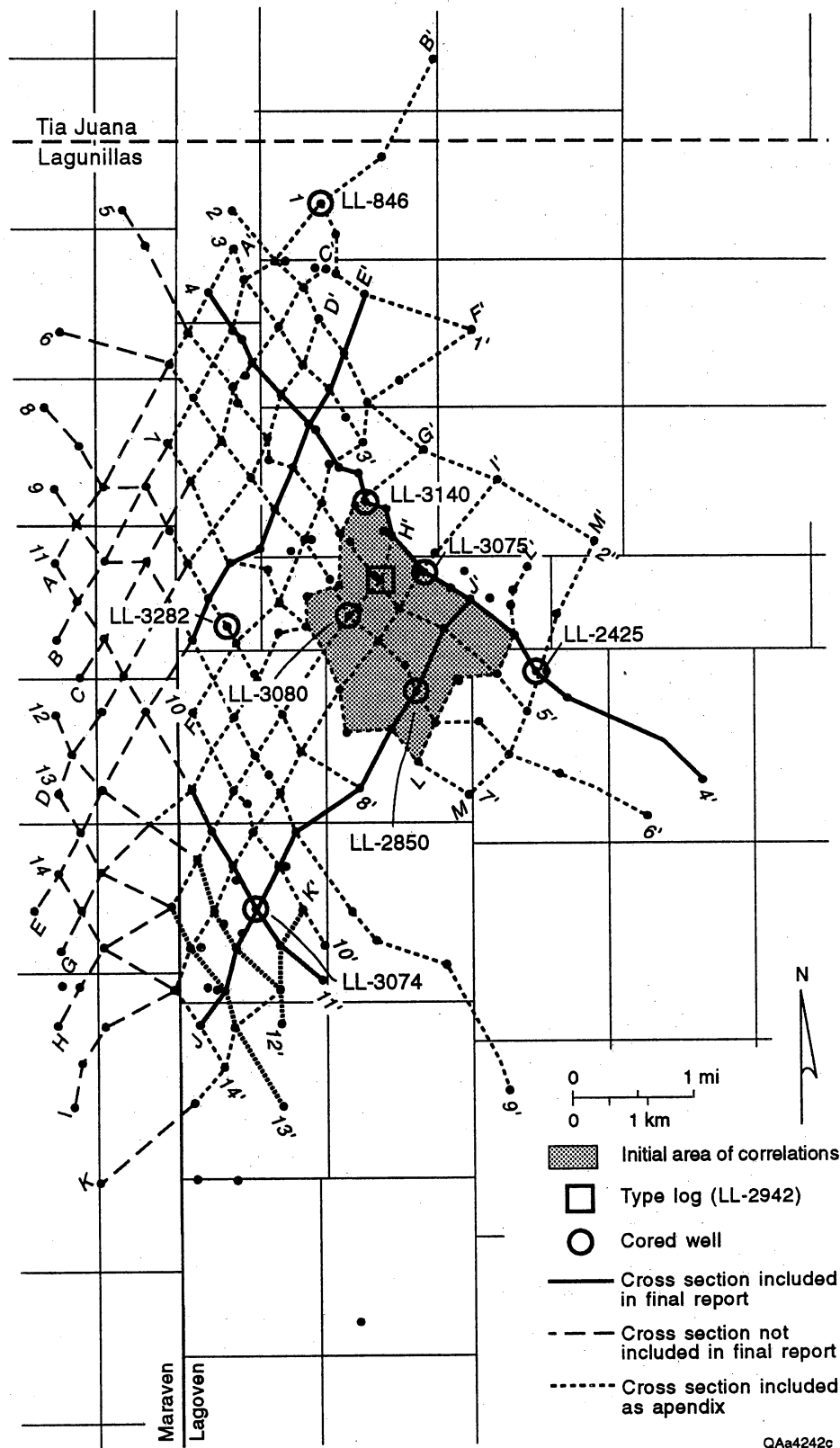
Figure 6. Well control, core control, and location of stratigraphic cross sections in the LL-652 area.

11
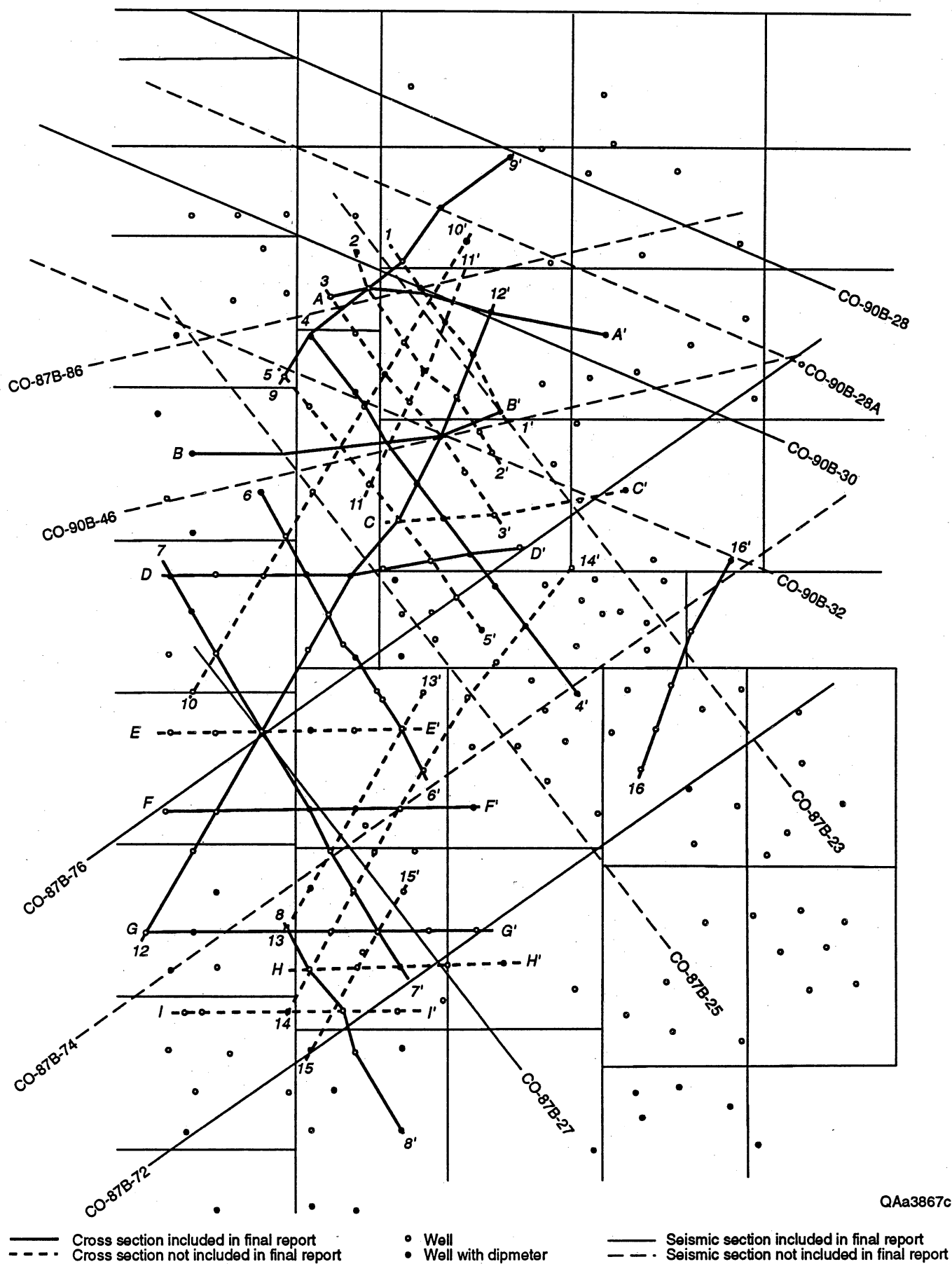
Figure 7. Structural cross section and seismic section grid.

12

A method for determining net-sandstone thickness from well logs was established by calibrating the core descriptions to the gamma-ray curve. This was done by comparing the core descriptions to the gamma-ray curve at the same scale, measuring net-sandstone thickness from the core descriptions, and then adjusting a vertical cutoff line of the gamma-ray curve to match the amount of net-sandstone thickness determined from the core descriptions. Based on this procedure, a 33-percent of greatest leftward gamma-ray deflection from a normalized shale baseline was used as a cutoff for counting net-sandstone thickness in the C-3-X and C-4-X Members. For the C-5-X, C-6-X, and C-7-X Members, this cutoff was 28 percent. For logs without the gamma-ray curve, resistivity and SP curves were used to measure net-sandstone thickness.

A depositional model was developed by integrating information from core descriptions and maps of net-sandstone thickness, percent sandstone, and log facies. Percent-sandstone values were determined by dividing thickness of stratigraphic unit by net-sandstone thickness. Log-facies maps, showing distribution of gamma-ray or SP responses for an individual stratigraphic unit or the most common log response in a thick stratigraphic unit containing several sandstone beds, were prepared for selected submembers. The types of log responses mapped included upward-coarsening, upward-fining, blocky, serrate, and baseline deflections.

Phase 5 consisted of petrographic description. Seventy-six thin sections were selected from the cores for analysis. Where possible, these thin sections were selected at the same depths as core plugs so that the petrographic descriptions could be calibrated against permeability, porosity, and other data derived from core analyses. Features described in the petrographic study included mineral composition of grains and clays, cement types, estimates of each type of porosity (primary, secondary, or microporosity), volume of total clay, and diagenetic sequence. Scanning electron microscopy (SEM) was conducted to evaluate calcite-cement dissolution and to assess differences in pore types among different sandstones and facies. The effects of diagenetic processes and type and distribution of clay that may influence the production performance of reservoirs was assessed to evaluate the affects of clays in waterflooded reservoirs.

Phase 6 was a structural interpretation of the LL-652 area, beginning with the construction of accurate fault-surface maps for all recognized faults. These maps were checked for three-dimensional geometric validity and integrated with structure maps. A paleostructural map was made of the C-3-X Member to define and compare the general tendency of the Eocene structure and to evaluate anomalies in net thickness of the interval from the top of the C-3-X Member to the Eocene unconformity. Twenty-two structural cross sections at exaggerated vertical scales across the LL-652 area were prepared in order to interpret the structural framework and solve problems related to faulting, dip of strata, and folds (fig. 7). The sections were later used in conjunction with structure maps to provide a three-dimensional analysis of the LL-652 area. Special detailed sections were prepared to evaluate the continuity of individual reservoir sandstones.

Twelve seismic cross sections were analyzed to visualize the structure, to prepare accurate structure maps, and to document the continuity of large-scale stratigraphic sequences. Most of these sections were oriented perpendicular to the strike of the fold areas and faults. Fault trends were projected from electric-log cross sections to the seismic sections. Dipmeter logs were interpreted to resolve local structural anomalies and complexities. Forty-seven dipmeter logs in the Lagoven area and 32 in the Maraven area (see app. A) were analyzed to estimate the direction of dip and strike and apparent changes in thickness of stratigraphic intervals.

Structural-top data were tabulated for all members and submembers in 195 wells (150 Lagoven and 45 Maraven) in the study area (see app. A). The test of faults and the structural framework was whether interpretations fit on a series of horizons at various depths. Multiple- horizon mapping was essential to support the integrity of structural interpretations, to provide an accurate and reasonable interpretation, and to validate the three-dimensional framework. Eight stratigraphic levels were selected, including the Miocene-Eocene unconformity and tops of C-1-X through C-7-X Members. Eight structure maps were based on structural-tops data, fault-surface maps, structural cross sections, seismic sections, dipmeter analysis and the preliminary structural marker map of the top of the C-3-X Member. A fault analysis was

conducted to characterize the principal faults in terms of their possible control on thickness variations in strata, relative age, and seal capacity.

Phase 7 was a production and pressure analysis conducted for each member and submember. These data were analyzed against a background of structural and stratigraphic maps to infer controls on anomalous production histories and pressures. The stratigraphic horizon of each perforated interval was identified, and producing wells in each member and submember were plotted on structural and stratigraphic maps. Fluid contacts were inferred from production and structural maps.

Phase 8 included construction of a petrophysical model by integrating core information, digitized well logs, production data, and key parameters such as porosity, permeability, V_{cl}, m, n, a, capillary pressure, S_{wirr}, and grain density. Permeability-porosity crossplots were prepared for major facies recognized from cores, with the objective of characterizing the fluid-flow potential. A transform function relating log response to rock and fluid properties was developed in order to make isopach maps of net oil sandstone, porosity, permeability, water saturation, porous hydrocarbon volume, original oil in place, and remaining oil.

In phase 9, three reservoirs were selected for detailed analysis and identification of potential areas for secondary recovery projects and development locations. A set of eight structural cross sections (four dip and four strike) presented detailed correlations of all major sandstones and mudstones in the C-3-X and C-4-X Members in the C-4-X.01 and C-4-X.03 reservoirs. Six cross sections were selected for similar analysis of the C-5-X.02 reservoir. The objectives of these cross sections were to document the vertical and lateral continuity of sandstones, to construct a three-dimensional model to predict probable fluid-flow paths for proposed waterflood operations, and to identify reservoir compartments that could be contacted by infill wells.

In phase 10, areas favorable for infill-well development were delineated for each reservoir by comparing maps of hydrocarbon volumetrics and production to structural and stratigraphic maps. Specific recommendations for extended development wells, recompletions, and geologically targeted infill locations were made on the basis of these comparisons, and the potential for secondary oil recovery for each member and submember was evaluated.

III. GENERAL GEOLOGIC SETTING

Structural Setting

Regional Setting

Five main structural trends exist in the Maracaibo Basin (fig. 8, Lugo, 1991). North-northeast-trending major faults (1) are mainly represented by the Icotea fault, the major fault in the Lake Maracaibo area, extending for more than 80 mi (130 km). West of the LL-652 area, it is a positive flower structure (Lugo, 1991). The Icotea fault is left-lateral-strike-slip (Lugo 1991), having associated minor faults in flower and horsetail patterns, and locally having abrupt, alongstrike increases in throw (scissor or trap-door structures). North-northeast-trending folds (2) are slightly oblique to the main north-northeast-trending faults; the LL-652 area is located in this trend (fig. 8). Northwest-trending normal faults (3), trending from N30°W to N50°W, commonly have normal displacement. Most of these faults offset upper Eocene units and are truncated by the Eocene-Miocene unconformity. North-trending thrust faults (4), representing the youngest faulting in the Maracaibo Basin, offset all strata and are associated with regional east-west compression in late Pliocene to Holocene time. Northwest-trending thrust faults (5) are located in the Central Lago, Lagunillas, and Bachaquero areas (fig. 8). The southwest movement of these faults indicates a tectonic transport from the northeast during early to middle Eocene time.

The structural framework evolved in discrete stages (fig. 9). The north-northeast trend of faults is pre-Cretaceous and was repeatedly reactivated during Cretaceous and Cenozoic tectonic episodes (Lugo, 1991). Additionally, transpression in the Maracaibo Basin occurred in four periods: first, middle to late Eocene transpression resulted in delineation of the main structural features, such as the Icotea fault. The structural interpretation for the post-late-Eocene and pre-middle-Miocene (fig. 10) is based on the observation that all Eocene strata are cut by faults that are, in turn, truncated by the Eocene-Miocene unconformity. Second, during late Eocene-early Miocene transpression quiescence, the Maracaibo Basin was exposed to regional erosion, interpreted as a tectonic uplift that tilted the basin to the west-southwest (Zambrano and others, 1972). The structural map of the Eocene-Miocene unconformity (fig. 11) shows that post-unconformity deformation increases to the north-northeast, particularly along the Icotea fault, where the unconformity gently dips 4° southward. Also, almost all of the en-echelon, northwest-trending normal faults terminate below the unconformity. Third, middle Miocene to Pliocene transpression, rejuvenation, and fault rotations occurred in the late Eocene to early Miocene erosional episode. The basin was subjected to renewed transpression during the middle Miocene, but this time the compressive component was greater and main faults were reactivated, offsetting the unconformity. Fourth, the last important event (Pliocene to Pleistocene) was east-west compression exemplified by north-trending thrust faults principally along the eastern flank of the La Sierra de Perijá and near the eastern coast of Lake Maracaibo. This compressional event reactivated the northern part of the Icotea fault.

Study Area

Structure of the LL-652 area is a north-northeast-trending, elongate anticline with a steeply dipping (25° to 45°) western and northwestern limb and a gently dipping (5° to 10°) east and southeast flank. In the Maraven area the structure is a monocline with a gentle 3° to 8° eastward dip (Maraven internal report).

The LL-652 area was affected by multiple tectonic events that generated three trends of normal faults and one trend of reverse faults, representing the local scale of the major regional trends defined by Lugo (1991). North-northeast-trending major faults are represented by a master normal fault located in the eastern part of the Maraven area. Maraven reports a "flank east fault" with an eastward dip and 500 ft (152 m) of throw. We interpreted 1,200 ft (366 m) of throw in the south that decreases to 800 ft (244 m) toward the north. This fault represents a geological boundary between the Maraven Block-I and Lagoven

Main faults

- A Icotea
- B Pueblo Viejo
- C Urdaneta
- D Lama
- E VLE
- F Alturitas
- G Centro Lago
- H Lagunillas
- I Bachaquero
- J Ambrosio

Main folds

- ① Urdaneta
- ② Urdaneta NE
- ③ Lama
- ④ Tia Juana
- ⑤ Centro Lago
- ⑥ Sur Lago
- ⑦ Bachaquero
- ⑧ Lagunillas
- ⑨ Ambrosio

Fault Fault showing downthrown side Thrust and reverse fault

Syncline Anticline

Study area

Lake Maracaibo

Carribbean Sea

Barranquilla

Maracaibo

Lake Maracaibo

COLOMBIA VENEZUELA

QAa3865c

Figure 8. Present structural styles in the Maracaibo Basin. Modified from Lugo (1991).
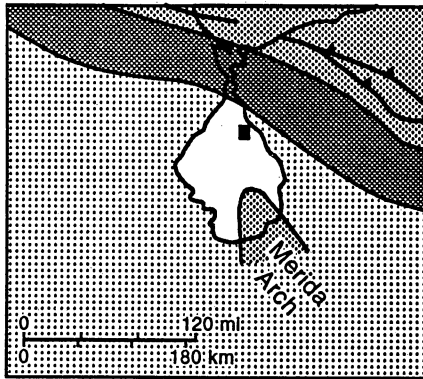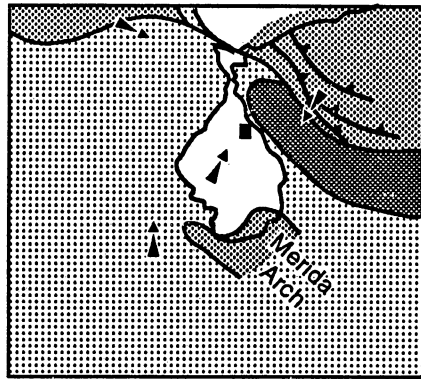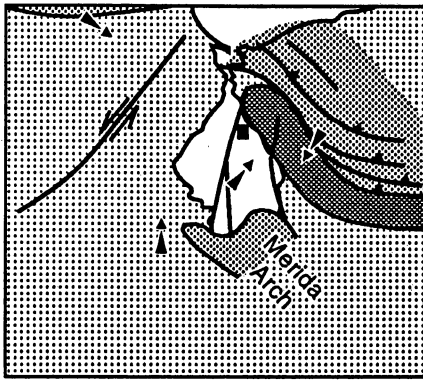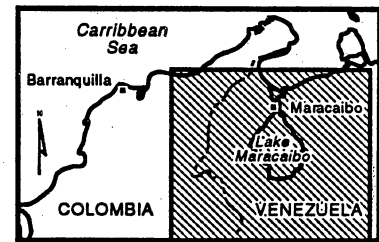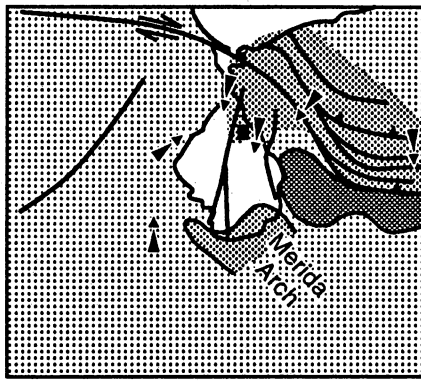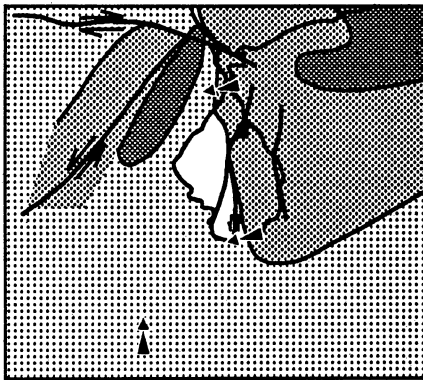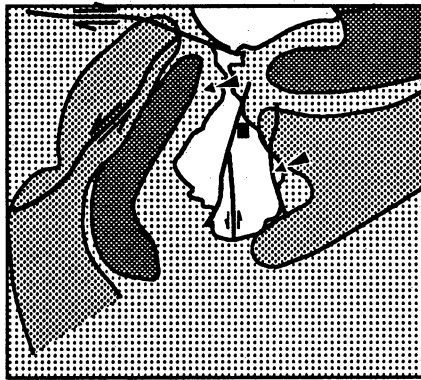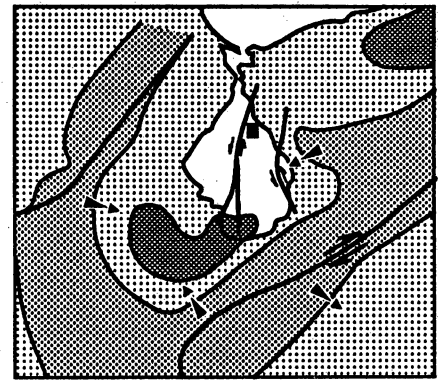
Figure 9. Paleotectonic maps showing chronology of tectonic episodes that affected the Misoa Formation. Modified from Lugo (1991).
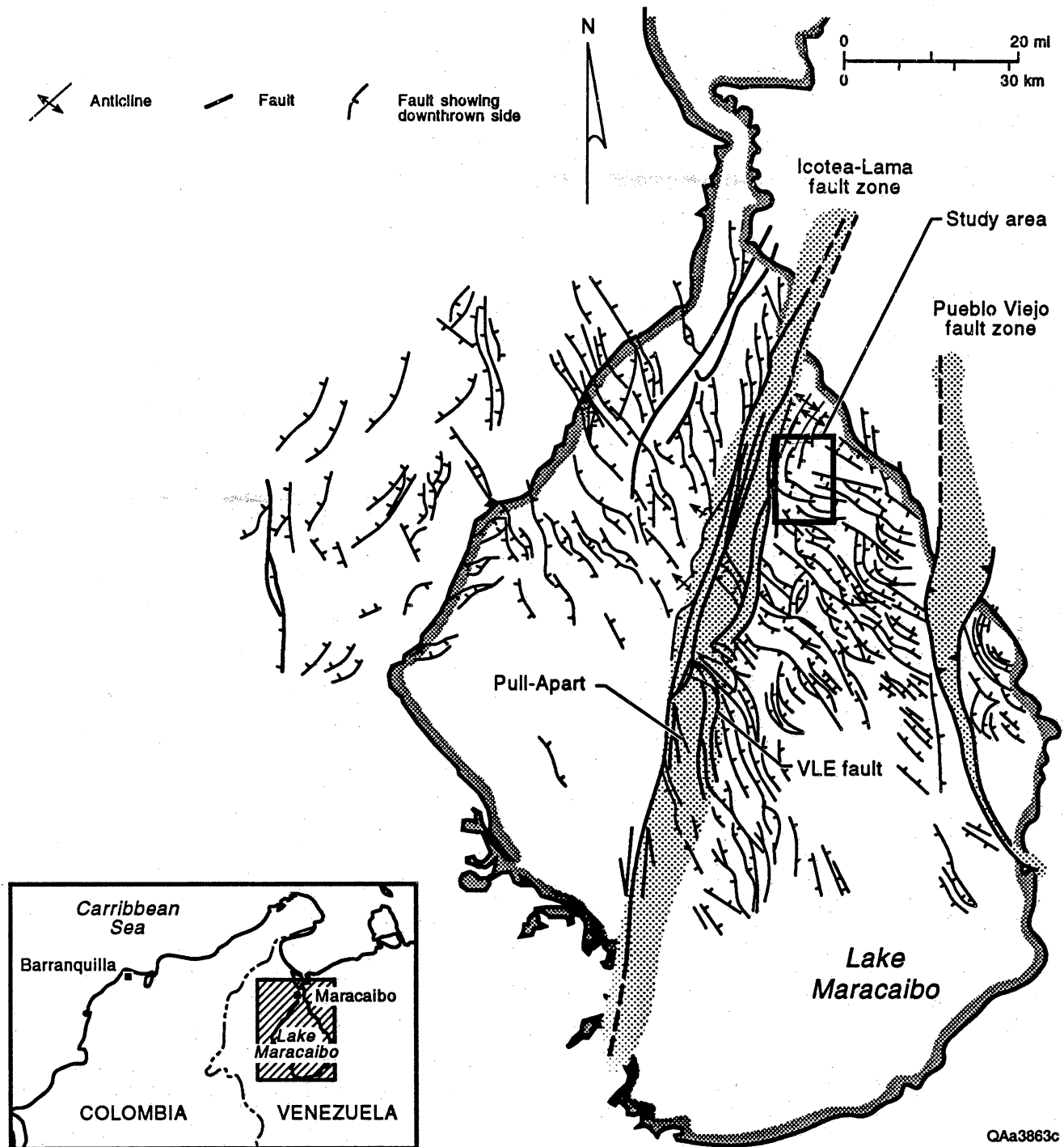
Figure 10. Fault maps of post-middle Eocene and pre-late-Eocene to Oligocene unconformity. From Lugo (1991).
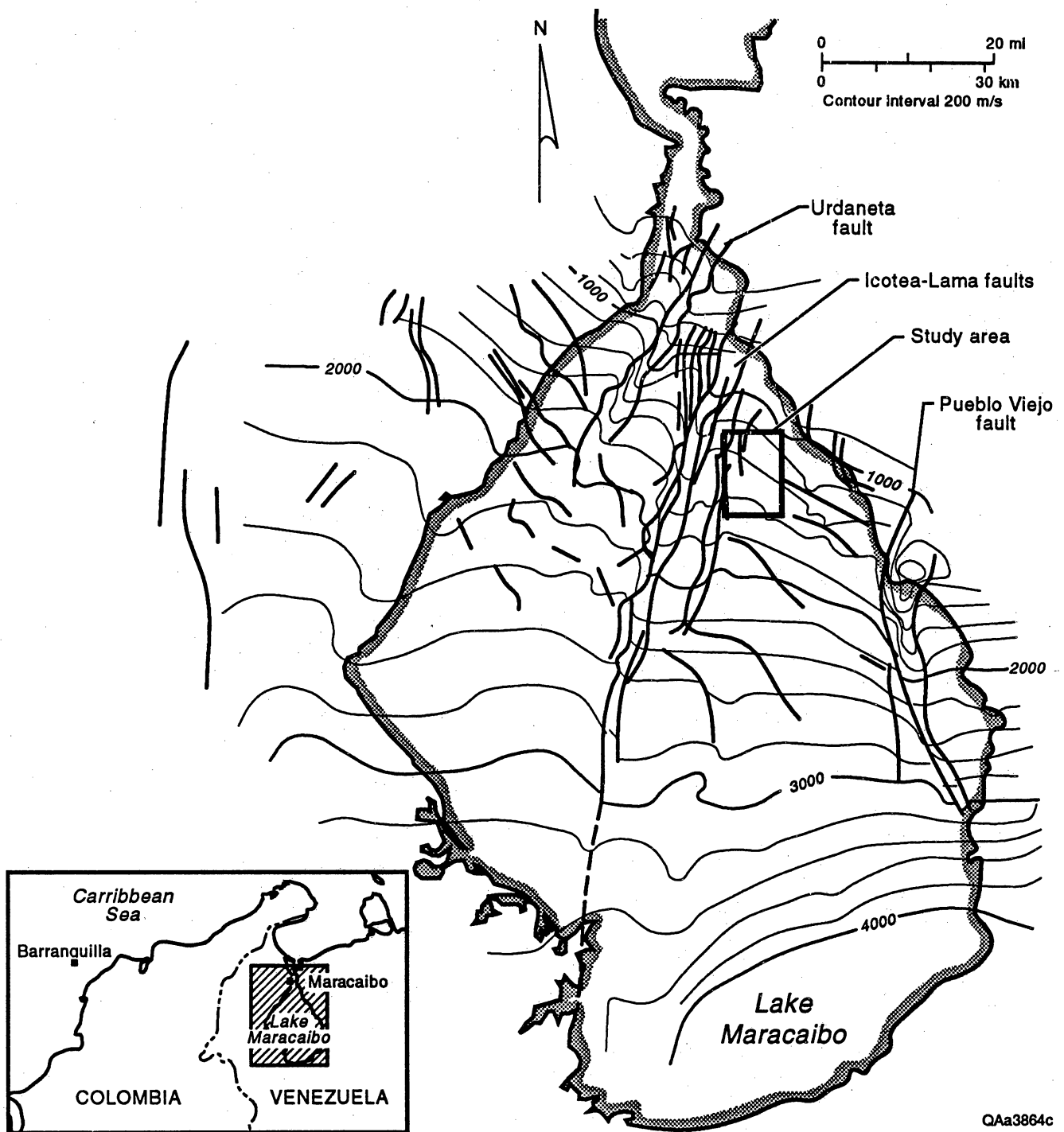
Figure 11. Structural map of the Eocene-Miocene unconformity. From Lugo (1991).

19

LL-652 area; the fault runs slightly oblique to the boundary between the two concessions. This master fault was reactivated after the Eocene-Miocene unconformity that is offset by up to 80 ft (24.4 m). North-northeast-trending folds are represented by an elongate anticline that is slightly oblique to the main north-northeast-trending fault. The northern area of the fold that includes the LL-2946 well is on the crest of an anticline. High dips (47°) occur in the LL-1293 well on the northwest limb and 54° in the LL-827 well on the east limb. The LL-827 well is located near the intersection of a reverse fault and the master normal fault. The southern area of the fold represents 80 percent of the LL-652 area. Three normal faults trend N20°-35°W, N40°-45°W, and N50°-60°W with multiple occurrences of missing section (vertical separation) ranging from 50 to 1,200 ft (15.2 to 366 m). Most of these faults offset the entire Eocene and are truncated by the Eocene-Miocene unconformity (fig. 11). A major normal fault is located northeastward with 400 to 800 ft (122 to 244 m) of throw. Northeast-trending normal faults are represented by two antithetic faults in the northern part of the field. They are located within 1,968 ft (600 m) of each other and have 550 ft (167 m) and 500 ft (152 m) of throw, respectively. Additionally, north-northeast-trending thrust faults cut across the older normal faults and represent the youngest deformation in the Maracaibo Basin (Lugo, 1991). Other evidence from the paleostructural and subcrop analysis shows that these faults were reactivated along older normal faults (Lugo, 1991). Seismic interpretation, described in a later section, "Structural Interpretation," shows evidence of reactivation along the western master fault in the Maraven area.

The principal reservoirs (C-4-X.01, C-5-X.02, and C-6-X.01) are separated from the C-4-X.03, C-5-X.08, and C-6-X.16 reservoirs on the southwest by a major normal fault (no. 6) that trends N60°W with 300 ft (91.5 m) of throw, extending to the northwest and being offset by reverse faults (fig. 12). The master normal fault in the east (no. 3) is the boundary of the C-4-X.01, C-5-X.02, and C-6-X.01 reservoirs. The southwest limit of the C-4-X.03, C-5-X.16, and C-6-X.08 reservoirs is a normal fault (south fault) trending N35°W with 600 ft (183 m) of throw.

The north-northeast-trending reverse faults are on the ridge-crestal area in the western part of the main reservoirs and are subparallel to the strike of the steeply dipping west limb of the reservoir. Several wells from the south to the north across the main reservoirs intersect faults with repeat section ranging from 60 to 150 ft (18 to 45.7 m) thick. These faults may internally divide the principal reservoirs (C-4-X.01, C-4-X.03, C-5-X.01, C-5-X.15, C-6-X.01, and C-6-X.08).

Stratigraphic Setting

Regional Setting

The Maracaibo Basin is centered on the southwest margin of Lake Maracaibo and covers approximately 19,300 mi^2 (50,000 km^2) (fig. 3). The Cretaceous platform of the basin consists of carbonates and marine mudstones of the Rio Negro to Mito Juan Formations (fig. 13) (Zambrano and others, 1972; Gonzalez de Juana and others, 1980). At the end of the Paleocene with deposition of the Guasare Formation, thick Eocene fluvial-deltaic sediments were deposited northeastward on the platform. The Eocene fluvial facies tract is the Mirador Formation, and the deltaic facies tract is the Misoa Formation (fig. 13). The lower Eocene, informally referred to as the "C" Sands (Walton, 1967), is composed of a major progradational cycle at the base (C-6-X and C-7-X Members) and two other major progradational cycles in a net retrogradational sequence (Bot and Perdomo, 1987; Graves and others, 1987) (fig. 13).

Maximum transgression in the Maracaibo Basin occurred during deposition of the C-1-X Member, and regressive conditions returned with subsequent deposition of major progradational clastic wedges of the upper Eocene "B" Sands (Gonzalez de Juana and others, 1980). The Eocene is truncated by a major angular unconformity (Eocene Unconformity). In the region of Lagunillas field the Misoa Formation is directly overlain by the Miocene La Rosa Formation (fig. 13).
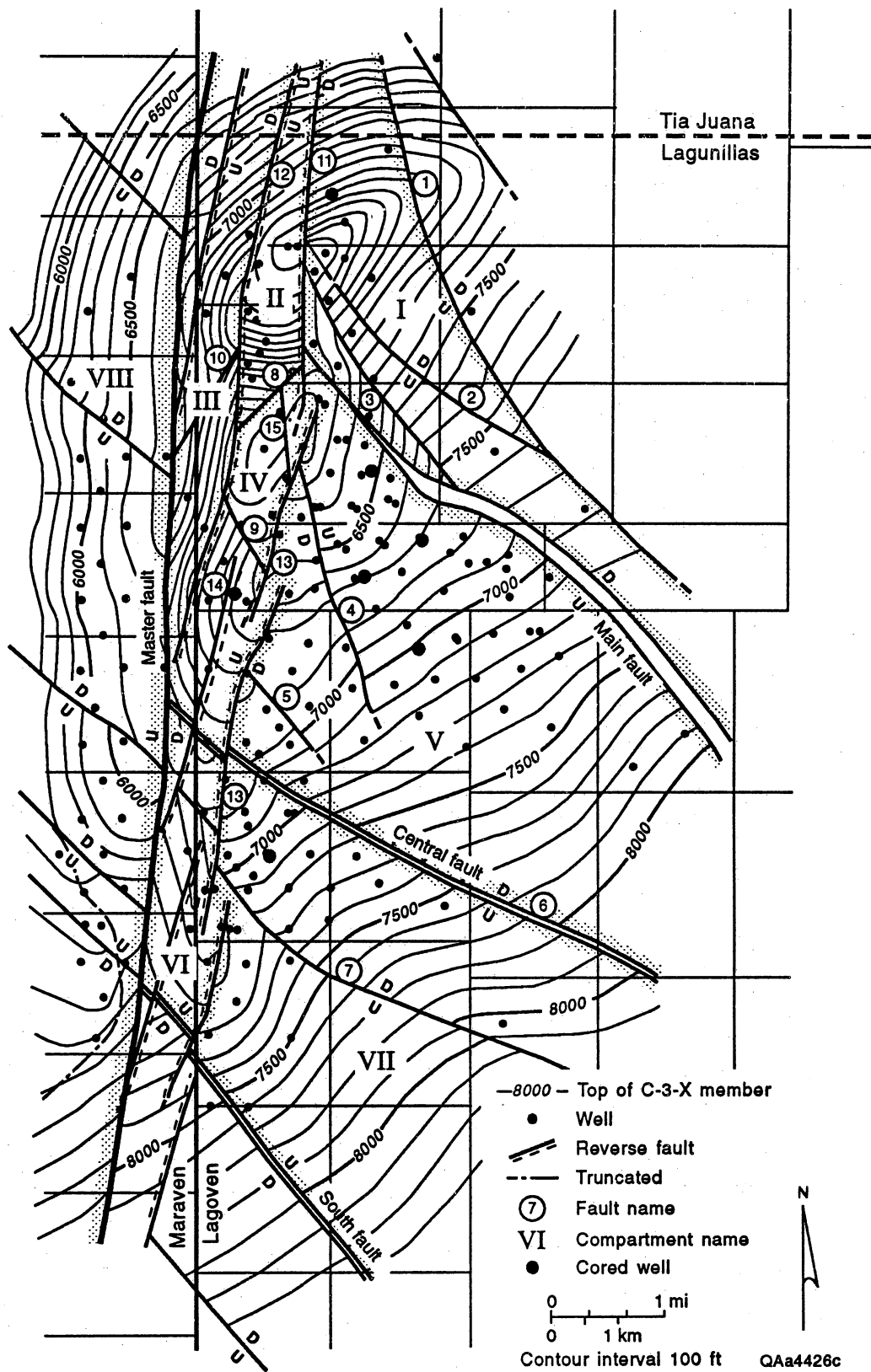
Figure 12. Fault compartment geometries in the LL-652 area.

The following labels appear within the figure:

Tia Juana
Lagunilias

II

I

VIII

III

IV

V

VI

VII

Master fault

Main fault

Central fault

South fault

Maraven

Lagoven

—8000 — Top of C-3-X member
● Well
Reverse fault
—·— Truncated
⑦ Fault name
VI Compartment name
● Cored well

N

0   1 mi
0   1 km
Contour interval 100 ft   QAa4426c

21
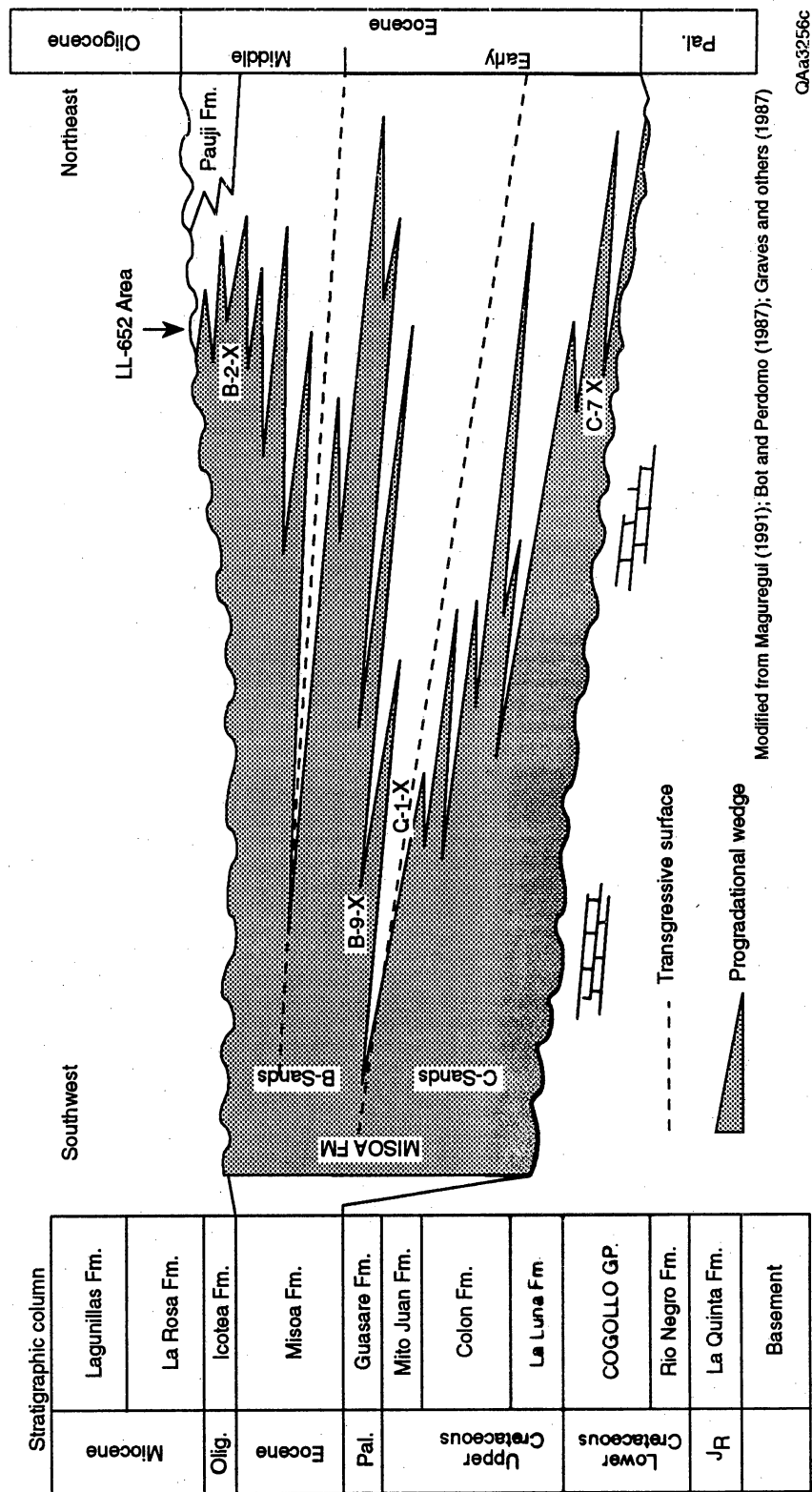
Figure 13. Major Eocene stratigraphic sequences in the Maracaibo Basin.

22

Local Setting

Most oil production in the lower Eocene in the LL-652 area (135 MMbbl) is from the combined C-3-X and C-4-X Members (fig. 5). The C-5-X Member has produced approximately 18 MMbbl, and the C-6-X Member accounts for 7.5 MMbbl. The sandstone-poor C-2-X Member has produced 1 MMbbl, the C-1-X Member has produced 0.8 MMbbl, and no oil has been produced from the C-7-X Member.

The lower Eocene in the LL-652 area is approximately 4,000 ft (1,220 m) thick and contains multiple regressive-transgressive cycles in a net-retrogradational sequence (fig. 5). The C-2-X through C-7-X Members, informally subdivided into two to three submembers, are bounded by laterally continuous shale marker beds that mark transgressive surfaces. The submembers range from 50 to 200 ft (15.2 to 61 m) thick and correspond to one or several paragenetic sequences that are each 50 to 80 ft (15.2 to 24.4 m) thick. Informal shale marker beds, numbered from 1 to 27 in the B and C members, were correlated throughout the LL-652 area.

The C-7-X Member represents a major progradational wedge truncated by an unconformity inferred to be caused by sea-level fall (fig. 5). Lower C-6-X progradational cycles above this unconformity are overlain by muddy Upper C-6-X retrogradational deposits. The C-5-X Member and the lower part of the C-4-X Member contain minor progradational cycles bounded by transgressive shales. In contrast, the Upper C-4-X Submember represents a major deltaic advance northeast of the LL-652 area. The Upper C-4-X Submember consistently exhibits excellent gamma-ray and resistivity responses, reflecting good reservoir quality and high oil saturation. Beginning with the C-3-X Member, there was a major retrogradational phase that continued throughout deposition of the Lower Eocene. The sandstone-rich Middle C-3-X Submember represents a brief phase of deltaic offlap, but the majority of the sequences in the C-3-X, C-2-X, and C-1-X Members are shale-dominated, highstand-systems tracts.

Four stratigraphic cross sections, located in figure 6 and shown in appendix F, across the LL-652 area exhibit lateral variability in stratigraphic sequences, continuous shale marker beds, and missing section due to faults. Large-scale stratigraphic sequences (for example, the Upper C-4-X Submember) and bounding shale markers are continuous across the field. However, there is much variability in individual sandstone thickness and log response reflecting facies variation within the sequences. Stratigraphic dip section E-E' (app. F) shows up to 2,000 ft (610 m) of relief on the Eocene unconformity, which progressively truncates older section southwestward. In the northeast part of the LL-652 area, the lowermost B members and the C-1-X Member are preserved below the unconformity, whereas in the Maraven concession the unconformity truncates the C-2-X and C-3-X Members. There are multiple occurrences of missing section ranging from 150 to 550 ft (45.7 to 167.7 m) in the C-3-X and C-4-X Members on the cross section.

Stratigraphic dip section J-J' (app. F) shows only 800 ft (244 m) of relief on the Eocene unconformity, and up to 200 ft (61 m) of the C-1-X Member is preserved below the unconformity in the Maraven concession. The LL-1176 well has 330 ft (101 m) of missing section due to faulting, and B Members are preserved northeast of the LL-992 well.

Stratigraphic strike section 4-4' (app. F) includes five wells that penetrate the C-7-X Member and shows the lateral extent of the unconformity at the base of the Lower C-6-X Submember. Additionally, the C members are also apparently thicker in the northwestern part of the section, due to the deviated LL-1316 well and steeply dipping strata in the LL-1695 well. Because this strike section is proximal and parallel to a major northwest-trending fault in the eastern part of the LL-652 area, it shows a continuous zone of approximately 1,000 ft (305 m) of missing section in the Lower B members and C-1-X Member. The Eocene unconformity also shows considerable relief and truncates more strata in the northwest than in the southeast, where strata as young as the B-6-X Member are preserved. Relief along this unconformity is much less (only 600 ft [183 m]) on stratigraphic strike section 11-11' (app. F).

The C members contain three major seismic stratigraphic units (lower, middle, and upper) that correspond approximately to the C-5-X to C-7-X, C-3-X to C-4-X, and C-1-X to C-2-X Members, respectively (table 1). Stratigraphic horizons were correlated to seismic reflectors partly by projections between prominent seismic reflectors (Eocene unconformity, Guasare Formation) identified by Lugo (1991) and by use of synthetic seismograms.

The lower seismic unit consists of a 0.1- to 0.3-s zone of low- to moderate-amplitude reflectors that are irregular, wavy, and discontinuous (fig. 14). The lower unit represents multiple regressive/transgressive couplets in the C-5-X and C-6-X Members that are individually too thin to be resolved seismically. These reflectors overlie a high-amplitude, continuous pair of prominent reflectors that correspond to the Guasare Formation (Lugo, 1991). The lower unit is overlain by a pair of moderate- to high-amplitude, semicontinuous reflectors that form the base of the middle seismic unit (fig. 14).

The middle seismic unit is defined as an upper pair of high-amplitude, continuous and parallel reflectors 0.15 to 0.20 s above a pair of moderate-amplitude, semicontinuous reflectors. Between these reflector pairs are low-amplitude, commonly inclined, and irregular reflectors (fig. 14). The middle seismic unit corresponds roughly to the C-3-X and C-4-X interval and represents a regressive/transgressive couplet (table 1). The pair of high-amplitude, continuous reflectors that forms the upper bounding surface of the middle seismic unit is the most distinctive seismic marker in the lower Eocene and is interpreted to represent a zone of high-velocity contrast between the shaly C-3-X Member and the sandy Upper C-4-X Submember (figs. 14 and 15). The upper reflector in this pair represents an onlapping, marine-flooding surface that marks the onset of a major retrogradational sequence in the upper C members (fig. 5). The marine onlapping surface merges updip (southwestward) with underlying low-amplitude clinoforms of a deltaic offlapping wedge in the C-4-X Member (fig. 14).

The upper seismic unit (upper C members) represents a major retrogradational highstand- systems tract that onlaps southwestward over the regressive progradational cycles of the C-4-X Member. The upper seismic unit consists of several, moderate-amplitude reflectors in a zone that is 0.20 to 0.25 s thick (table 1 and figs. 14 and 15). These reflectors have good continuity but are not as continuous as those in the middle seismic unit. High-amplitude reflectors in the upper seismic unit may correspond to widespread sandstones at the top of upward-coarsening sequences that have high-velocity contrast with mudstones.

The Eocene unconformity is represented by a continuous, high-amplitude pair of parallel reflectors (table 1) that merge with and are inferred to truncate underlying reflectors to the west and southwest (fig. 14). In the LL-652 area, the lower B members are present below the unconformity but are absent west of the main fault along the concession boundary.

Table 1. Eocene and Paleocene seismic facies in the LL-652 area.

STRATIGRAPHIC UNITS	SEISMIC RESPONSES	INTERPRETATION
Eocene Unconformity	Strong pair of westward-dipping, continuous and parallel reflectors	Angular unconformity
Upper C Members (C-1-X/C-2-X)	Moderate to moderately strong reflectors with good to fair continuity	Retrogradational, highstand systems tract
Middle C Members (C-3-X/C-4-X)	Strong, continuous pair of parallel reflectors	Regressive/transgressive couplet
Lower C Members (C-5-X to C-7-X)	Poorly-defined zone of irregular, weak to fair reflectors with poor continuity	Multiple regressive/transgressive couplets overlying low-stand unconformity (C-6-X/C-7-X boundary)
Guasare Formation	Strong, continuous pair of reflectors	Mixed carbonate/clastic shelf
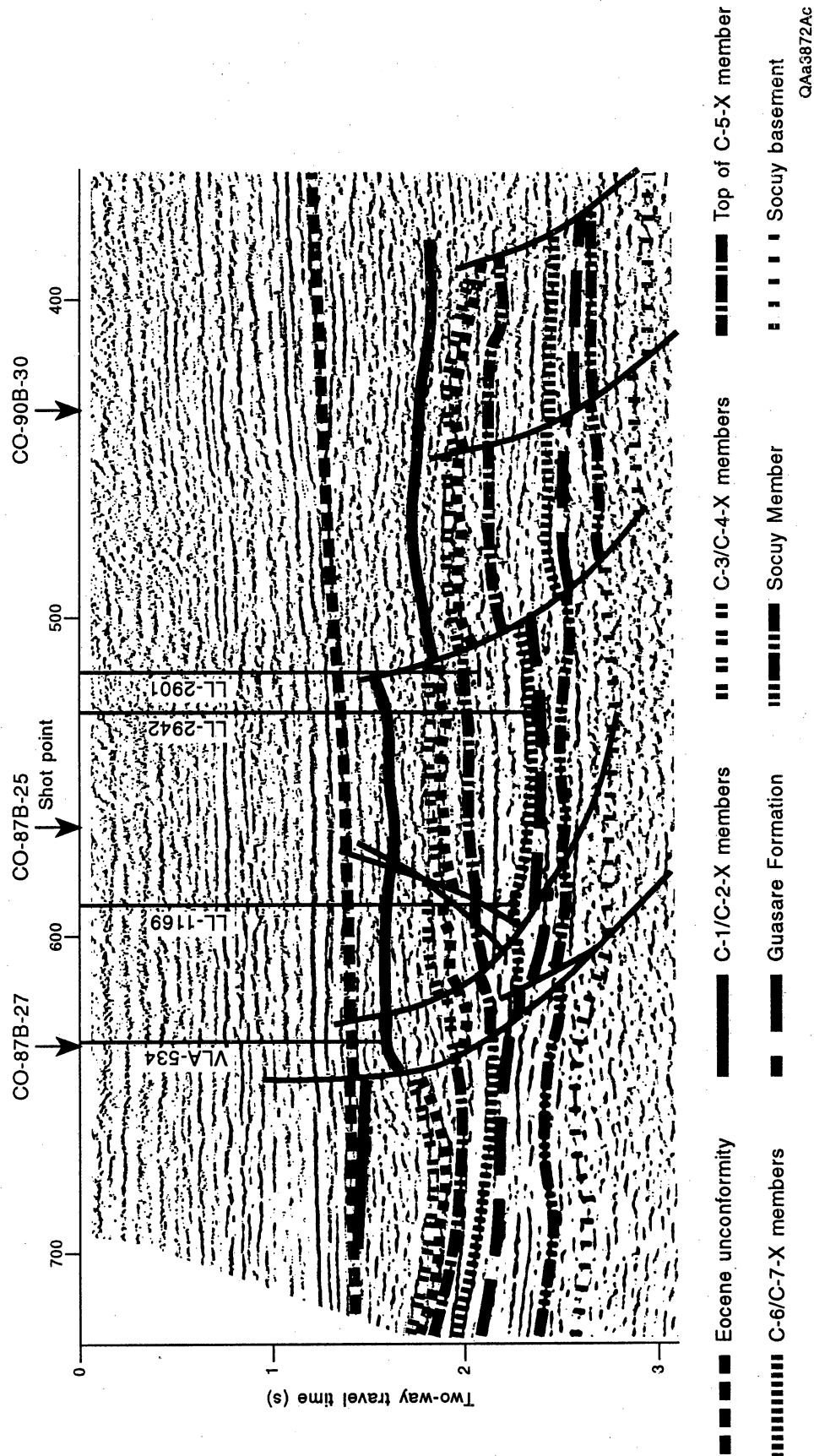
Figure 14. Seismic dip section CO-87B-76.

QAa3872Ac

26

Two-way travel time (s)

Shot point

QAa3872Bc
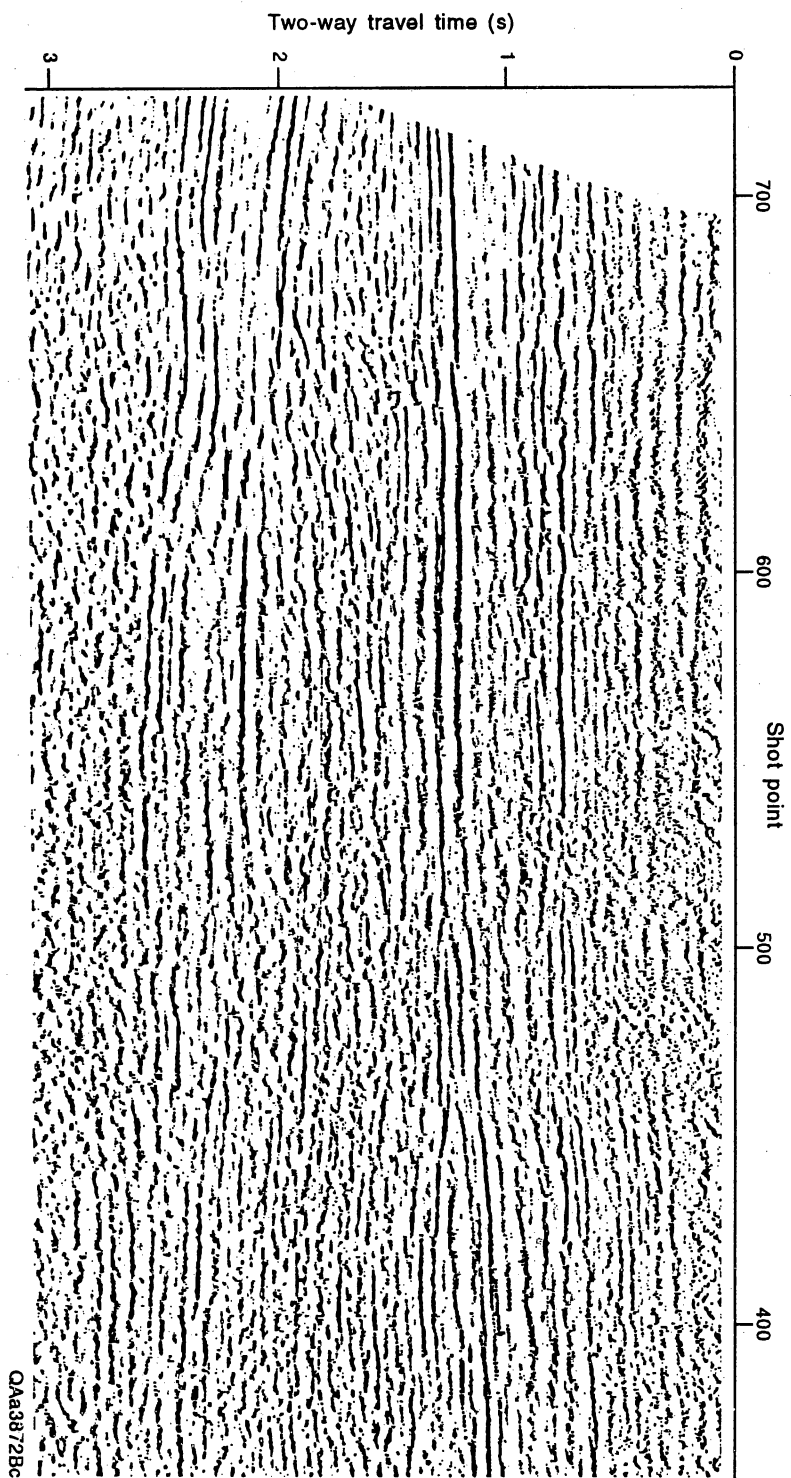
Figure 14. Continued
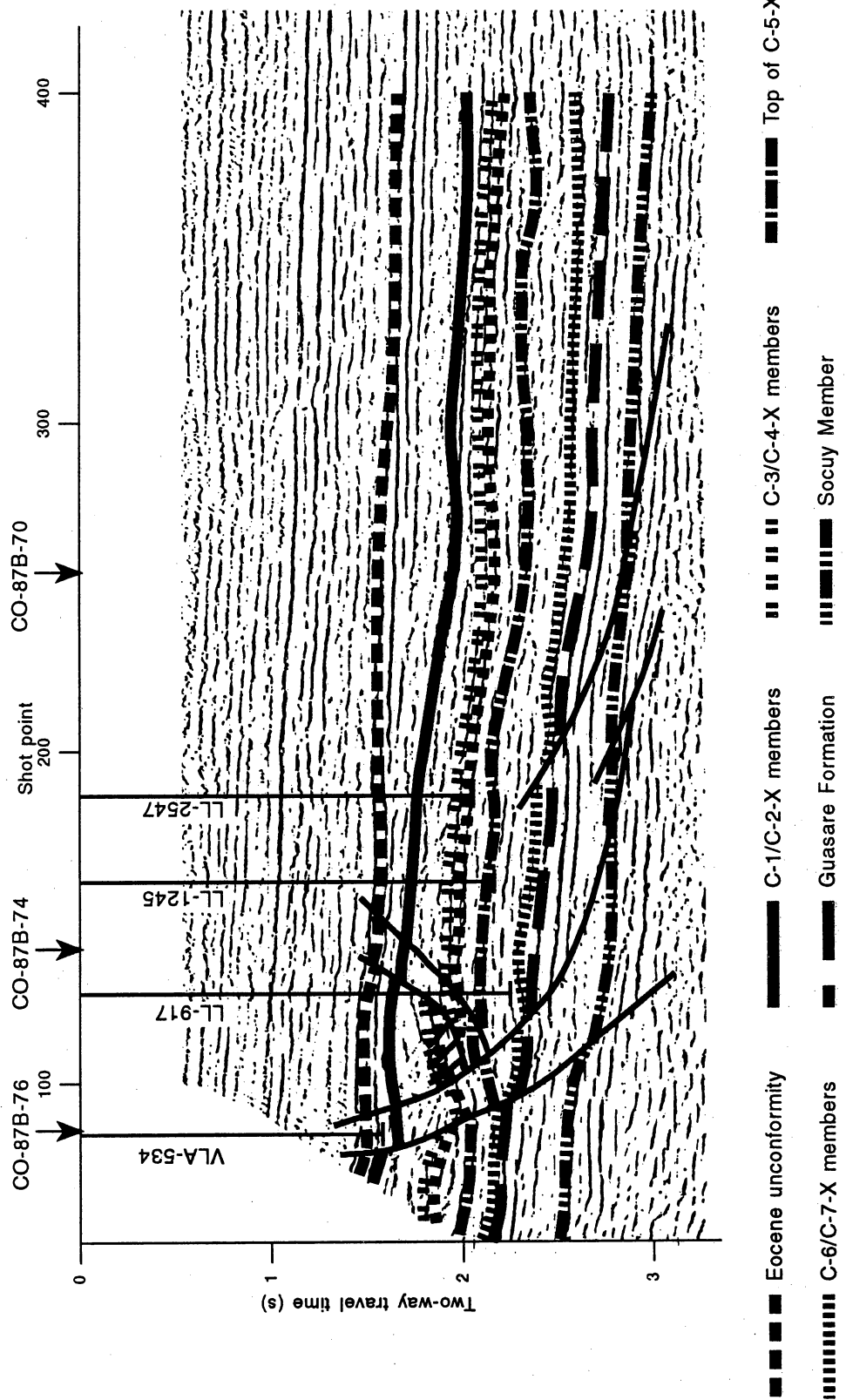
Figure 15. Seismic strike section CO-87B-27.

QAa3871Ac

28

Figure 15. Continued.

QAa3871Bc

Shot point

Two-way travel time (s)

29
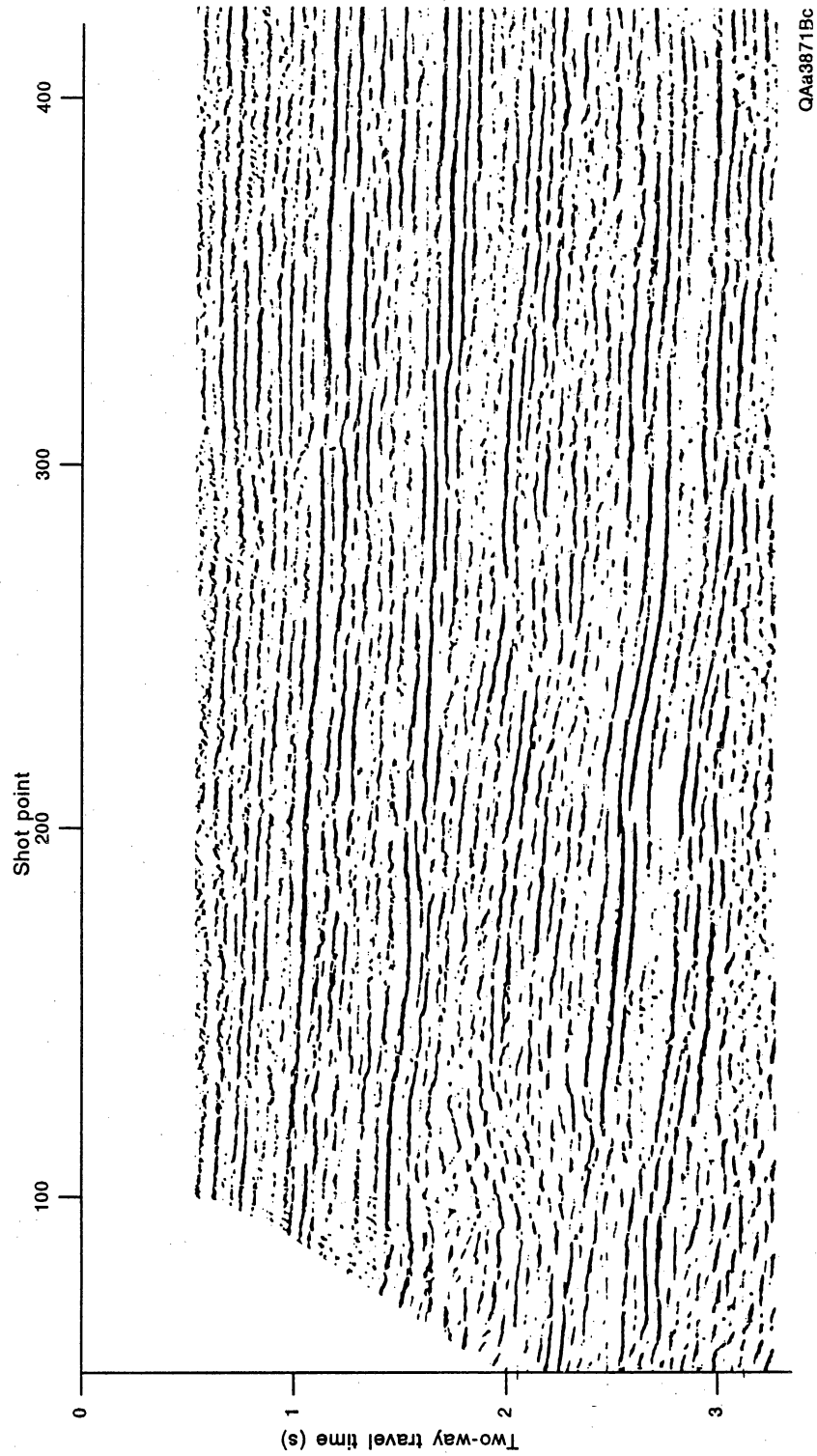
IV. STRUCTURAL INTERPRETATION

Fault-Surface Maps

Faults and folds play a significant role in the trapping of hydrocarbons in the LL-652 area and define reservoir boundaries. The preparation of accurate fault-surface maps required the integration of fault-surface maps with maps of several key structural horizons to determine the structural style.

The fault-surface map (fig. 16) was used to (1) aid in solving three-dimensional structural problems, especially to delineate complex fault patterns in the area, (2) define the location of the faults in both the horizontal and vertical dimensions, (3) supplement structure maps to accurately delineate the upthrown and downthrown fault traces in order to delineate the correct width of the fault gap or overlap, and (4) estimate the dip and strike (table 2) along 12 normal faults and 2 trends of reverse faults in the study area. Neither minor faults, with displacement of 70 ft (21.3 m) or less, nor the two antithetic normal faults are included in this map because of poorly documented, fault-intersection data. Compilation of fault data commenced with identification of fault-cut points that represent the intersection of a drilled well with a fault surface. The thickness of missing or repeated section (fault magnitude estimated from electric logs by correlation) was recorded in order to measure the vertical separation. An estimate of the subsea depth was also required for each fault-cut point.

Fault-trace positions were difficult to define without the use of the fault-structure map integration technique. Also, the width of a fault gap was documented, which is a function of the angle and direction of dip of the fault, as well as the dip of strata (Tearpock and Bischke, 1991). Therefore, the width of a fault gap for any given fault on a structure map could not be intuitively determined. Finally, fault maps were not finalized until a later stage of the structural interpretation when fault positions were fully documented with new data.

Paleostructural Map and C-3-X Structural-Top Marker

The net-thickness map of the interval between the Eocene-Miocene unconformity and the top of the C-3-X Member (fig. 17) shows five major and eight minor thickness anomalies in the LL-652 area. The strongest anomaly is located along the Maraven boundary, and there are three others in the northern and northeastern part of the field as well as one in the south. This tendency is consistent with regional patterns where the number of anomalies increase northward, subparallel to the Icotea fault. Additionally, this map represents local-scale variation and is consistent with the unrestored total isopach map of the Eocene (fig. 18), although both show a strong anomaly on the east side of the Icotea and Block-1 master faults.

To further interpret thickness anomalies in the net-thickness map we constructed a paleostructural map (fig. 19). This represents the "structural map" or topography on the top of the C-3-X Member at the time of deposition of the La Rosa Formation. This map does not reflect any structural feature that affected the area after formation of the unconformity. To define the paleostructure map, it was necessary to document (1) the total thickness between the Eocene unconformity and the top of the C-3-X Member, (2) distribution of faulted wells, and (3) changes or anomalies in structure. The paleostructural map of the C-3-X Member showed the structure on the top of the C-3-X Member at the time when the La Rosa Formation was deposited on the Eocene unconformity, with the assumption that the paleotopography of the unconformity was almost horizontal. In the LL-652 area the La Rosa Formation has few thickness changes (average thickness 190 ft [57.9 m]). In the Maracaibo Basin, the average thickness is 195 ft (60 m) (Bot and Perdomo, 1987). The northern part of the field was persistently a complex structural area.

There is also an elongate anticline with a relatively high-dipping (20°) northern and western limb and a gently dipping (6°) southeastern flank. The crest of the anticline is oriented subparallel to the eastern master fault, from the Maraven area in the southwest throughout the Lagoven concession in the north-
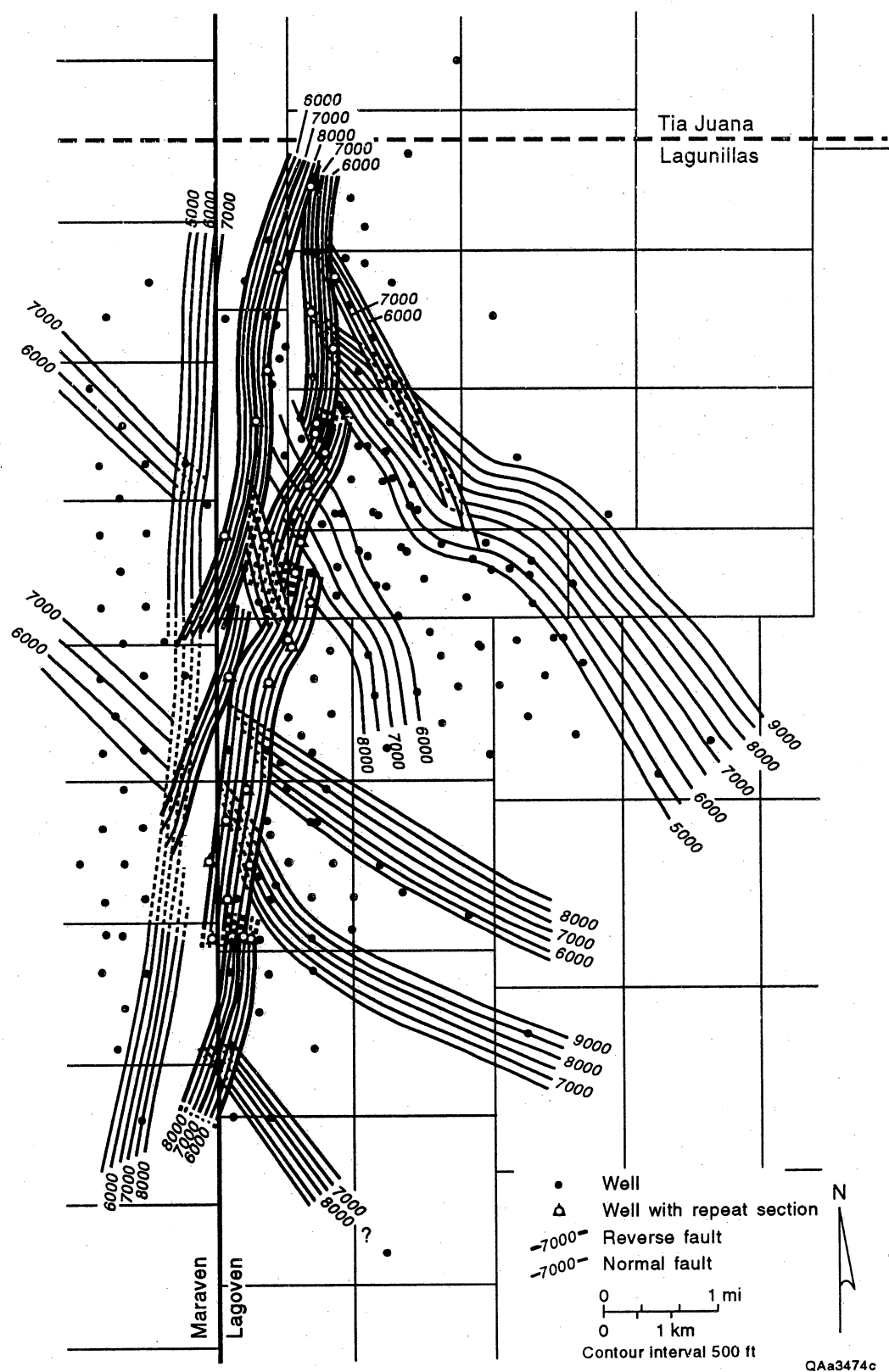
Figure 16. Fault-surface map of the LL-652 area.

Table 2. Fault characteristics in the LL-652 area.

Fault Name	Style	Dip	Strike	Throw (ft)	Cutting Wells
Master Fault	Normal	70° E	N5° E	900	VLA-613, VLA-13
Main Fault	Normal	58° NE	N45° W	800	LL-601, LL-1060, LL-2191, LL-1339, LL-2039, LL-2969, LL-2896, LL-3075, LL-2901, LL-3249, LL-1126, LL-3140, LL-2997, LL-1312, LL-3238, LL-3055, LL-3274, LL-1166, LL-2729, LL-851
South Fault	Normal	70° SW	N35° W	700	LL-1679
1	Normal	75° NE	N22° W	150	-
2	Normal	75° NE	N50° W	100	-
3	Normal	75° SW	N40° W	100	LL-1066, LL-1209, LL-1166
4	Normal	58° SW	N22° W	100	LL-1129, LL-2187, LL-2938, L-2940, LL-1172, LL-3261, LL-1061, LL-3173
5	Normal	60° SW	N40° W	50	LL-2280, LL-2038, LL-1218
Central Fault 6	Normal	62° NE	N60° W	250	LL-1748, LL-1176, LL-3059, LL-3155, LL-1310
7	Normal	65° NE	N45° W	50	LL-1022, LL-3149, LL-1307, LL-1196
8	Normal	80° NW	N45° E	500	-
9	Normal	65° SW	N25° W	200	LL-1803
10	Normal	80° SE	N30° E	550	-
11 (NE-R)	Reverse	78° W	N-S	500	LL-851, LL-827
12 (NW-R)	Reverse	75° E	N15° E	550	LL-3250, LL-LL-3204, LL-1089, LL-857
13 (CE-R)	Reverse	70° NW	N12° E	80	LL-1095, LL-1169, LL-3301, L-1782, LL-3282, LL-1218, LL-904, LL-1061
14 (CW-R)	Reverse	70° SE	N11° E	100	LL-997
15	Normal	55° SW	N10° W	100	LL-3144, LL-3286, LL-3263, L-3056
16 (SE-R)	Reverse	70° NW	N35° E	100	LL-1303, LL-1005, LL-1196, LL-946, LL-1023, LL-3284, LL-1001
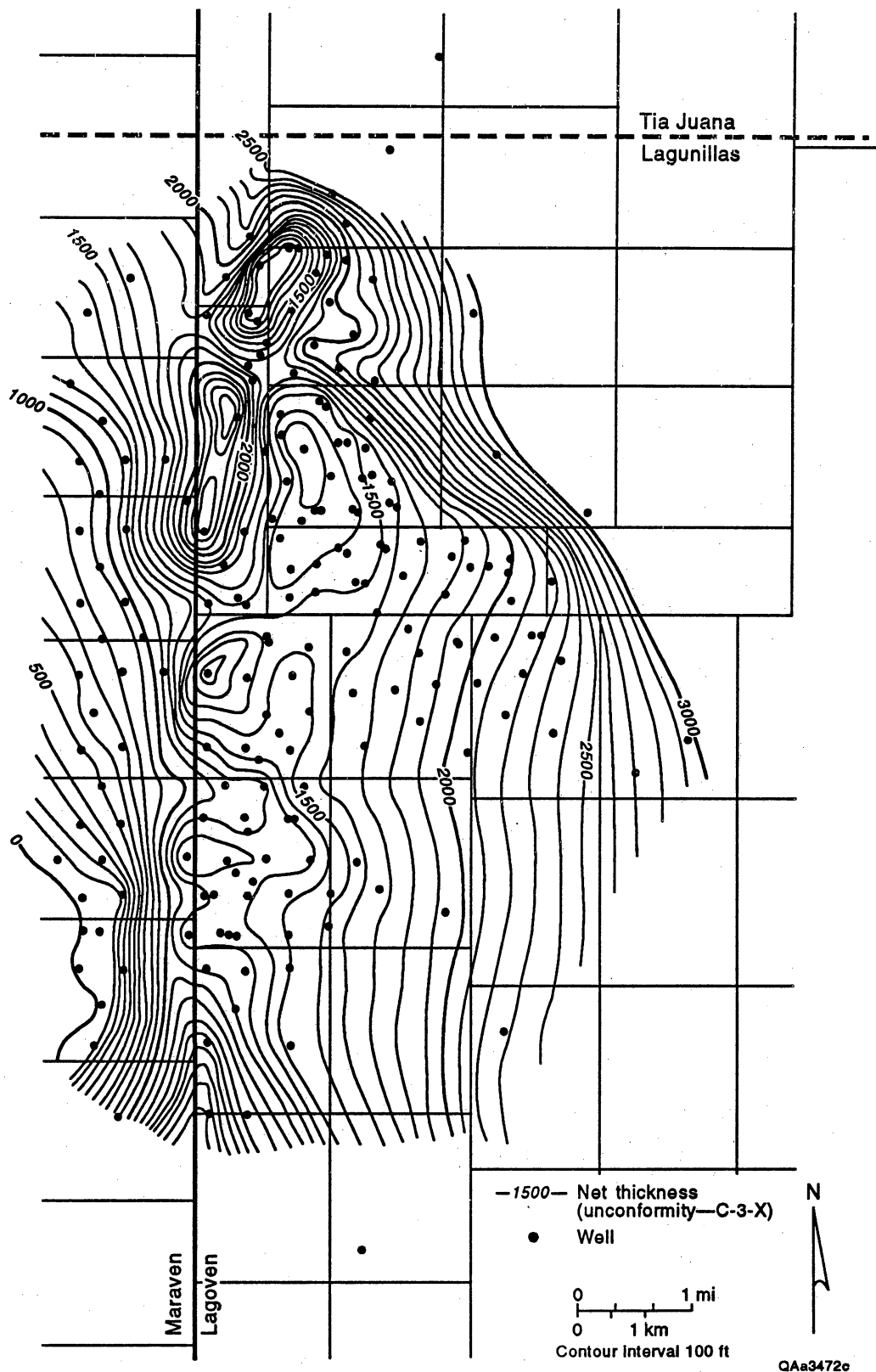
Figure 17. Net-thickness map of the interval between the Eocene-Miocene unconformity and the top of the C-3-X Member.
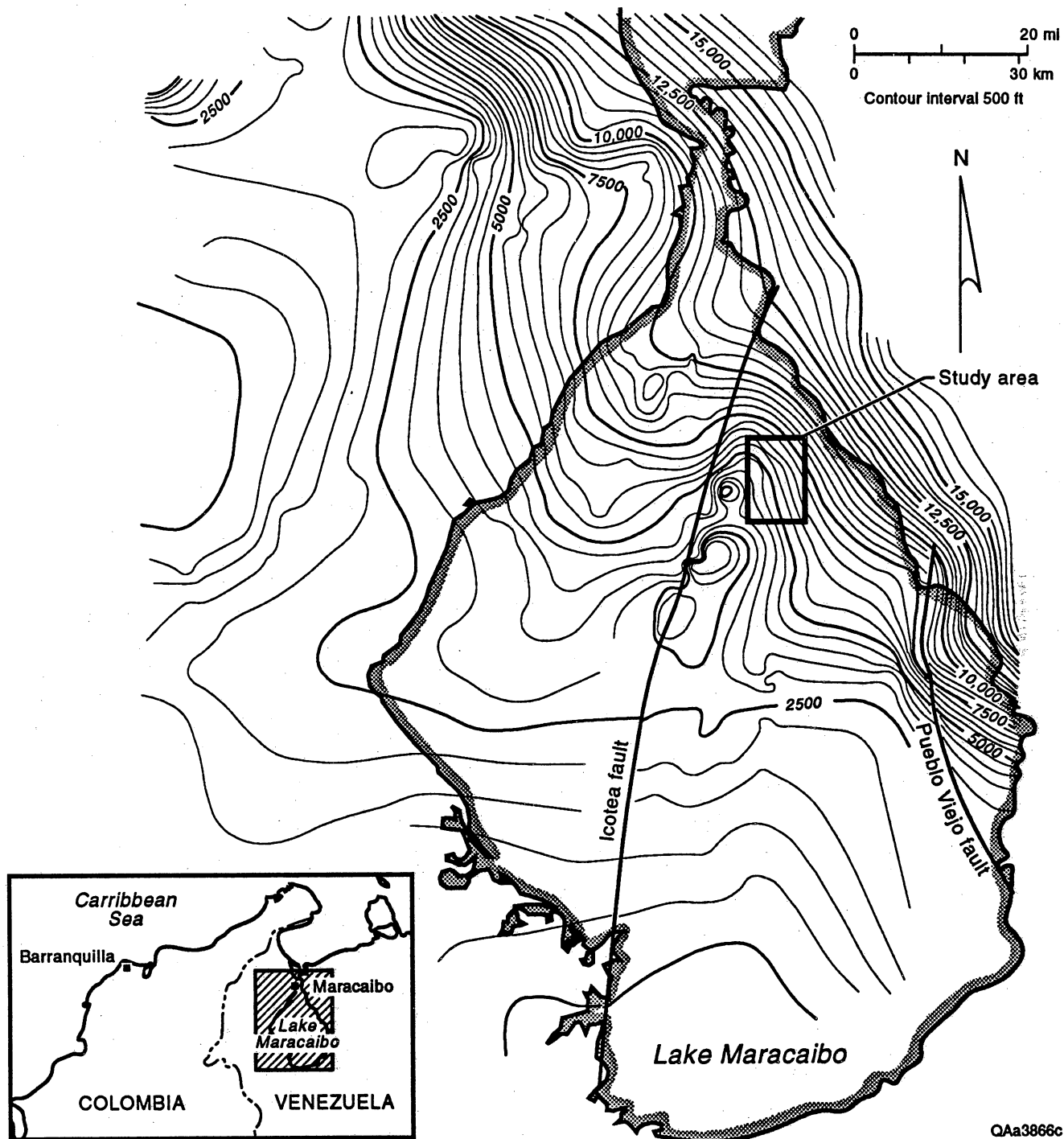
Figure 18. Unrestored total isopach map for the Eocene. From Lugo (1991).
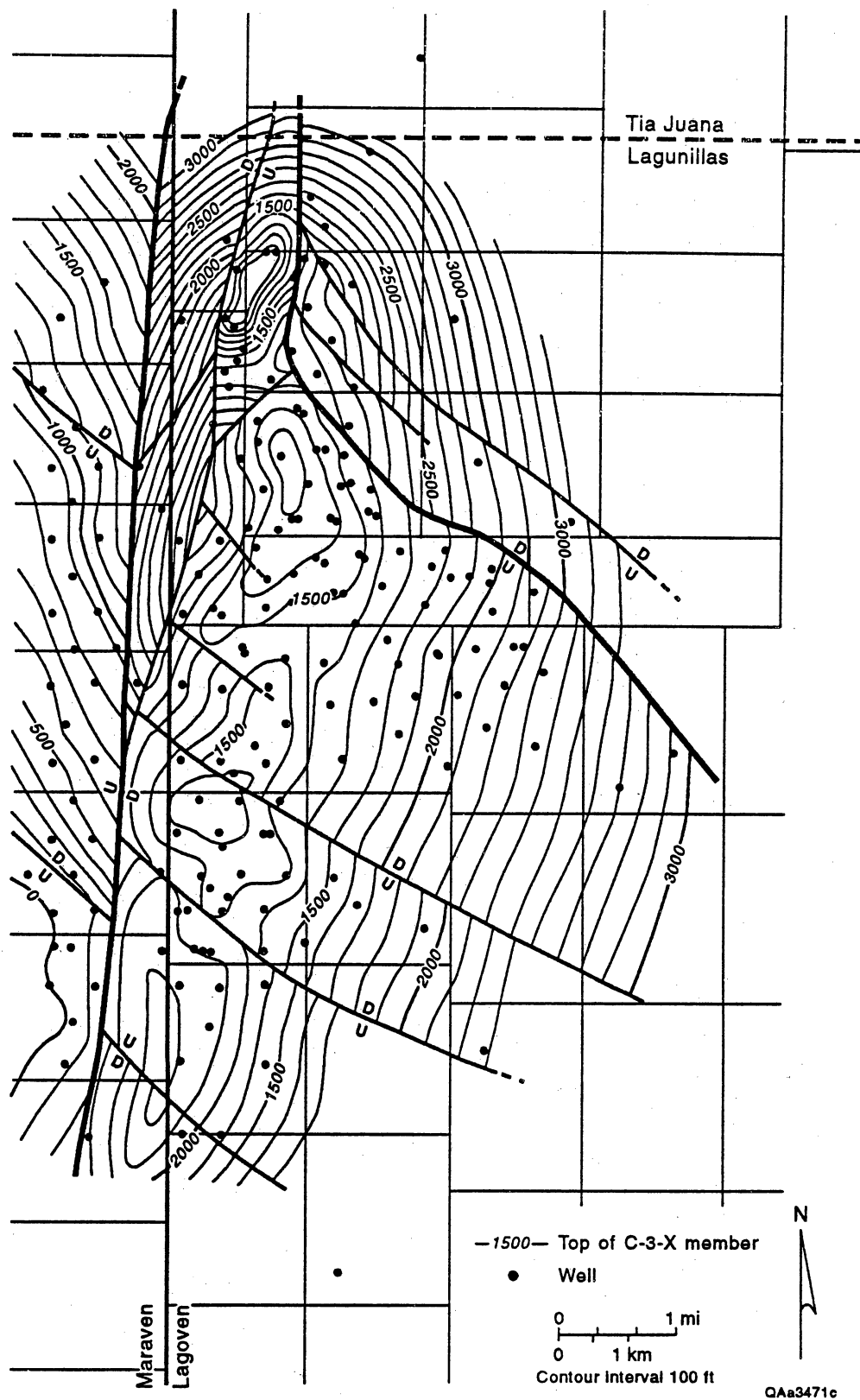
Figure 19. Paleostructural map on top of the C-3-X Member in the LL-652 area.

northeast. The northern part has a crest with a N22°E strike and is offset 0.9 mi (1.5 km) from the main crest (N12°E).

Structural Cross Sections

Twelve of twenty-two structural cross sections that were completed are included in this report to document the structural framework (fig. 7). All cross sections have a vertical exaggeration of 2:1 and do not represent the true attitude of the structure. However, they provide significant information to verify the existence of faults, relative changes in structural dip, stratigraphic discontinuities, folds, and other important structural features.

After several stages of revision to improve the accuracy of the interpretation, the final cross sections agreed with the completed structural maps and seismic interpretation and conformed to the structural style of the LL-652 area. These cross sections show that the youngest reverse faults offset the unconformity and truncate the oldest normal faults. The master fault also cuts the Eocene-Miocene unconformity. All the normal faults die below the unconformity, except the master fault, and some block rotation is associated with reverse faults.

Cross Section A

Cross section A is located in the northern part of the field and shows the LL-1695 well in the downthrown block (high-dip zone) of the reverse fault (fig. 20). The LL-3250 well is located between two reverse faults in the upthrown block, is intersected by the left reverse fault, and has a repeat section of 190 ft (58 m). The LL-827 well is located in a structurally high position and has a repeat section of 120 ft (36.6 m) at the reverse fault. The lower part of the LL-827 well is in the downthrown block and shows a rotation and 54° dip from the dipmeter log.

The main normal fault, located between the LL-827 and LL-2981 wells, has a throw of 400 ft (122 m); this fault may offset Paleocene strata. The LL-2981 well is located in an isolated block and is separated from the LL-637 well by a fault that offsets the Guasare Formation. The C members are truncated progressively westward from the LL-627 well.

Cross Section B

Cross section B contains the VLA-744 well, with 300 ft (91.5 m) faulted out at the bottom of the C-2-X Member and top of the C-3-X Member (fig. 21). The master fault, with a throw of 800 ft (244 m), is west of the VLA-89 well. The LL-1089 well is faulted 150 ft (45.7 m) by the reverse fault at the level of the B-9-X Member. This well is located in the downthrown block in a high-dip zone. The LL-3144 well is located in an upthrown block bounded by the reverse fault in the east and a normal antithetic fault on the west. The LL-3141 well shows a missing section of 900 ft (274 m) in the B-8-X, B-9-X and C-1-X Members. The LL-1166 well is located eastward and is intersected by the main fault in the C-5-X Member and in the Lower C-1-X Member by a secondary fault.

Cross Section D

Cross section D crosses the anticline from the west flank (VLA-598 and LL-857 wells, high-dip zone) to the east flank (LL-3249 well) where there is a gentle dip of only 5° (fig. 22). The VLA-90 and VLA-931 wells are located in the upthrown block of the master fault; on the downthrown side the VLA-598 well is bounded eastward by a reverse fault. The B members are preserved in this well. The LL-857 well is intersected by the reverse fault in the C-1-X Member. The downthrown block is in the high-dip (38°) zone, as interpreted from the dipmeter log.
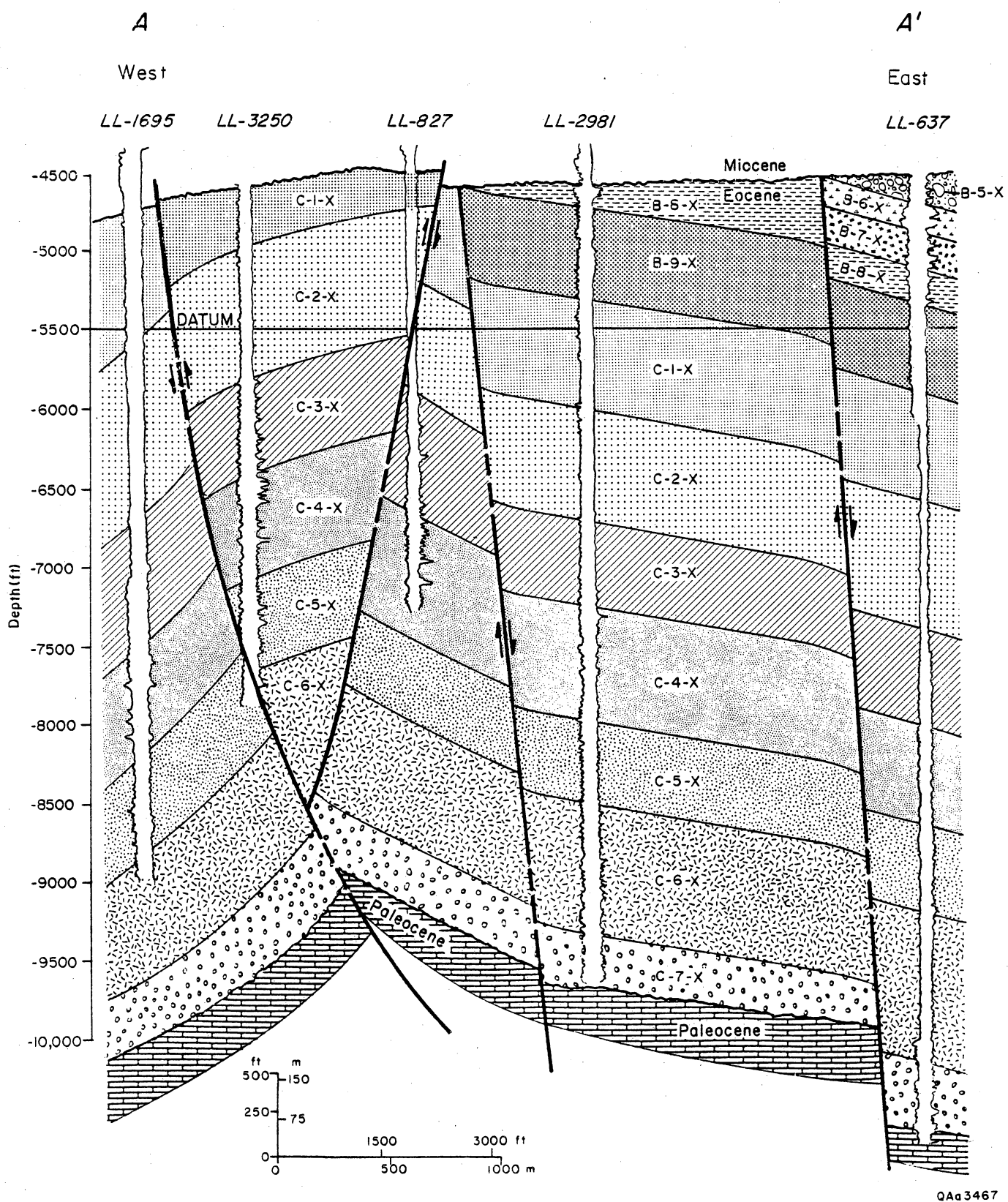
Figure 20. Structural cross section A–A'.

37
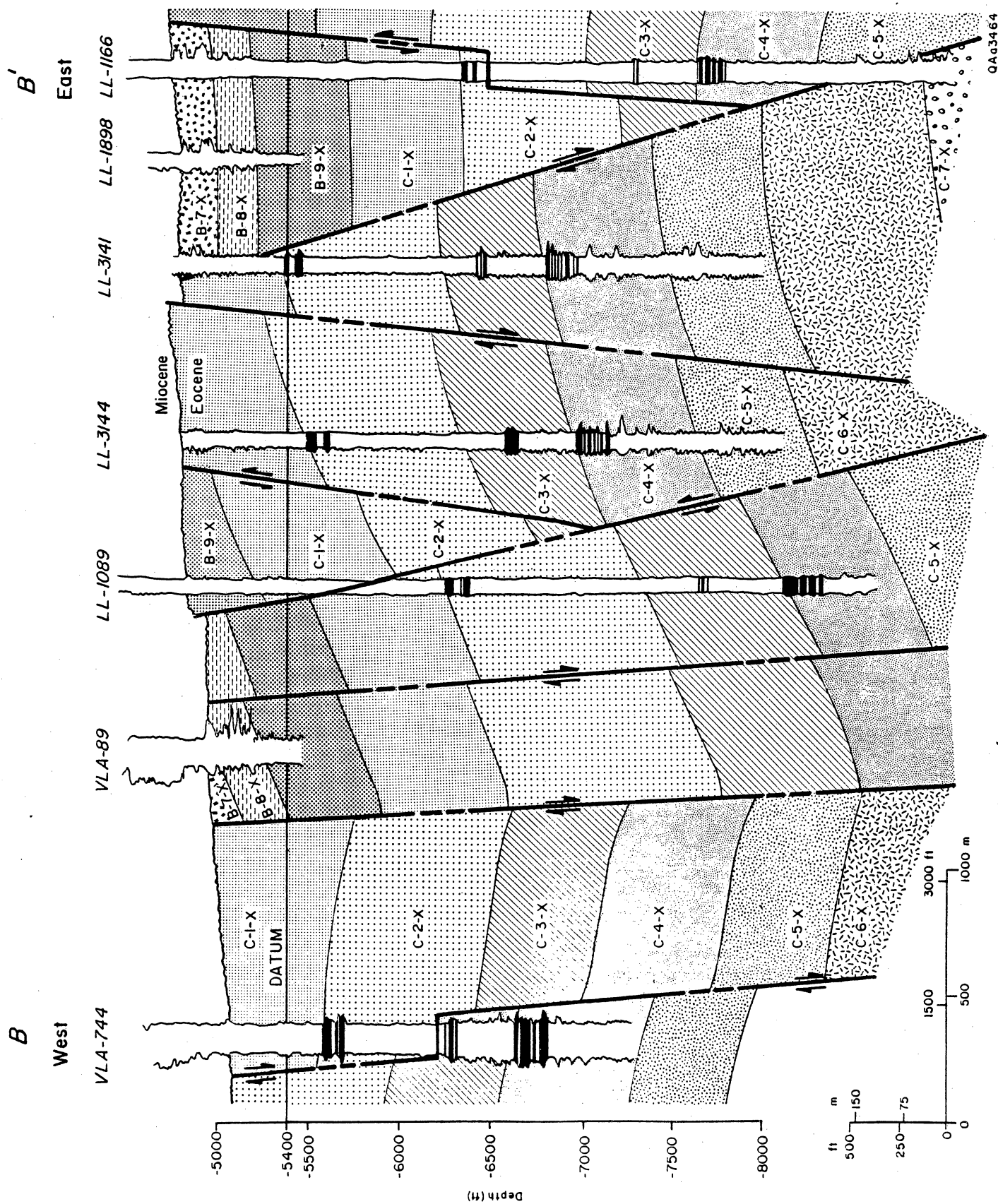
Figure 21. Structural cross section B–B'.

38
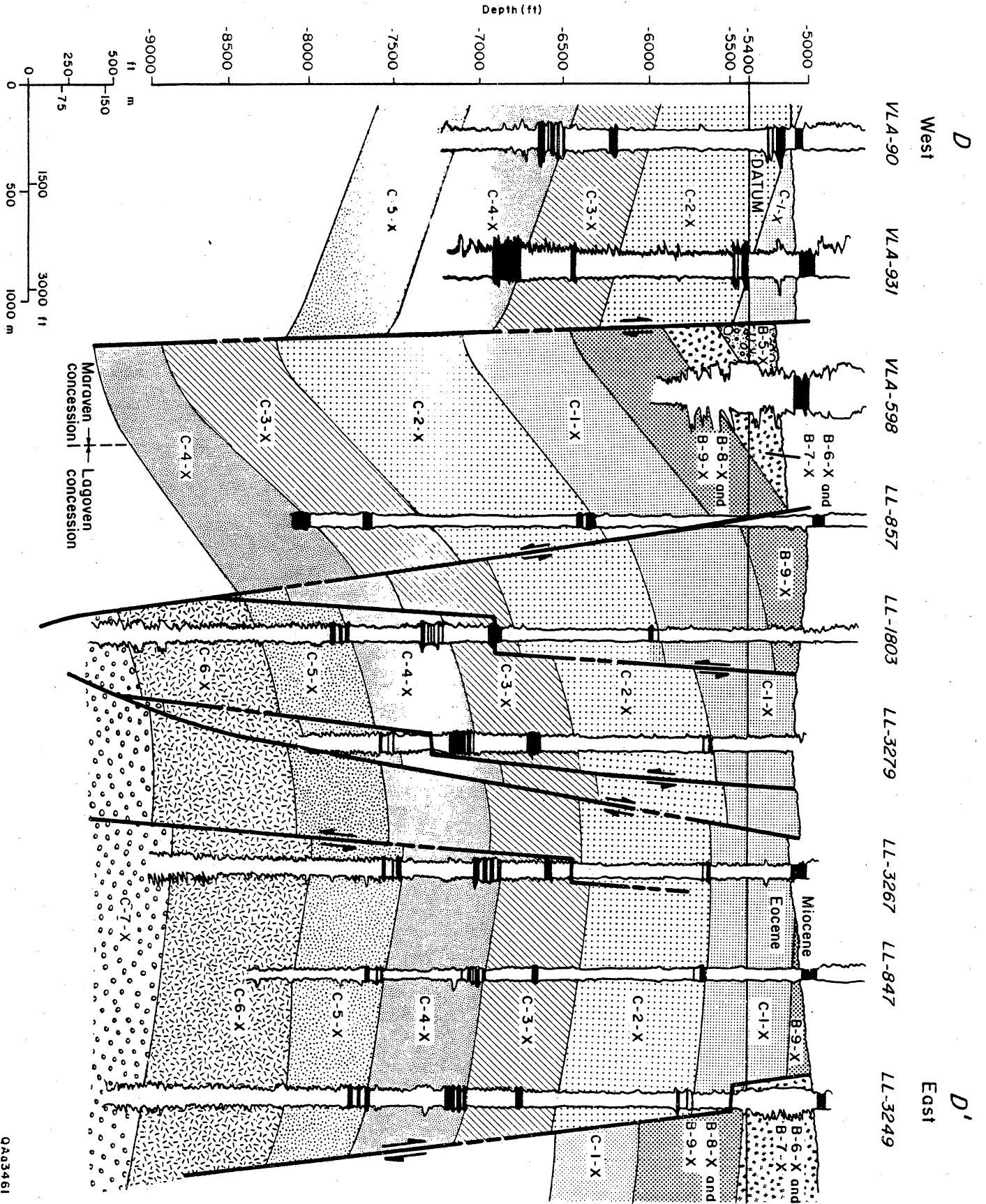
Figure 22. Structural cross section D–D'.

QAa3461

The LL-1803 and LL-3279 wells are intersected by minor faults and are located in the upthrown block bounded by two reverse faults. The LL-3267 well is intersected by a normal fault that cuts the top of the C-3-X Member and terminates in the shaly section of the C-2-X Member. The LL-3249 well is intersected by the master fault with a missing section of 1,180 ft (360 m) in the B-8-X, B-9-X, and part of the C-1-X Members. The downthrown block of the main fault (on the east, LL-3249 well) and master fault (on the west, VLA-598 well) contains the B-6-X Member.

Cross Section F

Cross section F contains the VLA-751 and VLA-28 wells, located in the upthrown block of the master fault (north horst, Maraven reports) (fig. 23). The relative dip is low (6° in the VLA-28 well) toward the east. The LL-917 well is located in an upthrown block, bounded by two reverse faults. One of these faults cuts the well at the base of the C-5-X Member (8,420 ft) with a repeat section of 110 ft (33.5 m). The LL-917 well is also intersected by a normal fault with 80 ft (24.4 m) of missing section in the C-2-X Member.

The LL-1310 well is faulted in the Upper C-4-X Submember at 7,580 ft with 80 ft (24.4 m) of missing section. The LL-866, LL-1106, and LL-1310 wells are located in a relatively undisturbed structural block with a low dip angle. The LL-1310 well is intersected by the central fault at 7,580 ft at the top of the C-4-X Member with a missing section of 180 ft (55 m).

Cross Section G

Cross section G is located in the southern part of the field and includes the VLA-281 and VLA-724 wells (faulted in the Lower C-4-X Submember), located in the upthrown block of the master fault (fig. 24). The VLA-96 well is located in the upthrown block, is bounded by two reverse faults, and is also cut by a reverse fault. The LL-1196 well is intersected by a reverse fault in the Upper C-2-X Member. The log response in this well shows a good contrast in the repeat section and is also intersected by a normal fault at 7,460 ft with a missing section of 60 ft (18 m).

Cross Section 4

Cross section 4 illustrates a faulted anticline with the crest at the LL-1095 well (fig. 25). In the northwest there is a relatively high dip and on the southeast a gentle dip. A trough associated with a fault occurs between the LL-3204 and LL-3144 wells, and the LL-975 well is located in a fold toward the northwest. The LL-3204, LL-3144, and LL-1095 wells are bounded by two reverse faults. The C-1-X Member is truncated by the Eocene-Miocene unconformity, which shows a high degree of angularity. Toward the southeast the truncation is less and the B-9-X Member is present. The LL-1276, LL-847, LL-2942, LL-1198, and LL-1986 wells are located in the structurally simple part of the southeast limb of the anticline.

Cross Section 6

Cross section 6 (fig. 26) includes the LL-3282 well that shows a repeat section in the Lower Middle C-5-X Submember associated with a reverse fault. Also, the LL-3301 well has a textbook example of a 90-ft (27.4-m) repeat section in the Middle C-3-X Submember. Figure 27 shows detailed correlations between this well and the LL-1782 well, located approximately 450 ft (137 m) southeastward from the LL-3282 well.

The VLA-613 well (fig. 26) is one of two wells (the other is VLA 13) with missing section (± 1,100 ft [335 m]) from the eastern master fault in the Maraven area. Cross section 6 also shows a transverse view of the anticline, with the high-dip zone on the northwest flank and the gently dipping southeast flank. The VLA-564 well intersects B members preserved in the downthrown block of the master fault. The

Figure 23. Structural cross section F-F'.

QAa3462

41
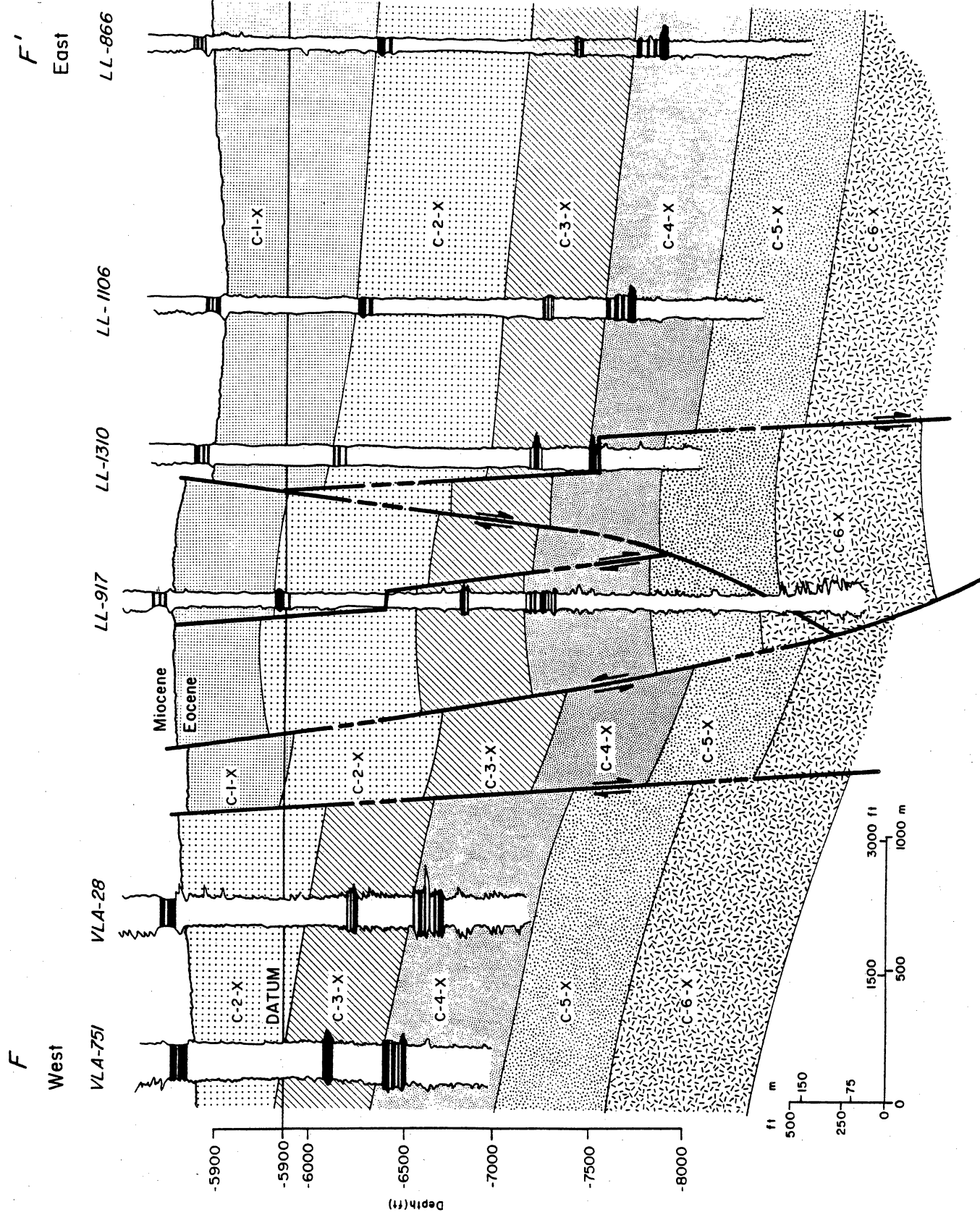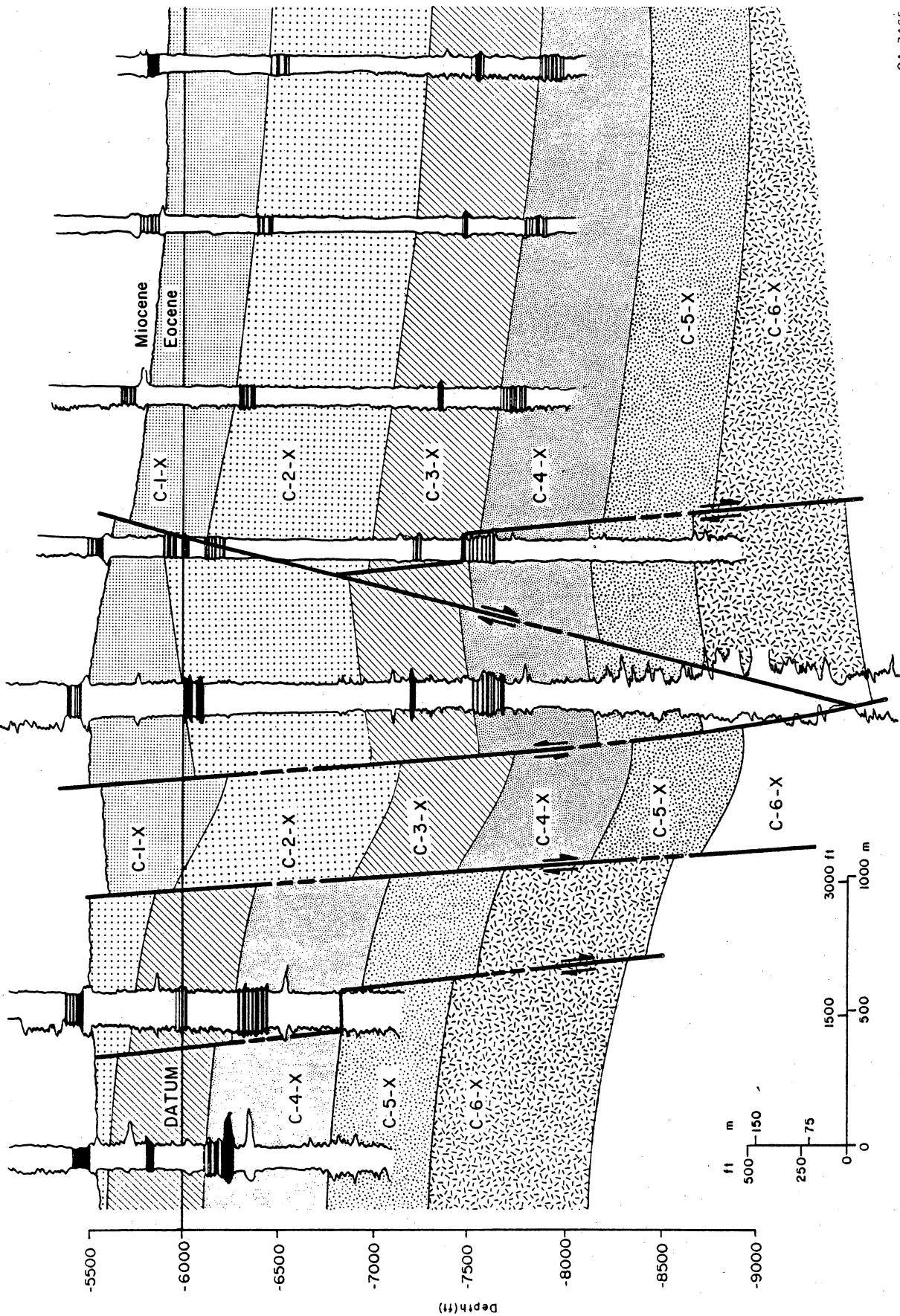
Figure 24. Structural cross section G-G'.

QAa3465

42
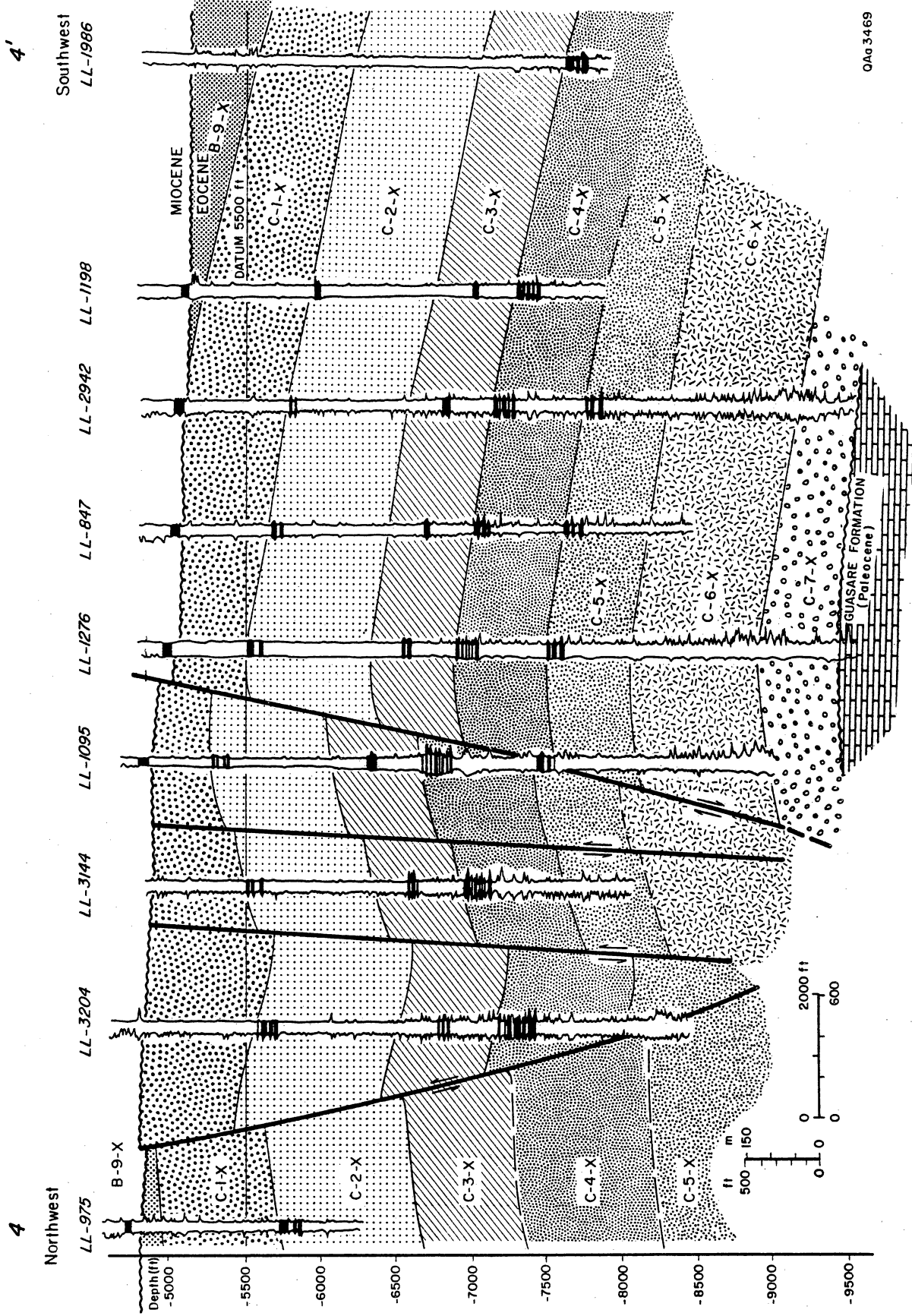
Figure 25. Structural cross section 4-4'.

43
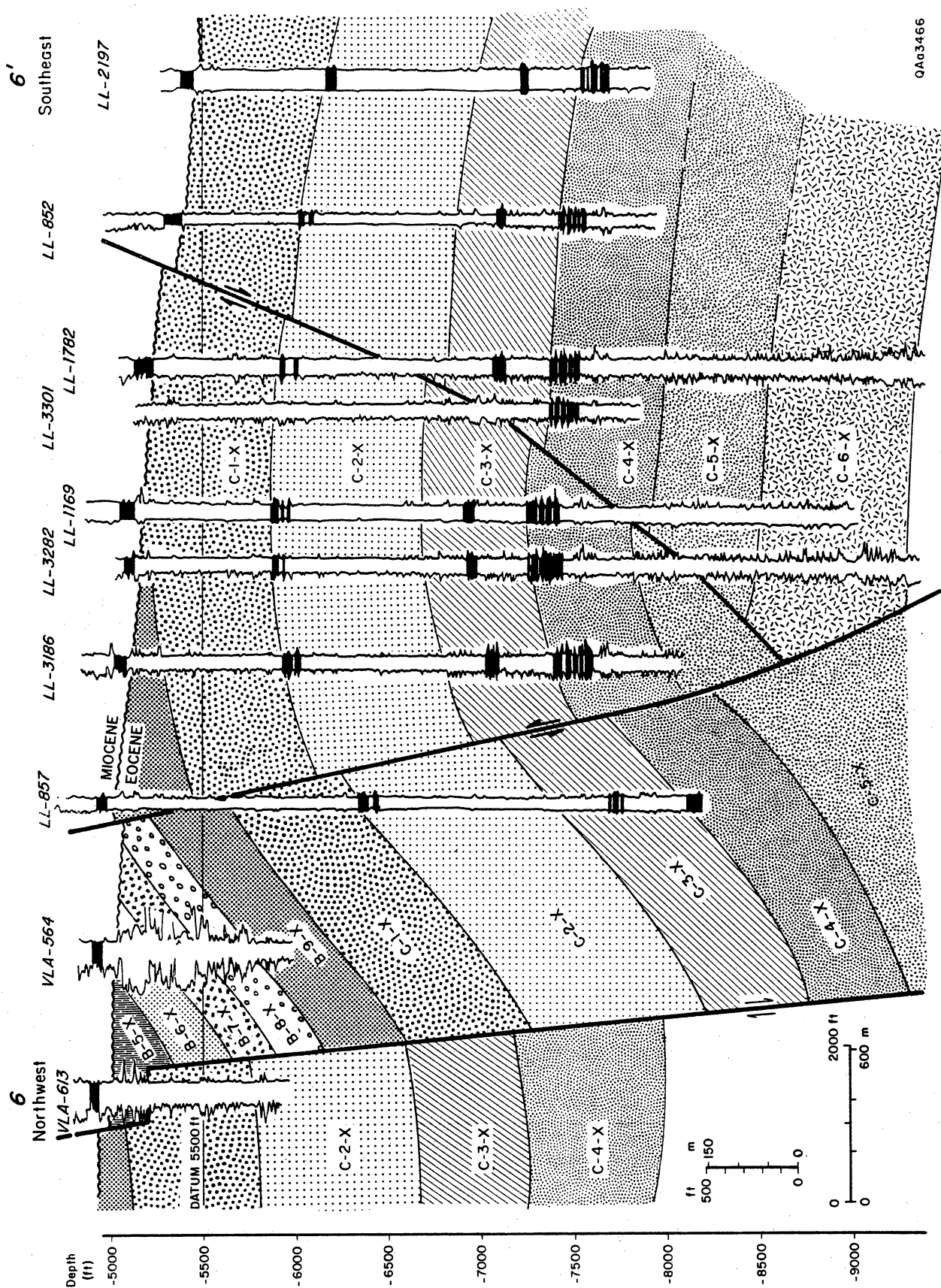
Figure 26. Structural cross section 6-6'.

QAa3466

44
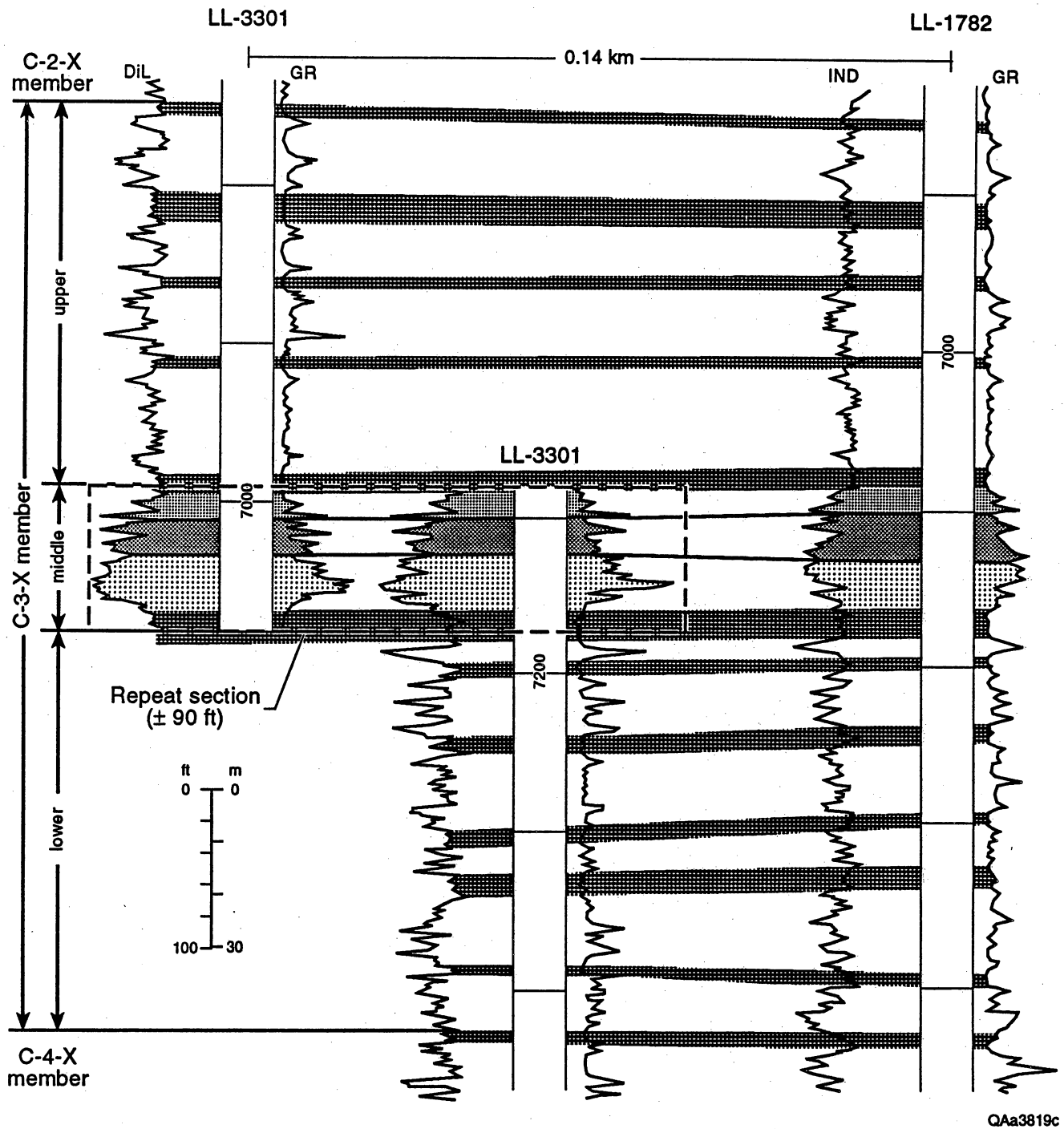
Figure 27. Detailed correlation between the repeat section in the C-3-X Submember in the LL-3301 and LL-1782 wells.

western reverse fault intersects the LL-857 well in the B-9-X Member, and the LL-3282, LL-1169, LL-3301, and LL-1782 wells are intersected by the eastern reverse fault with an average of 90 ft (27.4 m) of repeat section. The LL-852 and LL-2197 wells are located in the downthrown block of the reverse fault.

Cross Section 7

Cross section 7 includes the VLA-90, VLA-862, VLA-882, and VLA-874 wells, located in a structural block on the upthrown side of the master fault (fig. 28). This simple structural block dips 6° eastward and is bounded southeastward by the master fault. The VLA-534 well is located in a downthrown block between the master fault and a reverse fault. The LL-917 and LL-1303 wells are intersected by this reverse fault and are located in the upthrown block between two other reverse faults. The LL-1245, LL-3074, and LL-833 wells are located in a block that dips 5° southeastward (LL-833 dipmeter log).

Cross Section 8

Cross section 8 shows the VLA-96 well in an upthrown block of the reverse fault. The LL-946 well has a repeat section (70 ft [21.3 m]) in the Middle C-3-X Submember (fig. 29). The LL-3260, LL-1124, and LL-1010 wells are located in a 6° dipping block with a minor fold. The best evidence of the unconformity offset by a reverse fault is shown between the LL-946 and LL-3260 wells.

Cross Section 9

Cross section 9 is located in the northern fold and shows the VLA-105 and LL-975 wells in the southwest flank of the fold, dipping 25° (LL-975 dipmeter log) southwestward (fig. 30). The LL-3250 and LL-2946 wells are located in an upthrown block, bounded by two reverse faults. This block is the structurally highest area in the field. The LL-846 and LL-450 wells are located in an adjacent structural block, where the LL-846 well has a 20° dip, indicated from the dipmeter log. This block is extremely important for new well locations, as will be discussed in Chapter XI.

Cross Section 12

Cross section 12 shows structural complexity of the whole study area (fig. 31). It spans an area from the southwest in the Maraven area that includes the VLA-281, VLA-66, VLA-777, and VLA-28 wells, bounded by a minor fault in the upthrown block of the master fault, to the LL-907, VLA-534, LL-3186, LL-103, and LL-3056 wells associated with several normal and reverse faults. It also includes the LL-1095 well on the crest of an anticline intersected by a reverse fault, and the LL-1209 well intersected by two faults. It also shows downthrown B members preserved below the Eocene-Miocene unconformity in the northeast block.

Cross Section 16

Cross section 16 shows the main fault (fig. 32). On the southwest the LL-3235, LL-971, and LL-2425 wells are located in the upthrown block of the fault. This block shows an apparently high dip in the section, but the real dip is only 6° southeastward (dipmeter log of LL-895 well). The LL-2191 well is offset 1,000 ft (305 m) by a fault in the C-1-X and C-2-X Members. The LL-1258 well is located in the downthrown block and exhibits preservation of the B members (from B-9-X to B-5-X), whereas in the upthrown block the B-5-X, B-6-X, and B-7-X Members are eroded and the B-8-X Member is truncated.
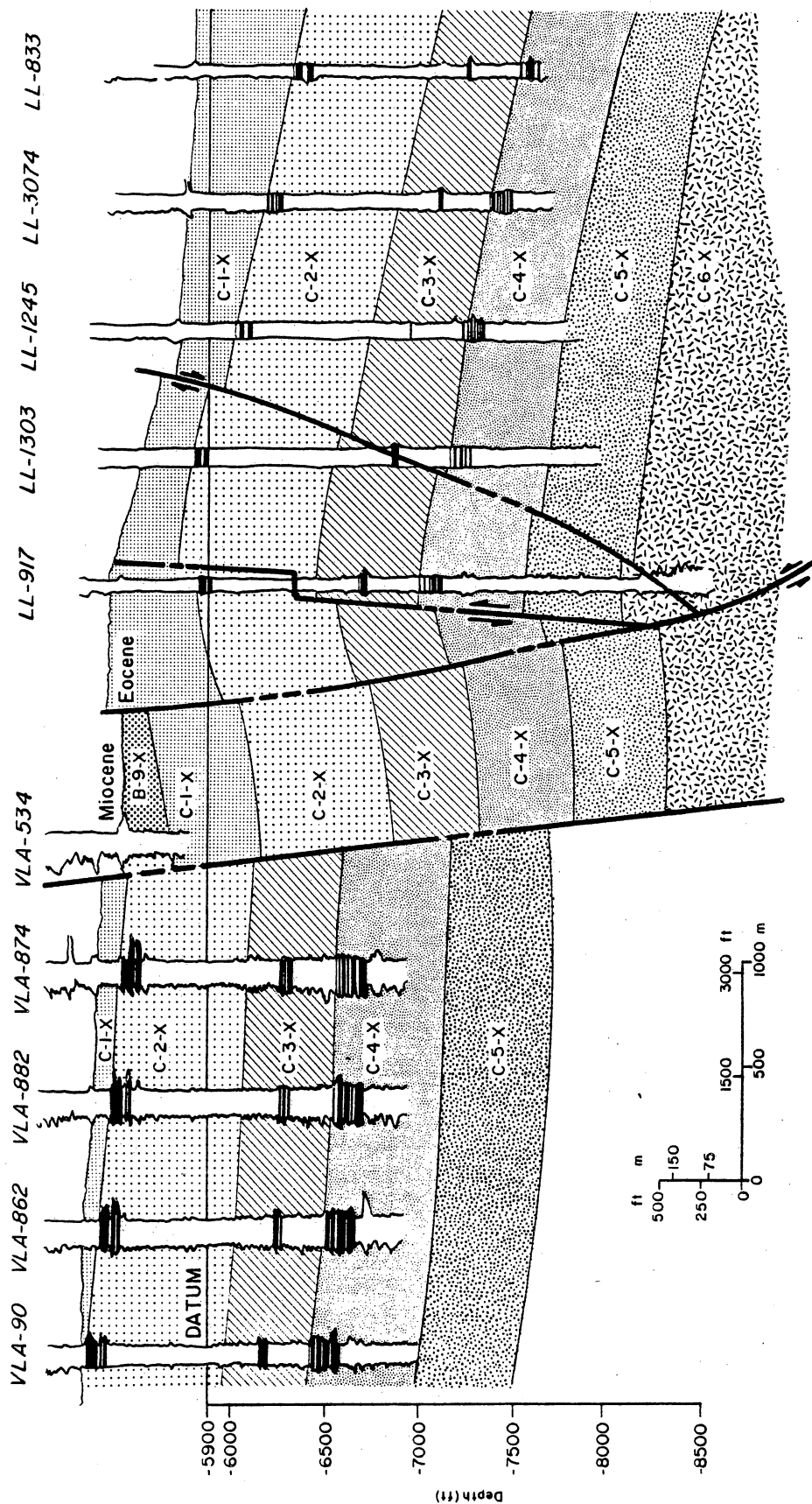
Figure 28. Structural cross section 7-7'.

47
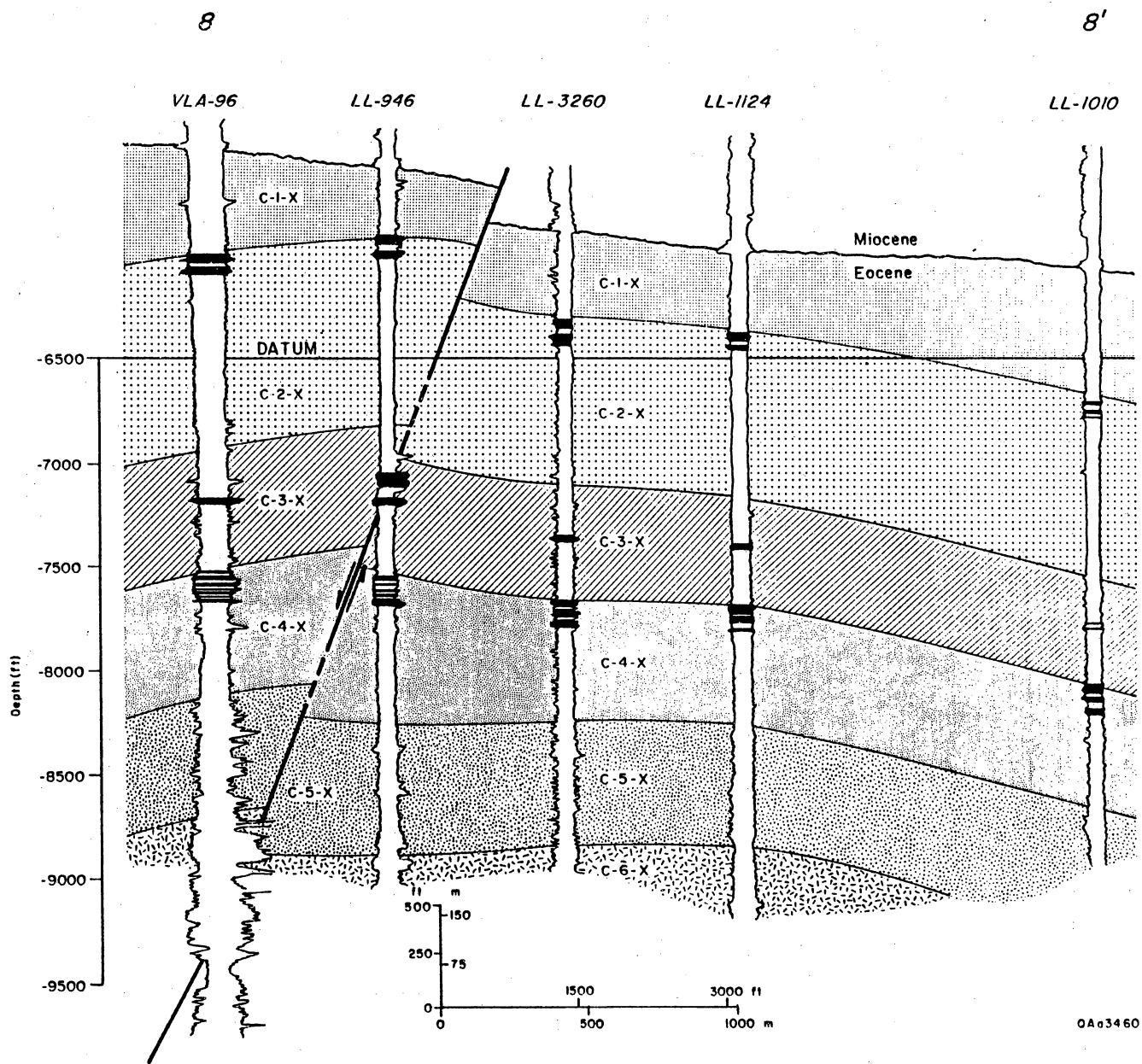
Figure 29. Structural cross section 8–8'.
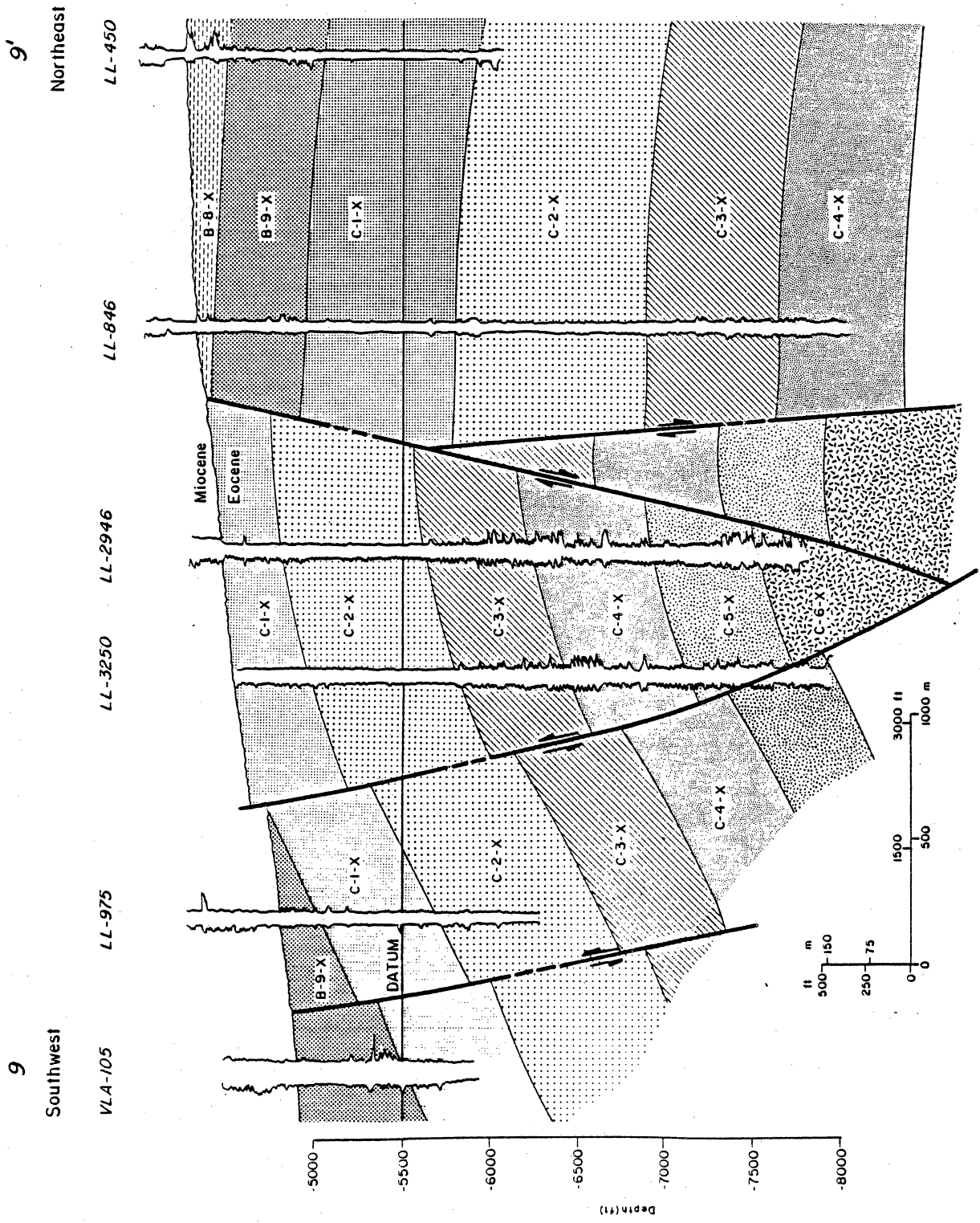
Figure 30. Structural cross section 9–9'.

49
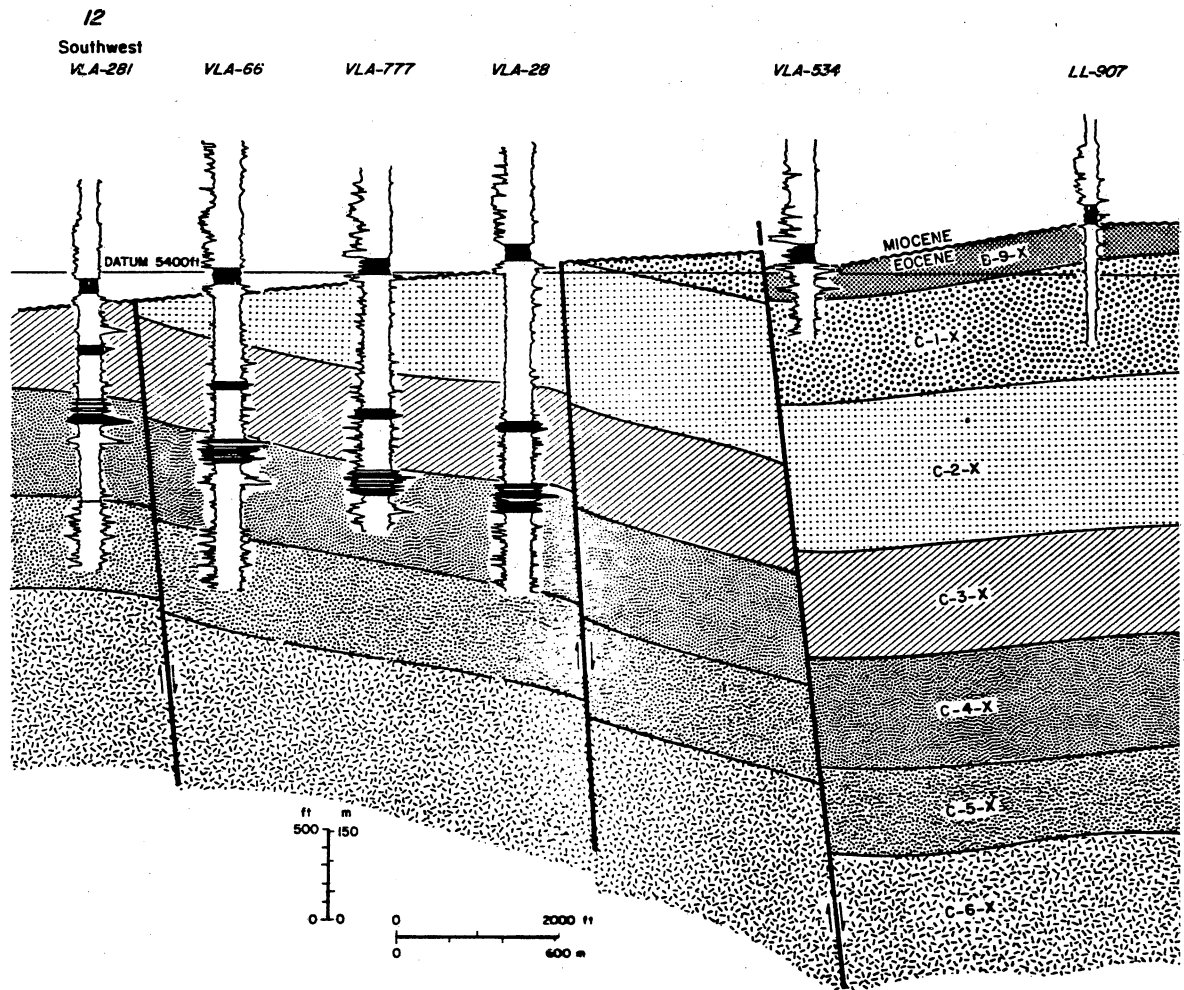
Figure 31. Structural cross section 12–12'.

51
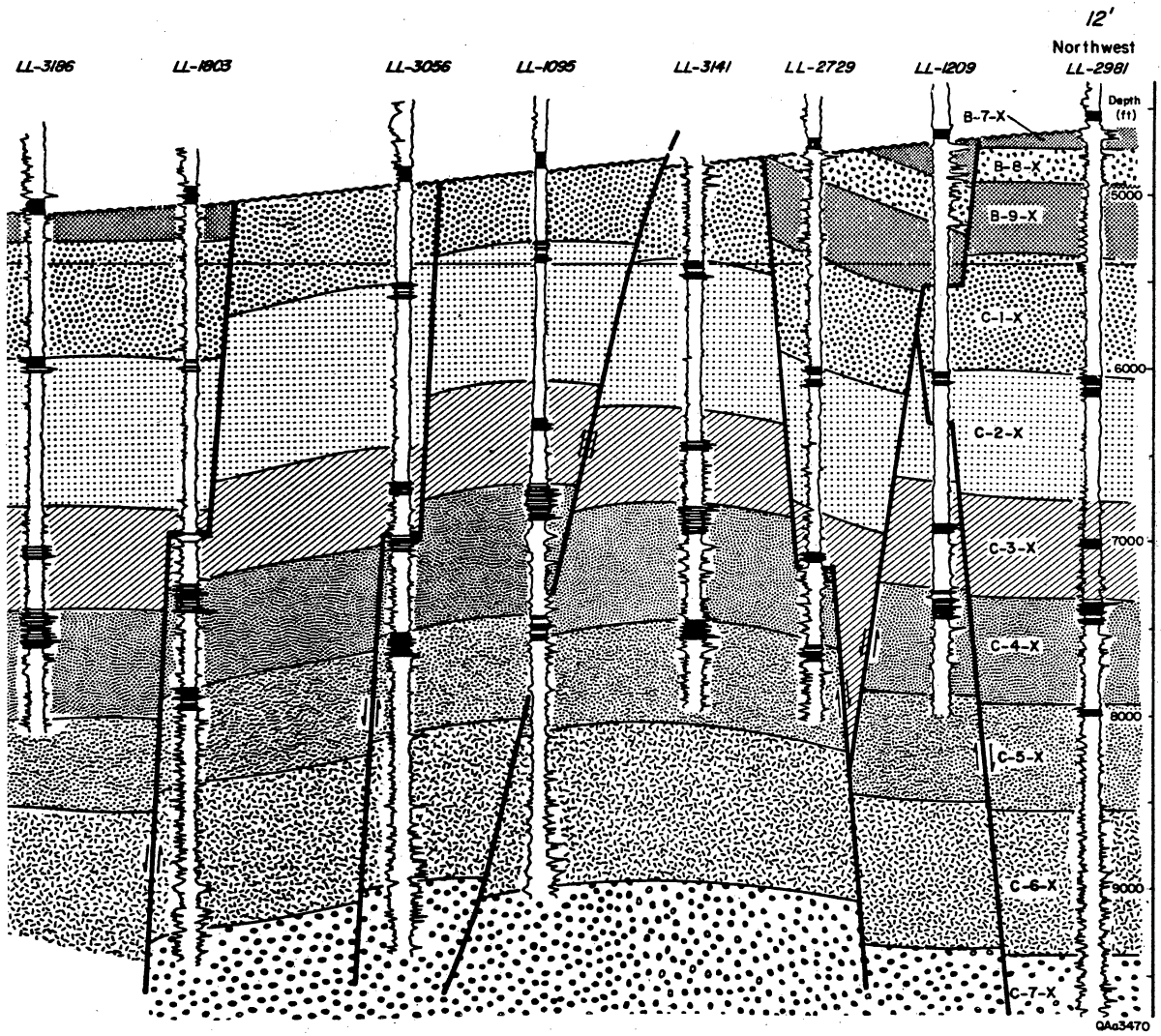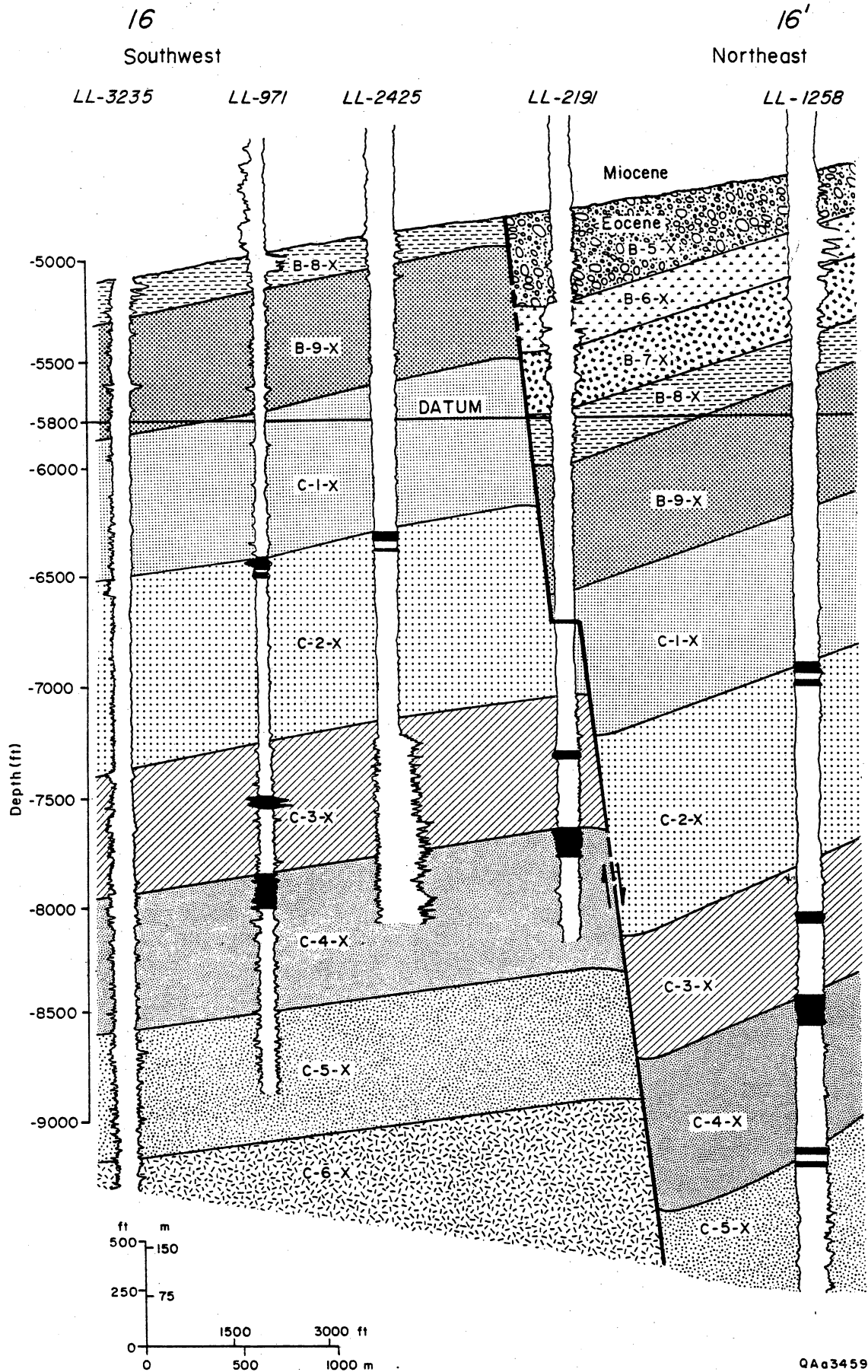
Figure 32. Structural cross section 16–16'.

52

In the LL-652 area, seismic data were used to further delineate the major faults and folds and provided general support for projection of the structural framework into areas with poor well control in the northern part of the field. Well data were tied to seismic sections with synthetic seismograms of five selected wells with high-quality sonic and bulk-density logs. The Eocene-Miocene unconformity, top of C-3-X Member, Guasare Formation, and Socuy Member were selected for correlations, as they correspond to the most prominent and most continuous seismic reflectors in the area. Four seismic reflectors (Eocene unconformity, Guasare formation, Socuy Member, and C-3-X/C-4-X interval) were selected to document the regional structural framework. The Eocene-Miocene unconformity is represented by two continuous, high-amplitude parallel reflectors that truncate underlying reflectors in the B and C members. The Guasare formation is represented by a high-amplitude, continuous pair of prominent reflectors. One high-amplitude, continuous reflector corresponds to the Socuy Member, which is overlain by three (0.15 s thick) moderate- to high-amplitude, semicontinuous reflectors that represent Cretaceous limestone. The middle seismic unit in the Eocene (between the unconformity and the Guasare Formation) corresponds approximately to the C-3-X and C-4-X Members and represents a pair of high-amplitude, continuous reflectors. These reflectors are the most distinctive seismic markers in the Eocene, and may represent a zone of high-velocity contrast between the shaly Lower C-3-X Submember and the sandstone-rich Upper C-4-X Submember.

Seismic Line CO-90B-28

The northwest part of this line shows the typical profile of the Icotea fault (fig. 33), an elongate anticline bounded longitudinally by upward- and outward-divergent strands of a wrench fault that has mostly reverse separation (Harding, 1985 and 1990). The fault splays upward from the basement, deforming the Cretaceous to Eocene section below the unconformity. The lower part of the post-unconformity sequence is also offset but is related to later reactivation that also deformed the LL-652 area (Lugo 1991).

At SP-345 (central part of the line) there is a normal fault with 0.25 s of throw. This fault offsets the whole section and represents the master fault in the study area. A low-angle reverse fault at SP-330 offsets the basement and has associated secondary reverse faults that offset mainly Cretaceous and Paleocene strata. A reverse fault at SP-270 offsets only the Eocene.

The LL-450 well, located at SP-260, penetrates the C-2-X Member. However, underneath there is an inferred closed fold in C-3-X/C-4-X reflectors. This interpretation is also supported by structural cross section A (fig. 20), which shows a fold between the LL-846 and LL-450 wells. Both elements of interpretation coincide and confirm this fold as the continuation of the north fold.

Seismic Line CO-90B-30

This line is parallel to the CO-90B-28 line and also shows a profile of the positive flower structure in the Icotea fault, where the unconformity is most deformed (fig. 34). At SP-320 the master fault cuts the entire sequence. The LL-1293 well (SP-235) is located on the downthrown side of the reverse fault that offsets the basement (where there is a detachment surface) up to the Eocene sequence. This is confirmed by the dipmeter of the same well that shows a 47° dip in the C-4-X Member. The LL-2946 well (SP-260) is located westward of the structure and is bounded by two reverse faults. The LL-2981 well (SP-235) is located in the downthrown block of a reverse fault. This block shows an apparent dip toward the LL-637 well (projected at SP-185), which is located downstructure in the southwest. This line is subparallel to structural cross section A (fig. 20). Two minor normal faults bound the LL-2981 well in the structural cross sections. However, the presence of these faults is questionable because of the poor vertical resolution of the seismic data, especially of faults of small throw.
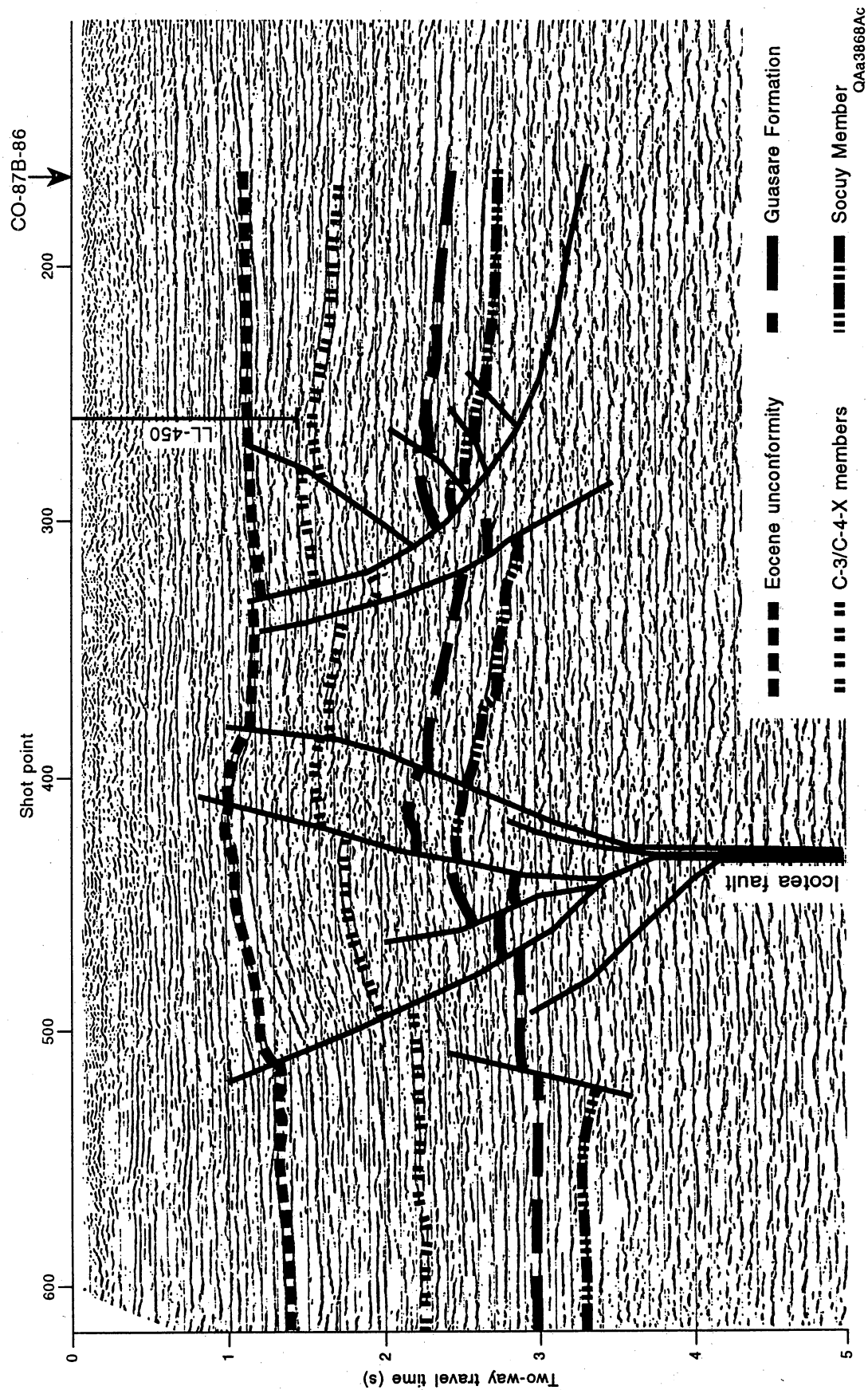
Figure 33. Seismic line CO-90B-28.

QAa3868Ac

54

Two-way travel time (s)

Shot point
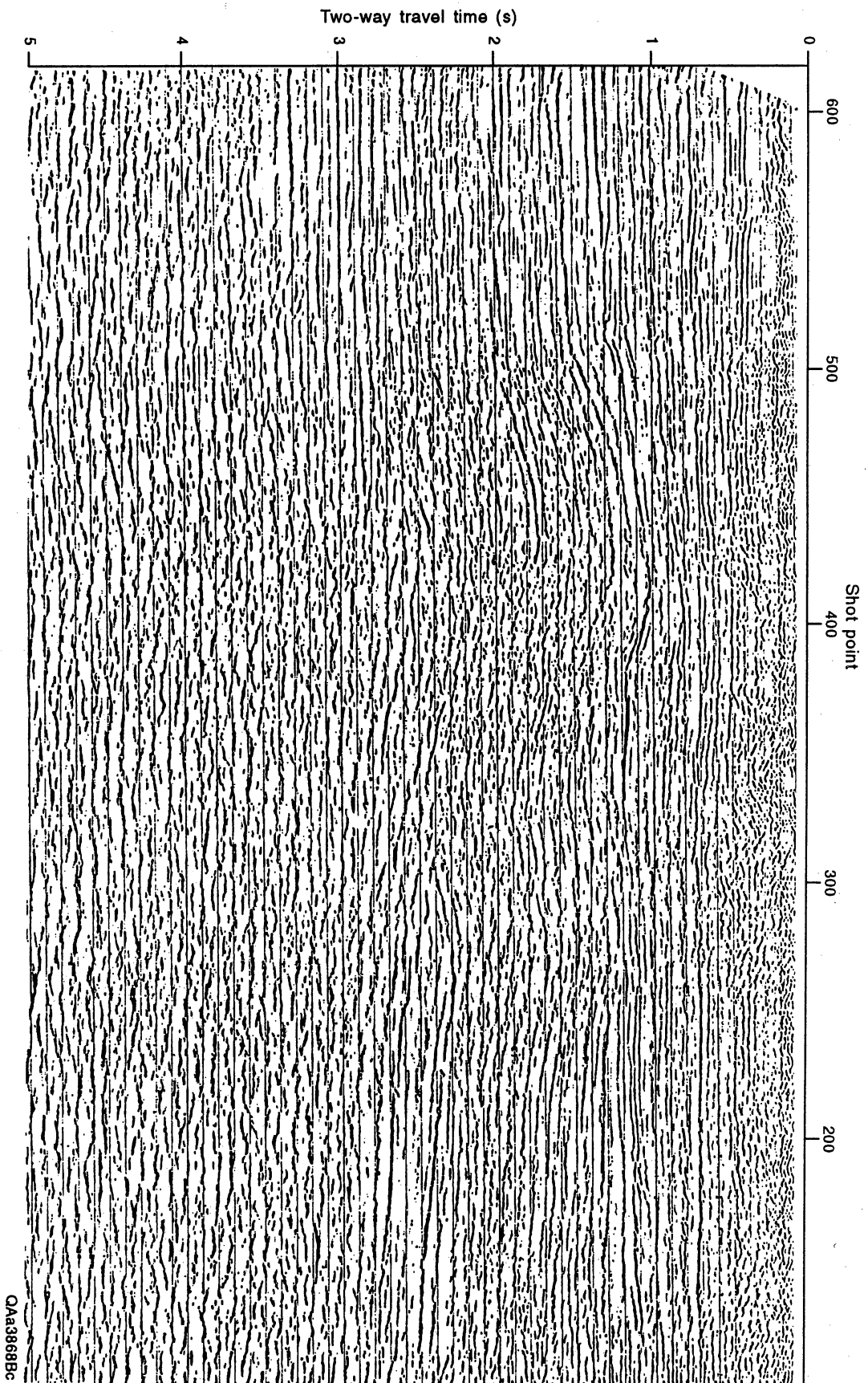
Figure 33. Continued.

QAa3868Bc
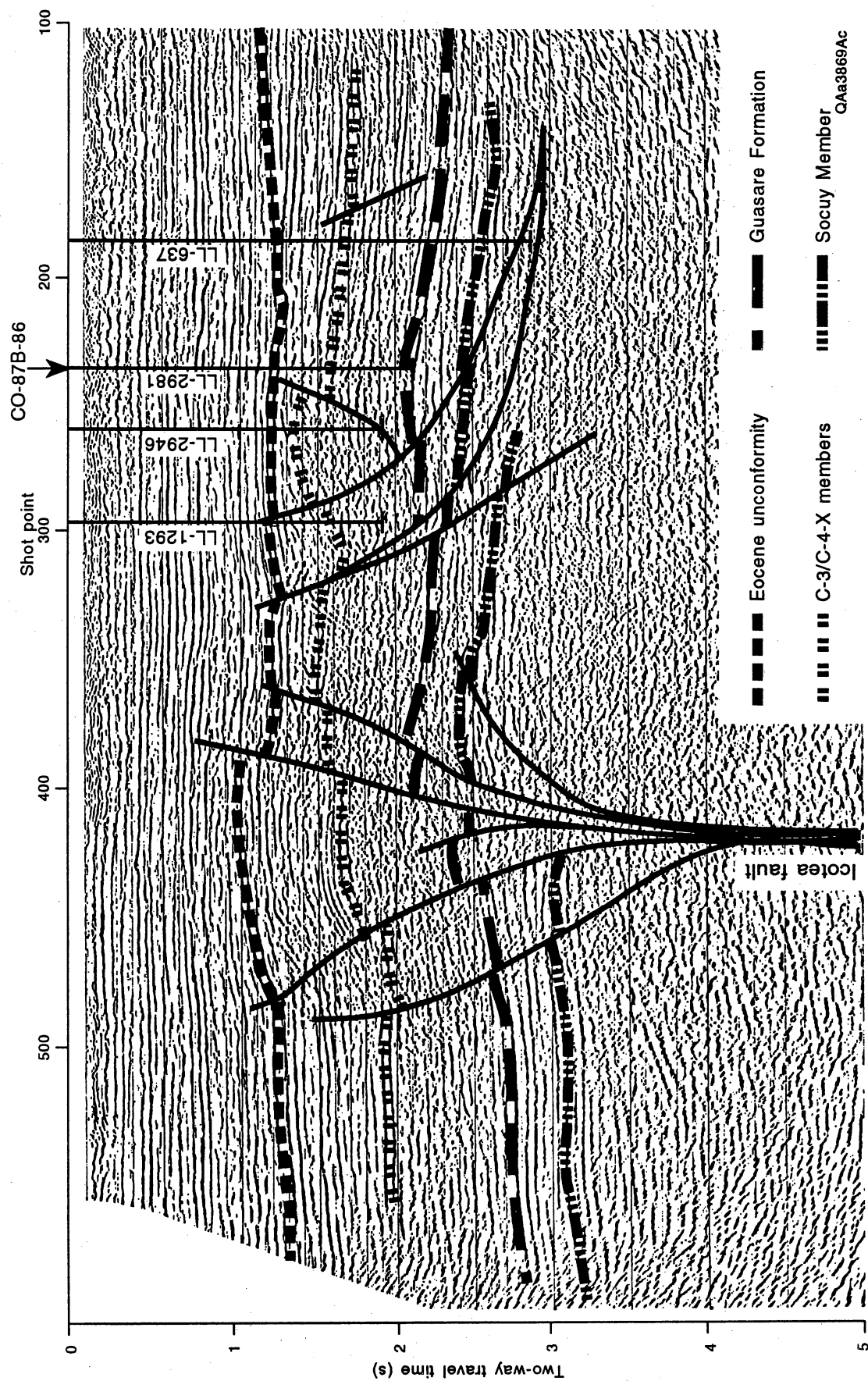
Figure 34. Seismic line CO-90B-30.

56
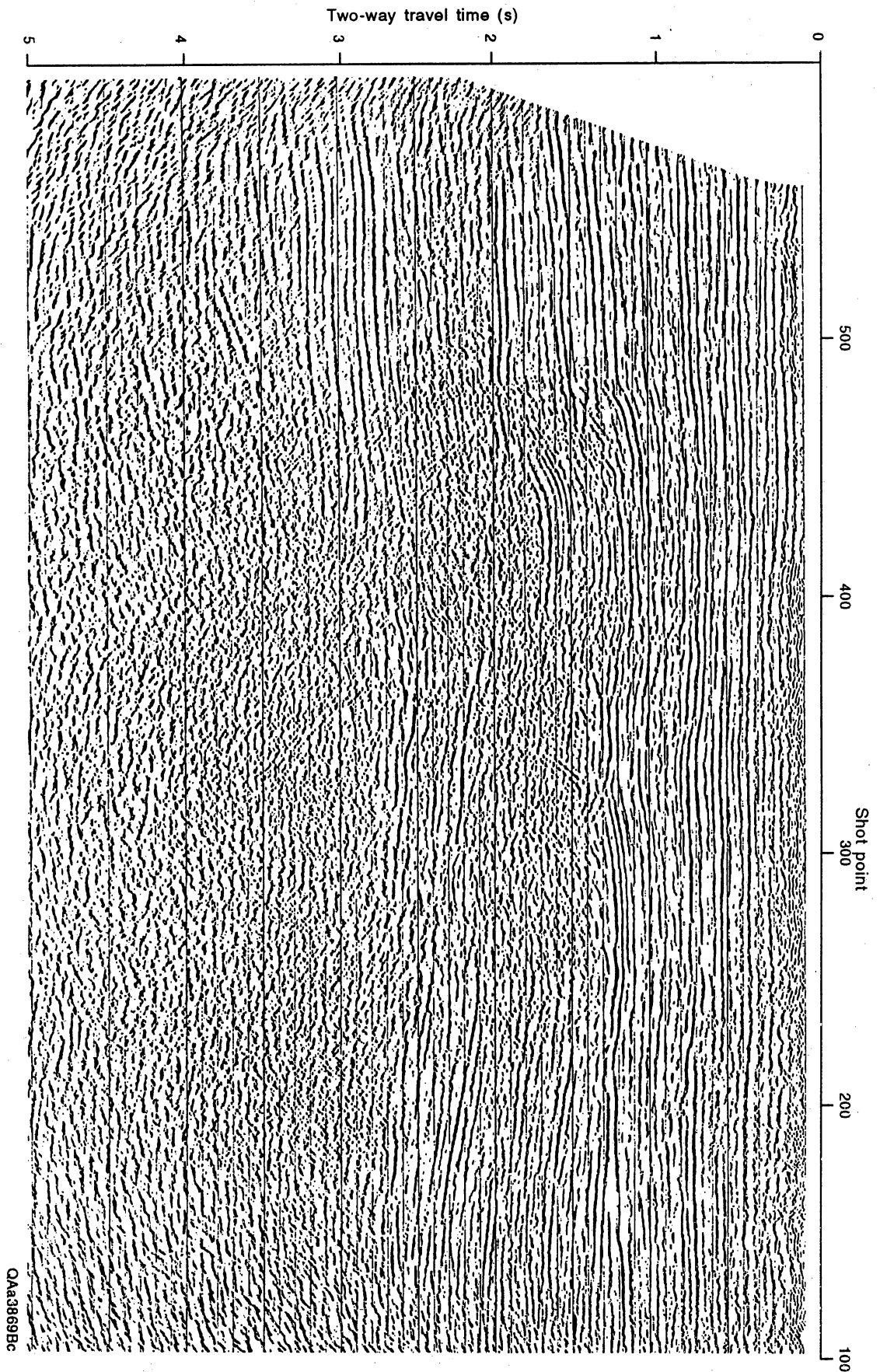
Figure 34. Continued.

QAa3869Bc

Seismic Line CO-87B-27

This line is a north-northwest (Maraven area) to south-southwest section that shows the VLA-534 well (SP-85), located on the downthrown side of the master fault that offsets the whole section from the basement to the unconformity (fig. 15). At SP-80 there is a reverse fault. The LL-917 well (SP-125) is located in an upthrown block bounded by two reverse faults. This area contains several splinter reverse faults. For example, well LL-917 is intersected by a normal fault in the C-2-X Member and a reverse fault in the C-6-X Member. The LL-1303 well, projected to SP-140, is intersected by the reverse fault that was earlier recognized in log correlations where there is 130 ft (39.6 m) of repeat section in the C-3-X Member. The LL-1245 and LL-2547 wells are located in an area where the seismic resolution is poor. Between SP-190 and SP-260 there are two thrust faults that offset lower Eocene, Paleocene, and Cretaceous strata. This seismic line is parallel to structural cross section 7 (fig. 28) where there are several major structural features that include reverse faults intersecting the LL-917 and LL-1303 wells. In contrast, the LL-2547 well is in an unfaulted block.

Seismic Line CO-87B-72

This line is a southwest-northeast seismic profile that transversely crosses the southern part of the master fault and terminates near the main fault in the east (fig. 35). The VLA-761 well is located in the upthrown block of the master fault. A reverse fault that offsets the entire sequence is located at SP-940. To the right are two reverse faults that cut only Paleocene and Eocene strata. The LL-1001 well (SP-890) is also cut by a reverse fault that has 180 ft (54.9 m) of repeat section. The LL-833 well is located in a structural block, bounded by a fault (probably the central fault) toward the northeast. Cretaceous strata in this area are offset by reverse faults. The LL-895 well (SP-650) is located on the upthrown block of the main fault.

Seismic Line CO-87B-76

This section (fig. 14) is intersected by lines CO-87B-27 (SP-635) and CO-90B-30 (SP-435). The VLA-751 well is located in the south horst of the Maraven area (Maraven reports). The VLA-53 well (SP-85) is located in a downthrown block, between the master fault on the southwest and a reverse fault on the northeast in a structurally complex zone. The LL-1169 well (SP-590) is located in the area of reverse faults. This well has a repeat section of 60 ft (18 m) in the C-4-X Member and the LL-2937 and LL-2942 wells also have a repeat section of 60 ft (18 m) in the C-4-X Member. The LL-2937 and LL-2942 wells are located in the upthrown block of the main fault (SP-520). This fault intersects the LL-2901 well where there is 1180 ft (360 m) of missing section in the B and C Members.

Dipmeter Analysis

The 47 dipmeter logs available in the Lagoven area and 32 in the Maraven area (fig. 7) provided a large data base for dipmeter analysis. All the dipmeter interpretations (app. A) were incorporated in the seven structural maps (see figs. 41 through 47). However, no dipmeter data were available for the C-7-X Member. The dipmeter analysis allowed calculation of dip and strike, identification of areas with major dip changes in the northwest part of the field, and quantification of fault and fold attributes. Sixty percent of the dipmeter data were presented in tabular form, showing only selected levels that were used in the structural map of some level. Vectorial diagram (arrows) presentations composed the remaining 40 percent of the dipmeter data, showing a graphic presentation of direction and magnitude of dip versus the depth of the well at the correlation point. We used these either for interpretation of the structural maps or for interpretation of major dip change on transverse sections, faults, and folds.

Identification of folded and faulted areas is useful for targeting sites for further field development. For example, the LL-827 well in structural cross section A (fig. 20) is in a structurally complicated zone that has a 54° southeast dip associated with the reverse fault and another minor normal fault. The dipmeter

log of the LL-1169 well, located in section 6 (fig. 26), indicates dip changes in all members along the crest of a small fold near reverse faults that intersect the C-4-X Member.

LL-1310 Well

The LL-1310 well (fig. 36) exhibits a missing section of 180 ft (54.9 m) in the C-4-X Member. The dipmeter log of this well shows a normal dip of 3° (azimuth 80°) in the Upper C-3-X Submember. Dip gradually changes in the Middle C-3-X Submember and finally reaches a maximum of 12° (azimuth 210°) in the drag zone, below which the fault zone is present. Below the level of the fault strata have a normal dip of 3° (azimuth 85°).

LL-1293 Well

Figure 37 shows part of the Lagunillas and La Rosa Formations that have an average dip of 4°. Below, separated by the Eocene unconformity, the B-9-X and C-1-X Members have an average dip of 28°. The correlation between the LL-1293 and LL-3250 wells (fig. 38) in the C-4-X Member illustrates the use of a dipmeter log to aid in determining true stratigraphic thickness compared to true vertical thickness. Figure 38 also illustrates the difficulty in correlating the high-dip zone in structurally complex areas.

VLA-724 Well

This well is faulted in the Lower C-4-X Submember at 6,800 ft and has 100 ft (30.5 m) of missing section (fig. 39). The dipmeter log of this well shows a structural dip that increases from 6° to 12° adjacent to the fault in the footwall block, an erratic distribution in the faulted zone at 6,800 ft and the drag zone of the other block, and finally the normal dip of approximately 5°. The transverse section shows the interpretation and the drag zone in the upthrown block at 6,850-6,950 ft, the drag zone in the downthrown block at 6,650-6,775 ft, and in the faulted zone at 6,775-6,850 ft.

LL-1095 Well

Figure 40 illustrates the correlation in the Middle to Lower C-4-X Submembers and C-5-X Member between the LL-1095, LL-3286, and LL-3055 wells. Below the top of the C-5-X Member there are few thickness changes. The LL-1095 well shows a slightly thicker section in the C-4-X Member as well as a repeat section (90 ft [27.4 m]) by reverse faulting at the top of the C-5-X Member. Above this level the dipmeter log shows dips over 35°, and below, average dips of only 6°.

Another well with the same dipmeter response to a reverse fault is the LL-946 well that is faulted in the C-3-X Member and exhibits a maximum dip of 53° in the upthrown block and 10° in the downthrown block. This is a typical dipmeter response in the LL-652 area in beds cut by reverse faults where the dip of the beds reaches a maximum dip on the upthrown block, indicating a drag zone and return to lowest values in the downthrown block.

Structure Maps

Structure plays a significant role in the trapping of hydrocarbons in the advanced stages of development and depletion of the field. The integration of fault-surface maps, structural cross sections, paleostructural maps, seismic interpretations, dipmeter analyses, and structural tops allowed the mapping of the important horizons that include the Eocene-Miocene unconformity and tops of the C-1-X, C-2-X, C-3-X, C-4-X, C-5-X, C-6-X, and C-7-X Members (figs. 41 to 48).
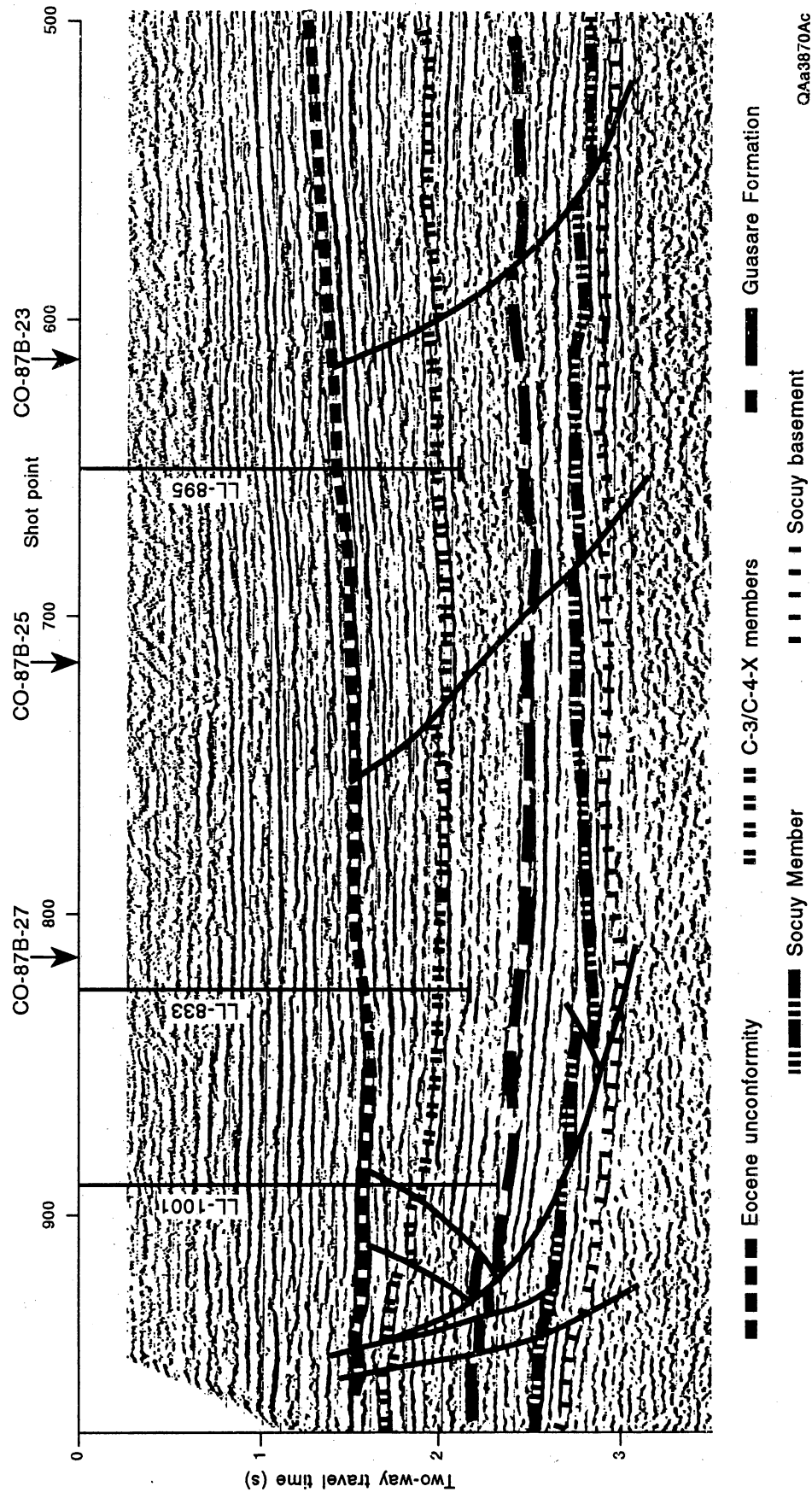
Figure 35. Seismic line CO-87B-72.

Legend:
- Eocene unconformity
- Socuy Member
- C-3/C-4-X members
- Socuy basement
- Guasare Formation
- Ac

QAa3870Ac

60

Figure 35. Continued.

QAa3870Bc

Shot point

Two-way travel time (s)

61
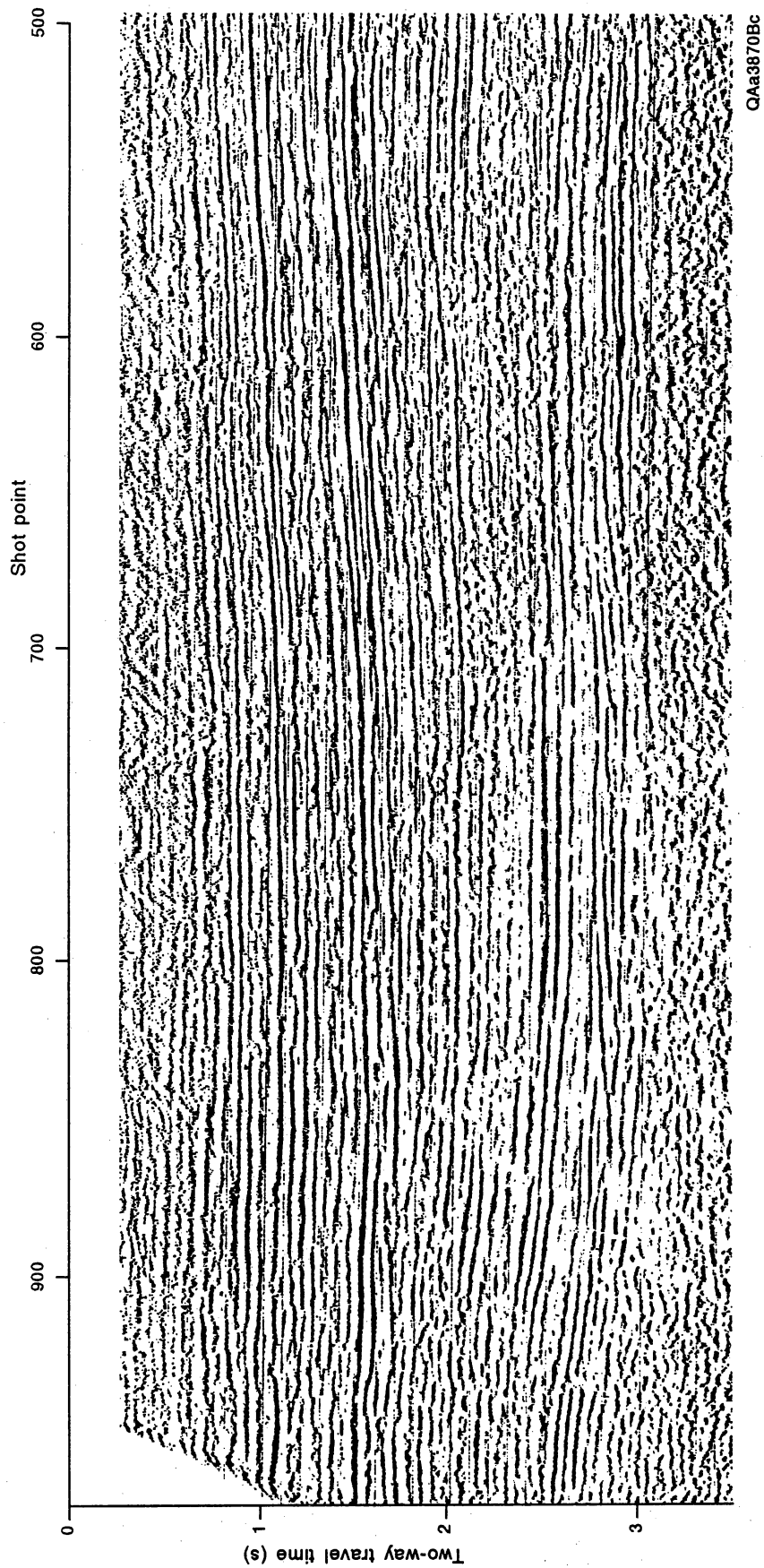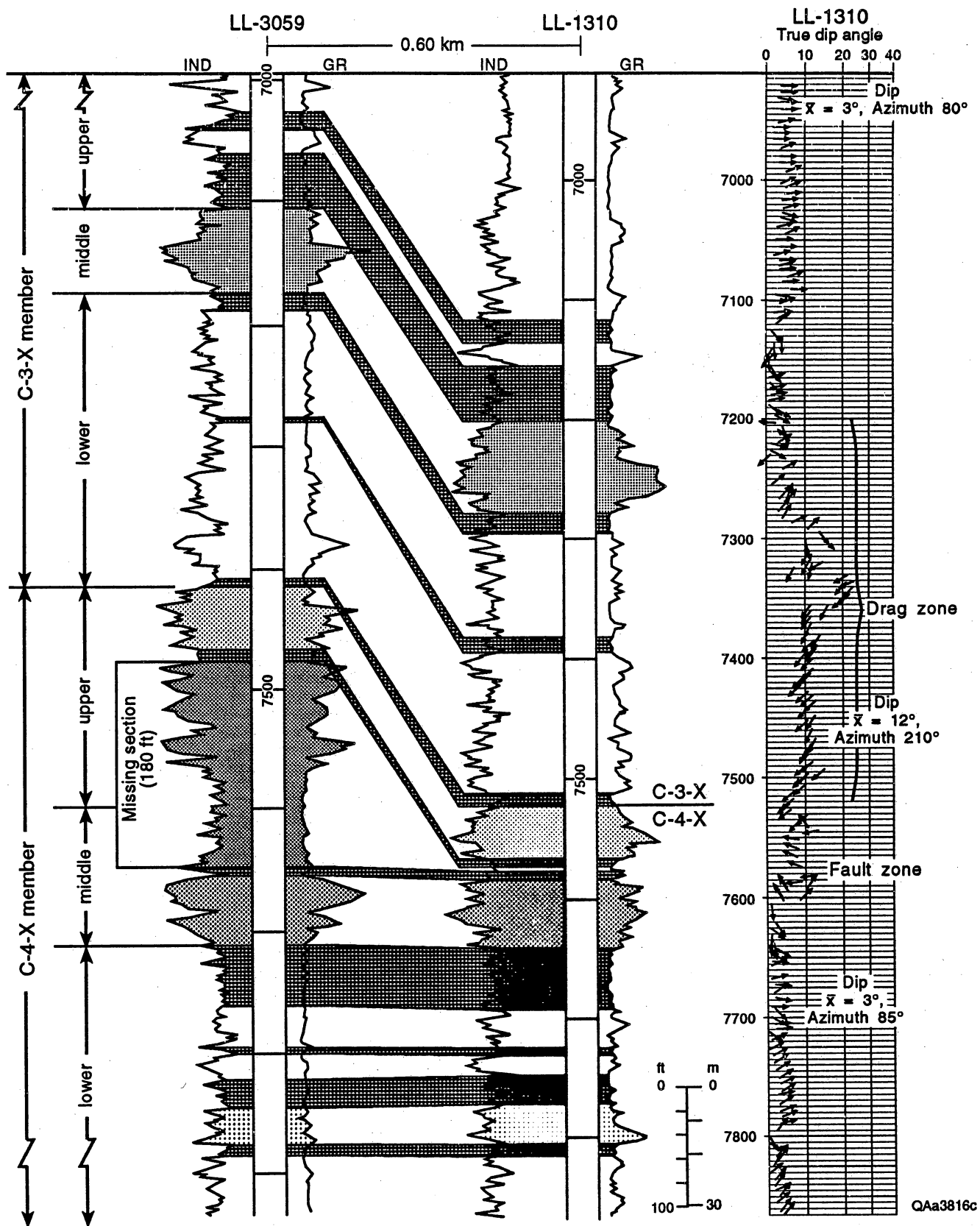
Figure 36. Major dip change due to faulting in the LL-1310 well interpreted from dipmeter log.

62
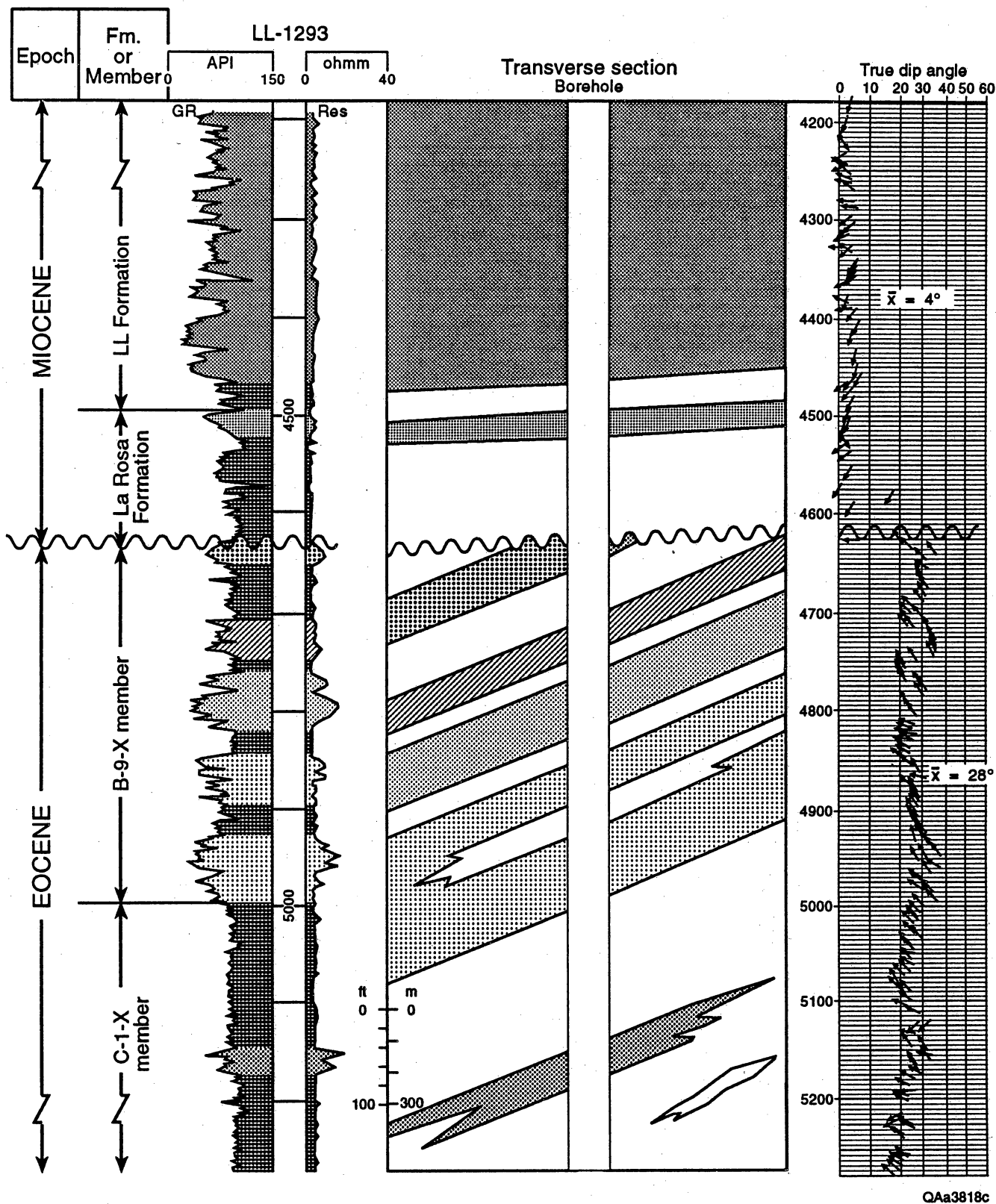
Figure 37. The LL-1293 well with dipmeter showing an angular unconformity.
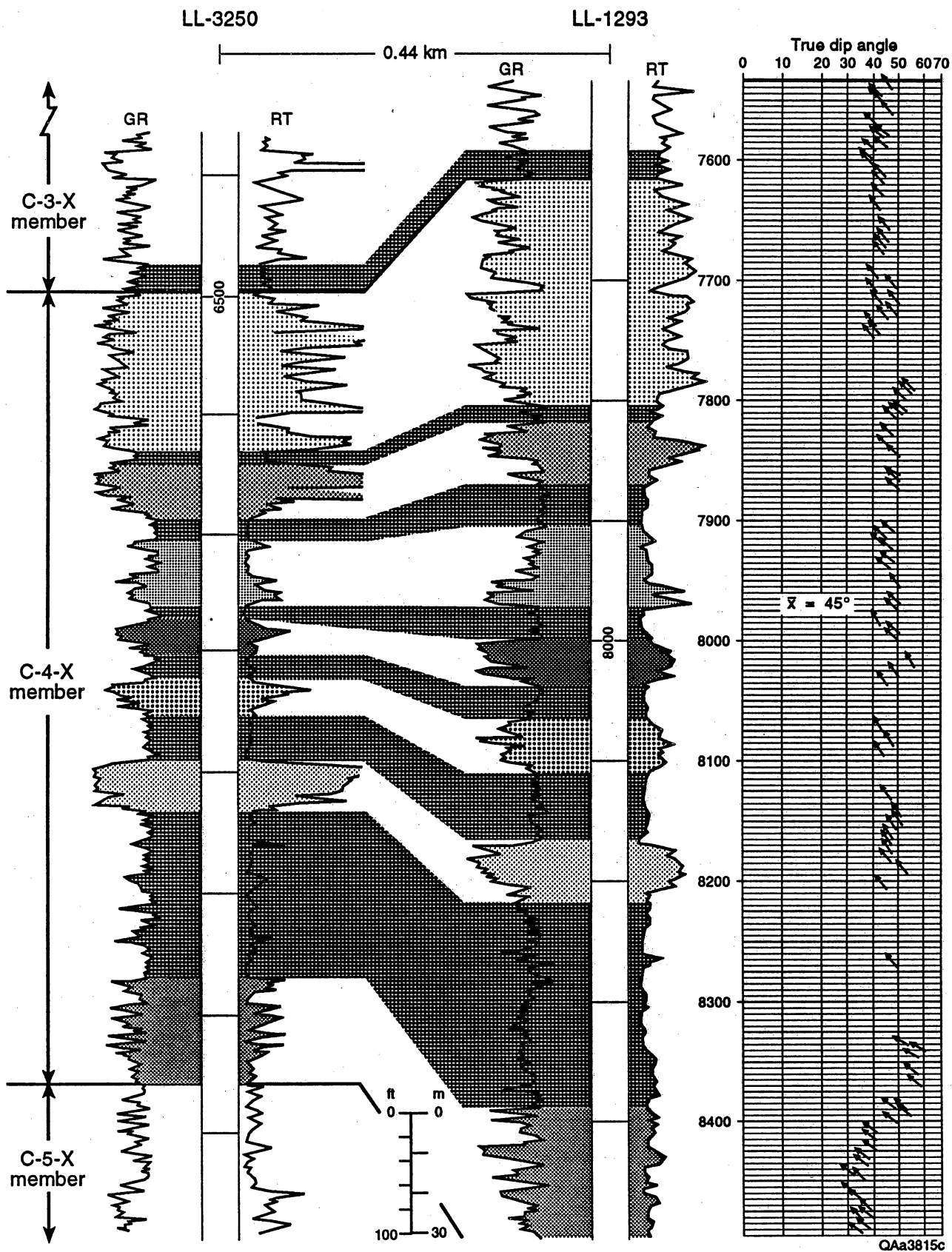
Figure 38. Stratigraphic correlation between the LL-1293 (high-dip zone) and LL-3250 (low-dip zone) wells.

64

Figure 39. Drag zone associated with normal fault in the transverse section of VLA-724 well.

65

Figure 40. Dipmeter response to reverse fault that intersects LL-1095 well.
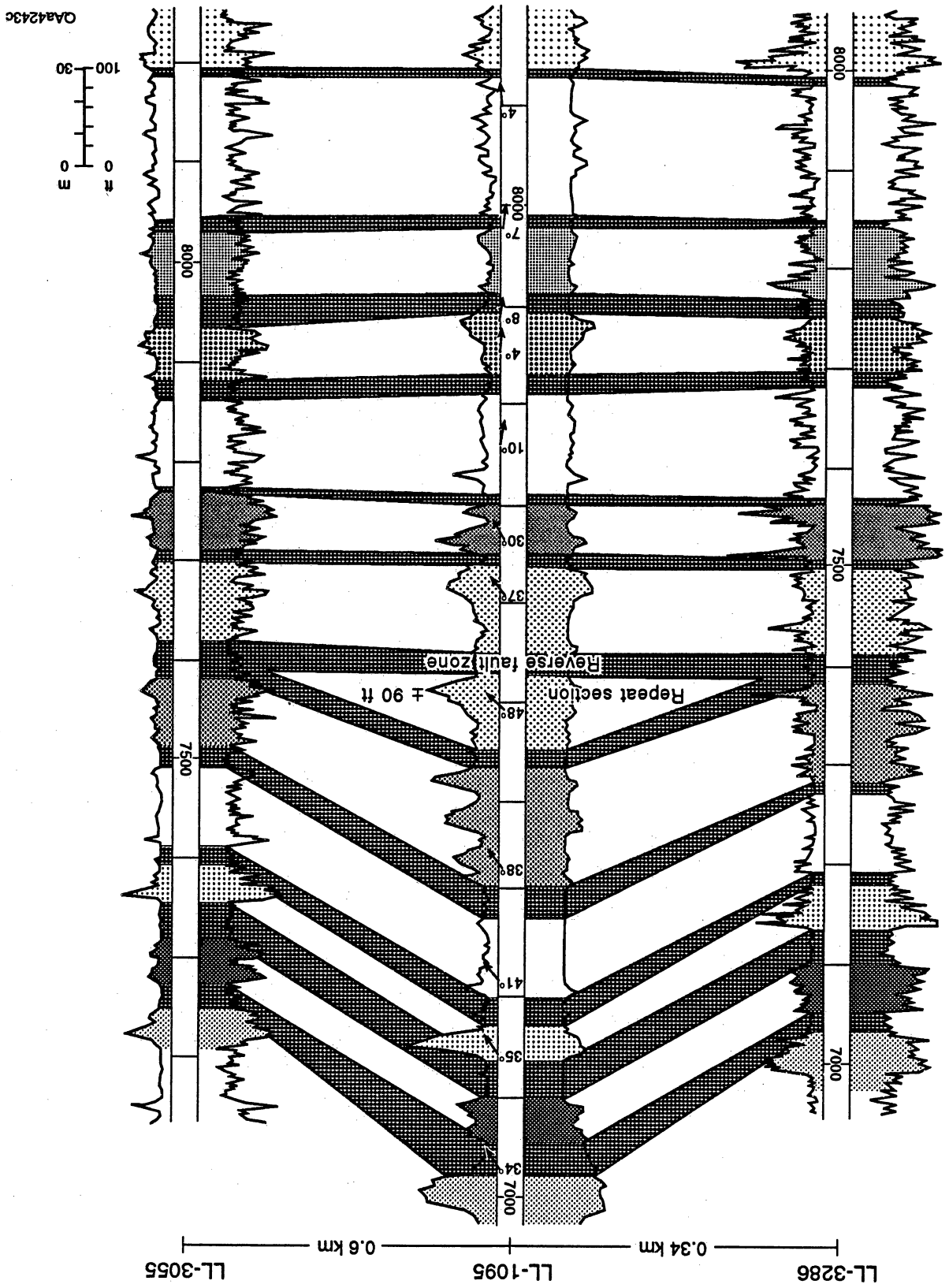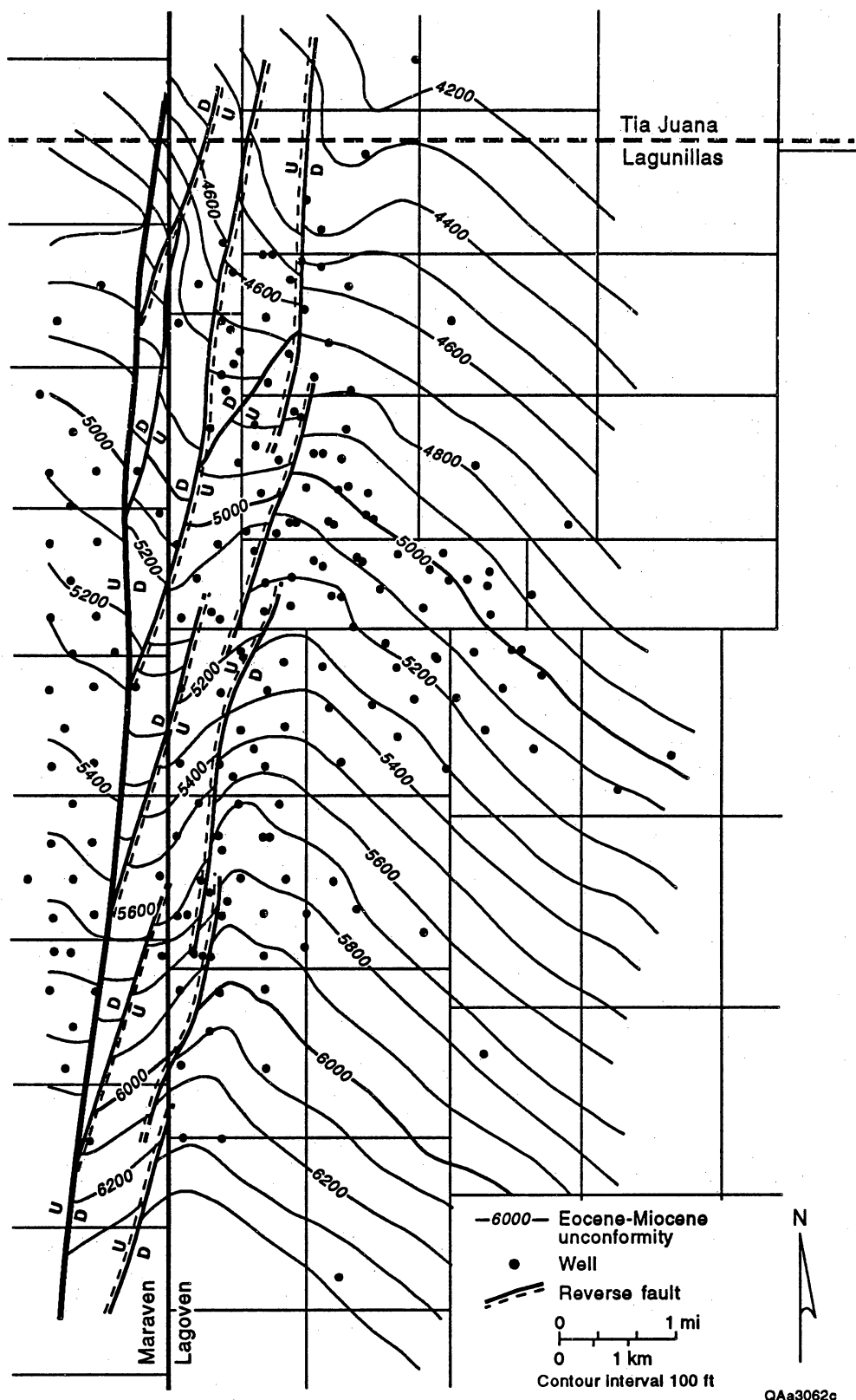
Figure 41. Structure map contoured on the Eocene-Miocene unconformity.

67
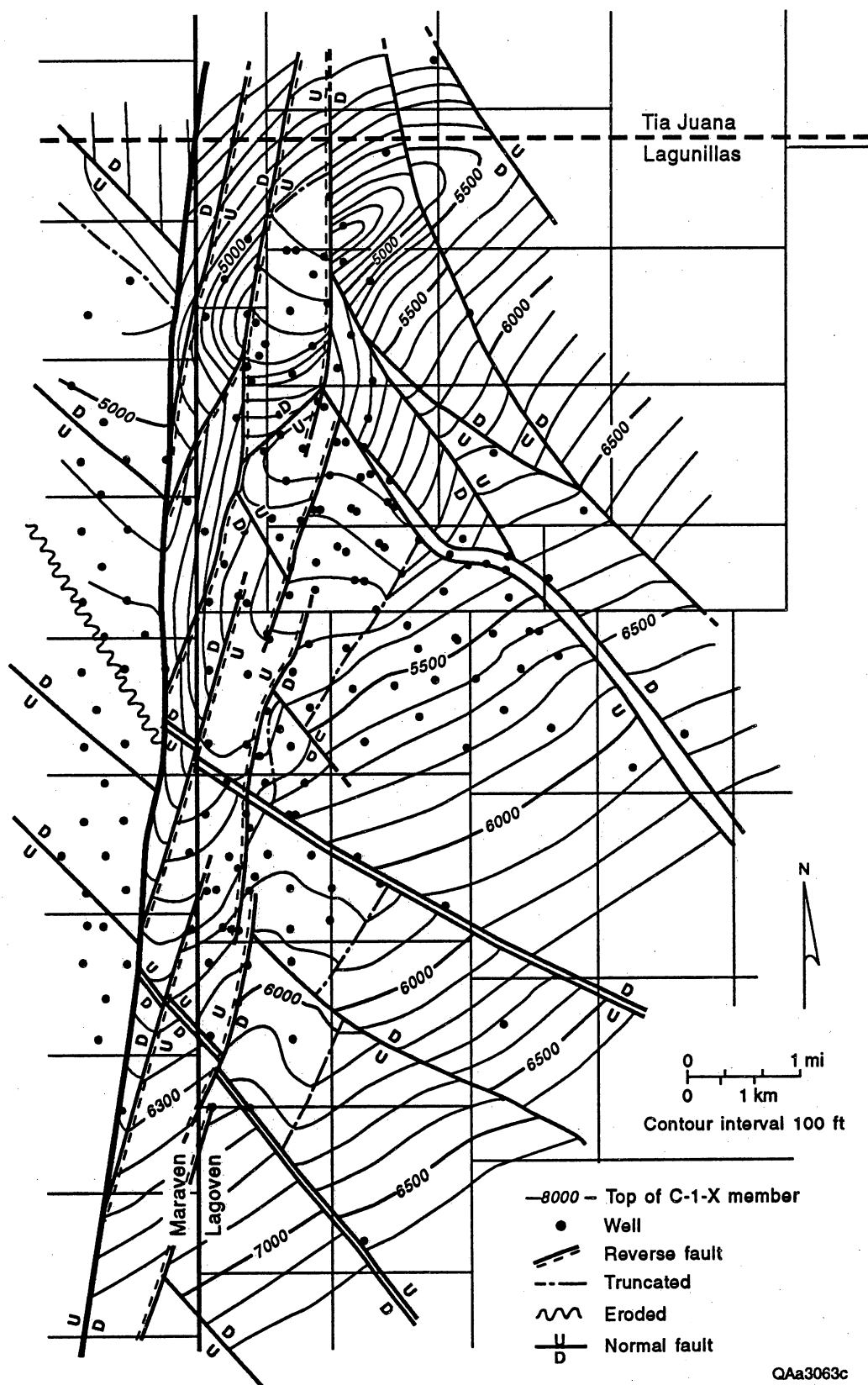
Figure 42. Structure map contoured on top of the C-1-X Member.

Tia Juana
Lagunillas

5000
5500
6000
6500
5500
6500
5500
6000
6000
6500
6000
6500
6300
6500
7000

Maraven
Lagoven

N

0   1 mi
0   1 km
Contour interval 100 ft

—8000— Top of C-1-X member
●   Well
⫽⫽   Reverse fault
---   Truncated
∿∿   Eroded
U
—   Normal fault
D

QAa3063c

68
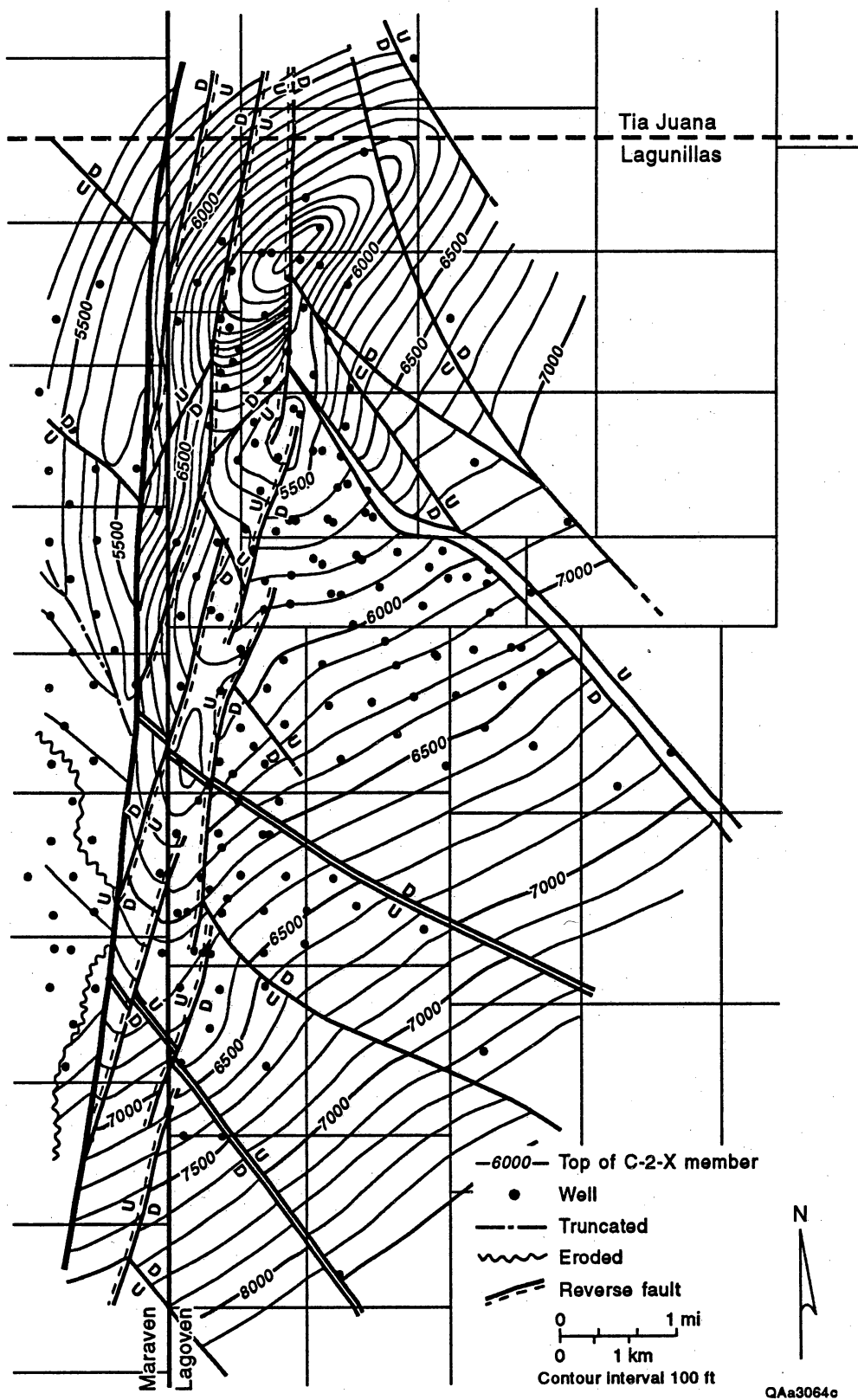
Figure 43. Structure map contoured on top of the C-2-X Member.

69
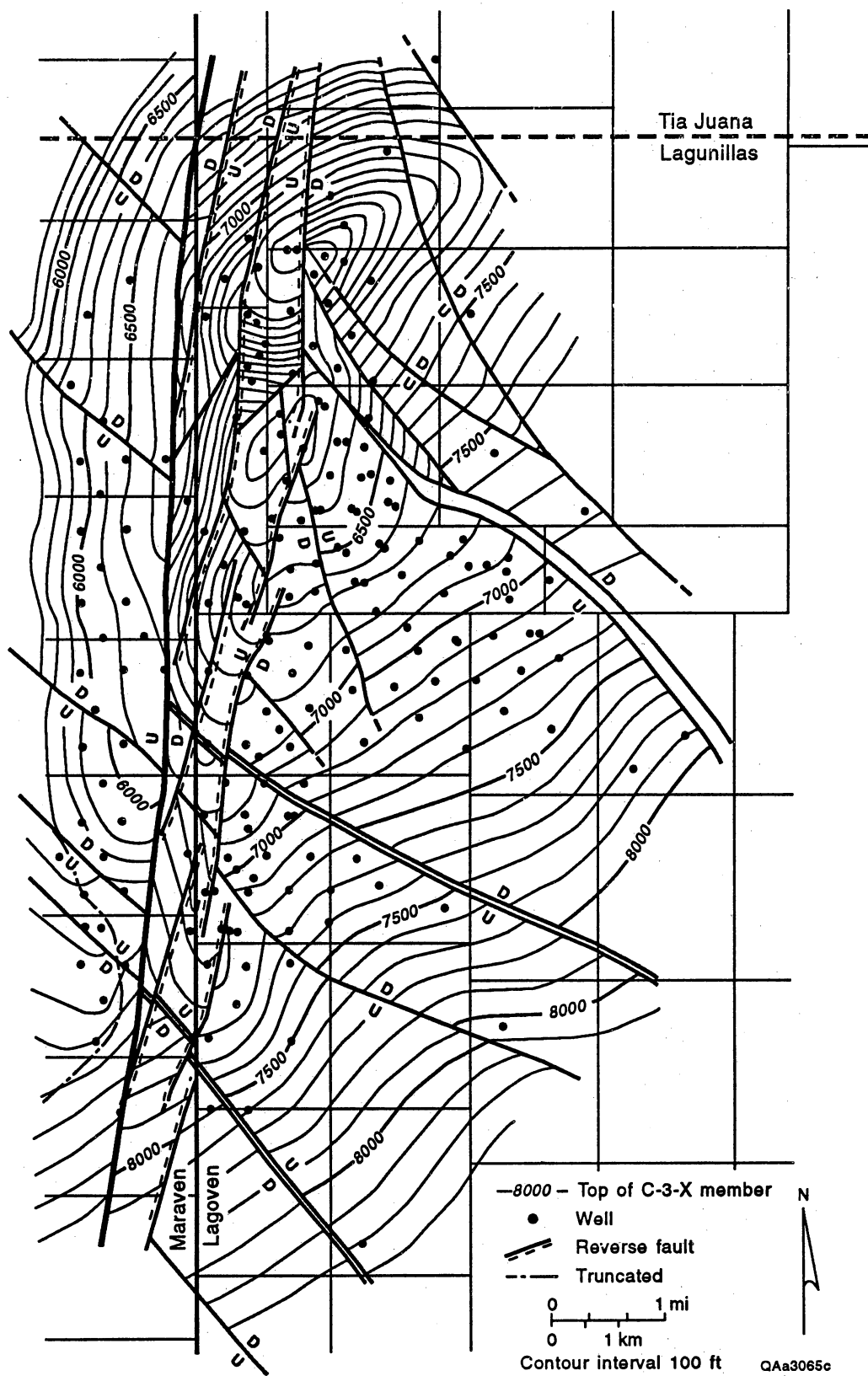
Figure 44. Structure map contoured on top of the C-3-X Member.

70
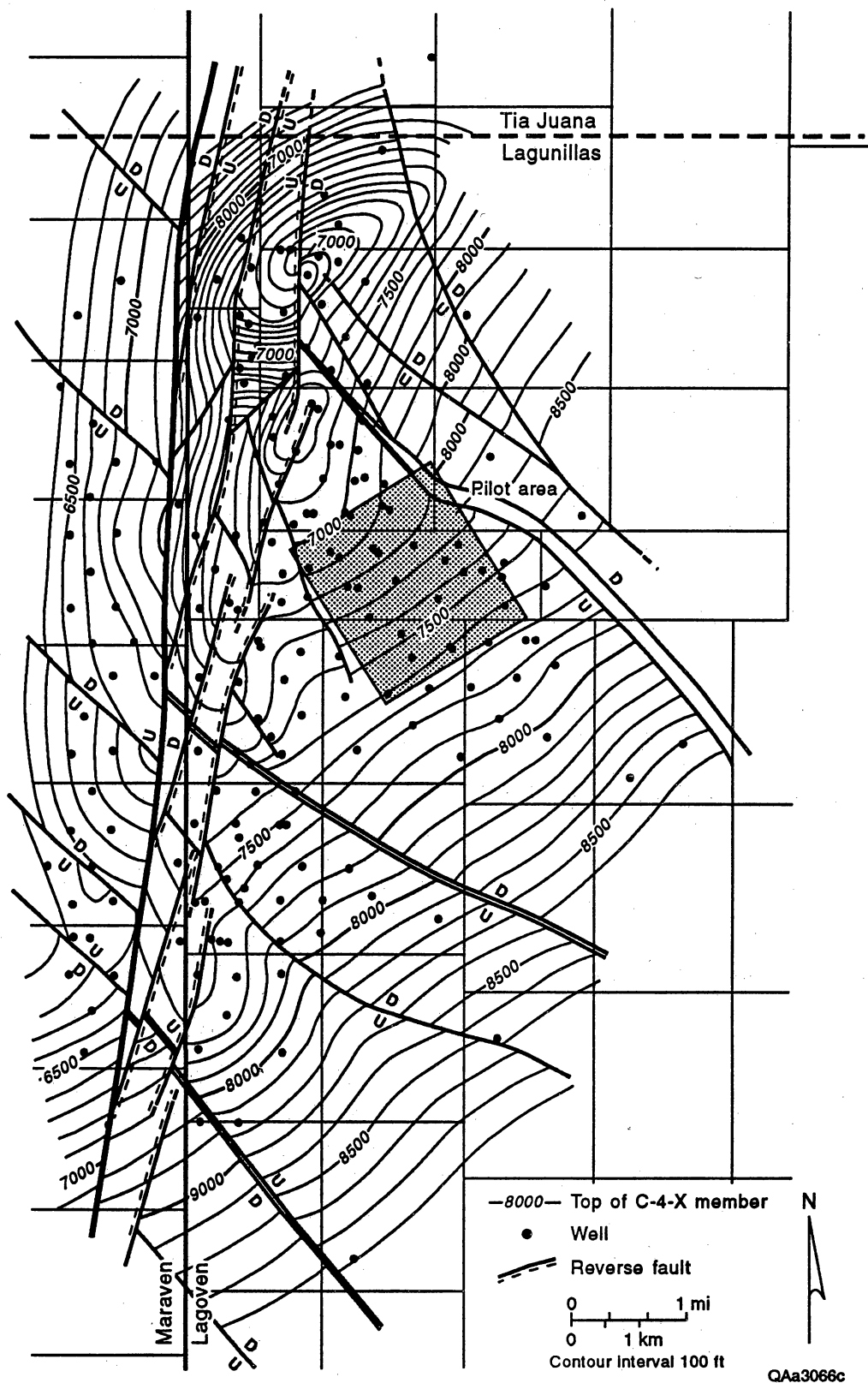
Figure 45. Structure map contoured on top of the C-4-X Member, with location of waterflood pilot area in the Upper C-4-X Submember.
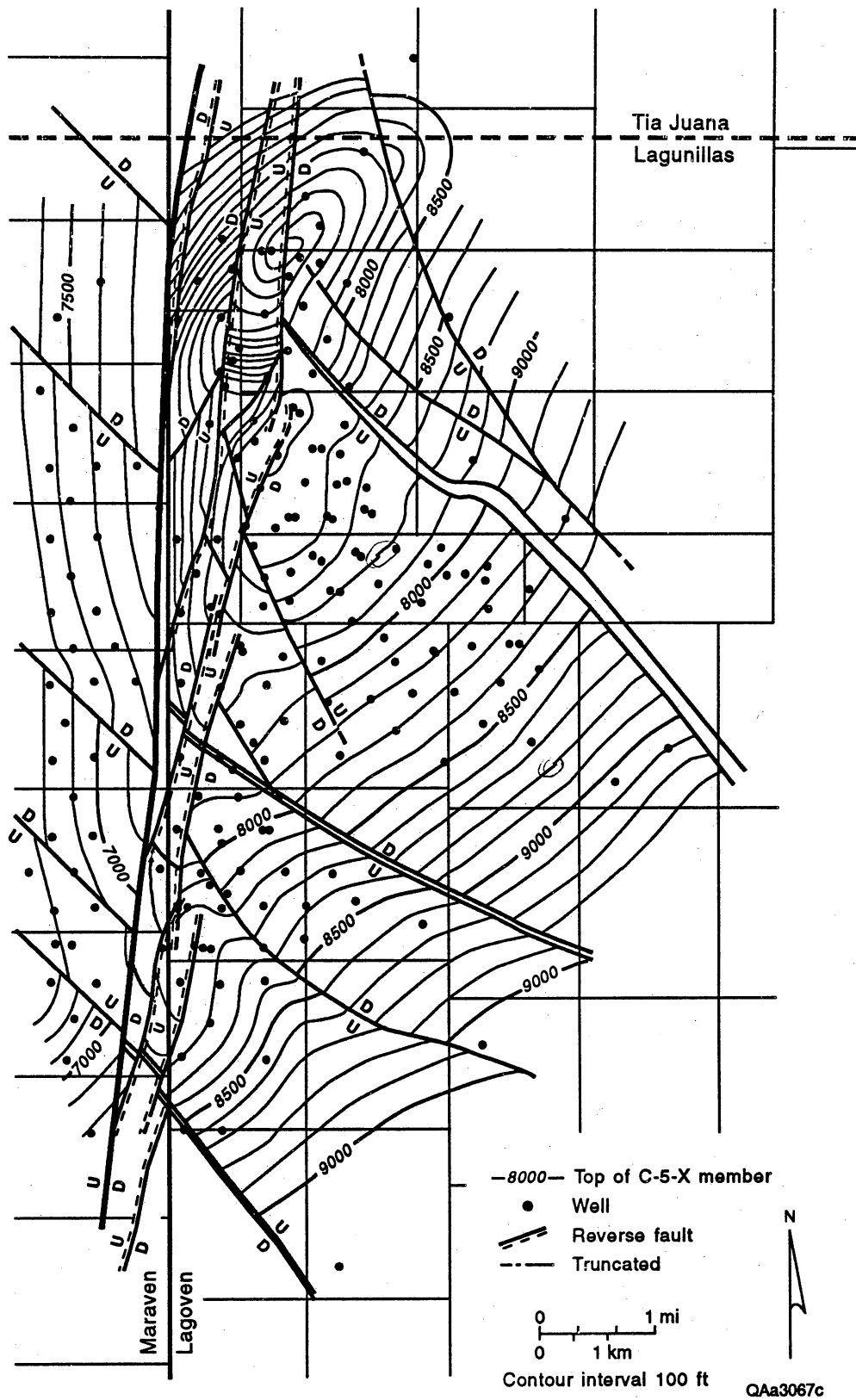
Figure 46. Structure map contoured on top of the C-5-X Member.

Tia Juana
Lagunillas

Maraven
Lagoven

—9000— Top of C-6-X member
● Well
Reverse fault

0   1 mi

0   1 km

Contour interval 100 ft

N

QAa3068c
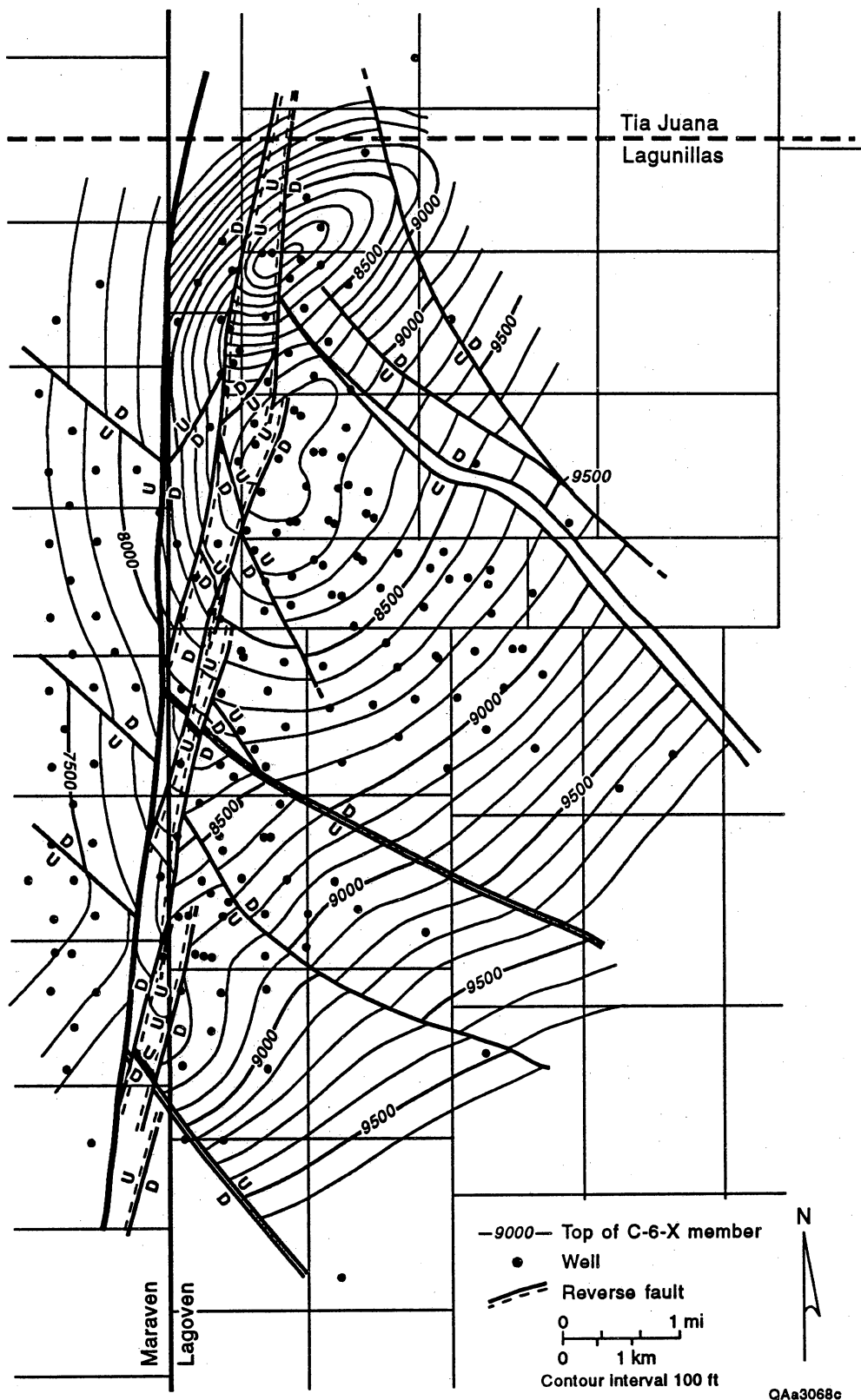
Figure 47. Structure map contoured on top of the C-6-X Member.
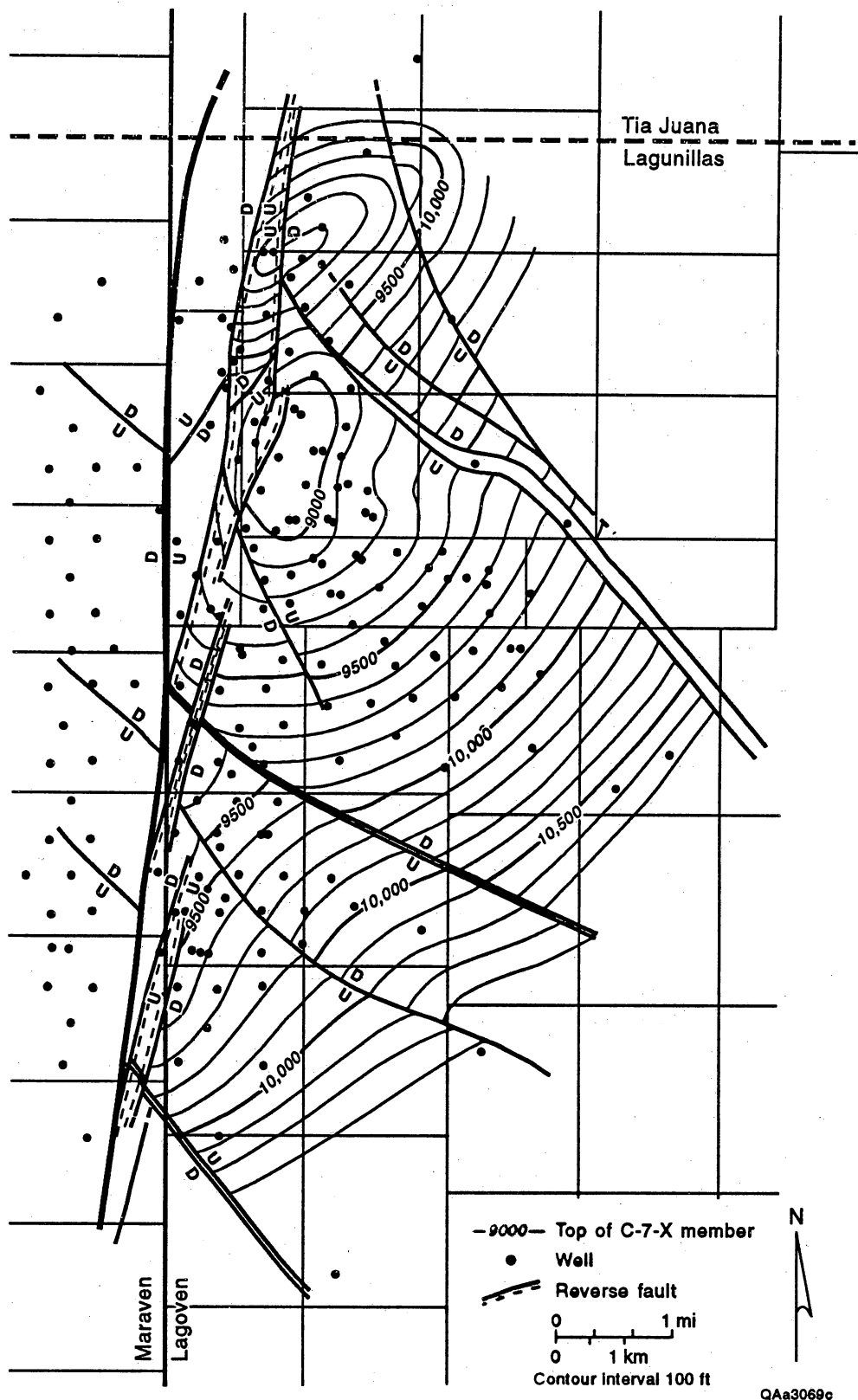
Figure 48. Structure map contoured on top of the C-7-X Member.

The following labels appear within the figure:

Tia Juana
Lagunillas

Maraven
Lagoven

—9000— Top of C-7-X member
● Well
Reverse fault

0 — 1 mi
0 — 1 km
Contour interval 100 ft

N

QAa3069c

The structure map of the Eocene-Miocene unconformity indicates a gentle dip to the south-southwest (3° to 8°). Post-unconformity deformation in the western part of the study area increases slightly northward and was caused by northwest-southeast compression after the unconformity, reflected by the north-northeast-trending reverse faults.

From the C-1-X to the C-7-X Members the maps show similar trends in the central and southern parts of the field. The main north-northeast-trending, elongate anticline has a steeply dipping (25°) west-northwest limb and a gently dipping (5°) southeast limb. The crest of the anticline is deformed by subparallel reverse faults. The reverse faults have a N12°E strike in the central part and N5°E in the southern part of the field. The anticlinal crest in the central part of the area is in the vicinity of the LL-1095 well (concession A-225).

The crest of the "north fold" has a strike of N40°E, with a northwest-dipping flank and 7° dipping flank to the southeast. The crest of this fold is located between the LL-2946 and LL-827 wells and is offset 0.9 mi (1.5 km) from the crest of the main anticline. The area between the two crests (fig. 43) is the most structurally complex in the field because (1) local structures are discontinuous and untraceable across reverse faults, (2) it is associated with a reactivation zone between the main fault and the reverse fault, (3) three fault patterns are present in this area, where some displacement was transferred to other faults or folds at terminations against other faults, (4) abrupt dip increases occur in the upthrown block of the reverse fault, and (5) it is associated with two antithetic faults. The structure maps, supported by seismic lines CO-90B-28 (fig. 33) and CO-90B-30 (fig. 34) and structural cross section 9 (fig. 30) clearly show that the "north fold" continues to the north-northeast. In areas affected by the reverse fault the dipmeter response is erratic, with dips in several directions.

The C-1-X Member (fig. 42) shows a continuously steep slope toward the crestal high with flattening of dip, indicating that this member was deeply eroded over the whole area, especially on the crest of the main anticline and the north fold. In the Maraven area the C-1-X Member is absent in the central and southern part and is truncated in the north. The C-2-X Member is eroded in the southern part of the Maraven area. Overlapping of structural contours is a mapping problem with the construction of the reverse fault overlap. Confusion is eliminated by dashing a line parallel to the fault on the upthrown block, indicating a zone of fault overlap.

Several normal faults and one zone of reverse faults are present in maps of C-1-X to C-7-X Members. Faulted wells area summarized in table 4. The study area was divided into eight fault-bounded zones (fig. 12). Zone I is located in the northeast part of the study area in the downthrown block of the north reverse fault and the main fault. This zone is in part the continuation of the "north fold" toward the northeast. Zone II is the upthrown block between two reverse faults in the north crest of the "north fold." Zone III is located in the western, high-dip flank in a downthrown block between a reverse fault on the east and the master fault on the west. Zone IV is the central part of the area bounded by two reverse faults in the east and west, an antithetic fault in the north and the central fault in the south. Zone V is located in a structurally simple area, bounded by the main fault in the north, the central fault on the south, and a reverse fault on the west. Zone V is the largest and most productive area in the field. Zone VI is located in the southwestern part of the field and is associated with the reverse fault and the master fault. Zone VII is located in the southeastern part of the study and is bounded by the central fault to the north, the south fault to the south, and the reverse fault to the west. Zone VIII is the western part of the Maraven area.

Fault Analysis

The LL-652 area contains multiple fault patterns that reflect a multistage tectonic history. Because of the structural complexity, all available data were used to characterize the field. Net-thickness maps of key intervals as well as subcrop maps were made to best evaluate the structural heterogeneity and fault history. The objective of the fault analysis was to characterize all 17 of the principal faults in the field and consisted of the following steps: (1) analysis of the net-thickness map of the C-3-X Member (fig. 49), with the objective of determining controls on thickness variations across faults possibly related to

NET THICKNESS (ft)

≥670

630-670

590-630

550-590

510-550

≤510

● Well

—·—·— Truncated

Reverse fault

0   1 mi

0   1 km

Contour interval 40 ft

QAa3473c
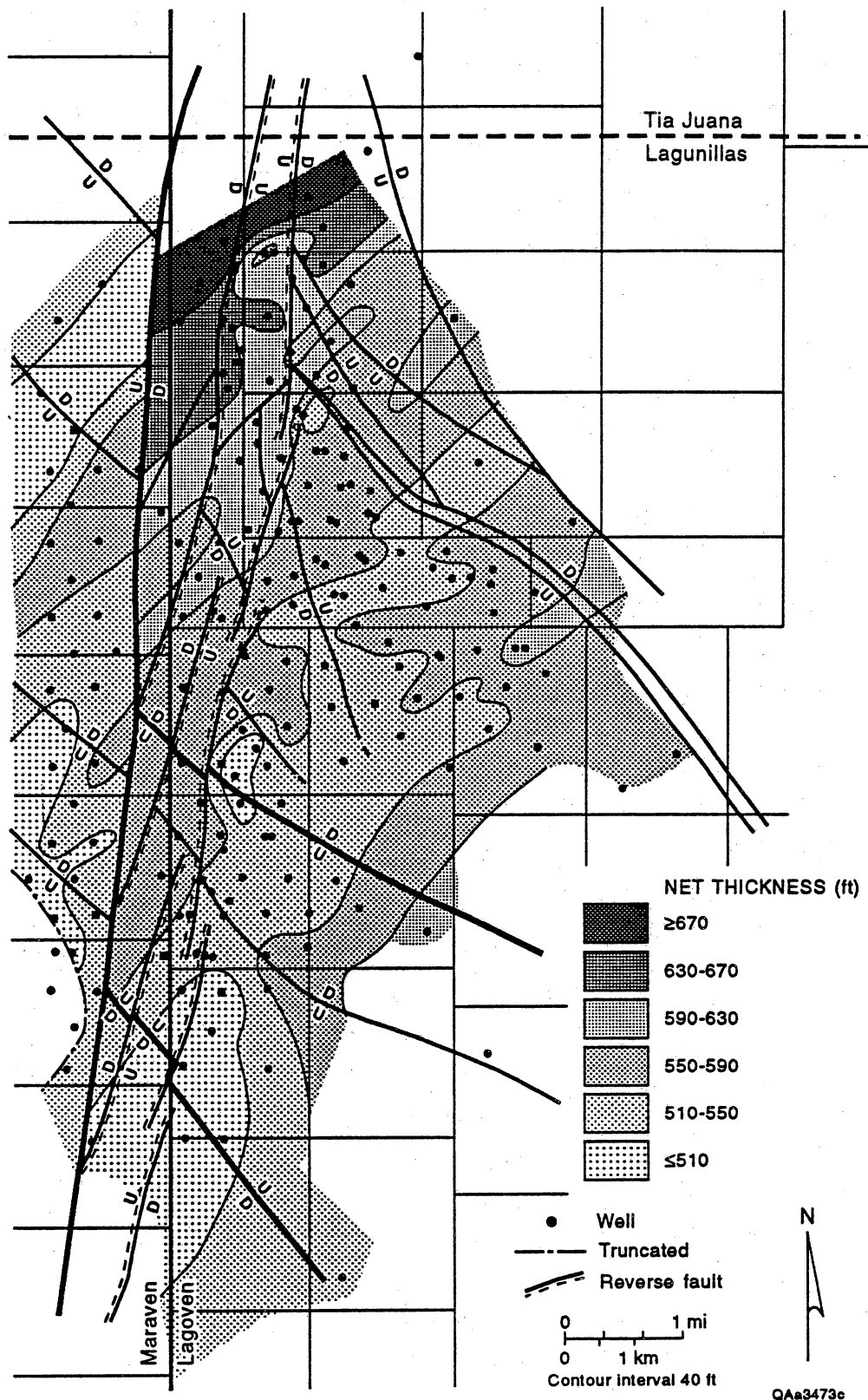
Figure 49. Total thickness map of the C-3-X Member.

syndepositional tectonism, (2) compilation of a subcrop map to analyze the intensity of the faulting and determine the relative age of faults, used in combination with the Miocene-Eocene unconformity structural map, and (3) analysis of fault characteristics, with the final objective of documenting the basic elements (dip, strike, and displacement) of the faults and fault type and seal. Horizontal separation of faults was determined to evaluate reservoir connectivity as an important factor in the evaluation of the potential hydrocarbon accumulation. This analysis was conducted in conjunction with investigation of pressure variations across faulted blocks. Fault-compartment geometries were delineated to document structural compartmentalization.

Net Thickness of C-3-X Member

Net thickness of the C-3-X Member was mapped to evaluate syndepositional tectonism because (1) the C-1-X and C-2-X Members were truncated on the western side of the master fault, and (2) 40 percent of the wells are not deep enough to entirely penetrate the C-4-X Member. The net-thickness map of the C-3-X Member (fig. 49) reflects the general northeast-trending depositional patterns. East of the master fault there is a constant increase in thickness toward the north, from less than 500 ft (152 m) in the south to more than 650 ft (198 m) in the north. On the western side of the master fault thickness varies from less than 500 ft (152 m) in the south to 590 ft (180 m) in the central part of the field and less than 500 ft (152 m) in the north. These net-thickness trends are different on either side of the master fault, reflected by an abrupt increase in interval thickness along the downthrown side of the fault, especially in the north part of the field. These variations can be explained by either deposition controlled by syntectonic growth faults or by strike-slip fault movement. Syntectonic deposition could have produced a rollover anticline associated with a normal listric growth fault as a result of bending of the hanging-wall fault block as it conformed to the curve of the fault. However, this theory is problematic because the majority of growth faults dip toward the basin and are parallel or subparallel to the coastline. The master fault is also associated with net-thickness changes in the northern part of the field, away from the southern depocenter where such net-thickness changes are expected. Strike-slip movement could also have occurred, because lateral displacements may juxtapose dissimilar stratigraphic sequences as observed in the LL-652 area. Strike-slip tectonics can also be inferred from anomalous variations in the amount of stratigraphic separation across the fault profile (Harding, 1985). A credible identification of strike-slip faults requires several combinations of profile and map criteria in regional areas (Harding, 1990) and should be confirmed with other criteria that refute alternative interpretations, but they are beyond the scope of this study.

Subcrop Map

A subcrop map of stratigraphic intervals below the Miocene unconformity (fig. 50) exhibits erosion of the B members along the crest of the anticline in the north fold and in the main anticline to the south fault. On the limbs of the anticline there is a gradual truncation of the C-1-X Member, and the B members appear away from the crest. On the downthown side of the main fault the B-9-X to B-4-X members were not eroded. Also in the high-dip zone, many B members were preserved on the downthrown side of the master fault in the central and northern parts of the fields.

In the Lagoven concession erosion was controlled by normal faults. Greatest erosion occurred in the Maraven area. The degree of erosion increases from north to south; in the north, only the B-9-X Member is preserved, and in the south the C-3-X Member is truncated. On the east side of the master fault all the normal faults control the degree of erosion and truncation between individual blocks, but on the west side the normal faults do not control the degree of erosion and truncation between blocks.

Reverse faults represent the youngest deformation in the area and do not control the degree of truncation between individual blocks. This is evident in the southern and central part of the study area, where there are few important differences between the downthrown and upthrown fault blocks where the same member is normally present. However, in the north fold there is a marked difference in thickness of
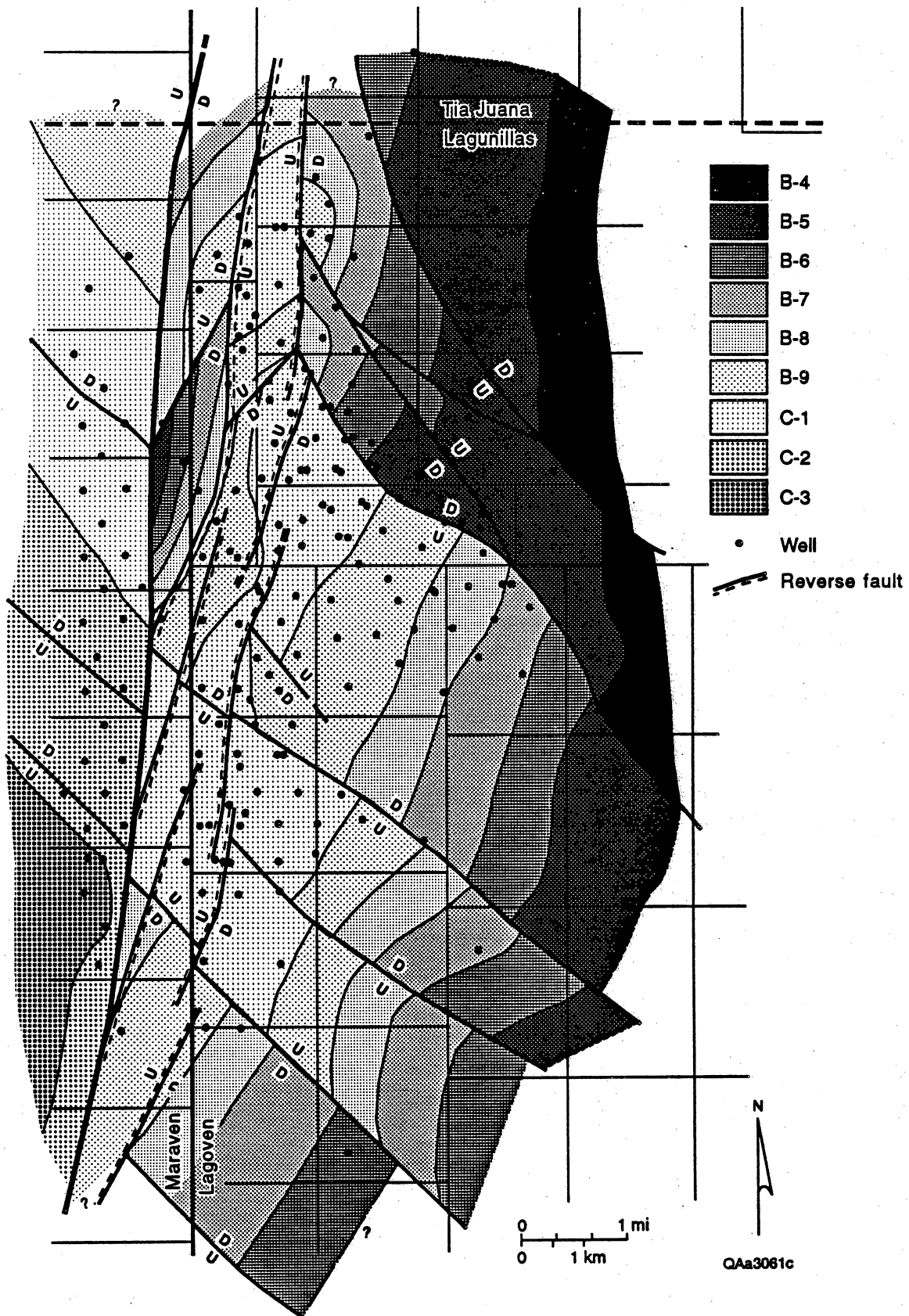
Figure 50. Subcrop map of stratigraphic intervals below the Eocene-Miocene unconformity.

preserved section between the central upthrown block where the C-1-X Member is truncated and the downthrown block, an important indication of reactivation of two reverse faults along the older normal faults. The paleostructural map of the C-3-X Member (fig. 19) reinforces this interpretation and shows that the main fault is continuous northward, where it changes strike in concession A-224 and forms a reactivation surface for the eastern reverse faults.

Fault Characteristics

Tectonic Features in Cores

The structure map on top of the C-3-X Member (fig. 44) shows the location of the eight cored wells in the LL-652 area. Tectonic features from cores are summarized in table 3. Tectonic features include microfaults, fractures, fault breccia, and faulted zones.

Microfaults are present in the C-3-X to C-7-X Members in all the cored wells, except in the LL-846 well, which contains most disrupted core in this study. Figure 51 shows an example of a normal microfault (8,826 ft) and a reverse microfault (8,952.5 ft) in the LL-3080 well. Another example of a normal microfault is at 7,737.5 ft in the LL-3074 well (fig. 52b).

There are excellent examples of fractures in the C-3-X to C-7-X Members in the LL-2850, LL-3074, LL-3075, LL-3080, LL-3140, and LL-3282 wells. The LL-3282 well has the greatest abundance of fractures, followed by the LL-3140 well. Figures 53 and 54 show examples of fractures in the LL-3140 (9,075 ft and 8,902 ft) and LL-3074 wells (7,752 ft) and multiple combinations of fractures and microfaults at 7,429 ft in the LL-2425 well.

Zones of fault breccia, occurring at 9,036 ft and 9,168 ft in the LL-3140 well (fig. 52a), may be associated with minor faults not recognized from well correlation. There are also tectonically disrupted beds at 9,175 ft in this well.

The LL-3282 well represents the best example of a faulted zone (45 ft [13.7 m] thick) (fig. 55). The log response is anomalous, showing a 90-ft (27.4-m) trend (from 8,090 ft) of low resistivity with a reading of 6 ohm-m (shallow) and 10 ohm-m (deep) resistivity as an excellent example of fluid invasion in a fracture zone, with indications of pervasive fractures. The gamma ray (GR) log shows an average, almost unvarying trend of 75 API, caused by an effect that reflects nearly vertically tilted beds associated with a reverse fault (fig. 55). The cored section in the LL-3282 well has other zones with tectonic features such as beds tilted 30° (8,095 to 8,170 ft), 10-15° (8,074 to 8,078 ft), and an intensely fractured zone (8,115 to 8,134 ft) (fig. 56). The zone may represent post-depositional tectonism where a reverse and normal fault intersect in the area of the LL-3282 well.

Fault-Seal Analysis

Criteria for analyzing fault seals are based mainly on theoretical studies of rock types juxtaposed at faults (fig. 57). Additionally, Bouvier and others (1989) empirically derived the variation in clay-smear potential across the fault surface by relating clay source-bed thickness and position of clay source-beds to the displacement at a given point on the fault surface, thereby extending fault-sealing characteristics beyond simple sand-to-shale juxtaposition. Field studies indicate that complete smearing on fault surfaces may extend down fault planes from shale footwall-cutoffs for distances equivalent to at least six times the thickness of the shale source layer.

Two variables must be assessed when evaluating fault-plane seal: (1) juxtaposition of lithology, and (2) clay smear. Figure 57b is a diagrammatic illustration of these variables showing sandstone juxtaposition but separation by a clay-filled fault zone about 3 ft (0.9 m) wide. These variables for the evaluation of fault seals in hydrocarbon traps, as outlined by Smith (1980) and Bouvier and others (1989),

Table 3. Tectonic features observed in cores in the LL-652 area.

Well	Cored Interval (ft)	Member	Microfault Depth (ft)	Microfault Type	Fractures (ft or %)	Other Tectonic Features
LL-846	78	C-3/C4	-	-	-	-
LL-2425	206	C-3/C4	1) 7429 2) 7377	N N		Combination of fractures and microfaults
LL-2850	428	C-3/C4	7727	N	7612-15 (3), 7251-52 (1) 7276-85 (9)	
LL-3074	376	C-3/C4	1) 7738 2) 7577 3) 7582	N (1 cm offset) N (low angle) N	7651-52(1), 7675-76 (1) 7681-83 (2), 7691-92 (1) 7695-97 (2), 7246-48 (2)	
LL-3075	568	C-5	1) 8334 2) 7919 3) 7942	N N N	8004-05 (1), 8040-41 (1) 8038-39 (1), 8186-87 (1) 8391-92 (1), 8446-47(1)	7919 ft severely distorted SS– possibly microfaulted
LL-3080	646	C-6	1) 8726 2) 8739 3) 8826 4) 8922 5) 8953 6) 9006 7) 9013 8) 9099	N N N N R N N N	8817-19 (2), 8877-78 (1) 8723-24 (1), 9157-59 (2) 9173-74 (1), 9188-89 (1) 9196-97 (1), 9198-99 (1) 9201-03 (2), 9207-08 (1)	
LL-3140	308	C-6/C-7	9181	N	8885-8896 (30%) 8993-8910 (50%) 8917-19 (2), 8935-36 (1) 9076-85 (9), 9090-92 (2) 9118-21 (3), 9125-31 (6) 9143-45 (2), 9150-54 (4) 9156-62 (6), 9180-81 (1) 9193-98 (5), 9202-03 (1)	9036/9168 ft, fault breccia 8993 ft and 9083 ft, tectonically disrupted bed
LL-3282	662	C-4/ C-5/C-6	1) 7988	N	7292'-93 (1), 7309-10 (1) 7352'-53 (1), 7373-74 (1) 7397'-98 (1), 7935-36 (1) 7943'-73 (20%) 7974'-78 (4), 7983-86 (3) 7987'-90 (3), 7998-99 (1) 7997'-8024 (20%) 8027'-34 (7), 8041-47 (6) 8049'-53 (4), 8056-58 (2) 8074'-82 (8), 8093-98 (5) 8102'-34 (32), 8717-23 (6) 8727'-28 (1), 8742-46 (4) 8757'-59 (2), 8778-79 (1) 8677'-78 (1), 8683-85 (2) 8703'-05 (2)	8095'-70' Beds tilted about 30° 8074'-78' Everything tilted 10° to 15° 8102'-8115' intensely fractured in small pieces 8115-34' Beds tilted nearly vertically (fault effect)

N= Normal
R=Reverse

Table 4. Summary of faulted wells in the LL-652 area

Well	Conc.	Depth (ft)	Missing Section (ft)	Repeat Section (ft)	Member	Dipmeter Yes	Dipmeter No	Comments
LL-601	A-253	5550	600	-	B-X		x	
LL-827	A-224	5550	-	120	C-2-X	x		
LL-851	A-224	7490	480	-	C-4-X	x		
LL-851	A-229	6150	-	140	C-2-X	x		
LL-857	A-188	5500	-	200	B-9-X	x		
LL-904	A-229	5900	-	120	C-2-X	x		
LL-917	A-272	8410	-	110	C-6-X	x		
LL-917	A-272	6450	80	-	C-2-X	x		
LL-946	A-273	7150	-	70	C-3-X	x		
LL-962	A-226	8170	350	-	C-5-X	x		
LL-997	A-188	5970	-	160	C-1-X		x	
LL-1001	A-276	8290	-	180	C-5-X	x		
LL-1005	A-273	6790	160	-	C-3-X	x		Major dip change by fault
LL-1005	A-273	7780	-	90	C-5-X		x	
LL-1022	A-262	8630	200	-	C-4-X	x		
LL-1023	A-273	6470	-	80	C-2-X	x		
LL-1060	A-253	7200	450	-	C-2-X	x		
LL-1061	A-229	7310	150	-	C-4-X	x		
LL-1061	A-229	5700	-	90	C-2-X	x		
LL-1066	A-224	6650	180	-	C-3-X	x		
LL-1066	A-224	5650	200	-	C-1-X	x		
LL-1089	A-188	6150	-	150	C-1-X	x		
LL-1095	A-225	7550	-	90	C-5-X	x		Angle of dip increases near reverse fault
LL-1126	A-225	5840	1200	-	C-1/C-2		x	
LL-1129	A-271	7470	80	-	C-4-X		x	
LL-1159	A-229	5370	1150	-	B-X/C-1		x	
LL-1166	A-224	6490	180	-	C-3-X	x		
LL-1166	A-224	8600	450	-	C-5-X	x		
LL-1169	A-188	7705	-	60	C-4-X	x		
LL-1172	A-229	6925	100	-	C-3-X		x	
LL-1176	A-273	7520	350	-	C-4-X		x	

Table 4. Continued.

LL-1196	A-273	7470	60	-	C-3-X		x	
LL-1196	A-273	6100	-	140	C-2-X		x	
LL-1209	A-224	5540	300	-	C-1-X	x		
LL-1209	A-224	6350	180	-	C-2-X	x		
LL-1218	A-272	6940	180	-	C-2-X		x	
LL-1218	A-272	6590	-	140	C-2-X		x	
LL-1218	A-272	7590	-	60	C-4-X		x	
LL-1303	A-273	6960	-	130	C-3-X		x	
LL-1307	A-273	7700	100	-	C-4-X		x	
LL-1310	A-272	7580	180	-	C-4-X	x		Good dipmeter example in a faulted zone
LL-1312	A-225	5520	1190	-	C-1-X		x	
LL-1339	A-229	5580	900	-	B-X/C-1		x	
LL-1679	A-277	7560	650	-	C-2-X		x	
LL-1748	A-274	5950	180	-	C-1-X		x	
LL-1782	A-272	6410	-	80	C-2-X		x	
LL-1803	A-188	6970	200	-	C-3-X	x		
LL-2038	A-272	7135	140	-	C-3-X		x	
LL-2039	A-229	6040	1150	-	B-X/C-1		x	
LL-2187	A-271	7490	50	-	C-3-X		x	
LL-2191	A-228	6540	1000	-	C-2-X		x	
LL-2280	A-272	6900	70	-	C-2-X		x	
LL-2729	A-224	7240	550	-	C-4-X		x	
LL-2896	A-229	5890	1000	-	B-X/C-1		x	
LL-2901	A-225	5670	1180	-	B-X/C-1		x	
LL-2938	A-229	7070	140	-	C-3-X		x	
LL-2940	A-225	6530	50	-	C-3-X		x	
LL-2981	A-2274	6510	150	-	C-2-X		x	
LL-3055	A-225	5220	800	-	C-1-X		x	
LL-3056	A-225	6890	100	-	C-3-X		x	
LL-3056	A-225	7150	-	50	C-4-X		x	
LL-3059	A-273	6270	300	-	C-2-X		x	
LL-3060	A-225	5240	900	-	C-1-X		x	
LL-3075	A-229	5370	1150	-	B-X/C-1		x	
LL-3140	A-225	5310	1200	-	B-X		x	
LL-3141	A-225	5250	900	-	B-X/C-1		x	
LL-3144	A-225	6280	80	-	C-2-X		x	

Table 4. Continued.

LL-3149	A-273	8070	120	-	C-4-X	x		
LL-3155	A-272	7300	260	-	C-4-X	x		
LL-3173	A-225	6650	50	-	C-3-X	x		
LL-3204	A-188	8260	-	180'	C-5-X	x		
LL-3238	A-225	5200	800	-	B-X/C-1	x		
LL-3249	A-225	5670	1180	-	B-X/C-1	x		
LL-3250	A-187	7690	-	190	C-5-X	x		
LL-3261	A-229	7650	120	-	C-4-X	x		
LL-3263	A-188	6840	100	-	C-4-X	x		
LL-3267	A-225	6480	50	-	C-3-X	x		
LL-3274	A-225	7080	800	-	C-3/C-4	x		
LL-3279	A-225	7360	140	-	C-4-X	x		
LL-3282	A-188	*	*	-	C-5-X			*Faulted Zone 8090-8180 (90')
LL-3284	A-273	6490	100	70	C-2-X			
LL-3286	A-225	6350	100	-	C-3-X	x		
LL-3301	A-272	7080	920	90	C-3-X			
VLA-13	LAC-25	7500	920	-	C-3-X		x	
VLA-68D	LAC-21	8450		80	C-5-X			
VLA-93	LAC-13	6410	150	-	C-4-X	x		
VLA-96D	LAC-17	9180		100	C-6-X	x		
VLA-200	LAC-21	6220	150	-	C-3-X		x	
VLA-613	LAC-5	5300	1100	-	B-X/C-1		x	
VLA-724	LAC-17	6800	100	-	C-4-X		x	Major dip change by fault
VLA-744	LAC-5	6200	300	-	C-3-X		x	
VLA-758	LAC-5	6380	320	-	C-3-X		x	
VLA-860	LAC-13	6110	120	-	C-3-X		x	
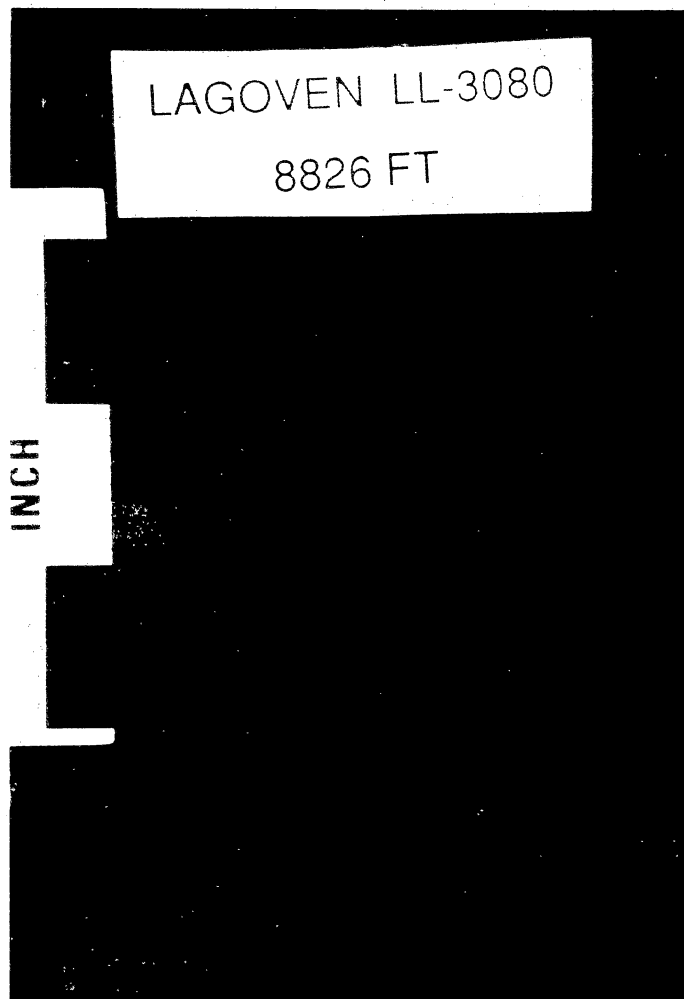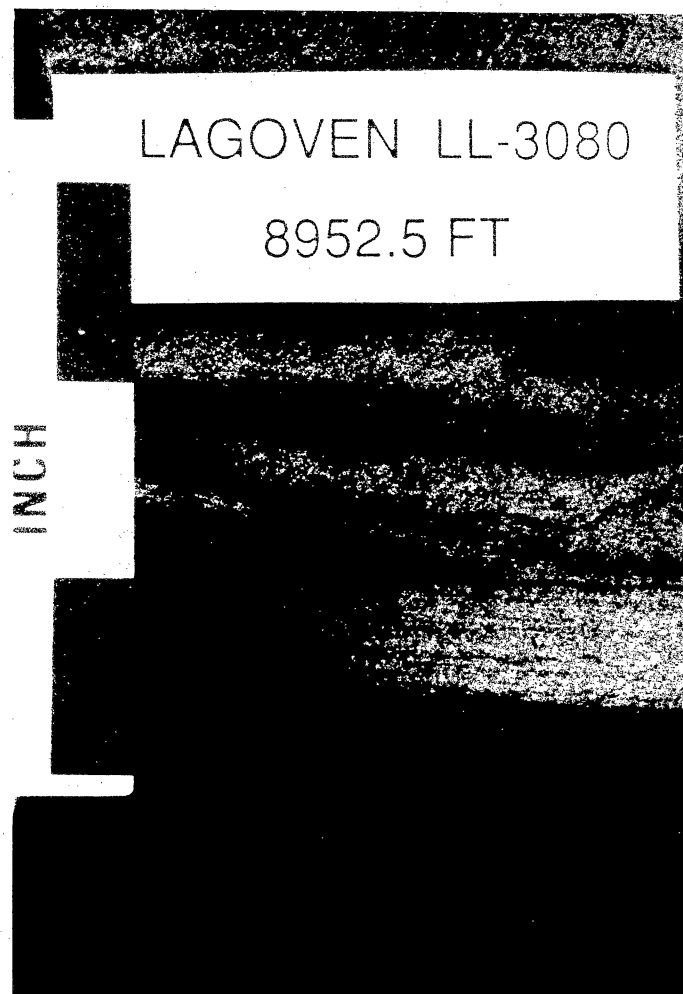
Figure 51. Photographs of (a) normal microfault and (b) reverse microfault in core of the LL-3080 well.
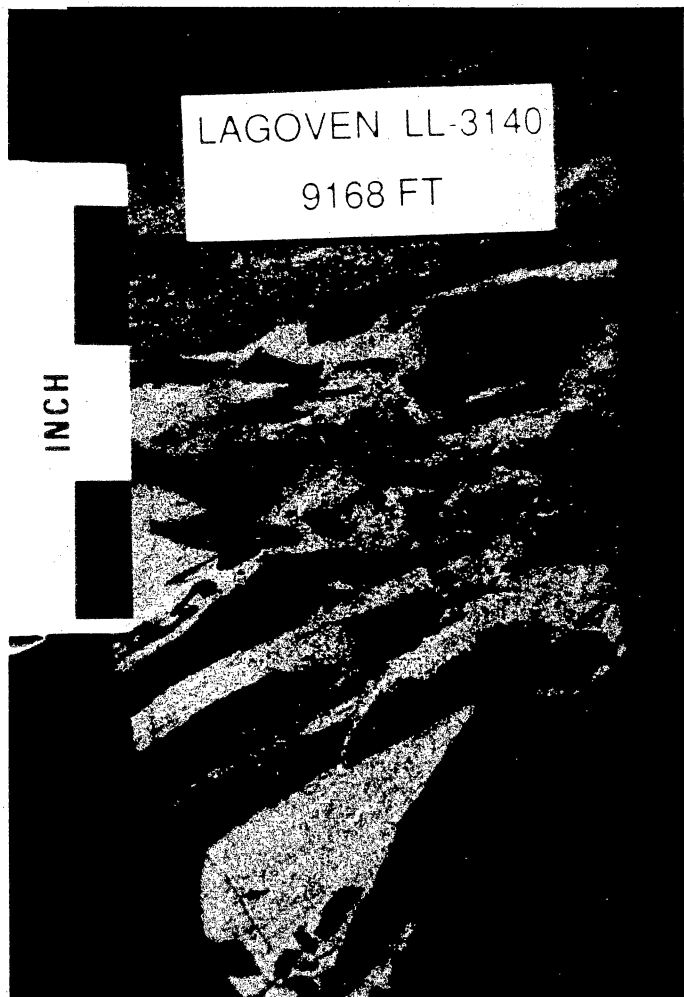
Figure 52. Photographs of (a) fault breccia in core of the LL-3140 well and (b) microfault in core of the LL-3074 well.
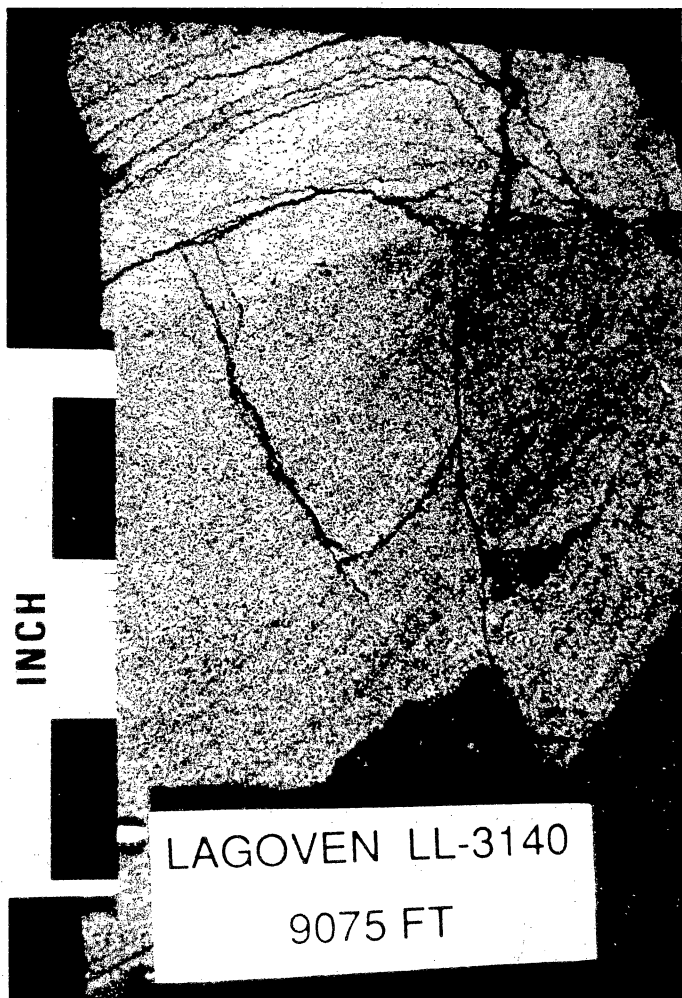
Figure 53. Photographs of fractures in core of the LL-3140 well.

(a)

LAGOVEN LL-2425

7429 FT

INCH

(b)

LAGOVEN LL 3074

7752 FT

INCH
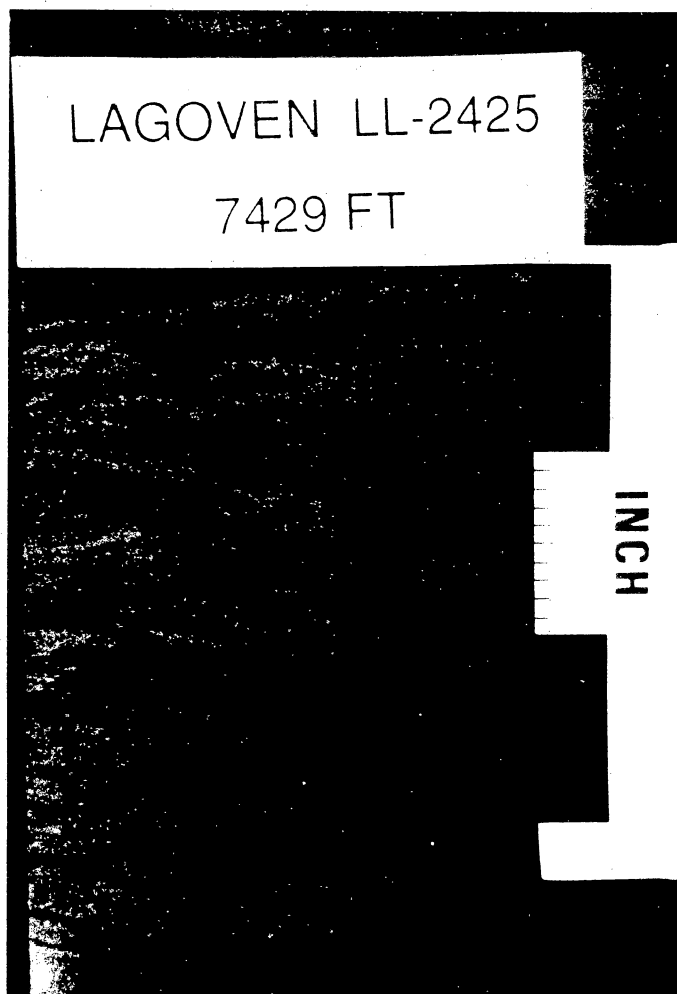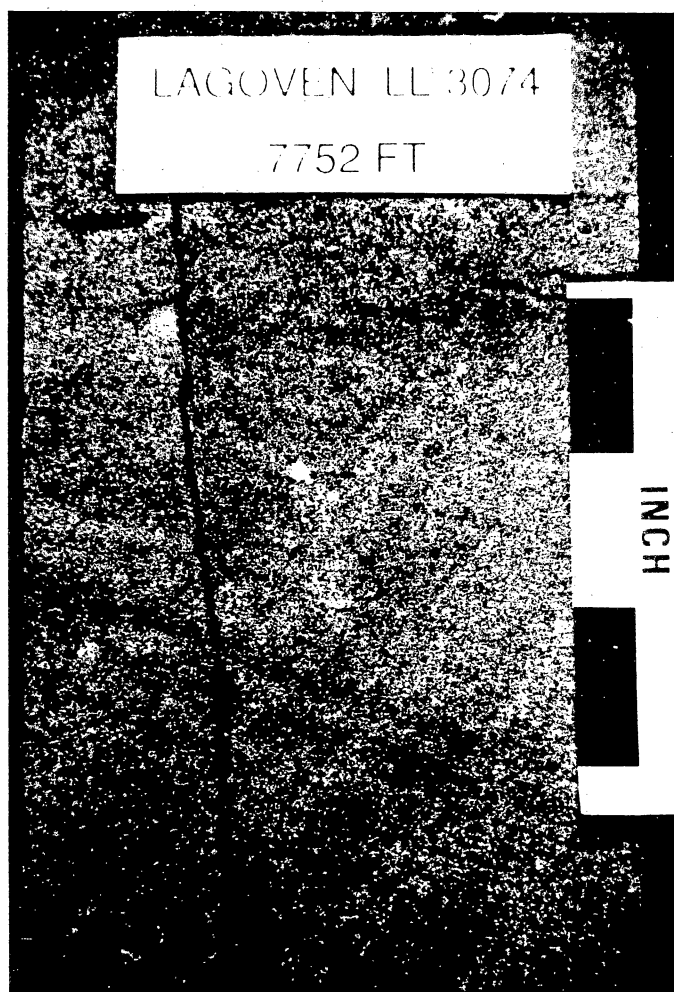
Figure 54. Photographs of (a) multiple fractures with microfault in core of the LL-2425 well and (b) fracture in core of the LL-3074 well.

GR
15   API   120

Res
0   ohm-m   35

Core Gamma
0   API   150

Core description

Ss.   Silt   Mud   Comments

— 7950 —

8000

8100

8200

RD

RS

8090

Faulted zone

8180

Cross stratified ripples

Ripples

Fractures

Microfault w/calcite fill

Fracture, inclined beds
Clay clasts

Fractures

Erosional contact
Fractures

Highly fractured, cross beds

Burrows

Fractures

Cross beds

Ophiomorpha

Fractures

Ophiomorpha, burrows

Beds tilted ≈ 30°

Fragmented shale

Beds tilted 10°-15°

Microfractured

Cross beds, fractures

Intensely fractured

Intensely fractured

Flaser ripples
Beds tilted nearly vertically

— 8135 —

ft   m
0   —   0

100 — 30

QAa3814c

Figure 55. Core description and log response of the LL-3282 well, located in a faulted zone.

88
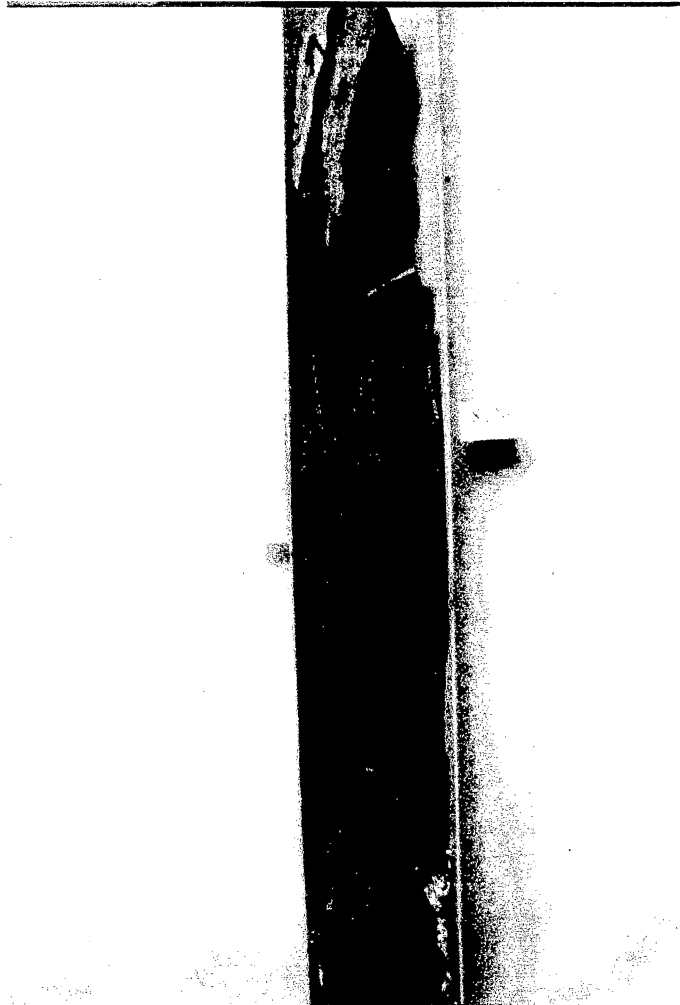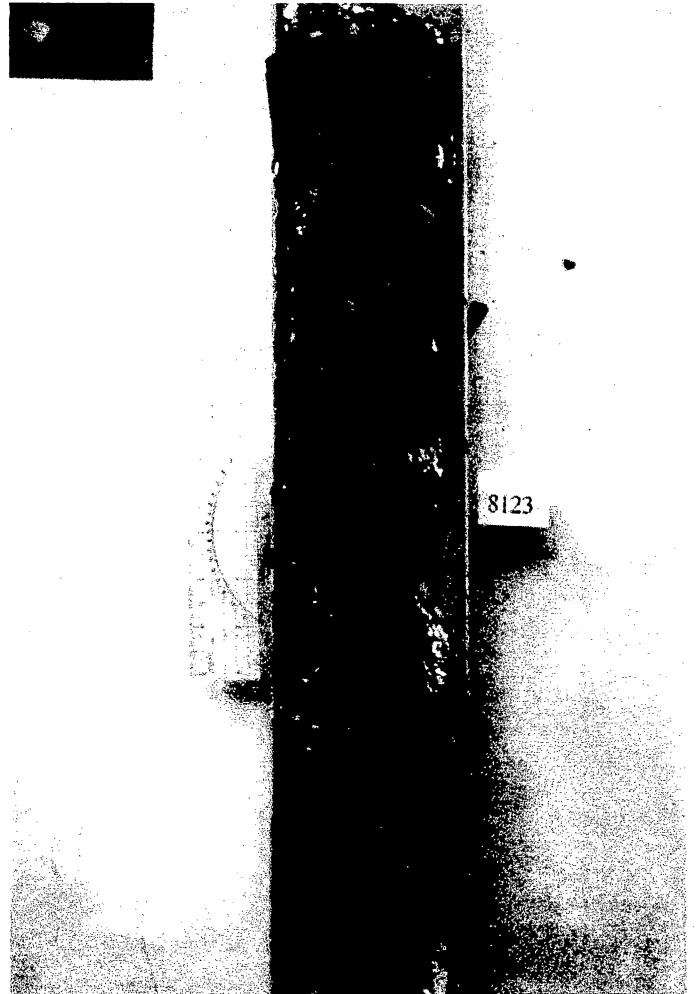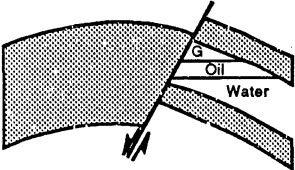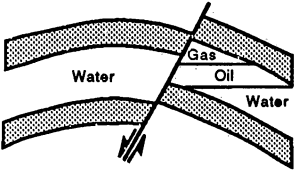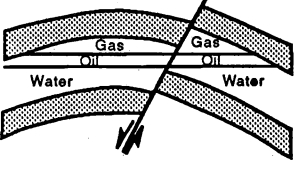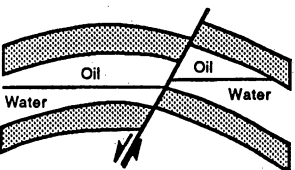
Figure 56. Photographs of (a) nearly vertically tilted beds associated with reverse fault and (b) intensely fractured zone in core of the LL-3282 well.

Hypothetical situation	Analysis of fault seal	
	Vertical migration	Lateral migration
Sand opposite shale at the fault. Hydrocarbons juxtaposed with shale.	Sealing	**Sealing** Reservoir boundary material may be the shale formation or fault zone material.
Sand opposite sand at the fault. Hydrocarbons juxtaposed with water.	Sealing	**Sealing** Seal may be due to a difference in displacement pressures of the sands or to fault zone material with a displacement pressure greater than that of the sands.
Sand opposite sand at the fault. Common hydrocarbon content and contacts.	Sealing	**Nonsealing** Possibility is remote that fault is sealing and the reservoirs of different capacity have been filled to exactly the same level by migrating hydrocarbons.
Sand opposite sand at the fault. Different water levels.	Sealing	**Unknown** Nonsealing if water level difference is due to differences in capillary properties of the juxtaposed sands. Sealing if water level difference is not due to differences in capillary properties of the juxtaposed sands.

(b)
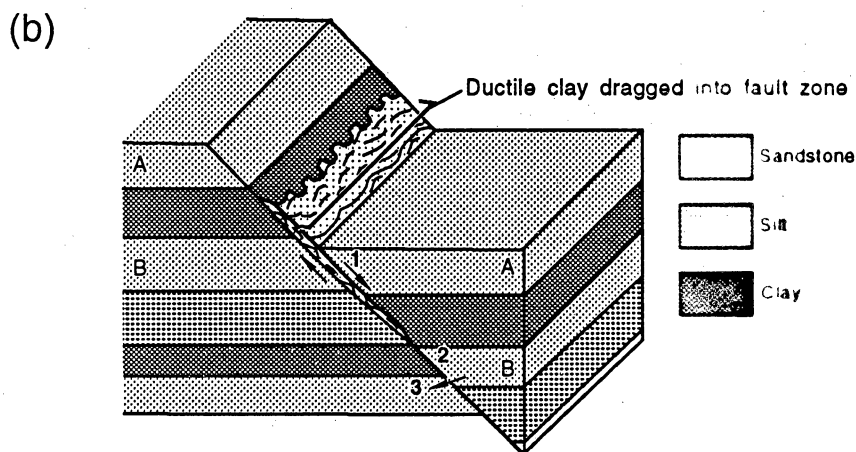
QAa4235c

Figure 57. (a) Hypothetical fault-lithology-accumulation relation from Smith (1980) and (b) diagram of clay smear and lithology juxtaposition. From Bouvier (1989).

are static geometric criteria (Harding and Tuminas, 1989). However these criteria are limited because dynamic phenomena such as the relative rates of migration into a trap versus rates of leakage out of the trap or production were not considered.

The probability of faults acting as pressure barriers is important in infield development and production, where fault-bounded compartments may not be in pressure communication. The best way to verify communication between individual blocks is with pressure data. Knott (1993) presented criteria for identifying whether a fault is sealing, based on pressure and fluid data (hydrocarbon type and hydrocarbon-water contact) from North Sea reservoirs.

The pattern of map-scale faults is known in the LL-652 area, but data are sparse on rock material in fault zones and associated features in cores near faults. To determine local pressure-sealing versus non-sealing cutoff values, individual pressure values must be calibrated against known trapped hydrocarbons in sandstone-to-sandstone windows along fault planes. The repeat formation tester (RFT) provides calibration and pressure evaluation and is a test for the presence of differential pressures across fault planes. It was used to measure pressure in the seven development wells (table 5).

In the LL-652 area seven RFT's (table 5) were run between March 1991 and May 1992 in the LL-3141, LL-3173, LL-3186, LL-3195, LL-3260, LL-3261, and LL-3263 wells to identify possible stratigraphic controls on pressure values. The most-productive three intervals (Middle C-3-X, Upper C-4-X, and Upper C-5-X Submembers) were analyzed in conjunction with facies and permeability maps. All RFT data were set for the same datum (7,300 ft for the C-3-X and C-4-X Members and 7,900 ft for the C-5-X Member) to make a direct comparison between values. As a result of these comparisons, 130 psi was determined as the minimum pressure differential between two wells in the same zone to infer reservoir compartments.

Middle C-3-X Submember—The LL-3173 well is not in complete communication with the LL-3195 well because it contacts a tidal-ridge deposit separated from a distributary-channel deposit (see also fig. 130) by an inferred facies boundary (fig. 58). In the LL-3173 well the log response is upward coarsening to serrate, the permeability is 39 md, and the average pressure is 2314 psi. The LL-3195 well in the Middle C-3-X Submember has an upward-fining to serrate log response, 192 md permeability, and 2,196 psi pressure. The contrast in log response and permeability is reflected in a 118-psi difference in pressure between the wells.

Upper C-4-X Submember—In the Upper C-4-X Submember the LL-3173 and LL-3195 wells contact different dip-elongate tidal-ridge sandstones that are separated by a narrow (less than 500 ft [152 m]) band of muddy interridge deposits (see also fig. 126). The permeability values are similar between the LL-3195 well (180 md) and the LL-3173 well (140 md), but they have a 206-psi pressure difference (fig. 58). Thus, even though both wells encounter permeable sandstones in the Upper C-4-X Submember, there are interwell heterogeneities (interridge clay laminae) that reduce interwell hydraulic communication. The low value of differential pressure (118 psi) in the Middle C-3-X Submember was expected because of good lateral continuity of sandbodies in this interval. In contrast, the high pressure differential (206 psi) in the Upper C-4-X Submember (fig. 58) is due to lateral restriction in hydraulic communication between the LL-3173 and LL-3195 wells, separated along depositional strike by interridge mudstones.

Upper C-5-X Submember—Three wells (LL-3186, LL-3195, and LL-3261) contact tidal-ridge sandstones in the Upper C-5-X Submember (see fig. 122). The LL-3195 and LL-3261 wells intersect axial parts of a tidal-ridge sandstone, whereas the LL-3186 well is in a muddy interridge area. Figure 59 shows a cross section incorporating these wells, where the log character indicates two upward-coarsening to serrate sandstones in the LL-3261 well with 4.6 md of permeability (fig. 59) and 1,915 psi of average pressure. The log response in the LL-3195 well is also upward coarsening in 5-md permeability sandstone and a pressure of 1,767 psi, with 148 psi of pressure differential between the two wells.

Figure 59 shows a fault between the LL-3261 and LL-3195 wells. The LL-3261 well is located on the downthrown side of the fault and tested 1,702 psi in the Upper C-4-X Submember, which juxtaposes at the fault surface the Middle C-4-X Submember in the upthrown block of the fault. The Middle C-4-X

Table 5. Summary of RFT data in the LL-652 area.

Well	Member	Depth (ft)	Formation Pressure (psi)	DATUM (ft)	Gradient (psi/ft)	DATUM Pressure (PSI)
LL-3141	C-3-X	6473	2310	7300	0.28	2542
(03/91)	C-3-X	6488	2311	7300	0.28	2538
	C-4-X	6847	1847	7300	0.28	1973
	C-4-X	6871	1844	7300	0.28	1964
	C-4-X	6892	1834	7300	0.28	1958
	C-4-X	6918	1832	7300	0.28	1939
	C-4-X	7060	2259	7300	0.28	2326
	C-4-X	7078	2263	7300	0.28	2325
	C-4-X	7161	2791	7300	0.28	2830
	C-5-X	7539	2302	7900	0.273	2400
	C-5-X	7562	2312	7900	0.273	2404
	C-5-X	7587	2262	7900	0.273	2347
	C-5-X	7600	2247	7900	0.273	2329
	C-5-X	7661	2481	7900	0.273	2546
	C-5-X	7720	2521	7900	0.273	2570
	C-5-X	7827	2920	7900	0.273	2940
LL-3173	C-3-X	6661	2189	7300	0.28	2368
(07/91)	C-3-X	6706	2104	7300	0.28	2259
	C-3-X	6747	2219	7300	0.28	2374
	C-3-X	6787	2224	7300	0.28	2368
	C-3-X	6852	2577	7300	0.28	2702
	C-3-X	6859	2580	7300	0.28	2703
	C-4-X	7026	1611	7300	0.28	1689
	C-4-X	7052	1659	7300	0.28	1728
	C-4-X	7070	1685	7300	0.28	1749
	C-4-X	7116	1814	7300	0.28	1866
	C-4-X	7136	1829	7300	0.28	1875
	C-4-X	7234	1603	7300	0.28	1621
LL-3186	C-3-X	7098	2258	7300	0.28	2315
(07/91)	C-3-X	7132	2272	7300	0.28	2319
	C-3-X	7267	2869	7300	0.28	2878
	C-3-X	7357	2406	7300	0.28	2390
	C-3-X	7402	2566	7300	0.28	2537
	C-4-X	7464	2043	7300	0.28	1997
	C-4-X	7482	2016	7300	0.28	1965
	C-4-X	7522	2005	7300	0.28	1943
	C-4-X	7556	2050	7300	0.28	1978
	C-4-X	7593	2270	7300	0.28	2182
	C-4-X	7614	2277	7300	0.28	2189
	C-4-X	7640	2291	7300	0.28	2196
	C-4-X	7726	2040	7300	0.28	1921
	C-5-X	8082	2892	7900	0.273	2842
	C-5-X	8064	2980	7900	0.273	2935

Table 5. Continued.

LL-3195 (08/91)	C-3-X	6782	2061	7300	0.28	2206
	C-3-X	6810	2048	7300	0.28	2185
	C-3-X	6943	2030	7300	0.28	2130
	C-3-X	7027	2089	7300	0.28	2165
	C-3-X	7047	2104	7300	0.28	2175
	C-4-X	7121	1506	7300	0.28	1556
	C-4-X	7148	1517	7300	0.28	1560
	C-4-X	7177	1532	7300	0.28	1566
	C-4-X	7216	1592	7300	0.28	1616
	C-4-X	7262	1492	7300	0.28	1503
	C-4-X	7336	1519	7300	0.28	1509
	C-4-X	7358	1518	7300	0.28	1502
	C-5-X	7760	1820	7900	0.273	1858
	C-5-X	7773	1641	7900	0.273	1676
	C-5-X	7851	2009	7900	0.273	2022
	C-5-X	7924	1480	7900	0.273	1473
	C-5-X	7968	1628	7900	0.273	1609
LL-3261 (05/92)	C-3-X	6757	2483	7300	0.28	2635
	C-3-X	6881	1898	7300	0.28	2015
	C-3-X	7136	2268	7300	0.28	2314
	C-4-X	7256	1690	7300	0.28	1702
	C-4-X	7360	1705	7300	0.28	1688
	C-4-X	7380	1722	7300	0.28	1700
	C-4-X	7470	2355	7300	0.28	2307
	C-5-X	7694	2158	7900	0.273	2214
	C-5-X	7716	1865	7900	0.273	1915
	C-5-X	7778	2319	7900	0.273	2352
	C-5-X	7813	2064	7900	0.273	2088
	C-5-X	7886	1371	7900	0.273	1378
	C-5-X	7930	1508	7900	0.273	1500
LL-3260 (05/92)	C-3-X	7229	2286	7300	0.28	2306
	C-3-X	7245	2245	7300	0.28	22 60
	C-3-X	7288	1948	7300	0.28	1951
	C-3-X	7519	3027	7300	0.28	2949
	C-3-X	7650	1684	7300	0.28	1586
	C-3-X	7681	2100	7300	0.28	1993
	C-4-X	7748	1805	7300	0.28	1680
	C-4-X	7795	1998	7300	0.28	1859
	C-4-X	7920	1901	7300	0.28	1727
	C-4-X	7920	1902	7300	0.28	1728
	C-5-X	8464	3778	7900	0.273	3624
	C-5-X	8598	3855	7900	0.273	3664
	C-5-X	8663	3851	7900	0.273	3643
	C-5-X	8709	4039	7900	0.273	3818
	C-5-X	8790	3819	7900	0.273	3576
	C-5-X	8830	3839	7900	0.273	3585
	C-5-X	8860	3418	7900	0.273	3156
	C-5-X	8880	3673	7900	0.273	3406

Table 5. Continued.

LL-3263 (05/92)	C-3-X	6544	2113	7300	0.28	2325
	C-3-X	6574	2114	7300	0.28	2317
	C-3-X	6710	1964	7300	0.28	2129
	C-3-X	6788	1665	7300	0.28	1808
	C-3-X	6853	1639	7300	0.28	1764
	C-4-X	6904	1652	7300	0.28	1753
	C-4-X	6914	1699	7300	0.28	1807
	C-4-X	6935	1628	7300	0.28	1730
	C-4-X	6960	1629	7300	0.28	1724
	C-4-X	7003	1687	7300	0.28	1770
	C-4-X	7148	2803	7300	0.28	2846
	C-4-X	7182	2857	7300	0.28	2890
	C-4-X	7400	2623	7300	0.28	2595
	C-5-X	7543	2752	7900	0.273	2850
	C-5-X	7583	2637	7900	0.273	2724
	C-5-X	7665	2570	7900	0.273	2634
	C-5-X	7779	3763	7900	0.273	3796
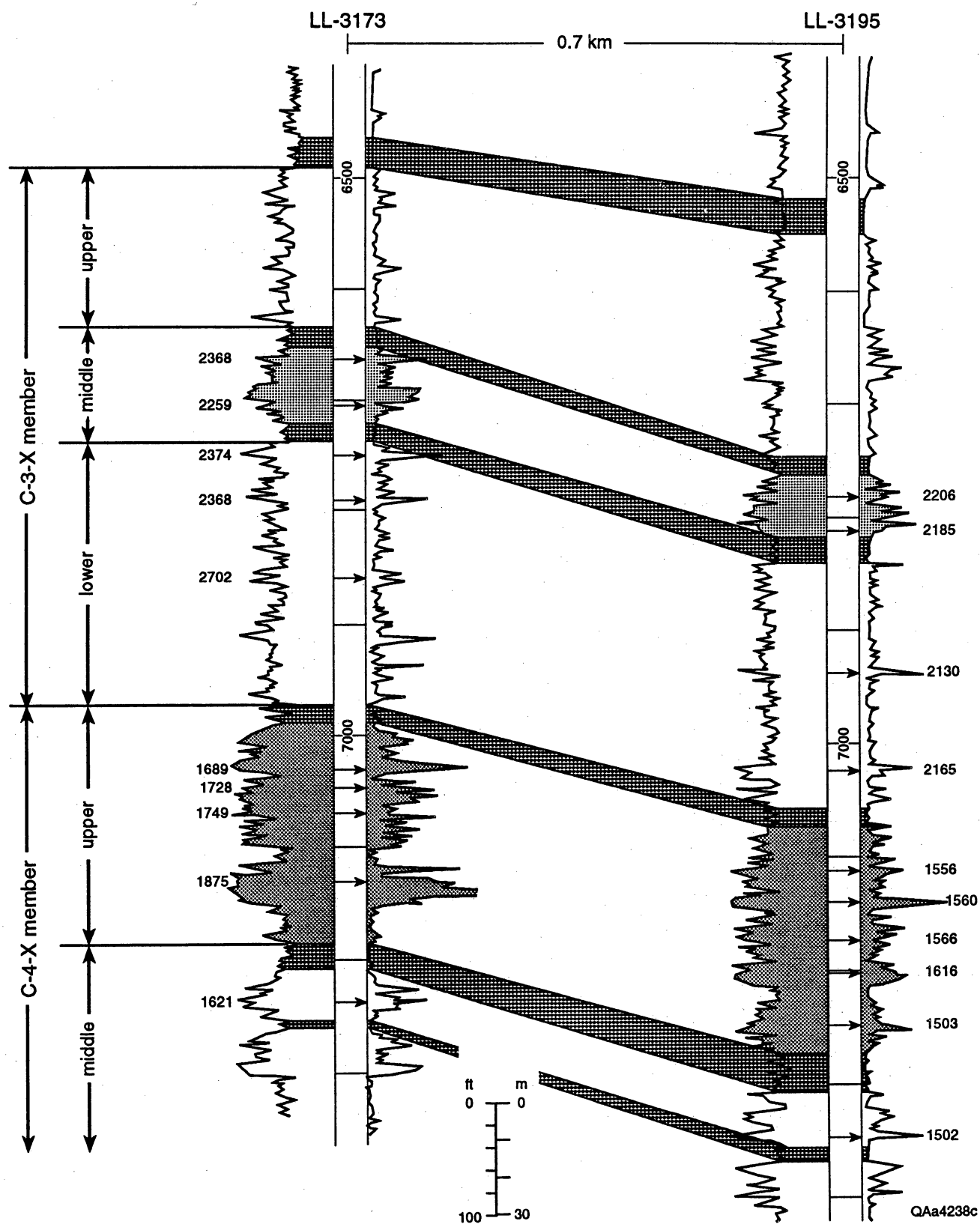
Figure 58. RFT data in the LL-3173 and LL-3195 wells.
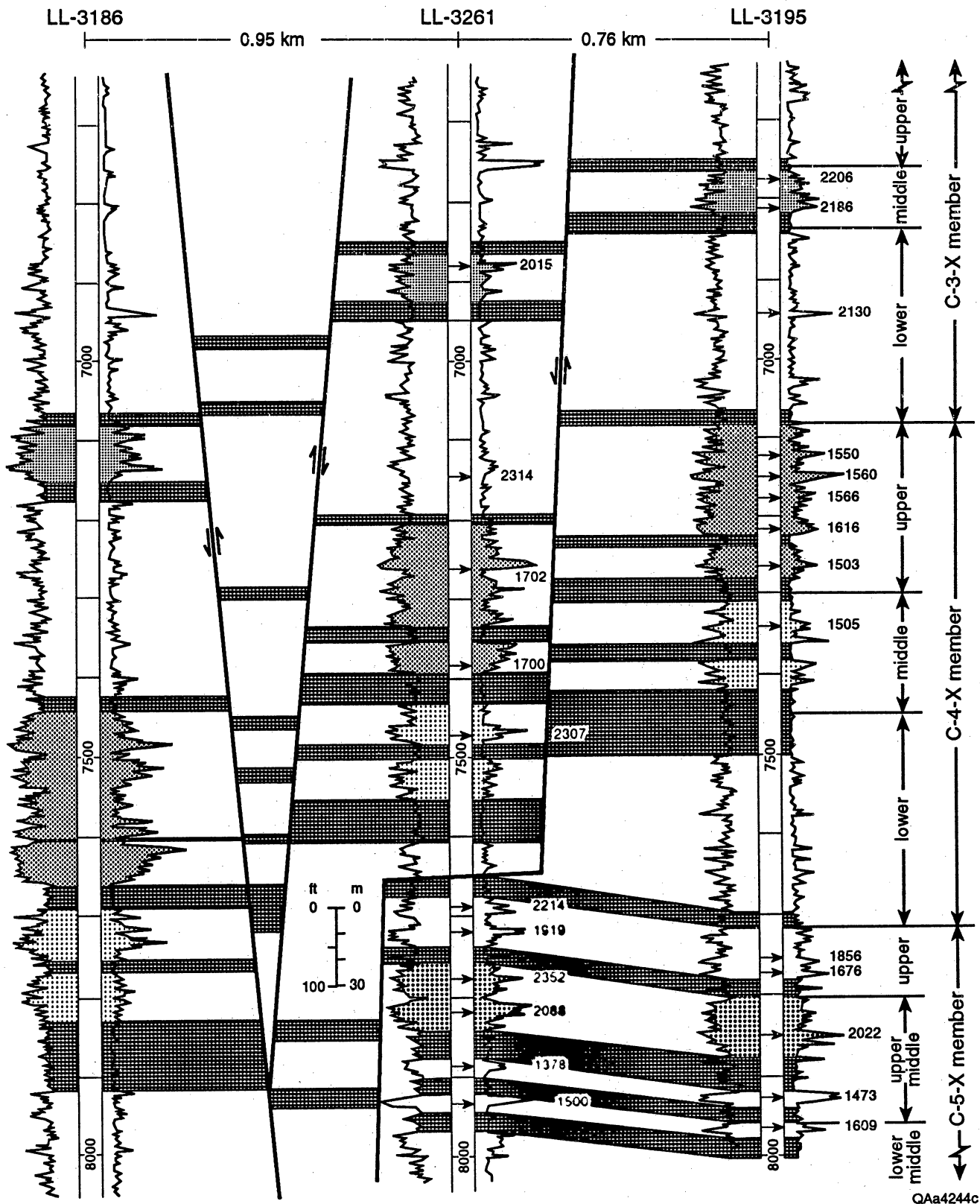
Figure 59. RFT data in the LL-3195 and LL-3261 wells.

Submember was measured at 1,503 psi in the LL-3165 well. The Lower C-3-X Submember was measured at 2,314 psi in the LL-3261 well. This zone juxtaposes the Upper C-4-X Submember in the LL-3195 well with a pressure of 1,575 psi; there is a difference of 739 psi between these two zones. The LL-3186 and LL-3261 wells are separated by two reverse faults (fig. 59); both wells are located in downthrown blocks. The individual pressures between juxtaposed sandstones show sealing between these two faults in the C-3-X and C-4-X Members.

Figure 60 shows a structural cross section between the LL-3263 and LL-3141 wells. The LL-3286 well documents the relative dip in this area. The reverse fault (#13) in this area has 80 ft (24.4 m) of throw. The Upper Middle C-5-X Submember in the LL-3263 well, located on the upthrown side of the fault, has 2,787 psi average pressure and is juxtaposed at the fault surface against the Upper Middle to Upper C-5-X Submembers in the LL-3141 well that was tested with an average pressure of 2,358 psi, indicating that there is 428 psi of pressure difference between the two blocks. The LL-3263 well has a pressure of 1,752 psi in the Upper C-4-X Submember, and the LL-3141 well has a pressure of 1,960 psi. This represents a 208-psi difference, indicating that the fault is sealing.

Another method to evaluate fault seal is to compare historical trends in pressure between fault blocks. As shown in Figure 61, this was made by selecting three wells (LL-1310, LL-3038, and LL-866) in the downthrown block (C-4-X.01 reservoir) of the central fault and three wells (LL-1245, LL-1103, and LL-1176) in the upthrown block (C-4-X.03 reservoir) of the fault. The pressure data for the C-4-X.01 reservoir has a linear trend, whereas in the C-4-X.03 reservoir the distribution is more erratic. However, the pressure-decline trend, although parallel between the two reservoirs, is offset by 1,100 psi in pressure, implying no communication across the fault seal.

Three sealing faults are identified in the LL-652 area: the reverse #13 (fig. 45), the central fault #6, and fault #4. To extrapolate to the rest of the field, we applied a parameter used by Knott (1993) for reservoirs in the Brent Group in the North Sea. This parameter is called "maximum fault throw versus reservoir thickness." Knott (1993) demonstrated that sealing is proportional to fault throw, normalized as a fraction of reservoir thickness. He also concluded that with faults with throws greater than reservoir thickness, there is a better-than-90-percent probability of sealing (fig. 62). These types of faults were interpreted as extrareservoir faults, and the seal is primarily by juxtaposition of different rock types. For example, because the C-3-X Member is 560 ft (171 m) thick, the C-4-X Member is 600 ft (183 m) thick, and the C-5-X Member is 550 ft (168 m) thick, there are probably only three extrareservoir faults in the LL-652 area.

The relation of member thickness to fault throw was plotted for each member (table 6). In comparison with the lower Eocene section, the Brent Group is thinner. As was expected, the three faults have a 90-percent probability of being sealed. Structural cross section 16 (fig. 32) shows an excellent example where the LL-1258 well, located in the downthrown block of the main fault, shows a shaly section (±700 ft [213 m] thick) of the C-2-X Member juxtaposed against the Middle and Lower C-3-X Submembers. The Upper C-4-X Member, located in the upthrown block that includes the LL-2191 well, has a missing section (main fault) of 1,000 ft (305 m) in the C-2-X Member.

For other faults, a method based on figure 62b (intrareservoir faults) was used where the fault throw is less than the average thickness 570 ft (174 m) of the C Members. The results are in table 6, along with an estimate of the probability of the fault providing a seal. The three faults inferred to be sealing by pressure analysis show a fault-seal probability (FSP) between 28 and 33 percent. A major conclusion is that different fault-sealing mechanisms are present and that it is difficult to determine the relative importance of each with only static geometric criteria like clay-smear potential (Bouvier and others, 1989) instead of dynamic pressure measurements. Finally, the most probable sandbody architecture for combined vertical and lateral seal is a top seal formation that is thicker (shaly section of C-1-X/C-2-X Members) than the magnitude of the fault displacement to provide both vertical and lateral seals.
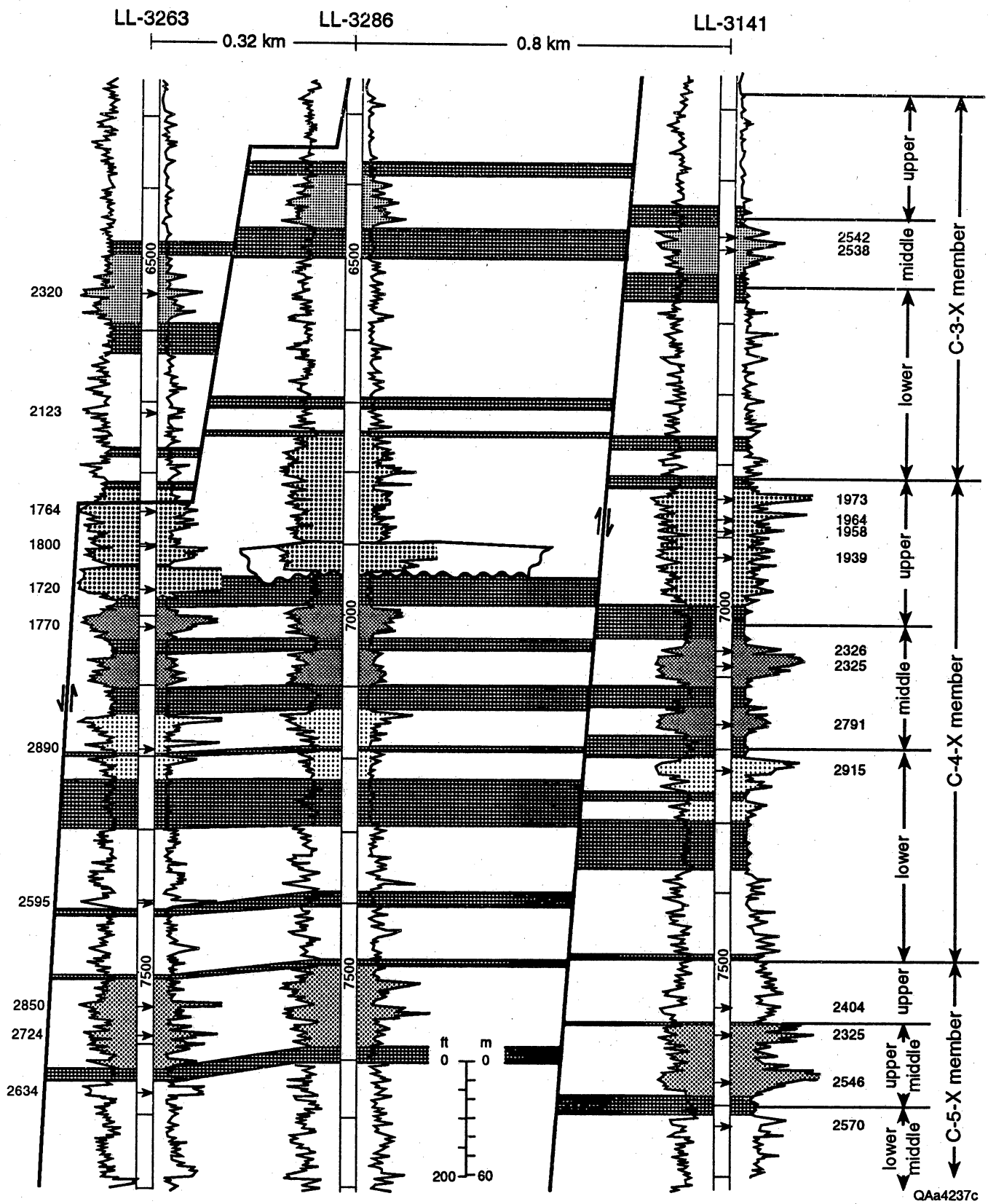
Figure 60. RFT data in the LL-3263 and LL-3141 wells.
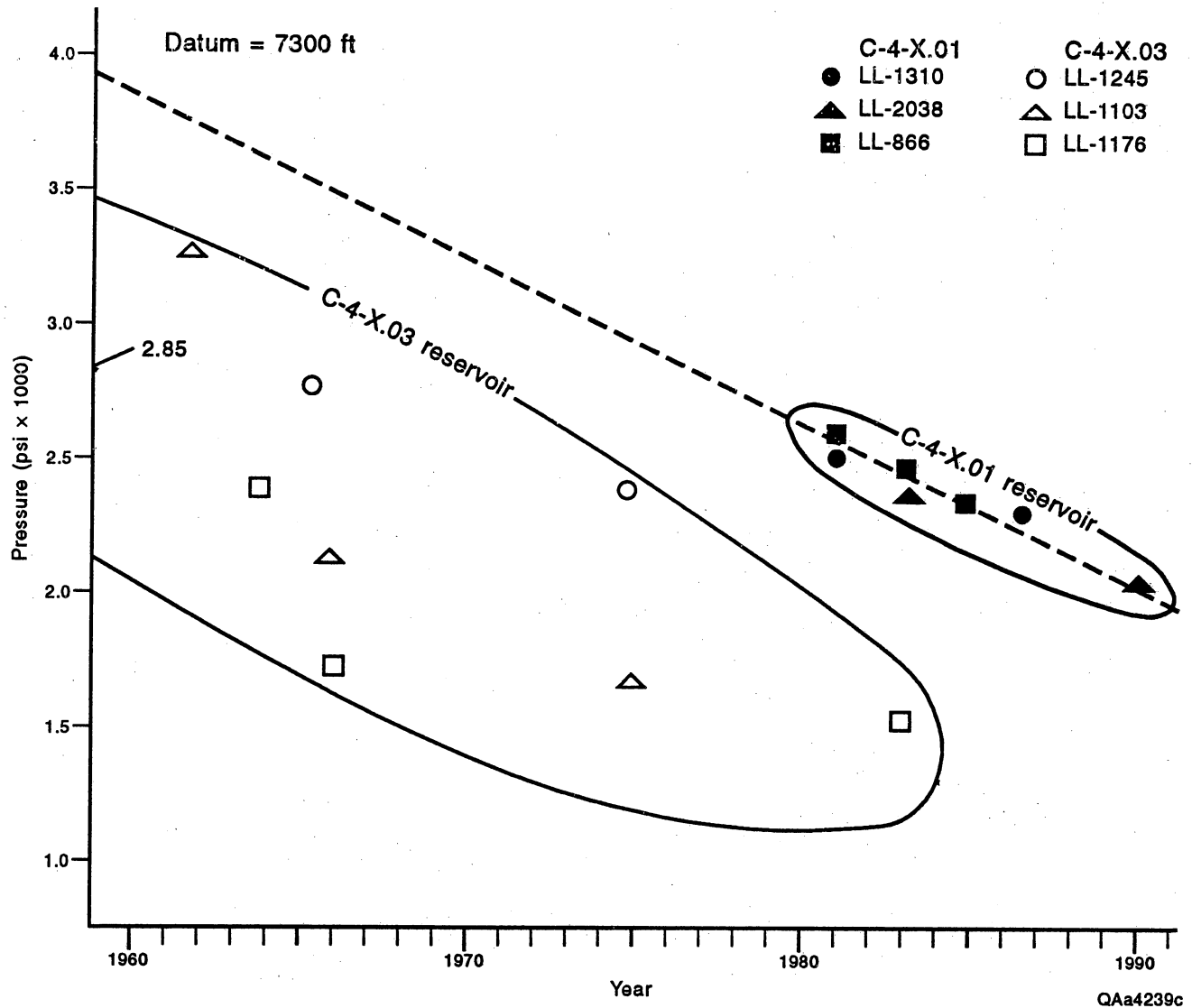
Figure 61. Historical trends in pressure between C-4-X.01 (downthrown block) and C-4-X.03 (upthrown block) reservoirs.
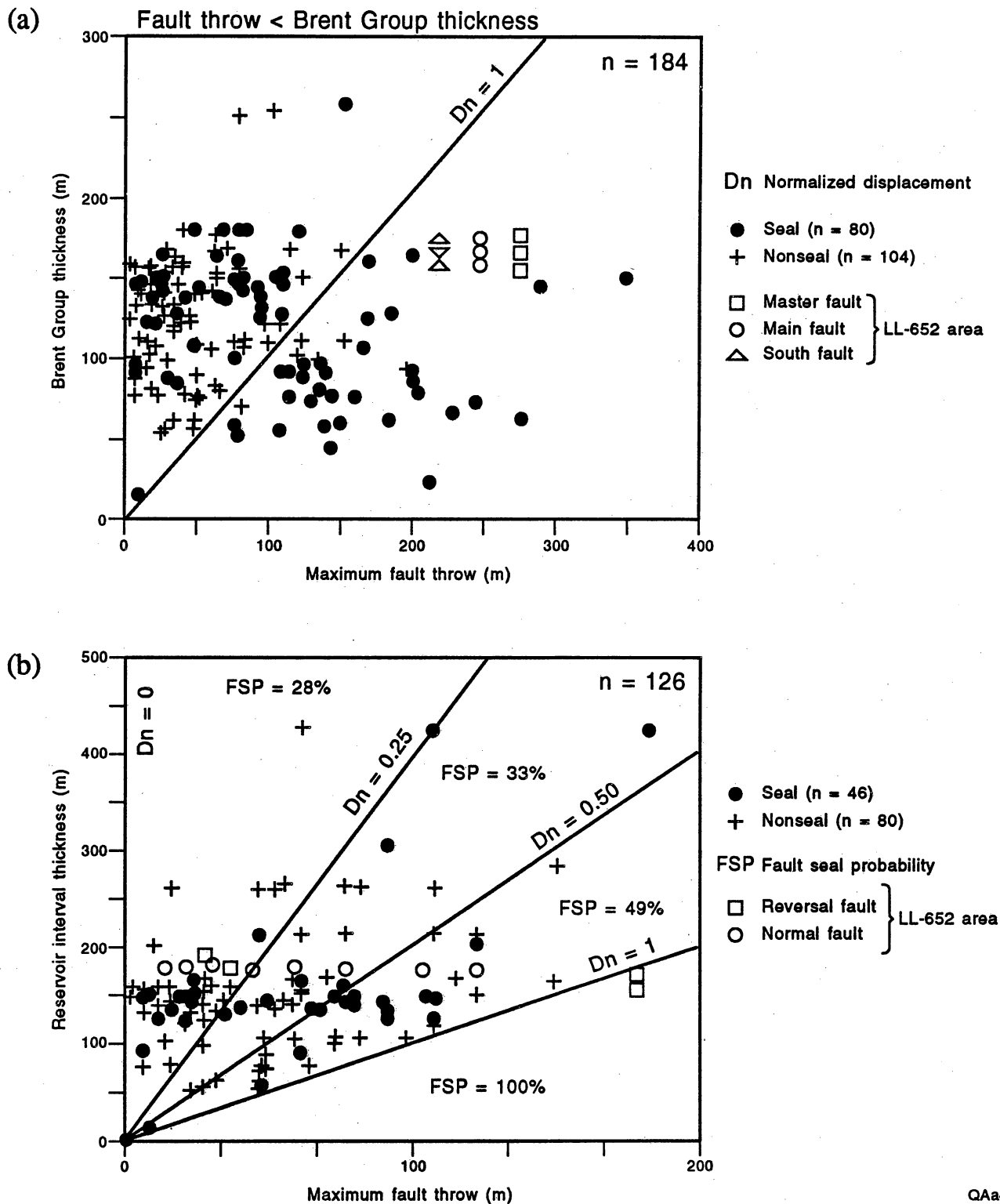
Figure 62. Brent Group thickness (North Sea) versus fault throw. (a) Extra-reservoir and intrareservoir faults and (b) intrareservoir faults derived from (a).

Table 6. Fault names in the LL-652 area.

Fault Name	Fault ft	Throw m	FSP(*) (%)	Comments
Master fault	900	274	90	Extrareservoir fault
Main fault	800	244	90	Extrareservoir fault
South fault	700	213	90	Extrareservoir fault
1	150	46	(-) 33	
2	100	30	(+) 28	
3	100	30	(+) 28	
4	100	30	(+) 28	Sealing toward the north, but communication expected in the south
5	50	15	(-) 28	
Central fault 6	250	76	(+) 33	Sealing by pressure analysis (historical tendency)
7	50	15	(-) 28	
8	500	152	49	
9	200	61	33	
10	550	167	49	
NE-Reverse 11	500	152	90	
NW-Reverse 12	550	167	90	
CE-Reverse 13	80	24	(+) 28	Sealing by pressure (RFT) analysis
CW-Reverse 14	100	30	28	
15	100	30	28	
SE-Reverse 16	100	30	28	

* Fault Seal Probability

101

The LL-652 area is divided into several fault-sealed compartments that in conjunction with structural closure provide the trapping mechanism (fig. 12). For example, the paleostructural map (fig. 19) shows that the north fold is structurally complex and separated from the main anticline, and structural cross section 12 (fig. 31) shows the intensity of compartmentalization due to faulting. The division of the field into eight zones (fig. 12) is defined by the fault-sealing probability and the pressure analysis.

Compartment I is isolated from other compartments by the northeast-trending reverse fault (90 percent FSP), and the main fault (90 percent FSP). On the northeast this compartment is bounded by fault #1, which has a 33 percent probability of being a seal. Southeastward, the limit is an oil-water contact, whereas the northern limit is unknown.

Compartment II is bounded on the east and west by reverse faults (each 90 percent FSP) and on the south by the number 8 fault (49 percent FSP). In contrast, the northern limit is unknown.

Compartment III is located in the high-dip limb of the anticline and is bounded by two sealing faults—the master fault (90 percent FSP) and the northwest reverse fault (90 percent FSP). Internally, this zone is divided into three smaller compartments.

Compartment IV is bounded by two reverse faults—a northwest reverse fault with 90 percent FSP and the east-central reverse fault with 28 percent FSP. This fault was analyzed with RFT pressure data and was inferred to be sealing. The southern boundary of this compartment has only 33 percent FSP but is sealing according to the pressure history in both fault blocks. To the north the limit is antithetic fault #8 with 49 percent FSP. This compartment occurs on the crest of the main anticline.

Compartment V is located in an unfaulted area and represents the best zone of production and reserves. This area, recommended for a pilot waterflood project, is bounded by three sealing faults—the main fault, fault #13, and the central fault. Internally this compartment has two minor faults that pinch out downstructure.

Compartment VI is located in the ridge-crestal area south of the anticline and is bounded by the master fault, the central fault, the south fault, and fault #16. Part of this compartment is located in the Maraven concession and the other in the Lagoven concession and represents the only compartment where C Members have been tested and produced on the downthrown side of the master fault (VLA-96 and VLA-68 wells). This compartment is very complex because it is intersected by several reverse faults.

Compartment VII is bounded by the central fault (33 percent FSP), the southeast reverse fault (28 percent FSP), and the southern fault (90 percent FSP). This compartment is divided by fault #7 (28 percent FSP) in two smaller compartments.

Compartment VII is in the Maraven concession and consists of several smaller compartments in the upthrown block of the master fault. The reverse faults control reservoir compartmentalization in the LL-652 area and define these seven compartments. Compartments II, III, IV, and V occur in the C-4-X.01, C-5-X.02, and C-6-X.01 reservoirs. Compartments VI and VII are in the C-4-X.03, C-5-X.08, and C-6-X.16 reservoirs. Distribution of these compartments is crucial to the viability of prospects. However, seals along normal faults are more variable and commonly less effective than seals along reverse or strike-slip faults, which may be a consequence of the more common formation of fault-parallel extension fractures associated with normal faults (Harding and Tuminas, 1989). The best examples of fractures in cores in the LL-652 area are associated either with normal faults (LL-3140 well) or with reverse faults (LL-3282 well). This means that fluid flow may occur along a temporary sealing fault as the result of increased pressure differential from production on one side of a fault block.

Structural Style

The differentiation of structural styles in local areas can be difficult and imprecise because a particular structural characteristic may have several tectonic origins. The most reliable and direct basis for identifying the styles is to determine the type of slip (reverse, normal, or strike) of the dominant faults (Harding, 1985). Identification includes the recognition of key structural elements such as en echelon folds and faults, trap-door blocks, critical differences in local trends, and regional structural patterns.

It was necessary in the analysis to consider both cross section and map characteristics, especially of the master fault and reverse faults where styles appeared similar in profile but where their structures had distinctly different areal distributions. This provided a clue for the configuration of the assemblage style.

The style of faulting in the LL-652 area is complex because of the combination of strike-slip movements and major extensional, compressional, and transpressional events. The master fault, main fault, northwest-trending normal faults, north fold, and main anticline are structures associated with or related to the wrench system of the Icotea fault. The north-northeast-trending reverse faults make up a structural style associated with the regional east-west compression in late Pliocene to Holocene time (Lugo, 1991). Finally, the overprints of several structural styles in the area, especially in the northern part of the field, resulted in complex patterns with a second-order or antithetic fault system having a transverse orientation with respect to the normal style of faulting in the area.

V. DEPOSITIONAL SYSTEMS

Facies Model

This section presents and discusses the tide-dominated deltaic facies model of the C Members in the LL-652 area. Tide-dominated deltaic reservoirs differ from fluvial- and wave-dominated types of deltaic reservoirs in that (1) the geometry of delta-front sandstones is both dip-elongate and dip-parallel, (2) the sandstones are extremely heterogeneous because of the high degree of interbedded mudstone, and (3) as a consequence of (1) and (2), tide-dominated deltaic reservoirs typically have a low recovery efficiency and therefore a high potential for secondary oil recovery.

The depositional model of the C members in the LL-652 area consists of dip-elongate, distributary- and tidal-channel sandstones that merge northeastward with extensive, dip-parallel delta-front sandstones in a tide-dominated deltaic system (fig. 63). Channel-mouth-bar sandstones occur at the distal (northeast) termini of the distributary-channel sandstones.

Muddy, non-framework facies separating reservoir sandstones consist of (1) lower delta plain (tidal-flat) deposits that encase distributary- and tidal-channel sandstones and (2) inner-shelf, transgressive mudstones that encase delta-front sandstones; seaward (northeastward), delta-front sandstones grade into thinner, distal delta-front sandstones interbedded with mudstones.

Criteria for the definition of the tide-dominated delta model for the LL-652 area were derived from two main sources: (1) maps of net-sandstone thickness and log-facies and (2) cores (table 7). Although these criteria are individually not conclusive, their combined occurrence strongly support the model.

The deltaic interpretation is based on consistent trends in upward-fining and blocky, northeast-trending and -bifurcating framework sandstones that pinch out downdip (northeastward) into sandy mudstones with upward-coarsening log responses. These sandstones are inferred to be marine in origin from burrow types (*Ophiomorpha, Planolites, Asterosoma,* and *Teichichnus*) and from accessory sedimentary structures such as symmetrical wave ripples and hummocky crossbedding.

The main criteria in distinguishing tide-dominated deltaic deposits from other types of deltaic deposits from maps are in the geometry of the delta-front sandstones. Although vertical profiles through fluvial- and tide-dominated deltaic deposits are similar (for example, both upward-coarsening, burrowed delta front), delta-front sandstones in the C members are strongly dip-elongate and dip-parallel (figs. 64 and 65). In wave-dominated deltaic systems, delta-front sands are reworked by waves into strike-elongate sheets (fig. 64a), whereas in fluvial-dominated, wave-modified deltas, delta-front sands are only slightly reworked into lobate patterns (fig. 64b). Delta-front sands in fluvial-dominated deltas are primarily dip-elongate (fig. 64c) as well as in fluvial- and tide-dominated deltas (fig. 64d), but commonly the delta-front sands in fluvial-dominated deltas are not parallel, flanked by point-sourced, lobate crevasse-splay deposits that fill muddy interdistributary areas. In tide-dominated deltaic systems, flood-and ebb-tidal currents rework delta-front deposits into parallel, upward-coarsening sand ridges (Off, 1963; Klein, 1970). However, elongate and dip-parallel delta-front sandstones can also occur in fluvial-dominated deltaic systems where distributaries prograde into lacustrine/interdistributary-bay areas (Tye and Coleman, 1989), but these types of delta-front deposits (1) are confined to small, discrete areas in the lower delta plain, (2) comprise only a fraction of the total delta-front deposits in the system, and (3) have a dip-parallel geometry partly controlled by the shape of the oblong lacustrine basin and the bathymetry of the lake floor. Additionally, delta-front deposits of the C members have a strong marine association, as inferred from burrow types, whereas the modern Achafalaya lacustrine delta is in a lower-delta-plain setting with weak marine processes (Tye and Coleman, 1989).

Other criteria supporting the interpretation of the tide-dominated deltaic model are numerous clay clasts and clay-draped reactivation surfaces. Abundant clay clasts result from repetitive, episodic scouring of a mud-rich substrate by flood- and ebb-tidal currents. Although they are most abundant in distributary-
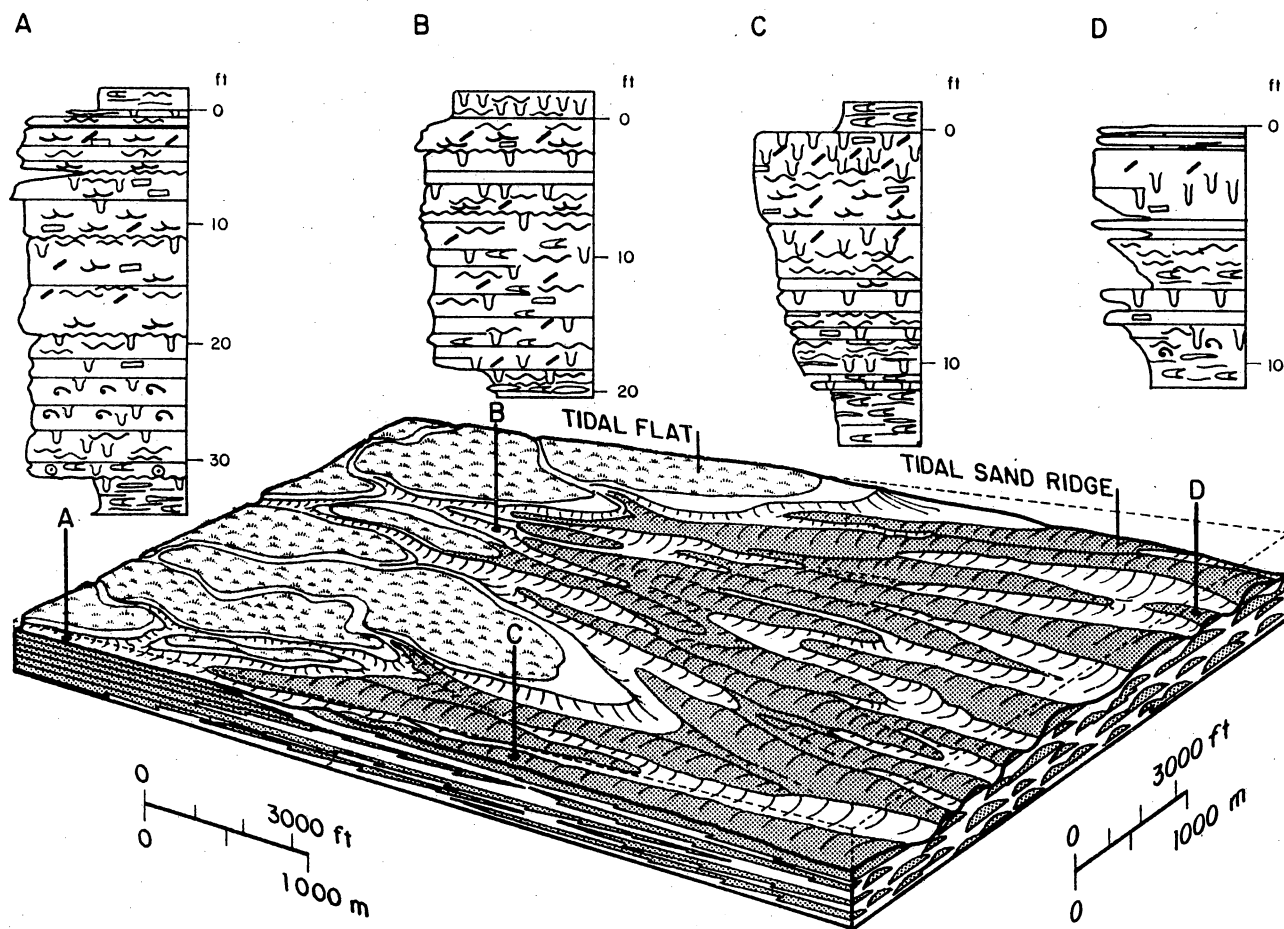
Figure 63. Tide-dominated deltaic depositional model of lower Eocene reservoirs in the LL-652 area. From Maguregui (1991).

Table 7. Criteria for tide-dominated deltaic model of reservoirs in the C Members.

SOURCE	CRITERION
MAPS	• Northeast-trending and -bifurcating sandbodies (upward-fining log response) Pinching out into muddy deposits (upward-coarsening log response)
	• <u>Dip-parallel delta-front sandstone geometry</u>
CORES	• Numerous repetitive, clay-draped reactivation surfaces and abundant clay clasts
	• Bi-directional ripples present but uncommon

(a)

Beach-barrier
shoreline

(b)

Lower delta plain   Delta front   Delta fringe   Crevasse splay

(c)

(d)

Tidal current
sand ridges

No scale
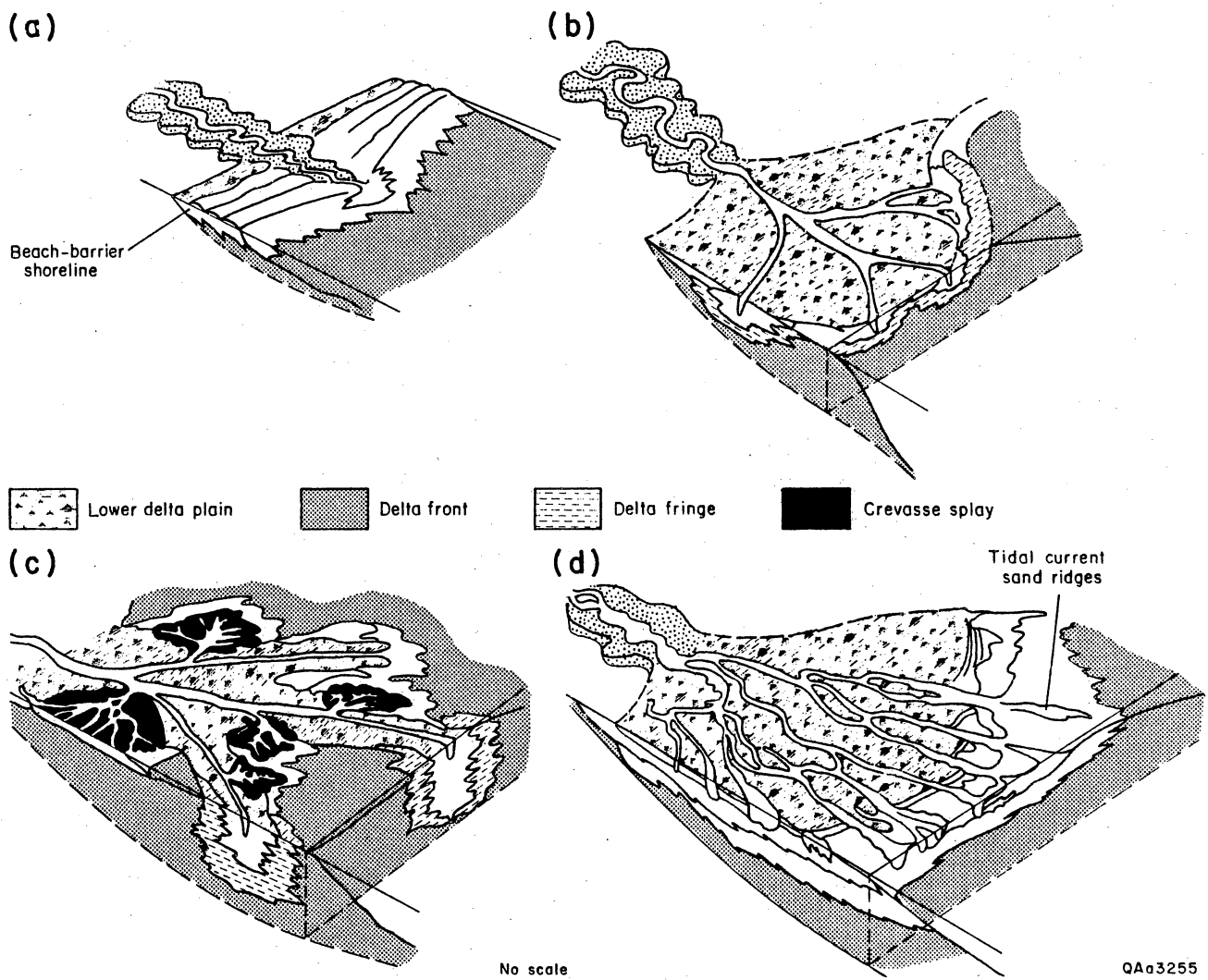
QAa3255

Figure 64. Spectrum of major delta morphologies. Modified from Fisher and others(1969).

(a)

Lower delta plain
Channel-mouth bar
Delta front
Delta fringe

Contour interval 20 ft

(b)

Contour interval 20 ft
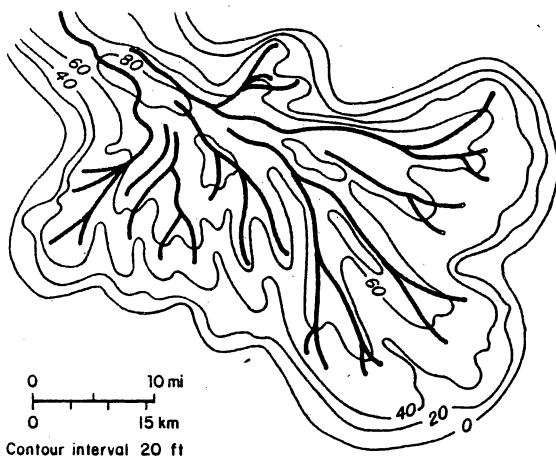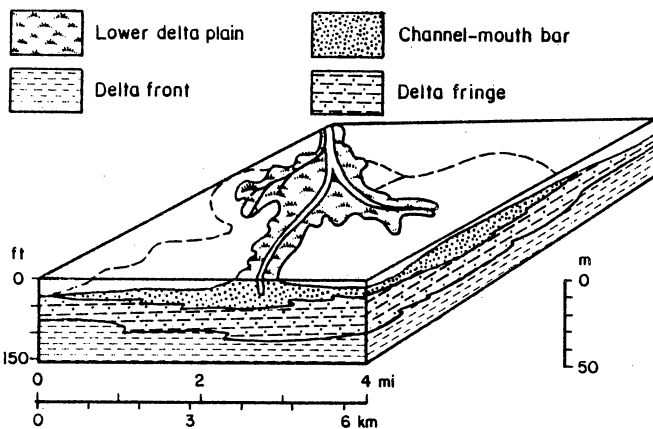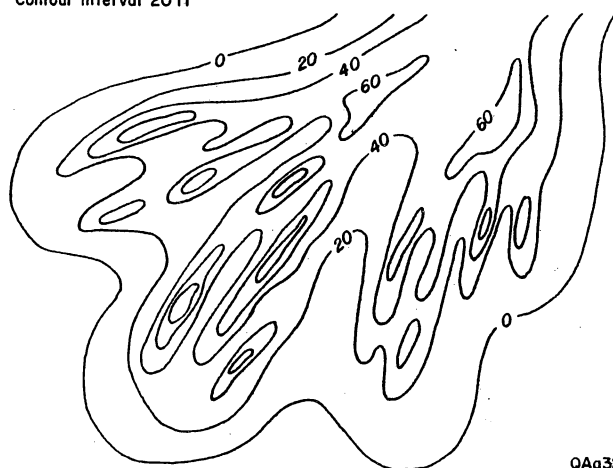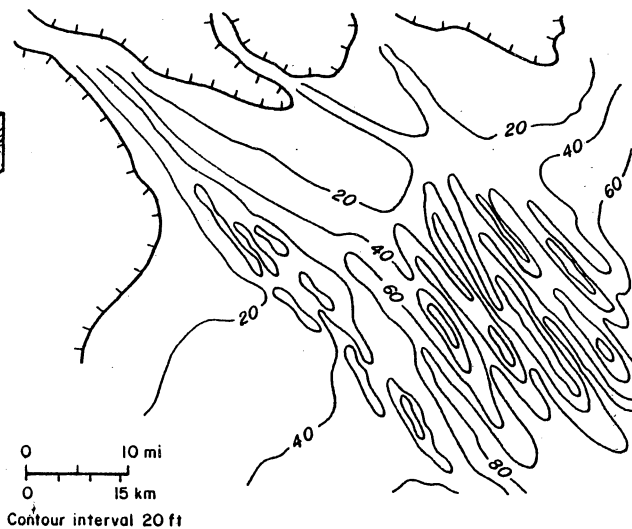
QAa3258

Figure 65. Comparison of net-sandstone thickness patterns in (a) fluvial-dominated deltas and (b) tide-dominated deltas. Modified from Coleman and Prior (1982).

and tidal-channel deposits, clay clasts are also scattered throughout tidal sand-ridge deposits in the delta front (Meckel, 1975; Maguregui, 1990; Maguregui and Tyler, 1991). Mud-draped reactivation surfaces that consist of flaser ripples and multiple, thin mud layers draping clean, moderately to well-sorted sand, indicate alternating high- and low-energy conditions that correspond to different phases of the tidal cycle (Reineck and Wunderlich, 1968; Reineck and Singh, 1973). Reactivation surfaces, although not restricted to tidal settings, commonly result from reworking of bedforms by the relatively weak reversing tidal current (Klein, 1970; de Mobray and Visser, 1984). Flaser ripples vary according to relative amounts of mud and sand. In sandy deposits, mud occurs as thin upward-concave lenses (Clifton, 1982); if mud and sand are in equal abundance, mud occurs as complex layers around sandy ripples; if mud is dominant as in the C members, sand occurs as isolated "starved" ripples.

Another important criterion for tidal conditions is bi-directionality of sedimentary structures such as ripples and crossbeds. In cores of the C members, bi-directional ripples are present but uncommon. However, in many settings in tide-dominated deltaic systems, there is a dominant tidal current that commonly results in unidirectional bedforms being preferentially preserved.

The presence of burrows does not exclusively support a tide-dominated deltaic interpretation, as they are common in all deltaic systems. However, the consistent and recurring presence of a wide variety of burrows in all major facies in the C members, especially lower-delta-plain, such as *Ophiomorpha*, *Asterosoma*, *Planolites*, and *Chondrites*, indicates a strong marine influence from tidal currents.

Facies

Distributary Channel

Distributary-channel deposits in the C members individually range from 5 to 20 ft (1.5 to 6 m) thick, are erosionally based and upward-fining, contain festoon crossbeds, clay clasts, and burrows, and exhibit a dip-elongate sandstone geometry (table 8). An example from the Middle C-5-X Submember shows an individual distributary channel deposit, 13 ft (4 m) thick, that truncates tidal-flat and tidal-channel deposits (fig 64a). This distributary-channel deposit consists of fine sandstone capped by siltstone and very fine sandstone. The lower 9 ft (2.7 m) is extensively crossbedded (fig. 64b), whereas the upper 4 ft (1.2 m) contains inclined beds and asymmetrical ripples. Organic fragments, burrows, and very coarse to gravel-sized clay clasts are present throughout the section. This distributary-channel deposit is part of a narrow (550 to 3,000 ft [168 to 915 m] wide), northeast-trending belt of more than 20 ft (6 m) of mostly upward-fining sandstone bounded by muddy deposits with either upward-coarsening or serrate log responses (see fig. 120). These muddy deposits are interpreted to have been formed in a lower-delta-plain (tidal-flat) setting transected by a network of distributary channels. The distributary-channel facies commonly truncate delta-front facies. An example from the Middle C-3-X Submember in the LL-3074 well (fig. 67) shows a 13-ft (4-m) upward-fining distributary-channel sandstone that truncates a 21-ft (6.4-m) section of upward-coarsening, burrowed delta-front mudstones and sandstones (fig. 68a). The distributary-channel sandstone is pervasively rich in gravel-sized clay clasts (fig. 68b) and exhibits a succession of low-angle inclined beds at the base to plane beds at the top. There are multiple erosional reactivation surfaces throughout the lower half of the sandstone and a 2.5-ft (0.8-m) zone of calcareous cement at the base that may have resulted from dissolution of shell lag at the base of the channel. This distributary-channel deposit differs from the previous example in figure 66 and is composed of multiple, thin (commonly less than 1-ft [0.3-m]) sandstone beds with clay clasts and reactivation surfaces instead of one main sandstone bed. These numerous, thin sandstone beds reflect a more distal setting of the distributary and deposition by episodic tidal currents.

Channel-Mouth Bar

Channel-mouth bar deposits occur at the termini of the distributary-channel facies and are distinguished by very clean, wavy bedded and tabular crossbedded medium sandstone at the top of burrowed,

Table 8. Diagnostic features and characteristics of distributary-channel facies in the C Members.

Diagnostic Features

- Interbedded sandstone and shale
- Flaser ripples
- Variable grain-size trends

Grain-Size Trend	Log Response	Basal Contact	Stratification	Sorting	Visual Porosity
None to slightly upward-fining	Baseline or serrate	Non-Erosional	Plane beds, asymmetrical and symmetrical ripples in sandstone interbedded with mudstone	Fair to poor	Poor

Thickness (ft)	Width (ft)	Sandbody Geometry
10 to 30	1,000 to 5,000	sheet

(a)

(b)

Depth
ft   m

Grain size and sedimentary structures
G | VC | C | M | Fine | VF | Silt | Mud

Rock type

8090 — 2466

2467
8095 —

*cc

*cc

2468   Distributary channel

8100 — 2469

*cc
*cc

2470

8105 — Tidal channel

2471

*cc *cc

8110 — 2472

2473

8115 — Tidal flat

2474

8120 — 2475

2476

8125 —

QAa3248c

LAGOVEN LL-3075

8099.5 FT

INCH
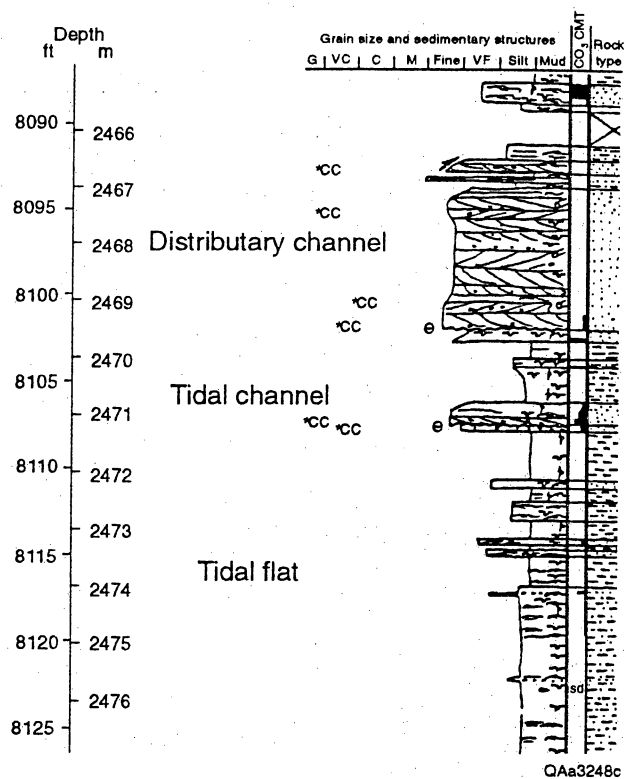
Figure 66. (a) Core description of distributary-channel and related facies in the Middle C-5-X Submember in the LL-3075 well and (b) photograph of distributary-channel facies (8,099.5 ft).

111
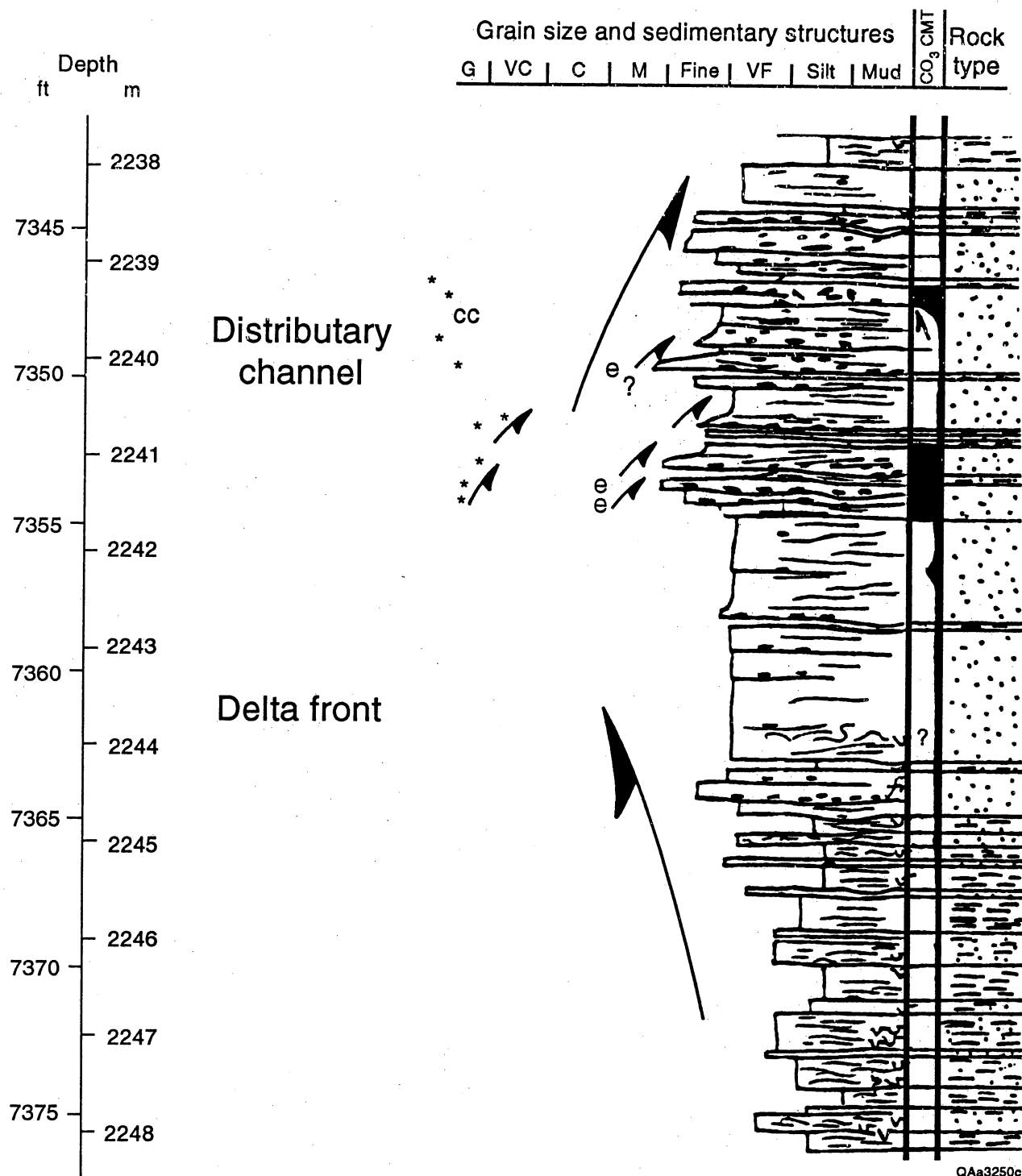
Figure 67. Core description of distributary-channel facies overlying delta-front facies in the Middle C-3-X Submember in the LL-3074 well. Photographs of delta-front (7,375 ft) and distributary-channel (7,354 ft) facies shown in figure 68.
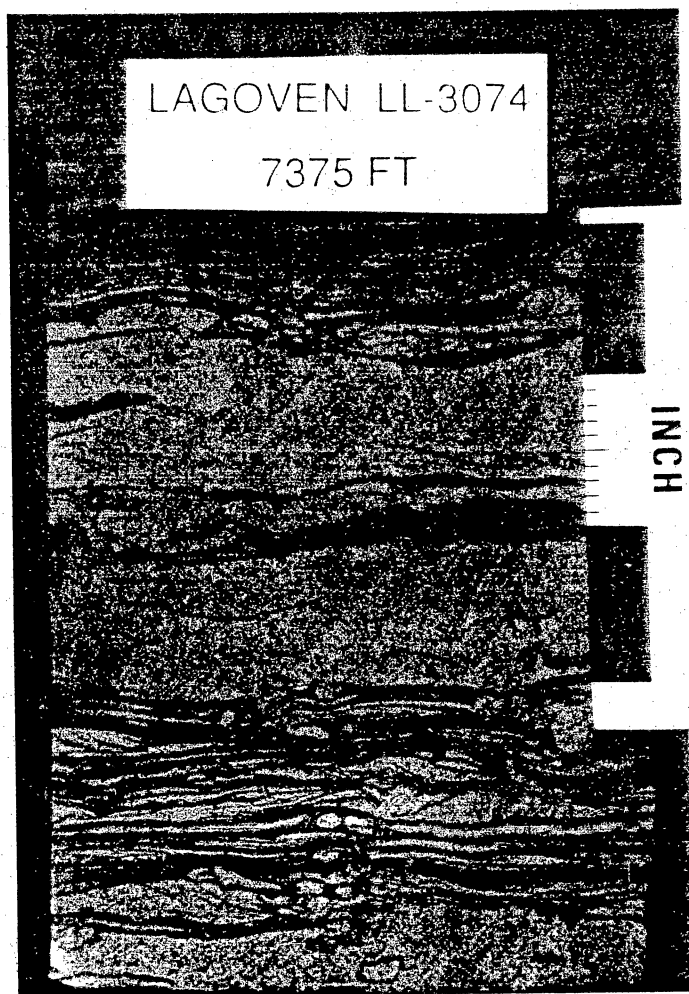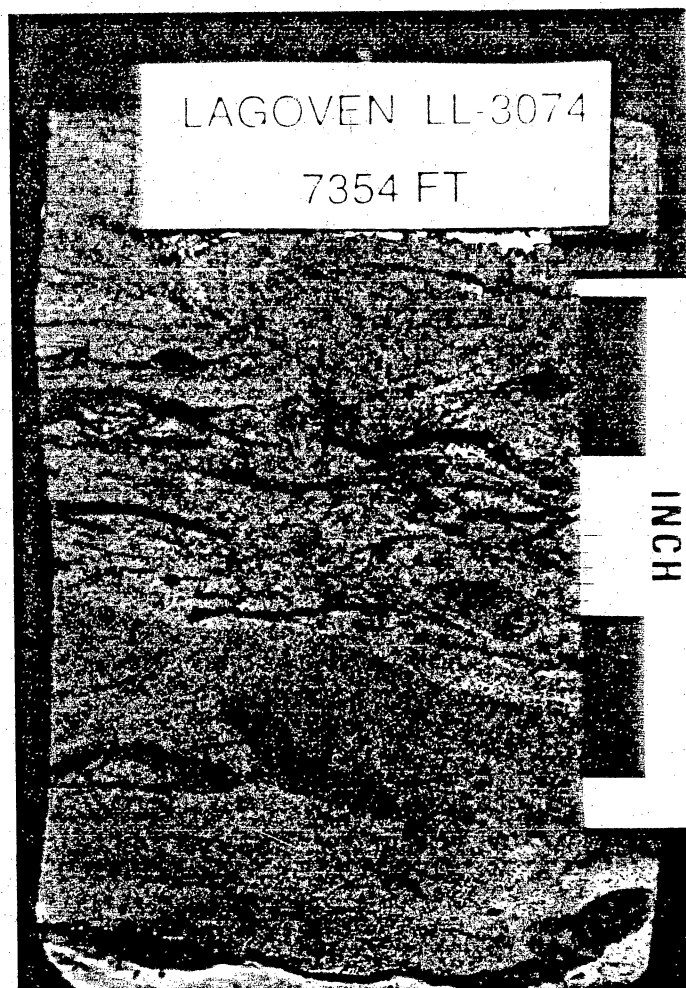
Figure 68. Photographs of (a) burrowed, interbedded mudstone and sandstones in delta-front facies and (b) clay-clast-rich distributary-channel facies in the Middle C-3-X Submember in core in the LL-3074 well. Core description is shown in figure 67.

upward-coarsening sequences (table 9 and fig. 69a). The crest of the channel-mouth bar, the coarsest part of the deposit, is only 3 ft (0.9 m) thick in this example and consists of oil-stained, crossbedded medium sandstone with minor clay clasts (fig. 69b), representing some of the best reservoir-quality rock in the C members. However, this facies is volumetrically insignificant as it commonly occurs as eroded remnants between younger distributary-channel deposits.

Delta Front

The delta front and distal delta front are collectively the most volumetrically significant facies in the C members (fig. 63). The delta-front facies is distinguished by (1) upward-coarsening grain-size trend, (2) stratification consisting of plane beds and ripples at the base and small crossbeds and inclined laminations at the top, (3) clay clasts and shell debris at the top, and most significantly, (4) a strong dip-elongate and parallel sandstone geometry (table 10).

The proximal delta front is relatively coarse, with an average grain size of fine sandstone in a range of siltstone at the base to medium sandstone at the top (fig. 70a). Sedimentary structures consist of asymmetric ripples in the lower one-third and small crossbedding and planar bedding in the upper two-thirds (fig. 70b). Clay clasts are common throughout, and the upper 6 ft (1.8 m) contains abundant Ophiomorpha burrows and shell debris.

In contrast to the proximal delta front, the medial delta-front facies averages from fine to very fine sandstone (fig. 71). Sedimentary structures range from bi-directional, asymmetrical ripples in the lower one-half (fig. 72a) to inclined beds and symmetrical ripples at the top (fig. 72b). Clay clasts are most common at the top of the section. Most medial delta-front deposits are thinner than proximal delta-front deposits and are also well burrowed (figs. 73 and 74), attesting to a strong marine influence. The most common burrow types are Planolites (fig. 74a) and Ophiomorpha (fig. 74b), which tends to be more common at the top of the delta-front section.

Distal Delta Front

Individual distal delta-front deposits in the C members are only 5 to 10 ft (1.5 to 3 m) thick and exhibit a spiky log response (table 11). Additionally, the distal delta-front facies may include load structures and slump deposits (figs. 75 and 76a). Other common features are bi-directional asymmetric ripples (fig. 77). The distal delta-front facies in the C members commonly occurs in multiple, upward-coarsening sequences, each no more than 6 ft (1.8 m) thick (fig. 78). These deposits typically have a dip-parallel net-sandstone thickness trend (see fig. 129).

Tidal Channel and Tidal Flat

Tidal channels are essentially small-scale creeks that transect the muddy tidal flat (fig. 63). In the C members, tidal-channel deposits are typically only 5 to 10 ft (1.5 to 3 m) thick, have an upward-fining or blocky grain-size trend, and are erosionally based (table 12). Tidal-flat deposits in the C members commonly have a slight upward-fining grain-size trend, reflecting progradation of the muddy tidal flat over the high-energy intertidal sand bar. Tidal-flat deposits are complexly stratified, with asymmetrical flaser and symmetrical ripples and plane beds in sandstone interbedded with mudstone (table 13).

An example of a tidal-channel deposit is a 9-ft (2.7-m), erosionally based section of upper fine sandstone overlain by upper very fine sandstone (fig. 79a). Stratification in the lower part of the deposit is poorly preserved, owing to incorporation of channel-margin, bank-collapse deposits (fig. 79b). Other important features are microfaults toward the base and clay clasts which decrease in size upward.

114

Table 9. Diagnostic features and characteristics of channel-mouth-bar facies in the C Members.

Diagnostic Features

- Wavy and cross bedding at top of upward-coarsening sequence

Grain-Size Trend	Log Response	Basal Contact	Stratification	Sorting	Visual Porosity
Blocky, at top of upward-coarsening trend	Upward-coarsening	Gradational with underlying delta front	Wavy beds Small crossbeds	Good to excellent	Good to excellent

Thickness (ft)	Width (ft)	Sandbody Geometry
5 to 10 at top of 20- to 40-ft sequences	2,000 ?	Lobate to dip-linear pods

(a)
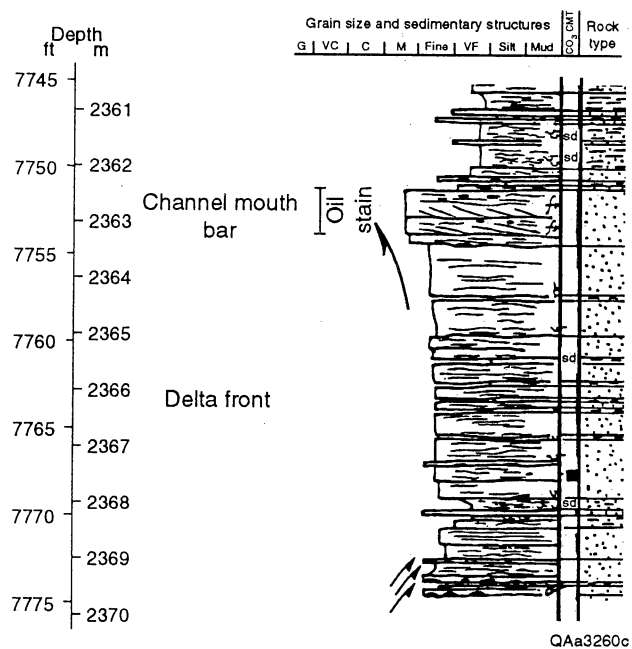
(b)
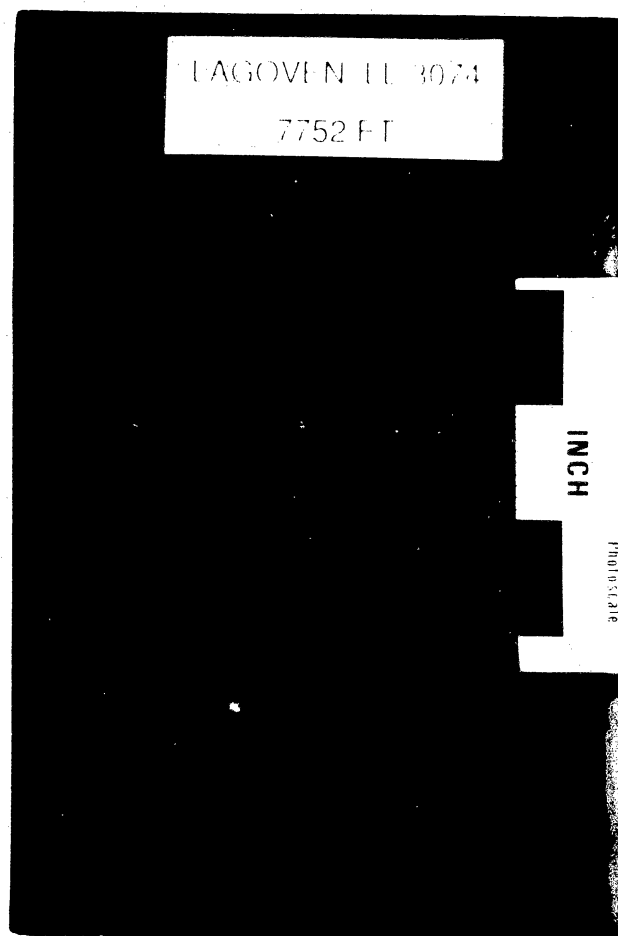
Figure 69. (a) Core description of channel-mouth-bar and delta-front facies and (b) core photograph of crossbedded, oil-stained channel-mouth-bar crest in the Upper C-4-X Submember in the LL-3074 well.

Table 10. Diagnostic features and characteristics of delta-front facies in the C Members.

Diagnostic Features

- Upward-coarsening
- Stratification mostly ripples and planar laminations
- Clay clasts and shell debris common at top
- Dip-elongate and parallel sand geometry

Grain-Size Trend	Log Response	Basal Contact	Stratification	Sorting	Visual Porosity
Upward-coarsening	Upward-coarsening	Gradational with sandy mudstone	Top: Small crossbeds and inclined laminations Base: Plane beds and ripples	Top: Good Base: Fair	Top: Good Base: Fair

Thickness (ft)	Width (ft)	Sandbody Geometry
5 to 18 individual Up to 40 composite	500 to 3,000	dip-elongate and parallel ribbons

Figure 70. (a) Core description of proximal delta-front (tidal sand-ridge) facies in the Upper C-4-X Submember in the LL-3282 well. Photograph of upper part of proximal delta-front (7,326 ft) is shown in figure 70b.
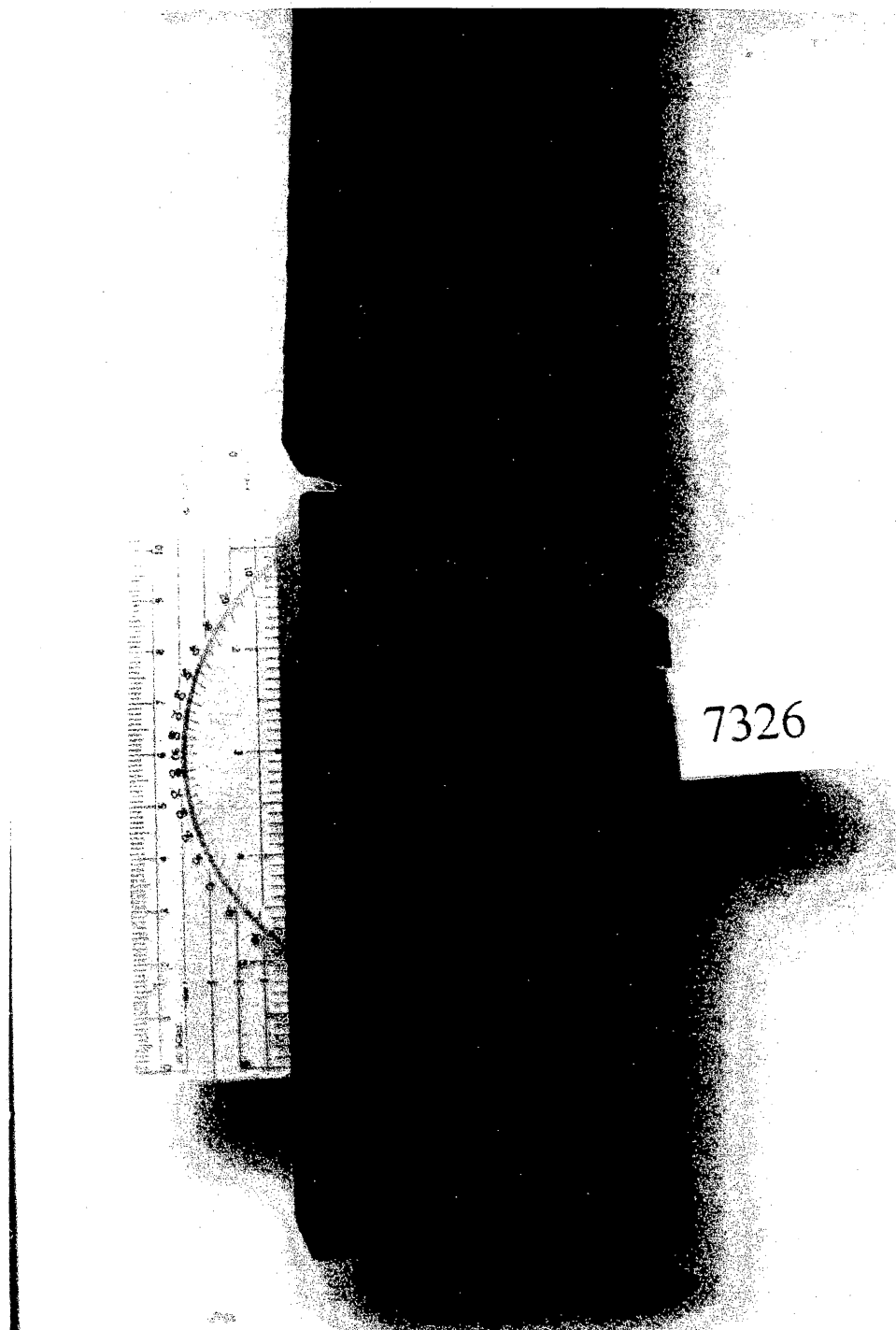
Figure 70. (b) Core photograph of sandstone-rich, mostly plane-bedded and burrowed proximal delta-front (tidal sand-ridge) facies in the Upper C-4-X Submember in the LL-3282 well. Core description is shown in figure 70a.

Grain size and sedimentary structures

| | G | VC | C | M | Fine | VF | Silt | Mud | CO₃ CMT | Rock type |

Depth
ft   m

8150 — 2484

*CC
*CC *CC

— 2485

*CC
*CC
*

8155 —

— 2486

8160 — 2487

Medial
delta front

*CC

*CC

— 2488

8165 — 2489

*CC

— 2490

8170 —

— 2491

8175 —

QAa3264c
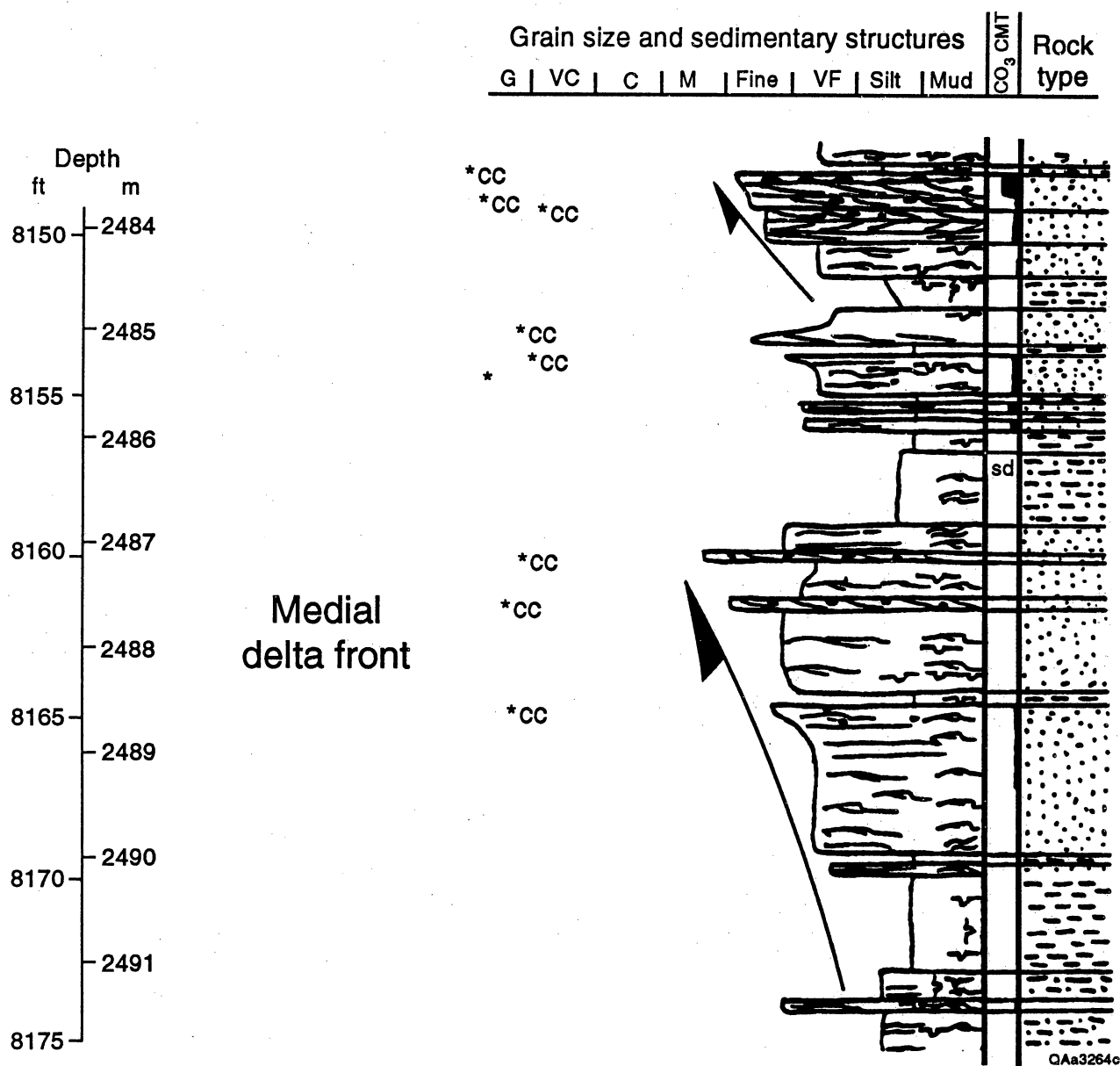
Figure 71. Core description of medial delta-front facies in the Middle C-5-X Submember in the LL-3075 well. Photographs of middle (8,164.5 ft) and upper (8,158 ft) part of delta-front sandbody are shown in figure 72.

(a)

LAGOVEN LL-3075

8164.5 FT

(b)

LAGOVEN LL-3075

8158 FT

INCH
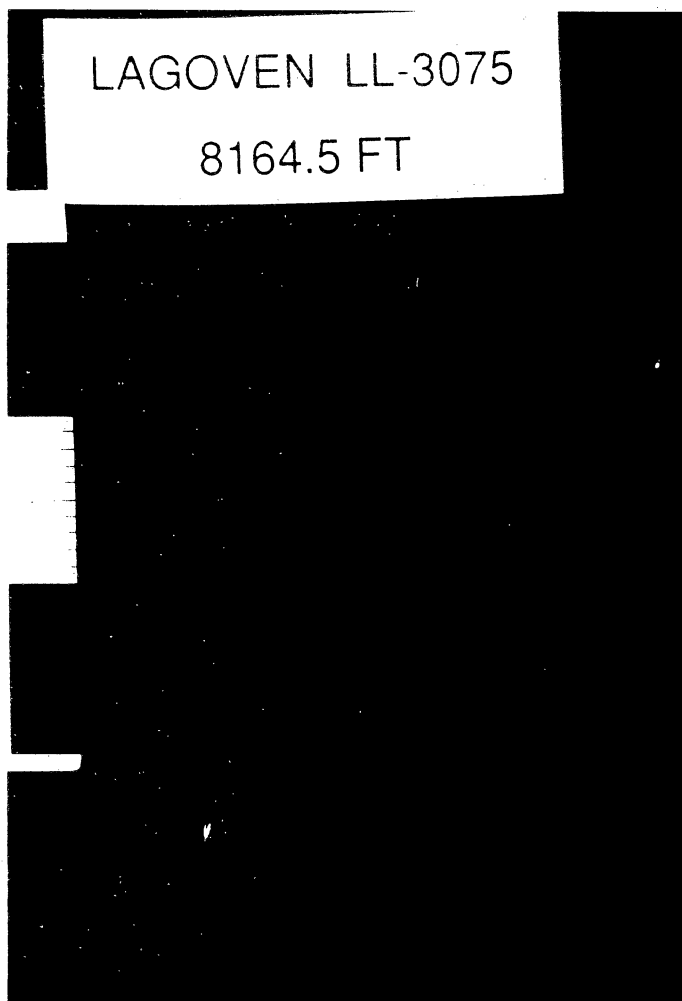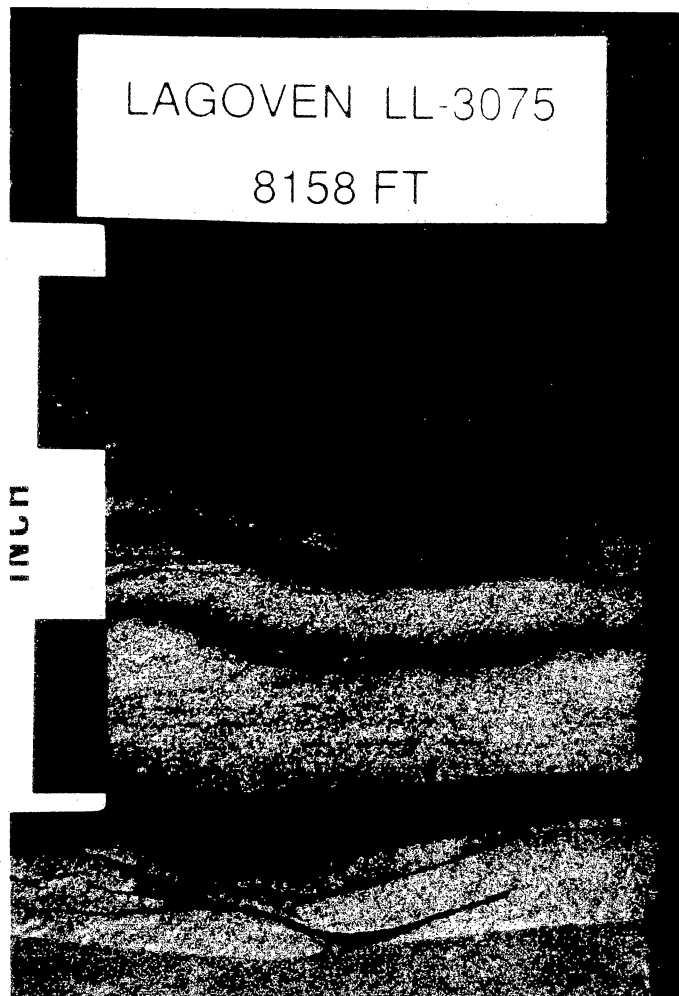
Figure 72. Photographs of the medial delta-front (tidal sand-ridge) facies in the Middle C-5-X Submember in core of the LL-3075 well. (a) Ripple-cross-stratified and laminated sandstones in the upper one-third of tidal sand-ridge and (b) symmetrical ripples at the crest of tidal sand-ridge, overlain by laminated, interridge siltstone. Core description is shown in figure 71.

Grain size and sedimentary structures | CO₃ CMT | Rock type

G | VC | C | M | Fine | VF | Silt | Mud

Depth
ft   m

7685

2343

7690 — 2344

2345

7695

2346

7700 — 2347

2348

7705

*cc

*cc

*cc

*cc (flat)

*cc
*cc

Medial
delta front

sd

QAa3266c
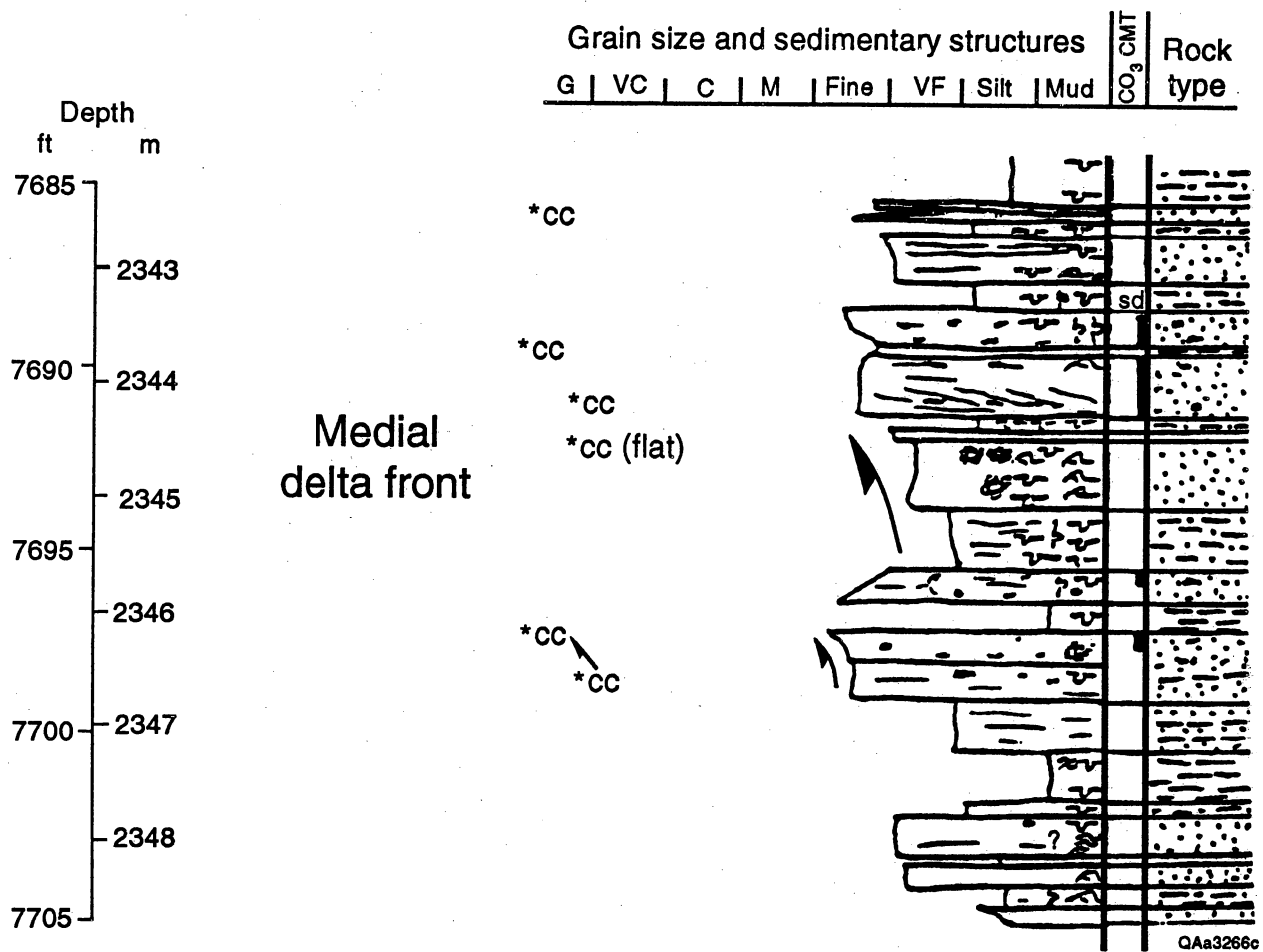
Figure 73. Core description of medial delta-front facies in the Upper C-4-X Submember in the LL-2850 well. Photographs of burrowed siltstones and sandstones (7,694.5 and 7,692 ft, respectively) are shown in figure 74.

(a)

(b)

LAGOVEN LL-2850

7692 FT
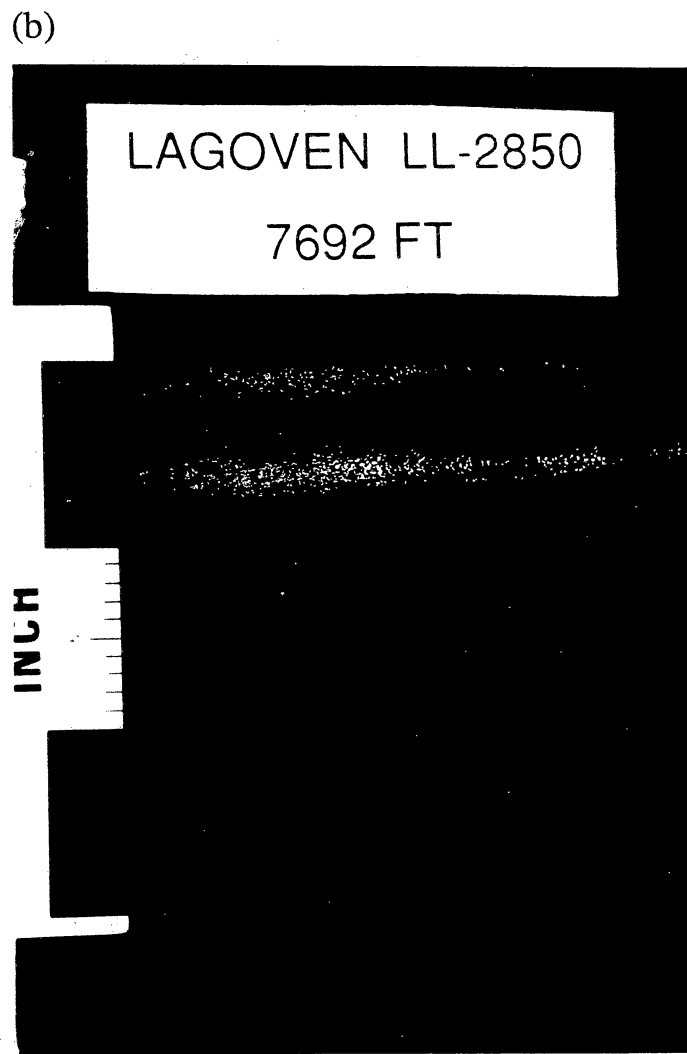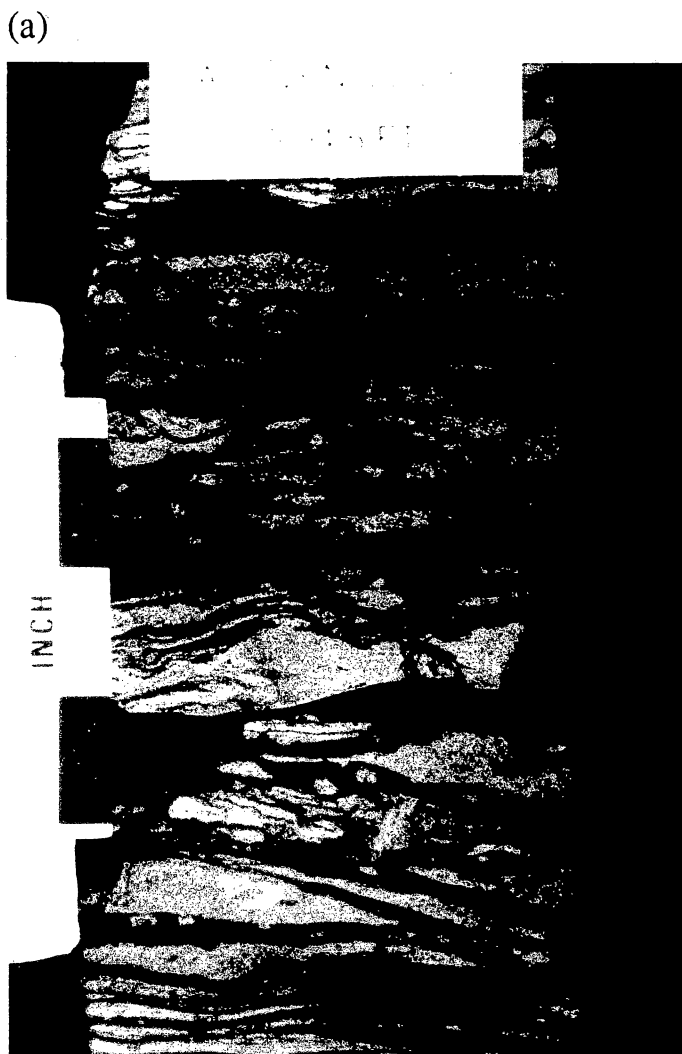
Figure 74. Photographs of medial delta-front facies in the Upper C-4-X Submember in core of the LL-2850 well. (a) Middle part of tidal sand-ridge deposit with *Planolites* burrows. (b) Upper part of tidal sand-ridge deposit with *Ophiomorpha* burrows. Core description is shown in figure 73.

Table 11. Diagnostic features and characteristics of distal delta-front facies in the C Members.

Diagnostic Features

- Upward-coarsening above marine shale
- Planar and ripple bedding
- May include load structures and slumps

Grain-Size Trend	Log Response	Basal Contact	Stratification	Sorting	Visual Porosity
Upward-coarsening	Upward-coarsening or spiky	Gradational with marine shale	Plane beds and ripples	Fair to poor	Poor

Thickness (ft)	Width (ft)	Sandbody Geometry
5 to 11 individual 20 to 40 composite	500 to 3,000	dip-elongate and parallel ribbons
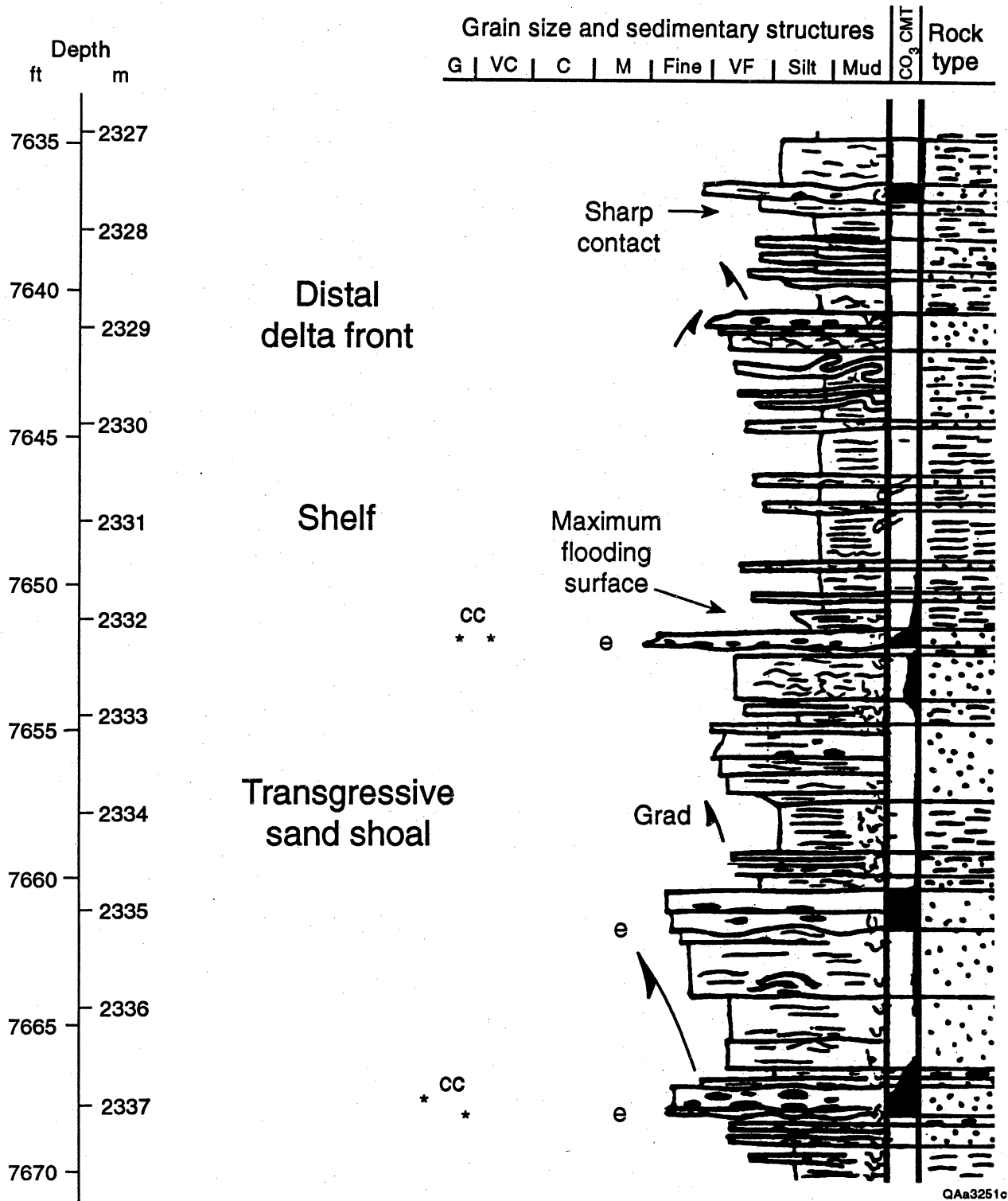
Figure 75. Core description of distal delta-front facies in the Lower C-3-X Submember, overlying shelf and transgressive sand-shoal facies in the Upper C-4-X Submember in the LL-3074 well. Maximum flooding surface at 7,681 ft correponds to boundary between C-3-X and C-4-X Members. Photograph of distal delta-front slump deposit (7,642 ft) is shown in figure 76.

125
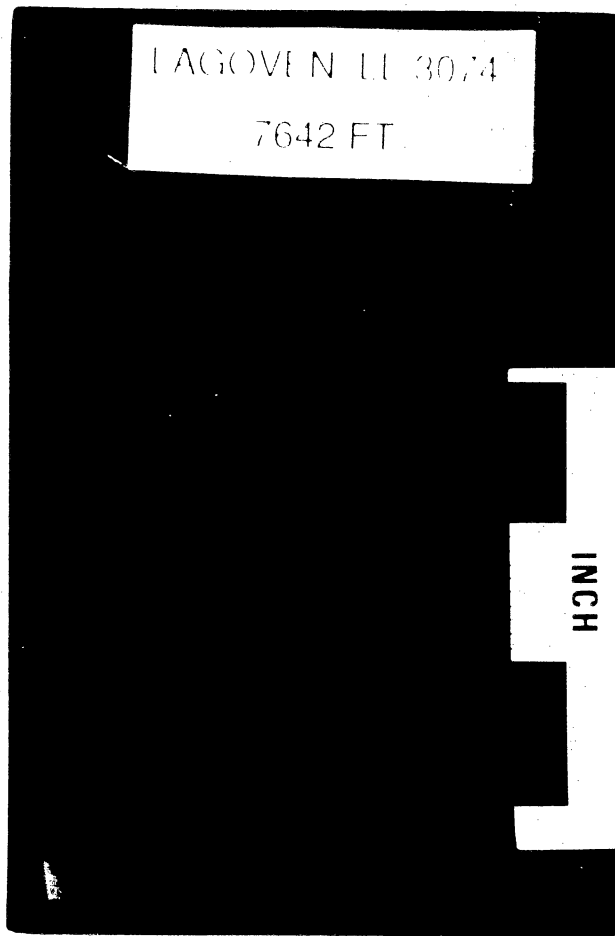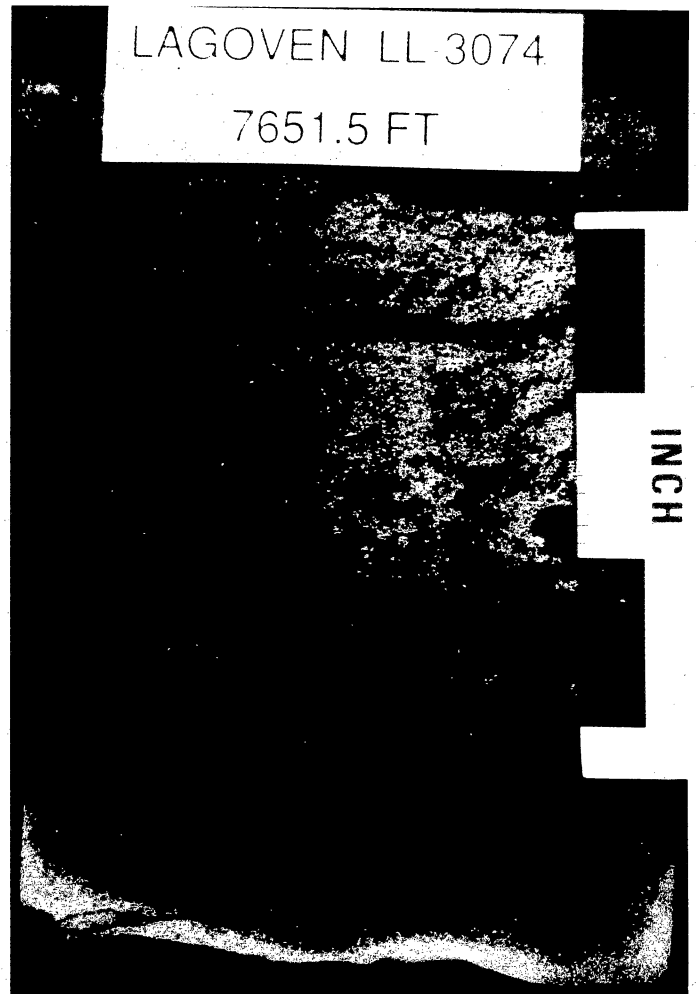
Figure 76. Photographs of (a) slump deposits in distal delta-front facies in the Lower C-3-X Submember and (b) transgressive, sand-shoal facies in the Upper C-4-X Submember.
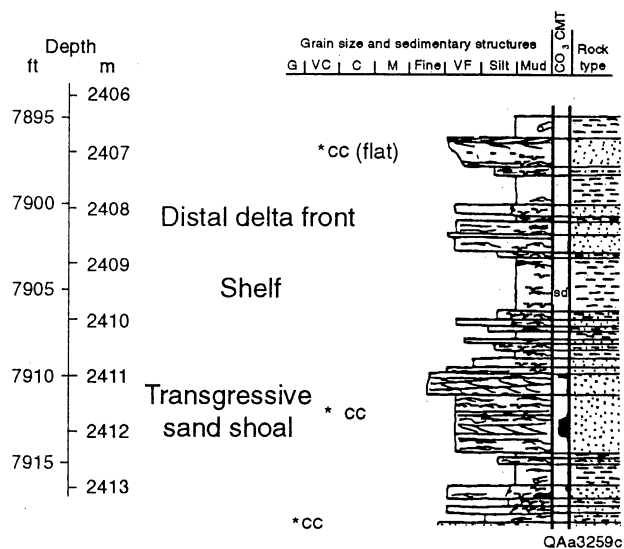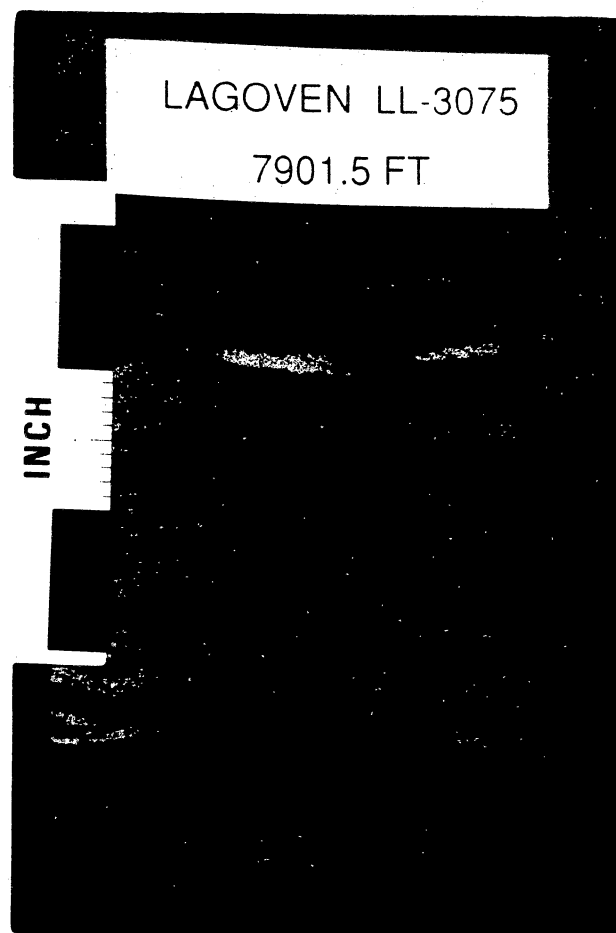
Figure 77. (a) Core description of distal delta-front facies in the Lower C-4-X Submember and (b) core photograph of asymmetrical, bidirectional ripples in distal delta-front facies.
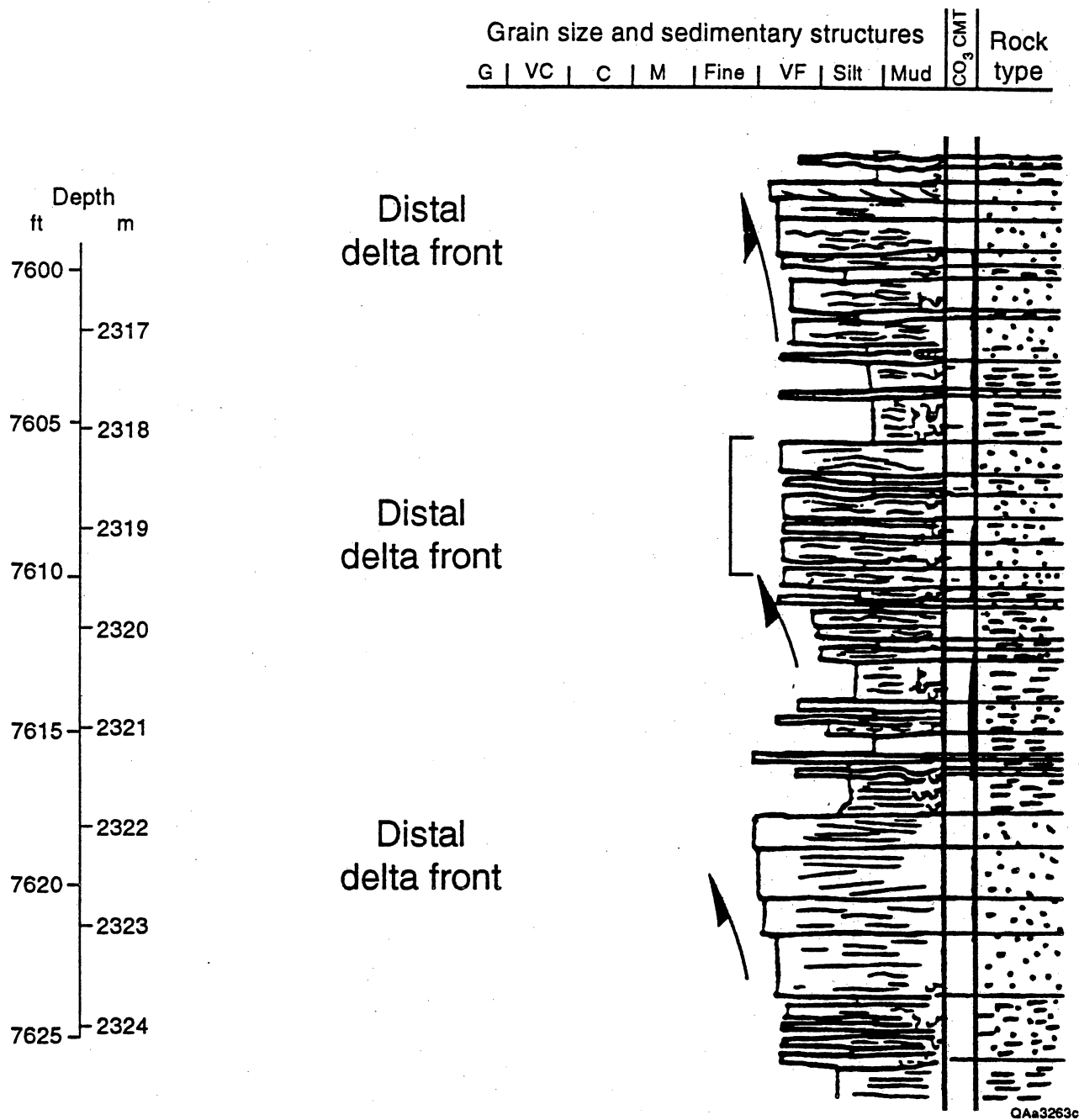
Figure 78. Core description of multiple distal delta-front deposits in the Lower C-3-X Submember in the LL-3074 well. Individual deposits are upward-coarsening and 6 to 9 ft (1.8 to 2.7 m) thick and interbedded with mudstone.

Table 12. Diagnostic features and characteristics of tidal-channel facies in the C Members.

Diagnostic Features

- Erosional base
- Small unit thickness

Grain-Size Trend	Log Response	Basal Contact	Stratification		Sorting	Visual Porosity
Upward-fining or blocky	Spiky (thin-bed response)	Erosional	Top: Asymmetrical ripples Base: Crossbeds		Variable moderate	Good to fair

Thickness (ft)	Width (ft)	Sandbody Geometry
5 to 10 individual 10 to 25 composite	1,000 to 2,500	sinuous dip-elongate ribbons

Table 13. Diagnostic features and characteristics of tidal-flat facies in the C Members.

Diagnostic Features

- Erosional base
- Upward-fining
- Basal crossbeds and clay clasts
- Dip-elongate sand geometry
- Commonly contains marine burrows

Grain-Size Trend	Log Response	Basal Contact	Stratification	Sorting	Visual Porosity
Upward-fining and blocky	Upward-fining and blocky	Erosional	Top: Plane beds, asymmetrical ripples Base: Tabular crossbeds	Variable	Variable but generally good

Thickness (ft)	Width (ft)	Sandbody Geometry
5 to 20 individual Up to 45 composite	1,000 to 4,000	dip-elongate and bifurcating ribbons

130
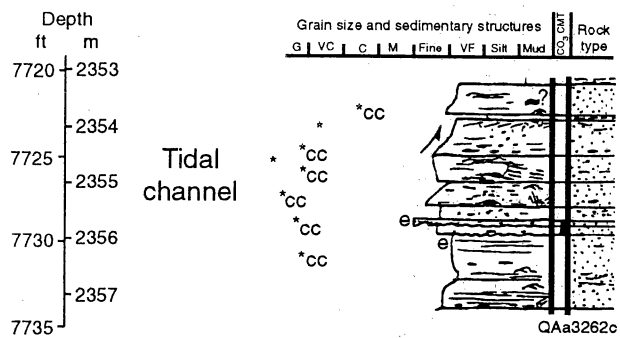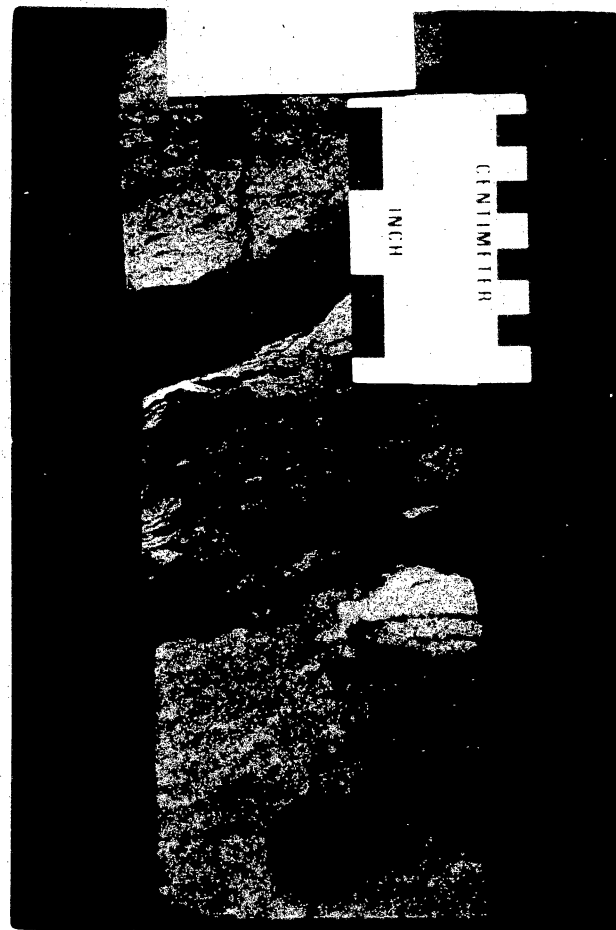
Figure 79. (a) Core description of tidal-channel facies in the Upper C-4-X Submember in the LL-2850 well and (b) core photograph of tidal-channel deposit.

A complete tidal-channel/tidal-flat sequence consists of a 15-ft (4.5-m), upward-fining section containing 9 ft (2.7 m) of erosionally based, crossbedded and rippled fine to very fine sandstone overlain by 6 ft (1.8 m) of rippled siltstone (fig. 80a). The ripples are primarily shale-draped, lenticular flaser ripples with minor reactivation surfaces (fig. 79b), reflecting fluctuating depositional energy.

Transgressive Sand Shoal and Shelf

The transgressive sand-shoal facies represents destructional delta-front deposits overlain by marine shelf deposits. Some sand-shoal deposits record autocyclic deltaic abandonment and subsidence, whereas others resulted from a general rise in sea level. The transgressive sand-shoal facies is distinguished by thin (2- to 10-ft [0.6- to 3-m]), upward-coarsening sandstones with numerous internal erosion surfaces and thin, calcareous zones (table 14). The shelf facies is distinguished by (1) fine grain size, (2) marine burrows, (3) high degree of lateral continuity, and (4) its stratigraphic position (commonly directly overlies the transgressive sand-shoal facies) (table 15).

An example of a transgressive sand-shoal/shelf facies couplet (fig 75) is a 16-ft (4.9-m) complex of multiple upward-coarsening, calcareous sandstones overlain by a 6-ft (1.2-m) section of siltstone with thin (approximately 6-in [2.4-cm]) sandstone interbeds. The lower section of sandstones contains large, irregular gravel-sized clay clasts, shell fragments, and numerous internal scour surfaces (fig. 76b). A similar transgressive sand-shoal/shelf facies couplet (fig. 81) consists of a pair of two upward-coarsening sandstones, each 5 to 7 ft (1.5 to 2.1 m) thick, overlain by a 4-ft (1.2-m) section of burrowed silty mudstone. One calcite-cemented zone contains cone-in-cone structures and stylolitic horizons (fig. 82a). The burrowed silty mudstones (shelf facies) contain numerous, thin lenses of very fine sandstone and siltstone (fig. 82b).

Fluvial-Estuarine Channel

The fluvial-estuarine channel facies, present in the Lower C-6-X Submember, consists of non-marine, valley-fill channel sandstones deposited during periods of sea-level fall. The diagnostic features of the fluvial-estuarine channel facies are (1) thick, massively crossbedded sandstones, (2) erosional base that commonly truncates marine shale, and (3) few or no marine burrows in the lower part of the section (table 16).

With subsequent rise in sea level, the narrow (less than 5 mi [8 km] wide) paleovalley carved by the entrenched, lowstand fluvial system became the locus of deposition for tidally influenced deltas in an embayed receiving basin (fig. 83). The fluvial-estuarine channel-fill sandstones are thickest in a northeast-trending belt in the LL-652 area (see figs. 106 and 107) and occupy paleotopographic low areas above an angular unconformity.

Examples of fluvial-estuarine, channel-fill sandstones (figs. 84 and 85) show a 30-ft (9-m) or more section of erosionally based, upward-fining sandstone in the Lower C-6-X Submember that truncates burrowed marine shale in the underlying C-7-X Member. The unburrowed sandstone contains large tabular crossbeds at the base; higher in the section there are small tabular crossbeds overlain by ripples and plane beds. Clay clasts and organic fragments (fig. 84b), which decrease in size upward, are abundant in the lower 14 ft (4.3 m) of section. A similar succession of rock types and bedforms is present in a Middle Jurassic valley-fill sequence in Northeastern England (Eschard and others, 1991), where the basal valley fill consists of massively crossbedded, erosion-based fluvial sandstone overlain by thinner and lenticular, mixed fluvial-tidal sandstones that are overlain by estuarine sand-flat deposits and transgressive shales.

132

(a)

(b)

Figure 80. (a) Core description of progradational tidal-flat facies in the Middle C-4-X Submember in the LL-2850 well and (b) core photograph of tidal-flat facies.

133

Table 14. Diagnostic features and characteristics of transgressive sand-shoal facies in the C-Members.

Diagnostic Features

- Thin and calcareous
- Internal erosion surfaces
- Overlain by shelf facies

Grain-Size Trend	Log Response	Basal Contact	Stratification		Sorting	Visual Porosity
Upward-coarsening	Spiky (thin-bed response)	Gradational, but may contain internal erosion surfaces	Top:	Inclined laminations, small crossbeds, symmetrical ripples	Variable	Variable, due to calcareous zones
			Base:	Plane beds and ripples		

Thickness (ft)	Width (ft)	Sandbody Geometry
2 to 10 individual 15 to 30 composite	many thousands of feet, but irregular	irregular sheet

134

Table 15. Diagnostic features and characteristics of shelf facies in the C Members.

Diagnostic Features

- Fine grain size
- Marine burrows
- High degree of lateral continuity

Grain-Size Trend	Log Response	Basal Contact	Stratification	Sorting	Visual Porosity
None	Baseline	May overlie calcareous and erosional zones	Planar laminations and starved ripples	Poor	None

Thickness (ft)	Width (ft)	Sandbody Geometry
Variable; Transgressive shales 2 to 10	>10,000	sheet

135
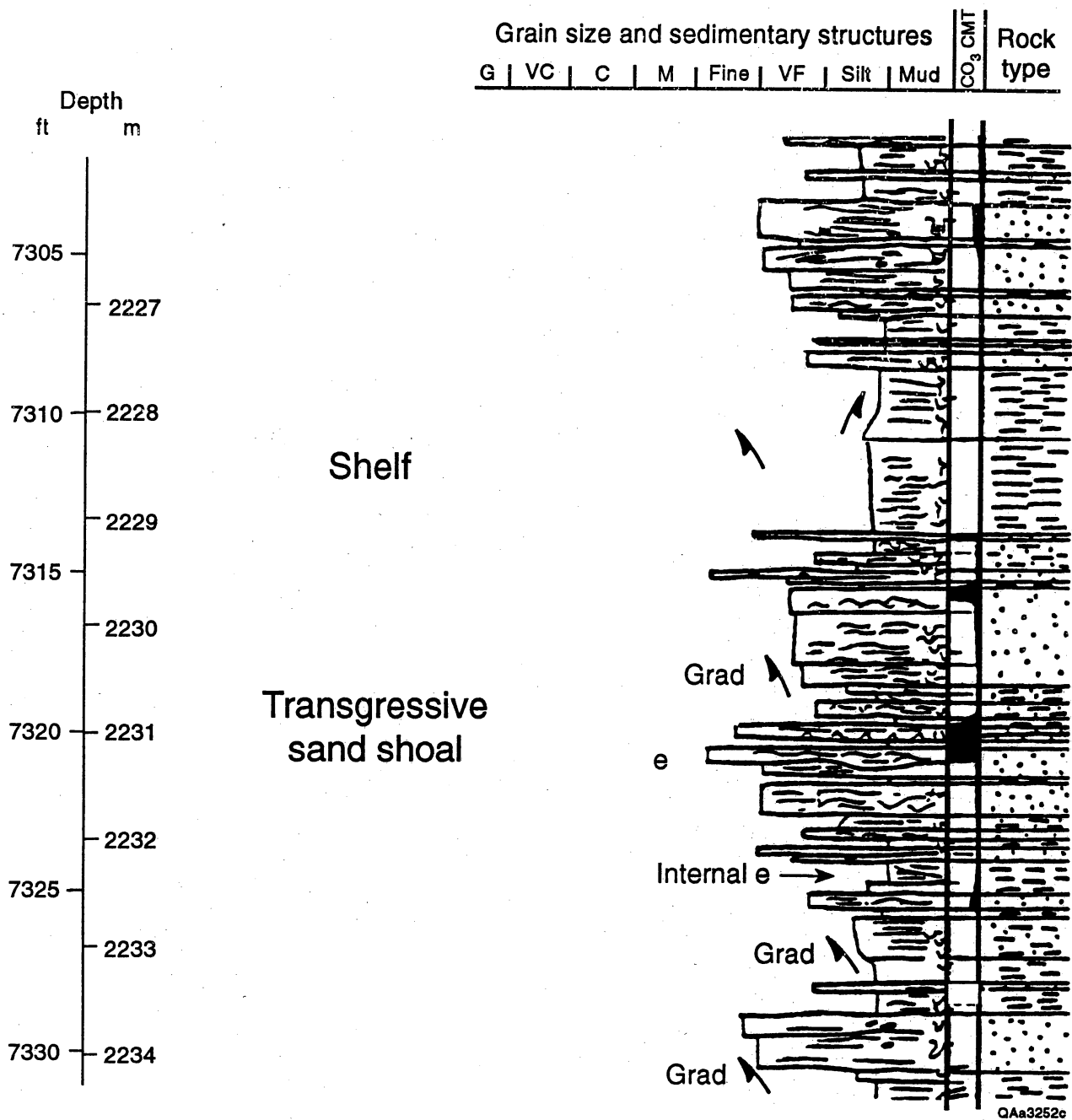
Figure 81. Core description of shelf and transgressive sand-shoal facies at the top of the Middle C-3-X Submember in the LL-3074 well. Photographs of stylolitic limestone (7,319.5 ft) and starved ripples in mudstone (7,311 ft) are shown in figure 82.

(a)
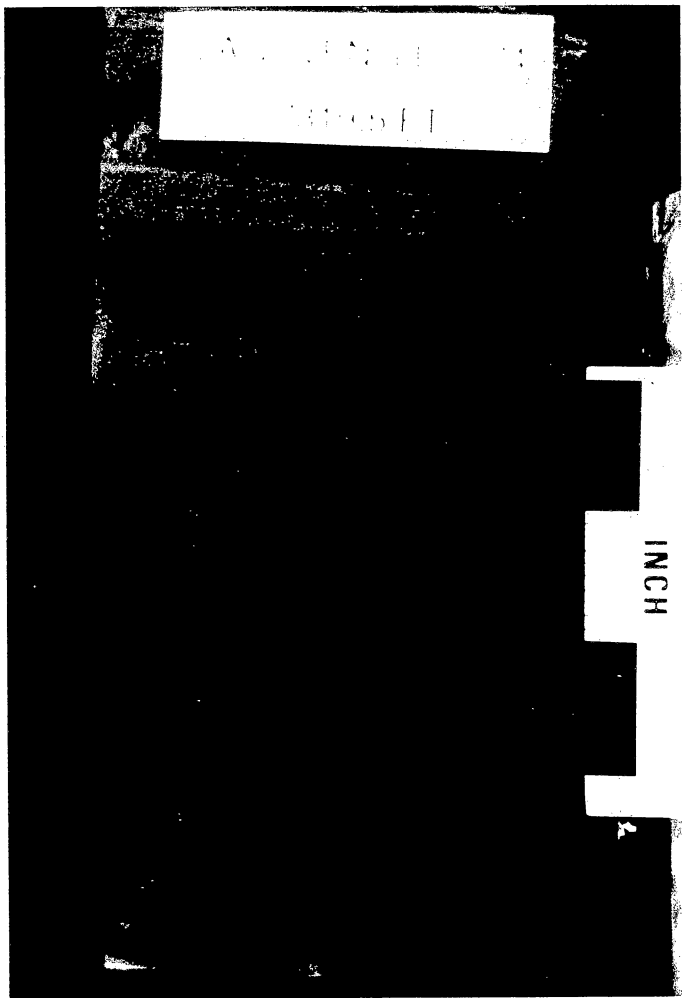
(b)
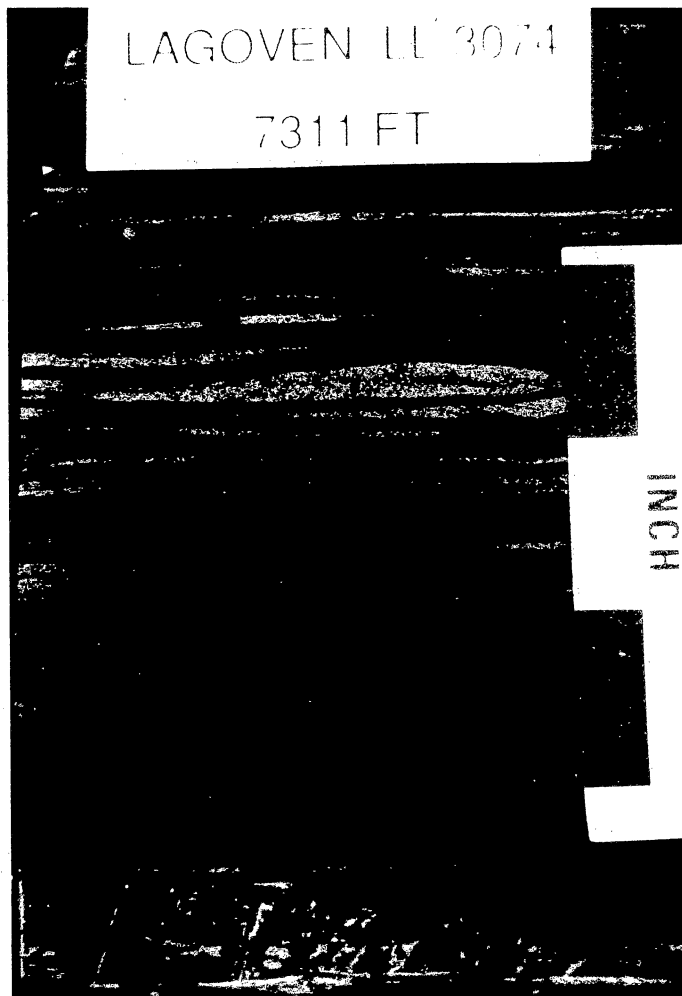
Figure 82. Photographs of (a) stylolitic limestone in transgressive sand-shoal facies and (b) lensoid beds and starved ripples in mudstone in shelf facies at the top of the Middle C-3-X Submember in the LL-3074 well. Core description is shown in figure 81.

Table 16. Diagnostic features and characteristics of fluvial-estuarine channel facies in the C Members.

Diagnostic Features

- Thick succession of multiple, massively crossbedded sandstones
- Erosional base; commonly truncates marine shale
- Few or no marine burrows in basal section; marine burrows in upper section

Grain-Size Trend	Log Response	Basal Contact	Stratification		Sorting	Visual Porosity
Upward-fining	Upward-fining or blocky	Erosional	Top:	Small crossbeds, plane beds, and ripples	Fair to poor	Good; decreases upward
			Base:	Large crossbeds with clay clasts		

Thickness (ft)	Width (ft)	Sandbody Geometry
20 to 40 individual 60 to 100 composite	2,000 to 6,000	dip-elongate belts

138

Legend:
- Floodplain
- Basal valley-fill
- Older deltaic deposits
- Younger deltaic deposits
- Upper valley-fill
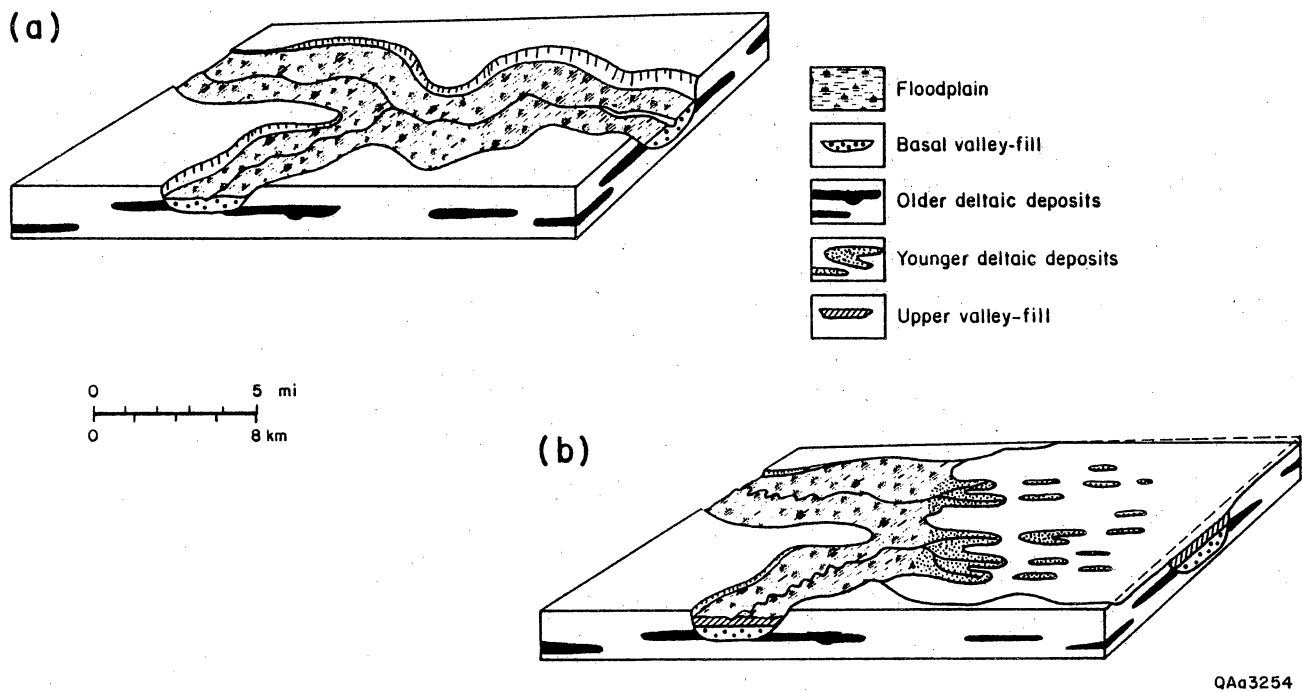
Figure 83. Schematic block diagram of (a) lowstand, entrenched paleovalley system with subsequent rise in sea level resulting in deposition of (b) highstand, tidally influenced deltaic system in an embayment. Unconformity corresponds to base of C-6-X Member in the LL-652 area..

139
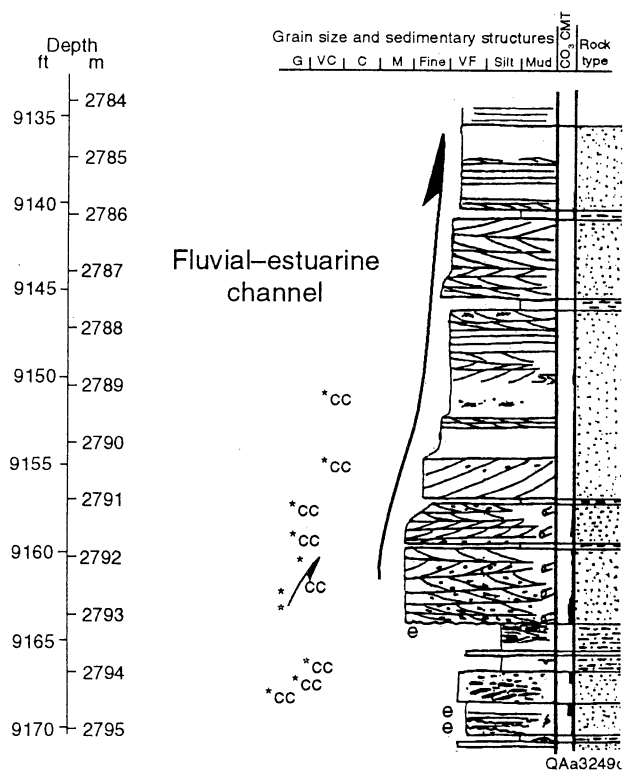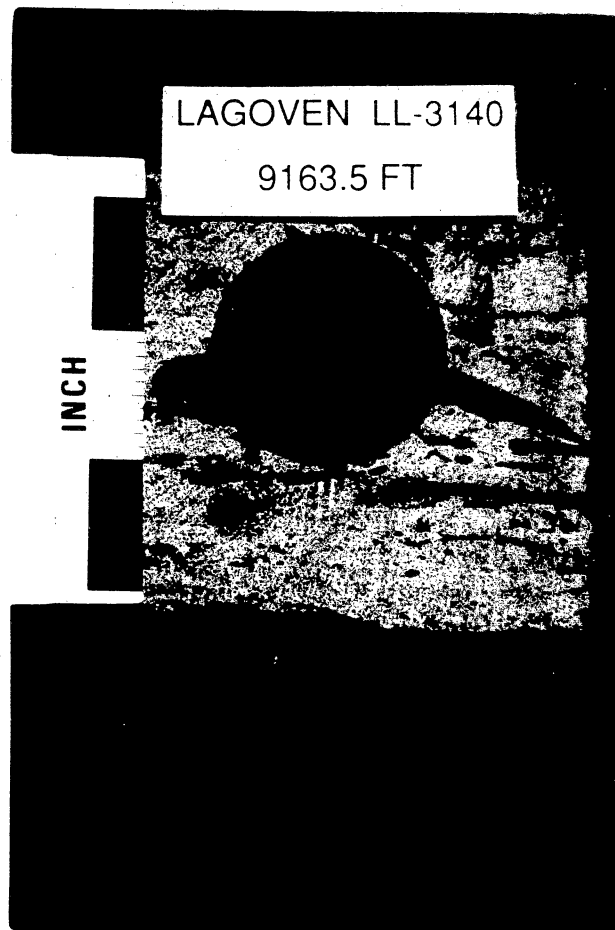
Figure 84. (a) Core description of fluvial-estuarine channel facies in the Lower Lower C-6-X Submember that truncates delta-front deposits in the C-7-X Member in the LL-3140 well and (b) core photograph of basal part of fluvial-estuarine channel facies in the LL-3140 well.

- Depth (ft)
- Permeability (MD)
- Depositional environments
- Grain size and sedimentary structures
- CO₃ cement / Rock type

Depositional environments (top to bottom):
DELTA FRONT
FLOODING SURFACE
TRANSGRESSIVE SAND SHOAL
UPPER ESTUARINE CHANNEL-FILL
FLOODING SURFACE
FLUVIAL
C-6-X
C-7-X
TIDAL CHANNEL AND TIDAL FLAT
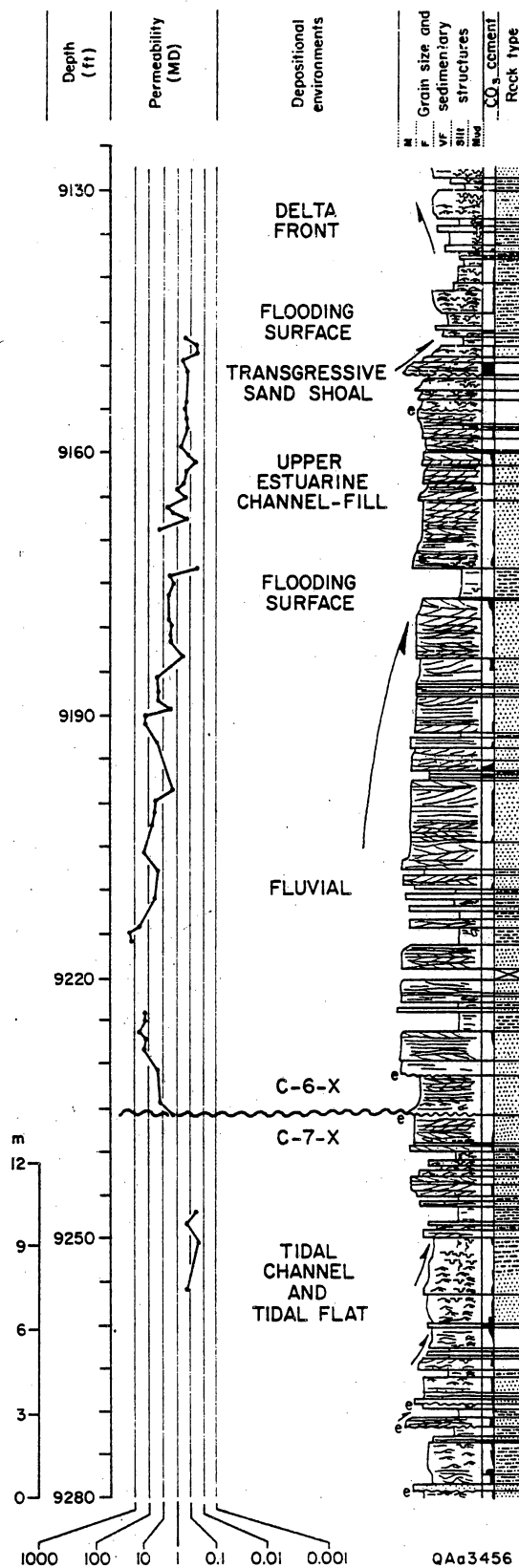
Figure 85. Core description of fluial-estuarine channel, upper estuarine channel-fill, and transgressive sand-shoal facies in the Lower Lower C-6-X Submember in the LL-3080 well. Permeability decreases upward in the sequence.

141

Three-Dimensional Architecture

Reservoirs in the C members are extremely heterogeneous as a result of the three-dimensional sandstone architecture, a function of deposition in a tide-dominated deltaic system. Sandstone architecture is dominated by a system of narrow (less than 2,000 ft [610 m] wide), dip-elongate and dip-parallel, northeast-trending sandbodies (fig. 63). The strong northeast-trending grain of the sandbodies may result in anisotropic reservoir drainage patterns and must be considered in new infill well locations, recompletions, and waterflood programs in the LL-652 area.

The primary facies that together comprise the bulk of the C reservoirs are (1) delta-front, (2) distal delta-front, and (3) distributary-channel (table 17). Minor facies are (4) tidal-channel, (5) channel-mouth-bar, and (6) fluvial-estuarine channel. The other facies, (7) transgressive sand-shoal, (8) shelf, and (9) tidal-flat, are poor-quality reservoir facies because of either diagenetic heterogeneities (complex, calcite-cemented zones) or high mudstone content.

The tide-dominated deltaic facies tract in the LL-652 area forms a strongly dip-elongate system. However, within this system there are specific changes in sandstone geometry and in sandstone partitioning (figs. 86 to 88). Net- and percent-sandstone patterns in the lower delta plain are typically complex and reticulated, whereas in the transition between lower delta plain and proximal delta front (distributary-channel and channel-mouth bar facies) they are dip-elongate and bifurcating (fig. 86). Both the proximal and distal delta-front facies contain dip-parallel sandstone bodies that are progressively thinner downdip.

In progradational sequences the sandiest parts of the deltaic system are the delta-front and distributary-channel/channel-mouth bar facies, whereas the distal delta-front and lower delta-plain facies are relatively muddy (fig. 87). Examples of progradational sequences in the LL-652 area are the Middle C-5-X Submember and the Upper C-3-X Submember (table 18). These submembers are sandstone-rich, averaging a maximum of 50 to 70 percent sandstone in distributary-channel and delta-front facies. However, the upper part of the Middle C-4-X Submember (fig. 5), which represents mainly interdistributary and tidal-flat deposits in the LL-652 area, is relatively muddy.

In retrogradational sequences the sandiest part of the deltaic system is the distributary channel/channel mouth bar, whereas both the proximal and distal delta front are sandstone-poor (fig. 88). Examples in the LL-652 area include the Upper 21-22 interval in the Lower Upper C-6-X, Lower C-5-X, Lower C-4-X, and Lower C-3-X Submembers (table 18). Delta-front deposits in these submembers typically contain only 20 to 30 percent sandstone, in contrast to the relatively sandstone-rich, distributary-channel system.

In aggradational sequences where deposition was sufficient to keep pace with rising sea level, the dominant preserved facies are distributary-channel, channel-mouth bar, and proximal delta-front (table 18). However, the distributary-channel facies is sandier than the delta-front facies. In the Middle C-3-X Submember, the distributary-channel facies correspond to relatively thick belts of more than 50 percent sandstone, but delta-front deposits contain only 30 to 40 percent sandstone. In the Lower 21-22 interval (Lower Upper C-6-X Submember) and the Upper C-3-X Submember the proximal delta-front deposits contain only 20 to 30 percent sandstone.

In sequences with base-level fall and extreme offlap northeast of the LL-652 area, net- and percent-sandstone patterns are dominated by linear, fluvial sandstone belts that locally contain more than 60 percent sandstone (table 18). Sandstones, locally more than 70 ft (21.3 m) thick, were deposited in a coarse-grained fluvial system that incised into older delta-front deposits (fig. 83). These belts are separated by sandstone-poor, interfluvial areas that escaped channel incision.

The infield development potential of reservoirs in the C members, based on net-sandstone distribution of the different deltaic facies, varies between the different types of sequences. Distributary-channel and channel-mouth bar facies are excellent targets, especially in progradational sandstones that were

142

Table 17. Summary of three-dimensional facies geometry and heterogeneity in the C Members.

A. Volumetrically Significant Facies

Facies	Individual Thickness (ft)	Width (ft)	Sandbody Shape	Sandbody Trend	Internal Heterogeneities	Common Bounding Facies
(1) Delta Front	5-20	500-3,000	Dip-elongate ribbon	dip	Minor shale interbeds in lower half channel	(l) distal delta front (v) shelf (l, v) distributary
(2) Distal Delta Front	5-10	500-3,000	Dip-elongate ribbon	dip	Multiple shale interbeds	(l) delta front (v) shelf
(3) Distributary Channel	5-20	1,000-4,000	Bifurcating ribbon	dip	Shale interbeds in upper half; clay clasts in lower half	(l) tidal flat (l, v) delta front

B. Volumetrically Less Significant Facies

Facies	Individual Thickness (ft)	Width (ft)	Sandbody Shape	Sandbody Trend	Internal Heterogeneities	Common Bounding Facies
(4) Tidal Channel	5-10	1,000-2,500	Sinuous ribbon	dip	Similar to Distributary channel	(l,v) Tidal Flat
(5) Channel-Mouth Bar	5-10	2,000?	Lobate pod	dip?	Few	(l,v) distributary channel (l,v) delta front
(6) Fluvial-Estuarine Channel	20-40	2,000-6,000	Dip-elongate belt	dip	Clay clasts at base	(l,v) any, particularly delta front

C. Other Facies

Facies	Individual Thickness (ft)	Width (ft)	Sandbody Shape	Sandbody Trend	Internal Heterogeneities	Common Bounding Facies
(7) Transgressive Sand Shoal	2-10	?	Irregular sheet	?	Calcite-cemented zones, clay clasts	(v) shelf (v) delta front
(8) Shelf	2-10	> 10,000	Sheet	?	Mudstone-dominated	(v) transgressive sand shoal (v) delta front (v) distal delta front
(9) Tidal Flat	10-20	1,000-5,000	Sheet	strike	Mudstone-dominated	(l) distributary channel (l, v) tidal channel

(l) Lateral
(v) Vertical
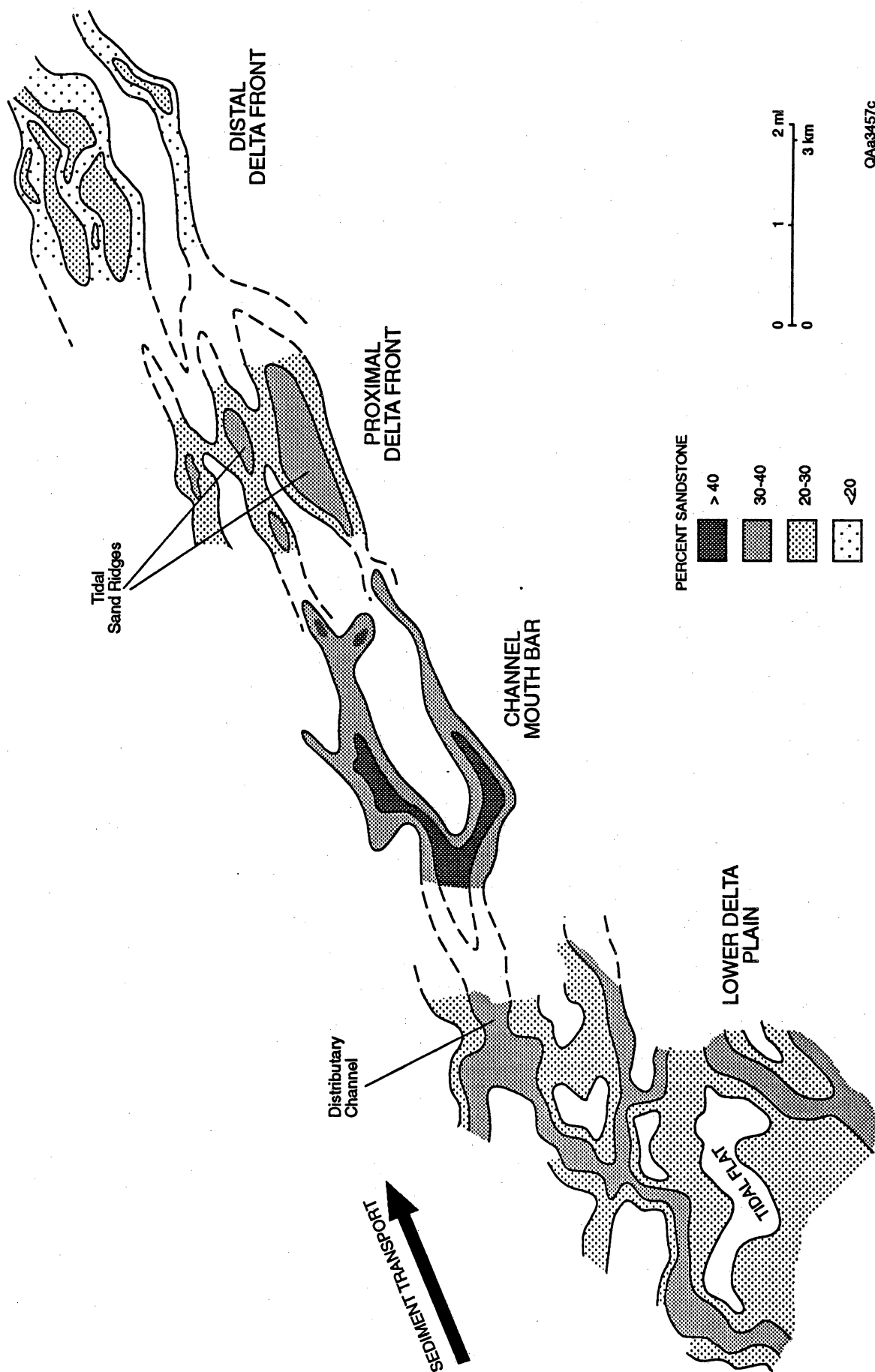
Figure 86. Relative percent-sandstone values in the tide-dominated deltaic facies tract in C members in the LL-652 area. The sandiest part of the deltaic system is the channel-mouth bar and proximal delta front. Percent-sandstone patterns are from maps of representative C submembers: lower delta plain (Middle C-4-X Submember), channel-mouth bar (#4 Unit in Upper C-4-X Submember), proximal delta-front (Lower Middle C-5-X Submember), and distal delta-front (Lower C-3-X Submember).

144
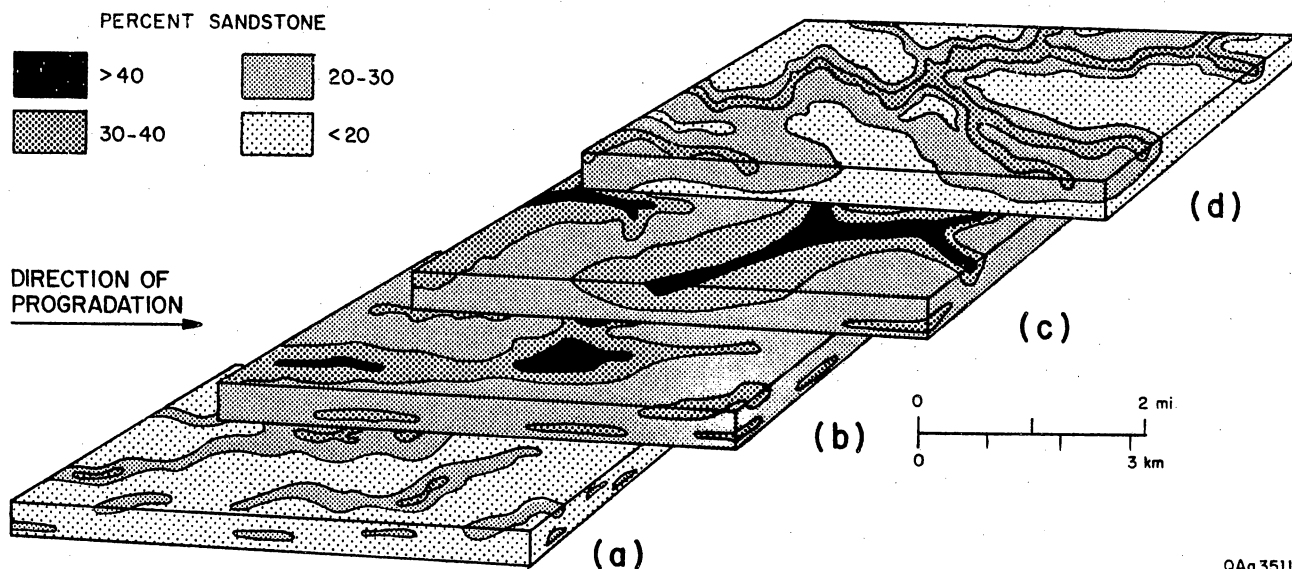
Figure 87. Typical percent-sandstone patterns in offlapping, progradational sequences in the tide-dominated deltaic facies tract in the C members in the LL-652 area, showing superposition and basinward progradation of (a) distal delta-front, (b) proximal delta-front, (c) distributary-channel and channel-mouth-bar, overlain by (d) lower delta-plain facies. The sandiest part of the facies tract is the distributary-channel and channel-mouth bar.

145
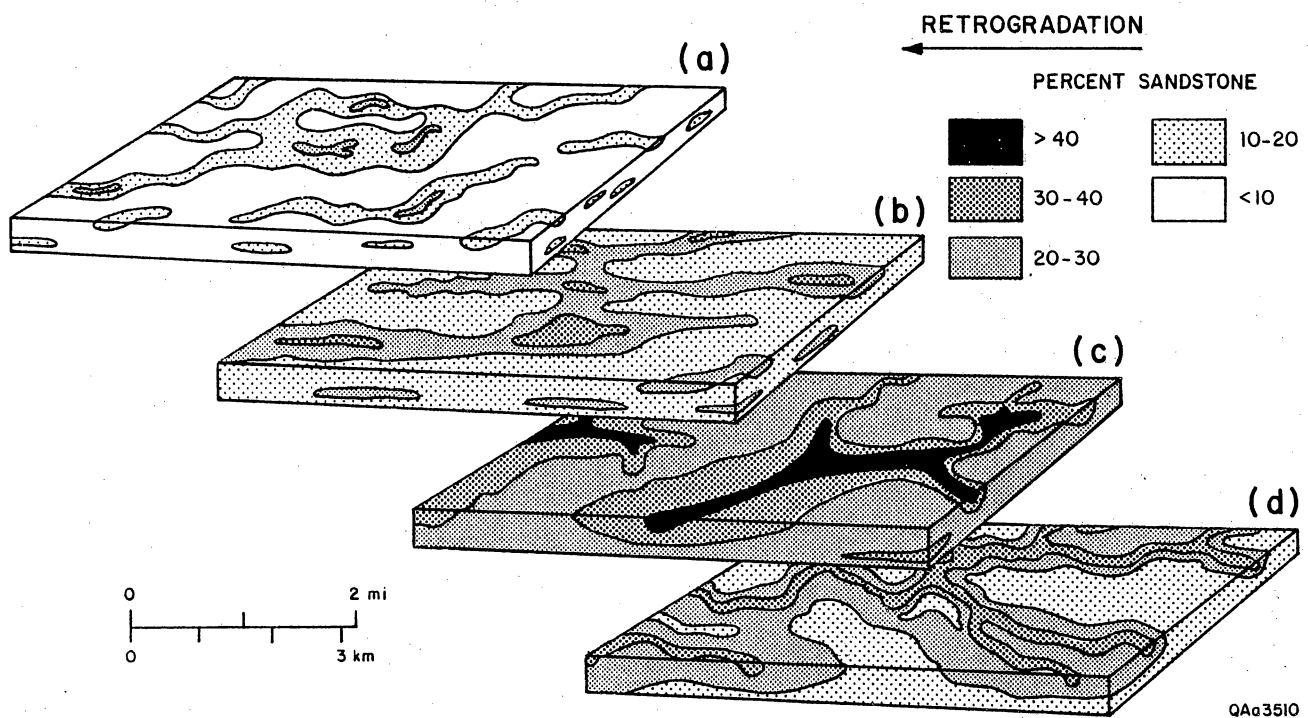
Figure 88. Typical percent-sandstone patterns in retrogradational sequences in the tide-dominated deltaic facies tract in C members in the LL-652 area. The sandiest part of the facies tract is the distributary-channel and channel-mouth bar, whereas both the proximal and distal distal-front are sandstone-poor.

146

Table 18. Variations in net-sandstone-thickness patterns in facies in different types of stratigraphic sequences in the C Members.

Cycle	Examples	Type of Net-Sandstone Patterns	% Sandstone	Net Sandstone (ft)	Thickness of Interval	Dominant Facies
Extreme Offlap (Base-Level Fall)	Upper Lower C-6-X	Linear belts of locally thick sandstone	locally >60	locally >70	~150	Fluvial valley fill and delta front
	Lower Lower C-6-X	Linear belts of locally thick sandstone w/erosional base	locally >60	locally >100	150-200	Fluvial valley fill
Offlap	Upper C-4-X	Elongate belts of variable width	Belts of 50-70	Belts of >100	100-150	Distributary channel and delta front
	#4 Sandstone in Upper C-4-X	Narrow, bifurcating, dip-elongate belts pinching out downdip	Belts of 60-80	Belts of 30-40	50-80	Distributary channel >delta front
	15-16 interval in Middle C-4-X	Narrow, sinuous and reticulated belts	~30*	Belts of 20-30	80-100	Tidal channel/tidal flat
	Middle C-5-X	E- and NE-trending and bifurcating dip-elongate system	wide (>2 mi) belts of 40-50	wide belts of 80-100	200-250	Distributary channel and delta front
Progradation during Retrogradation	Upper C-3-X	Narrow, downdip-bifurcating dip-elongate system	Belts of 20	Belts of 30-40	~200	Proximal delta front
	Middle C-3-X	Sinuous, interconnected dip-elongate belts of variable width	1-2 mi wide belts of >50	Belts of 40-50	100	Distributary channel truncating delta front
	Lower 21-22 interval in Lower Upper C-6-X	Dip-elongate, bifurcating belts, 1 mi wide	~30*	Belts of >40	~100	Proximal delta front
Retrogradation	Lower C-3-X	Narrow, parallel belts of sandstone, downdip of depocenter	~20	Belts of >50	300	Delta front
	Lower C-4-X	Dip-elongate belts	Belts of 15-25	60-80	250	Delta front
	Lower C-5-X	Dip-elongate, east-trending belts, 1-2 mi wide	Narrow belts of >30	70	250	Delta front
	Upper 21-22 interval in C-6-X	1-2 mi-wide belts, dip-elongate and subparallel	~30*	Belts of >30	100	Delta front

* Calculated from net sandstone thickness

147

deposited during periods of net retrogradation, because in these sequences there is a relatively greater net-sandstone and permeability contrast between these facies and the sandstone-poor, delta-front facies. Intrareservoir stratigraphic traps are favorable in these areas of permeability contrasts, whereas progradational sequences deposited during periods of offlap may contain fewer permeability contrasts between the distributary-channel and delta-front facies that are both sandstone-rich.

In contrast, there is little variation in relative sandiness in the interdistributary/tidal-flat facies (lower-delta-plain) between progradational and retrogradational cycles in the LL-652 area. This part of the deltaic facies tract was an area of sediment bypass in progradational cycles when sediment was stored in the delta-front and channel-mouth-bar facies. During retrogradation, relatively more sediment was stored in the distributary channels than in the delta front, but interdistributary areas were relatively muddy. Therefore, the lower-delta-plain facies tract is heterogeneous in the C members and is inferred to contain multiple sites of permeability contrasts that may represent numerous but small stratigraphic traps for remaining mobile oil. Excellent examples of genetic depositional episodes (submembers) with high-reservoir-quality sandstone encased in muddy interdistributary deposits are the Upper C-4-X and Middle C-3-X Submembers. These two submembers together account for most of the production in the combined C-3-X/C-4-X Members and yet still contain a high potential for secondary oil production.

In both the volumetrically significant and less significant facies, the dominant sandbody trends and shapes are ribbons and belts, whereas in the other facies the sandbodies occur as sheets with no dominant trend (table 17). Each facies contains component heterogeneities that limit internal reservoir sandstone continuity. The most homogeneous facies is channel-mouth bar; however, it is uncommon in the C members. Facies with moderate internal heterogeneities—delta-front, distributary-channel, tidal-channel, and fluvial-estuarine channel—differ slightly in where these internal heterogeneities occur. For example, in the delta-front facies, maximum reservoir-quality sandstone is at the top of the upward-coarsening section, where silt and mud were winnowed out by wave and tidal processes. Distributary-, tidal-, and fluvial-estuarine channel facies are expected to contain the best reservoir-quality sandstone toward the base (for example, fig. 85), where the grain size of the sandstone is maximum, but the lower part of the channel facies also commonly contains clay clasts, organic fragments, and intraformational channel-margin, bank-collapse material that limit reservoir quality. The distal delta-front facies, although volumetrically significant, contain numerous internal heterogeneities (multiple shale interbeds) that limit vertical reservoir communication. The remaining facies (transgressive sand-shoal, shelf, tidal-flat) are internally heterogeneous or muddy and may be difficult to develop efficiently.

The tide-dominated deltaic facies architecture and diagenetic history together control reservoir permeability (fig. 86 and table 17). Fieldwide unconformities associated with sequence boundaries (base-level changes) and phases of deltaic abandonment (ravinement surfaces) may constitute significant permeability barriers. Additionally, local permeability barriers that extend over short distances (2,000 ft [610 m] or less) are controlled by facies pinchouts such as distributary- and tidal-channel sandstone into tidal-flat mudstone and superposition of distributary-channel onto delta-front deposits. For example, lateral pinchouts of sandy tidal-channel deposits into the muddy tidal flat are expected to form permeability barriers, but superposition of sandstone-rich distributary-channel deposits onto delta-front sandstones may only constitute permeability barriers if the base of distributary-channel deposits contains abundant clay clasts and organic fragments that can retard vertical fluid flow along the facies contact. Similarly, the seaward (northeastward) transition from distributary channel, channel-mouth bar, delta front, to distal delta front is gradational, with inferred permeability loss over only great distances northeastward.

Permeability and Porosity Characteristics

The main control on reservoir quality (permeability and porosity) in the C members is depth (table 19). The median permeability of coreplug samples in each member decreases from 30.4 md in the C-3-X Member to 0.61 md in the C-7-X Member (figs. 89a and 90). The cumulative-frequency curves of the C-3-X and C-4-X Members differ substantially from those of C-5-X through C-7-X Members. However, this may

Table 19. Statistical summary of porosity and permeability in the C-3-X to C-7-X Members.

Statistic Summary of Porosity

UNIT	C3	C4	C5	C6	C7
Minimum	4.5	1.8	1.6	0.30000001	2.0999999
Maximum	25.4	155.89999	19.799999	17.9	12.7
Sum	2027.4	5209.4	1768.5	4164.7	571.5
Points	116	329	136	412	64
Mean	17.477586	15.834043	13.003677	10.108495	8.9296875
Median	17.6	16.1	13.5	10.2	9.3499999
RMS	17.816415	17.902733	13.639193	10.522183	9.2577754
Std Deviation	3.4731288	8.366822	4.1300598	2.924966	2.4620729
Variance	12.062624	70.00371	17.057394	8.5554264	6.0618031
Std Error	0.32247192	0.46127783	0.35414971	0.14410273	0.30775912
Skewness	-0.65341832	14.227036	-0.61921384	-0.49572763	-0.78173056
Kurtosis	1.0076929	237.31314	-0.34621651	1.0614017	0.042629948

Statistic Summary of Permeability

Unit	C3	C4	C5	C6	C7
Minimum	0.019999	0.10000	0.0010000	0.0019999	0.019999
Maximum	784.00	1572.9	105.93	1392.0	71.900
Points	115.00	323.00	134.00	392.00	59.000
Mean	20.183	14.724	1.2841	0.88964	0.60700
Median	30.400	15.999	1.1588	0.64498	0.61000
RMS	40.799	28.088	10.411	11.673	8.3949
Std Deviation	8.8748	7.2113	10.363	11.677	8.0525
Variance	7.9250	5.4474	10.745	13.777	6.6177
Std Error	1.2258	1.1162	1.2238	1.1322	1.3120
Skewness	0.20820	0.62612	0.79511	3.0831	1.6358
Kurtosis	0.52228	0.25029	0.18677	0.71966	0.26177

(a)
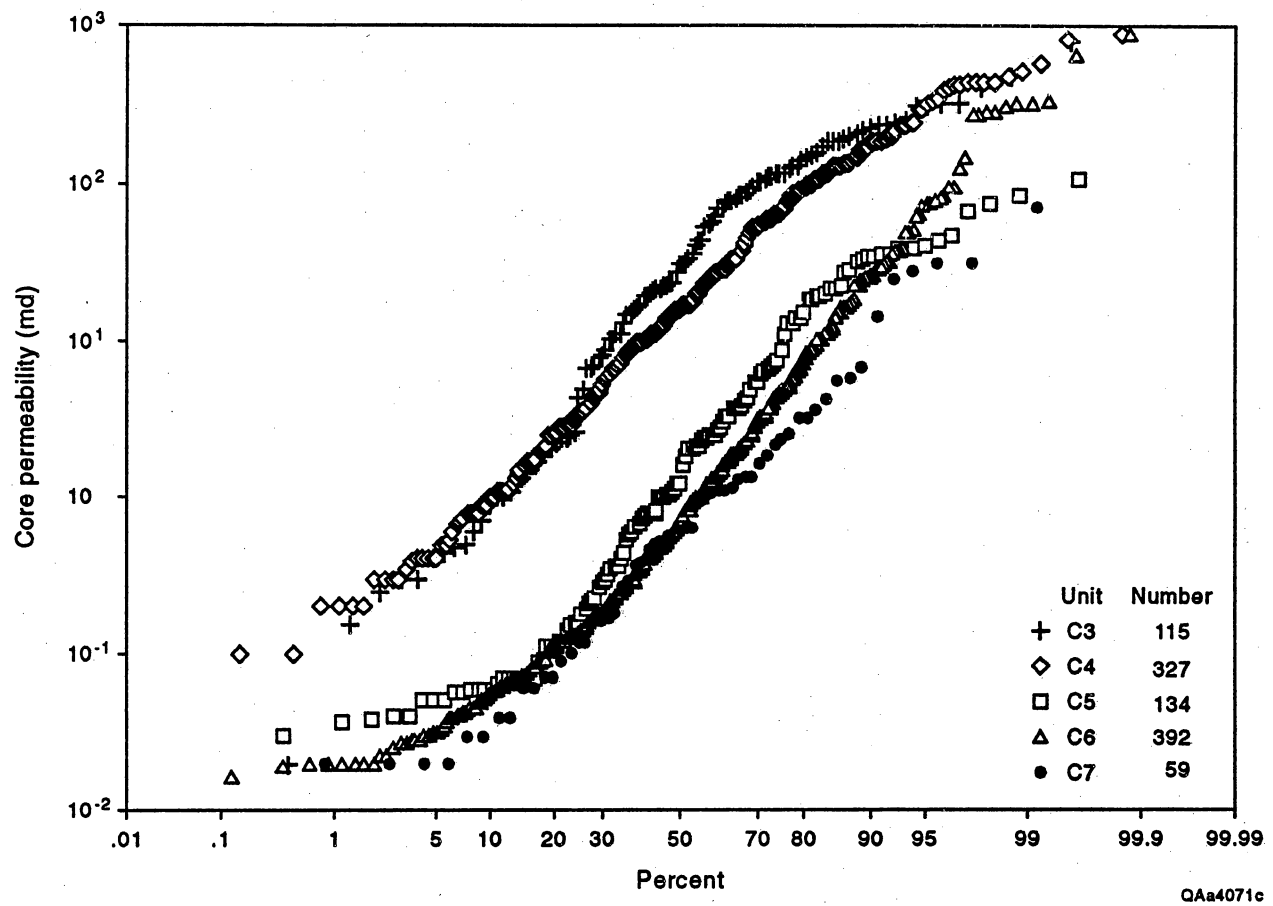
Figure 89. (a) Cumulative frequency plot of whole-core permeability in the C-3-X to C-7-X Members in the LL-652 area.

150

(b)
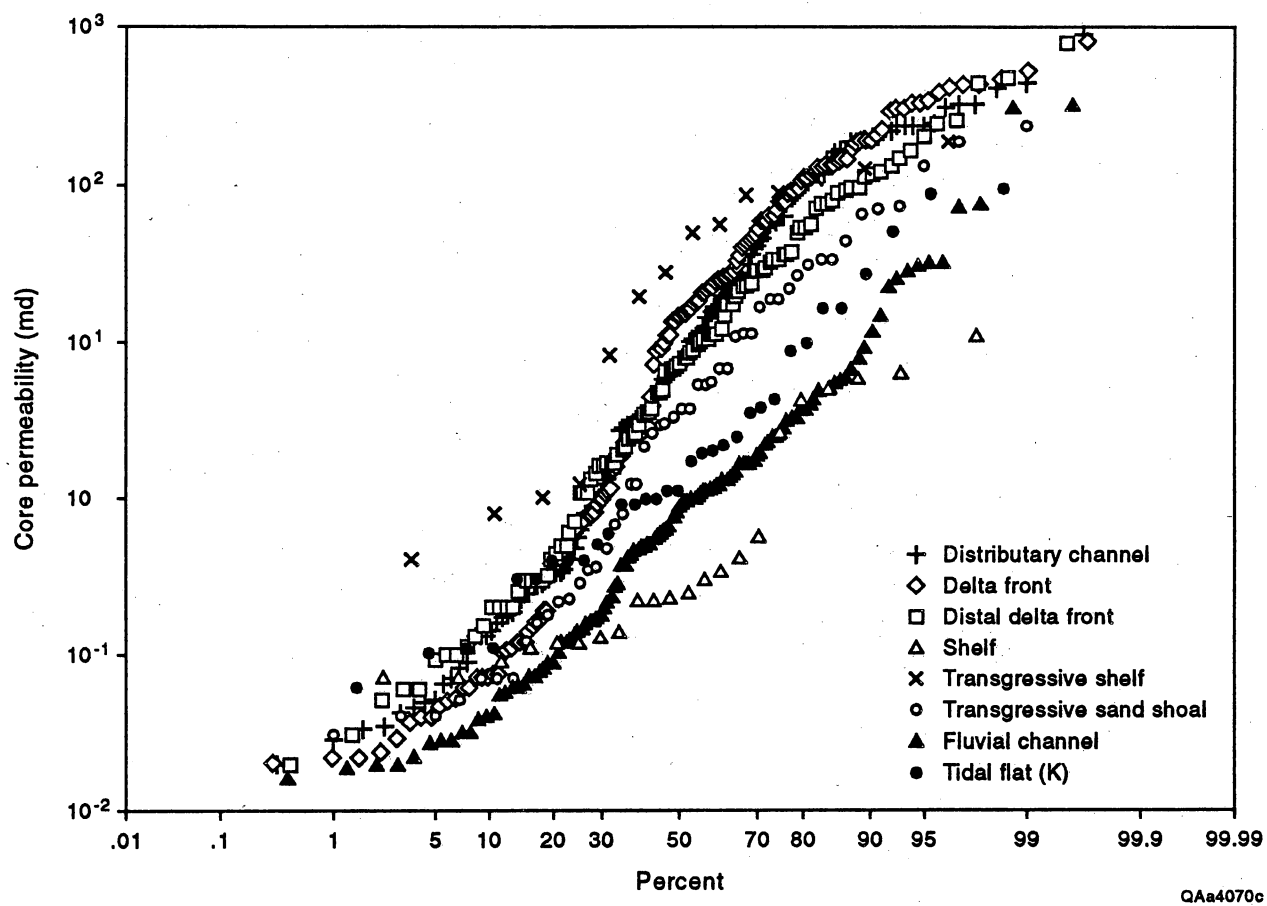
Figure 89. (b) Cumulative frequency plot of facies permeability in the C-3-X to C-7-X Members in the LL-652 area.
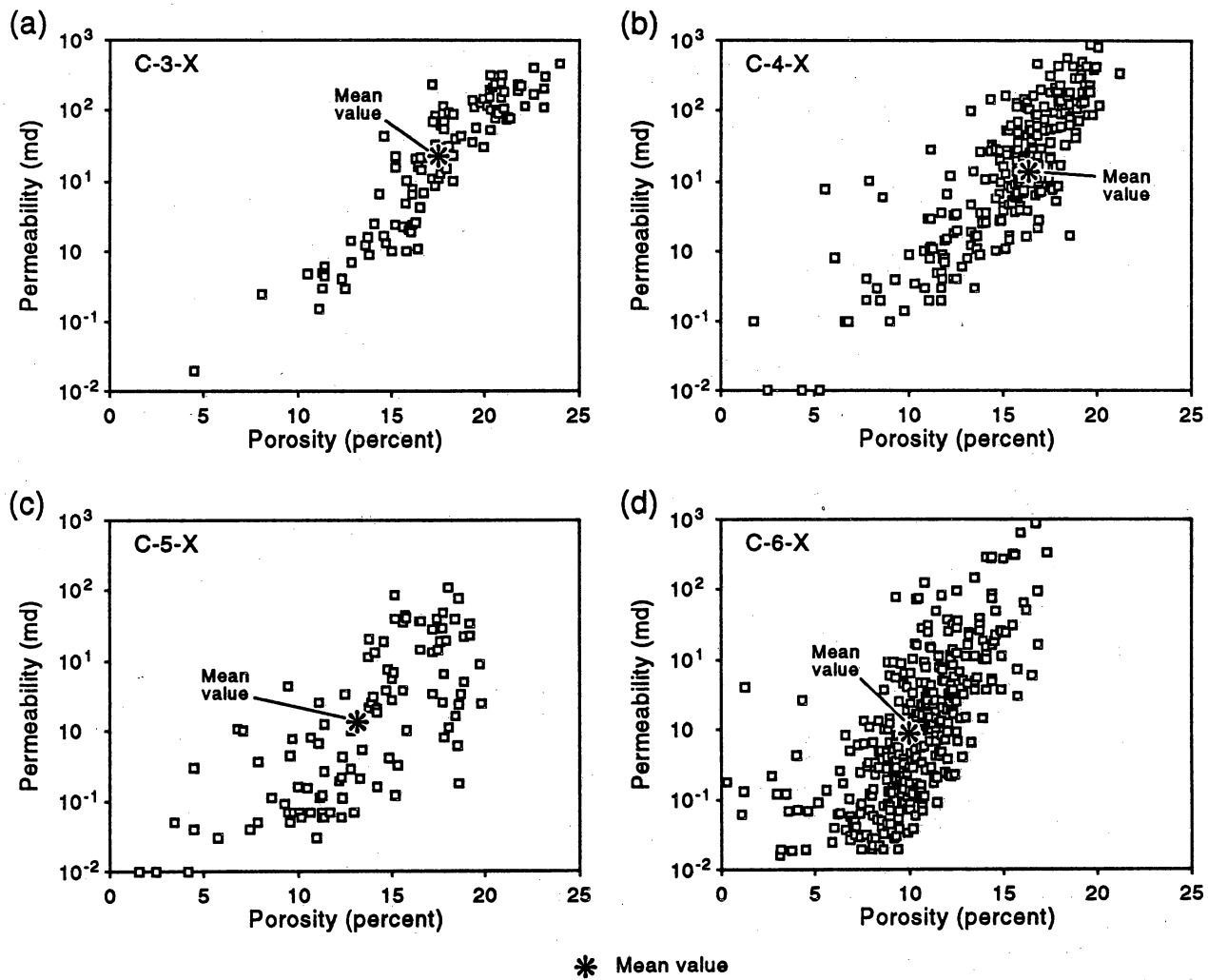
Figure 90. Permeability-porosity crossplots of the C-3-X to C-7-X Members.

152

be partly due to sampling bias: the depth differential between the Middle and Lower C-3-X Submembers and the Upper C-4-X Submember is commonly only 250 ft (76 m). In contrast, the depth differential between the Upper C-4-X Submember and Middle to Upper C-5-X Submembers is commonly as much as 600 ft (183 m).

A cumulative-frequency plot of permeability of different facies in the combined C-3-X to C-7-X Members shows great similarity in the volumetrically important distributary-channel, delta-front, and distal delta-front facies (fig. 89b). However, the volumetrically less important facies show clear departures from the trend of the main facies. For example, the transgressive shelf facies (sandy, basal part of shelf facies) is the most permeable; however, this facies was sampled only in the shallow C-3-X Member, where permeability values in almost all facies are high. Likewise, the fluvial-estuarine channel facies in the C-6-X Member has a low-permeability trend because of great sample depth. The two volumetrically unimportant facies with expected permeability trends are tidal-flat and shelf; these facies are mudstone-rich and are therefore expected to have low permeability values. Furthermore, the tidal-flat and shelf facies were sampled throughout the C-3-X to C-7-X Members, thereby removing the effects of sample depth from the permeability trends of these facies. In virtually all cases, permeability and porosity values in each facies decrease with depth from the C-3-X to C-6-X Members (figs. 91 to 97), whereas differences between facies in the same member are only slight to non-existent (figs. 98 to 101). For example, there are no significant differences in permeability and porosity between the distributary-channel and delta-front facies, except in the C-5-X Member (fig. 98). Likewise, few differences exist between distributary-channel and distal delta-front facies (fig. 99), although a clear difference exists between distributary-channel and tidal-flat facies in the C-3-X and C-4-X Members (fig. 100), as well as a slightly higher average porosity in tidal-channel compared to the tidal-flat facies in the C-4-X Member (fig. 101a).

The permeability-porosity distribution data, although indicating great similarity in facies, do not assess the importance of permeability and porosity contrasts along facies boundaries. For example, there is an order-of-magnitude difference in permeability across the distributary-channel/delta-front facies boundary in the LL-2850 well in the Middle C-3-X Submember, although the average permeability for each of these facies is virtually the same (fig. 102). In addition, there is up to a two order-of-magnitude difference in permeability across the distributary-channel/tidal-flat facies boundary in this well.

Permeability differences also exist along certain segments of the unconformity associated with the fluvial-estuarine channel facies; for example, there is a two to three order-of-magnitude difference in permeability across the fluvial-estuarine channel/tidal-flat facies boundary in the LL-3080 well (fig. 103). However, where the fluvial-estuarine channel facies truncates the distributary-channel facies, there is no permeability contrast.

The permeability-porosity crossplots (figs. 98-101) also ignore differences in reservoir quality that exist over short intervals within individual facies. For example, the permeability varies from less than 1 md to almost 1,000 md in 5-ft (1.5-m) intervals within individual distal delta-front and distributary-channel deposits in the LL-2850 well in the Upper C-4-X Submember (fig. 104). These small-interval permeability variations reflect the depositional style, which in turn controls the rock fabric (sedimentary structures) and degree of shaly interbeds, clay clasts, and burrows. Another control on these small-interval permeability variations is diagenesis (calcite-cemented zones, clay type, etc.). These permeability variations, caused by both depositional and diagenetic factors, can be integrated to make an improved model of reservoir heterogeneity.
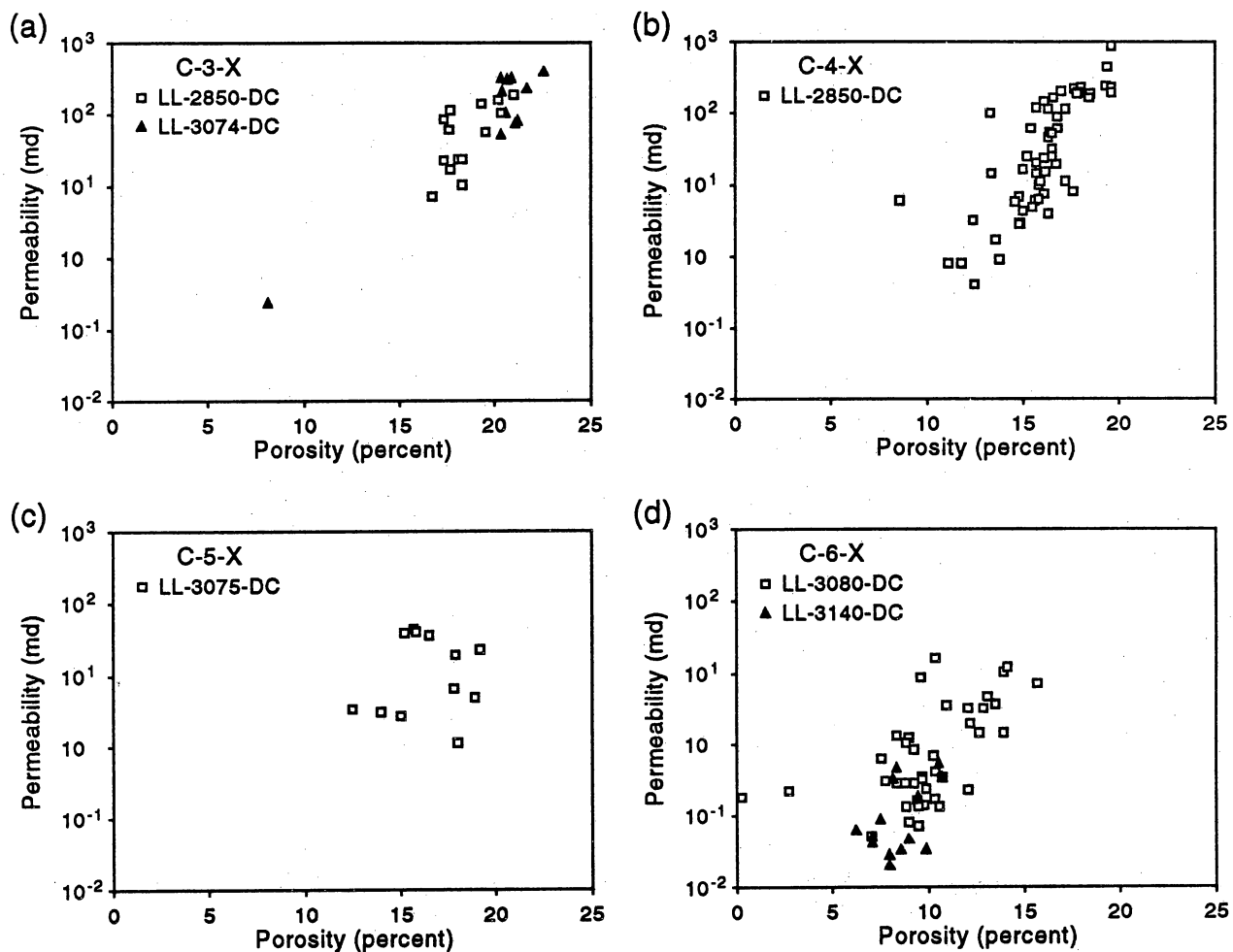
Figure 91. Permeability-porosity crossplots of distributary-channel facies per member. Data from whole-core analysis.
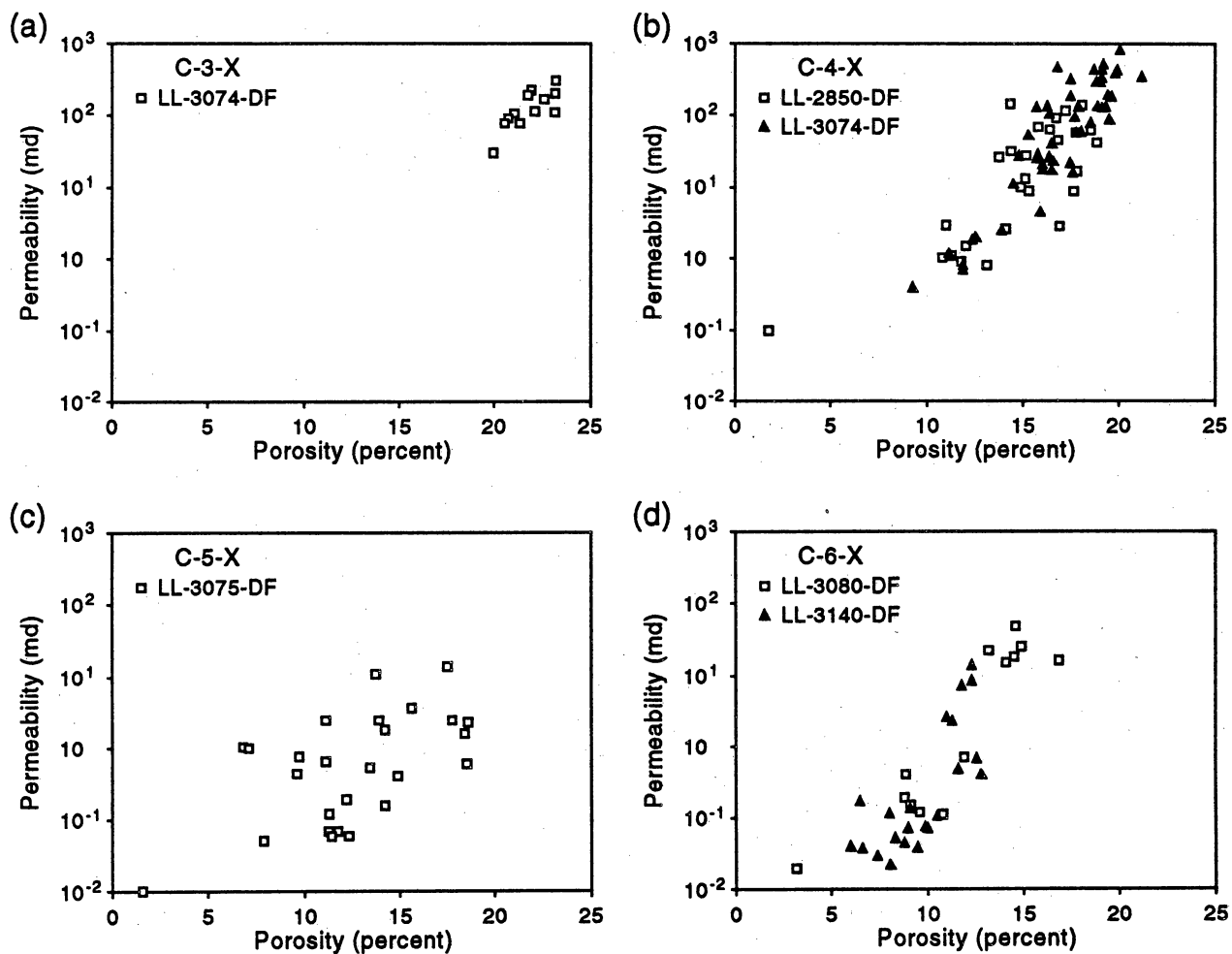
Figure 92. Permeability-porosity crossplots of delta-front facies per member. Data from whole-core analysis.
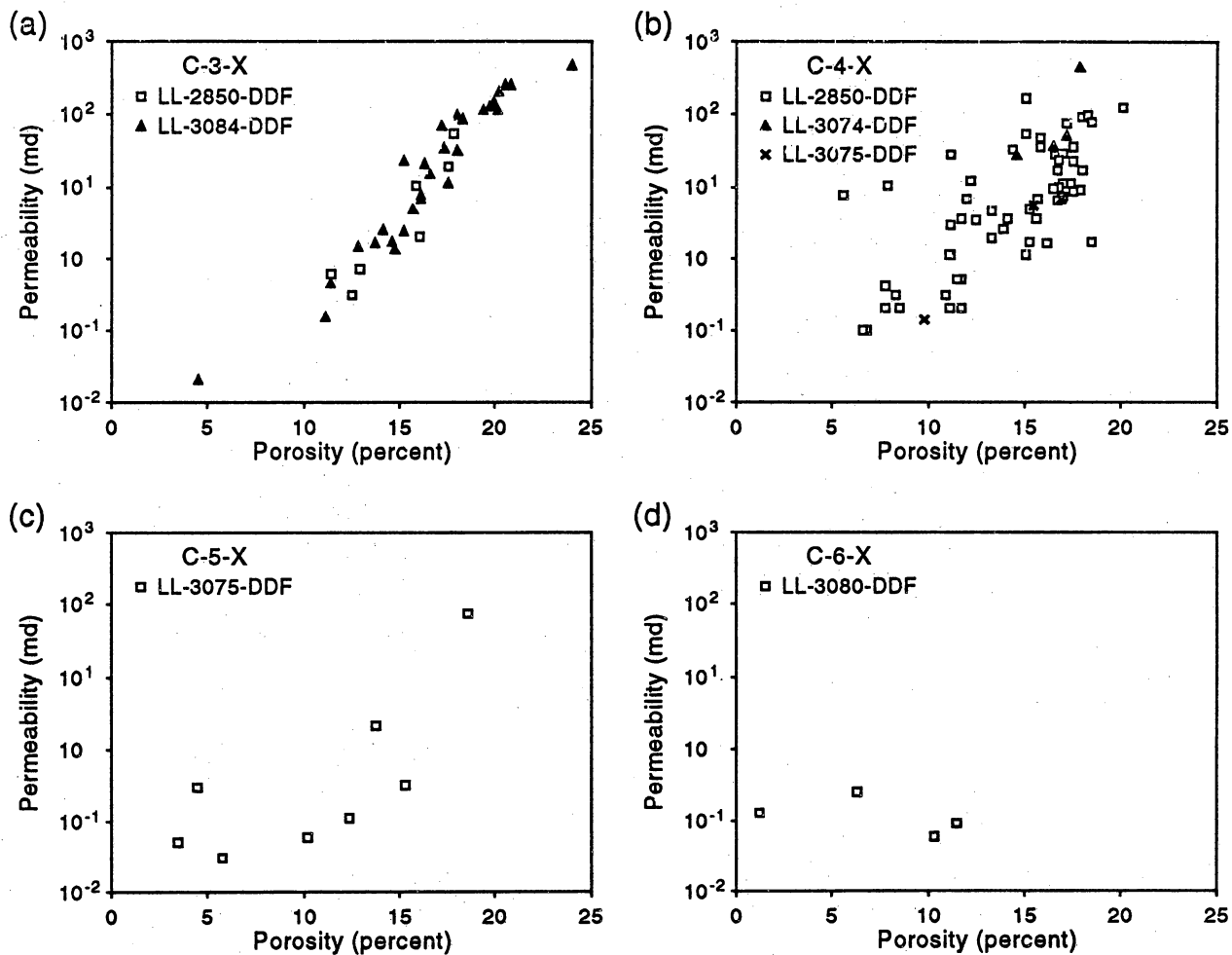
Figure 93. Permeability-porosity crossplots of distal delta-front facies per member. Data from whole-core analysis.

156
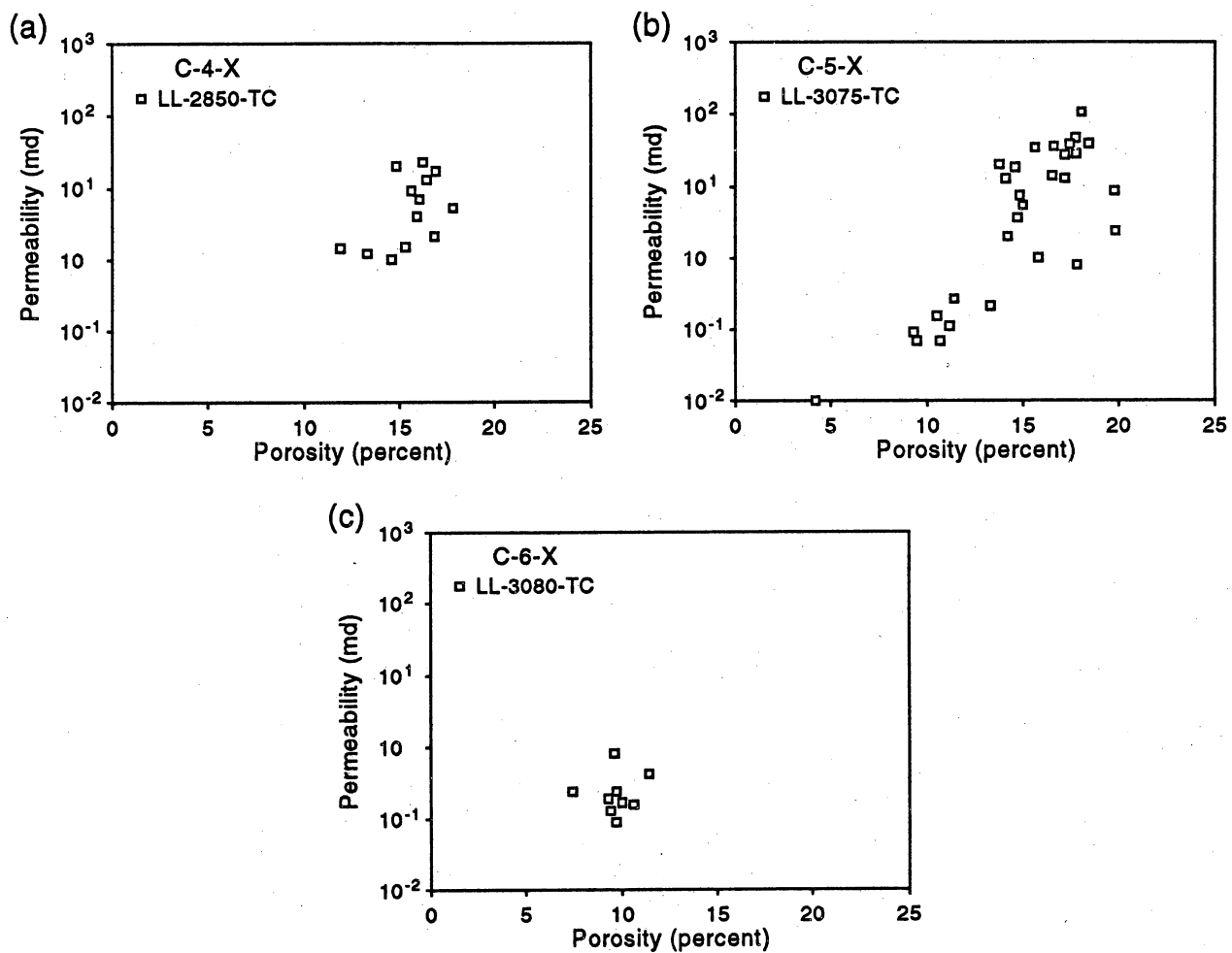
Figure 94. Permeability-porosity crossplots of tidal-channel facies per member. Data from whole-core analysis.
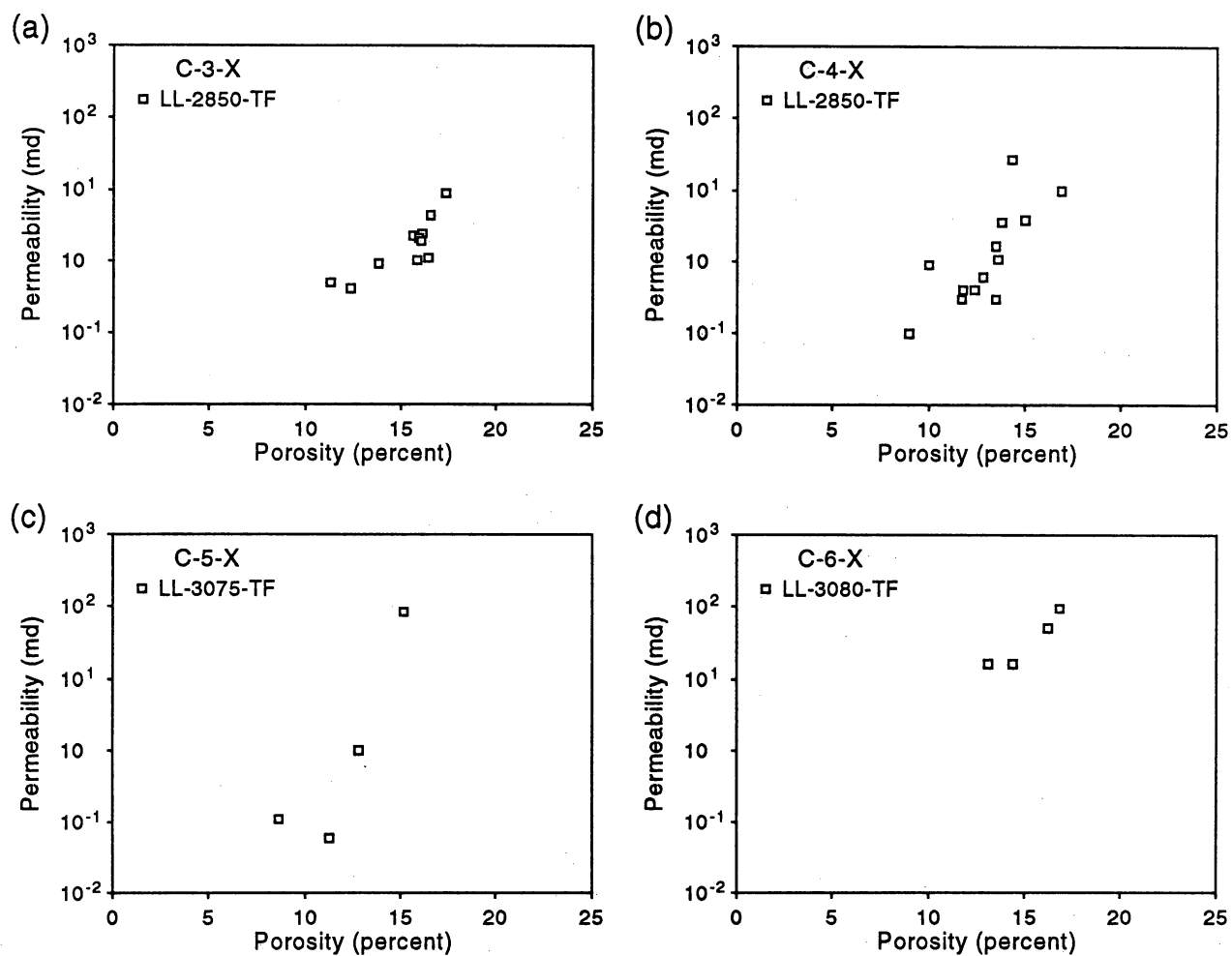
Figure 95. Permeability-porosity crossplots of tidal-flat facies per member. Data from whole-core analysis.
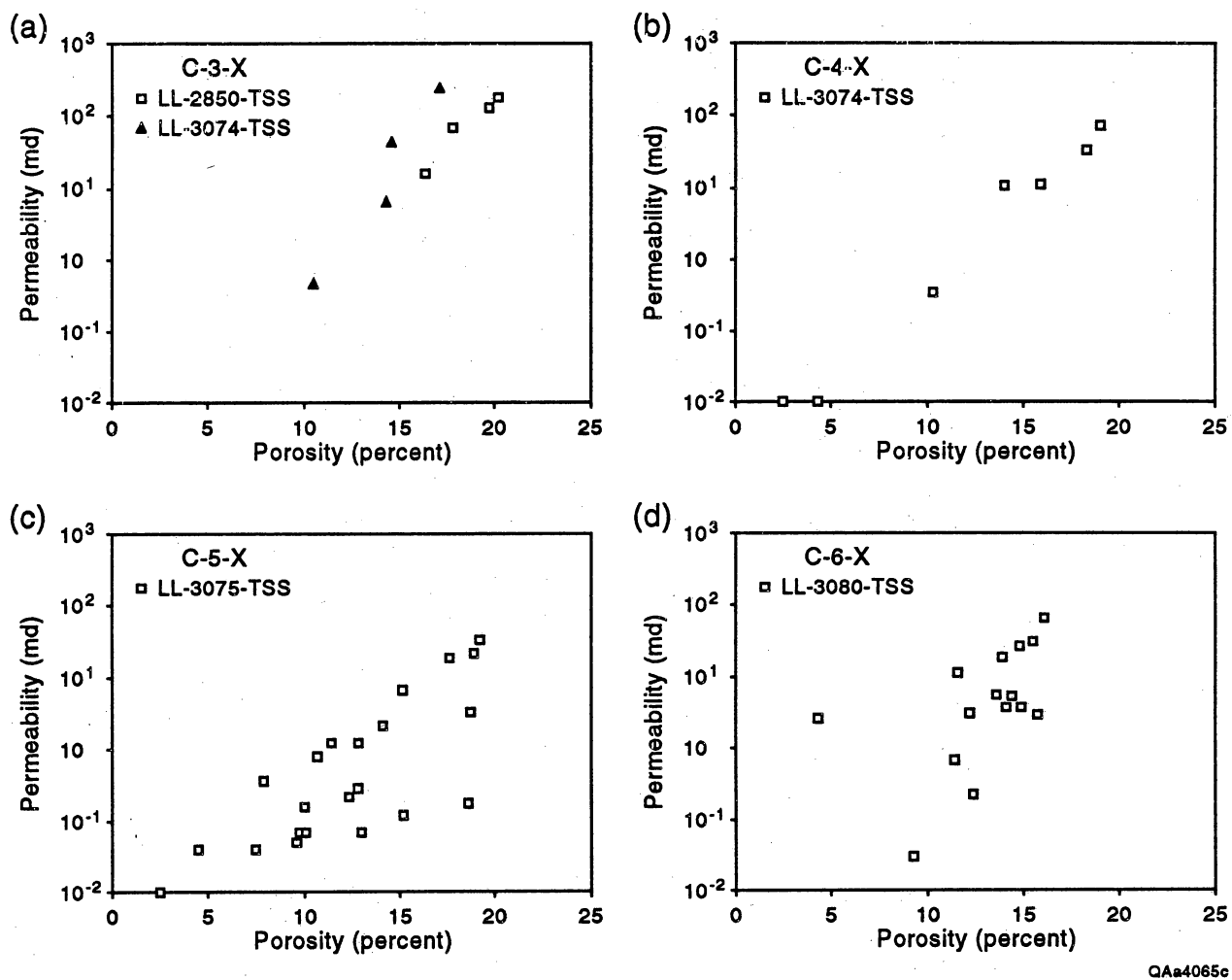
Figure 96. Permeability-porosity crossplots of transgressive sand-shoal facies per member. Data from whole-core analysis.

159
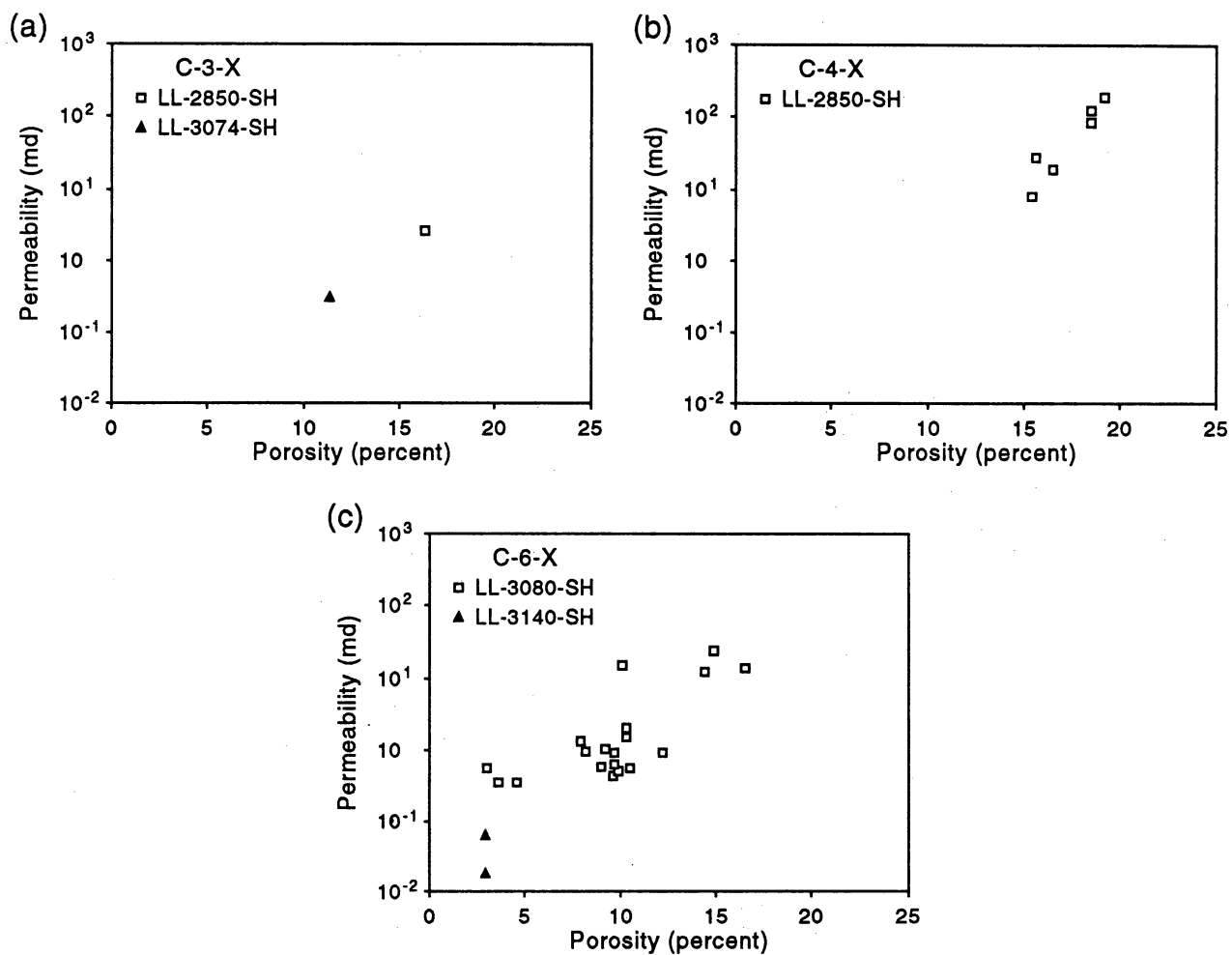
Figure 97. Permeability-porosity crossplots of shelf facies per member. Data from whole-core analysis.
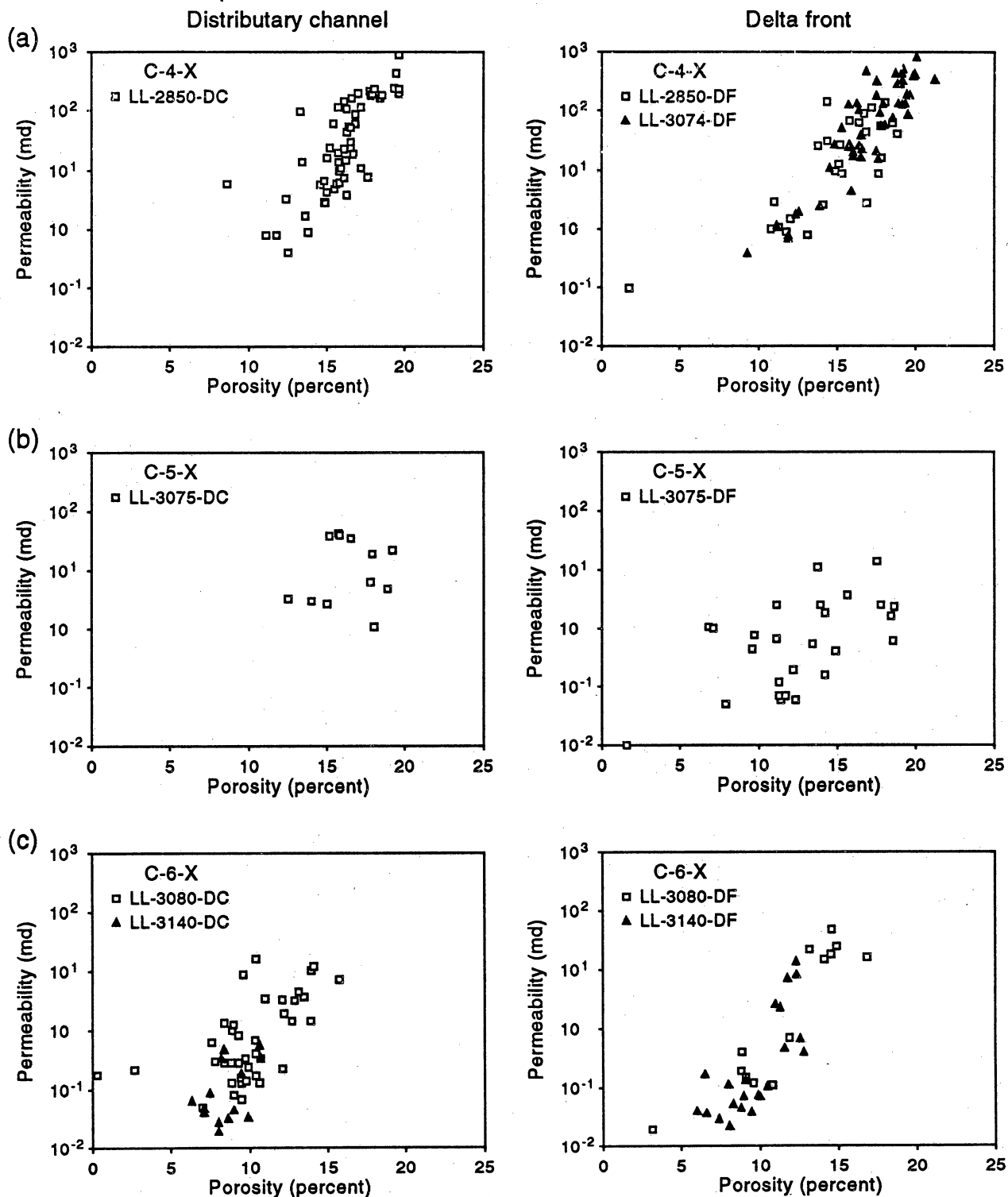
QAa4068c

Figure 98. Permeability-porosity crossplots of distributary-channel versus delta-front facies in the C-4-X, C-5-X, and C-6-X Members.
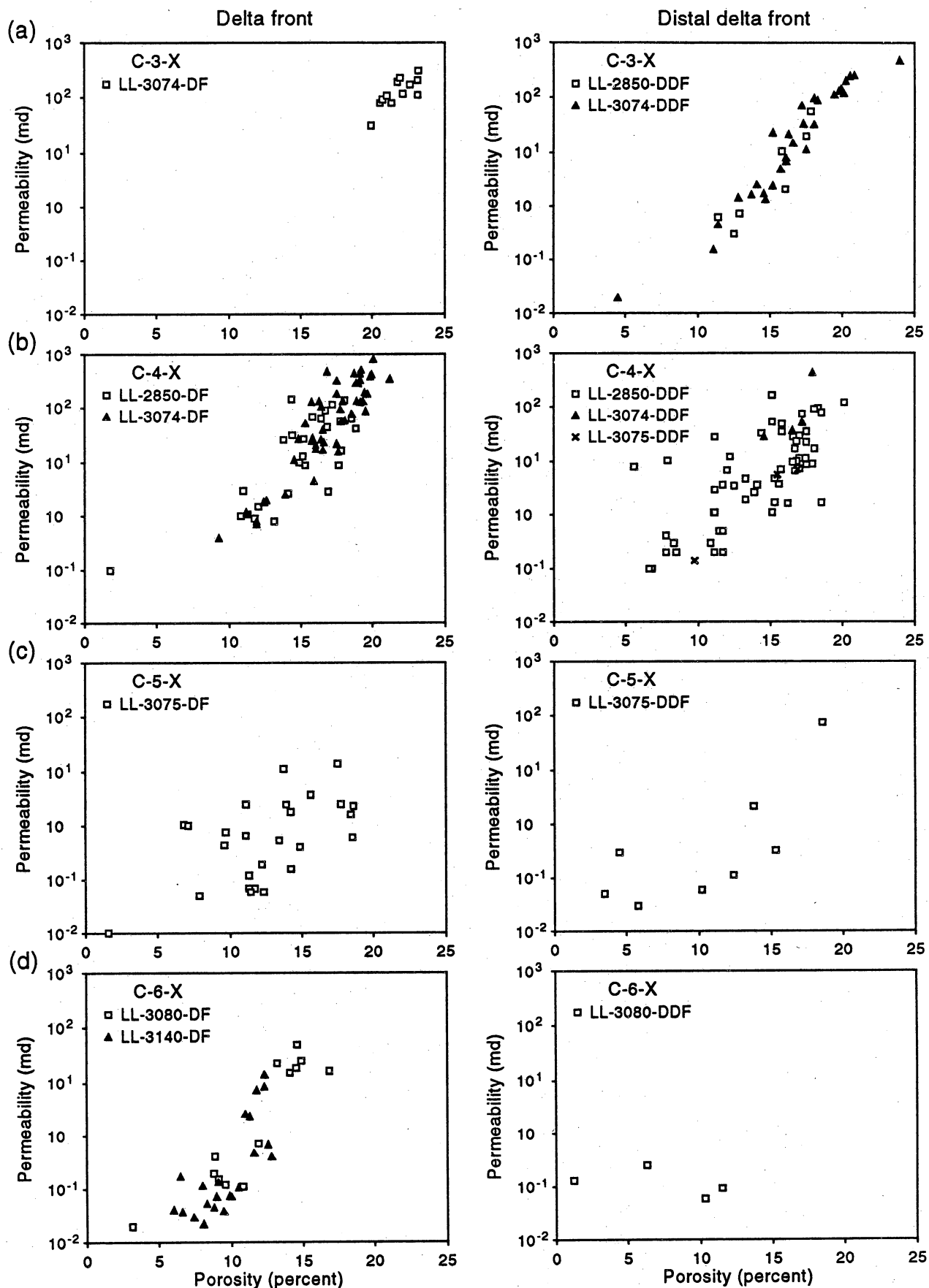
Figure 99. Permeability-porosity crossplots of delta-front versus distal delta-front facies in the C-3-X to C-6-X Members.

162
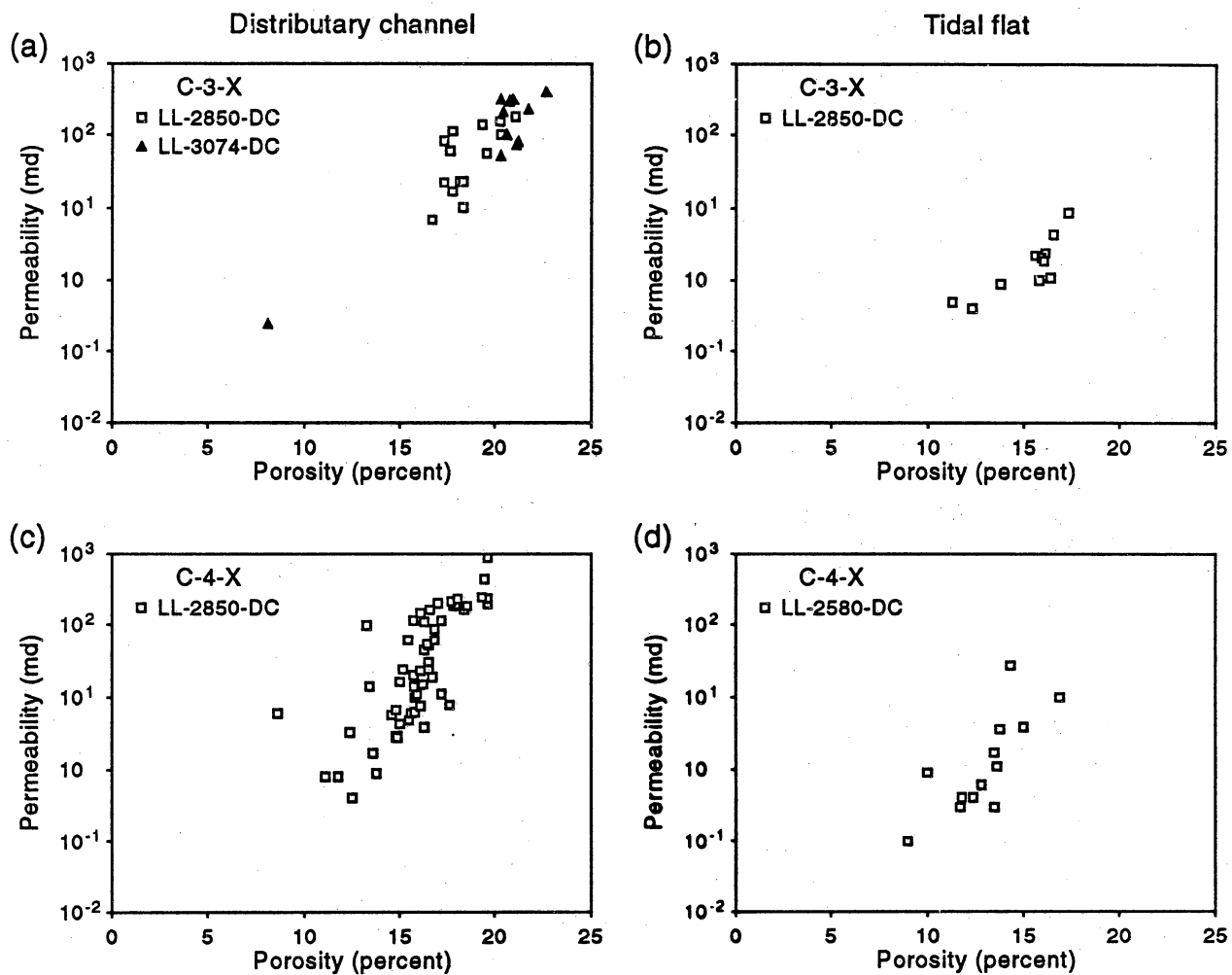
Figure 100. Permeability-porosity crossplots of distributary-channel versus tidal-flat facies in the C-3-X and C-4-X Members.
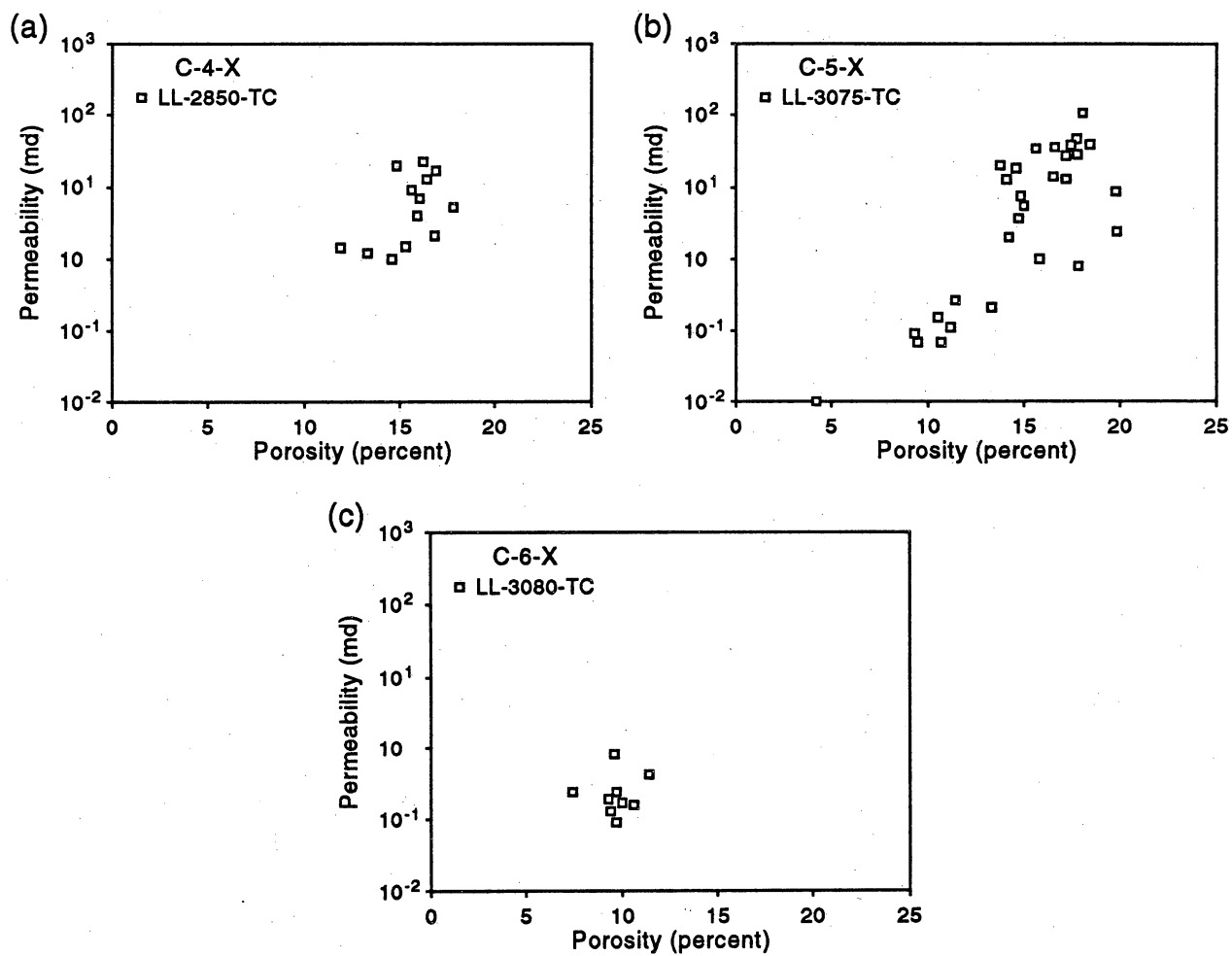
Figure 101. Permeability-porosity crossplots of tidal-channel (TC) versus tidal-flat (TF) facies in the (a) C-4-X, (b) C-5-X, and (c) C-6-X Members.
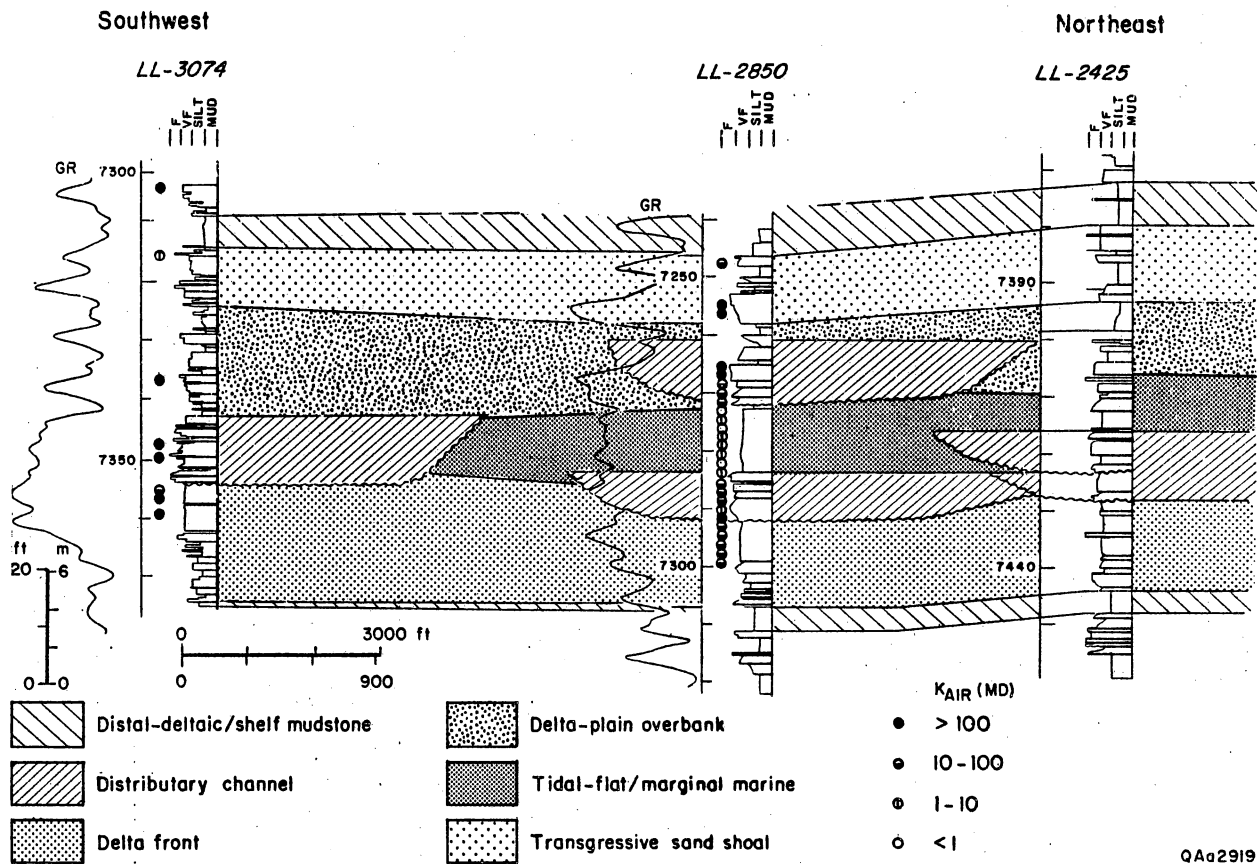
Figure 102. Stratigraphic dip section from cores in the Middle C-3-X Submember, showing distributary-channel deposits that truncate delta-front deposits and high permeability contrast between tidal-flat and distributary-channel deposits. Cored wells are located in figures 81 and 82.
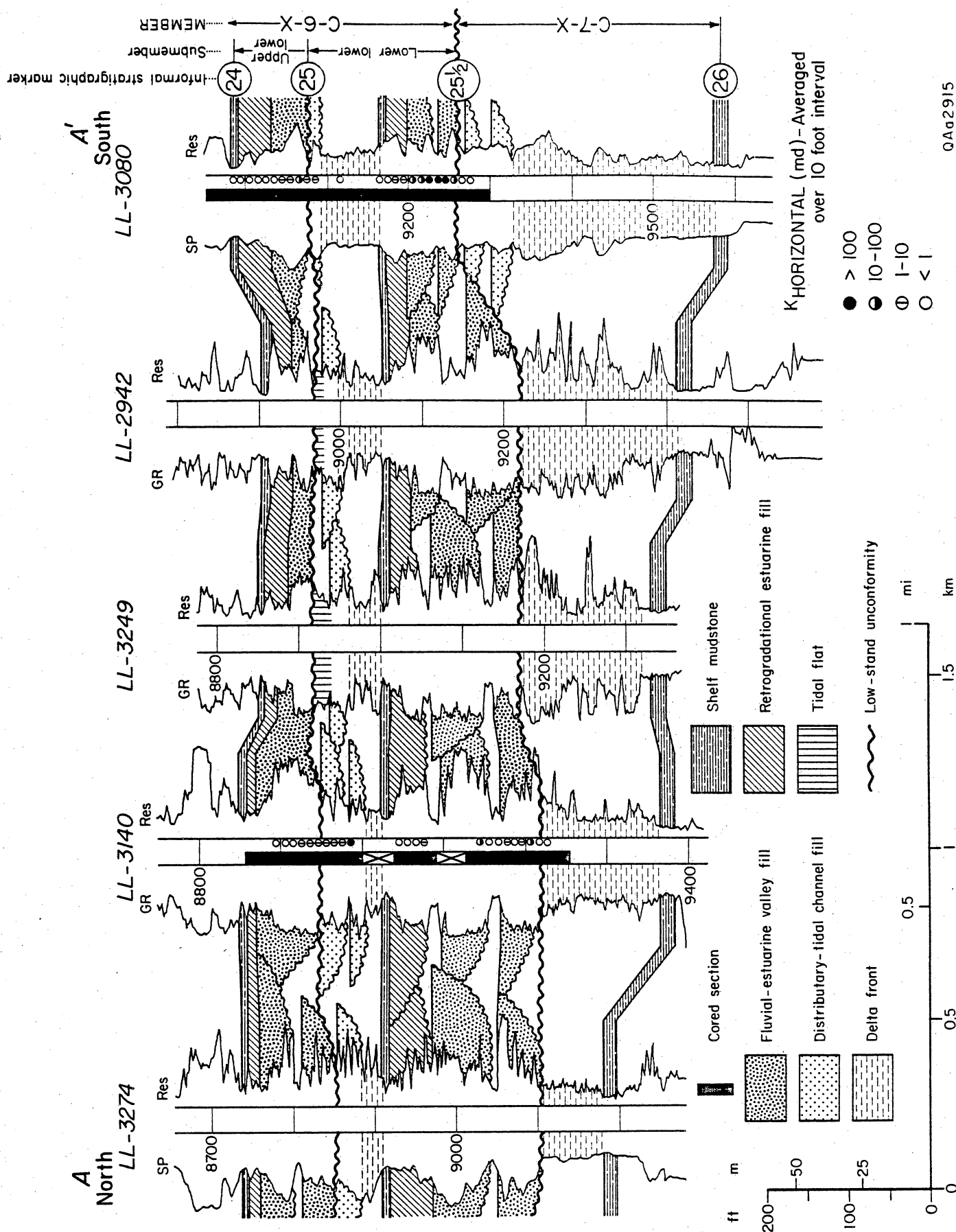
Figure 103. Stratigraphic strike section A–A', showing incised-valley, fluvial-estuarine deposits in the Lower Lower C-6-X Submember that truncate deltaic deposits of the C-7-X Member and high permeability contrast across the unconformity at the base of the C-6-X Member in the LL-3080 well. Cross section is located in figures 106, 107, and 108.

166
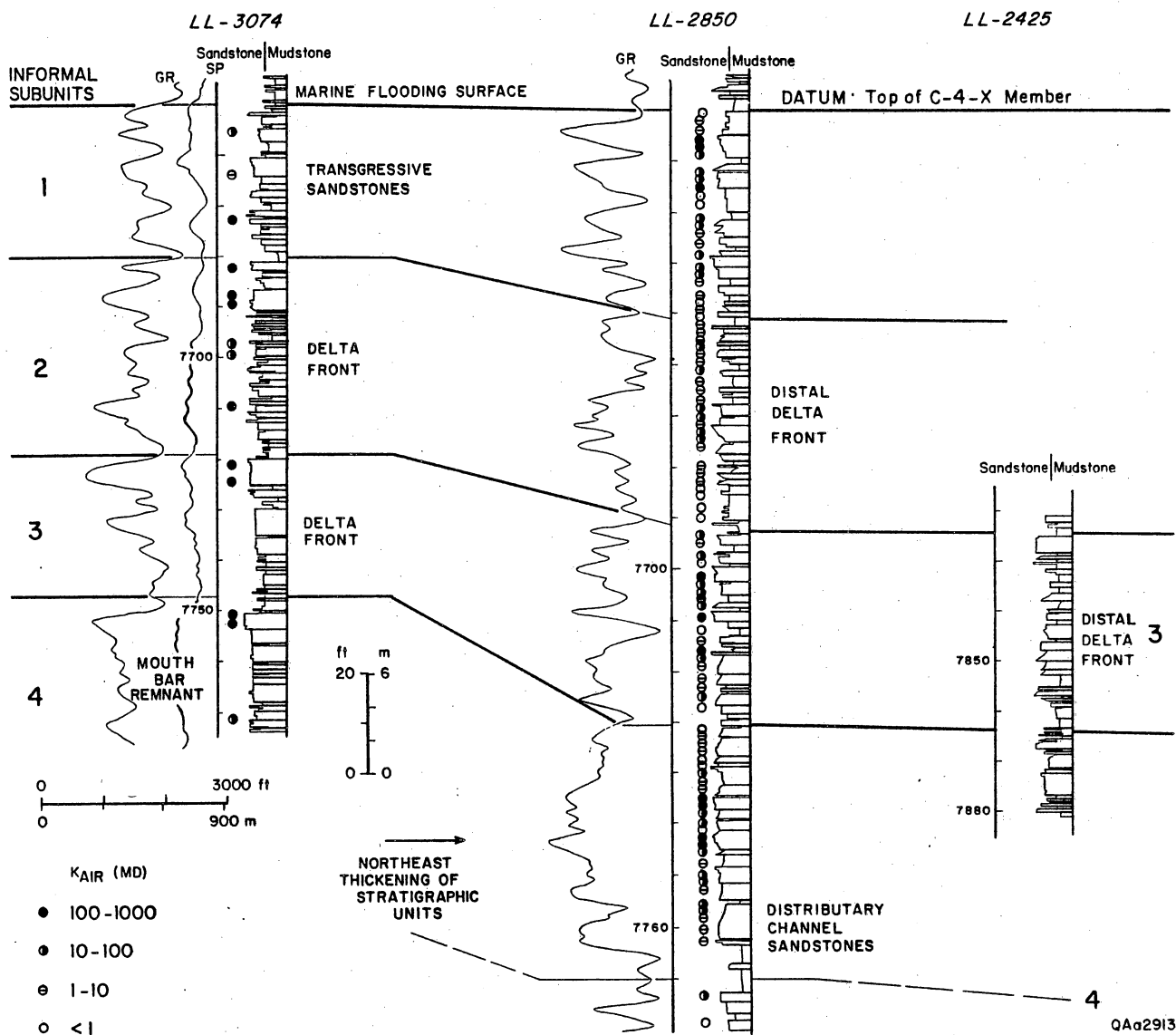
Figure 104. Stratigraphic dip section from cores in the Upper C-4-X Submember, showing permeability variation and basinward thickening of subunits 1–4 in the transition from delta-front to distal delta-front facies. Cored wells are located in figure 126.

VI. DEPOSITIONAL AND SANDSTONE ARCHITECTURAL TRENDS OF C MEMBER RESERVOIR INTERVALS

Introduction

Depositional trends of the tide-dominated deltaic sandstones of the C members exert a strong control over reservoir heterogeneity and consist of a system of narrow (less than 2,000 ft [610 m] wide), dip-parallel sandbodies that are poorly contacted at the current well spacing of approximately 80 acres. Most of the framework distributary-channel and delta-front sandbodies are northeast-trending and may preferentially influence reservoir drainage in this direction, a factor to be considered in future infield development.

The C members in the LL-652 area were deposited in multiple progradational and retrogradational stages in a net-retrogradational megasequence (fig. 5). The C-7-X Member was deposited as a major offlapping progradational clastic wedge; the upper, aggradational part of the C-7-X Member was eroded by fluvial systems associated with a major fall in sea level. Valley-fill, fluvial-estuarine sandstones of the Lower C-6-X Submember were deposited in northeast-trending bands along axes of maximum fluvial incision.

The Middle C-6-X Submember, not mapped in this study, consists of a series of progradational wedges bounded by marine flooding surfaces, whereas the sandstone-poor Upper C-6-X Submember represents a backstepping, retrogradational system (fig. 5). Marine highstand conditions persisted during deposition of the mudstone-dominated Lower C-5-X Submember, but with deposition of the Middle C-5-X Submember, regressive conditions returned with an offlapping deltaic wedge. The top of the C-5-X Member is marked by a marine-dominated, retrogradational system.

The Lower C-4-X Submember, deposited during highstand conditions, is overlain by two progradational deltaic wedges of the Middle C-4-X Submember (fig. 5). Deposition of the C-4-X Member culminated in a major progradational wedge in the Upper C-4-X Submember that extended northeastward beyond the LL-652 area in a phase of maximum offlap in the lower Misoa Formation. However, within the Upper C-4-X Submember, the net sequence was backstepping. The Upper C-4-X Submember consistently exhibits the greatest gamma-ray and resistivity deflections in the C members, reflecting high-reservoir-quality sandstones deposited in a delta-front and lower delta-plain setting.

The C-3-X Member marks the beginning of a major retrogradational phase that continued with deposition of the C-2-X and C-1-X Members (fig. 5). The base of the C-3-X Member, defined by a laterally continuous marine flooding surface, is overlain by distal delta-front deposits of the Lower C-3-X Submember. The thin (approximately 100-ft [30.5-m]) but sandstone-rich Middle C-3-X Submember represents a short-lived phase of offlap during this extended period of net retrogradation. The sandstone-poor Upper C-3-X Submember records a possible reorganization of the basin as indicated by anomalous southeast-trending and lobate net-sandstone thickness patterns.

C-7-X Member

Sandbody Geometry

The C-7-X Member is the basal stratigraphic unit in the lower Misoa Formation and is a 150- to 300-ft (45.7- to 91.4-m), upward-coarsening interval truncated by the C-6-X Member (fig. 5). Sandbody geometry of the C-7-X Member is sheetlike (table 20), except in a northeast-trending band of less than 80 ft (24.4 m) of net sandstone, 2,000 to 6,000 ft (610 to 1,829 m) wide, centered on the LL-3140 well (fig. 105). This band corresponds to a zone of relatively deep erosion by the overlying C-6-X Member. Net-sandstone thickness in the C-7-X Member is commonly over 100 ft (30.5 m), except in the zone of deep erosion, where it is locally less than 30 ft (9 m) (figs. 103 and 105).

Table 20. Depositional systems and reservoir characteristics of the C-7-X Member.

Sand-body Geometry	Sheetlike (?) sandstones more than 100 ft thick and locally truncated by overlying C-6-X Submember in northern part of the map area where net-sandstone thickness is as low as 45 ft.
Depositional Facies	Delta-front deposits locally truncated by incised-valley fluvial deposits of overlying C-6-X Member.
Cored Wells	LL-3080 (upper 25 ft only), LL-3140 (upper 40 ft only).
Perforated Wells	Central area: LL-1803, 2942, 3056 wells.
General Area(s) of Greatest Potential for Secondary Oil Recovery	Along erosional contact with overlying C-6-X Member where permeability barriers may exist.
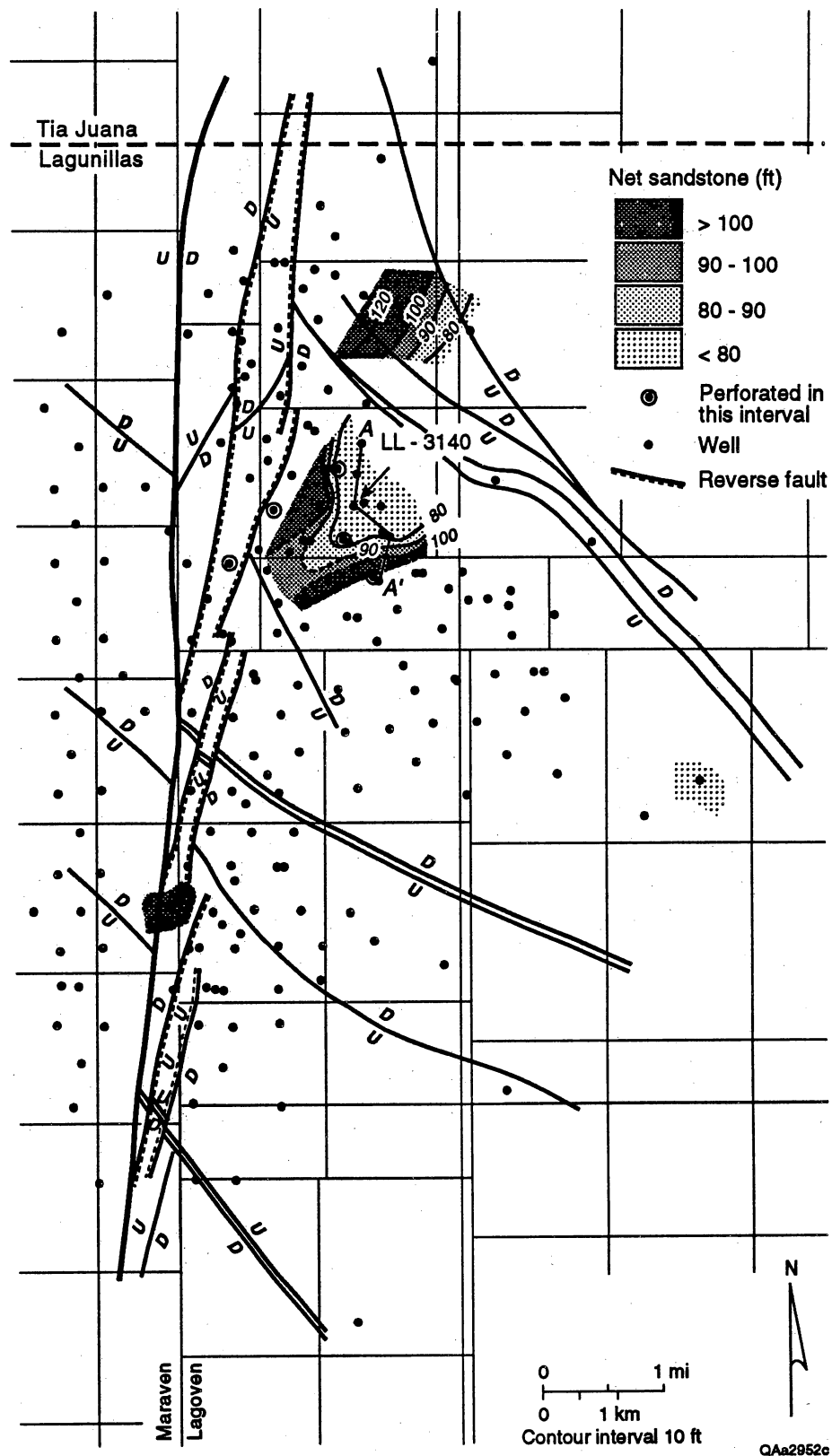
Figure 105. Net-sandstone thickness map of the C-7-X Member in the LL-652 area.

Lithology and Depositional Systems

Deposits of the C-7-X Member consist of thin (individual beds less than 2 ft [0.6 m] thick), finely laminated, upward-coarsening sandstones interbedded with moderately burrowed shale (app. D, LL-3140 well, 9,164-9,202 ft). Load structures, slump deposits, and microfaults are common in the lower part of the section, whereas multiple, erosion-based clay-clast beds overlain by shale drapes are present in the upper part of the section. These shales and sandstones were deposited in distal delta-front and delta-front settings; the distal delta front is the lower upward-coarsening section with load structures and slumps, and the delta front contains multiple clay-clast beds deposited in frontal splays.

Reservoir Development

Three wells (LL-1803, LL-2942, and LL-3056) have been perforated in the C-7-X Member (fig. 105). However, there has been no oil production from any of these wells, due to high water saturation in the C-7-X Member.

Lower Lower C-6-X Submember

Sandbody Geometry

The Lower Lower C-6-X Submember consists of a northeast-trending belt of mainly upward-fining sandstone, 90 to 130 ft (27.4 to 39.6 m) thick and 2,500 to 3,500 ft (762 to 1,067 m) wide, bounded by areas of less than 80 ft (24.4 m) of mainly upward-coarsening sandstone (table 21 and figs. 106 and 107). This northeast-trending belt is a the zone of relatively deep incision by the C-6-X Member into the C-7-X Member (see fig. 105).

Lithology and Depositional Systems

The Lower Lower C-6-X Submember in the LL-3140 well consists of approximately 130 ft (39.6 m) of net sandstone in a sequence with a lower 50-ft (15.2-m) upward-fining sandstone overlain by an upper 50-ft (15.2-m) sandstone with blocky to upward-coarsening log responses. A third, 30-ft (9-m) sandstone caps the sequence (fig. 103). The lower sandstone is massively crossbedded and erosionally based, containing abundant clay clasts and organic fragments (fig. 84, and app. D, LL-3140 well, 9,118 to 9,164 ft). This sandstone is overlain by a 23-ft (7-m), poorly burrowed shale with thin (1- to 2-ft [0.3- to 0.6-m]), interbedded sandstones (app. D, LL-3140 well, 9,095 to 9,118 ft). The overlying sandstone is crossbedded and also contains erosional surfaces.

Thickest sandstones in the Lower Lower C-6-X Submember represent valley-fill deposits deposited after an inferred sea-level fall; the lower sandstone was deposited by fluvial channels that occupied the valley floor, incising into older delta-front deposits of the C-7-X Member. With subsequent sea-level rise and drowning of the valley, estuarine mudstones and thin sandstones were deposited over the fluvial section (fig. 83). The upper sandstones represent distributary-channel and delta-front deposits of an estuarine deltaic system. These sandstones are in turn overlain by retrogradational, estuarine-fill and shelf mudstones that mark the maximum transgression of the incised valley (fig. 103).

Reservoir Development

Drilling activity in the Lower Lower C-6-X Submember has been limited mainly to the central part of the LL-652 area. Of the seven wells perforated in this zone, only two have intersected the relatively thick fluvial-estuarine facies (figs. 106 and 107).

Table 21. Depositional systems and reservoir characteristics of the Lower Lower C-6-X Submember.

Sand-body of Geometry	Northeast-trending belts of sandstone, 90-130 ft thick and 2,000-6,000 ft wide, bounded by broad (?) areas less than 80 ft of net sandstone. The thicker sandstones have upward-fining and blocky log responses.
Depositional Facies	Incised valley fluvial deposits that truncate older delta-front and distributary-channel deposits in the underlying C-7-X Member. These fluvial deposits are overlain by transgressive estuarine-fill deposits.
Cored Wells	LL-3080 and LL-3140 (entire interval).
Perforated Wells	Central area: LL-1782, 1803, 2942, 3055, 3056, 3075, 3080 wells.
General Area(s) of Greatest Potential for Secondary Oil Recovery	See comments for Upper Lower C-6-X Submember.
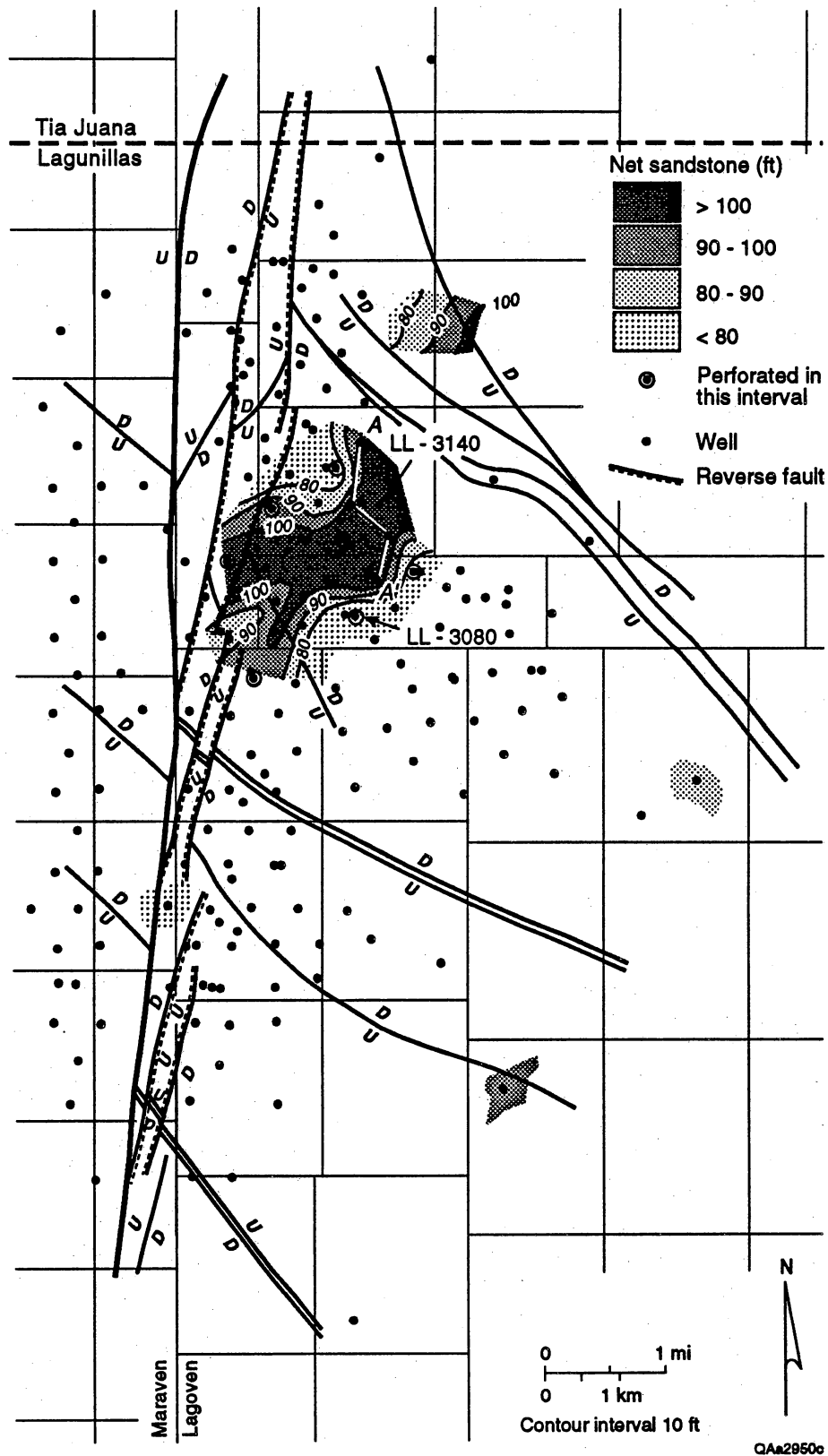
Figure 106. Net-sandstone thickness map of the Lower Lower C-6-X Submember in the LL-652 area. Cross section A–A′ is shown in figure 103.

173
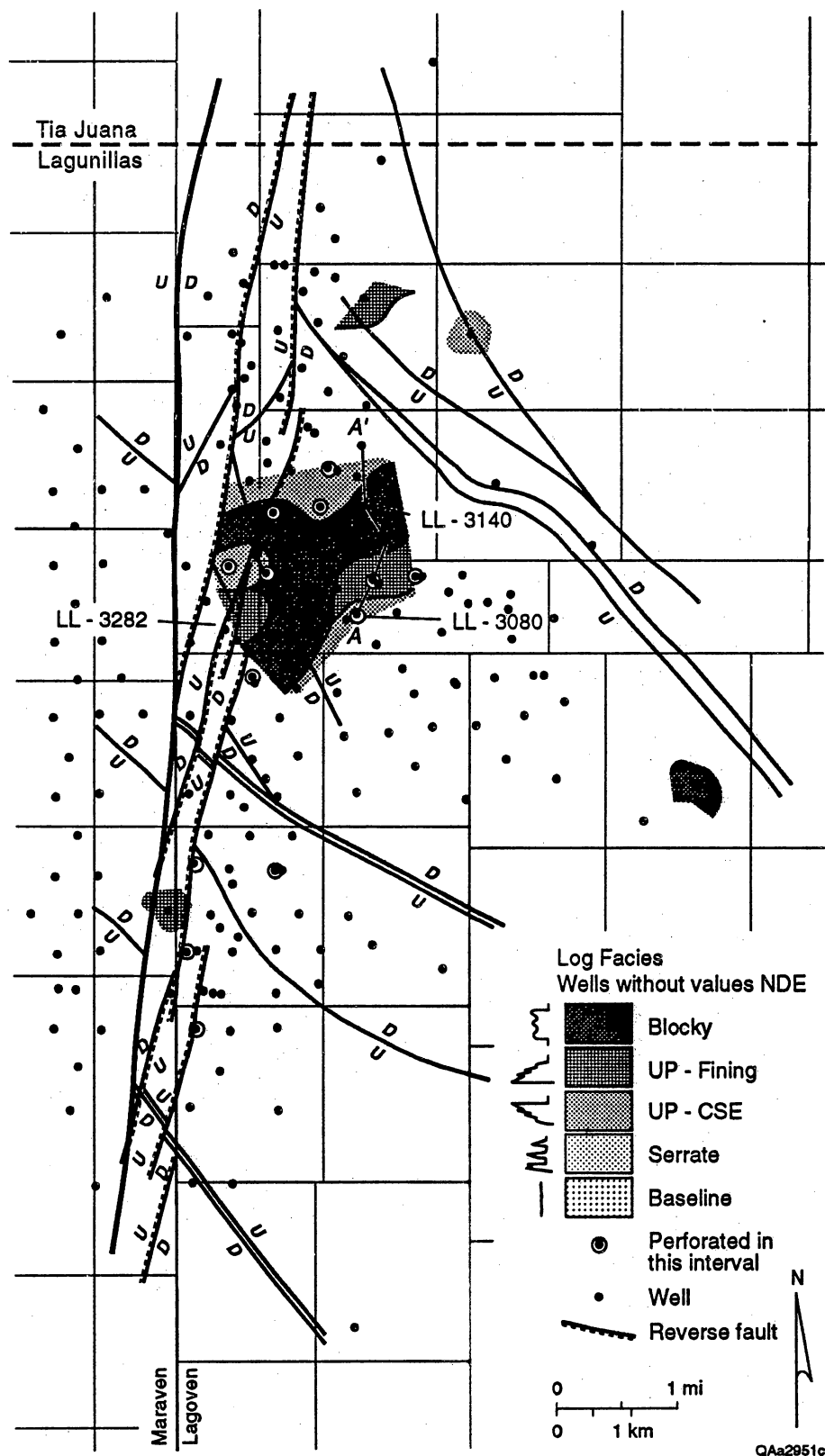
Figure 107. Log-facies of the Lower Lower C-6-X Submember in the LL-652 area. Cross section A–A' is shown in figure 103.

174

Upper Lower C-6-X Submember

Sandbody Geometry

The Upper Lower C-6-X Submember consists of one main northeast-trending belt of upward-fining sandstone in the northern part of the field, locally more than 80 ft (24.4 m) thick, bounded laterally by upward-coarsening sandstones less than 50 ft (15 m) thick (table 22 and fig. 108). There are other northeast-trending sandstone remnants in the southern part of the field (fig. 108).

Lithology and Depositional Systems

The Upper Lower C-6-X Submember consists of a lower upward-coarsening interval, approximately 80 ft (24.4 m) thick (fig. 103), overlain by a thick (approximately 75-ft [22.9-m]), upward-fining sandstone, which in turn is overlain by a thin (20-ft [6-m]) laterally continuous silty shale. The lower upward-coarsening interval consists of burrowed delta-front sandstones truncated by a 12-ft (3.7-m) section of crossbedded distributary-channel sandstones (app. D, LL-3140 well, 8,987 to 9,036 ft). The upper section is a thick, multistoried succession of upward-fining, erosionally based, crossbedded and unburrowed sandstones of a fluvial-estuarine channel complex that truncates older marine strata (app. D, LL-3140 well, 8,880 to 8,935 ft). This fluvial-estuarine channel complex is similar to that of the underlying Lower Lower C-6-X Submember (fig. 103). The uppermost 20 ft (6 m) of silty mudstone are transgressive deposits that cap the sequence.

Reservoir Development

The Upper Lower C-6-X Submember has been developed mainly in the central part of the LL-652 area, with minor activity toward the southwest (fig. 108). As in the Lower Lower C-6-X Submember, most of the perforated wells have been away from the main depositional axis, with three wells perforated with less than 50 ft (15.2 m) of net sandstone.

Lower Upper C-6-X Submember (21-22 Interval)

The Lower Upper C-6-X Submember is an upward-fining interval, 150 to 200 ft (45.7 to 61 m) thick (fig. 5); it is composed of a lower sandstone-rich unit (lower 21-22 interval) and an upper sandstone-poor unit (upper 21-22 interval) that together constitute a retrogradational, transgressive sequence.

Lower 21-22 Interval

Sandbody Geometry

The Lower 21-22 interval in the LL-652 area is defined as two main dip-elongate and digitate upward-fining sandbodies more than 40 ft (12 m) thick and approximately 2,000 ft (610 m) wide (table 23 and figs. 109 and 110). These sandbodies thin laterally into muddy areas with less than 30 ft (9 m) of net sandstone (fig. 109).

Lithology and Depositional Systems

The lower two-thirds of the lower 21-22 interval, cored in the LL-3080 well, consist of a lower 33-ft (10-m) upward-coarsening section of burrowed mudstone interbedded with thin (0.5- to 2.5-ft [0.2- to 0.8-m]) rippled sandstones that increase upward in thickness (app. D, LL-3080 well, 8,677 to 8,710 ft). The upper section of the lower 21-22 interval is a 42-ft (12.8-m) sandstone-rich unit with a 17-ft (5.2-m) sharp-based,

Table 22. Depositional systems and reservoir characteristics of the Upper Lower C-6-X Submember.

Sand-body bounded Geometry	Northeast-trending sandstones, more than 70 ft thick with upward-fining and blocky log responses, laterally by upward-coarsening sandstones less than 50 ft thick.
Depositional Facies	Incised-valley fluvial deposits that truncate deltaic deposits. The sequence is capped by transgressive estuarine-fill deposits.
Cored Wells	LL-3080 (entire interval), LL-3140 (all but 40 ft in lower half).
Perforated Wells	Central area: good density of perforated wells; southwestern area: poor density.
General Area(s) of GreatestPotential for Secondary Oil Recovery	Possible permeability boundaries at contacts of fluvial sandstones and underlying deltaic deposits. Other permeability contrasts possible lateral to and overlying these fluvial sandstones.

176
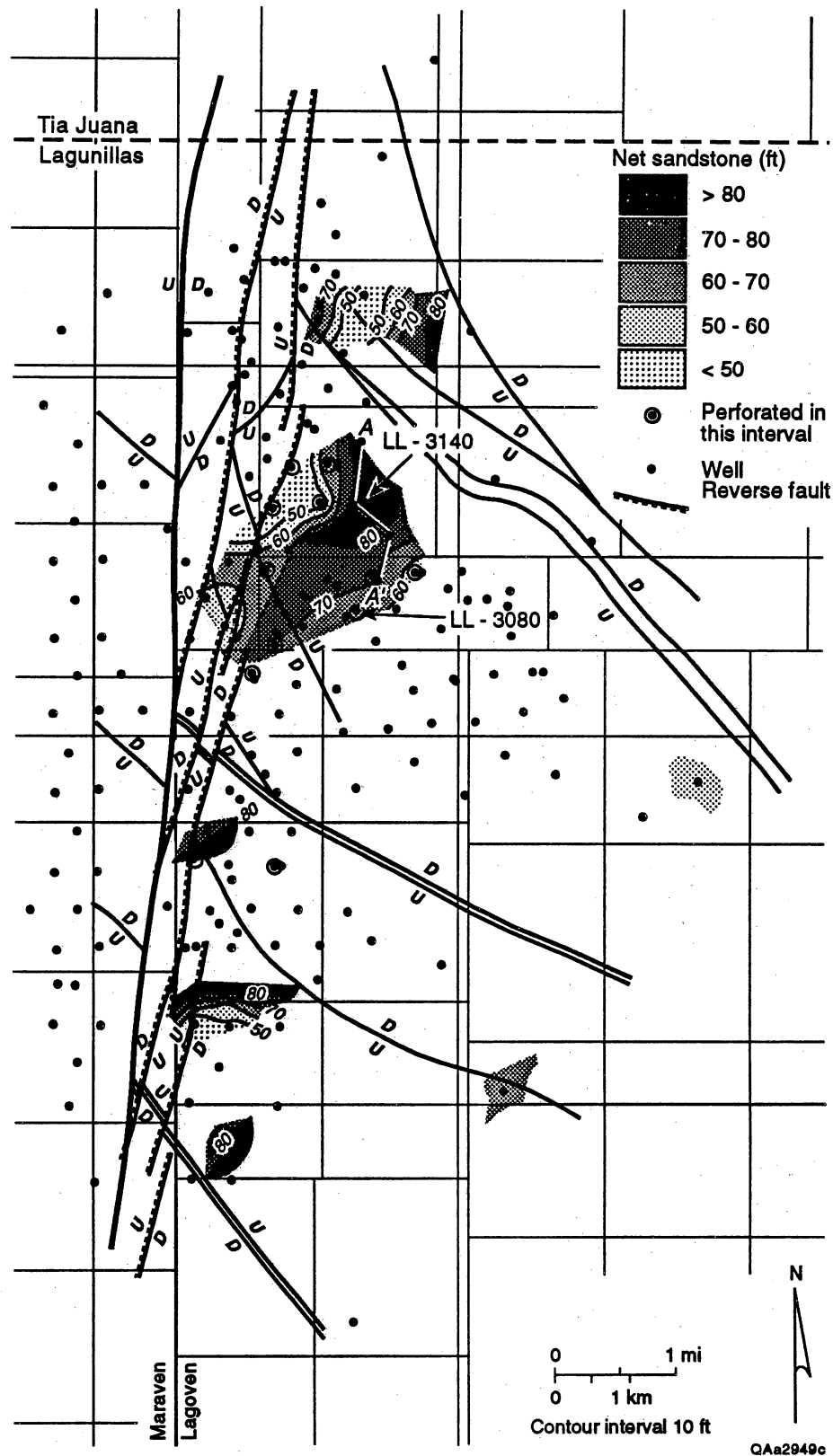
Figure 108. Net-sandstone thickness of the Upper Lower C-6-X Submember in the LL-652 area. Cross section A–A' is shown in figure 103.

177

Table 23. Depositional systems and reservoir characteristics of the Lower 21-22 Interval in the Lower Upper C-6-X Submember.

Sand-body Geometry	Northeast-trending, dip-elongate and upward-fining sandstones 40-58 ft thick and approximately 2,000 ft wide, bounded laterally by areas of generally less than 30 ft of sandstone and merging northeastward with areas of less than 40 ft of net sandstone.
Depositional Facies	Distributary-channel deposits, overlying delta-front deposits in a offlapping progradational parasequence.
Cored Wells	LL-3080 (lower 70%), LL-3282 (lower 90%).
Perforated Wells	Southwest: LL-946, 992, 1001, 1005 wells; Central: Multiple perforated wells.
General Area(s) of Greatest Potential for Secondary Oil Recovery	Channel-mouth-bar sandstones pinching out into sandstone-poor delta-front deposits and narrow, isolated distributary-channel deposits.
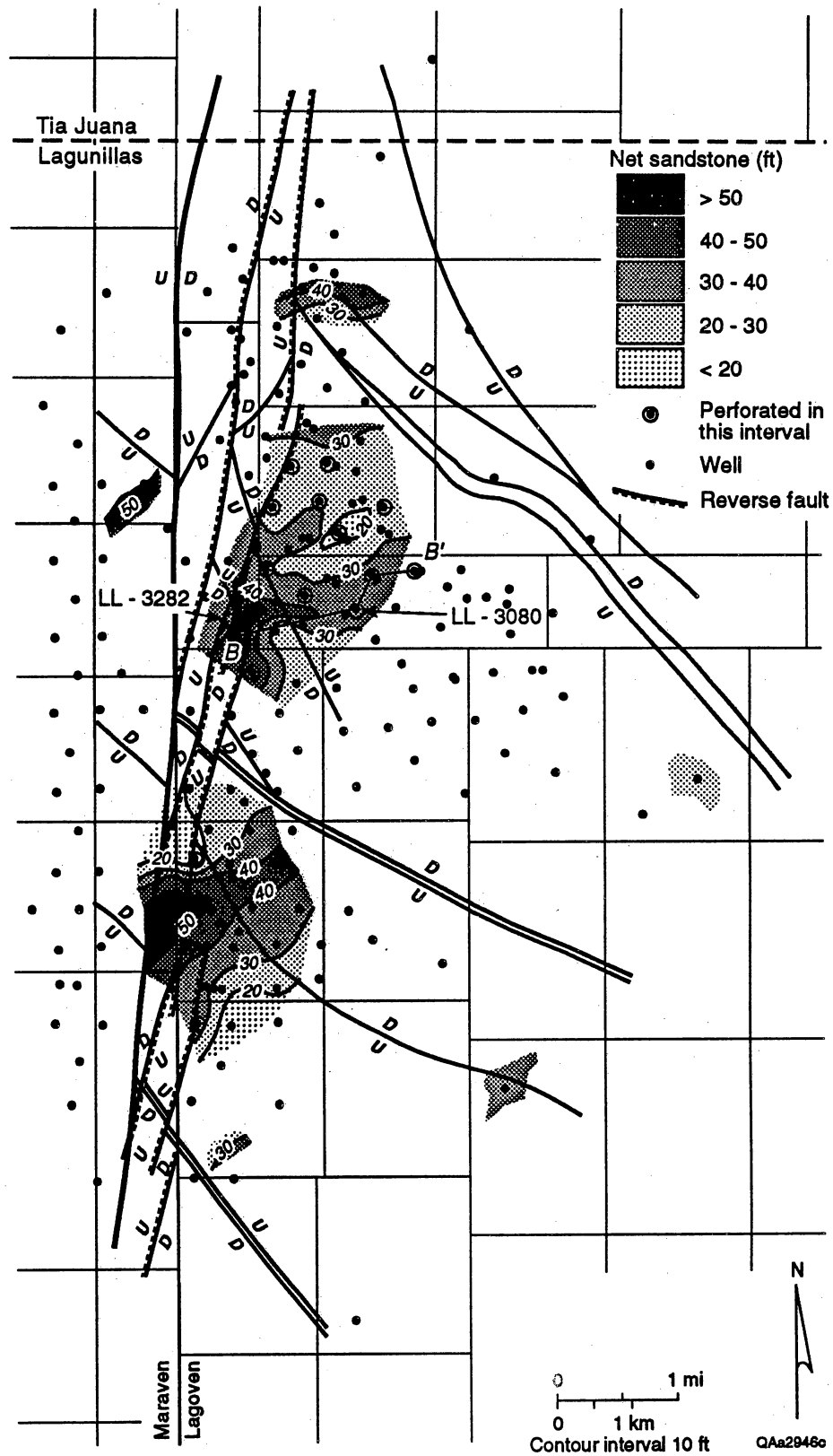
Figure 109. Net-sandstone thickness of the Lower 21-22 Interval in the Lower Upper C-6-X Submember in the LL-652 area. Cross section B–B′ is located in figure 111.

179
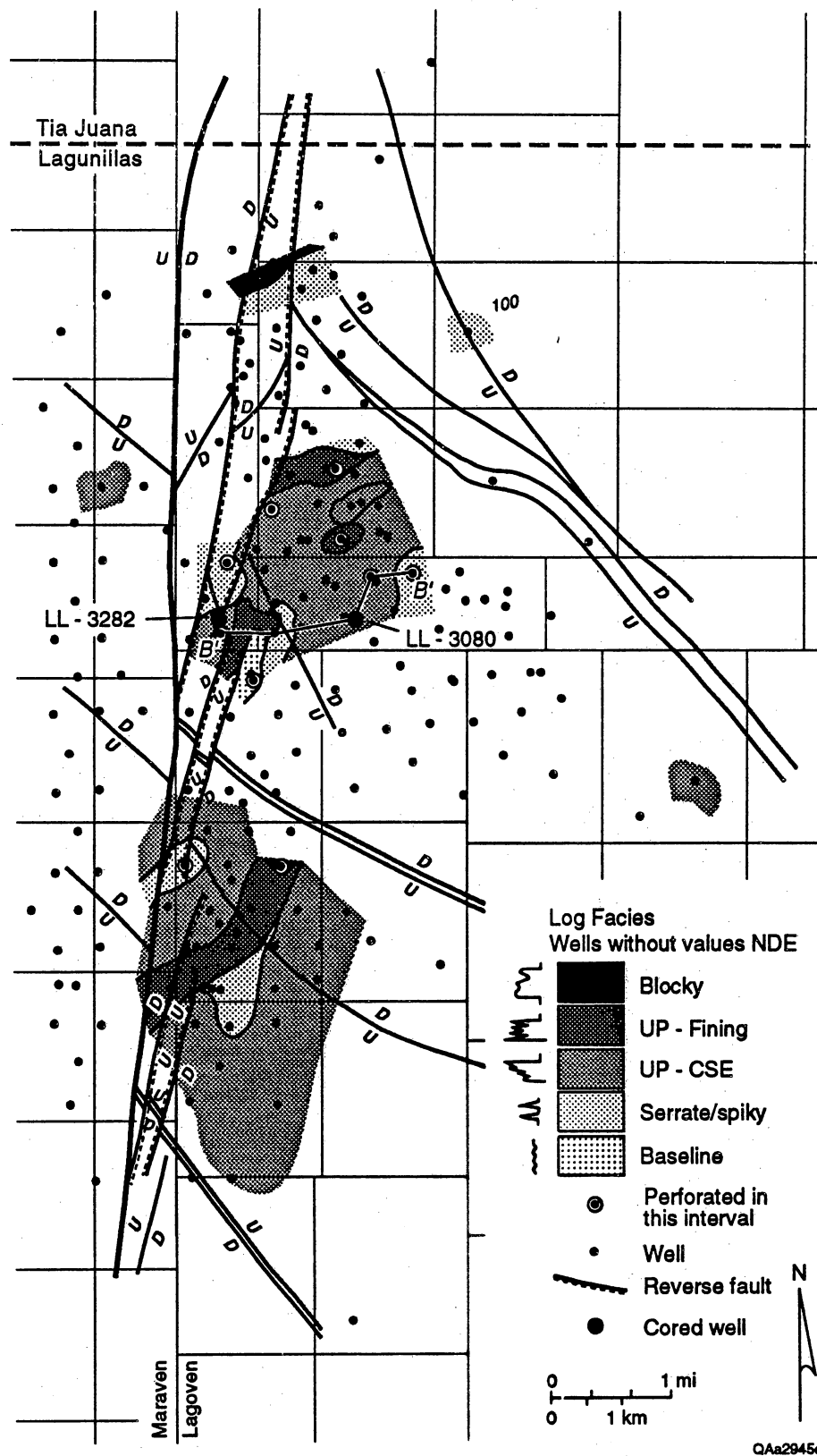
Figure 110. Log-facies of the Lower 21-22 Interval in the Lower Upper C-6-X Submember in the LL-652 area. Cross section B–B′ is located in figure 111.

crossbedded and rippled organic-rich sandstone overlain by a 12-ft (3.7-m) rippled and crossbedded, calcite-cemented sandstone that is capped by a thin, 10-ft (3-m) zone of rippled siltstone and very fine sandstone (app. D, LL-3080 well, 8,634 to 8,677 ft).

This cored segment represents a single regressive-transgressive couplet composed of a lower offlapping, progradational deltaic wedge (distal delta-front, delta-front, and distributary channel) overlain by an upper retrogradational, transgressive sandstone. Two regressive-transgressive couplets, each no more than 60 ft (18 m) thick, comprise the lower 21-22 interval. Across a 1.7-mi (2.8-km) dip section (fig. 111) along the axis of a deltaic depocenter in the central part of the LL-652 area, a lower offlapping deltaic wedge, approximately 60 ft (18 m) thick, thins eastward to less than 5 ft (1.5 m). This wedge is overlain by a retrogradational sandstone that thins westward from 25 ft (7.6 m) to only 3 ft (0.9 m). The upper offlapping deltaic wedge is separated from the lower wedge by a continuous, 5-ft (1.5-m) shale inferred to be a marine flooding surface. In contrast to the lower deltaic wedge, the upper wedge contains a retrogradational unit that pinches out in the LL-652 area.

Reservoir Development

Development of the Lower 21-22 interval has been fairly uniform throughout the central part of the LL-652 area (figs. 109 and 110). However, there are no perforated wells in the northern and only limited development in the southwest parts of the field. There is no correspondence between net-sandstone thickness, log-facies, and location of perforated wells in the Lower 21-22 interval.

Upper 21-22 Interval

Sandbody Geometry

The Upper 21-22 interval is a muddy unit that is composed of multiple northeast-trending, dip-elongate sandstones that range in thickness from 30 to 45 ft (9 to 15 m) and in width from 1,500 to 2,500 ft (457 to 762 m) (table 24 and fig. 112). These sandstones pinch out into extensive muddy areas of less than 15 ft (4.5 m) of net sandstone.

Depositional Systems

Although there are no cores in the Upper 21-22 interval in the LL-652 area, net-sandstone thickness trends and the overall mudstone-rich nature of this unit suggest a distal delta-front or inner-shelf setting. All of the sandstones in the Upper 21-22 interval have upward-coarsening or serrate log responses, except for thick (more than 40-ft [12-m]) upward-fining sandstones in the southwest part of the LL-652 area, near the Maraven concession boundary. These upward-coarsening and serrate log responses are consistent with progradational, offlapping sandbodies located distally from a deltaic platform.

Reservoir Development

Development of the shaly Upper 21-22 interval is extremely limited. In the three areas where the Upper 21-22 interval has been penetrated, there have been no perforations in the northern, two in the central, and only three in the southern part of the LL-652 area (fig. 112). In the central area, sandstone-poor areas have been perforated rather than sandstone-rich depositional axes. In the southern area, only one well (LL-946) has been perforated in a depositional axis, which is projected to extend northeastward into the southeastern corner of the central area.

181
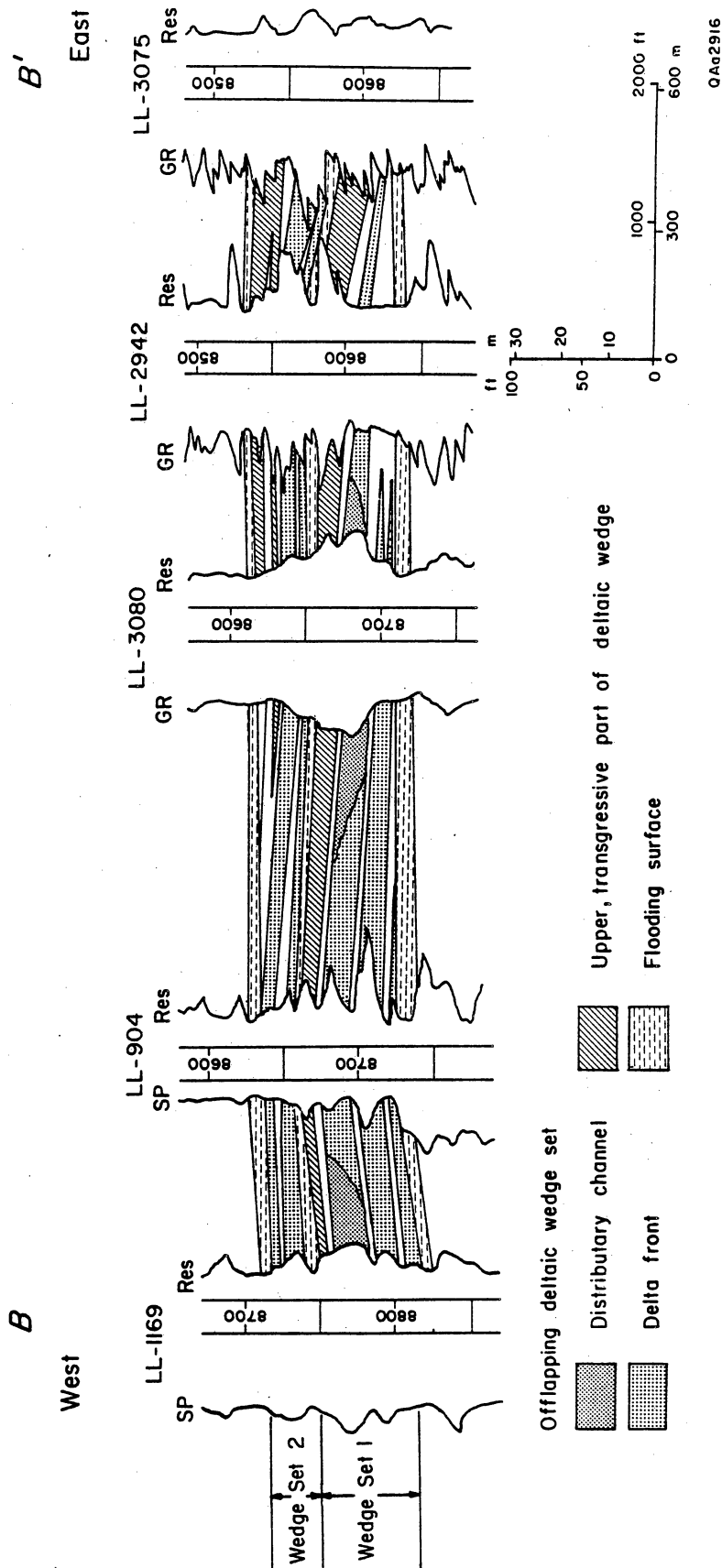
Figure 111: Stratigraphic dip section B-B' in the Lower 21-22 Interval in the Lower Upper C-6-X Submember, showing eastward-thinning, progradational deltaic wedges overlain by westward-thinning transgressive sandstones deposited during phases of deltaic abandonment. Individual depositional cycles (parasequences) are 40 to 80 ft (12 to 24 m) thick. Cross section is located in figures 109 and 110.

Table 24. Depositional systems and reservoir characteristics of the Upper 21-22 Interval in the Lower Upper C-6-X Submember.

Sand-body Geometry	Northeast-trending, dip-elongate sandstones, 30-45 ft thick and 1,500-2,500 ft wide, bounded by sandstone-poor areas with minimum of 10-15 ft of net sandstone.
Depositional Facies	Distal delta-front and shelf deposits.
Cored Wells	None
Perforated Wells	Southwest: LL-946, LL-992, LL-1001 wells. Central: LL-1172, LL-1782 wells.
General Area(s) of Greatest Potential for Secondary Oil Recovery	Isolated distal delta-front tidal ridge deposits.

183
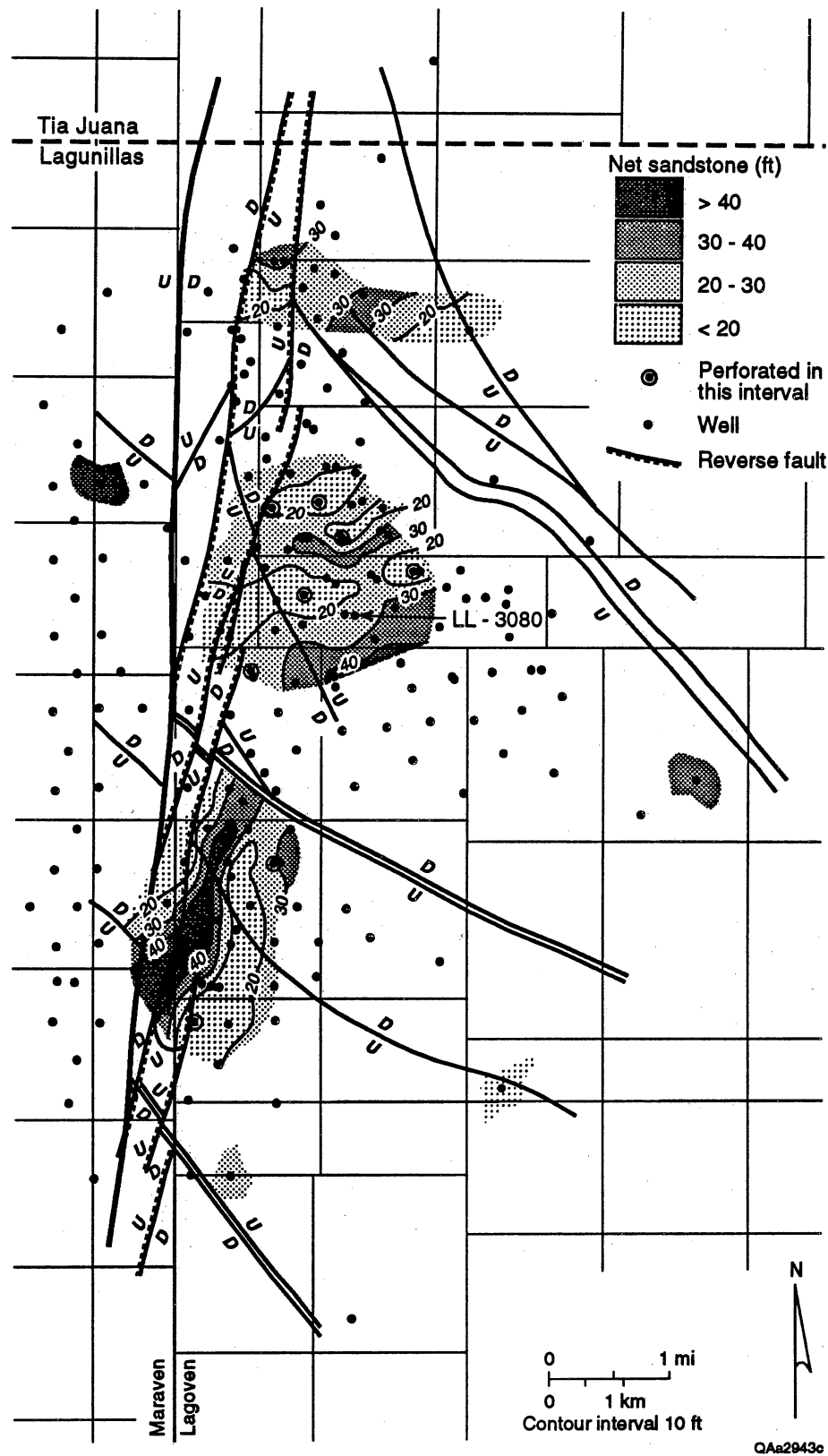
Figure 112. Net-sandstone thickness of the Upper 21-22 Interval in the Lower Upper C-6-X Submember in the LL-652 area.

184

Upper Upper C-6-X Submember

Sandbody Geometry

The Upper Upper C-6-X Submember is a thin (average 70-ft [21.3-m]), typically upward-coarsening interval at the top of the C-6-X Member (fig. 5). This unit is composed of dominantly upward-coarsening, northeast-trending, dip-elongate sandstones, 40 to 50 ft (12 to 15.2 m) thick and 500 to 3,500 ft (150 to 1,067 m) wide (table 25 and fig. 113). A major depocenter exists in the southwestern part of the LL-652 area, near the Maraven concession, where there is a single dip-elongate trend of more than 40 ft (12 m) of net sandstone.

Depositional Systems

The Upper Upper C-6-X Submember, dominated by upward-coarsening sandstones, represents delta-front deposits throughout most of the LL-652 area. However, in the southwestern part of the LL-652 area, there is a single dip-elongate trend of distributary-channel sandstones that represent the updip equivalent of these delta-front sandstones.

Reservoir Development

The Upper Upper C-6-X Submember is only moderately developed; there are extensive undeveloped areas in the LL-652 area, particularly in the north and southeast (fig. 113). Of the main depositional axes defined by more than 40 ft (12 m) of net sandstone, only one well (LL-946) has been perforated.

Lower C-5-X Submember

Sandbody Geometry and Depositional Facies

The Lower C-5-X Submember, which is divided into lower and upper intervals, is a sandstone-poor, approximately 250-ft (76-m) thick interval composed of multiple, thin sandstones interbedded with mudstones (fig. 5). These sandstones form semi-continuous, narrow (1,500 to 3,000 ft [457 to 915 m] wide) belts more than 70 ft (21.3 m) thick (table 26 and fig. 114) in a system of inferred upward-coarsening tidal sand-ridge deposits in a distal delta-front setting.

Reservoir Development

The Lower C-5-X Submember has been moderately developed, although there are some areas in the LL-652 area that have not been tested. For example, there are virtually no perforations in the north and in the southwest, except for four wells close to the Maraven-Lagoven concession boundary. The pattern of perforations is random, with little or no correspondence to depositional axes (fig. 114).

Lower Lower C-5-X Submember

Sandbody Geometry

The Lower Lower C-5-X Submember is defined as the 100- to 150-ft (30.5- to 45.7-m) interval between the 20 shale marker and the top of the C-6-X Member (fig. 5). Sandbodies in this interval are inferred to be dip-elongate, discontinuous belts, 40 to 55 ft (12 to 16.8 m) thick and 1,000 to 2,000 ft (305 to 610 m) wide (table 27 and fig. 115).

185

Table 25. Depositional systems and reservoir characteristics of the Upper Upper C-6-X Submember.

Sand-body Geometry	Northeast-trending, dip-elongate sandstones, 40-50 ft thick and 500-3,500 ft wide, bounded laterally by sandstone-poor areas 10-30 ft thick.
Depositional Facies	Upward-coarsening delta-front (tidal-ridge) sandstones in central part of map area and upward-fining distributary-channel sandstones in the southwest part of map area.
Cored Wells	None
Perforated Wells	Central area: fair level of development (LL-847, 1129, 1172, 1276, 3056, 3075 wells); southwestern area: poor level (LL-946, 1001 wells).
General Area(s) of Greatest Potential for Secondary Oil Recovery	Narrow distributary-channel and tidal ridge sandstones.
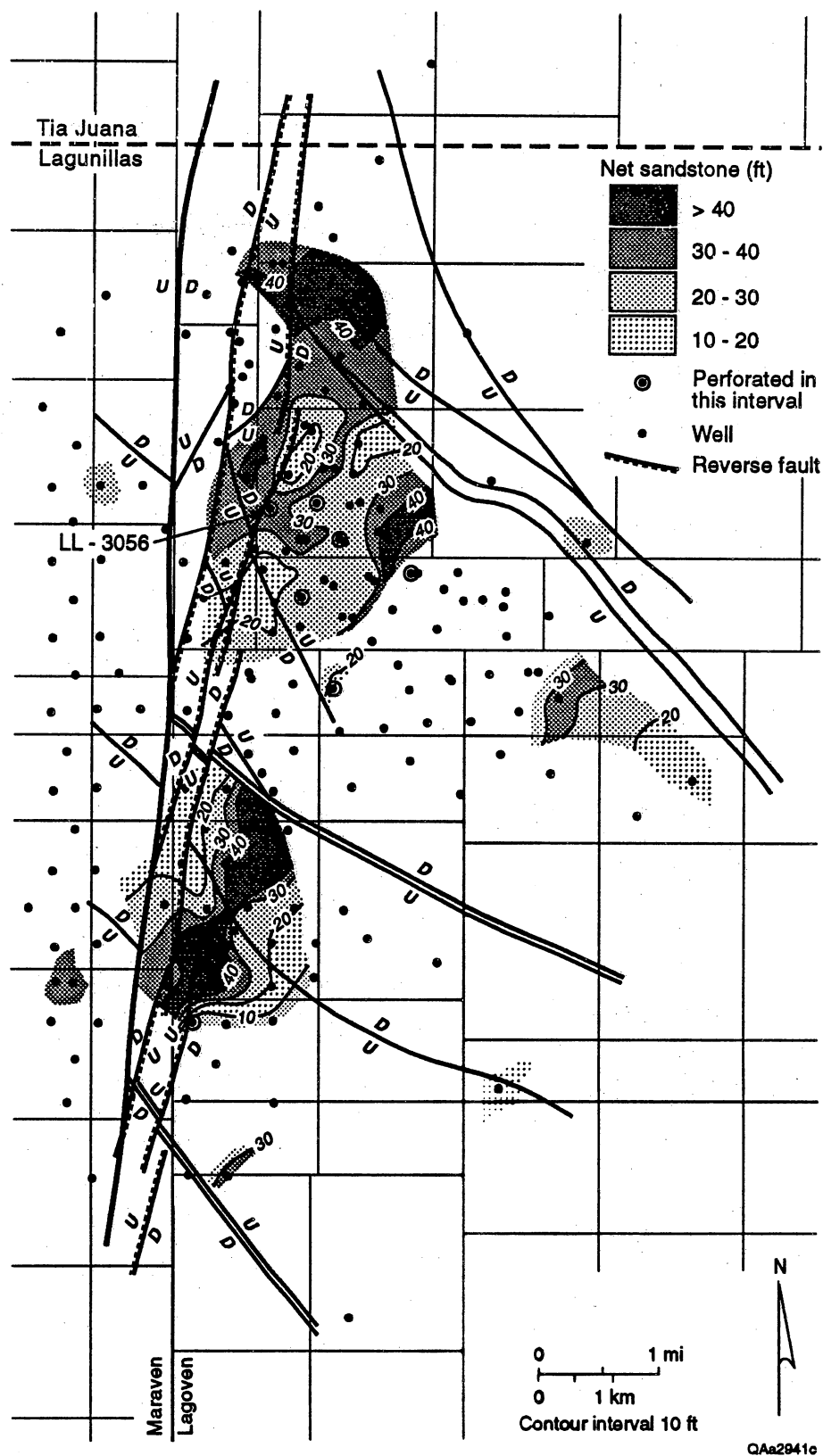
Figure 113. Net-sandstone thickness map of the Upper Upper C-6-X Submember in the LL-652 area.

187

Table 26. Depositional systems and reservoir characteristics of the Lower C-5-X Submember.

Sand-Body Geometry	Narrow (1,500-3,000 ft wide), dip-parallel and semi-continuous belts of more than 70 ft (30%) sandstone.
Depositional Facies	System of upward-coarsening tidal sand ridges (distal delta-front) consisting of interbedded sandstone and mudstone.
Cored Wells	LL-3075 (entire interval).
Perforated Wells	North-central area: moderate level of development (LL-904, LL-1111, LL-1126, LL-1172, LL-1276, LL-1782, LL-2938, and LL-2940 wells); southwestern and northern areas: poor levels of development.
General Area(s) of Greatest Potential for Secondary Oil Recovery	Tidal ridge sandstones that are isolated by faults or muddy interridge areas.

188
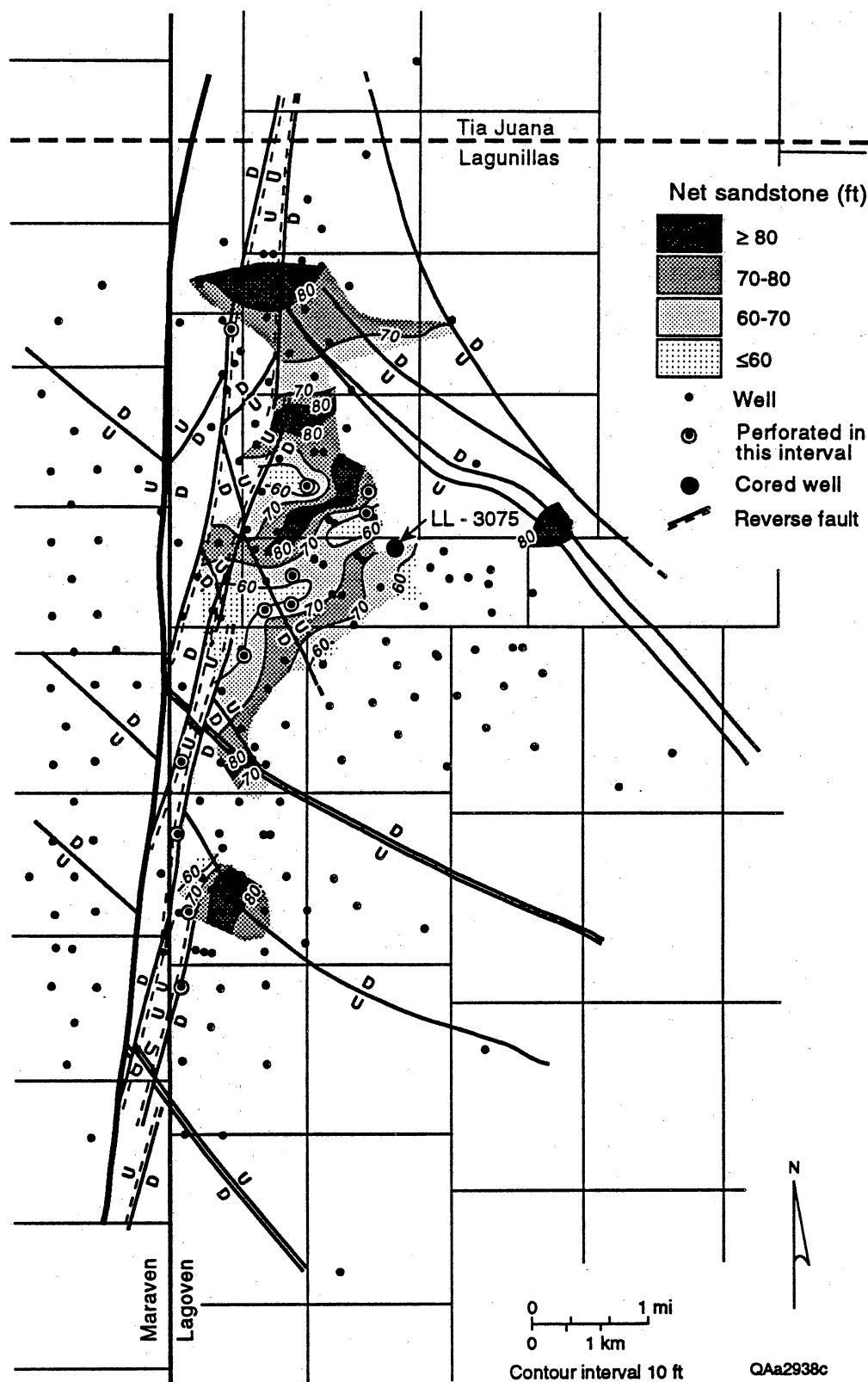
Figure 114. Net-sandstone thickness map of the Lower C-5-X Submember in the LL-652 area.

Table 27. Depositional systems and reservoir characteristics of the Lower Lower C-5-X Submember.

Sand-body Geometry	Dip-elongate (?), discontinuous belts of sandstone, 40-55 ft thick and 1,000-2,000 ft wide, thinning laterally into 20-30 ft of muddy sandstone.
Depositional Facies	Distal delta-front and shelf deposits.
Cored Wells	LL-3075 (entire interval).
Perforated Wells	Central area: LL-1111, 1129, 1172, 1782 wells; southwestern area: LL-946, 1001 wells.
General Area(s) of Greatest Potential for Secondary Oil Recovery	Relatively thicker (individual sandstones 5-10 ft thick) sandstones encased in marine mudstone.

190
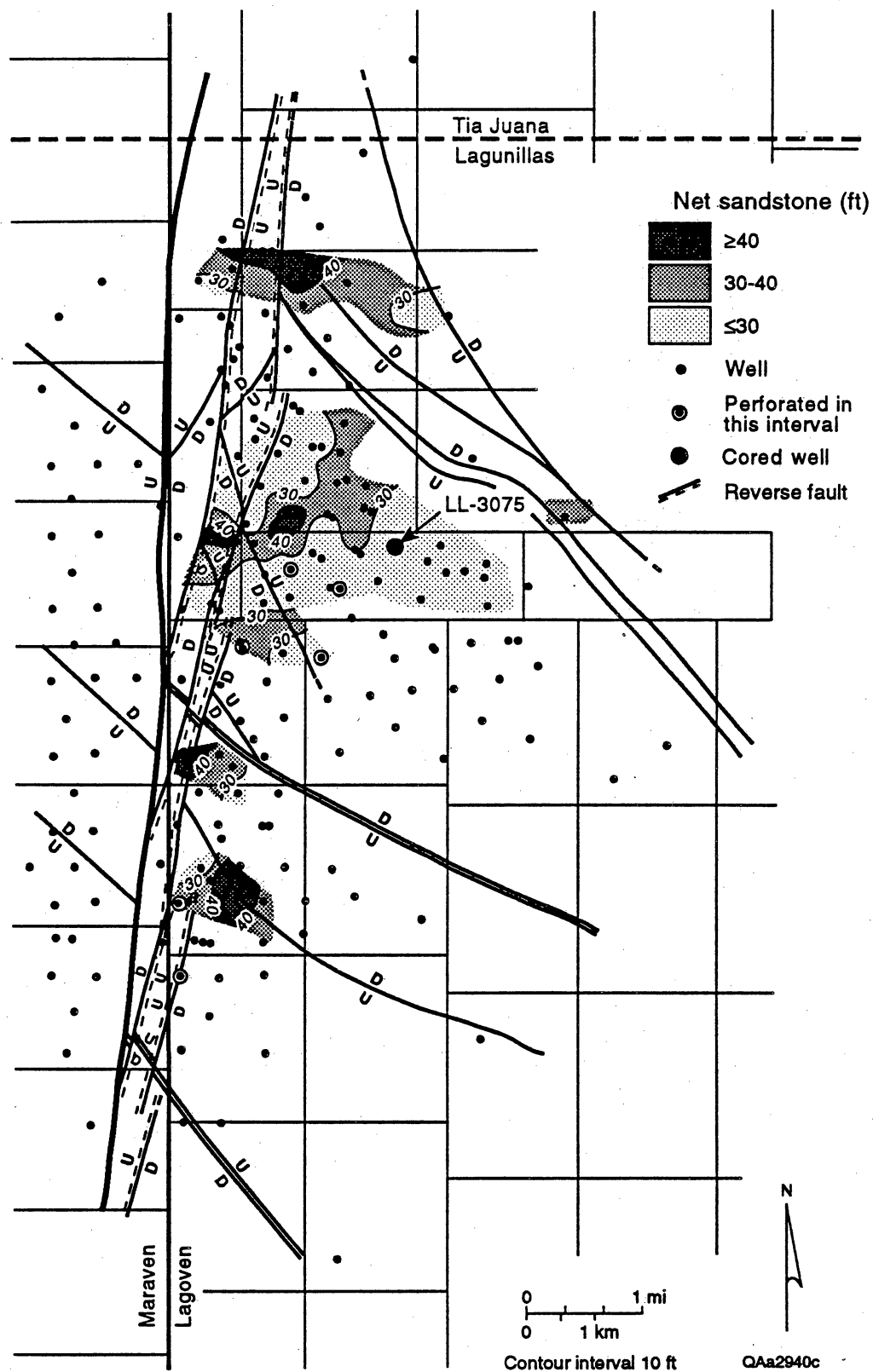
Figure 115. Net-sandstone thickness map of the Lower Lower C-5-X Submember in the LL-652 area.

191

Lithology and Depositional Systems

Sandstones in the Lower Lower C-5-X submembers are thin (1 to 3 ft [0.3 to 0.9 m]) and interbedded with burrowed mudstone (app. D, LL-3075 well, 8,330 to 8,452 ft). Sedimentary structures in the sandstones consist of asymmetrical starved ripples, plane beds, and minor inclined beds. These thin sandstones represent distal delta-front deposits located seaward (northeastward) of an inferred distributary-channel system in the Maraven concession.

Reservoir Development

Development in the Lower Lower C-5-X Submember is limited to four wells in a 0.58-mi^2 (1.5-km^2) area in the central part of the field and two wells in the southwest part of the field (fig. 115). In the central area, almost all of the wells have been perforated in shaly locations away from the main depocenter of more than 30 ft (9 m) of net sandstone. Likewise, the depocenter in the north has not been developed.

Upper Lower C-5-X Submember

Sandbody Geometry

The Upper Lower C-5-X Submember, defined as the interval from the 19 to the 20 shale markers (fig. 5) is 100 to 150 ft (30.5 to 45.7 m) thick and consists of a system of east-trending, dip-parallel sandstones, 40 to 60 ft (12 to 18 m) thick and 2,000 to 5,000 ft (610 to 1,524 m) wide (table 28 and fig. 116). The most common log responses are upward-coarsening to serrate.

Lithology and Depositional Systems

As in the Lower Lower C-5-X Submember, the Upper Lower C-5-X Submember contains multiple sandstones interbedded with mudstone. However, individual sandstones are up to 5 ft (1.5 m) thick and are separated by comparatively thinner mudstones (app. D, LL-3075 well, 8,177 to 8,330 ft). The sandstones are also more commonly crossbedded, although asymmetrical ripples and plane beds are abundant. The two intervals in the Lower C-5-X Submember (upper and lower) together represent the distal facies tract of a deltaic system; the lower unit is distal delta front and the upper unit is delta front. No distributary-channel deposits are inferred in either of the units in the LL-652 area, as the deltaic system had not prograded very far eastward.

Reservoir Development

The Upper Lower C-5-X has undergone a moderate level of development: 10 wells have been perforated in the north-central part of the field in an area that covers approximately 0.97 mi^2 (2.5 km^2) (fig. 116). However, there has been no development in two sandy depositional axes in the northern part of the field and none toward the southwest, except for three wells near the Maraven lease.

Middle C-5-X Submember

The Middle C-5-X Submember consists of all strata between the 18 and 19 shale markers and is typically 250 ft (76 m) thick (fig. 5). It is a composite of three units (lower, middle, and upper) that are each 50 to 100 ft (15.2 to 30.5 m) thick.

Table 28. Depositional systems and reservoir characteristics of the Upper Lower C-5-X Submember.

Sand-body upward-Geometry	East-trending, dip-parallel sandstones, 40-60 ft thick and 2,000-5,000 ft wide. These sandstones have coarsening and/or serrate log responses.
Depositional Facies	Distal delta-front.
Cored Wells	LL-3075 (entire interval).
Perforated Wells	Moderate density of perforated wells only in central area.
General Area(s) of Greatest Potential for Secondary Oil Recovery	Areas where tidal ridge sandstones are isolated by faults or muddy interridge areas.

193
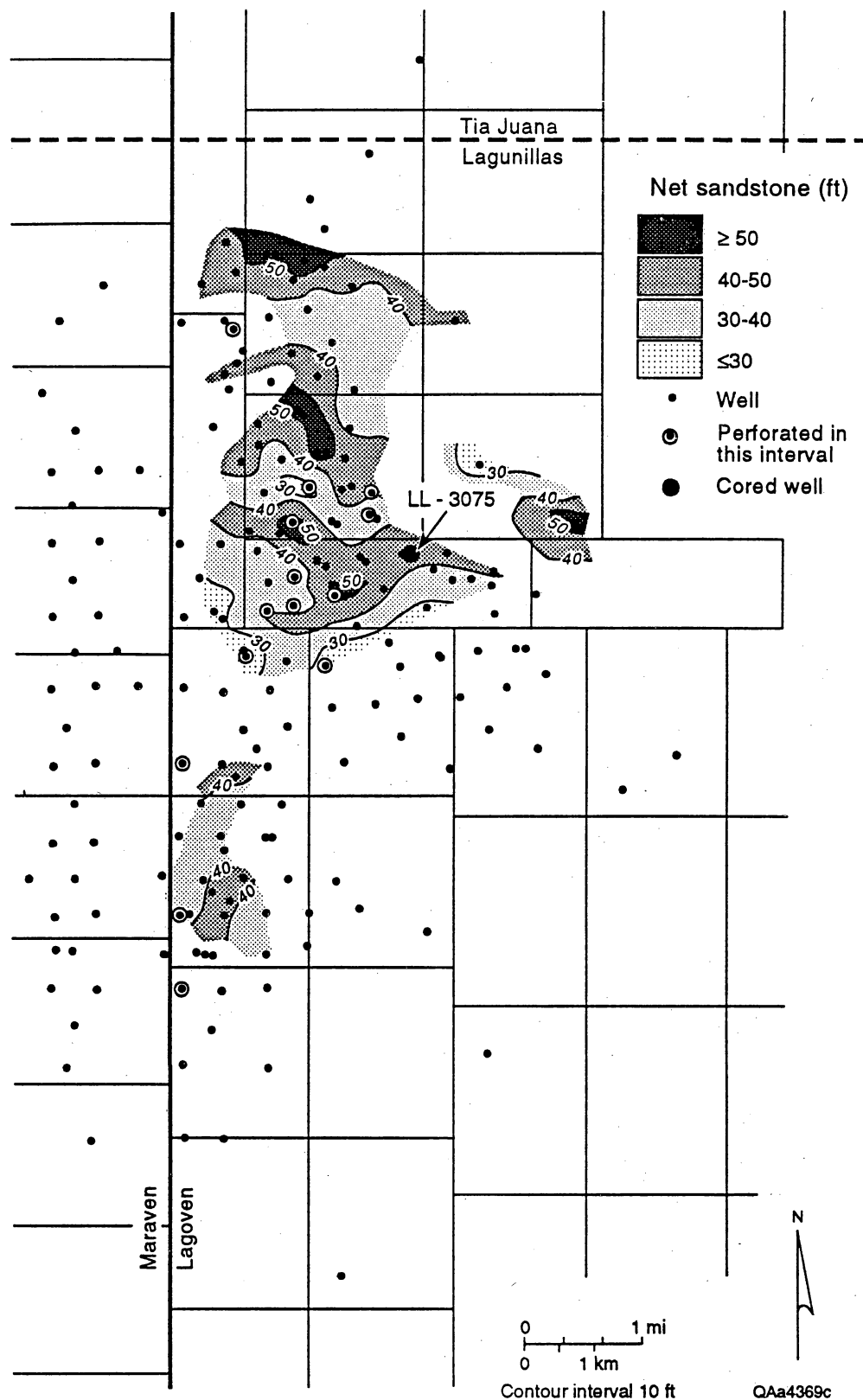
Figure 116. Net-sandstone thickness map of the Upper Lower C-5-X Submember in the LL-652 area.

194

Sandbody Geometry

The Middle C-5-X Submember is composed of multiple, east- and northeast-trending belts of sandstone, 80 to 110 ft (24.4 to 33.5 m) thick and 2,000 to 8,000 ft (610 to 2,439 m) wide (table 29 and fig. 117). In the northern part of the LL-652 area, the sandstone trends eastward to southeastward, whereas in the southwest they trend northeastward.

Lithology and Depositional Systems

Individual units in the Middle C-5-X Submember consist of (1) a lower upward-coarsening unit, (2) a middle unit composed of mudstone and erosion-based sandstones, and (3) an upper sandstone-rich unit (app. D, LL-3075 well, 7,993 to 8,177 ft). These units correspond to (1) delta-front, (2) proximal delta-front and lower delta-plain, (3) and inner estuarine bay-fill units, respectively, overlain by a retrogradational, marine-dominated interval. These three units together make up an offlapping progradational wedge. A stratigraphic strike section that displays log-facies responses (fig. 118) shows the (1) lower system of mainly upward-coarsening tidal sand-ridge deposits overlain by the (2) middle unit consisting of proximal delta-front (upward-coarsening log response) and tidal-flat deposits (upward-fining and serrate log responses), and (3) the upper estuarine bay fill with thick (more than 35-ft [11-m]) distributary-channel deposits capped by transgressive deposits. An upward increase in upward-fining sandstones in the Middle C-5-X Submember reflects progradation of the delta plain over the delta front in the LL-652 area.

Reservoir Development

The Middle C-5-X Submember has been extensively developed, especially in the north and north-central parts of the LL-652 area (fig. 117). Much of the southwest part of the field, near the Maraven concession, has also been perforated. However, since the Middle C-5-X Submember is a complex of three depositional subunits, these perforations are distributed among different stratigraphic horizons, resulting in numerous opportunities for additional infield development.

<div align="center">Lower Middle C-5-X Submember</div>

Sandstone Geometry

This basal unit in the Middle C-5-X Submember is typically a 100-ft (30.5-m), upward-coarsening section (fig. 5). The sandstone geometry is strongly dip-parallel throughout most of the LL-652 area (table 30 and fig. 119). The sandstones range from 30 to 45 ft (9.1 to 13.7 m) thick and from 1,000 to 6,000 ft (305 to 1,829 m) wide.

Lithology and Depositional Systems

The Lower Middle C-5-X Submember is composed of upward-coarsening sandstones, 5 to 12 ft (1.5 to 3.7 m) thick, interbedded with burrowed siltstone and mudstone (app. D, LL-3075 well, 8,128 to 8,177 ft). These sandstones have a succession of bedforms that range from asymmetric ripples at the base to clay-clast-rich, inclined beds and crossbeds at the top. Each sandstone is a tidal-ridge deposit in a delta-front setting and contains maximum reservoir quality at the top.

Table 29. Depositional systems and reservoir characteristics of the Middle C-5-X Submember.

Sand-body Geometry	East- and northeast-trending sandstones, 80-110 ft thick and 2,000-8,000 ft wide. In northern part of field, net-sandstone thickness generally decreases eastward from 90-100 ft to 60-80 ft.
Depositional Facies	Composite unit of three offlapping depositional cycles, consisting of an aggregate of distributary-channel, delta-front and transgressive sandstones.
Cored Wells	LL-3075 (entire interval), LL-3282 (upper 30%).
Perforated Wells	Good density of perforated wells throughout, except for southwestern and extreme northern areas.
General Area(s) of Greatest Potential for Secondary Oil Recovery	See maps of individual depositional cycles (upper, middle, and lower).
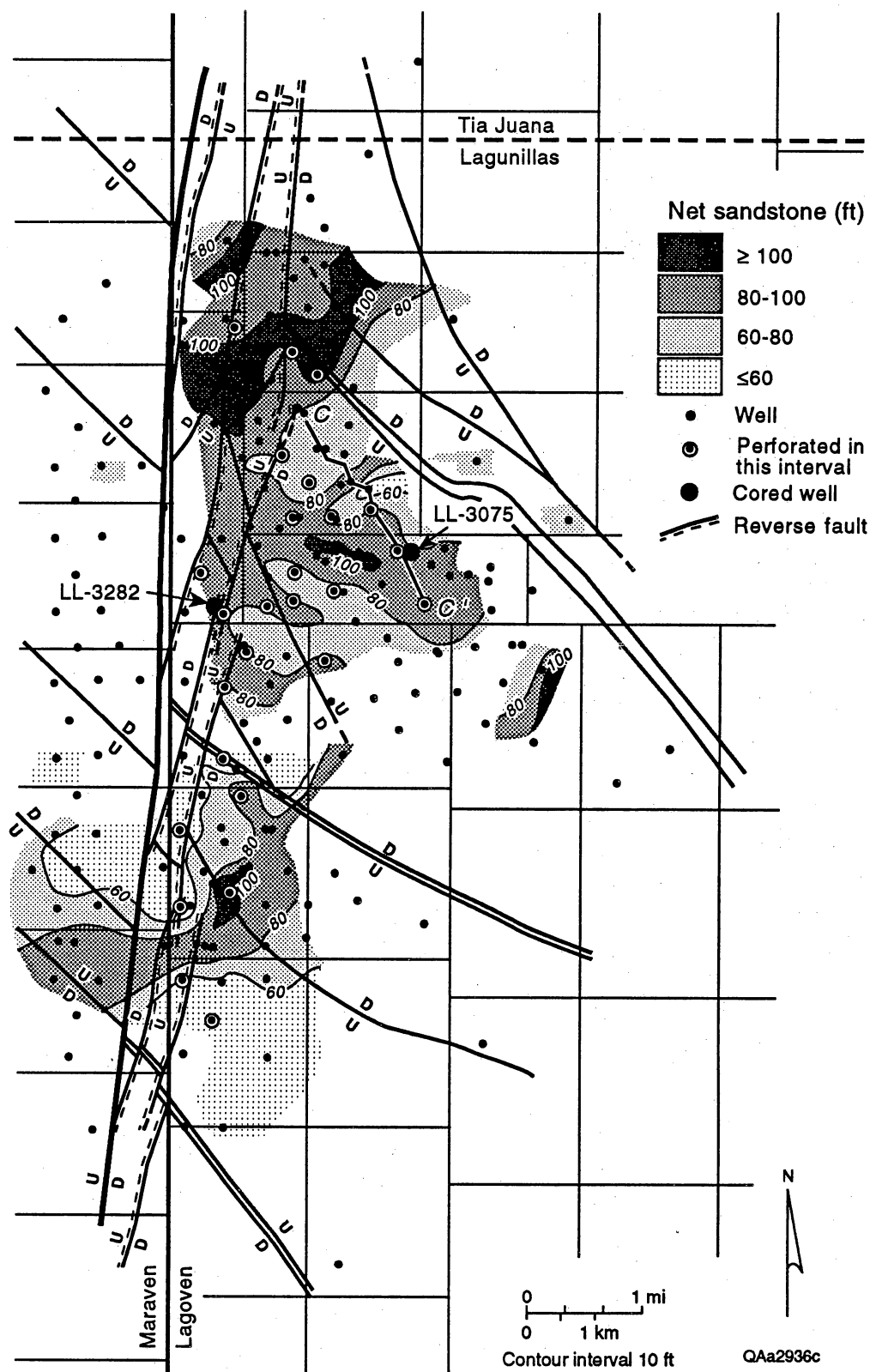
Figure 117. Net-sandstone thickness map of the Middle C-5-X Submember in the LL-652 area. Cross section C–C' is shown in figure 118.
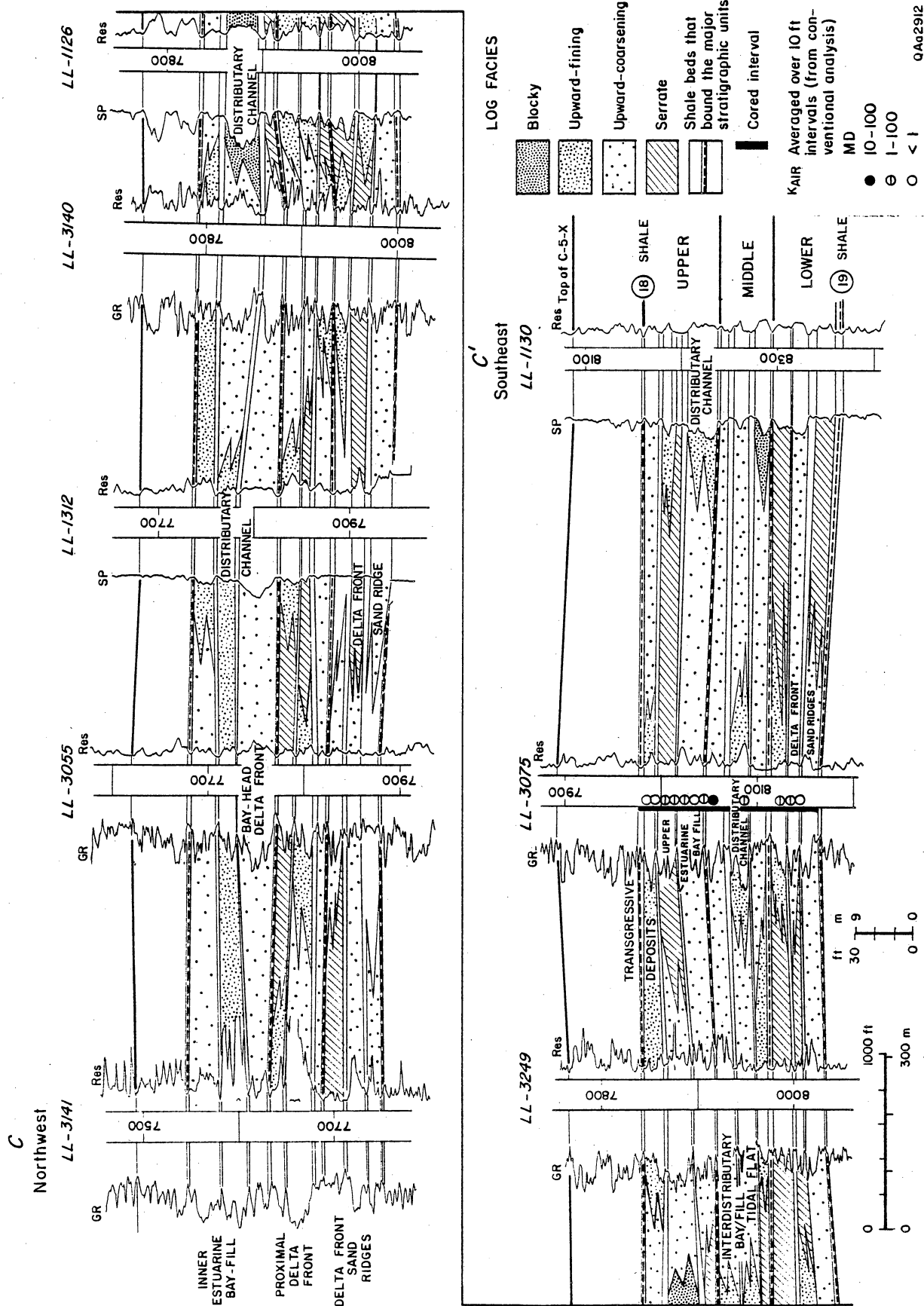
Figure 118. Stratigraphic strike section C–C' in the Middle C-5-X Submember, an offlapping deltaic sequence with tidal sand-ridge deposits overlain by proximal delta-front and lower delta plain deposits. Cross section is located in figures 117, 119, 120, and 121.

Table 30. Depositional systems and reservoir characteristics of the Lower Middle C-5-X Submember.

Sand-body Geometry	Dip-parallel, mainly upward-coarsening sandstones, 30-45 ft thick and 1,000 to 6,000 ft wide, separated by broad areas of 15-30 ft of muddy sandstone.
Depositional Facies	Delta-front (tidal ridge) sandstones bounded by muddy interridge deposits. Possible distributary-channel system in southwest corner of map area in Maraven concession.
Cored Wells	LL-3075 (entire interval).
Perforated Wells	Main concentration of perforated wells in central area; all other areas have poor density of perforated wells.
General Area(s) of Greatest Potential for Secondary Oil Recovery	
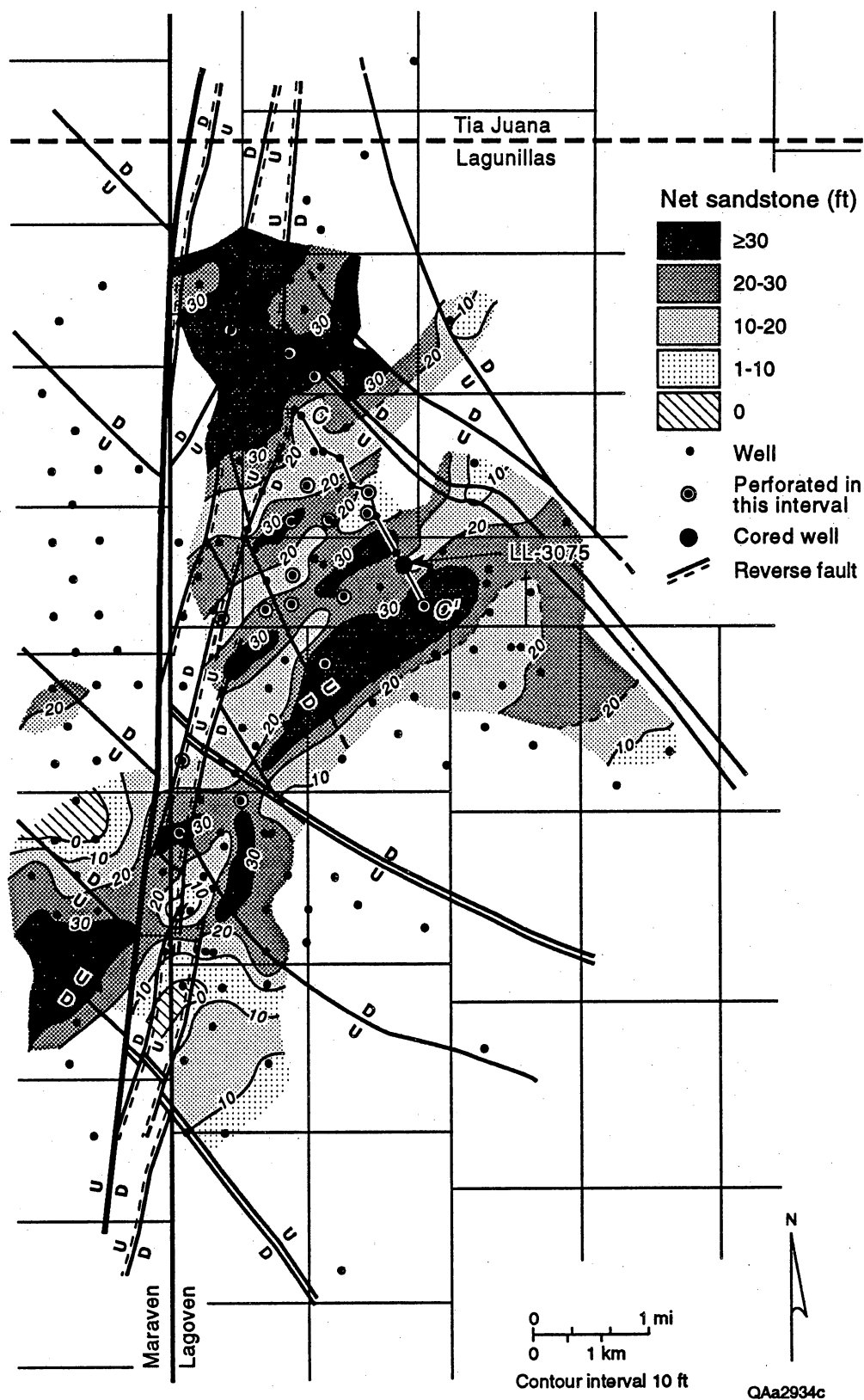
Figure 119. Net-sandstone thickness map of the Lower Middle C-5-X Submember in the LL-652 area. Cross section C–C' is shown in figure 118.

Reservoir Development

Greatest development of the Lower Middle C-5-X Submember has been in the central part of the LL-652 area (fig. 119). All of the thickest sandstone bodies in this area have been perforated by at least two wells. However, there are sites in each of these sandstones that can still be targeted for additional development. Other areas where the current perforation density is sparse include the far northern part of the field and selected areas in the updip (southwestern) part of the facies tract in the vicinity of the LL-3062 well.

Middle Middle C-5-X Submember

Sandstone Geometry

The Middle Middle C-5-X Submember is a thin (50- to 100-ft [15.2- to 30.5-m]) interval that consists of narrow (550 to 3,000 ft [168 to 915 m] wide), northeast-trending bands of upward-fining sandstones more than 20 ft (6 m) thick pinching out laterally into mudstones (table 31 and fig. 120). These sandstones have northeast-bifurcating trends in the northern part of the LL-652 area.

Lithology and Depositional systems

The Middle Middle C-5-X Submember (app. D, LL-3075 well, 8,058 to 8,128 ft) consists of a lower section of thick (20-ft [6-m]) mudstone and thin (1- to 1.5-ft [0.3- to 0.5-m]) sandstones truncated by a crossbedded, upward-fining 12-ft (3.7-m) sandstone. The upper part of the section contains several upward-coarsening, rippled and crossbedded sandstones interbedded with burrowed mudstone. The base of this sequence is composed of muddy tidal-flat deposits truncated by a single distributary-channel deposit; the upper part of the section is composed of progradational bay-fill deposits.

Reservoir Development

The Middle Middle C-5-X Submember has been extensively developed (fig. 120). However, as in the Lower Middle C-5-X Submember, these sandstone bodies have been incompletely developed and contain locations for additional wells or recompletions. There are areas of sparsely perforated wells in the southwest and extreme northern part of the field. Additionally, the thickest parts of the dip-elongate sandstone body in the central part of the field have not been contacted, especially where this sandstone has been intersected by the northeast-trending zone of partly-sealing reverse faults.

Upper Middle C-5-X Submember

Sandbody Geometry

The Upper Middle C-5-X Submember represents the last stage in the offlapping progradational wedge in the Middle C-5-X Member and consists of a system of dip-elongate and digitate sandbodies more than 40 ft (12 m) thick with a complex geometry (table 32 and fig. 121). In the southern part of the LL-652 area, the sandstone bodies are simple, northeast-trending belts that extend across the field, whereas in the northern part they are northeast-bifurcating pods that pinch out downdip (northeastward).

Lithology and Depositional Systems

The lower part of the Upper Middle C-5-X Submember (app. D, LL-3075 well, 7,995 to 8,088 ft) consists of a 15-ft (4.6-m) interval of rippled, burrowed sandstones overlain by another 15-ft (4.6-m) interval of erosion-based, crossbedded and clay-clast-rich sandstone. The upper 24 ft (7.3 m) contains two intensely

Table 31. Depositional systems and reservoir characteristics of the Middle Middle C-5-X Submember.

Sand-body sandstones Geometry	Narrow (550-3,000 ft wide), northeast-trending bands of more than 20 ft of mostly upward-fining bounded laterally by broad areas of 5-15 ft of muddy sandstone with either upward-coarsening or serrate log responses.
Depositional Facies	Distributary- and tidal-channel deposits bounded by muddy lower delta-plain (tidal-flat) deposits.
Cored Wells	LL-3075 (entire interval).
Perforated Wells	North-central and central areas: moderate to good density of perforations; southwestern area: fair density.
General Area(s) of Greatest Potential for Secondary Oil Recovery	Distributary- and tidal-channel sandstones isolated in fault compartments or partly encased in tidal-flat mudstone.

Net sandstone (ft)

- ≥30
- 20-30
- 10-20
- 1-10

• Well

◉ Perforated in this interval

● Cored well

⟋⟋ Reverse fault

LL-3075

Tia Juana
Lagunillas

Maraven   Lagoven

N

0   1 mi

0   1 km

Contour interval 10 ft   QAa2932c
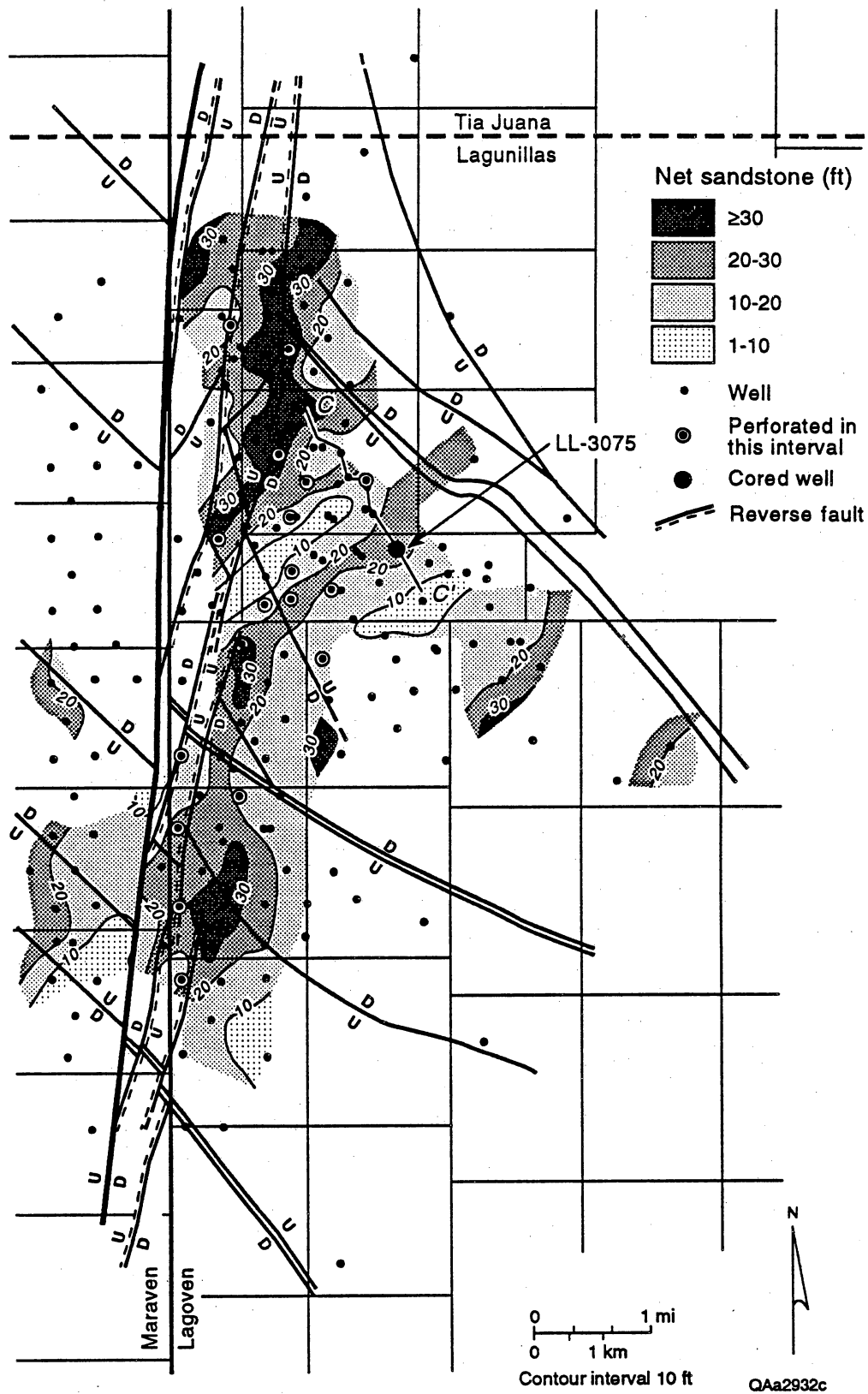
Figure 120. Net-sandstone thickness map of the Middle Middle C-5-X Submember in the LL-652 area. Cross section C–C′ is shown in figure 118.

Table 32. Depositional systems and reservoir characteristics of the Upper Middle C-5-X Submember.

|	
Sand-body Geometry	Digitate, dip-elongate, northeast-trending and -bifurcating sandstones more than 40 ft thick and 1,550 to 4,000 ft wide, extending across map area. These sandstones have upward-fining and blocky log responses and are flanked by thinner (10-30 ft) sandstones with upward-coarsening and serrate log responses.
Depositional Facies	Distributary-channel (bayhead delta?) and channel mouth-bar deposits overlain by transgressive delta-front sandstones.
Cored Wells	LL-3075 (entire interval), LL-3282 (upper 80%).
Perforated Wells	Central area: moderate to good density of perforated wells; southwestern area: fair density; all other areas: poor density.
General Area(s) of Greatest Potential for Secondary Oil Recovery	Narrow distributary-channel sandstones and channel-mouth-bar sandstones where they pinch out into delta-front deposits.
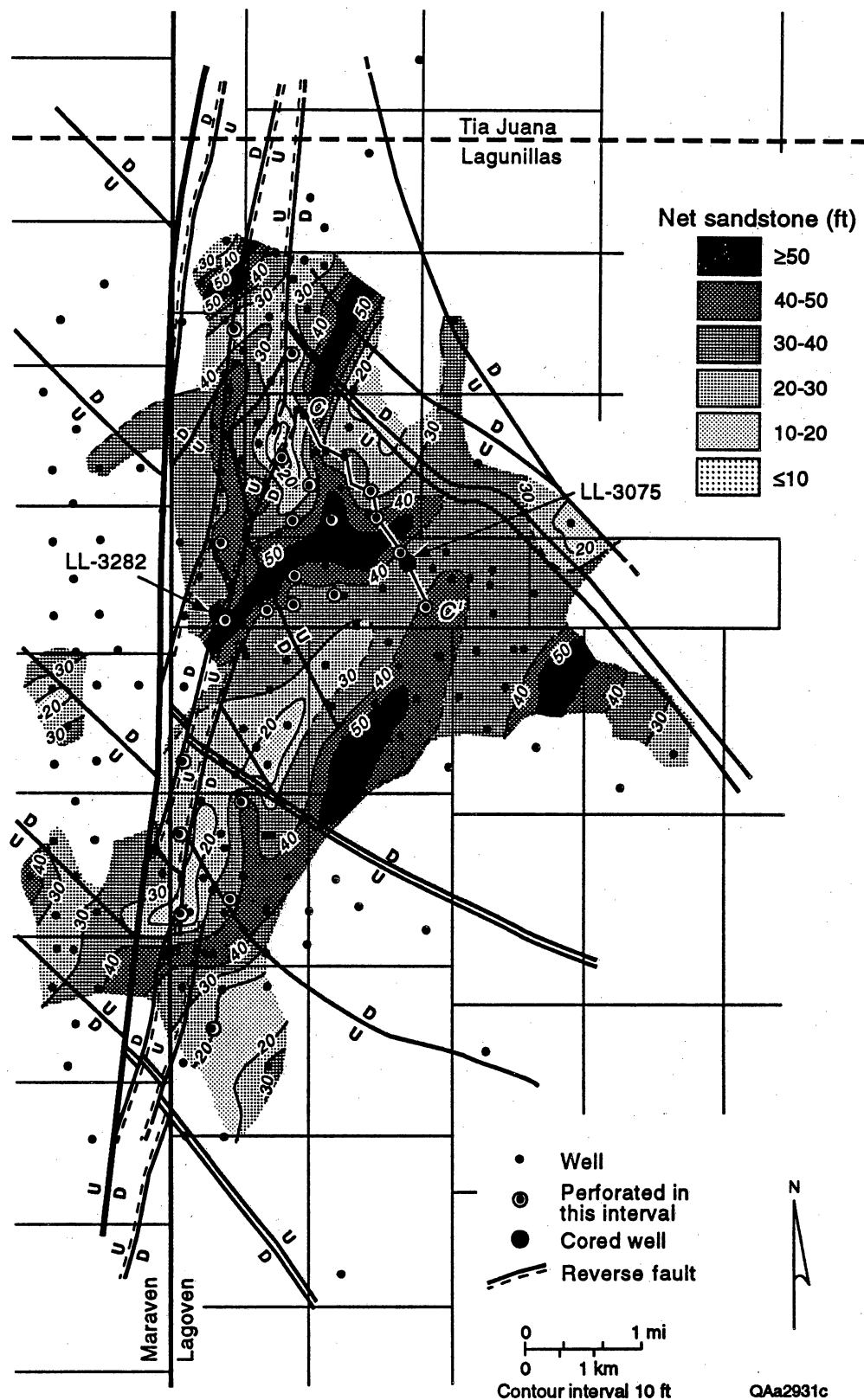
Figure 121. Net-sandstone thickness map of the Upper Middle C-5-X Submember in the LL-652 area. Cross section C–C' is shown in figure 118.

burrowed, upward-coarsening sandstones, each 5 to 7 ft (1.5 to 2.1 m) thick; burrow types include *Ophiomorpha, Skolithos,* and *Planolites.* This stratigraphic succession includes a basal delta-front deposit truncated by distributary-channel deposits. The upper part of the sequence consists of transgressive-shoreface (reworked delta-front) deposits, indicated by clean, upward-coarsening sandstones with marine burrows and symmetrical wave ripples.

Reservoir Development

Although the Upper Middle C-5-X Submember has been intensely perforated in the central part of the LL-652 area, there are still areas where thick sandstones have not been tested or developed (fig. 121). For example, the distributary-channel sandstone in the northeast part of the LL-652 area, centered on the LL-2729 well, has not been perforated. The southern belt of sandstone (more than 40 ft [12 m] thick) between the LL-946 and LL-1001 wells has been incompletely perforated.

Upper C-5-X Submember

Sandbody Geometry

The Upper C-5-X Submember is the uppermost 50 to 100 ft (15.2 to 30.5 m) of the C-5-X Member (fig 5) and features an east-trending system of interconnected belts of more than 30 ft (9 m) of net sandstone 2,000 to 3,500 ft (610 to 1,067 m) wide in the northern part of the LL-652 area (table 33 and fig. 122). These sandstones have dominantly upward-coarsening or serrate log responses.

Lithology and Depositional Systems

The Upper C-5-X Submember (app. D, LL-3282 well, 7,920 to 8,028 ft and app. D, LL-3075 well, 7,905 to 7,995 ft), consists mostly of multiple upward-coarsening sandstones interbedded with burrowed mudstone. Individual upward-coarsening sequences range from 3 to 8 ft (0.9 to 2.4 m) thick in the LL-3282 well and 5 to 16 ft (1.5 to 4.9 m) thick in the LL-3075 well, along the depositional axis of one of the dip-elongate sandbodies (fig. 122). The sandstones commonly have asymmetrical ripples and plane beds at the base and crossbeds and clay clasts at the top, although clay clasts are also abundant throughout most of the sandstones. Large, symmetrical ripples are present at the top of some of the upward-coarsening sequences. The multiple upward-coarsening sandstones of the Upper C-5-X Submember were deposited in delta-front and distal delta-front settings. The lack of upward-fining and blocky log responses indicates that the delta-plain facies tract was not present in the LL-652 area and is inferred to have been westward in the Maraven area.

Reservoir Development

The Upper C-5-X Subunit has been intensely developed (fig. 122). However, the northern dip-elongate sandstone body has not been perforated, and because this is an area of complex structure, it may present an opportunity for development.

Lower C-4-X Submember

The Lower C-4-X Submember includes all strata from the 16 shale marker to the top of the C-5-X Member and is approximately 250 ft (76 m) thick in the LL-652 area (fig. 5). Sandstones in the Lower C-4-X Submember occur in northeast-trending, dip-elongate belts that merge into a broad, 2-mi (3.2-km) wide area toward the north (table 34 and fig. 123). These sandstones have upward-coarsening and serrate log responses and were deposited in delta-front and distal delta-front environments. Although there is an

Table 33. Depositional systems and reservoir characteristics of the Upper C-5-X Submember.

Sand-body Geometry	East-trending, interconnected belts of more than 30 ft (>30%) sandstone 2,000 to 3,500 ft wide in the northern part of the map area. In the southern part of the map area, sandstones are generally less than 30 ft thick. Sandstones have a dominantly upward-coarsening or serrate log response.
Depositional Facies	Mainly delta-front and distal delta-front deposits.
Cored Wells	LL-3075 (entire interval), LL-3282 (entire interval).
Perforated Wells	Central area: good density of perforated wells; southwestern area: fair density; all other areas: poor density.
General Area(s) of Greatest Potential for Secondary Oil Recovery	Areas where delta-front and distal delta-front tidal ridge sandstones pinch out into interridge mudstones.
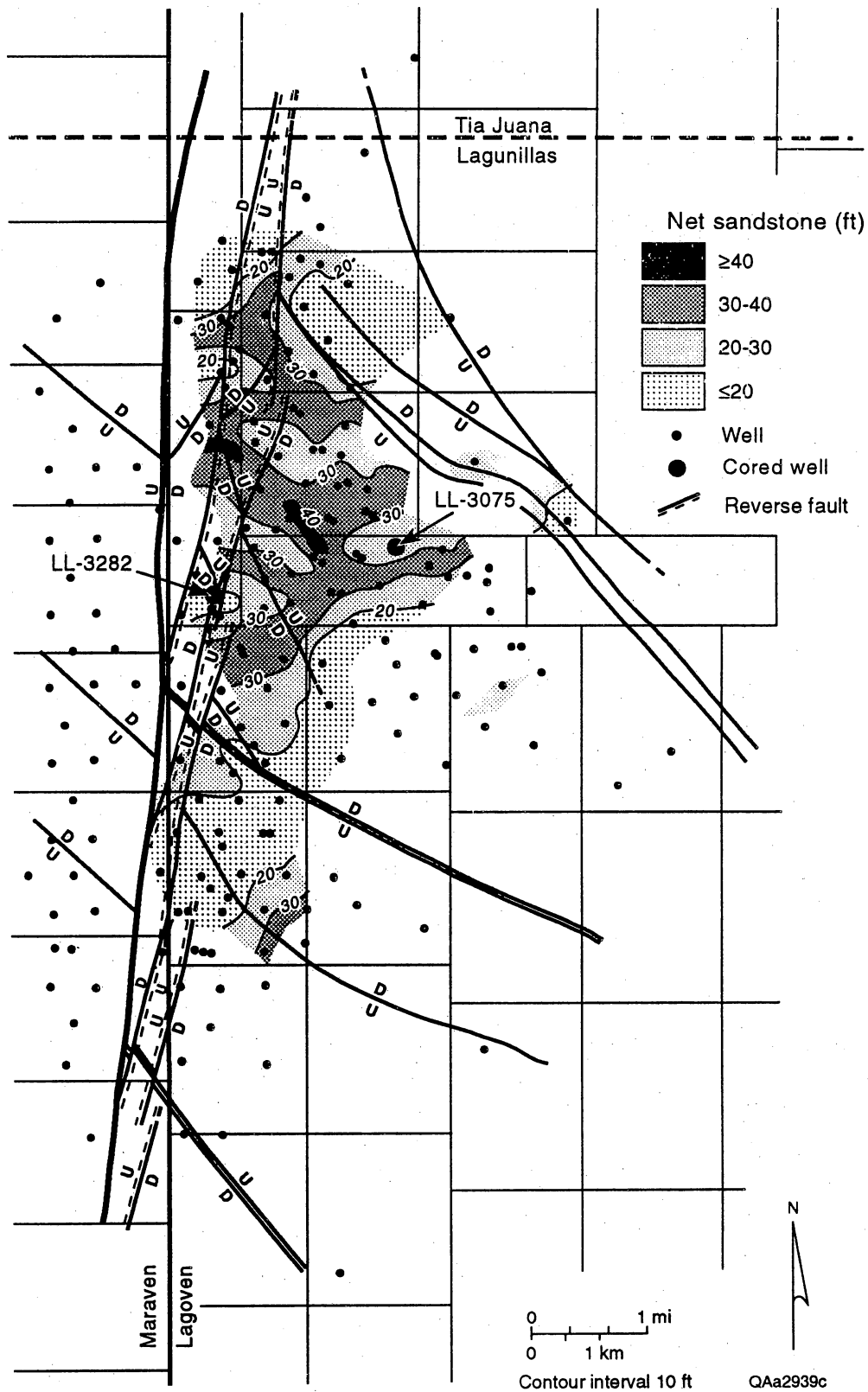
Figure 122. Net-sandstone thickness map of the Upper C-5-X Submember in the LL-652 area.

Table 34. Depositional systems and reservoir characteristics of the Lower C-4-X Submember.

Sand-body Geometry	Northeast-trending, dip-elongate sinuous belts of sandstone, more than 40 ft thick (>15% sandstone) in the central and southwest part of the map area, merging into wide (>2 mi) area in the northern part of the map area where there is more than 60 ft (>20%) of sandstone. Almost all sandstones have upward-coarsening and serrate log responses.
Depositional Facies	Delta-front and distal delta-front tidal ridge sandstones.
Cored Wells	None
Perforated Wells	Good completion density throughout, except for southwestern area.
General Area(s) of Greatest Potential for Secondary Oil Recovery	Areas where tidal ridge sandstones are encased in interridge mudstones.
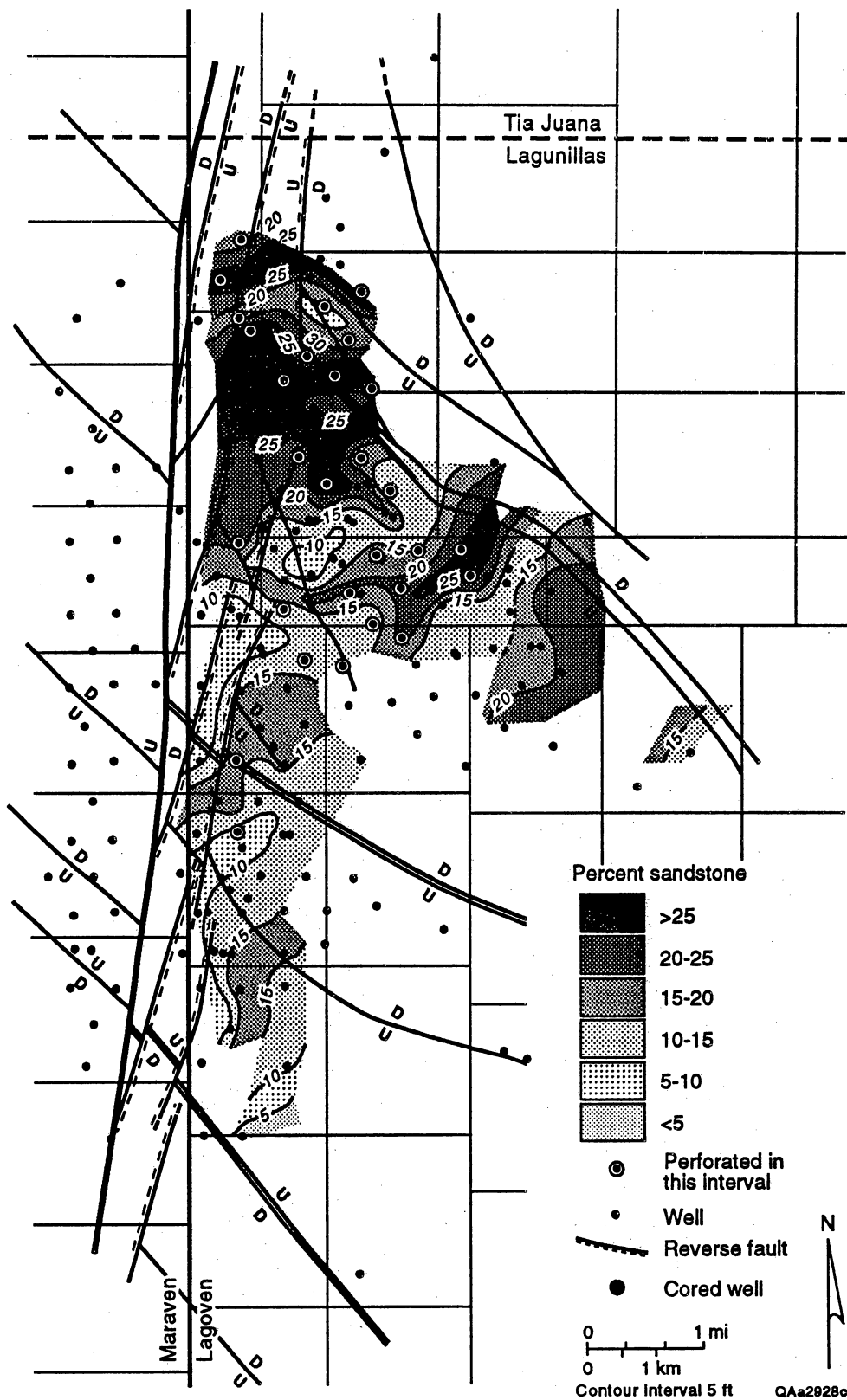
Figure 123. Percent sandstone map of the Lower C-4-X Submember in the LL-652 area.

absence of upward-fining and blocky log responses that indicate distributary-channel deposits, a depocenter is inferred in the northern part of the Maraven concession, west of the broad, relatively sandstone-rich area in the northern part of the field.

Reservoir Development

The Lower C-4-X Submember has been perforated throughout the central and north-central part of the LL-652 area, where it contains more than 20 percent sandstone (fig. 123). However, the thinner belt of 15 to 20 percent sandstone between the LL-1310 and LL-1162 wells has not been perforated, as well as the entire belt of 15 ft (4.5 m) of sandstone in the extreme southern part of the field.

Middle C-4-X Submember

The Middle C-4-X Submember includes all strata from the 14 to 16 shale markers and is typically 200 ft (61 m) thick (fig. 5). This submember is a composite of two separate depositional units: the lower unit is bounded below by the 16 shale marker and above by the 15 shale marker, and the top of the upper one is the 14 shale marker. Each depositional unit is composed of lower delta-plain (tidal-flat, distributary-, and tidal-channel) deposits overlying delta-front deposits. The two units together contain north- to northeast-trending belts of sandstone more than 40 ft (12 m) thick and 2,000 to 7,500 ft (610 to 2,287 m) wide. Locally, these sandstones are as much as 60 ft (18 m) thick (table 35 and fig. 124).

Five main facies, in ascending order in the core of the LL-2850 well (app. D, 7,770 to 7,898 ft) from (1) tidal-channel, (2) tidal-flat, (3) delta-front, (4) distributary-channel, and (5) distal delta-front make up the Middle C-4-X Submember. Tidal-channel deposits are defined by multiple, erosion-based and upward-fining sandstones, each 2 to 4 ft (0.6 to 1.2 m) thick and stacked into two composite intervals 12 to 16 ft (3.7 to 4.9 m) thick. A 7-ft (2.1-m) tidal-flat section overlies the upper tidal-channel sequence from 7,846 to 7,854 ft and is composed of upward-fining siltstone with burrows and flaser ripples (fig. 80). The delta-front deposit that forms the basal part of the Upper Middle C-4-X Submember (14 to 15 interval) extends from 7,825 to 7,839 ft and is an upward-coarsening interval of fine and very-fine sandstone interbedded with burrowed and rippled siltstone and mudstone. A 15- to 20-ft (4.6- to 6.1-m) distributary-channel deposit directly overlies the delta-front sequence and consists of crossbedded and plane-bedded fine to upper-fine sandstone with organic fragments and minor burrowing. Some crossbeds are oversteepened and have been distorted by soft-sediment deformation. The uppermost part of the section is a 15-ft (4.6-m), distal delta-front deposit that contains three 2- to 3-ft (0.6- to 0.9-m), very fine sandstone beds interbedded with burrowed mudstone and siltstone.

Reservoir Development

The Middle C-4-X Submember is in an advanced stage of development. Virtually every major sandstone in this interval has been perforated, especially in the east-central part of the LL-652 area (fig. 124). However, some of these sandstones can still be contacted in less-developed areas. For example, the narrow (less than 600 ft [182.9 m] wide), northeast-trending sandstone body more than 40 ft (12 m) thick, located in the southwestern part of the LL-652 area, has not been tested south of the LL-1245 well and may contain remaining mobile oil, especially in the zone of the reverse faults.

Upper C-4-X Submember

The Upper C-4-X Submember consists of all strata from the 14 shale marker to the top of the C-4-X Member (fig. 5). The Upper C-4-X Submember is composed of four main, dominantly upward-coarsening units that represent a depositional parasequence as part of the major progradational cycle that makes up the C-4-X Submember (fig. 125). Of these four main units, the lowest (#4) is the thickest unit and was

211

Table 35. Depositional systems and reservoir characteristics of the Middle C-4-X Submember.

Sand-body Geometry	North-northeast-trending belts of sandstone, more than 40 ft thick and 2,000 to 7,500' ft wide. These sandstones are locally as much as 60 ft thick.
Depositional Facies	Composite interval of two depositional parasequences, consisting mostly of distributary-channel, tidal-channel, and delta-front sandstones.
Cored Wells	LL-2850 (upper 90% of interval).
Perforated Wells	High density of perforated wells throughout the field, except west-northwest area (A-188 concession).
General Area(s) of Greatest Potential for Secondary Oil Recovery	Thick distributary- and tidal-channel sandstones and overbank deposits partly encased in muddy tidal-flat deposits.

212
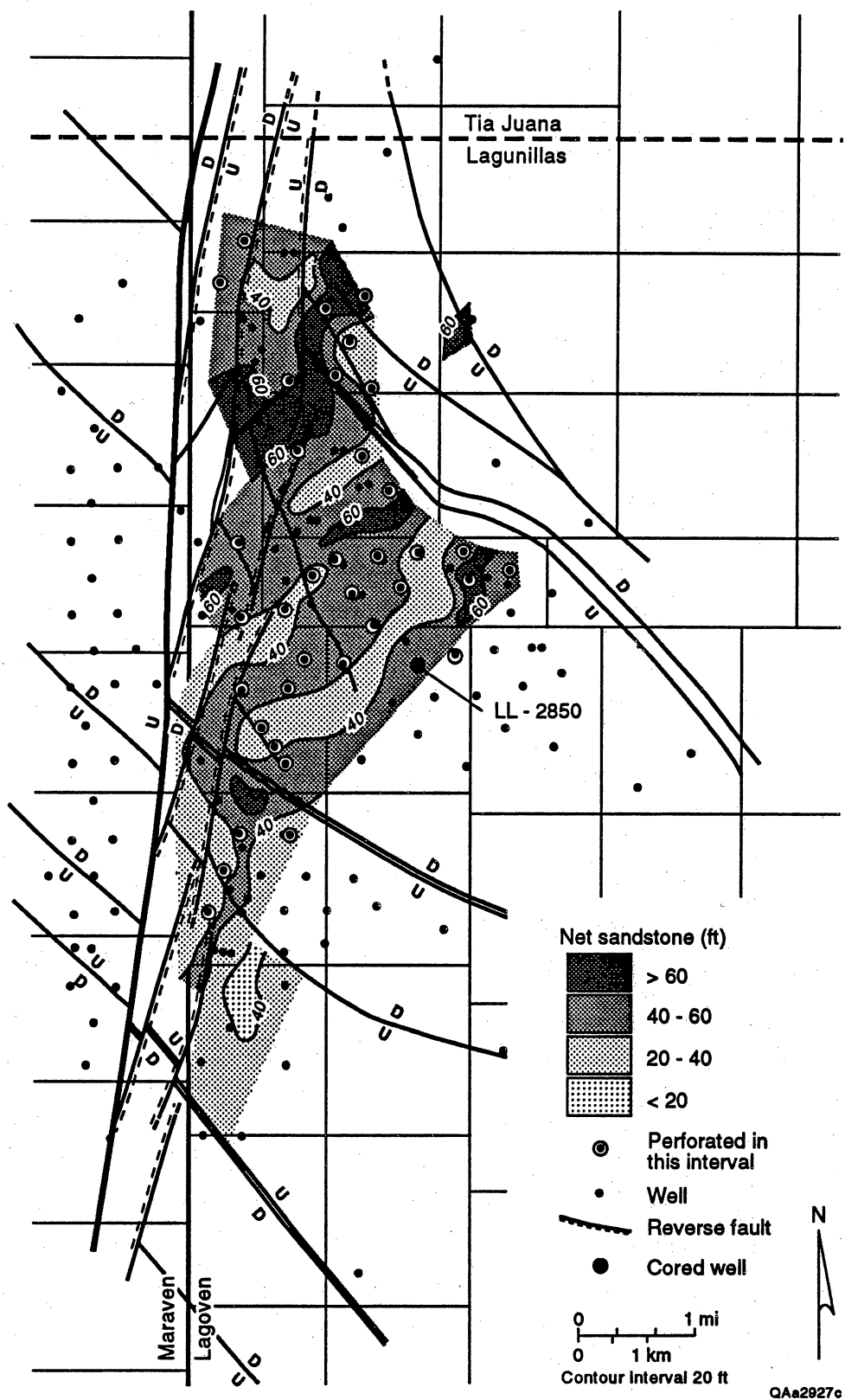
Figure 124. Net-sandstone thickness map of the Middle C-4-X Submember in the LL-652 area.

213
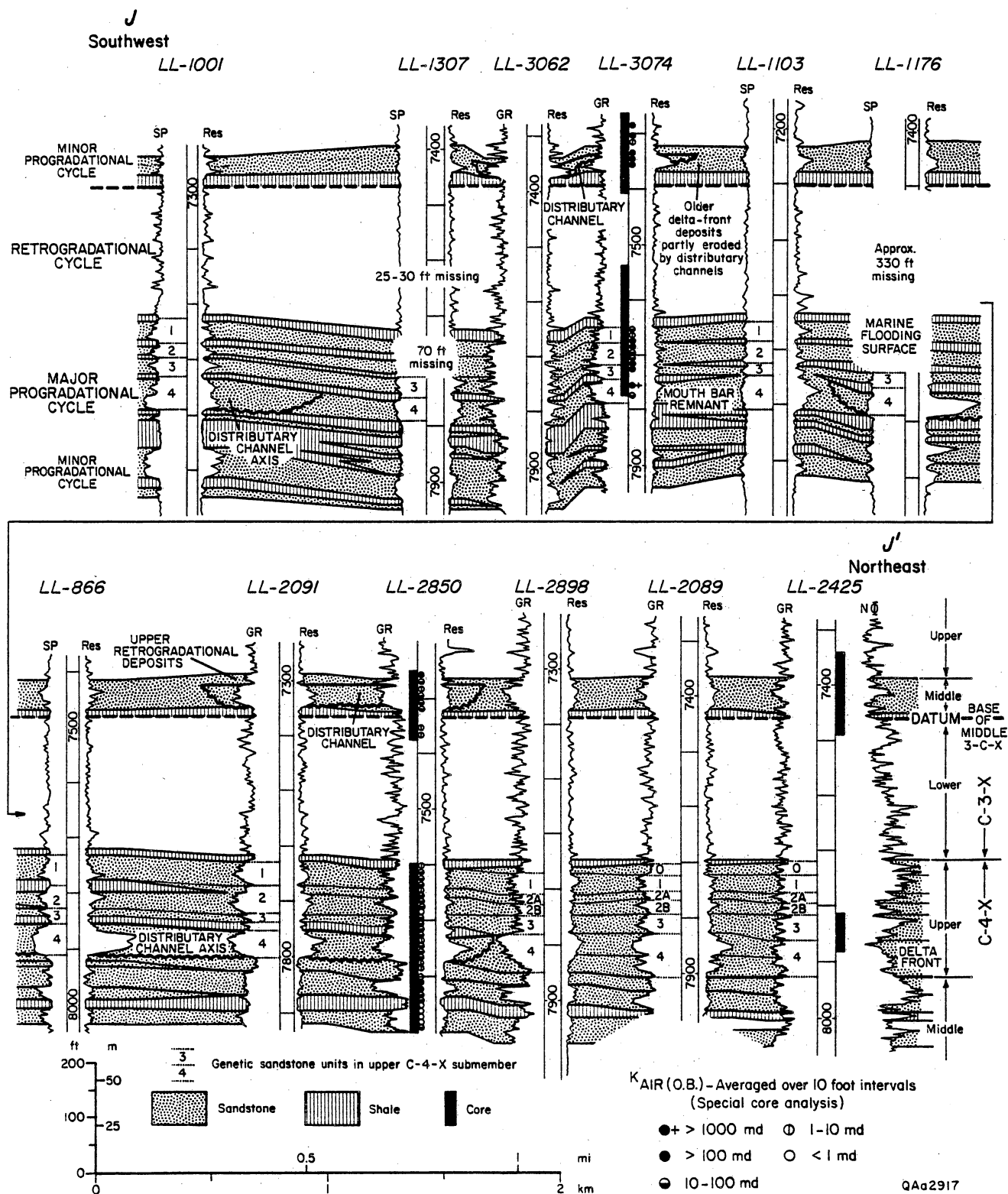
Figure 125. Stratigraphic dip section J–J′ in the Middle C-4-X to Middle C-3-X Submembers, showing major depositional cycles and lateral variability in facies and sandbody thickness. Sandstone depositional cycles are bounded by thin (less than 10-ft [3-m]) shale beds, too thin to be depicted at this scale. Cross section is located in figure 126 through 128 and figures 130 and 131.

214

mapped separately; the others (#1, #2, and #3) are thinner, are partly bounded by thin (typically less than 10-ft [3-m]) discontinuous shales, and were not mapped separately.

Sandbody Geometry

The Upper C-4-X Submember is composed of northeast-trending, dip-elongate sandbodies with a combined thickness of 90 to 140 ft (27.4 to 42.7 m), separated by sandstone-poor areas with less than 50 ft (15.2 m) of net sandstone (table 36 and fig. 126). The trends of thickest net sandstone (more than 100 ft [30.5 m]) occur in four main belts in the LL-652 area.

Lithology and Depositional Systems

Each of the four main units that compose the Upper C-4-X Submember consist of multiple upward-coarsening sandstones (app. D, LL-3074 well, 7,650 to 7,775 ft). The #4 unit, incompletely cored in this well, consists of upward-coarsening and upward-thickening, wavy-bedded sandstones separated by thin (less than 5-in [12.7-cm]) mudstones. The upper 3 ft (0.9 m) is medium, oil-stained sandstone with clay clasts (fig. 69).

The #3 unit consists of two upward-coarsening sandstones, each 6 to 10 ft (1.8 to 3 m) thick (app. D, LL-3074 well, 7,719 to 7,749 ft). Maximum grain size in the lower sandstone is fine, whereas it is lower medium in the upper sandstone. Sedimentary structures in each sandstone range from plane and wavy beds at the base to inclined laminations and ripples at the top; *Planolites* burrows are common in the lower sandstone, and clay clasts are present in the upper sandstone, also oil-stained at the top.

The #2 unit is a complex, 39-ft (11.9-m) interval of at least four heterogeneous, upward-coarsening sandstones finely interbedded with siltstone and mudstone (app. D, LL-3074 well, 7,680 to 7,719 ft). Each sandstone is 4 to 10 ft (1.2 to 3 m) thick and contains clay clasts, organic fragments, and burrows. These units have an average grain size of very fine to fine sandstone, whereas the #3 and #4 units have an average grain size of fine sandstone.

The #1 unit contains several 0.5- to 1-ft (0.15- to 0.3-m), calcite-cemented zones associated with erosional surfaces and shell fragments (app. D, LL-3074 well, 7,650 to 7,680 ft). These sandstones, which range in thickness from 5 to 8 ft (1.5 to 2.4 m), are also rich in large (cobble- to gravel-sized), irregular clay clasts.

The main four units of the Upper C-4-X Submember compose successive progradational wedges in a net retrogradational, backstepping clastic wedge (fig. 104). The #4 unit represents proximal delta-front and lower delta-plain deposits in an initial advance of a delta in the LL-652 area. Deltaic progradation was from the southwest to the northeast, and individual units in the Upper C-4-X Submember thicken slightly northeastward, reflecting the direction of deltaic progradation. Delta-front sandstones of the #1, #2 and #3 units are progressively shalier northwestward due to increasing amounts of thin mudstone interbeds. An exception is the #4 unit that features a channel-mouth-bar remnant updip (southwest) of a distributary-channel complex in the LL-2850 core (fig. 104). This channel-mouth-bar remnant is approximately 1,500 ft (457 m) from a major depositional axis of distributary-channel sandstones that had cannibalized older channel-mouth bar deposits (fig. 126). The #1 unit (fig. 104) differs from the two underlying units and represents retrogradational deposits associated with the laterally extensive marine flooding surface at the top of the Upper C-4-X Submember (fig. 104).

Reservoir Development

The Upper C-4-X Submember is in a mature stage of development, has been perforated extensively throughout the LL-652 area (fig. 126), and is currently undergoing rapid pressure depletion. Although the sandstone geometry of the Upper C-4-X Submember is dominantly northeast-trending, a rapidly north- to

Table 36. Depositional systems and reservoir characteristics of the Upper C-4-X Submember.

Sand-body Geometry	Northeast-trending, dip-elongate sandstones, 90-140 ft thick (>50% sandstone) and 1,050-5,000 ft wide, distributed throughout the map area. These sandstones are bounded laterally by sandstone-poor areas with a minimum of 40 ft of sandstone.
Depositional Facies	System of dip-elongate, mainly upward-coarsening delta-front sandstones. Proximal delta-front sandstones are located in the western and southwestern part of the map area and merge northeastward into distal delta-front sandstones. However, the lower part of this submember (#4 sandstone) consists mostly of distributary-channel sandstones.
Cored Wells	LL-2425 (60 ft from middle), LL-2850 (entire), LL-3074 (all except lower 30 ft), LL-3282 (all except 35 ft).
Perforated Wells	Multiple perforated wells in east-central area; fewer perforated wells in south and north-central areas.
GeneralArea(s) of Greatest Potential for Secondary Oil Recovery	Thick delta-front and distributary-channel sandstones isolated by faults or areas on the margin of these sandstones where they form stratigraphic traps by pinching out laterally into interridge or interdistributary mudstones.

216
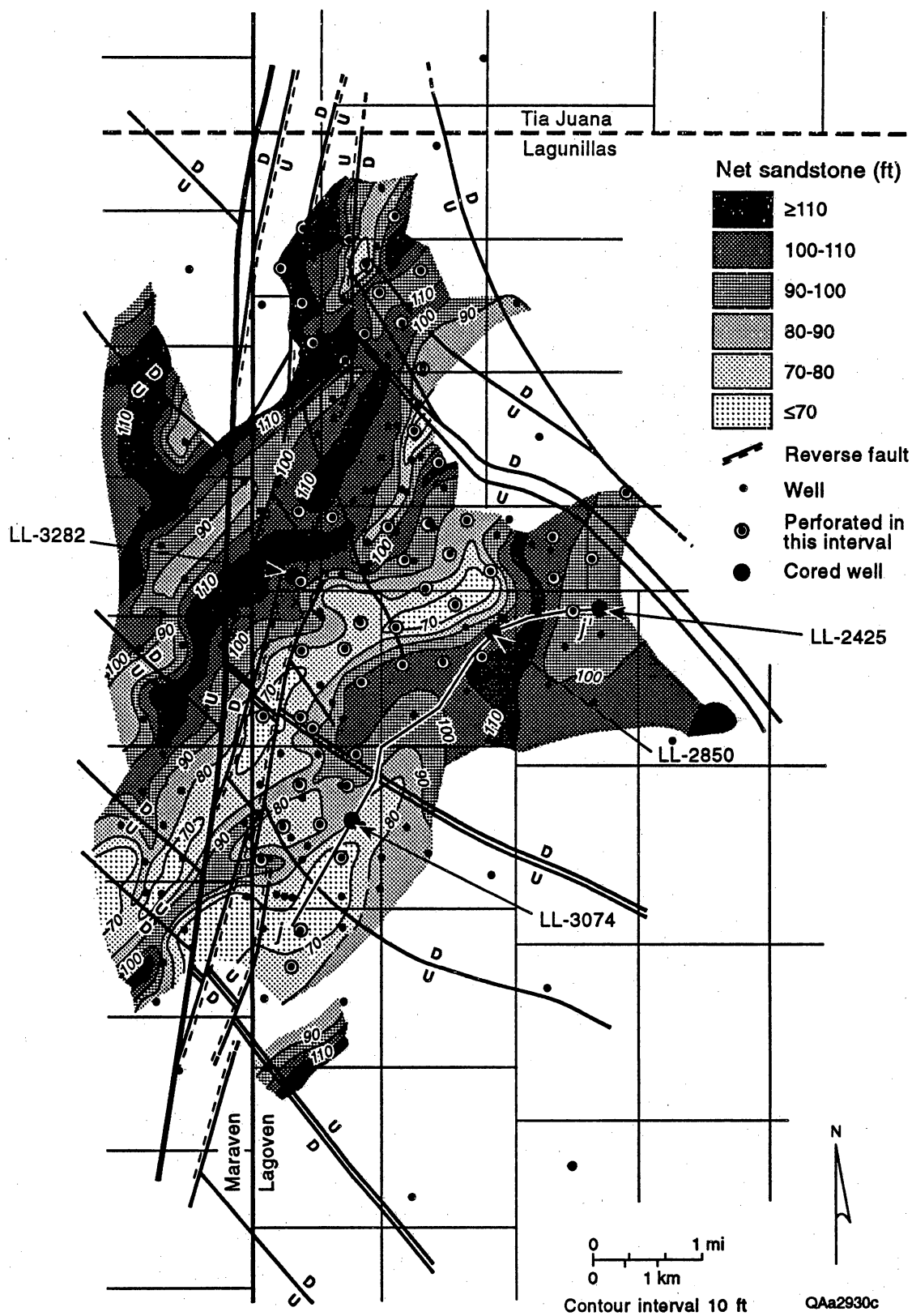
Figure 126. Net-sandstone thickness map of the Upper C-4-X Submember in the LL-652 area. Cross section J-J′ is shown in figure 125.

217

northwest-advancing zone of water encroachment is present just south of the LL-2850 well. The reason why the water encroachment is north- to northwest-trending is that the thick sandstones in the Upper C-4-X Submember together have a great net-sandstone thickness in this part of the field (fig. 126) and the structural gradient is up toward the northwest.

Because of the high number of previous perforations in the field, the Upper C-4-X Submember is a primary target for a strategic waterflood program (see fig. 234). Areas north of the LL-2850 well that are relatively shalier and stratigraphically heterogeneous in the Upper C-4-X Submember can be efficiently swept with water-injection wells located along axes of narrow, northeast-trending sandbodies that may feature anisotropic reservoir drainage patterns because of the strong depositional geometry.

#4 Unit in Upper C-4-X Submember

Sandbody Geometry

The #4 Unit, representing the initial and furthest advance of a deltaic system in the Upper C-4-X Submember, consists of a system of multiple, northeast-trending and -bifurcating upward-fining sandstones defined by more than 70 percent (30 ft [9 m]) of net sandstone (table 37 and fig. 127). In the southern part of the LL-652 area, these sandstone belts extend across the map area, but in the north they pinch out into muddy areas with less than 40 percent sandstone that have serrate and upward-coarsening log responses (figs. 127 and 128).

Lithology and Depositional Systems

The #4 Unit in the LL-652 area and the eastern part of the Maraven concession represents a system of mainly distributary-channel sandstones grading downdip (northeastward) into sandy channel-mouth-bar deposits and pinching out into muddy delta-front deposits. Interdistributary areas consist of either channel-mouth-bar remnants or tidal-flat mudstones. The #4 Unit is extremely heterogeneous; percent sandstone values range from less than 10 percent in interdistributary areas to as much as 100 percent along narrow (only 1,000 ft [305 m] wide) distributary-channel axes (fig. 127).

Reservoir Development

Although the #4 Unit has been perforated throughout the field and is part of a thick (150-ft [45.7-m]) package of sandstones composing a potential target for a secondary-recovery waterflood program, it also contains numerous opportunities for strategic infill drilling or recompletion. For example, the dip-elongate, northeast-bifurcating distributary-channel sandbody in the northern part of the A-188 concession (north and south of the LL-1089 well) has not been perforated, even though it is in a structurally complex area (fig. 127). Thick (locally more than 80 ft [24.4 m] of net sandstone) areas of high-reservoir quality in channel-mouth-bar deposits may be excellent targets for recompletion (fig. 127). Additionally, the southern segment of this distributary-channel system, centered on the LL-3186 well, is poorly developed and could be a target for infill drilling.

Lower C-3-X Submember

Sandbody Geometry

The Lower C-3-X Submember is a 250- to 300-ft (76- to 91.5-m), sandstone-poor interval (fig. 5). Two depocenters in the Lower C-3-X Submember are defined by more than 70 ft (21.3 m) of net sandstone in the Maraven concession; the main depocenter is located in the east-central part of the Maraven concession, and a minor depocenter exists in the extreme southern part of the area (table 38 and fig. 129).

Table 37. Depositional systems and reservoir characteristics of the #4 Sandstone Unit in the Upper C-4-X Submember.

Sand-body Geometry	Northeast-trending and -bifurcating system of upward-fining sandstones more than 30 ft thick (70%) sandstone pinching out into and merging with and muddy areas of less than 20 ft (40%) sandstone in the northern part of the map area. In the southern part of the map area, the sandstones are continuous.
Depositional Facies	System of distributary-channel sandstones pinching out into channel-mouth bar and delta- front deposits in the northern part of the map area. Interdistributary areas consist of sandstone-poor tidal-flat deposits.
Cored Wells	LL-2425 (top 16 ft only), LL-2850 (entire), LL-3074 (all except lower 30 ft), LL-3282 (top 6 ft only).
Perforated Wells	Densely perforated area in south-central and southeastern areas; moderate to fair perforation density elsewhere.
General Area(s) of Greatest Potential for Secondary Oil	Areas where distributary-channel and channel-mouth bar deposits pinch out northeastward into muddy delta-front deposits (northern part of map area) and laterally into muddy tidal-flat deposits (other areas).
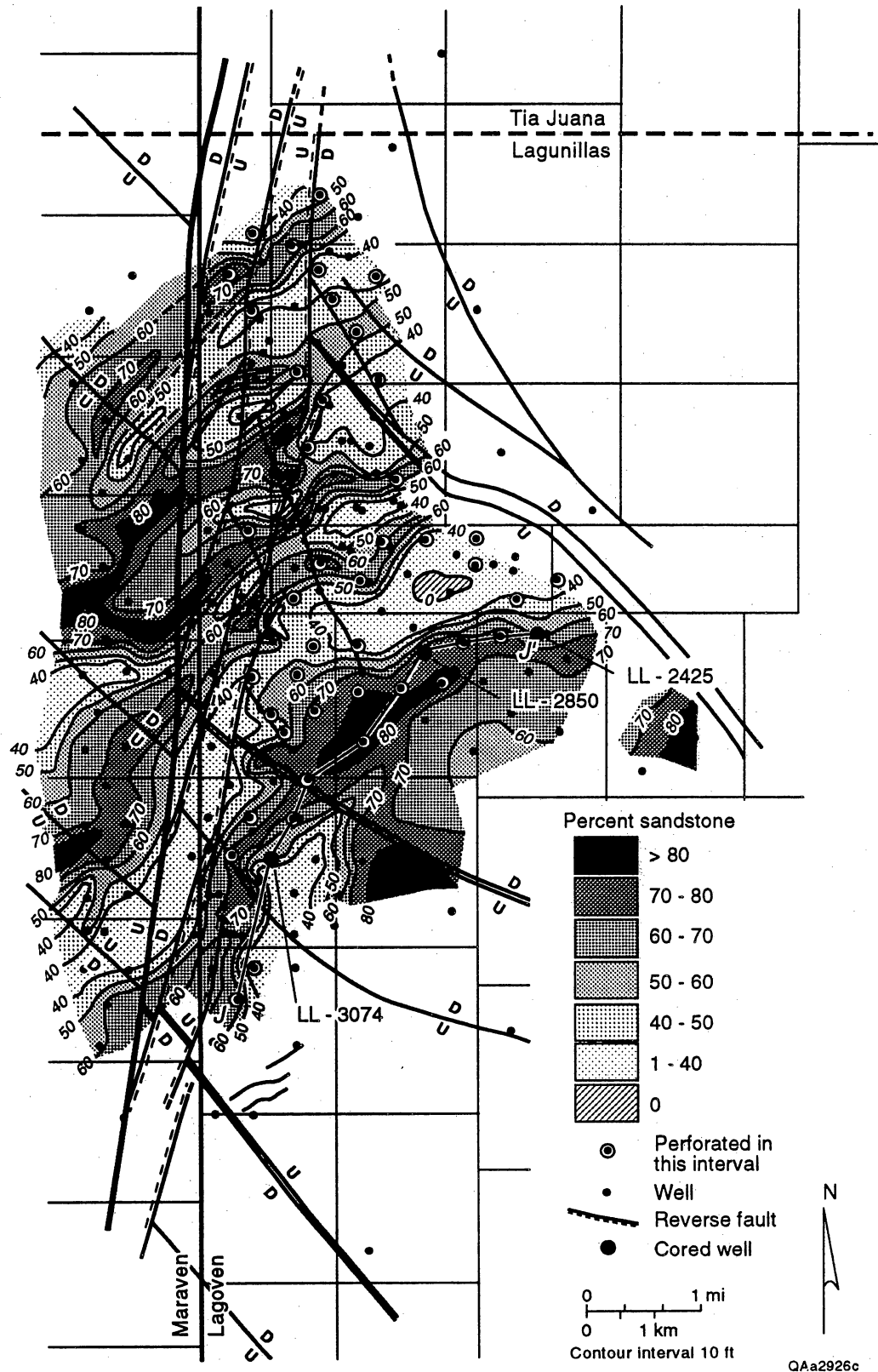
Figure 127. Percent sandstone map of the #4 Sandstone Unit in the Upper C-4-X Submember in the LL-652 area. Cross section J-J' is shown in figure 125.

220

Legend:
- Blocky
- Up-fining
- Up-coarsening
- Serrate/spikey
- No response (mud)
- Reverse fault
- Perforated in this interval
- Well
- Cored well

Tia Juana
Lagunillas

LL-2425

LL-2850

LL-3074

Maraven

Lagoven

N

0   1 mi
0   1 km
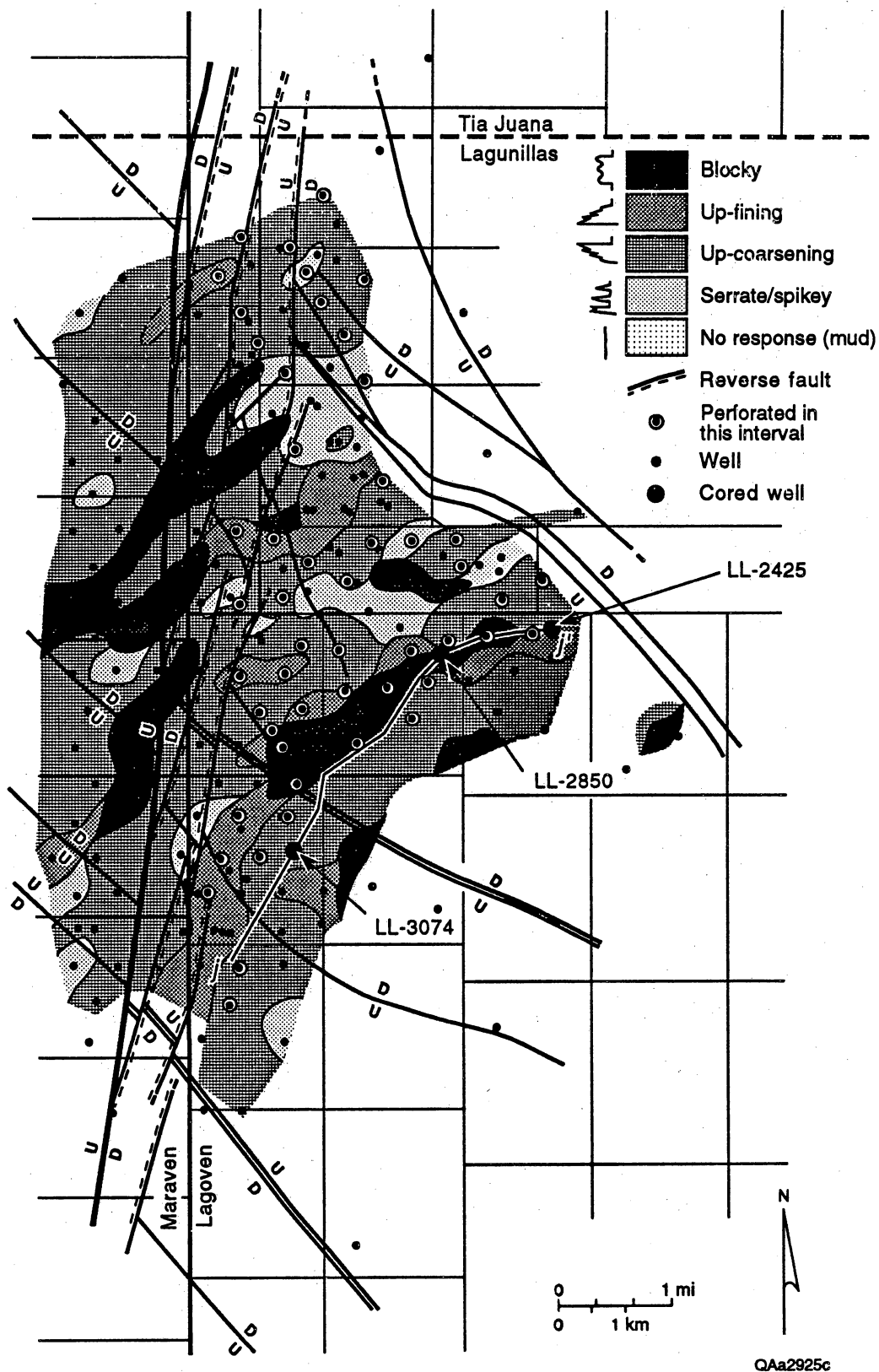
QAa2925c

Figure 128. Log-facies map of the #4 Sandstone Unit in the Upper C-4-X Submember in the LL-652 area. Cross section J–J' is shown in figure 125.

Table 38. Depositional systems and reservoir characteristics of the Lower C-3-X Submember.

Sand-body Geometry	Two lobes of more than 70 ft of sandstone in Maraven concession (main one in west-central part of map and minor one in southwestern part of map), connected to narrow (500-2,000 ft wide), continuous lands of sandstone more than 50 ft thick. Log response of sandstone in lobes is variable, whereas log response in bands is upward-coarsening and serrate.
Depositional Facies	Depocenters consisting of distributary-channel complexes in Maraven concession located updip (westward and southwestward) of dip-elongate, narrow tidal sand ridge deposits that occur throughout the Lagoven concession.
Cored Wells	LL-2850 (lower 7 ft only), LL-3074 (lower 110 ft), LL-03282 (lower 10 ft only).
Perforated Wells	Southeastern and southern areas: high density of perforated wells; northern area: good density; all other areas: poor density.
GeneralArea(s) of Greatest Potential for Secondary Oil Recovery	Where narrow tidal sand ridges pinch out laterally into muddy interridge areas; also in channel-mouth-bar sandstones along boundary between Maraven and Lagoven concessions in area between LL-917 and LL-933.
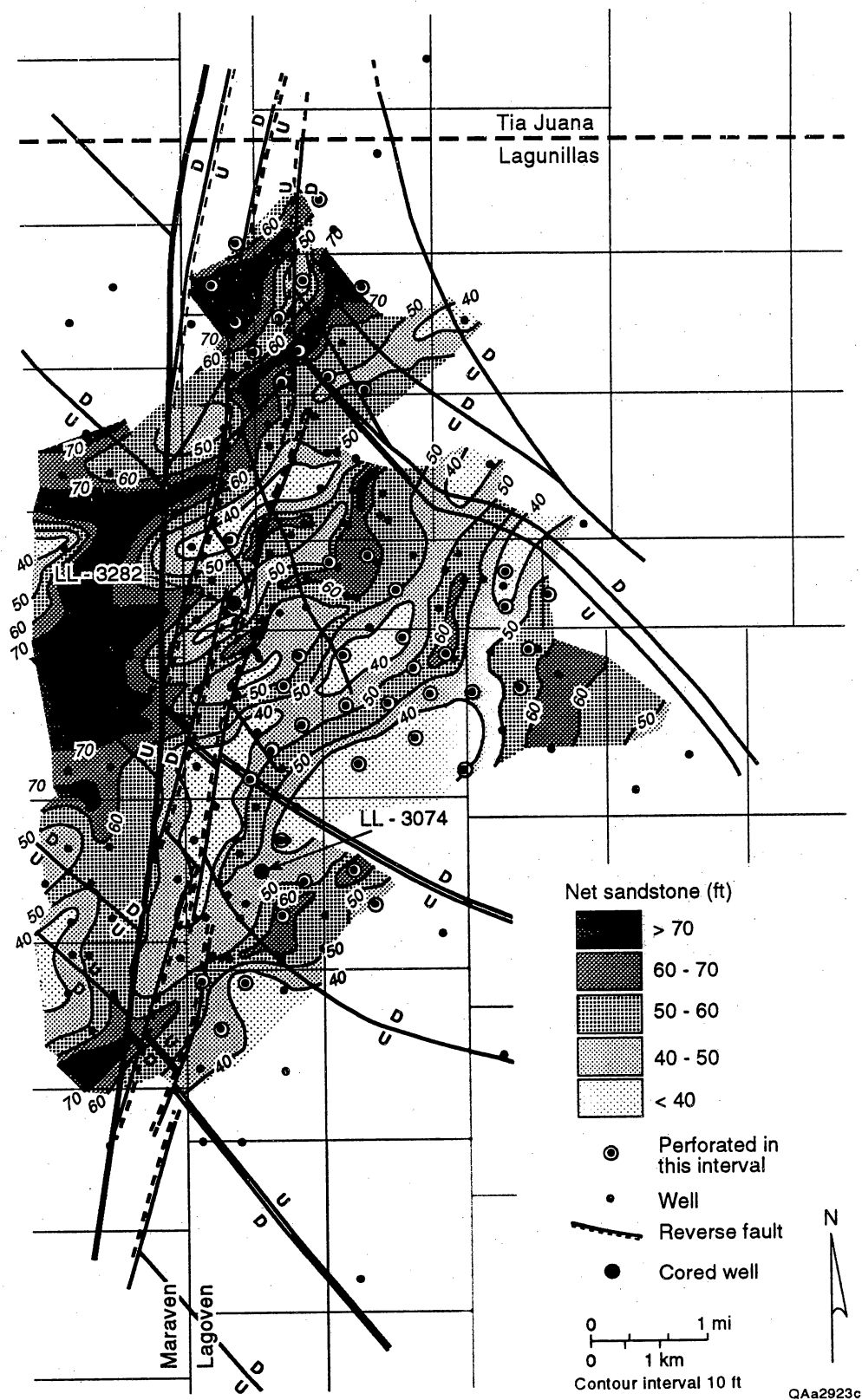
Figure 129. Net-sandstone thickness map of the Lower C-3-X Submember in the LL-652 area.

These depocenters are connected to narrow (500 to 2,000 ft [152 to 610 m] wide), continuous bands of sandstone more than 50 ft (15.2 m) thick in the LL-652 area. The log responses in the depocenters are blocky and upward-fining with numerous variations, whereas the log responses of the narrow bands are upward-coarsening and serrate.

Lithology and Depositional Systems

The Lower C-3-X Submember is extremely heterogeneous. Virtually all of the sandstone beds are very fine and are interbedded with mudstone (app. D, LL-3074 well, 7,535 to 7,645 ft). The thickest individual sandstone bed is only 5 ft (1.5 m) thick; most sandstone beds are only 1 ft (0.3 m) thick. Most of the sandstones in the Lower C-3-X Submember occur in multiple, upward-coarsening sequences that range in thickness from 1.5 to 10 ft (0.5 to 3 m). Each upward-coarsening sequence typically exhibits a succession of bedforms that range from plane beds and asymmetrical ripples at the base to inclined beds and symmetrical ripples at the top. Marine burrows, including *Planolites*, *Teichichnus*, and *Rhizocorallium* are common, and clay clasts are present at the top of some upward-coarsening sequences. The lowest 18 ft (5.5 m) contains slump deposits and thin (1- to 2-ft [0.3- to 0.6-m]), sharp-based and upward-fining sandstones with very-coarse and small-gravel clay clasts.

The basal part of the Lower C-3-X Submember was deposited in an inner-shelf setting following the transgression that marked the end of deposition of the C-4-X Member. Thin, sharp-based and upward-fining sandstones in this interval were deposited as frontal splays on the inner shelf. Multiple, upward-coarsening sequences in the Lower C-3-X Submember represent distal delta-front deposits downdip (eastward and northeastward) of deltaic depocenters in the Maraven concession; these delta-front deposits were reworked by tidal currents along depositional dip into narrow (commonly less than 1,000 ft [305 m] wide), parallel tidal sand ridges (fig. 129).

Reservoir Development

The Lower C-3-X Submember is an aggregate of numerous, thin (individual units less than 10 ft [3 m]) sandstone beds that are interbedded with thin, low-permeability shaly zones. These sandstone beds have a combined thickness of more than 50 ft (15.2 m) in multiple, dip-elongate belts with greater-than-average net-pay thickness that represent areas of potential infill wells.

Middle C-3-X Submember

Sandbody Geometry

The Middle C-3-X Submember is a thin, 70- to 100-ft (21.3- to 30.5-m) sandstone-rich interval (fig. 5). The sandstone geometry consists of northeast-trending patterns of more than 50 ft (15.2 m) of net sandstone in dip-parallel bands, 1,500 to 3,500 ft (457 to 1,067 m) wide (table 39 and fig. 130). The log-facies map of the Middle C-3-X Submember also exhibits northeast-trending patterns in a system of upward-coarsening and serrate log responses transected by a system of upward-fining and blocky log responses in the southern part of the area (fig. 131). The majority of the dip-elongate belts of upward-fining and blocky log responses are approximately 2,000 ft (610 m) wide. The trend of blocky log responses approximately coincides with more than 50 ft (15.2 m) of net sandstone (fig. 130).

Lithology and Depositional Systems

The Middle C-3-X Submember, cored in the LL-2425, LL-2850, and LL-3074 wells, contains a lower upward-coarsening section of delta-front deposits, 14 to 20 ft (4.3 to 6.1 m) thick, commonly truncated by 8- to 14-ft (2.4- to 4.3-m) upward-fining, distributary-channel sandstones (fig. 102). The upper part of the

Table 39. Depositional systems and reservoir characteristics of the Middle C-3-X Submember.

Sand-body Geometry	Northeast-trending, dip-elongate and upward-fining sandstones 40-60 ft thick and 1,500-3,500 ft wide, transecting a system of northeast-trending, upward-coarsening sandstones, 30-50 ft thick and 1,500-5,000 ft wide. Net-sandstone thickness generally increases northeastward.
Depositional Facies	A system of northeast-trending distributary-channel sandstones in the southern part of the field area that truncates a dip-elongate system of upward-coarsening delta-front sandstones.
Cored Wells	LL-2425 (entire interval), LL-2850 (entire interval), LL-3074 (entire interval).
Perforated Wells	Southern, south-central, and eastern areas: high density of perforated wells; northern area: moderate density; north-central area: virtually none.
General Area(s) of Greatest Potential for Secondary Oil Recovery	Where distributary-channel sandstones pinch out laterally into delta-plain (tidal-flat) mudstones in the southern part of the field, or where lenticular tidal-ridge sandstones are partly isolated in muddier interridge sandy mudstones.

225
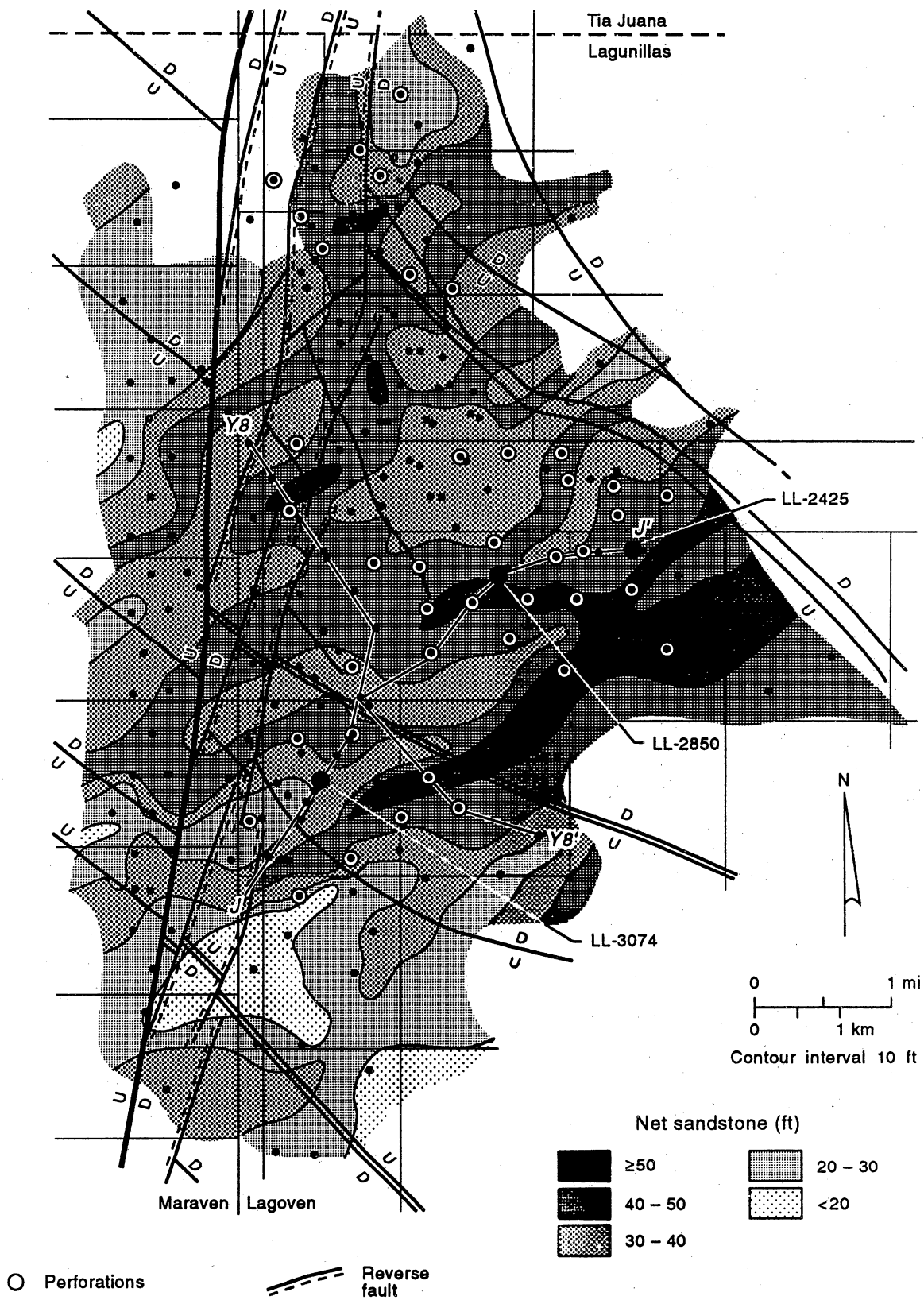
Figure 130. Net-sandstone thickness map of the Middle C-3-X Submember in the LL-652 area. Cross sections J–J' and Y8–Y8' are shown in figures 125 and 132, respectively.
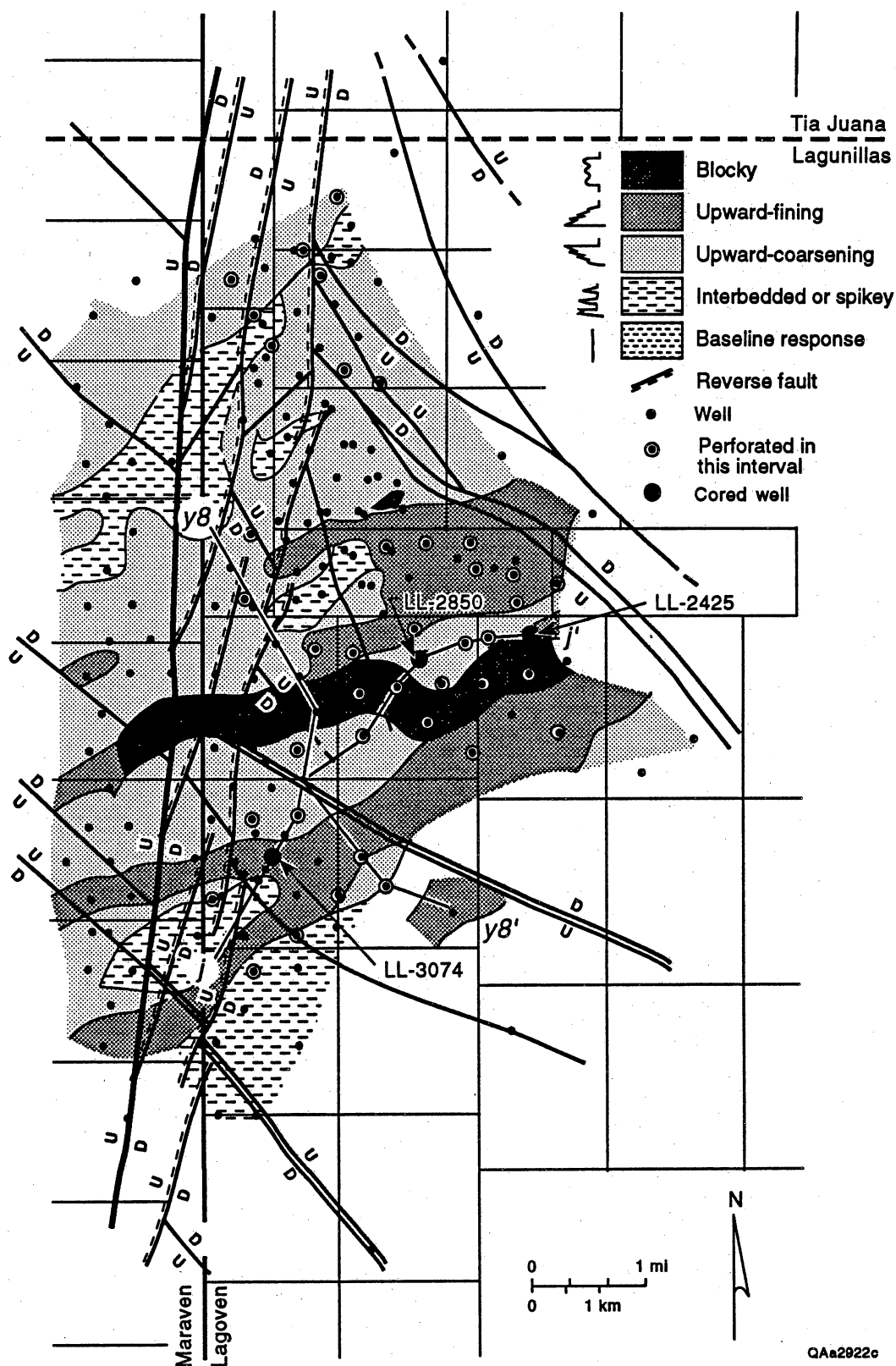
Figure 131. Log facies map of the Middle C-3-X Submember. Cross sections J–J′ and Y8–Y8′ are shown in figures 125 and 132, respectively.

section contains a variety of different types of sandbodies, including upward-coarsening, interbedded overbank deposits (LL-3074 well), very fine and fine, rippled tidal-flat sandstones with no grain-size trends (LL-2425 and LL-2850 wells), and erosion-based, upward-fining tidal-channel sandstones (LL-2850 well). The Middle C-3-X Submember is bounded above by a 10-ft (3-m) laterally continuous, mainly upward-coarsening zone of irregularly calcite-cemented, transgressive sand-shoal deposits that are in turn overlain by a 4- to 6-ft (1.2- to 1.8-m) laterally continuous, burrowed mudstone representing a marine flooding surface.

A stratigraphic strike section that cuts across the grain of the sandbodies in the Middle C-3-X Submember shows the deltaic facies architecture (fig. 132). Lenticular distributary-channel sandbodies, individually about 2,000 ft (610 m) wide, locally truncate an extensive system of delta-front sandstones. These distributary-channel sandstones are bounded laterally by muddy tidal-flat deposits that have an irregular sheet geometry. This paragenetic sequence is bounded below by a laterally extensive shelf mudstone and above by an irregular transgressive sandsheet and associated shelf mudstone. Areas where high permeability and porosity contrasts may occur are along (1) distributary channel-delta front contacts, particularly at the base of channel deposits where clay clasts and organic fragments may comprise flow barriers and (2) lateral pinchouts of distributary-channel sandstones into tidal-flat mudstones. Other flow barriers may exist in the transgressive sand shoal/sheet facies between numerous thin and impermeable, calcite-cemented zones. However, these zones are not easily recognized from electric logs, and their lateral continuity is difficult to predict.

Reservoir Development

The Middle C-3-X Submember has been perforated throughout the LL-652 area (figs. 130 and 131). However, this submember continues to be an active producer and is experiencing a pressure decline less severe than that of the Upper C-4-X Submember. Therefore, undrained or partly drained compartments may exist in this unit and recompletions, infill wells, or even strategically implemented waterfloods may be necessary to most efficiently produce the remaining mobile oil. Areas in the field where this oil could be targeted by recompletions and infill wells are defined by structurally and stratigraphically complex areas distant from previously existing completions. A limited waterflood may be appropriate in the central, unfaulted part of the LL-652 area that has been extensively perforated, where it may be able to sweep remaining mobile oil that remains along facies contacts between distributary-channel and delta-front facies or tidal-channel and tidal-flat facies.

Upper C-3-X Submember

Sandbody Geometry

The sandstone-poor Upper C-3-X Submember makes up the upper 200 ft (61 m) of the C-3-X Member (fig. 5). Unlike most C submembers, the sandstone geometry of the Upper C-3-X Submember is east- and southeast-trending and -bifurcating; these trends are defined by more than 40 ft (12 m) of net sandstone or more than 20 percent sandstone and are 700 to 1,600 ft (213.4 to 487.8 m) wide (table 40 and fig. 133). The sandbodies define the depositional axes of a system of inferred distributary-channel deposits that pinch out into interdistributary-bay deposits and delta-front mudstones. Because of the lobate and digitate nature of the sandstones, the Upper C-3-X Submember is interpreted as having been deposited in a fluvial-dominated setting with low tidal influence.

Reservoir Development

Despite the shallow depth of the Upper C-3-X Submember, there are many areas in the LL-652 area where reservoir development has been minimal (fig. 133). One reason for this lack of development is because the Upper C-3-X Submember is shaly and contains only a few sandstones that individually are up to 10 ft
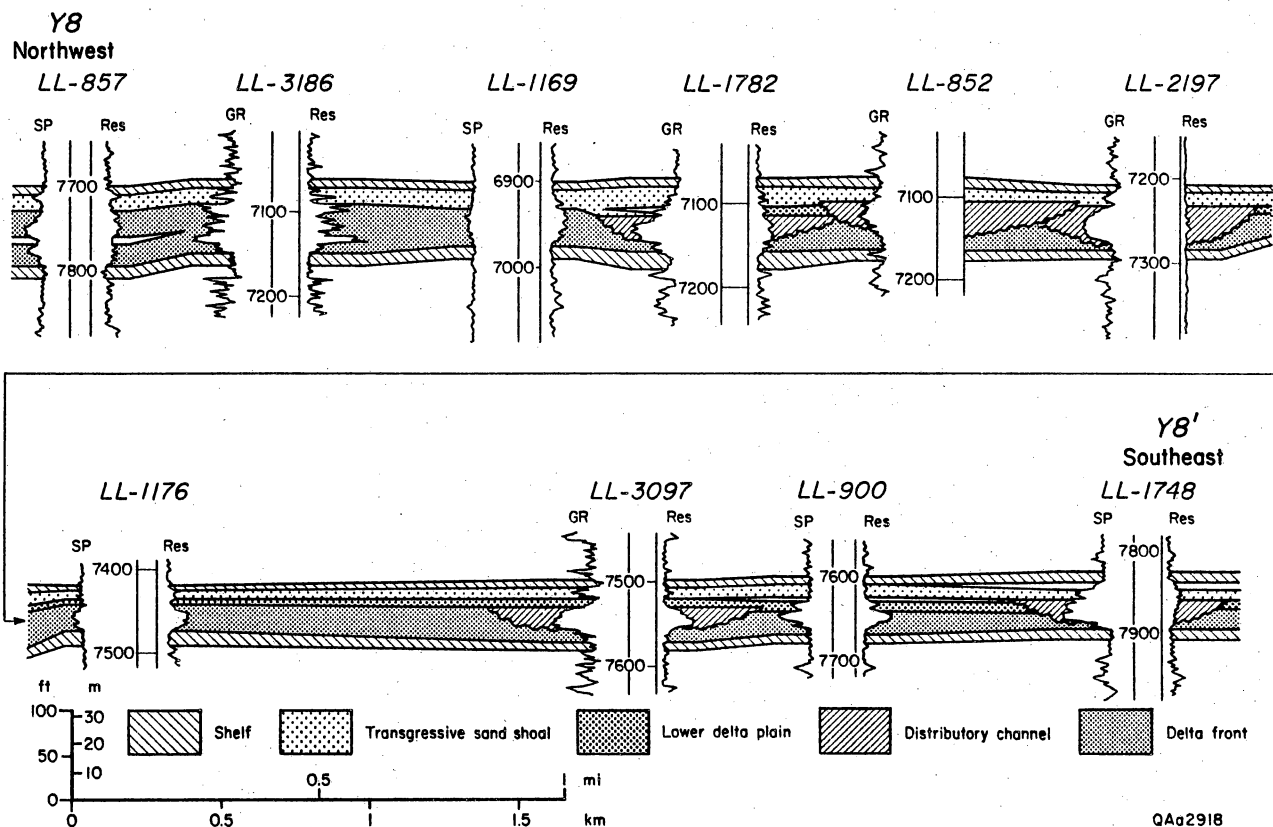
Figure 132. Stratigraphic strike section Y8–Y8′ in the Middle C-3-X Submember, showing sandbody architecture and facies heterogeneity resulting from multiple, lenticular distributary-channel sandstones locally truncating muddy delta-front sandstones. The top reservoir seal is partly provided by a sheetlike, calcareous transgressive sand-shoal deposit. Cross section is located in figures 130 and 131.

Table 40. Depositional systems and reservoir characteristics of the Upper C-3-X Submember.

Sand-body Geometry	Multiple, east-trending, dip-elongate, bifurcating lenticular sandstones more than 40ft thick (>20% sandstone) and 700 to 1,600 ft wide.
Depositional Facies	Distributary-channel deposits in the Maraven concession merging eastward with delta-front and interdistributary bay deposits in the Lagoven concession.
Cored Wells	LL-2425 (lower 35 ft only), LL-3074 (lower 70 ft only).
Perforated Wells	Southern and south-central areas: good density of perforated wells; northern area: moderate density; north-central and extreme western areas: poor density.
GeneralArea(s) of Greatest Potential for Secondary Oil Recovery	Where distributary-channel deposits pinch out laterally into indistributary bay deposits or where channel-mouth-bar deposits pinch out into delta-front deposits.
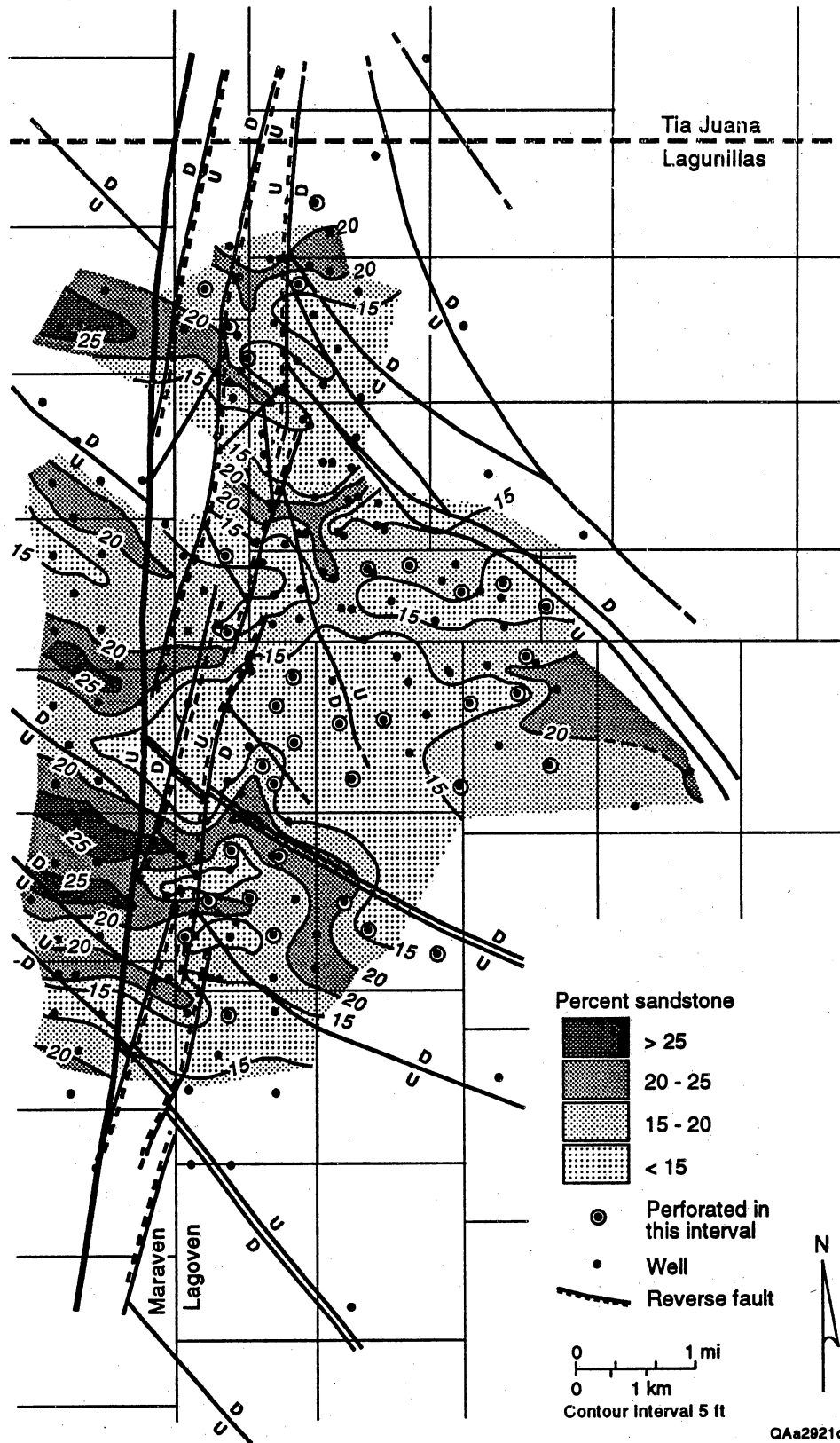
Figure 133. Percent-sandstone map of the Upper C-3-X Submember. In contrast to other C-3-X submembers, percent sandstone in the Upper C-3-X Submember is southeast-trending and exhibits bifurcating trends.

231

(3 m) thick. Areas of relatively thick net sandstone (20 ft [6 m] or more) that correspond to distributary-channel and channel-mouth-bar deposits exist with few or no perforations. For example, all perforations in the extreme northern part of the field have missed the thickest sandstone bodies (fig. 133). Although the density of perforations is greater in the southern part of the field, there still exist certain areas that can be targeted for development.

VII. PETROGRAPHY OF MISOA C SANDSTONES: COMPOSITIONAL, TEXTURAL, AND DIAGENETIC CONTROLS ON POROSITY DISTRIBUTION AND EVOLUTION

The goal of the petrographic study was to identify the main influences on porosity and permeability distribution in the Misoa C sandstones. Original porosity and permeability of Misoa sandstones were determined by their grain size and sorting, which were controlled, in turn, by depositional environment. However, diagenesis has significantly altered reservoir characteristics since deposition by the processes of compaction and cementation. This study indicates that diagenesis, not depositional environment, is the main control on porosity and permeability distribution in Misoa sandstones. In particular, volume of quartz cement is the main influence on reservoir quality, and because the volume of quartz cement increases significantly with depth, reservoir quality decreases.

Methodology

A key to our approach is to conduct petrographic analyses in the context of the stratigraphic framework. The composition of Misoa sandstones was determined from 76 thin sections made from representative samples of the different members (C-3-X through C-6-X) and facies. It was then possible to quantify the petrographic characteristics of each sandstone and facies—grain size, detrital mineralogy, authigenic cements, and porosity. Matrix-free (clean) sandstones were sampled preferentially because most reservoirs are in clean sandstones. Many of the chips used to make the thin sections were taken immediately adjacent to core-analysis plugs so that petrographic parameters could be compared to porosity and permeability. The plugs were not available for this study, but in general it is preferable to make thin sections from end trims off the core-analysis plugs. Composition of Misoa sandstones was determined by standard thin-section petrography and scanning electron microscopy (SEM) with an energy dispersive X- ray spectrometer (EDX).

Sampling concentrated on the five key wells, LL-2850, LL-3074, LL-3075, LL-3080, and LL-3140, from which a total of 66 thin sections were made. Thin sections also were made from two other wells, LL-846 and LL-2425, in order to sample the facies they contained, but these wells had no core-analysis data that could be compared with petrographic data. All sample depths in this report have been converted to log depths so that petrographic data can be directly compared to log response.

Point counts were done on all 76 thin sections chosen as representative of the range of Misoa sandstones. A total of 200 counts were made on each thin section. This number of counts allows reasonable statistical accuracy compared with counting 300 points, but because each sample takes less time, more samples can be completed. Counting error varies with the percentage of the constituent. For a sample in which 200 points are counted, a constituent that composes 50 percent of the sample has an error of ±3.6 percent, whereas a constituent that is 10 percent has an error of ±2.1 percent and one that is 2 percent of the sample has an error of ±0.9 percent (Folk, 1974). In comparison, if 300 points were counted, a constituent that composes 50 percent of the sample has an error of ±3.0 percent, one that is 10 percent has an error of ±1.7 percent, and a constituent that is 2 percent of the sample has an error of ±0.7 percent.

Framework grain size was estimated by comparing the thin sections to standardized grain-size charts. Grain size estimated from viewing thin sections averages only 85 percent of grain size measured by sieving (Folk, personal communication, 1975), so raw values of grain size should be divided by 0.85 to give actual grain size. All values of grain size reported in text and tables in this report are the raw values determined from thin section and should be divided by 0.85 if the sieve-equivalent size is desired.

Point counts recognize four major categories of rock volume: detrital framework grains, matrix, authigenic cements and replacive minerals, and pores. Framework grains are subdivided by composition. The essential framework grains are those used to classify the sandstone: quartz, feldspar, and rock fragments, including chert. Other framework grains, such as biotite or tourmaline, are counted but are excluded from the calculation of sandstone type.

Detrital clay matrix is defined as grains too small to be identified in thin section. Detrital clay was distinguished from authigenic clay by using many of the criteria summarized by Wilson and Pittman (1977), including the following: (1) detrital clay commonly fills primary pores and occurs at grain-to-grain contacts; (2) it may form distinct laminae; (3) it has been compacted and does not contain porosity visible in thin section between clay particles; and (4) crystal size is generally smaller than that of authigenic clays. Where sand-sized detrital clay clasts were recognized, they were counted separately from clay matrix. However, where clay clasts were deformed by compaction and no longer recognizable as distinct grains, they were counted as matrix.

Authigenic cements were categorized by composition and location, that is, whether they filled intergranular pores or occurred within secondary pores that formed by dissolution of a framework grain. It is necessary to make this distinction in order to calculate "minus-cement porosity," which is the sum of primary porosity plus the volume of cements that occur in primary pores. Minus-cement porosity provides an indication of the relative amount of porosity lost by compaction, and the total volume of cements in primary pores provides an estimate of the amount of porosity lost by cementation.

Porosity is identified during point counting as primary, intergranular porosity or secondary porosity that formed by dissolution of a framework grain or cement. It is difficult to recognize intergranular pores that were filled with carbonate cement that has subsequently completely dissolved. Unless the cement enlarged the intergranular pore space by dissolving adjacent framework grains or overgrowths, cement-dissolution porosity generally cannot be recognized except in places where part of the cement remains.

The point count data from each of the thin sections in this study are tabulated in appendix B in tables 1-7. Each sample is identified by well number and core depth. The values listed in the tables are in percent of total rock volume, including porosity. Thus, mineral percentages listed in these tables and mentioned throughout the report refer to percent of whole-rock volume, as distinct from the percent of the solid-rock volume. The data for each sample continue on two pages; detrital minerals and detrital clay matrix are on one page and authigenic minerals and porosity are on the second page. Mean grain size is also listed on the second page.

Texture

Most Misoa sandstone samples viewed in this study are very fine grained (3.0 to 4.0 phi [0.062 to 0.125 mm]) or fine grained (3.0 to 2.0 phi [0.125 to 0.25 mm]). They are well sorted (0.35 to 0.5 phi) to moderately sorted (0.5 to 1.0 phi), according to the definition of Folk (1974). Differences in grain size are slight among the C-3-X to C-6-X sandstones (table 41) and among facies (table 42). C-6-X sandstones are the coarsest grained of the sandstone intervals, having an average grain size of 0.14 mm, and C-3-X sandstones are the finest, averaging 0.11 mm. The reason that the C-6-X sandstones are somewhat coarser than the other sandstones is probably that those sampled in the C-6-X Member were deposited in a fluvial-estuarine channel environment (see fig. 106), which is the coarsest grained facies (table 42).

Framework Mineralogy

Misoa sandstones are sublitharenites (fig. 134), and the average composition is $Q_{82}F_6R_{12}$. C-3-X, C-4-X, and C-6-X sandstones are slightly more quartz-rich than are C-5-X sandstones. Detrital quartz composes an average of 58 percent of the total rock volume and forms between 61 and 97 percent of the essential constituents. Plagioclase, the most abundant type of feldspar, has an average volume of 3.5 percent; orthoclase, which is rare, has an average volume of only 0.04 percent. Some feldspar was dissolved during diagenesis, and the volume is now occupied by secondary pores or secondary pores filled with kaolinite or calcite cement. If we assume all the open secondary pores and all the secondary pores filled by calcite or kaolinite were originally feldspar grains, the original detrital sandstone was a subarkose with composition $Q_{76}F_{13}R_{11}$.

Table 41. Petrographic data summary of C-3-X, C-4-X, C-5-X, and C-6-X sandstones.

	C3 Sandstone	C4 Sandstone	C5 Sandstone	C6 Sandstone
Number of samples	8[1]	15[1]	16	27
Depth (ft)	7300	7700	8000	9000
Framework-grain composition	$Q_{83}F_6R_{11}$	$Q_{85}F_5R_{10}$	$Q_{79}F_8R_{13}$	$Q_{84}F_4R_{12}$
Quartz cement (%)	7.1	9.2	9.3	11.2
Siderite cement (%)	2.6	2.2	3.5	2.4
Calcite + ankerite cement (%)	2.6	1.2	3.7	0.7
Kaolinite cement(%)	1.9	1.7	1.3	1.2
Illite cement (%)	1.1	1.2	1.3	1.1
Chlorite cement (%)	1.1	0.4	0.9	0.4
Total cement (%)	16.3	16.1	19.6	17.3
Primary-pore-filling cement (%)	11.6	12.6	14.8	13.8
Minus-cement porosity (%)	18.9	19.6	19.6	17.6
Primary porosity (%)	7.4	7.0	4.8	3.8
Secondary porosity (%)	6.2	7.1	4.6	4.4
Porosimeter porosity (%)	21.3	17.2	17.1	12.0
Permeability (geometric mean) (md)	184	66	11	4
Grain size (mm)	0.11	0.13	0.12	0.15

Values determined by counting 200 points per thin section.
[1]Only includes petrographic data from the five key wells.

Table 42. Petrographic data summary by facies.

	DF	DDF	DC	F/EC	TC	TSS
Number of samples	20	5	21	14	6	5
Depth (ft)	7900	7400	8000	9100	8200	7800
Framework-grain composition	$Q_{83}F_6R_{11}$	$Q_{84}F_5R_{11}$	$Q_{78}F_7R_{15}$	$Q_{89}F_3R_9$	$Q_{75}F_9R_{16}$	$Q_{84}F_6R_{10}$
Quartz cement (%)	8.3	8.6	9.0	12.4	10.1	8.8
Siderite cement (%)	2.6	6.3	1.6	0.6	4.5	6.6
Calcite + ankerite cement (%)	2.2	1.4	4.1	0.4	3.6	2.8
Kaolinite cement(%)	1.7	0.8	1.6	1.0	1.3	0.9
Illite cement (%)	1.3	1.0	1.4	0.5	1.8	1.6
Chlorite cement (%)	0.8	1.2	0.3	0.4	1.3	0.3
Total cement (%)	17.1	19.7	18.4	15.4	22.5	21.2
Primary-pore-filling cement (%)	12.4	14.2	12.9	13.6	17.0	15.3
Minus-cement porosity (%)	18.4	18.5	17.6	17.8	21.5	19.9
Primary porosity (%)	5.9	4.3	4.7	4.3	4.5	4.6
Secondary porosity (%)	5.7	4.2	5.0	5.1	5.0	3.4
Porosimeter porosity (%)	17.6	16.0[1]	14.8	12.3	16.3	17.0
Permeability (geometric mean) (md)	56	6[2]	12	11	4	10
Grain size (mm)	0.12	0.11	0.12	0.17	0.13	0.14

Values determined by counting 200 points per thin section.
[1]Based on one sample only.

DF = Delta front; DDF = Distal delta front; DC = Distributary channel; F/EC = Fluvial/estuarine channel; TC = Tidal channel;
TSS = Transgressive sand shoal

236

Quartz

Quartzarenite

95

o C3
● C4
□ C5
■ C6

Subarkose   Sublitharenite

75

Arkose | Lithic arkose | Feldspathic litharenite | Litharenite

50

Feldspar   Rock fragments

QAa3607c
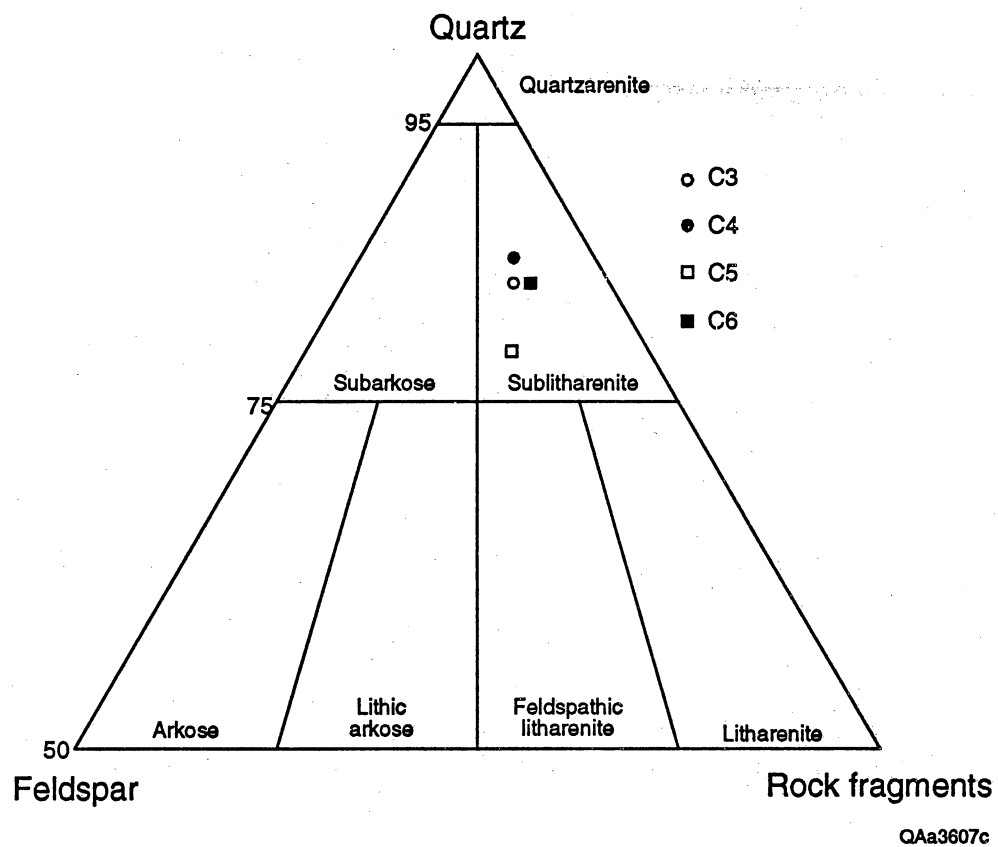
Figure 134. Compositional classification of Misoa sandstones by sandstone interval. Note that this diagram shows only the upper half of Folk's (1974) sandstone classification triangle, from 50 to 100 percent quartz.

237

Rock fragments range from 1 to 30 percent of the essential framework grains. Metamorphic rock fragments, which are composed predominantly of muscovite and quartz, are the most common lithic grains (average = 3.9 percent). Most of the metamorphic rock fragments are of low-rank rocks such as slate, phyllite, and slightly metamorphosed chert grains. Sedimentary rock fragments (average = 3.6 percent) include detrital grains of sandstone, siltstone, shale (many of which may be contemporaneous mud rip-up clasts), and chert. Minor volumes of plutonic rock fragments (average = 0.6 percent) composed of quartz and plagioclase occur in most sandstones. Most rock fragments in the Misoa sandstones are ductile and deform during compaction. Ductile grain deformation, a form of mechanical compaction, is an important cause of porosity loss in these sandstones (plate 1a and b).

Other framework grains in Misoa sandstones include biotite and muscovite, which are each present in volumes of ≤1.0 percent in most samples. Tourmaline, zircon, glauconite, leucoxene (altered ilmenite), and hematite (altered magnetite) occur in many samples in volumes of ≤0.5 percent. Organic matter is present in volumes ranging from 0 to 8 percent and averaging 0.6 percent.

Framework-grain composition of Misoa sandstones varies among facies (fig. 135). The most quartz-rich samples occur in the fluvial/estuarine channel facies in the Lower Lower C-6-X Submember (fig. 106). The transgressive-sand-shoal, distal-delta-front, and delta-front facies have intermediate framework-grain compositions, and the distributary-channel and tidal-channel facies contain the greatest volume of rock fragments (fig. 135). Delta-front and transgressive sand-shoal sandstones probably contain a higher percentage of detrital quartz because wave and current abrasion removed more of the mechanically unstable rock fragments and because differences in hydraulic properties allowed wave and current action to winnow quartz from rock fragments. Distributary- and tidal-channel sandstones contain more abundant rock fragments because they were not winnowed. The high percentage of quartz in the fluvial/estuarine-channel deposits cannot be explained by depositional processes, and it is likely that these incised channels tapped a different, more quartz-rich source area.

Detrital Clay Matrix

Detrital clay matrix composes only 0 to 6 percent of the volume of Misoa sandstones in the samples chosen for this study. However, these samples were particularly chosen to emphasize clean sandstones and thus do not accurately represent the average volume of detrital clay in all Misoa sandstones. In many cases it is difficult to distinguish detrital and authigenic clays, so some of the volume of clay reported as authigenic may actually be detrital (table 41). No X-ray diffraction analyses of matrix were done for this study, but previous X-ray work by Ghosh and others (1988a, b) indicates that kaolinite, chlorite, illite, and mixed-layer illite-smectite (MLIS) with 70 to 80 percent illite layers occur in varying proportions in Misoa C sandstones. Ghosh and others did not specify whether the X-ray samples contained detrital clay, but their data suggest that the Misoa matrix is composed of a mixture of clay mineral types. Clay-sized quartz probably also is a component of matrix.

Cements

Cements and replacive minerals constitute between 9 and 49 percent of the sandstone volume in Misoa samples. Cement is most abundant in clean sandstones that contain little detrital clay matrix. Because clean sandstones were preferentially sampled for this study, the average volume of 18 percent cement may not accurately represent the average volume of cement in all Misoa sandstones. It should, however, be representative of the volume of cement in reservoir sandstones. The highest average volume of cement is in C-5-X sandstones (table 41), which contain particularly abundant carbonate cements—calcite, ankerite, and siderite. The facies with the highest average volumes of total cement are tidal channel, transgressive sand shoal, and distal delta front, all of which have abundant carbonate cement (table 42). The volume of quartz cement is 8 to 10 percent in all facies, with the exception of the fluvial/estuarine-channel samples, which have an average of 12 percent.
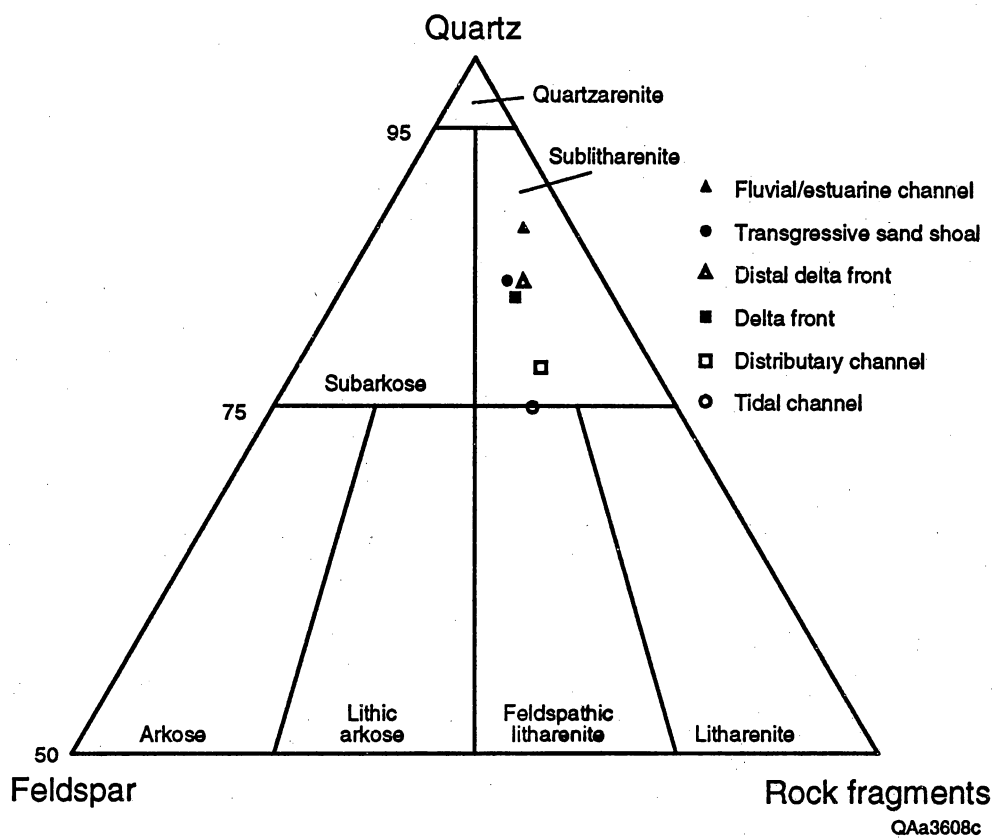
Figure 135. Compositional classification of Misoa sandstones by facies. Note that this diagram shows only the upper half of Folk's (1974) sandstone classification triangle, from 50 to 100 percent quartz.

Plate 1a.

Loss of porosity by deformation of ductile biotite (B) and metamorphic rock fragment (M). Sample of C-6-X sandstone from a depth of 9,174 ft in the LL-3140 well. Long dimension of photo = 0.65 mm. Plane-polarized light.

Plate 1b.

Typical Misoa sandstone with abundant detrital quartz grains and sedimentary and metamorphic rock fragments. Quartz cement fills much of the intergranular porosity, typical of deeper Misoa C-X sandstones. Sample of C-6-X sandstone from a depth of 9,174 ft in the LL-3140 well. Long dimension of photo = 2.6 mm. Cross-polarized light.

Plate 1c.

Shallow Misoa C-3-X sandstone with high primary and secondary porosity and little quartz cement. Sample from a depth of 7,272 ft in the LL-2850 well. Long dimension of photo = 2.6 mm. Plane-polarized light.

Plate 1d.

Deep Misoa C-6-X sandstone, in which most intergranular porosity is occluded by quartz cement. Same sample and field of view as in photo (b) but plane-polarized light.

(a)

B

M

(b)

(c)

(d)
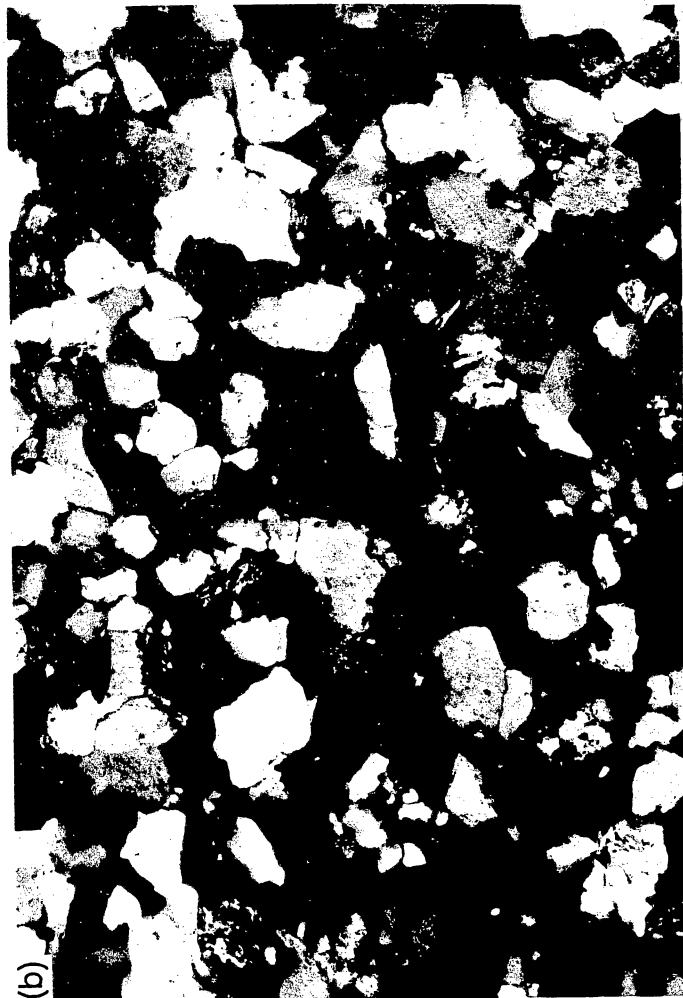
Quartz, carbonates, and clay minerals are the most common cements in Misoa sandstones. The relative proportion of these cements varies in the different sandstone intervals, with C-6-X sandstones containing the greatest proportion of quartz cement and C-3-X sandstones containing the most carbonate cements (fig. 136a). The relative proportions of cement types by facies are quite similar among all the facies except for the fluvial/estuarine channel sandstones, which contain the highest proportion of quartz cement (fig. 136b). Thus, the reason for the relatively abundant quartz cement in C-6-X sandstones is that many of those sampled were deposited in fluvial/estuarine-channel environments.

The only other authigenic mineral observed in Misoa sandstones was pyrite, which is uncommon and generally occurs in volumes of <0.5 percent. Reservoir bitumen ("dead oil"), a solid hydrocarbon residue that occurs in some sandstones, is also considered a cement in this study, although it is not a mineral.

On the basis of petrographic evidence, the relative order of occurrence of the major events in the diagenetic history of the Misoa sandstones was (1) precipitation of siderite rims and nodules, (2) formation of illite, and minor chlorite, rims, (3) mechanical compaction by grain rearrangement and deformation of ductile grains, (4) precipitation of quartz overgrowths, (5) precipitation of calcite cement, (6) generation of secondary porosity by dissolution of feldspars, rock fragments, and calcite cement, (7) precipitation of kaolinite and minor illite and chlorite in secondary pores, (8) precipitation of ankerite cement, (9) precipitation of additional quartz cement, and (10) migration of hydrocarbons into the reservoirs. Many of these events overlapped in time (fig. 137).

Quartz

Quartz is volumetrically the most abundant cement in Misoa sandstones; the volume ranges from 0 to 19 percent and averages 10 percent. Quartz cement increases with depth, from an average of 7.8 percent at 7,200 ft to 12.5 percent at 9,200 ft (fig. 138; plates 1c and d and 2a and b); the relationship is significant at the 99-percent confidence level. (Four outliers were omitted from the calculation of the linear regression equation relating quartz cement and depth. Some of these atypical samples have low volumes of quartz cement because they were extensively cemented by early siderite, others because they have such abundant ductile grains and organics that they lost all porosity by compaction.) The reason for the high average volume of quartz cement in fluvial/estuarine-channel sandstones is that their average depth is 9,100 ft, considerably deeper than the other facies (table 42). Quartz-cement volume is the main control on porosity and permeability in C-3-X through C-6-X sandstones in the study area, as will be discussed further in the section "Diagenetic Controls on Reservoir Quality."

Weak positive correlations (significant at the 90-percent confidence level) exist between volume of quartz cement and (1) the volume of detrital quartz (r = 0.36) and (2) grain size (r = 0.27). Inverse correlations exist between quartz cement and (1) volume of detrital clay (r = -0.33) and (2) volume of rock fragments (r = -0.26). Grain size and detrital-quartz content both increase with depth in this set of Misoa sandstone samples. Thus, one explanation for the increasing volume of quartz cement with depth is that quartz cement precipitated preferentially in the coarser-grained, more detrital-quartz-rich sandstones, and these occur in the deeper part of the stratigraphic section. The trend of quartz cement with depth in this case would simply be a consequence of the fact that the coarsest, most quartz-rich sandstones are oldest.

Alternatively, the volume of quartz cement may increase with depth because the deeper sandstones have higher thermal maturities and more quartz cement precipitated in them during their longer, hotter burial. A correlation between increased quartz cement and higher thermal maturity has been noted in other basins (for example, the East Texas Basin [Dutton and Diggs, 1990] and the Green River Basin [Dutton, 1993]). The increase of quartz cement with depth suggests that quartz cementation occurred throughout the burial history of Misoa sandstones, probably during discrete episodes (fig. 137). Later episodes of quartz cementation apparently enlarged existing quartz overgrowths in optical continuity and without dust lines or other inclusions, making it difficult to distinguish different generations of quartz cement. If this hypothesis is correct, then the correlation of quartz cement with grain size and detrital-quartz content is simply a consequence of the fact that the coarsest, most detrital-quartz-rich sandstones occur in the part

(a)

Quartz

Carbonates

Clay minerals

(b)

Quartz

▲ Fluvial/estuarine
□ Distributary channel
■ Delta front
△ Distal delta front
○ Tidal channel
● Transgressive sand shoal

Carbonates

Clay minerals

QAa3609c
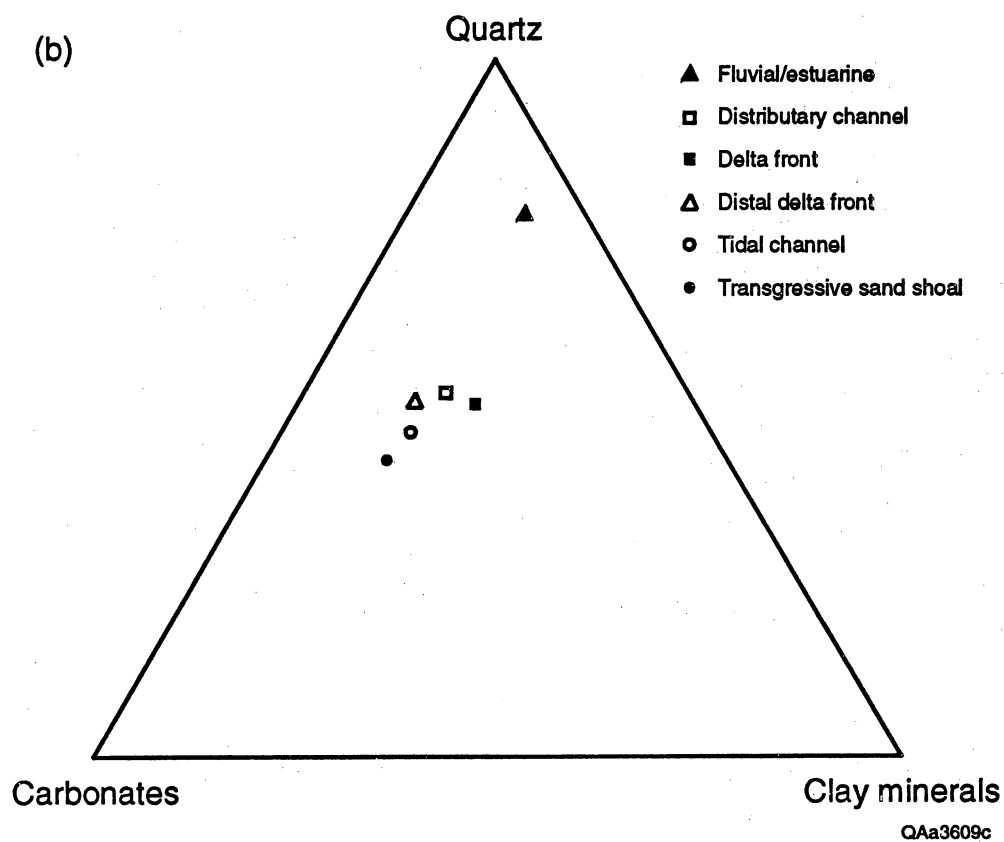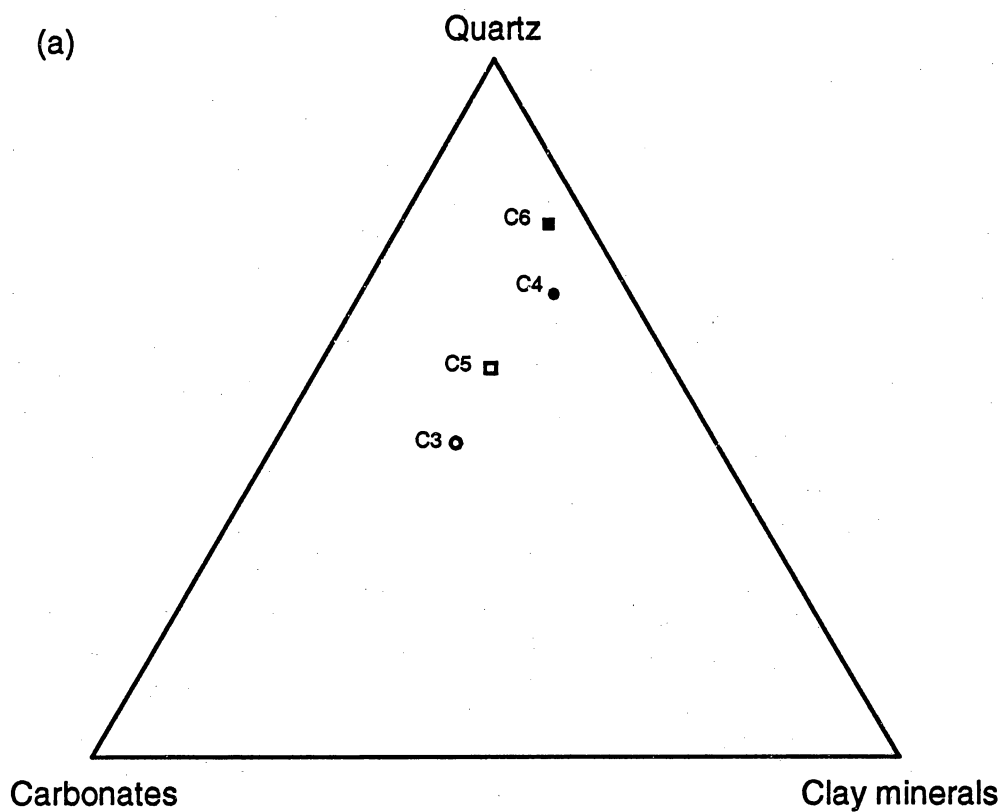
Figure 136. (a) Relative proportions of quartz, carbonate, and clay cements by Misoa sandstone intervals. (b) Relative proportions of cements by facies.

Process	Stage	
	Early	Late
Siderite rims, nodules	—	
Illite rims	—	
Mechanical compaction	—— -- ·	
Quartz overgrowths	——	- - - -
Calcite cement	—	
Dissolution feldspar, calcite		—— -- --
Authigenic kaolinite		—— -- --
Ankerite		——
Oil migration		—

QAa3610c

Figure 137. Generalized paragenetic sequence for Misoa C-3-X through C-6-X sandstones, Lagunillas field, LL-652 area, Lake Maracaibo.
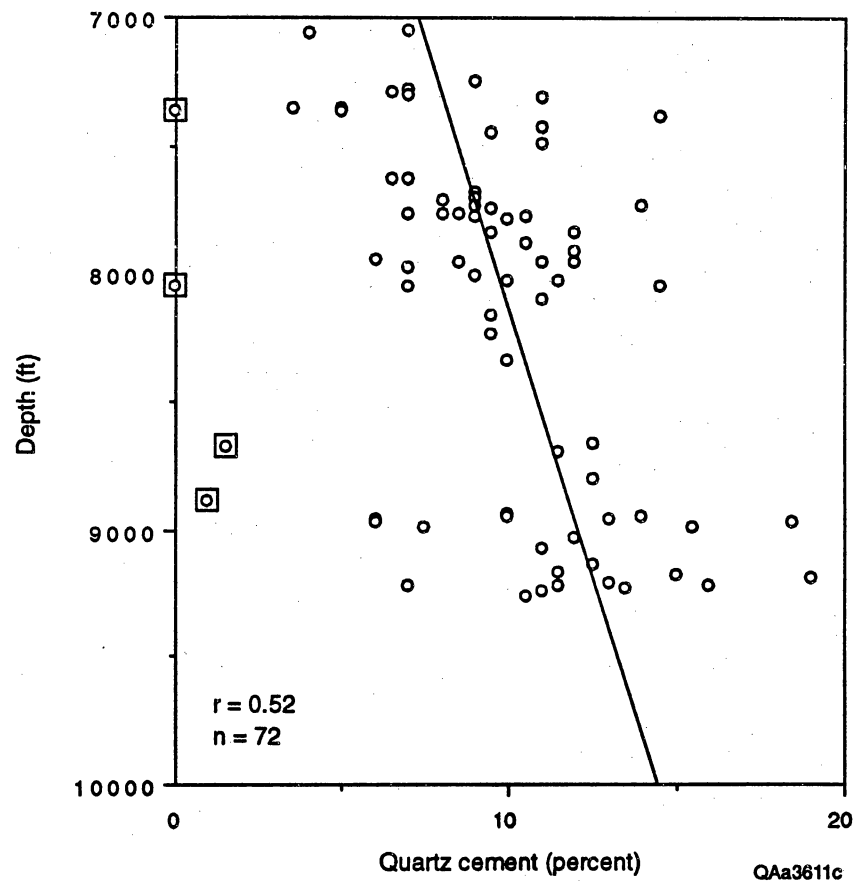
Figure 138. Quartz cement volume in Misoa C-3-X through C-6-X sandstones as a function of present burial depth. Quartz cement increases significantly with depth. Linear regression equation relating depth and quartz cement is:

quartz cement (percent) = 9.03 + 2.34 × depth (ft) × 10^{-3}.

Four outliers (boxed) were not included in the calculation of the regression equation.

of the section with the highest thermal maturity. Because quartz cement has been observed to increase with thermal maturity in other formations and basins, we favor this second hypothesis to explain the increase in quartz cement with depth in Misoa sandstones.

Authigenic Clays

Authigenic kaolinite and illite were identified by thin-section and SEM examination of Misoa sandstones. Illite and mixed-layer illite-smectite (MLIS) cannot be distinguished by these techniques, but on the basis of previous X-ray analyses (Ghosh and others, 1988a, b) some of the clays identified as illite probably included MLIS as well. Some illite and MLIS occur as rims of tangentially oriented flakes that developed around detrital grains early in the diagenetic history (plate 2c). In some places the illite rims apparently were thick enough to inhibit the precipitation of quartz cement. Other illite and MLIS have a flaky to fibrous morphology and extend into and across primary pores (plate 2d). The distribution and morphology of the illite and MLIS bridging and lining intergranular pores and pore throats causes a reduction in permeability in samples with abundant illite. Authigenic illite is most abundant in the tidal-channel and transgressive-sand-shoal sandstones (table 42), which each contain an average of 2 percent illite. All of the other facies contain an average of 1 percent illite.

Kaolinite is a reaction product of feldspar dissolution, and it is found mainly within secondary pores (plate 2c). Kaolinite probably has less impact on permeability in Misoa sandstones because it is somewhat isolated within secondary pores. However, much of the kaolinite appears loosely packed and thus may be susceptible to being dislodged during production, creating a mobile fines problem.

Chlorite is less abundant than either illite or kaolinite. It was tentatively identified in thin sections as coating some detrital grains and occurring in secondary pores. However, no chlorite was observed in the SEM samples, so perhaps most of what was called chlorite in thin section is actually illite or kaolinite.

Carbonate Cements

Siderite, iron-bearing calcite, and ankerite all occur in Misoa C sandstones. Textural relations indicate that siderite was one of the first cements to precipitate (fig. 137; plate 3a and b). Most Misoa sandstones contain only a few percent siderite cement (average volume = 3 percent), but a wide range of volumes, from 0 to 30 percent, were observed. Five samples contain more than 10 percent siderite—one sample each from delta-front, distal-delta-front, tidal-channel, transgressive-shelf, and transgressive-sand shoal facies. On average, siderite is most common in the distal delta-front, tidal-channel, and transgressive sand-shoal facies, but this may simply reflect the relatively small sample sizes of these facies (table 42) and the presence of one extensively cemented zone in each. The extensively siderite-cemented layers have very low porosity and permeability and may compartmentalize reservoirs, but their distribution and lateral extent cannot be predicted with current information.

Iron-bearing calcite cement precipitated after quartz (plate 3c). The average volume of calcite cement is 2 percent, but its distribution is highly variable, ranging from 0 to 46 percent. A few samples are extensively cemented by calcite (5 samples contain >10 percent calcite, and 10 samples contain 0.5 to 10 percent), but most samples (61) contain no calcite. Of the five samples with >10 percent calcite, two are from distributary-channel, two from delta-front, and one from tidal-channel facies. As with siderite, the controls on distribution of calcite cement could not be determined.

Dissolution of calcite cement was recognized as an important mechanism of porosity enhancement in the shallower Misoa B sandstones in this area (Ghosh and others, 1988a, b; Maguregui, 1993). Dissolution of calcite cement is interpreted to have taken place during post-Eocene uplift, when meteoric water penetrated the formation (Ghosh and others, 1988a, b). On the basis of thin-section and SEM observations of Misoa C samples in this study, it does not appear that calcite cement dissolution was as important in the C sandstones as in the B sandstones. Most calcite in Misoa C sandstones shows no evidence of

Plate 2a.

Typical C-3-X distributary-channel sandstone from a depth of 7,304 ft in the LL-2850 well. Abundant primary porosity and well developed quartz overgrowths are characteristic of sandstones at this depth. SEM photo by J. M. Mendenhall. Scale bar is 100 μm.

Plate 2b.

Typical C-6-X fluvial/estuarine channel sandstone from a depth of 9,215 ft in the LL-3140 well. Primary pores (P) remain at this depth, but quartz overgrowths (Q) are well developed and occlude much of the inter-granular porosity. SEM photo by J. M. Mendenhall. Scale bar is 100 μm.

Plate 2c.

Illite rim (I) developed around what was probably a detrital feldspar grain. The feldspar later dissolved, and kaolinite (K) precipitated in the resulting secondary pore. Sample is from well LL-2425 from a depth of 7,422.5 ft. SEM photo by J. M. Mendenhall. Scale bar is 10 μm.

Plate 2d.

Authigenic illite extending into an intergranular pore. Sample is from well LL-2425 from a depth of 7,422.5 ft. SEM photo by J. M. Mendenhall. Scale bar is 10 μm.
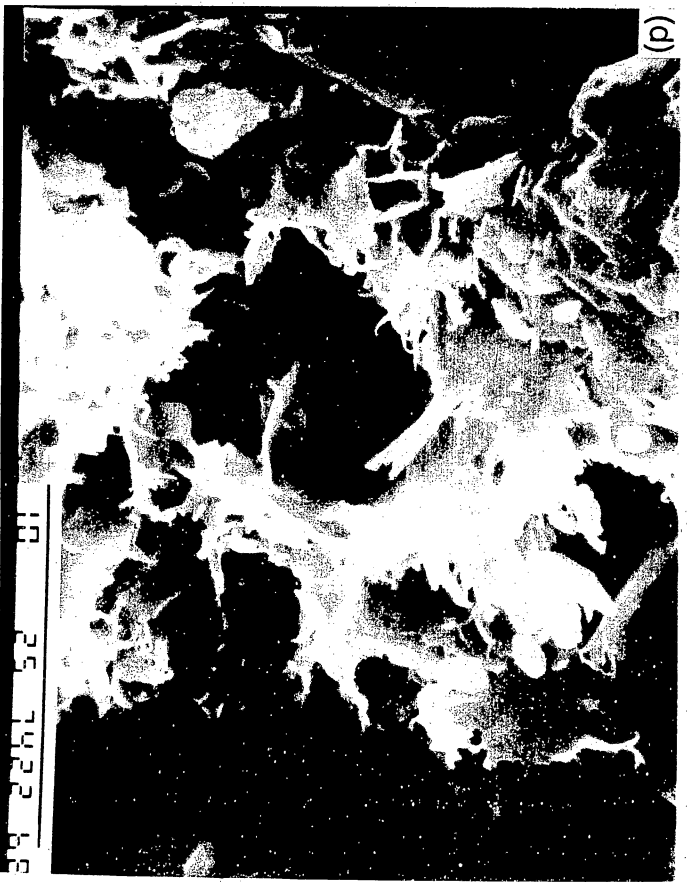
dissolution when it is viewed in thin section or SEM. Most detrital quartz grains and overgrowths observed in SEM lack the calcite-replacement textures described by Burley and Kantorowicz (1986) and Bloch (1991), although abundant authigenic clay may obscure these features. However, dissolution of pore-filling and grain-replacing calcite did open up pores in some C sandstones. The former presence of calcite cement is inferred from remnants of calcite, enlarged intergranular pores, and irregular, corroded margins of detrital grains (plate 3d). Oversize secondary pores may or may not represent framework grains that were replaced by calcite at one time. Therefore, it seems likely that calcite dissolution occurred in the C sandstones but was relatively restricted, and most secondary pores were not previously cemented by calcite. Instead, secondary pores probably formed directly by dissolution of feldspars and other framework grains, without going through an intermediate stage of being replaced by calcite cement. However, zones of particularly abundant secondary porosity and enlarged intergranular pores probably represent porosity enhancement by dissolution of grain-replacing and pore-filling calcite.

The C sandstones are deeper than the B sandstones, which probably explains the difference between them in the importance of calcite dissolution. In the LL-3074 well, which was the shallowest well in the study area at the time of the post-Eocene uplift, the C-3-X sandstone was still 1,500 ft deep at maximum uplift. This depth was probably too great for significant meteoric water penetration and calcite dissolution in the C sandstones.

Precipitation of ankerite cement was a late diagenetic event (fig. 137) that apparently followed feldspar dissolution. The average volume of ankerite is 0.6 percent, and the range is 0 to 6 percent. Because of the uniformly low volume of ankerite cement, it has little impact on porosity distribution in Misoa sandstones.

Porosity

Porosity in Misoa C sandstones observed in thin section ranges from 0 to 19 percent; porosimeter-measured porosity for the equivalent samples ranges from 6.9 to 25.4 percent. Average porosimeter porosity in the Misoa sandstones that were included in the petrographic study is 15.5 percent, compared with an average of 10.3 percent thin-section porosity. In general, thin-section porosity is lower than porosimeter porosity because accurately identifying the volume of microporosity in thin section is difficult. When the microscope cross hair lands on authigenic illite or kaolinite, it is counted as the clay mineral, but abundant microporosity actually exists between the clay flakes (plate 1c, d). The two measures of porosity in Misoa C sandstones are related by the following equation: porosimeter porosity = $10 + 0.5 \times$ (thin-section porosity) (r = 0.62).

Thin-section porosity was divided into (1) primary, intergranular pores and (2) secondary pores that result from dissolution of framework grains or cements. On the basis of thin-section identification, average primary porosity has been found to be 4.9 percent, and average secondary porosity, 5.1 percent. Most secondary pores formed by the dissolution of framework grains, particularly feldspar and rock fragments. Some secondary pores contain remnants of the original detrital grains and the reaction product kaolinite. Both primary and secondary porosity identified in thin section correlate significantly with porosimeter porosity (r = 0.59 and 0.50, respectively).

Microporosity, defined as pores having pore-aperture radii <0.5 m (Pittman, 1979), is moderately abundant in Misoa sandstones. Microporosity cannot be accurately quantified by routine thin-section point counts, but an estimate of the volume of microporosity can be obtained by taking the difference between porosimeter-measured porosity and thin-section porosity. This method is predicated on the fact that pores that cannot be distinguished in thin section are micropores. The average volume of microporosity in Misoa C sandstones estimated by this method is 5.2 percent. The different sandstone intervals and facies of the Misoa sandstones vary in their relative proportions of primary and secondary porosity and microporosity (fig. 139). Primary porosity is relatively most abundant in C-4-X sandstones, whereas microporosity is relatively most abundant in C-3-X sandstones (fig. 139a). The reason for the large difference between porosimeter and thin-section porosity in the C-3-X sandstones is unknown, but

Plate 3a.

Rims of siderite (brown) around detrital grains. Precipitation of early siderite rims may have inhibited later precipitation of quartz cement. Sample of C-4-X sandstone from a depth of 7,622 ft in the LL-2850 well. Long dimension of photo = 2.6 mm. Plane-polarized light.

Plate 3b.

Porosity completely occluded by early siderite cement (S). Sample of C-6-X sandstone from a depth of 8,667 ft in the LL-3080 well. Long dimension of photo = 0.65 mm. Cross-polarized light.

Plate 3c.

Iron-bearing calcite cement (C, stained blue) precipitated after quartz overgrowths. The irregular, corroded shape of grains indicates that calcite replaced some detrital framework grains and quartz cement. Sample of C-3-X sandstone from a depth of 7,345 ft in the LL-3074 well. Long dimension of photo = 0.65mm. Plane-polarized light.

Plate 3d.

Enlarged intergranular pores (blue) and irregular margins of grains suggest that calcite cement previously filled this sandstone but has since been dissolved, resulting in high porosity. Sample of C-3-X sandstone from a depth of 7,244 ft in the LL-3074 well. Long dimension of photo = 0.65 mm. Plane-polarized light.

(a)

Primary porosity

Secondary porosity

Microporosity

C4
C6
C5
C3

(b)

Primary porosity

▲ Fluvial/estuarine channel
■ Delta front and distributary channel
○ Tidal channel
△ Distal delta front
● Transgressive sand shoal

Secondary porosity

Microporosity

QAa3612c
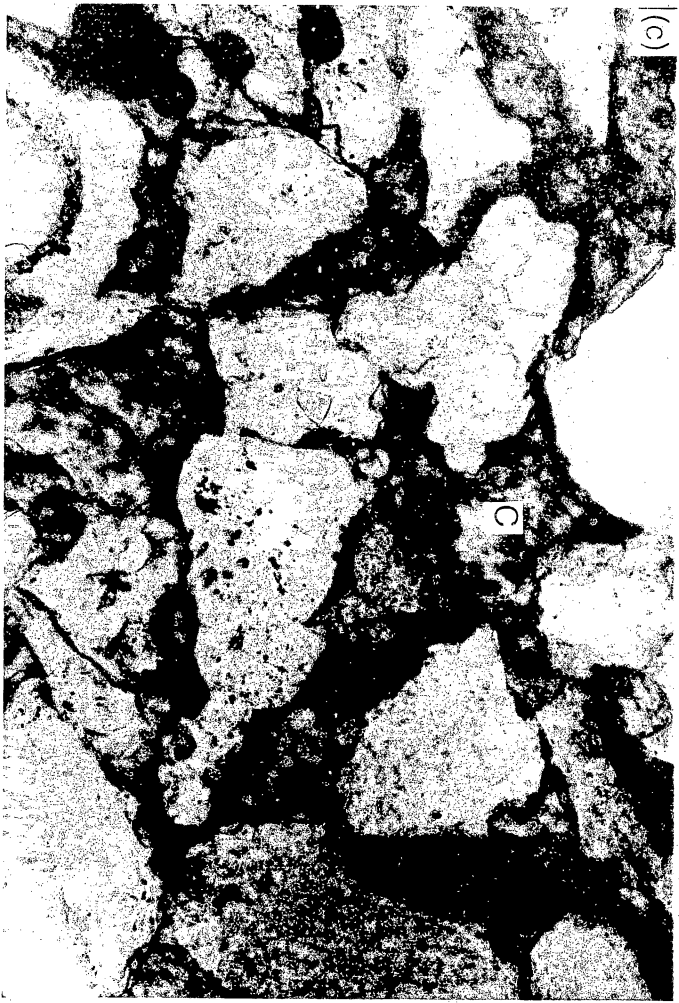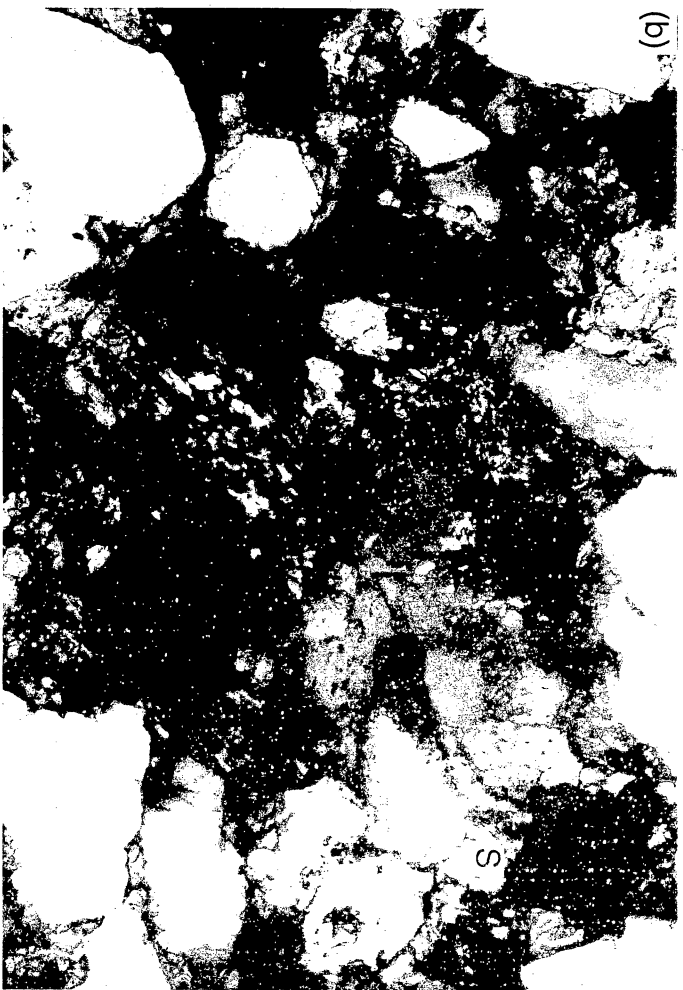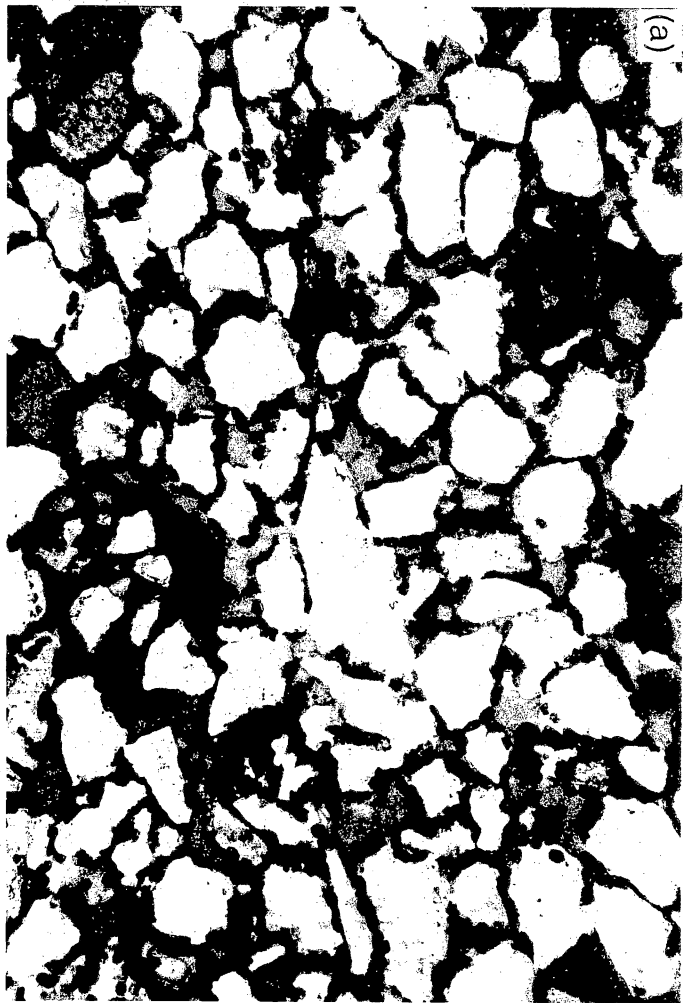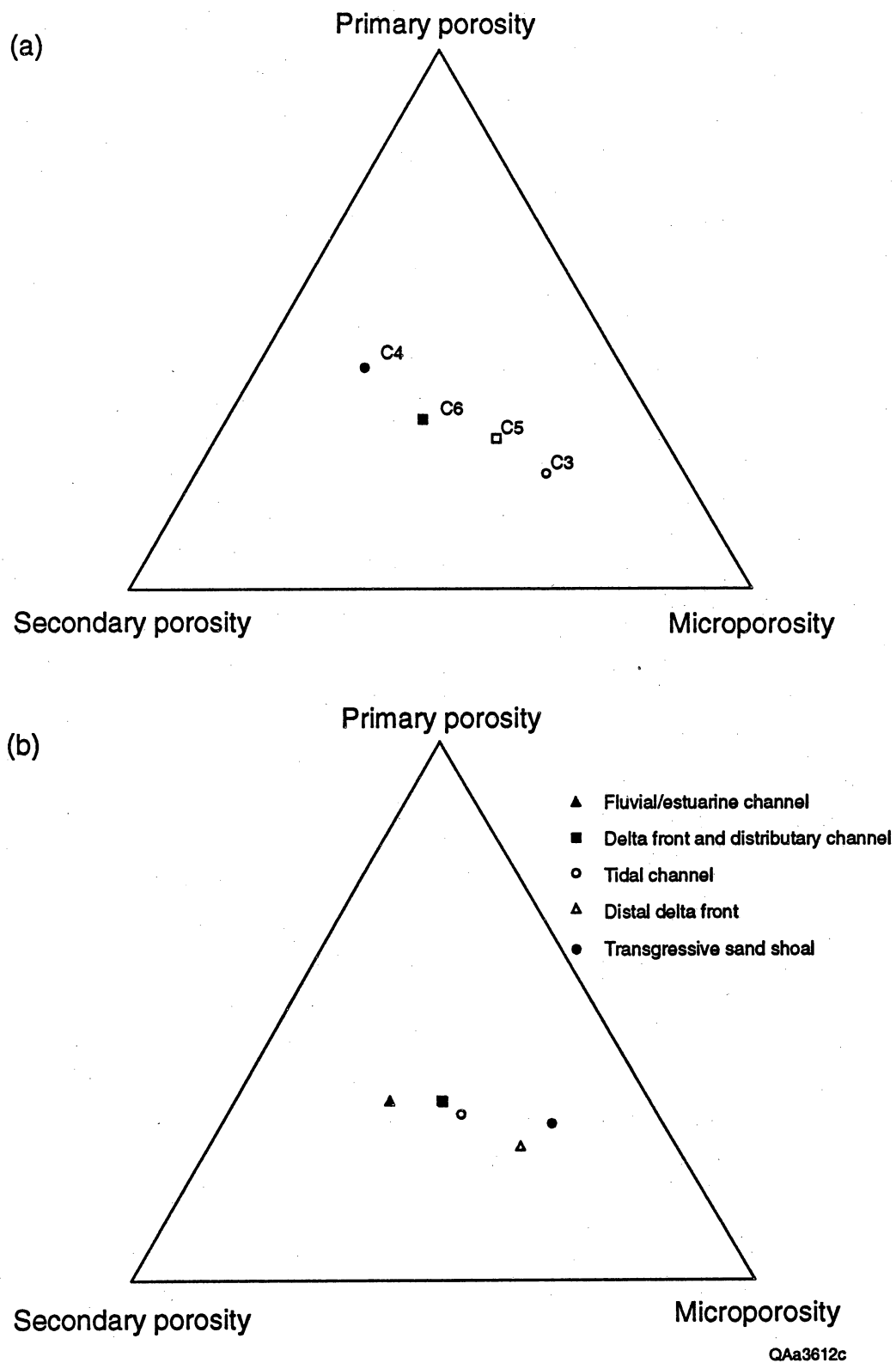
Figure 139. (a) Relative proportions of primary, secondary, and micropores by Misoa sandstone intervals and (b) relative proportions of pore types by facies.

255

it is this difference that results in the estimate of a large volume of microporosity in C-3-X sandstones. The high average permeability in C-3-X sandstones (table 41) suggests that most porosity is actually effective and interconnected and that for some reason the measurements of thin-section porosity in the C-3-X sandstones are too low. The fluvial/estuarine-channel facies has the highest proportion of macroporosity (primary + secondary porosity), and microporosity is most common in the transgressive sand-shoal and distal delta-front facies (fig. 139b).

Much of the depositional porosity in Misoa sandstones was lost by mechanical compaction, such as reorientation of competent grains and deformation of ductile grains (Houseknecht, 1987). Many of the sedimentary and metamorphic rock fragments in Misoa C sandstones are ductile and have been deformed during compaction, causing a reduction of primary porosity. Minus-cement porosity, which is a measure of the amount of porosity remaining after compaction, averages 19 percent in Misoa sandstones. At the time of deposition, moderately well sorted Misoa sandstones probably had a porosity of about 40 percent (Pryor, 1973; Atkins and McBride, 1992). Thus, about 21 percent porosity (53 percent of the original porosity) was lost by compaction. Much of the remaining intergranular porosity was occluded by precipitation of an average of 14 percent primary-pore-filling cement, leaving an average of about 5 percent intergranular porosity.

Diagenetic Controls on Reservoir Quality

By comparing point-count data of thin sections with core analyses, the influence of parameters such as grain size, compaction, detrital mineralogy, volume of authigenic cements, and pore type (primary versus secondary) on porosity and permeability were analyzed (table 43). Only 57 of the thin-section samples were taken directly adjacent to core-analysis plugs, so only those samples were used to compare petrographic and petrophysical parameters. These samples were mostly chosen from sandstones with the best reservoir quality within each C interval; thus, the petrographic samples are not representative of the entire range of porosity and permeability in each sandstone.

When the Misoa sandstone petrographic data base is taken as a whole, combining samples from all sandstones, two parameters emerge as having the major control on porosity: depth and volume of quartz cement. Although depth is not a petrographic property of the rocks, it is the best predictor of porosity in Misoa sandstones (fig. 140a). Porosity decreases with increasing depth in the 57-sample petrographic data base, from an average of 21 percent at 7,200 ft to 11 percent at 9,200 ft (fig. 140a). Porosity shows the same significant decrease with depth when samples from only one facies are considered. Distributary-channel samples have an average porosity of 20 percent at 7,200 ft and 10 percent at 9,200 ft. Differences in average porosity among facies are mainly a function of the depth from which the samples were taken. Thus, delta-front and transgressive sand-shoal samples have high average porosity because those samples are from relatively shallow depths, whereas fluvial/estuarine channel samples have low average porosity because they are from greater depths (table 42).

The other parameter that correlates strongly with porosity is volume of quartz cement (fig. 140b). Because quartz-cement volume increases with depth (fig. 138), porosity decreases. The scatter in the relationship between quartz-cement volume and porosity (fig. 140b) indicates that quartz cement is not the only control on porosity, although it is the single most important petrographic factor (table 43). Thus, the decrease in porosity with depth is explained mainly by the increase of quartz cement with depth.

Relationships between permeability and various textural and mineralogic parameters in Misoa sandstones also were quantified by least-squares linear regression (table 43). As is true for porosity, permeability in the petrographic data base decreases significantly with depth (fig. 141a). Average permeability at 7,200 ft is 136 md, compared with 2.8 md at 9,200 ft.

Porosity is the best predictor of permeability (fig. 141b), and there is a good linear trend between porosity and log permeability when data from all sandstone intervals are combined. Both primary and secondary porosity contribute to permeability (table 43), which indicates that secondary pores are not isolated but

Table 43. Porosity and permeability versus petrographic parameters in Misoa sandstones.

Porosimeter porosity vs petrographic parameters

Parameter	Correlation Coefficient
Depth	-0.82*
Total thin-section porosity (%)	+0.62*
Primary porosity (%)	+0.59*
Quartz cement (%)	-0.57*†
Secondary porosity (%)	+0.50*
Ductile grains (%)	-0.32
Kaolinite cement (%)	+0.26
Chlorite (%)	+0.22
Grain size (phi)	+0.21
Total cement (%)	-0.17
Illite cement (%)	-0.11
Total carbonate cement (%)	+0.03

Permeability vs petrographic parameters

Parameter	Correlation Coefficient
Porosimeter porosity (%)	+0.74*
Ductile grains (%)	-0.63*
Total thin-section porosity (%)	+0.57*
Depth	-0.52*
Primary porosity (%)	+0.52*
Secondary porosity (%)	+0.47*
Quartz cement (%)	-0.38*†
Illite cement (%)	-0.36*
Kaolinite cement (%)	+0.19
Grain size (phi)	-0.18
Total cement (%)	-0.17
Total carbonate cement (%)	0

Linear regression correlation coefficients are shown for porosimeter porosity versus various textural and mineralogic parameters; n = 57. Linear regression correlation coefficients are shown for log permeability versus various parameters; n = 57.

*Significant at the 99 percent confidence level.
†Omitting two outliers.
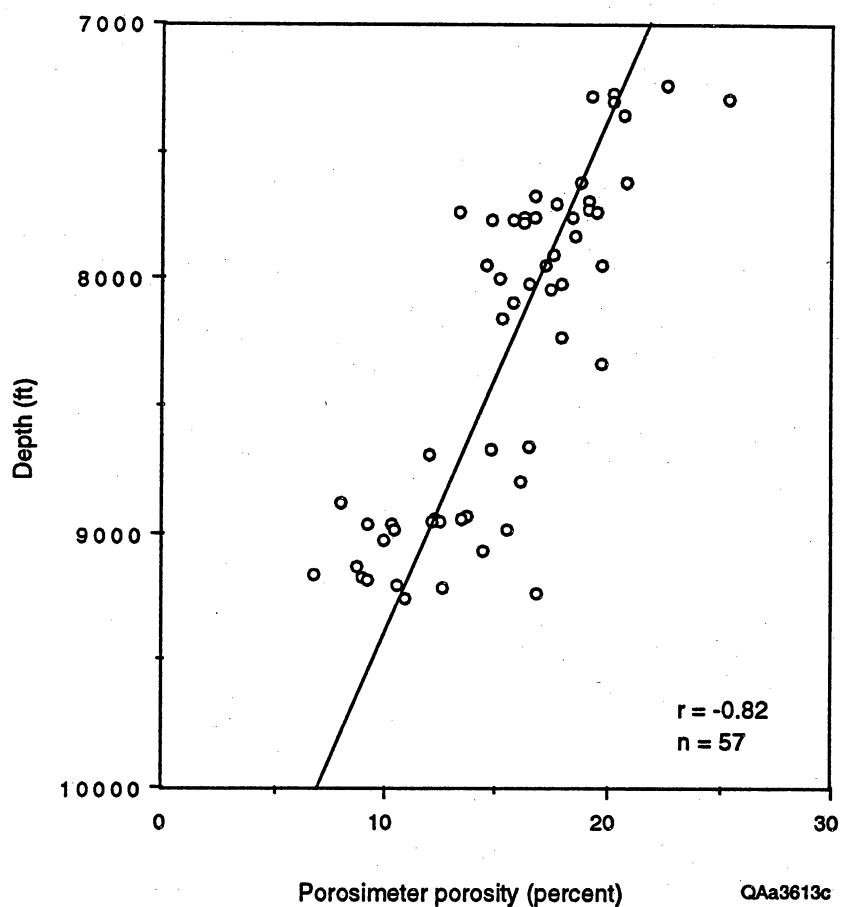
Figure 140. (a) Porosimeter-measured porosity as a function of present burial depth of Misoa C-3-X through C-6-X sandstones. Porosity decreases significantly with depth. Linear regression equation relating depth and porosity is:

porosity (percent) $= 56.62 - 4.97 \times$ depth (ft) $\times 10^{-3}$.
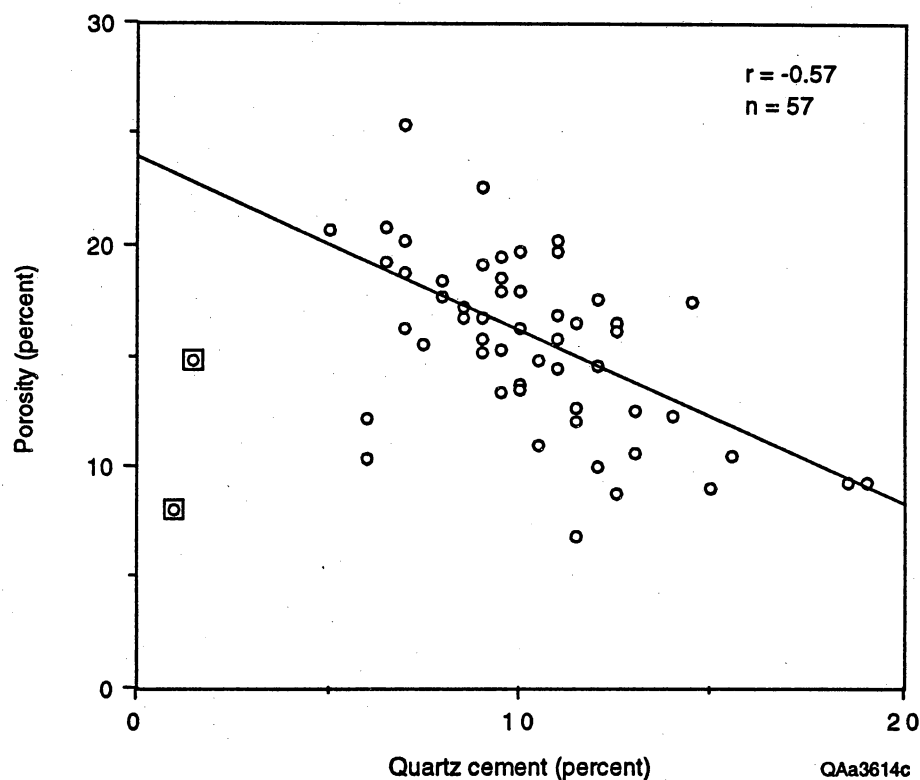
Figure 140. (b) Porosimeter-porosity as a function of quartz cement volume in Misoa C-3-X through C-6-X sandstones. Porosity decreases significantly with increasing quartz cement. Linear regression equation relating porosity and quartz cement is:

porosity (percent) = 23.7 − 0.78 × quartz cement (percent).

Two outliers (boxed) were not included in the calculation of the regression equation.
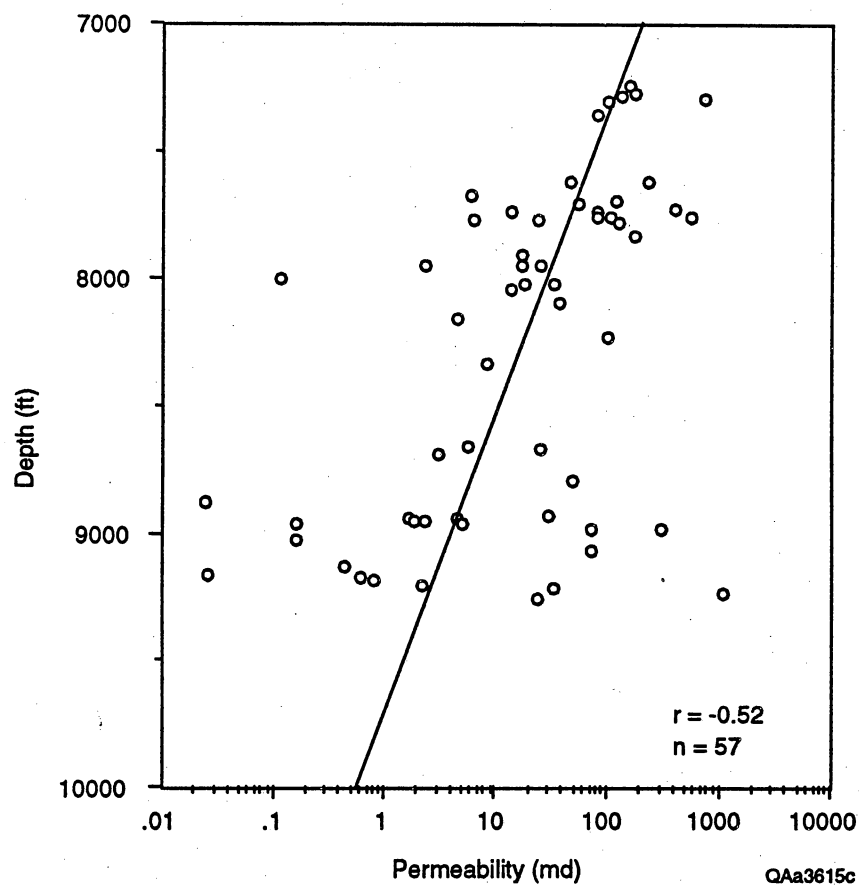
Figure 141. (a) Semilog plot of permeability versus depth for 57 Misoa C-X sandstones. Linear regression equation relating depth and permeability is:

log permeability = $8.21 - 8.44 \times$ depth (ft) $\times 10^{-4}$.
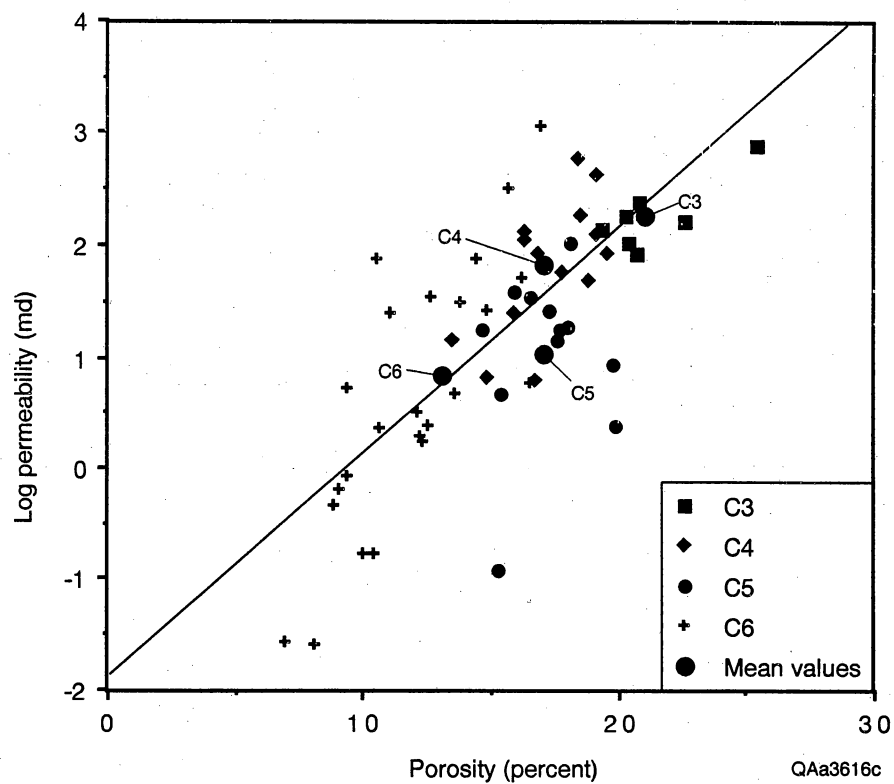
Figure 141. (b) Plot of log permeability versus porosity for 57 Misoa C-X sandstones. Mean values for each sandstone interval are shown. Linear regression equation relating porosity and log permeability is:
Log permeability = -1.87 + 0.20 × porosity (percent).

are connected to the flow paths by primary pores. Porosity and permeability decrease systematically from the C-3-X to the C-6-X sandstones (fig. 141b). Although C-4-X and C-5-X sandstones have the same average porosity, average permeability is higher in C-4-X sandstones because they contain a higher proportion of macroporosity than do C-5-X sandstones (fig. 139a).

Porosity is not an independent variable but is in turn controlled by other factors. The independent petrographic parameters that correlate significantly with permeability are volume of (1) ductile grains, (2) quartz cement, and (3) authigenic illite (table 43). Ductile grains are defined in this study as metamorphic rock fragments, sedimentary rock fragments (sandstone, siltstone, and shale, but not chert), biotite, muscovite, and organic matter. All of these grains are easily deformed during burial, resulting in a loss of porosity and permeability by mechanical compaction. Thus, as the volume of ductile grains increases, permeability decreases (table 43). Quartz and illite volume also correlate significantly (at the 99-percent confidence level) with permeability (table 43). Grain size is not an important control on permeability in Misoa sandstones. The coarsest grains occur in C-6-X sandstone, but they have low permeability because of deep burial and resulting abundant quartz cement.

Conclusions

Misoa C sandstones are fine to very fine sublitharenites. Quartz, plagioclase, and metamorphic and sedimentary rock fragments are the most abundant detrital grains. Quartz overgrowths, siderite, calcite, illite, and kaolinite are the major cements in these sandstones. An average of 5 percent primary porosity remains in these sandstones even after compaction and cementation. Porosity is further enhanced by dissolution of feldspar, rock fragments, and some calcite cement to form secondary pores.

The main control on porosity in Misoa C sandstones in the study area is the volume of quartz cement; because quartz cement increases significantly with depth, porosity decreases. Variations in average porosity among facies are a function of the average depth from which the samples were taken. Thus, delta-front and transgressive sand-shoal samples have high average porosity because those samples are from relatively shallow depths, whereas fluvial/estuarine channel samples have low average porosity because they are from greater depths. The main parameters that influence permeability are volume of ductile grains, quartz cement, and illite cement; grain size is not an important control on permeability. Permeability decreases significantly with increasing depth because of the increase in quartz cement with depth.

In these Misoa C sandstones, diagenesis, specifically the precipitation of quartz cement, is the main control on reservoir quality. More deeply buried sandstones contain more quartz cement and thus have lower permeability than do shallower sandstones, no matter what their grain size or depositional environment. Original variations in permeability that resulted from differences in depositional energy have been overwhelmed by the subsequent diagenetic overprint.

VIII. PRODUCTION ANALYSIS

Kh Production

Cumulative production to March 1993 in 130 active wells in the LL-652 area was 165.5 MMbbl of oil (table 44), mainly 37° API, and 8.3 MMbbl of water. Eighty-two percent (135.8 MMbbl) of the oil production comes from the C-3-X and C-4-X Members (fig. 5) with an average of 1.5 MMbbl of cumulative production per well and average of 155 barrels of oil per day (BOPD) (figs. 142 and 143). Twelve percent (20.5 MMbbl) comes from the C-5-X Member (fig. 5), which as an average of 0.6 MMbbl of cumulative oil per well and 215 BOPD of 41° API (figs. 144 and 145). The C-6-X Member has 5 percent (8.4 MMbbl) of cumulative production with an average of 0.4 MMbbl per well and 80 BOPD of 40° API (figs. 146 and 147). The C-2-X Member has only 1 percent (0.8 MMbbl) (fig. 5) with an average of 109 BOPD of 37° API.

Each of seven structural compartments in the LL-652 area (fig. 12) produces from multiple reservoirs. For example, compartment V has produced from the C-4-X.01 reservoir (C-3-X and C-4-X Members), the C-5-X.02 reservoir (C-5-X Member), and the C-6-X.01 reservoir (C-6-X Member). Compartment I has produced from 9 wells with a cumulative production of 17 MMbbl and 1.9 MMbbl average production per well. The LL-851 well has the best cumulative production (table 45) in this compartment with 5.3 MMbbl. The LL-1066, LL-1209, and LL-3273 wells are producing more than 200 BOPD, and the LL-2981 well is producing 432 BOPD. Compartment II has a cumulative production of 5.7 MMbbl from 10 wells. The LL-652 well has the best cumulative production with 4.2 MMbbl, and the LL-1316 well is producing 238 BOPD. Compartment III, located in the steeply dipping flank of the anticline in the north, is drained by only two wells that have a cumulative production of 5.10 MMbbl. The LL-1293 well has produced 2.6 MMbbl, and the LL-1695 has produced 2.5 MMbbl and is still producing 201 BOPD. Compartment I has produced from eight wells with 4.5 MMbbl of cumulative production. The LL-1169 well has produced 2.1 MMbbl, and the LL-3186 well is the best producer in the entire field with 635 BOPD and only 33 barrels of water per day (BWPD). Compartment V (central structural block) has the biggest production area of the field and includes 76 wells with a cumulative production of 85.8 MMbbl. Seventy-seven percent (66.1 MMbbl) of this production comes from the C-4-X.01 reservoir. The LL-852, LL-971, and LL-1106 wells have produced more than 4 MMbbl each, and seven wells are currently producing more than 200 BOPD, and four wells are producing more than 320 BOPD. The LL-3238 well is the best producer, with 480 BOPD (table 45). Compartment VI has produced from 11 wells with a cumulative production of 14.5 MMbbl. This compartment has also produced in the Maraven area from the VLA-68 and VLA-96 wells, which have 2.4 MMbbl and 1.2 MMbbl of cumulative production, respectively. The best cumulative production in the LL-652 area in this compartment is from the LL-1006 well with 5.3 MMbbl. Compartment VII has produced from 28 wells with a cumulative production of 32.9 MMbbl of oil and 1.2 MMbbl of water. The LL-833 and LL-900 wells have produced 6.1 MMbbl and 4.2 MMbbl, respectively. Four wells are currently producing more than 230 BOPD, and the LL-3059 and LL-3155 wells are excellent producers with more than 460 BOPD.

It was difficult to evaluate production maps at the level of submembers because open intervals in each well commonly include several submembers. We therefore had to compare production logs, but only six good production logs from the LL-2938, LL-2089, LL-1876, LL-3074, LL-3156 and LL-3062 wells were available. These wells are located in different blocks and produce from different members. Figures 148 and 149 show an example of production logs in the LL-3156 and LL-3074 wells.

The combined C-3-X/C-4-X Members account for 82 percent of oil production in the LL-652 area. The C-5-X Member has produced 12 percent, and the C-6-X Member has produced 5 percent. The productivity is directly related to the average kh calculated by pressure (table 46) that is highest in the C-3-X/C-4-X Members (590 md-ft), C-5-X Member (490 md-ft), and C-6-X Member (155 md-ft).

263

Table 44. Cumulative production (MMbbl) of C Members.

Compartments	Member C-2-X Oil	Member C-2-X Water	Member C-2-X Wells	Members C-3-X/C-4-X Oil	Members C-3-X/C-4-X Water	Members C-3-X/C-4-X Wells	Member C-5-X Oil	Member C-5-X Water	Member C-5-X Wells	Member C-6-X Oil	Member C-6-X Water	Member C-6-X Wells
I	-	-	-	17.05	0.23	8	0.04	0.03	1	-	-	-
II	-	-	-	5.43	0.31	6	0.17	0.02	3	0.10	0.01	1
III	-	-	-	5.07	0.10	2	-	-	-	-	-	-
IV	-	-	-	3.77	0.06	5	0.67	0.01	2	0.02	0.01	1
V	-	-	-	66.05	1.99	47	14.20	0.28	15	5.50	0.50	14
VI	0.83	0.11	2	8.20	2.98	4	3.58	0.04	33	1.87	0.49	2
VII	-	-	-	30.24	1.06	18	1.81	0.09	8	0.89	0.02	2
LL-652 Area	0.83	0.11	2	135.81	6.73	90	20.47	0.47	32	8.38	1.03	20

Compartments	Total Oil	Total Water	Total Well-Member	Total Average Production
I	17.06	0.26	9	1.9
II	5.71	0.34	10	0.6
III	5.07	0.10	2	2.5
IV	4.46	0.08	8	0.6
V	85.75	2.77	76	1.1
VI	14.47	3.62	11	1.3
VII	32.94	1.17	28	1.2
LL-652 Area	165.49	8.34	144	1.2

Figure 142. Cumulative production (bbl) by well in the C-3-X/C-4-X Members.
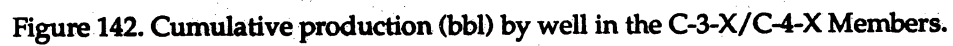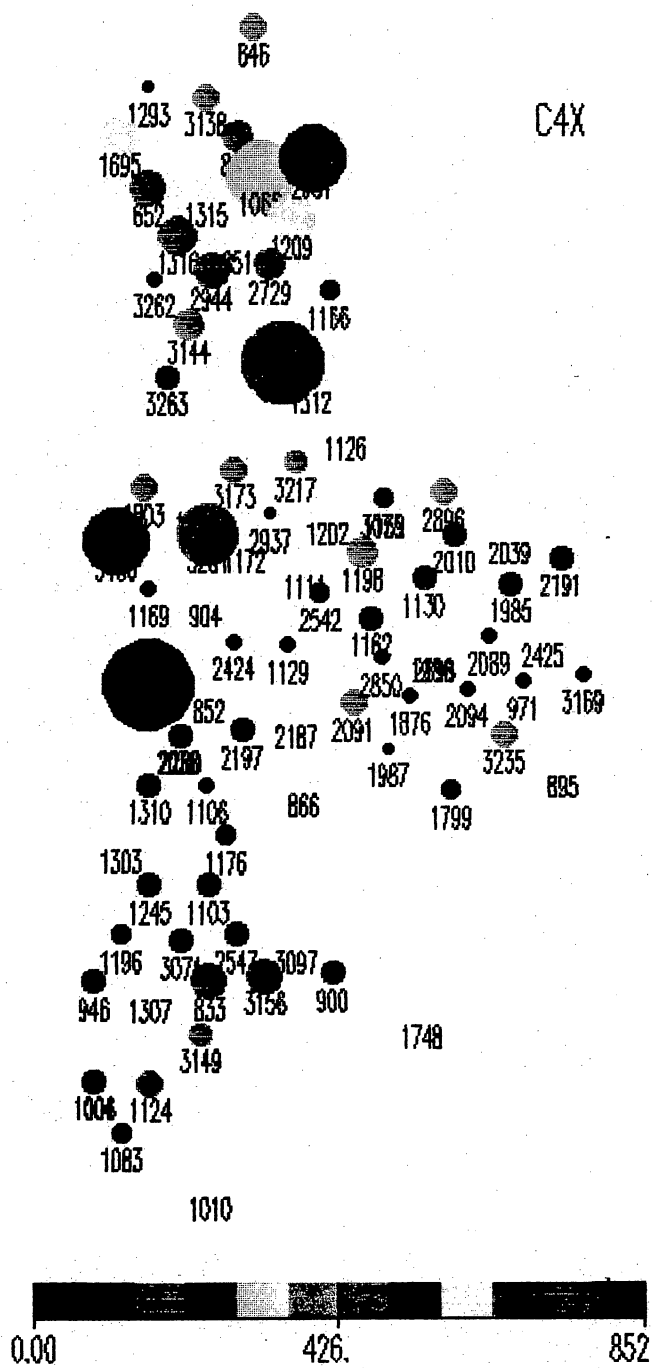
Figure 143. Average daily oil production (bbl) by well in the C-3-X/C-4-X Members.
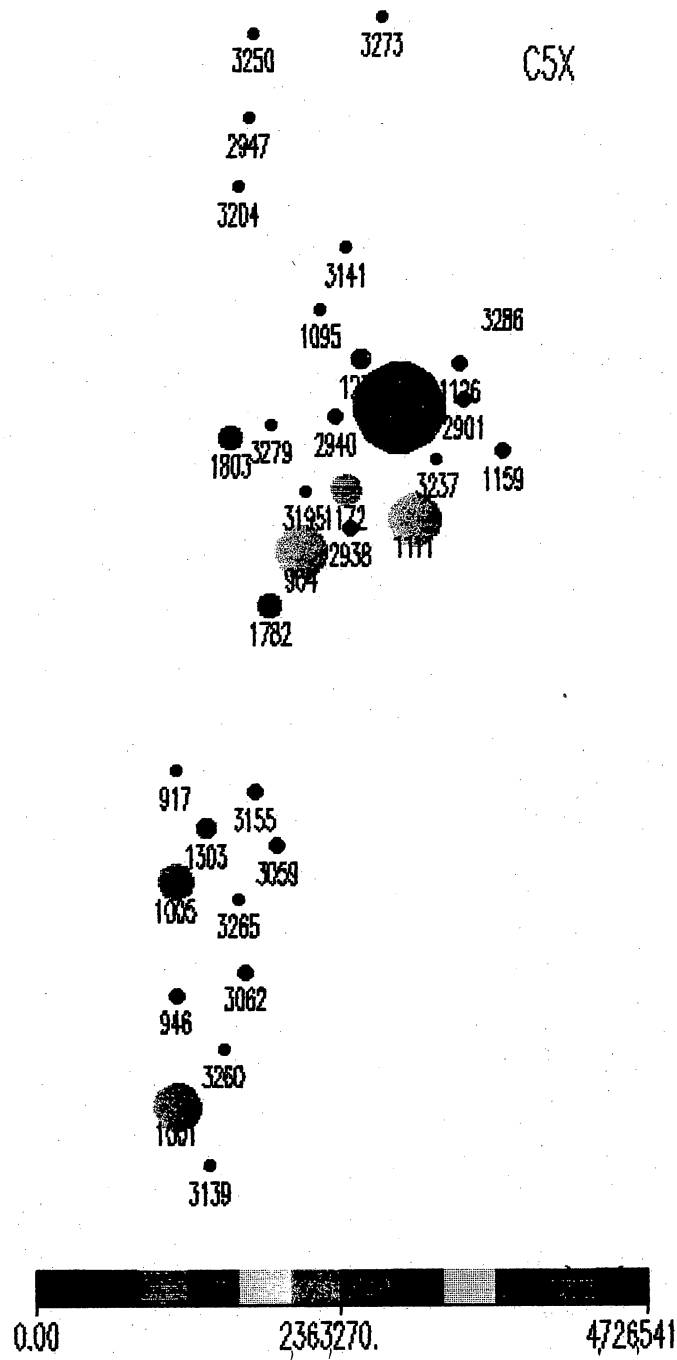
Figure 144. Cumulative production (bbl) by well in the C-5-X Member.

267
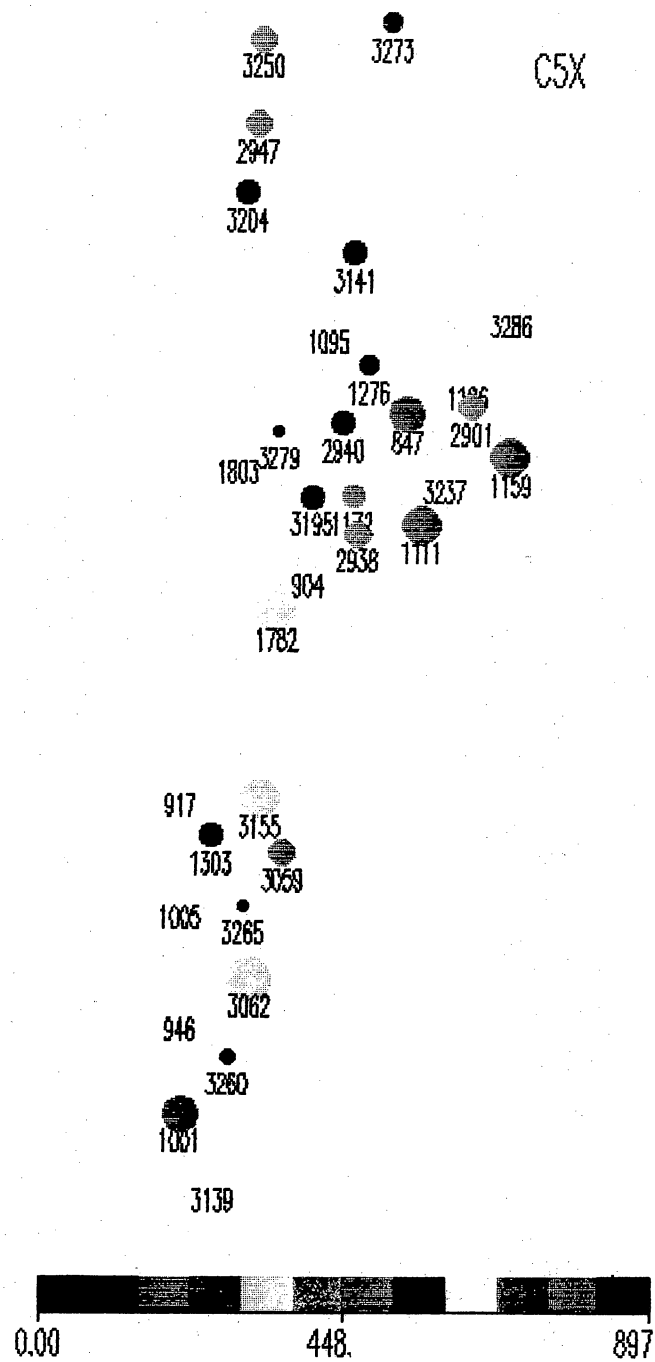
Figure 145. Average daily oil production (bbl) by well in the C-5-X Member.
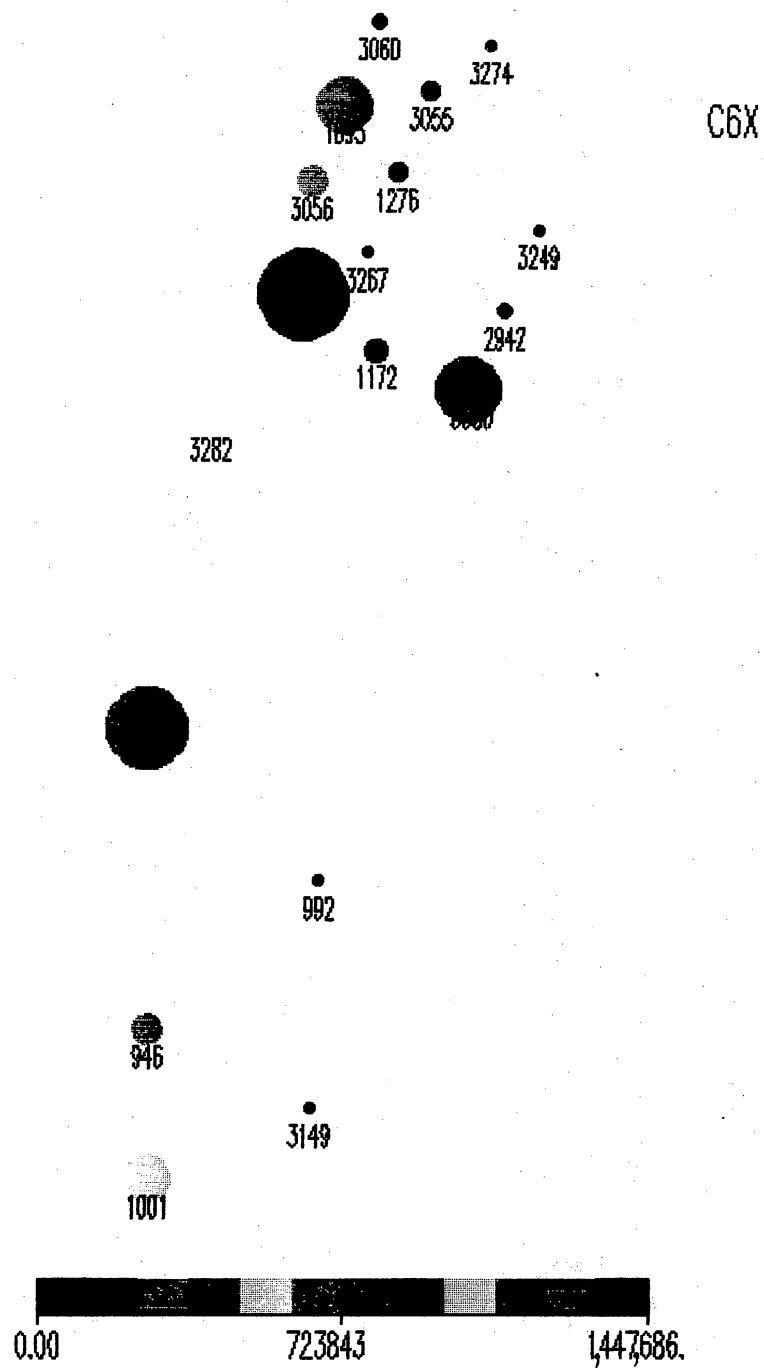
Figure 146. Cumulative production (bbl) by well in the C-6-X Member.

269
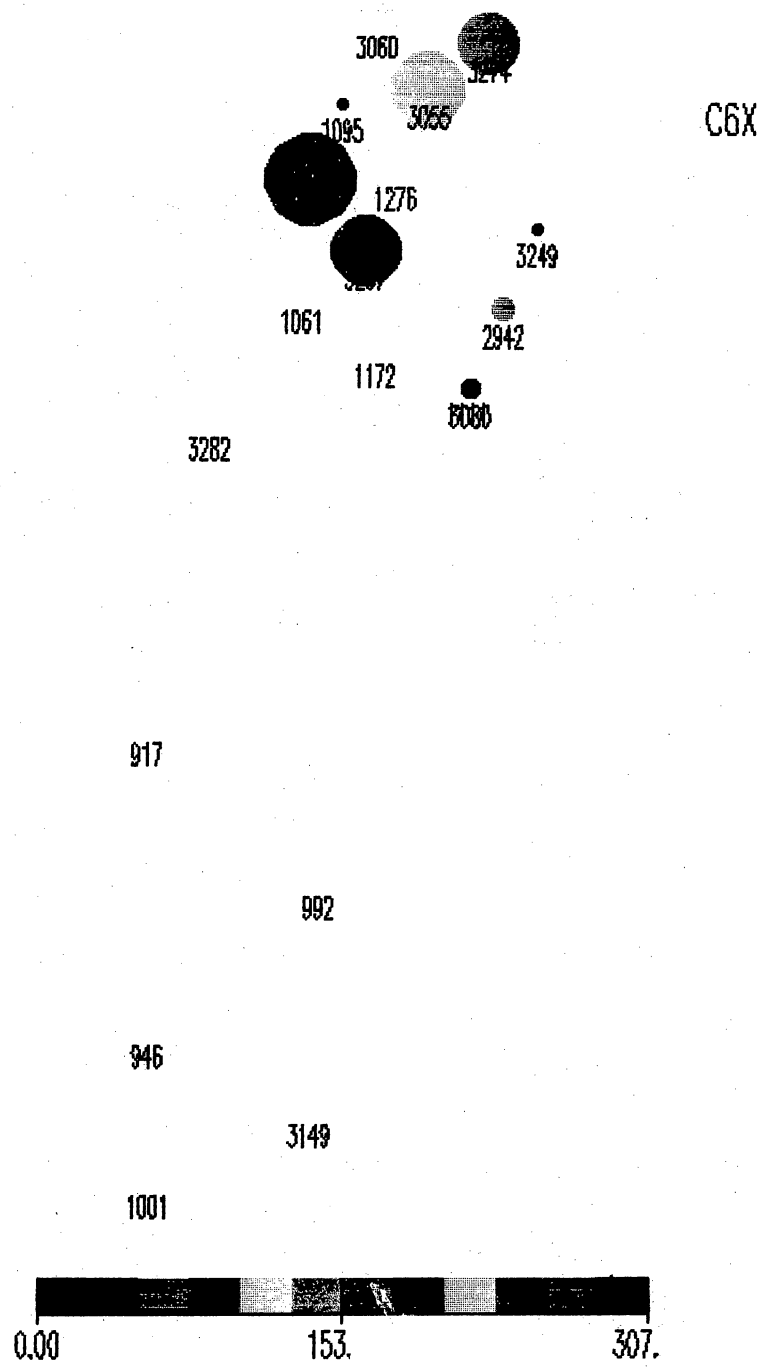
Figure 147. Average daily oil production (bbl) by well in the C-6-X Member.

Table 45. Best production by well and compartment.

Compartment	Cumulative Well	Cumulative MMbbl	Current Well	Current Date	Current Reservoir	Current Oil (BOPD)	Current Gas (MCFD)	Current Water (BWPD)	API
I	LL-851	5.3	LL-1066	03/93	C-4-X.01	296	2800	0	36
			LL-1209	01/93	C-4-X.01	219	1092	2	37
			LL-2981	03/93	C-4-X.01	432	1400	0	36
			LL-3273	03/93	C-5-X.02	235	585	2	37
II	LL-652	4.2	LL-1316	02/93	C-4-X.01	238	1092	10	38
III	LL-1293	2.6	LL-1695	03/93	C-4-X.01	201	1960	7	36
IV	LL-1169	2.1	LL-3186	03/93	C-4-X.01	635	516	33	37
V	LL-852	4.5	LL-1111	03/93	C-5-X.02	346	1357	5	36
			LL-1198	01/93	C-4-X.01	217	1960	0	36
	LL-971	4.1	LL-2091	11/92	C-4-X.01	212	1577	7	37
			LL-2197	01/93	C-4-X.01	223	3645	12	36
	LL-1106	5.8	LL-2896	03/93	C-4-X.01	249	1926	3	38
			LL-3056	03/93	C-6-X.01	324	1344	0	40
			LL-3217	02/93	C-4-X.01	215	952	1	38
			LL-3235	03/93	C-4-X.01	220	560	19	36
			LL-3238	03/93	C-4-X.01	480	2632	0	38
			LL-3261	02/93	C-4-X.01	358	3037	0	37
			LL-3267	02/93	C-6-X.01	243	555	1	38
VI	LL-1006	5.3	-	-	-	-	-	-	
VII	LL-833	5.9	LL-1124	02/93	C-4-X.03	250	1204	7	39
			LL-1245	02/93	C-4-X.03	231	1681	1	39
	LL-900	4.2	LL-3059	11/92	C-5-X.16	511	1011	162	41
			LL-3062	03/93	C-5-X.16	253	1262	5	42
			LL-3155	02/93	C-5-X.16	464	1888	0	42
			LL-3284	02/93	C-4-X.03	250	1800	0	38
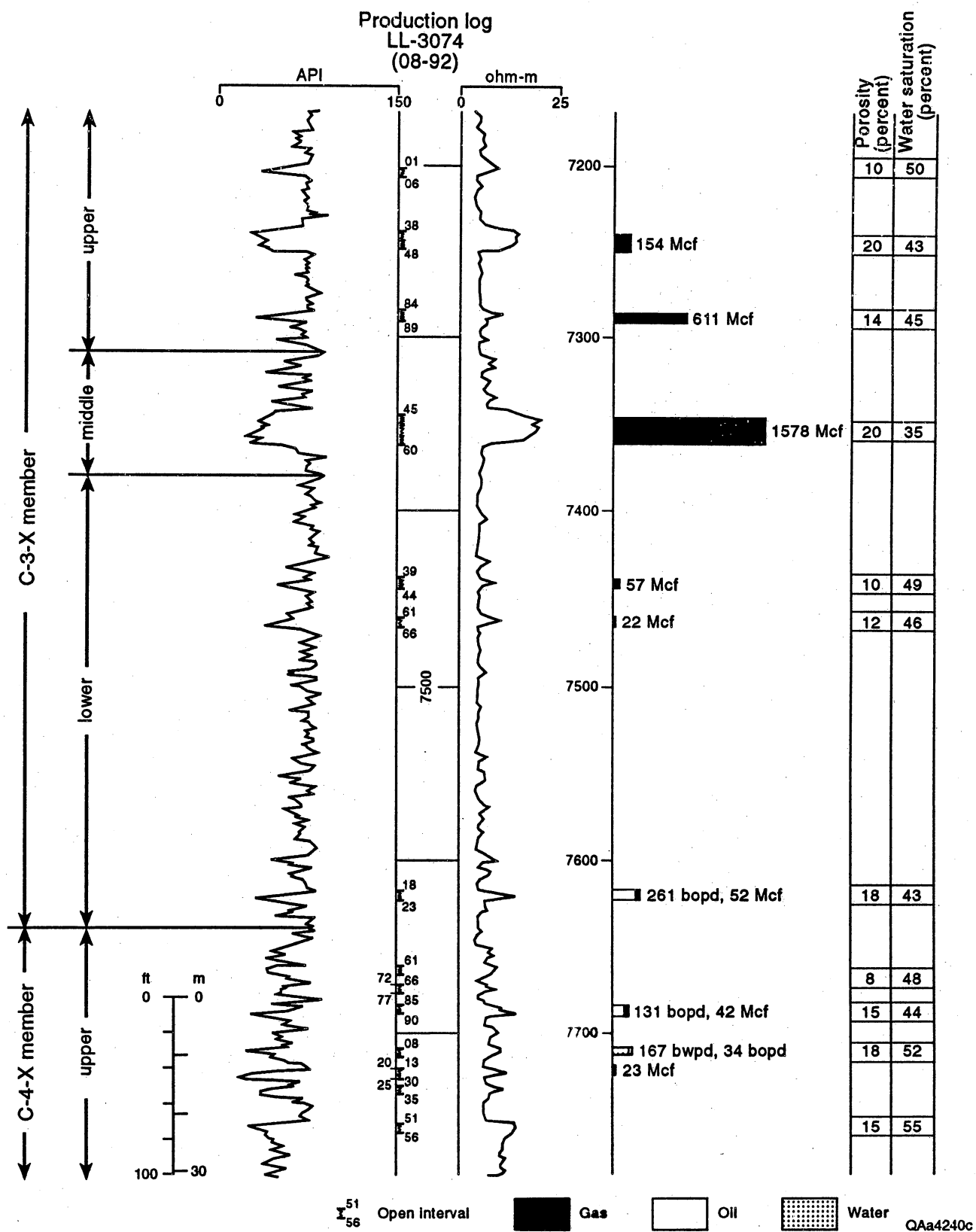
Figure 148. Production log of the LL-3074 well.
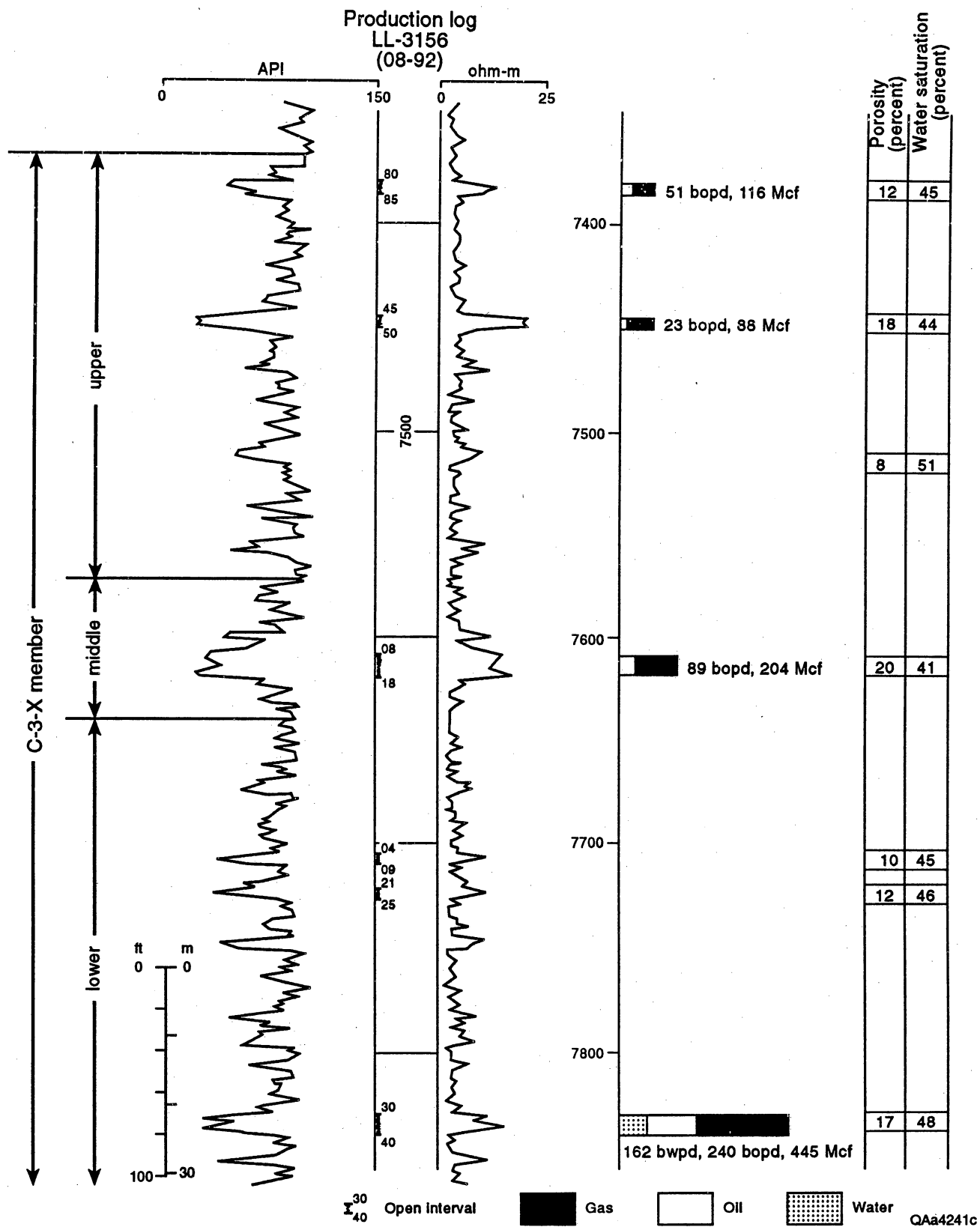
Figure 149. Production log of the LL-3156 well.

Table 46. Kh from pressure tests in wells.

Member	Well	Kh (md•ft)	Average (md•ft)
C-3-X/C-4-X	LL-895	428	590
	LL-1162	337	
	LL-1169	533	
	LL-1293	241	
	LL-1803	1789	
	LL-1876	200	
	LL-2010	997	
	LL-2089	196	
	LL-2094	593	
C-5-X	LL-1111	876	490
	LL-1276	296	
	LL-2905	298	
C-6-X	LL-847	154	155
	LL-1001	185	
	LL-1061	170	
	LL-1095	197	
	LL-1111	149	
	LL-1276	76	

An aquifer exists in the southeastern flank of compartments I, V, and VII. The movement of this aquifer is partially active as inferred from production and pressure data. Water is moving laterally along and subparallel to structural contours and sandstone bodies. There are also multiple oil-water contacts in each member and submember that are poorly defined as a single surface because of high degree of sandstone and mudstone interbedding. Irregular production and lateral stratigraphic changes introduce barriers to the normal movement of the oil-water contacts not parallel with the structure. Therefore, in the absence of data, we assumed that the oil-water contacts are parallel to the structure.

Positions of oil-water contacts were estimated from (1) production history, (2) log analysis (resistivity and density log response by well), (3) water saturation from petrophysical evaluation (maps), and (4) structure and stratigraphy. Original oil-water contacts were revised from interpretations of the log response in older wells located downstructure and from production data. These contacts were also validated from the results of the petrophysical study. Table 47 shows the depths where the original oil-water contacts were interpreted in compartments I, V and VII. Current oil-water contacts were estimated from log response from new wells and production-history analysis.

Middle C-3-X Submember

The Middle C-3-X and Upper C-4-X Submembers contain the best examples in the field of multiple oil-water contact analysis because they are thick, sandstone-rich, and are well-documented with cores and production data. In compartment V the original oil-water contact in the Middle C-3-X Submember was estimated at 8,200 ft because the LL-1060 well (A-253) is located downstructure and contains 70 ft (21.3 m) of net pay from the petrophysical evaluation. The LL-895 well (A-254) shows the lowest oil-saturated sandstone at 8,200 ft. This well has a cumulative production of 1.7 MMbbl in the C-3-X Member and was recompleted with low production. Also, the old LL-866 and LL-971 wells produced 2.7 and 4.1 MMbbl, respectively, from the C-3-X Member. The current oil-water contact in compartment V was defined at 7,850 ft. The production history of the LL-895 well showed the oil-water contact was below 7,800 ft. Also, the newer LL-3235 well (A-254) was drilled 120 ft (36.6 m) upstructure of the LL-895 well and was opened only in the Middle C-3-X Submember (fig. 150) with more than 180 BOPD and only 8 percent water production (BWPD). The LL-1799 well, located in concession A-271, is still producing with moderate potential and shows an oil-water contact at 7,850 ft.

Another good example in the Middle C-3-X Submember is in compartment VII A (table 47). The original oil-water contact was defined at 7,850 ft from the LL-900 well (fig. 151), which has a cumulative oil production of 4.1 MMbbl and is still producing from the C-3-X Member. Also, the LL-1748 well, located 220 ft (67.1 m) downstructure from the LL-900 well, has produced from the Middle C-3-X Submember in low-resistivity sandstones. The current oil-water contact was defined at 7,880 ft from the new LL-3306 well, perforated in low-resistivity sandstones ($\pm$10 ohm-m) (fig. 152) and is producing more than 200 BOPD with only 4 percent water. The LL-3306 well is located at the same level of the LL-900 well, still producing without water, and is 150 ft (45.7 m) downstructure of LL-833 well, which has a cumulative production of 6.0 MMbbl and is still producing oil. Also, the production log of the LL-3156 well (fig. 149) shows that this submember is producing only oil.

Upper C-4-X Submember

The original oil-water contact in compartment V in the Upper C-4-X Submember was defined at 8,120 ft (fig. 153) because the LL-1060 well (A-253) is wet and the LL-895 well (concession A-254) contained original residual oil at 8,150 ft, inferred from the log response and petrophysical evaluation. The current oil-water contact in compartment V was defined at 7,800 ft mainly from the production history of the high-producing LL-1987, LL-866, LL-1876, LL-2089, and LL-2191 wells, but the water contact has reached these wells, especially the LL-1987 well located downstructure at 7,800 ft. The original oil-water contact in

Figure 47. Oil-water contacts (subsea depths).

		COMPARTMENT							
		I (FT)		V (ft)		VII A (North) (ft)		VII B (South) (ft)	
Member	Sub-M	Original	Current	Original	Current	Original	Current	Original	Current
C-3-X	U	7900	7750	8000	7800	7900	7800	7700	7500
	M	8000	7900	8200	7850	7950	7880	7850	7700
	L	8000	7900	8000	7850	7950	7800	7850	7700
C-4-X	U	8200	8080	8120	7800	7980	7950	8080	7950
	M	8150	8100	8200	7850	7950	7850	8000	7900
	L	8200	8150	8100	7950	7950	7900	8000	7900
C-5-X	U	8500	8400	8300	8200	8350	8300	8400	8300
	U•Mid	8500	8400	8300	8150	8350	8300	8400	8300
	L•Mid	8450	8350	8300	8150	8350	8300	8400	8350
	L	8450	8400	8250	8100	8300	8250	8350	8300
C-6-X	U•Up	8900	8850	8850	8750	8900	8900	9000	8950
	L•Up	8900	8850	8850	8750	8900	8900	9000	8450
	M	8850	8800	8850	8750	8900	8900	9050	9000
	U•Low	9200	9150	9100	9050	9200	9200	9200	9150
	L•Low	9200	9200	9100	9050	9200 Prosp. Arbitrary	—	9200 Prosp. Arbitrary	—
C-7-X		—	—	9300	9300	—	—	—	—
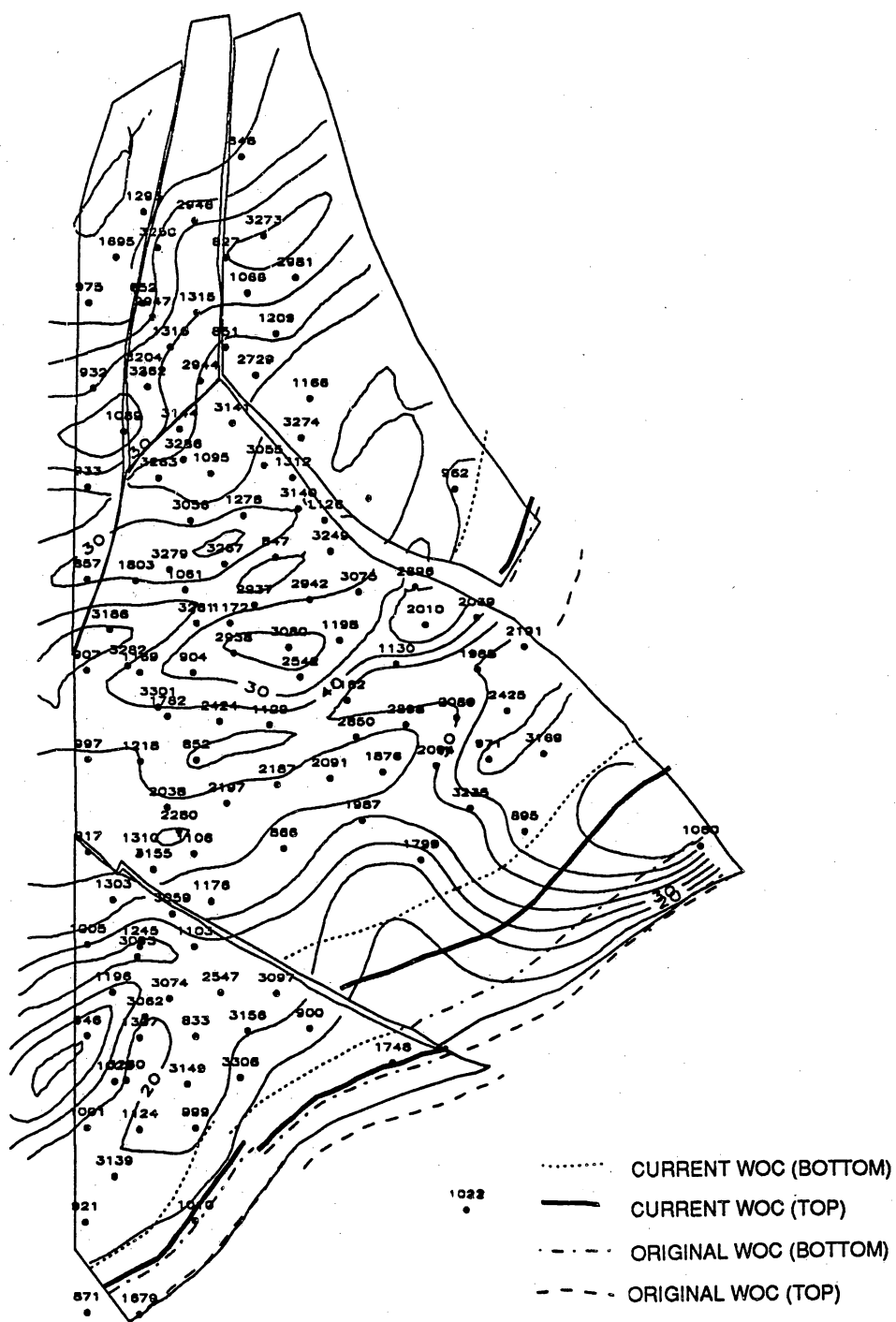
Figure 150. Original and current oil-water contacts in the Middle C-3-X Submembers.
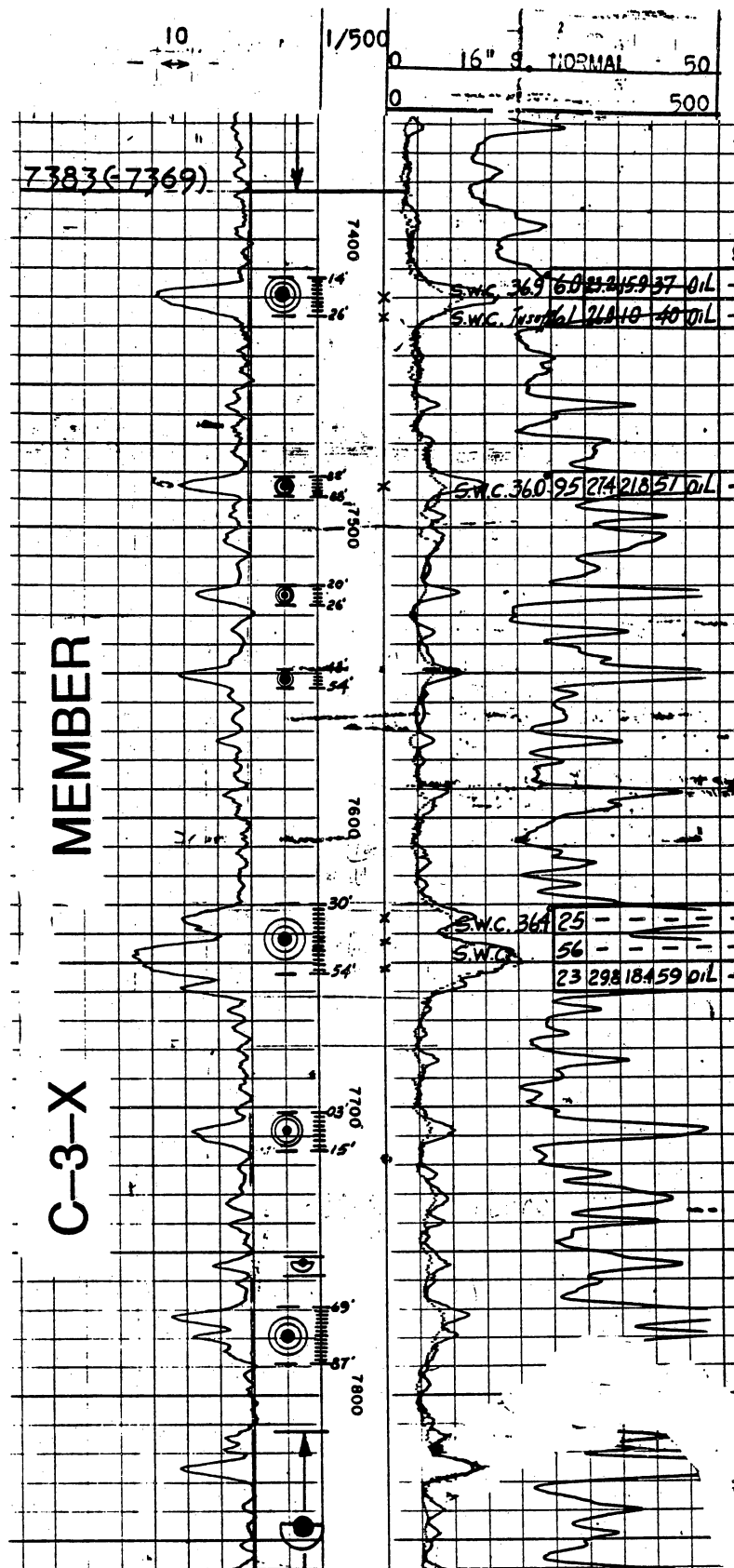
Figure 151. Open intervals in low-resistivity sandstones in the LL-900 well.
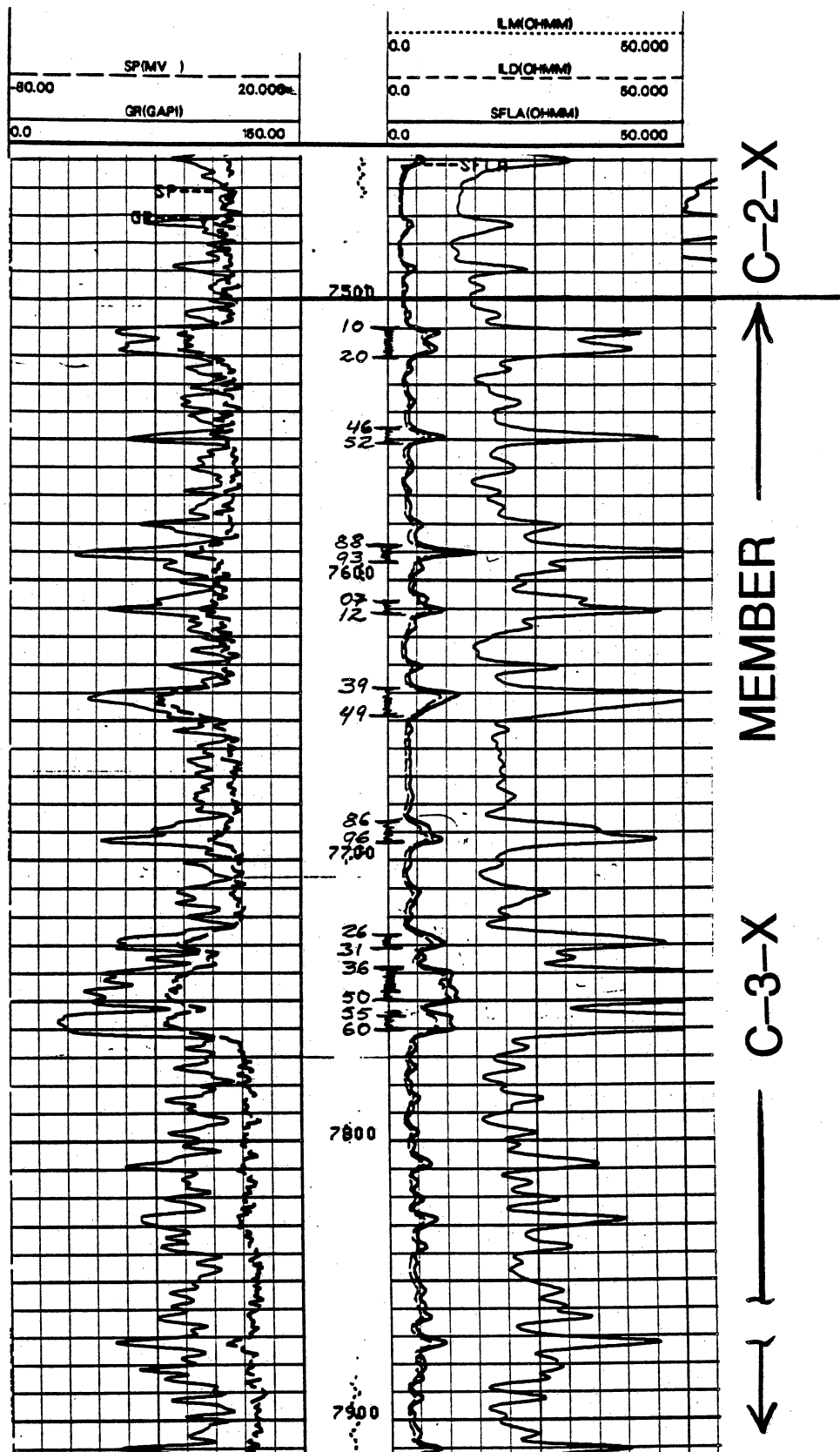
Figure 152. Open intervals in low-resistivity sandstones in the LL-3306 well.
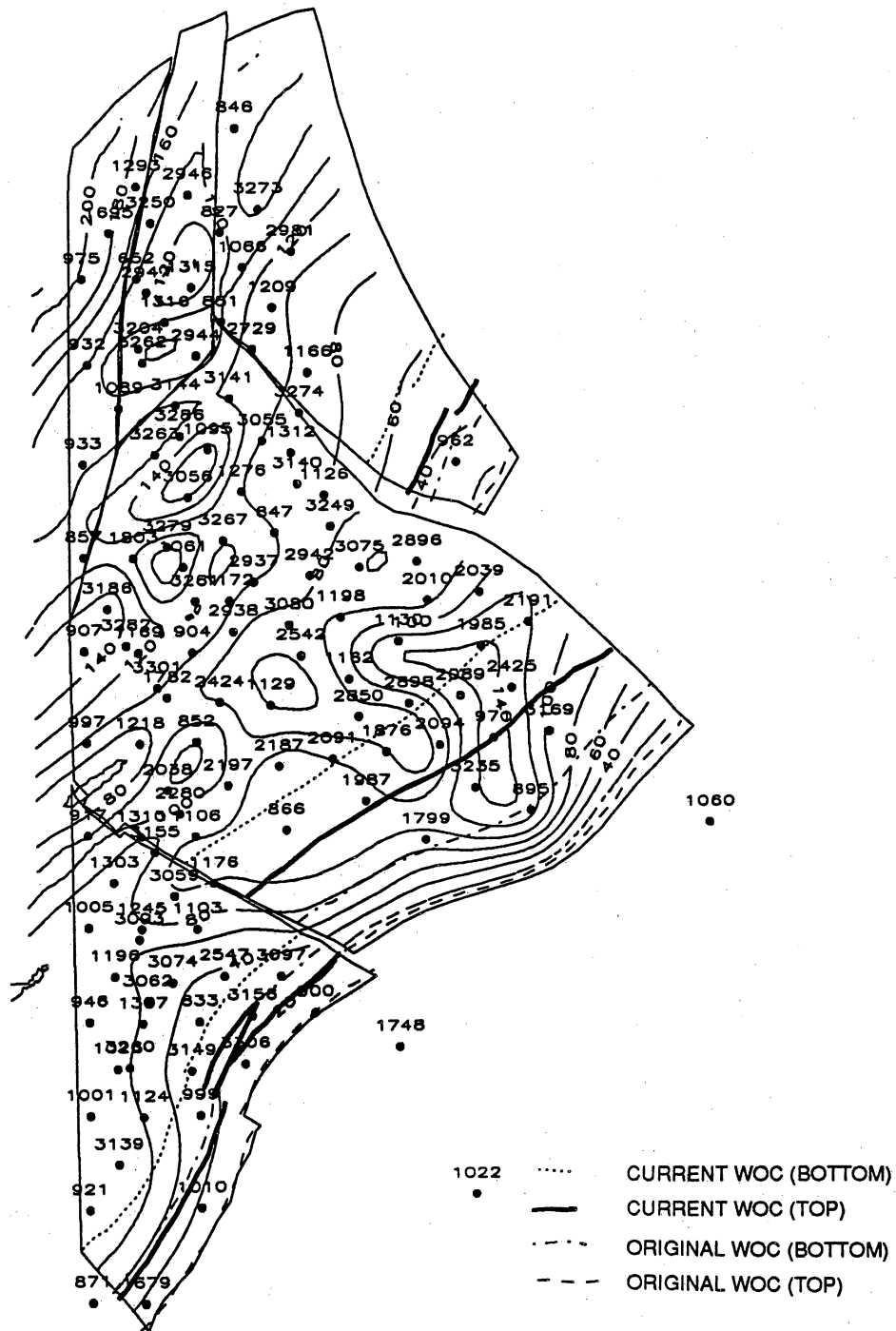
Figure 153. Original and current oil-water contacts in the Upper C-4-X Submember.

compartment VII A (north) was defined at 7,980 ft because the LL-900 well (A-274) is totally wet in this member and the top of the lowest oil sandstone was interpreted at 7,950 ft. The LL-833 well also shows a wet zone below 7,950 ft. The current oil-water contact is irregular but is interpreted at an average depth of 7,950 ft, because the newer LL-3149 well shows a contact at this level. The LL-3156 well (A-273) shows different internal levels of oil-water contacts in this submember that were interpreted at an average of 7,950 ft.

An additional area in the C-4-X.01 and C-5-X.02 reservoirs (compartment V) is now recognized because the original (official) oil-water contact was estimated too shallow. The Middle C-3-X Submember (part of the C-4-X.01 reservoir) has the old contact interpreted at 7,800 ft; with the new interpretation it is at 8,200 ft (cf. figs. 150 and 154). However, the Upper-Middle C-5-X.02 original oil-water contact is at 8,090 ft, and with the reinterpretation it is now inferred to be at 8,300 ft. Also, we recognize an additional area in the C-4-X.03 and C-5-X.16 reservoirs (compartment VII). For example, the original (official) oil-water contact was estimated in the Middle C-3-X Submember at 7,720 ft; with the new interpretation it is at 7,950 ft.

Low-Resistivity Sandstones

As part of the production analysis, a general review of wells producing from low-resistivity sandstones was made as a preliminary step for the petrophysical evaluation and consisted of identifying the open low-resistivity interval in each member with water production less than 5 percent to ascertain which intervals are producing oil. Table 48 is a summary of all producing wells with low-resistivity sandstones. The resistivity cutoff in the C-3-X and C-4-X Members was determined to be 10 ohm-m, and in the C-5-X Member it was determined to be 10-12 ohm-m. The resistivity cutoff in the C-6-X Member (14 ohm-m) was calculated from production logs. Also, the C-3-X, C-4-X, and C-5-X Members were validated by production logs. The LL-900 well (fig. 151) is an example of an old well of open intervals in low-resistivity (less than 10 ohm-m) sandstones in the C-3-X Member. The LL-3306 well (fig. 152) is a new example that shows open intervals with 10 ohm-m in the Upper and Middle C-3-X Member. This well is producing 220 BOPD with only 4 percent water (7 BWPD).

Table 48. Cutoff values for low-resistivity sandstones in the C Members.

Member	Well	Open Interv.	Low-Resist. Interval (ft)	Resistivity (OHM-M)	Production BOPD	GOR	Water %	Date	Comments
C-3-X C-4-X	LL-866	7214-7718 7746-7900	(several) 7746-60 7827-7837	10 10 10	281 186	772 1323	4.4 1.0	01/65 05/73	Production is from all the intervals.
	LL-900	7414-7787	7520-7526 7548-7554 7703-7715 7769-7787	10 10 12 12	923 455	961 1308	0.3 4.0	05/55 10/88	Still producing from original intervals.
	LL-904	6750-7720	6750-6755 7667-7673 7687-7697	10 13	940 520	1640 1269	0.0 0.0	01/63 09/85	
	LL-971	7424-7592	7424-7429 7460-7475	13 10	1008	658	0.0	04/57	Still producing 223 BOPD and 0.1% water.
	LL-1106	7087-7516	7087-7092 7414-7419	11	319	1749	5.0	03/78	
		7615-7800	7615-7640 7790-7800	12	1509	1074	0.1	04/63	
	LL-1124	7262-7830	7298-7323(2) 7534-7627(2) 7533-7538	11 11 12	1158 1151	1852 1033	1.2 0.4	10/72 09/62	
	LL-1126	7154-7703	7358-7458 (4 intervals)	11	2534	807	1.0	08/62	
	LL-1130	7508-7770	(9 intervals)	10-13	2189	946	1.6	10/62	
	LL-1159	7272-7816	7272-82 7224-7396(3) 7537-7559(2) 7727-7816(3)	11 10	1003 292	1512 8705	0.4 0.8	08/63 08/82	
	LL-1162	7504-7910	9 intervals	11-13	1321	1272	0.0	04/63	11/73 (310 BOPD, 0.2% water)
	LL-1192	7339-7756	6 intervals	11-12	1259	1050	0.4	12/63	08/87 (190 BOPD, 0.4% water)
	LL-1307	7323-7656	5 intervals	12	1014	1839	0.0		

Table 48. Continued.

C-3-X C-4-X	LL-1748	7634-7768	7670-7675 7748-7768	8-10	335	1391	5.0	05/73	
	LL-1799	7455-7820	7 intervals	8-12	459	915	0.0	06/72	
	LL-2039	7656-7861	7825-7830 7856-7861	12	328	1622	0.2	02/77	
	LL-2094	7402-7708	4 intervals	10	631	1464	0.0	04/78	03/86 (76 BOPD, 2.4% water)
	LL-2280	7472-7780	4 intervals	8-10	793	1280	0.3	11/79	
	LL-2424	6910-7380	5 intervals	10-12	148	8628	2.6	08/85	
	LL-2547	7362-7747	6 of 7 intervals	10-12	739	1138	3.4	12/81	Good example.
	LL-2850	7281-7591	All intervals (8)	10-12	85	3765	4.2	05/84	Cored well.
	LL-3306	7510-7744	4 of 5 intervals	9-12	224	480	4.0	03/93	The best example.
			C-3-X/C-4-X AVERAGE	10					
C-5-X	LL-946	8240-8560	8240-8256 8303-8310 8323-8328 8375-8380	10 12					The water production was less than 5%.
	LL-1001	8150-8622	8525-8540 8555-8575	12-13					High rate of oil with only 4% of water.
	LL-1126	7780-8063	7813-8063 (7 intervals)	12	461	1534	2.0	08/62	
	LL-1303	8016-8216	8016-8030 8135-8140	12-13	175	3657	1.2	08/80	11/87 (118 BOPD and 1.0% water).
	LL-2901	7771-8097	4 of 7 intervals	11	201	3761	0.7	02/86	04/91 (176 BOPD and 0.0% water).
			C-5-X AVERAGE	12					

Figure 154. Official net-pay map of the Middle C-3-X Submember with reservoir extensions.
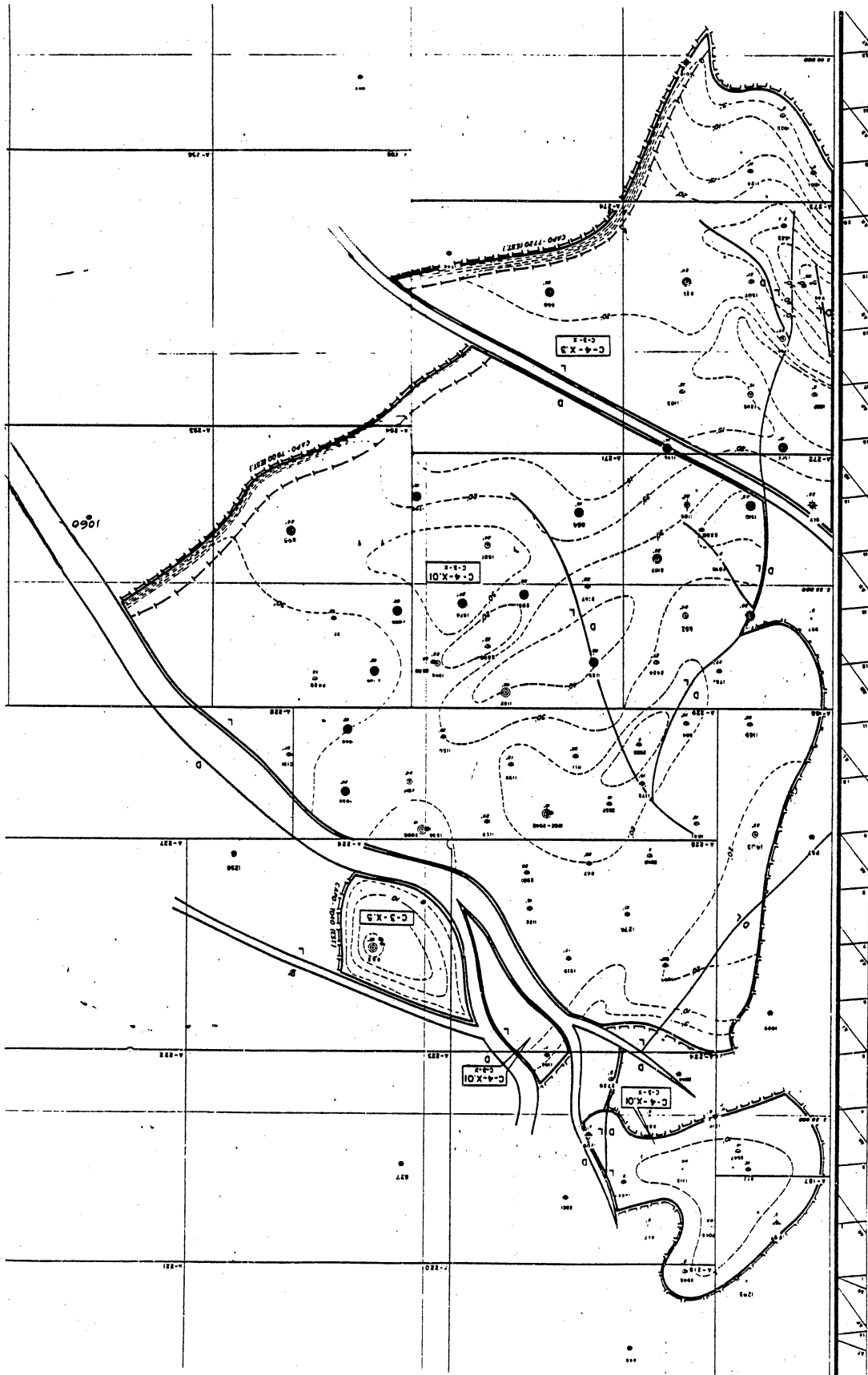
IX. PETROPHYSICS

Petrophysical characterization of the LL-652 area was accomplished through integrating core and log data, quantifying petrophysical properties from wireline logs and validating petrophysical properties by net-sandstone thickness and log facies maps, all ultimately leading to the calculation of reservoir volumetrics (fig. 155). One problem was the limited number of good porosity logs because of severe borehole washouts. This difficulty was successfully resolved by developing transforms between porosity and shale volumes determined from gamma-ray and resistivity logs.

Data Integration

Data integration consisted of building a core and log database and normalizing the data. TerraStation, a log analysis software package from Terra Science Corporation, was used to store the database and to perform well-log analysis. One hundred forty-five digitized well logs were transferred from Lagoven into TerraStation on the Bureau's computers. After a review of the digitized data, 47 wells were eliminated because of missing or anomalous curves. Of the remaining 98 well logs, 65 wells were determined to have complete electric and porosity log suites including SP, GR, caliper, neutron, density, and shallow- and deep-resistivity curves, and the other 33 wells had only the electric logs including SP and short and long normal curves. Core data were available in six key wells: LL-2850, LL-3074, LL-3075, LL-3080, LL-3140, and LL-3282 (fig. 6).

Standardization of log data and depth adjustment were required to normalize data. The sources of differences in logs were tool malfunction, inconsistent shop and field calibration, and the fact that wells were logged by different operators and logging companies. In the LL-652 area, wells were logged by five different companies over a period of 40 years. Differences in gamma-ray data have been observed. After a review of histograms of gamma-ray logs, we determined that differences were not necessarily caused by different company approaches. Figure 156a shows histograms of GR of the C-3-X Member from the LL-3074 and LL-3080 wells. Although both wells were logged by Schlumberger, the difference in these histograms is clear. When the volume of shale (V_{sh}) was used, the GR log was normalized on an individual well basis and the fieldwide standardization of gamma-ray logs became unnecessary.

Standardization of density-log data was not attempted because the variability in histograms of density data (fig. 156b) could have been caused by complex depositional facies. However, density-log data in the LL-2850 well were abnormally high. Core data from this well were used to correct the density-log data. A grain density of 2.9 g/cm^3 was required to match core porosity, whereas the mean grain density of 2.67 g/cm^3 from core data (fig. 157) was the same as from other cored wells. The abnormal density-log data were caused by overcorrection of the borehole effect. Therefore, a correction was made by subtracting 0.1 g/cm^3 from the original density-log values.

Depth adjustments were necessary because of differences in data depths from logging suites and core depth. Because of severe borehole washouts, porosity logs could not be used for depth shifting. Depth shifting between porosity and electric logs was done by mainly matching GR and SP curves or in some cases by matching GR and resistivity logs with high-quality SP logs. In the cored wells, depth shifting of core data versus log data was accomplished by comparing GR logs between core and log (table 49). For the LL-3140 well the core depth was shifted by 54 ft (16.5 m) because of differences in the core-gamma and GR logs (fig. 158).

Petrophysical Models and Key Well Evaluation

The objective in petrophysical characterization was to develop field-specific models for evaluating petrophysical properties from wireline logs. For shaly-sand log analysis, factors such as availability of porosity logs, core data, formation-water salinity and its variability, type and distribution of clay, and V_{sh}
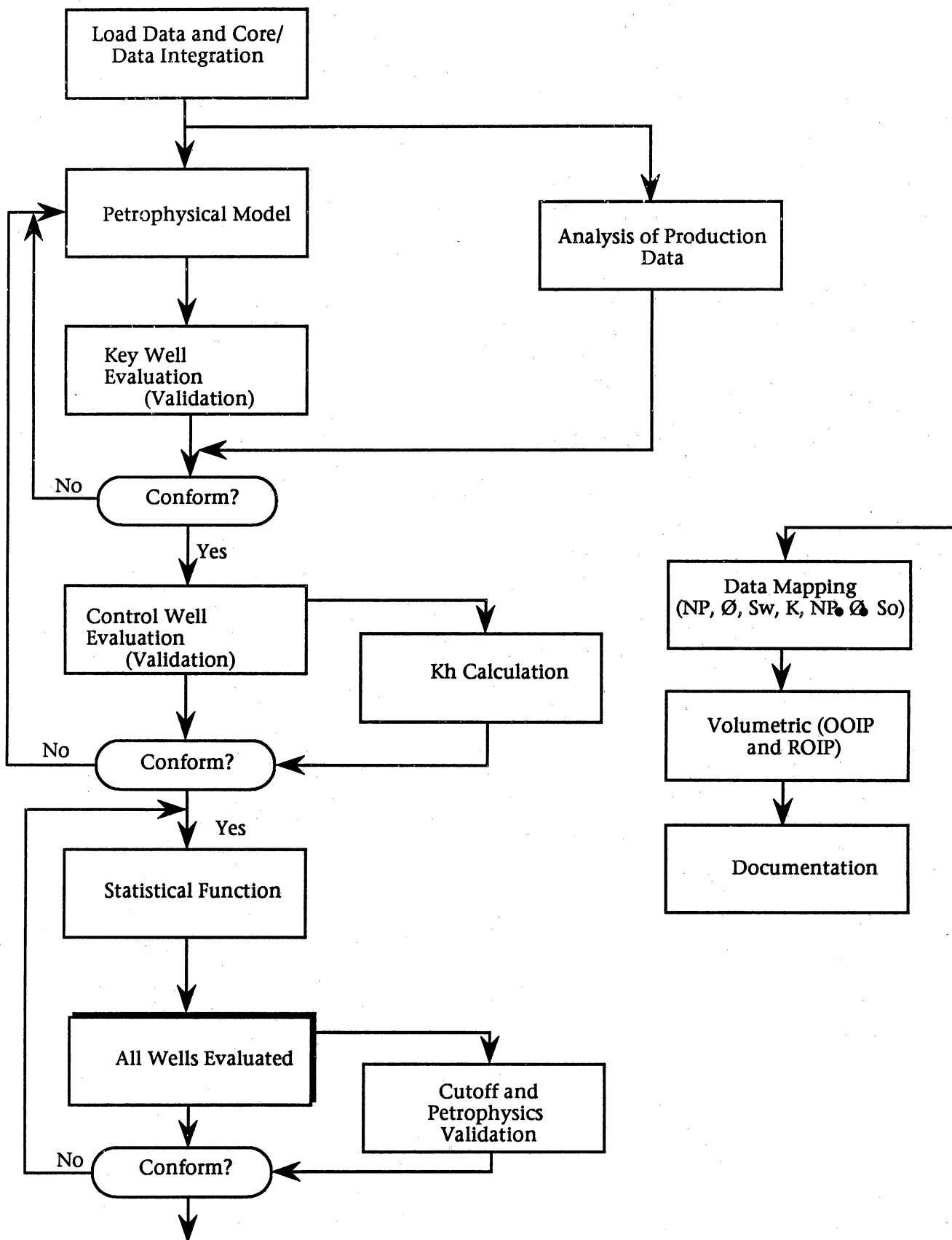
Figure 155. Flow chart of procedures for petrophysical characterization and volumetric calculations.
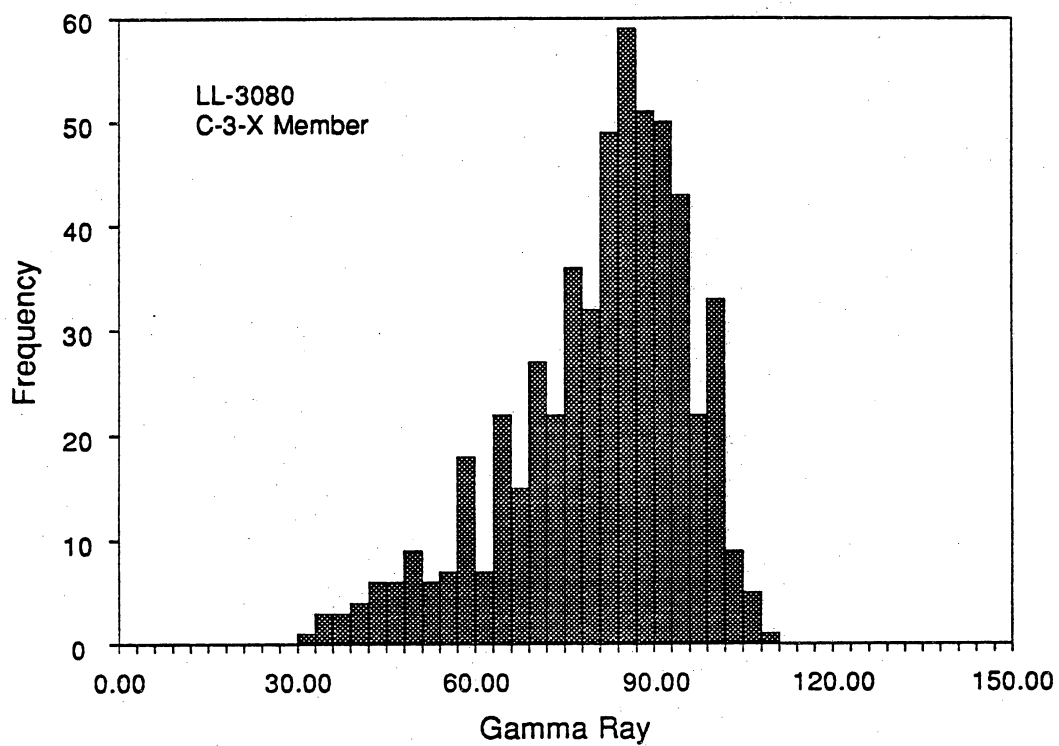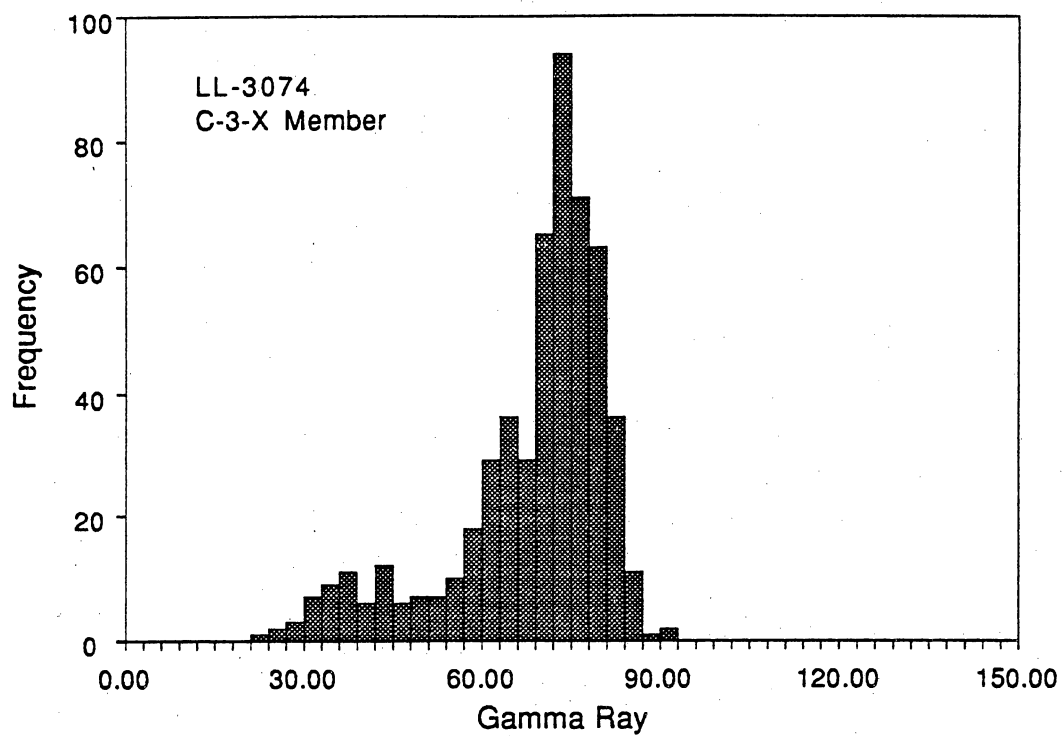
Figure 156. (a) Histograms of gamma-ray values from Schlumberger logs in the LL-652 area.
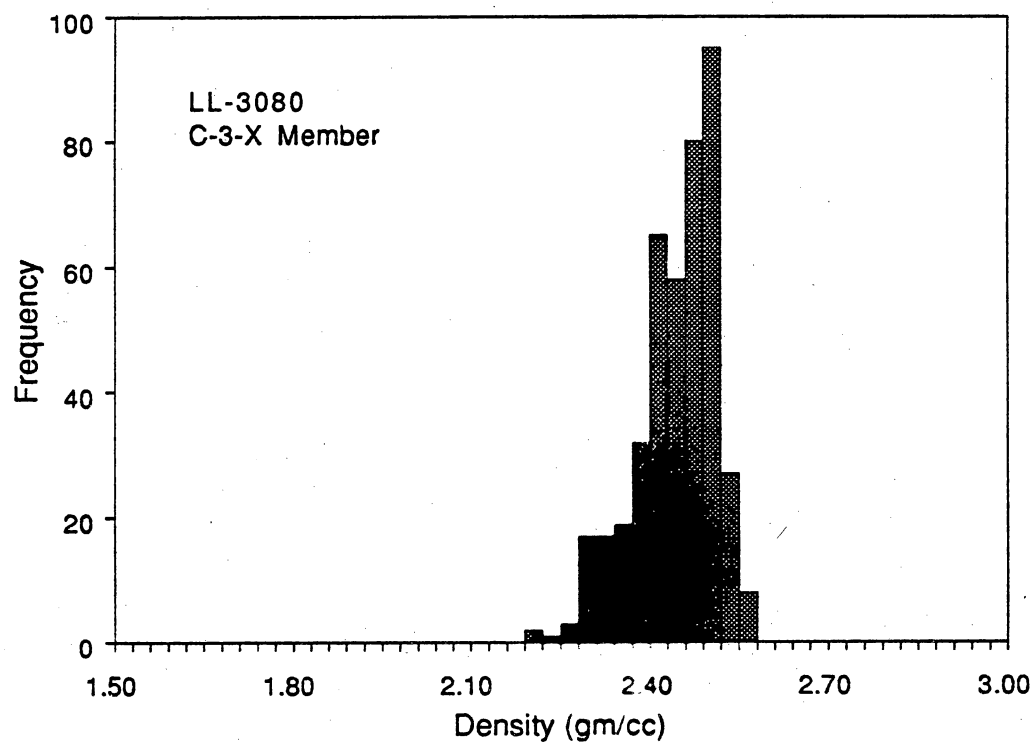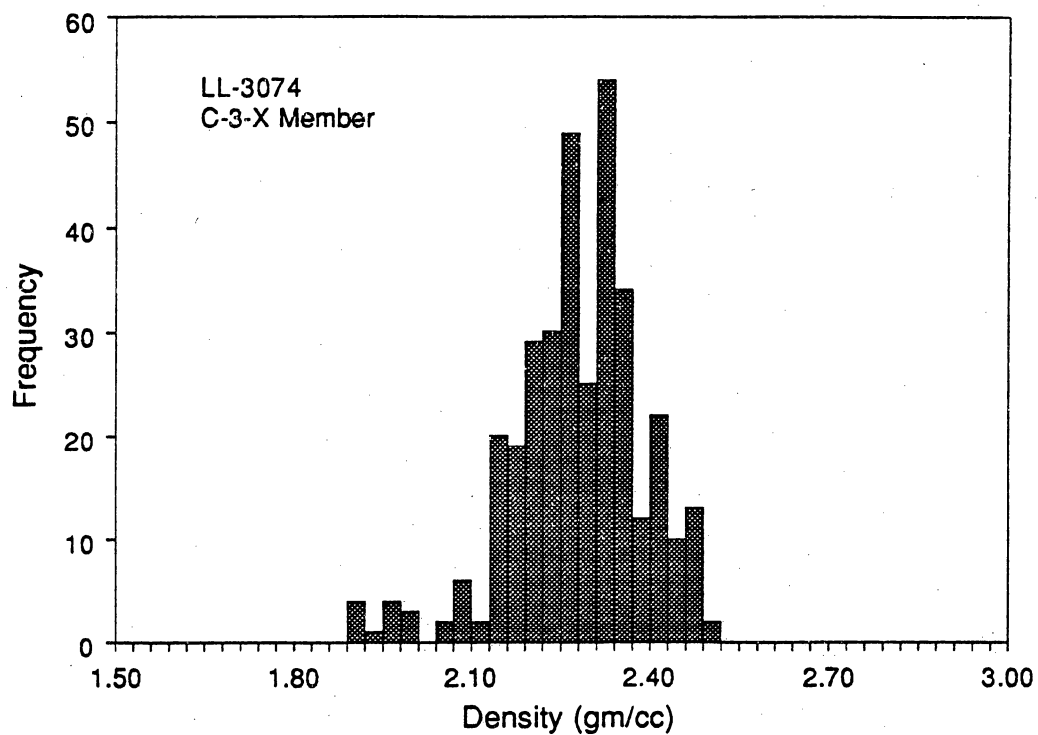
Figure 156. (b) Histograms of density-log values in the LL-652 area.
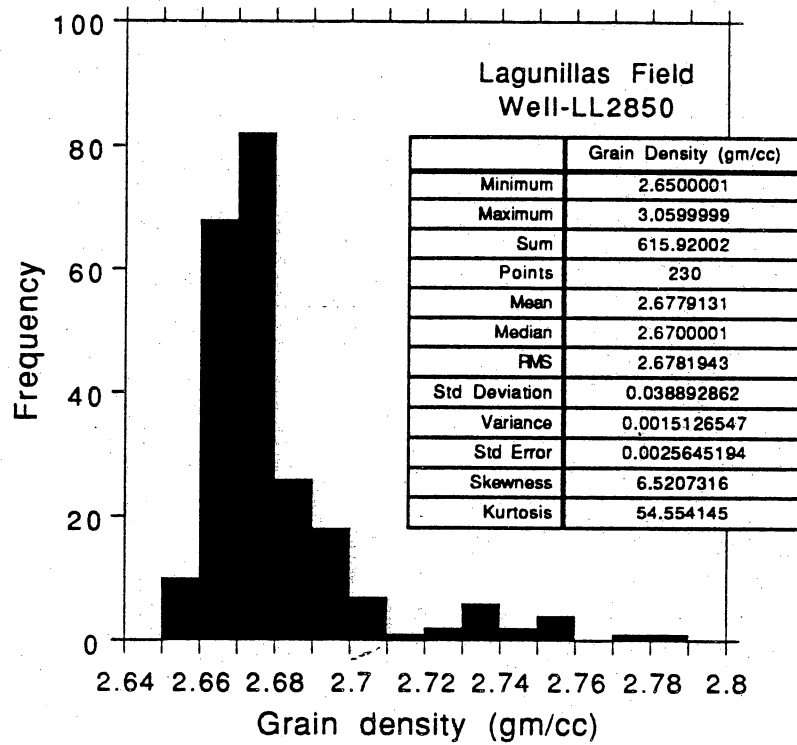
Figure 157. Histogram of core grain density with a mean of 2.68 g/cm^3 and a median of 2.67 g/cm^3.

Table 49. List of shifts in core depth in key wells.

Cored Well	Member	(1) Core-Depth (ft)	(2) Log-Depth (ft)	(2)-(1) (ft)	(3) Special Analysis (ft) (Core-Gamma/Ø, k)	(2)-(3) (ft)	Comments
LL-2850 (core lab)	C-3	7240-4362	7258-7274 7275-7322 7323-7374	18 14 12	7240-7256 7261-7308 7311-7362	18 14 12	
	C-4	7590-7898	7602-7620 7621-7776 7777-7846 7851-7910	12 10 8 12	7590-7608 7611-7766 7769-7838 7839-7898	12 10 8 12	
LL-3074 (core lab)	C-3	7240-7376	7240-7376	0	7240-7340 7341-7366 7367-7376	0 -2 0	
	C-4	7535-7775	7535-7775	0	7535-7775	0	
LL-3075 (Inpeluz)	C-5	7882-8452	7869-8439	-13	7871-7980 7981-8030 8031-8100 8101-8230 8231-8260 8261-8320 8321-8360 8361-8440	-2 -3 -2 0 -2 -1 0 -1	
LL-3080 (Inpeluz)	C-6	8633-9280	8651-9298	18	8650-8670 8671-8990 8991-9160 9161-9295	1 0 2 3	
LL-3140 (core lab)	C-6/C-7	8820-8948	8859-8882 8887-8992	39 43	8820-8843 8844-8948	39 43	
		8971-9203	9025-9257	54	8971-9203	54	
LL-3282 (core lab)	C-4	7280-7440	7275-7340 7344-7412 7412-7436	-5 -2 -4	7280-7345 7346-7414 7416-7440	-5 -2 -4	
	C-5	7920-8134	7918-8053 8055-8084 8086-8134	-2 -1 0	7920-8055 8056-8085 8086-8134	-2 -1 0	
	C-6	8670-8990	8668-8714 8715-8780 8782-8844 8846-8930 8931-8988	-2 -3 -2 -1 -2	8670-8716 8718-8783 8784-8846 8847-8931 8933-8990	-2 -3 -2 -1 -2	

Figure 158. Core gamma-ray log versus well gamma-ray log in the LL-3140 well.

and heavy minerals were determined as important parameters for selecting and developing petrophysical models for calculating porosity, permeability, and water saturation. Petrophysical models were determined by calibrating log with core data. The lack of good porosity logs as a consequence of severe borehole washouts made petrophysical characterization of LL-652 area especially difficult. Porosity, the key parameter required in petrophysical characterization, was derived indirectly from nonporosity logs such as GR, SP, and resistivity. The petrophysical models of LL-652 area were developed from a total of approximately 1,500 core data points and wireline logs in six key wells.

Model for Calculating Shale Volume (V_{sh})

The V_{sh} model was important for water saturation and porosity calculations for LL-652 area. Figure 159 shows the models for calculating shale volume from gamma-ray index (Hilchie, 1989). The gamma-ray index of shale volume (I_{GR}) is defined as

$$I_{GR} = \frac{GR - GR_{min}}{GR_{max} - GR_{min}}$$

(1)

where GR, GR_{min}, and GR_{max} are the gamma-ray values at well log depth, clean sandstone, and shale. The linear model is $V_{sh} = I_{GR}$, and the Johnson and Linke model (1978) for Tertiary deposits is nonlinear. Johnson and Linke's model (1978) was developed by calibrating I_{GR} with total V_{sh} values estimated from thin sections. In this study, thin sections were taken only in clean sandstones, and hence estimated V_{sh} values were not available in shaly intervals. The linear model was selected because both porosity and water saturation values derived from a linear model have a better match to core porosity, permeability, and water saturation.

Porosity Model (V_{sh}-Porosity Transforms)

Shale volume is solely a function of gamma-ray index. However, in the C members, there is a general trend of decreasing porosity with depth as a result of compaction and diagenesis (an increase in quartz overgrowths with depth). To account for this depth effect, V_{sh}-porosity transforms were developed for each member.

We used both core porosity and density porosity to develop V_{sh}-porosity transforms. Core porosity is biased toward clean sandstones, and density porosity is affected by borehole washouts. Since washouts are more serious in shaly intervals than in sandy intervals, good porosity data, obtained after filtering density porosity from caliper and porosity cutoffs, are also biased toward clean sandstones. Crossplots of V_{sh} versus core porosity and density porosity for the C-3-X to C-7-X Members are shown in figures 160 to 165. Although the data points are scattered, a trend of increasing porosity with decreasing V_{sh} can be defined in the C-3-X to C-7-X Members. Because both core and density porosities are biased toward sandstones, the relationships between V_{sh} and porosity (fig. 166) were determined initially by linear regression from the Reduced-Major-Axes (RMA) method and subsequently by adjusting the slope of the regressed lines to match foot-by-foot core porosities and permeabilities in the key wells. Because permeability is highly sensitive to the error in porosity estimation and because porosity obtained from the V_{sh}-porosity transforms depends on GR_{min} and GR_{max} values, GR_{min} and GR_{max} can be adjusted slightly to approach core porosity and permeability. The final equations developed for the V_{sh}-porosity transforms are

$$\phi = \frac{1.20 - V_{sh}}{4.5}$$

(2)

for the C-1-X to C-3-X Members,

$$\phi = \frac{1.20 - V_{sh}}{5}$$

(3)
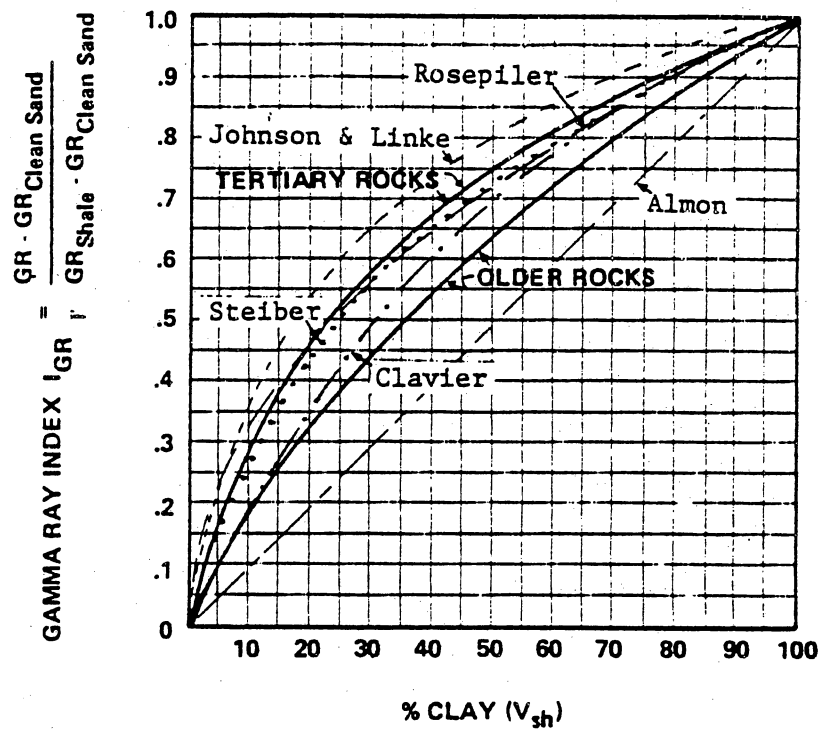
Figure 159. Model for calculating V_{sh} from gamma-ray logs. After Hilchie (1989).
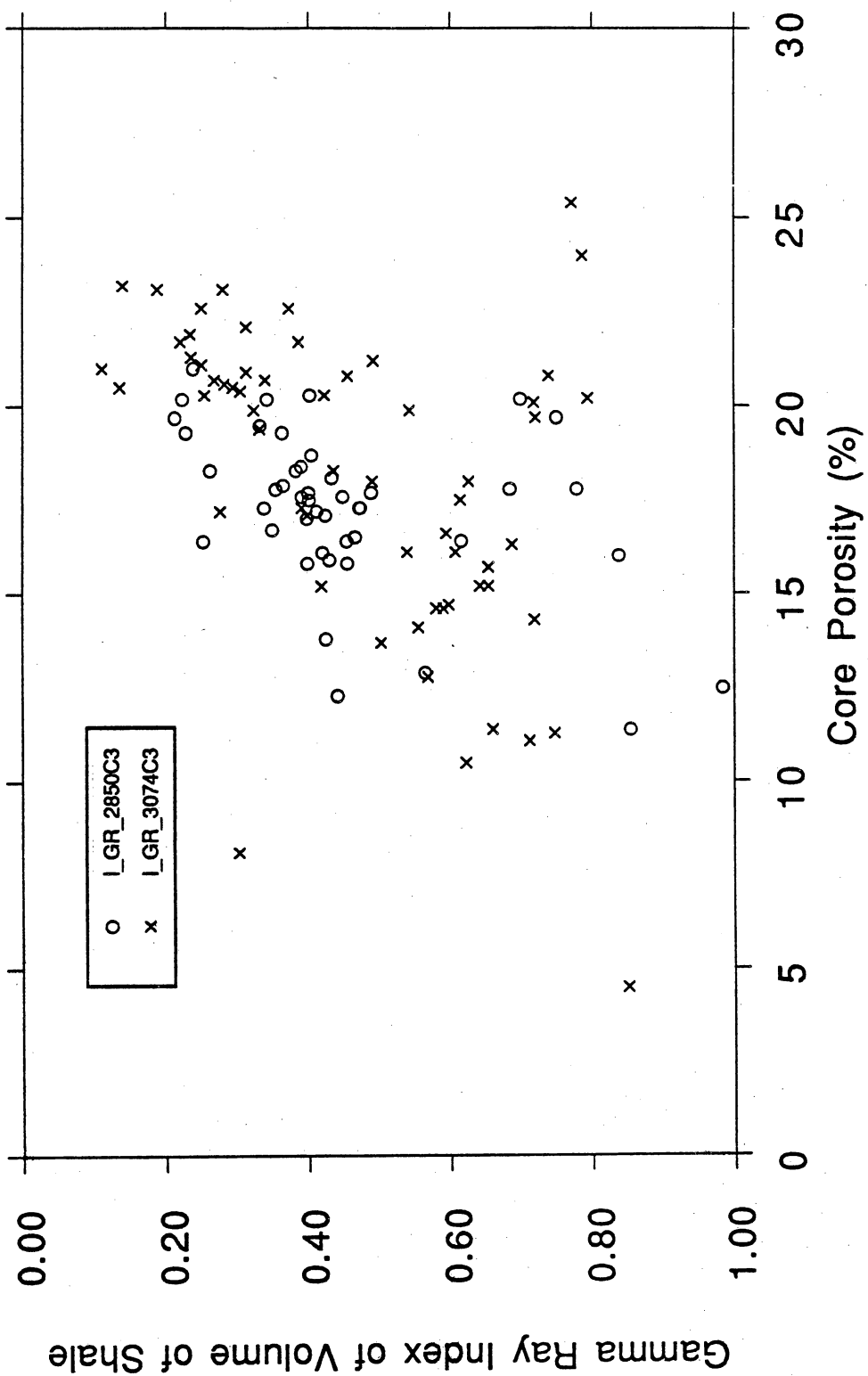
Figure 160. (a) Gamma-ray index versus core porosity of the C-3-X Member showing porosity decreasing with increasing V_{sh}.
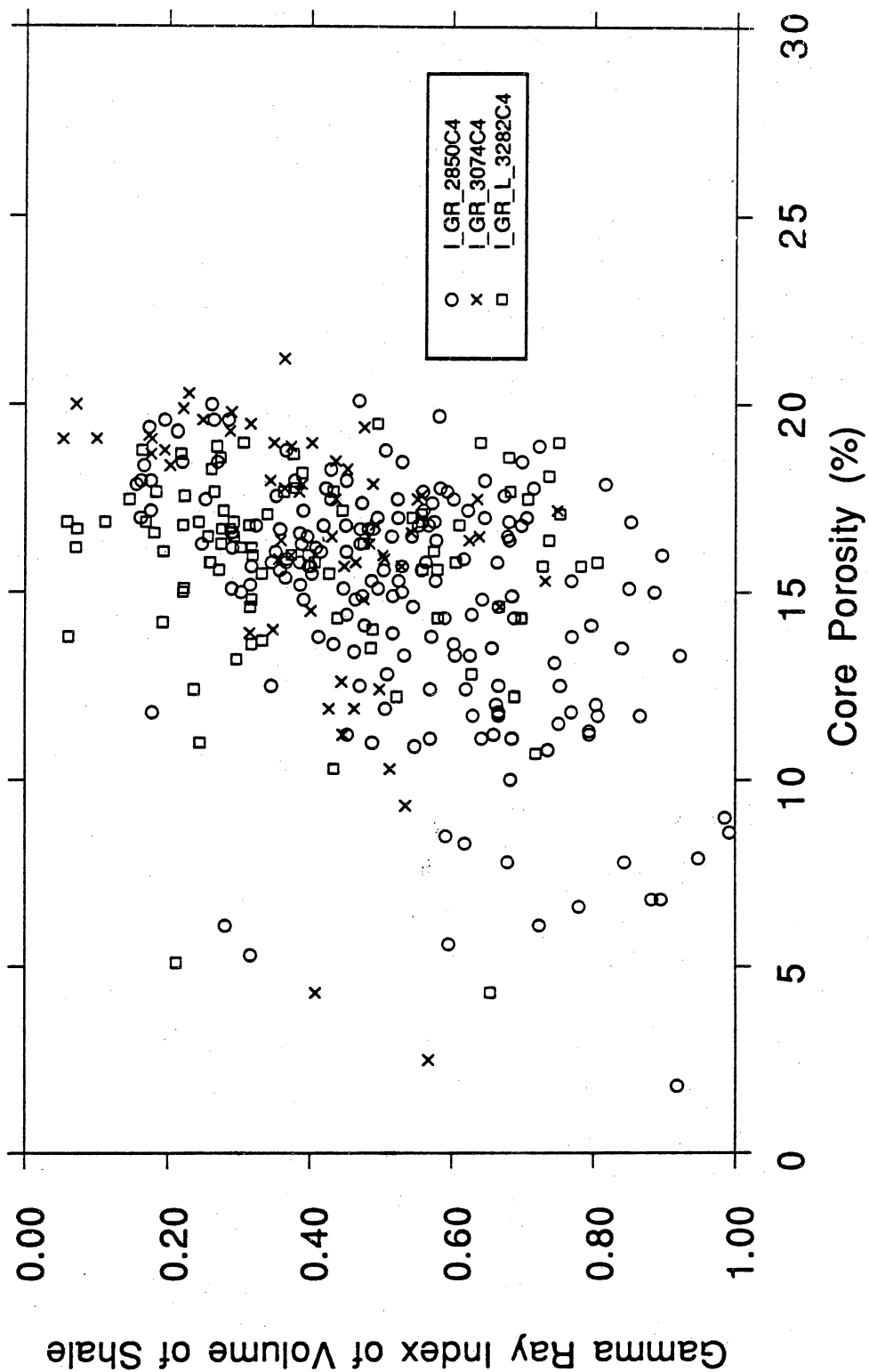
Figure 160. (b) Gamma-ray index versus core porosity of the C-4-X Member. Although data points are scattered, there is a trend of porosity decreasing with increasing V_{sh}.
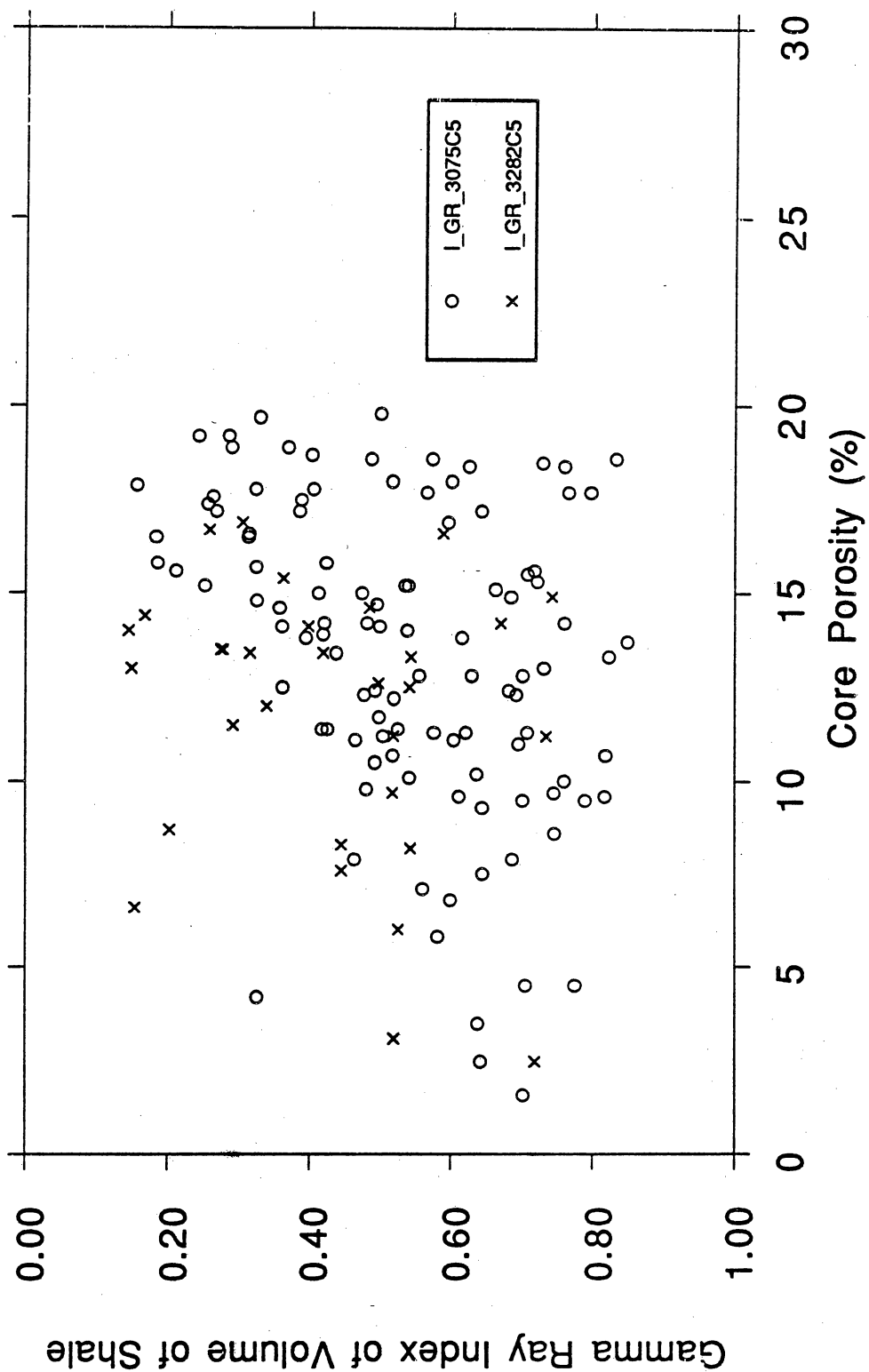
Figure 160. (c) Gamma-ray index versus core porosity of the C-5-X Member. There is no apparent trend of porosity decreasing with increasing V_{sh}.
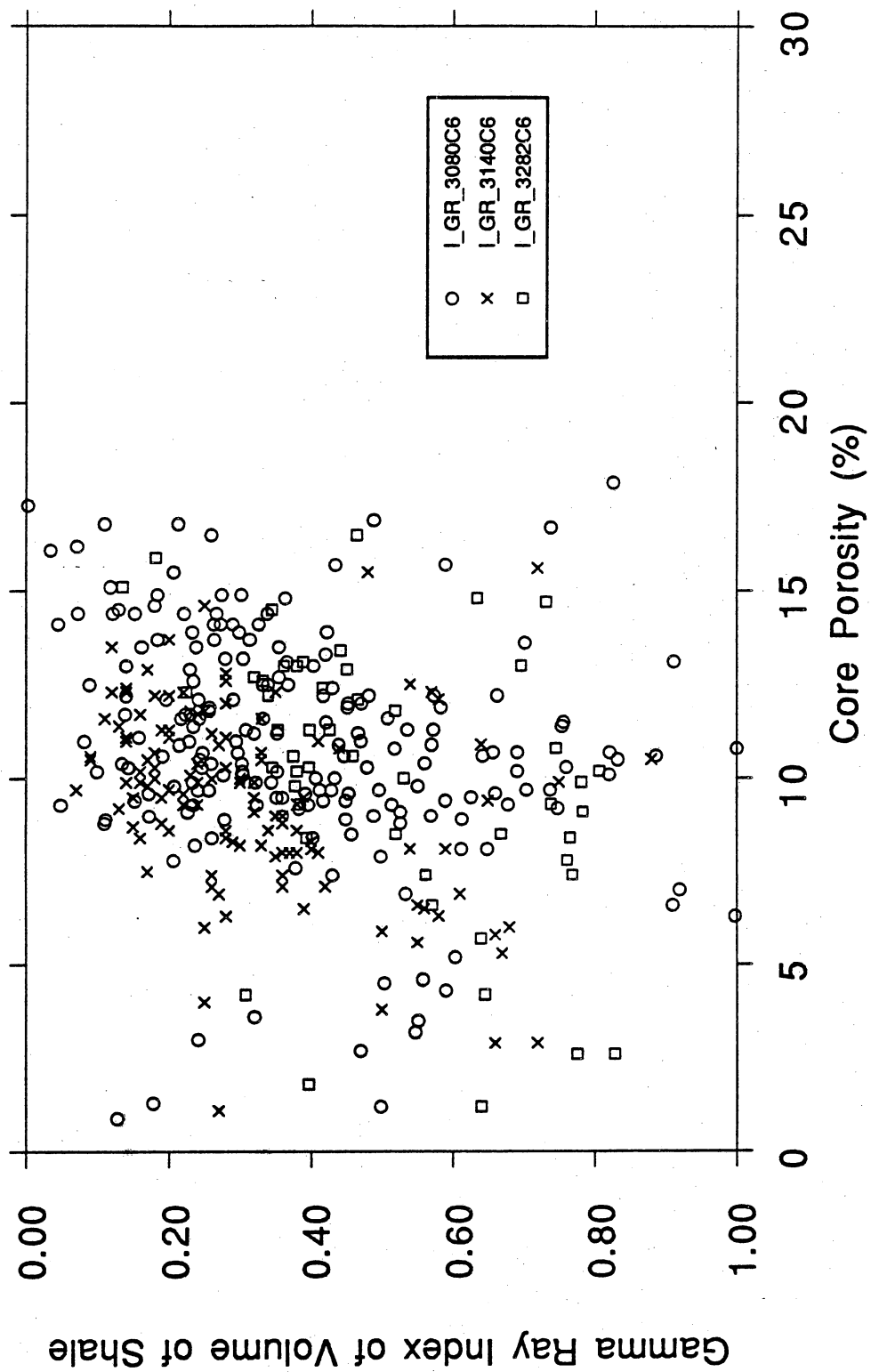
Figure 160. (d) Gamma-ray index versus core porosity of the C-6-X Member.
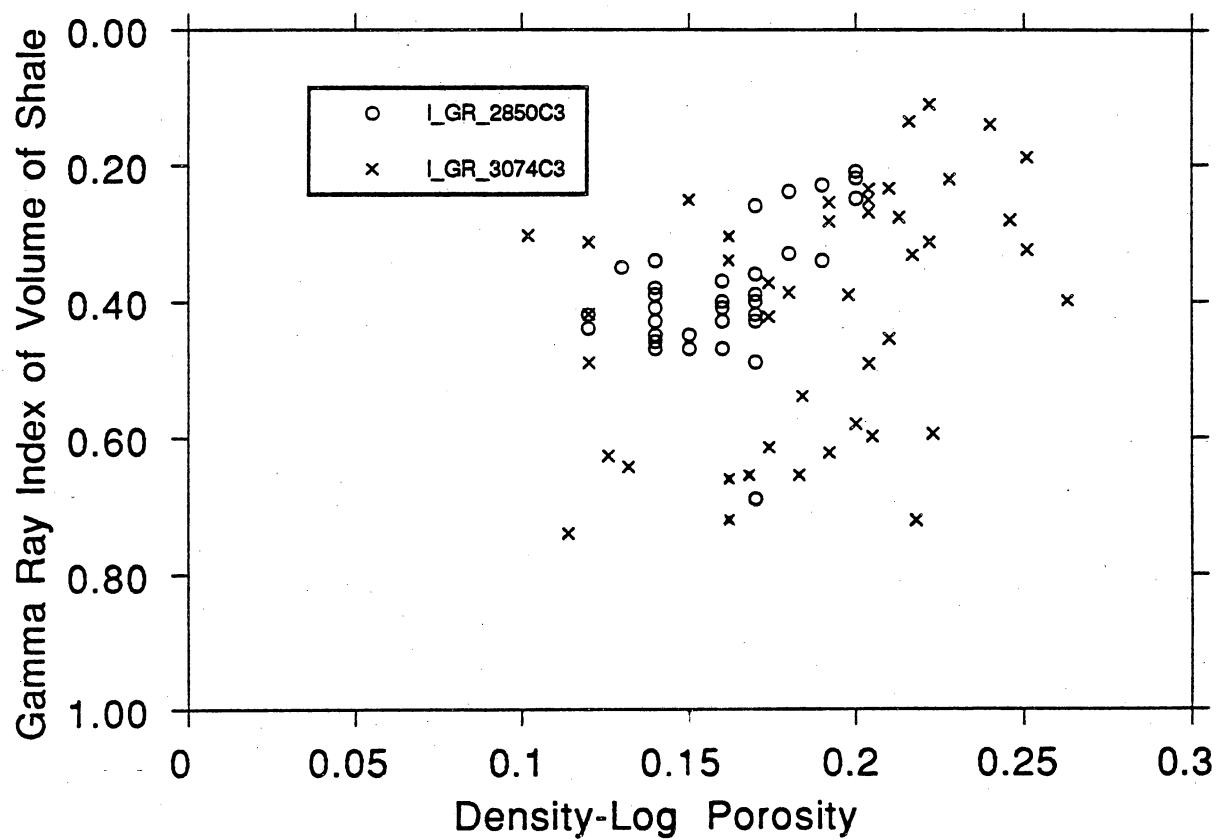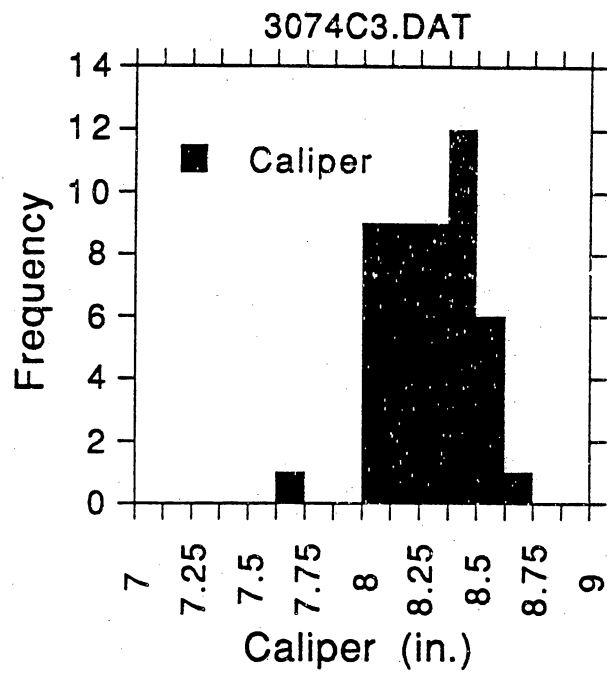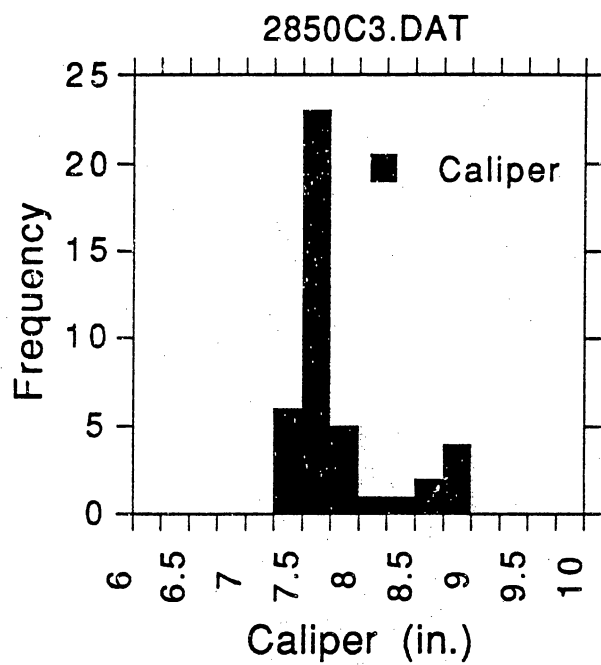
Figure 161. Gamma-ray index versus density porosity of the C-3-X Member.
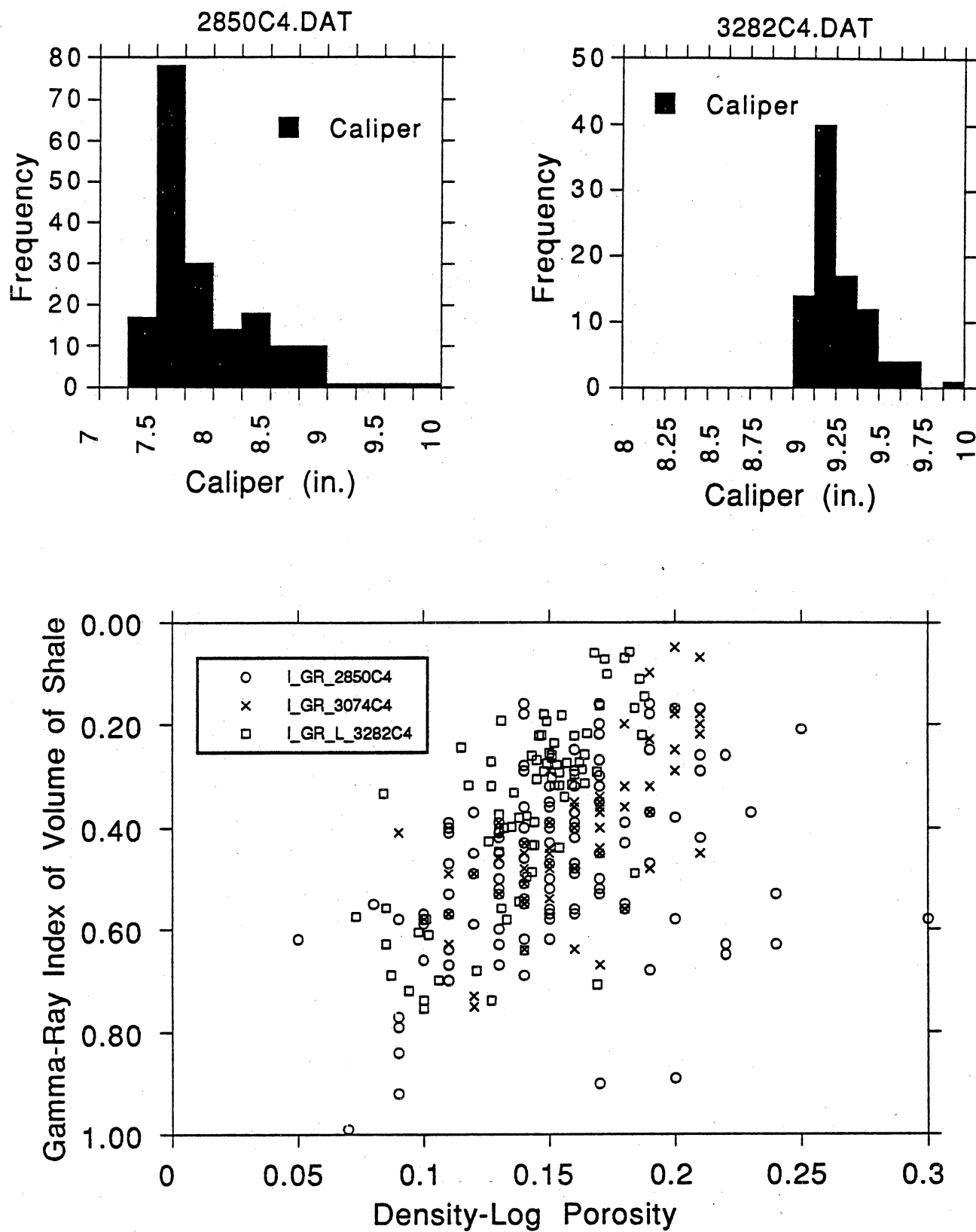
Figure 162. Gamma-ray index versus density porosity of the C-4-X Member.
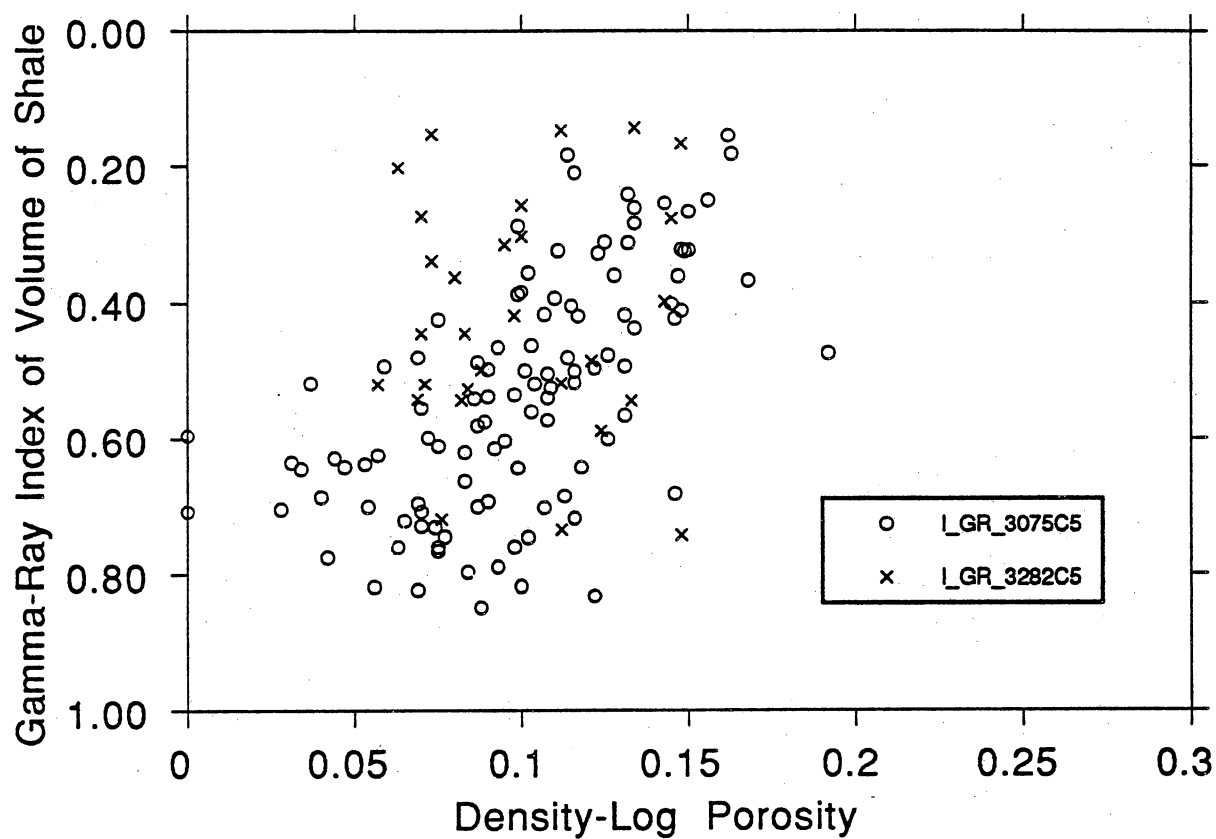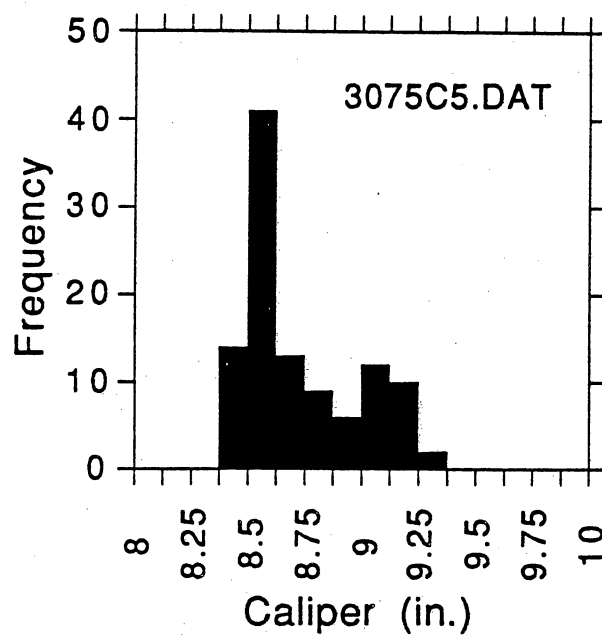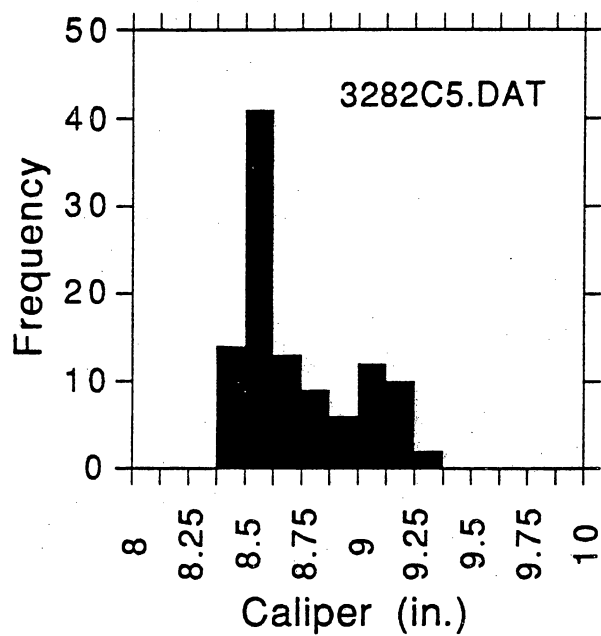
Figure 163. Gamma-ray index versus density porosity of the C-5-X Member.
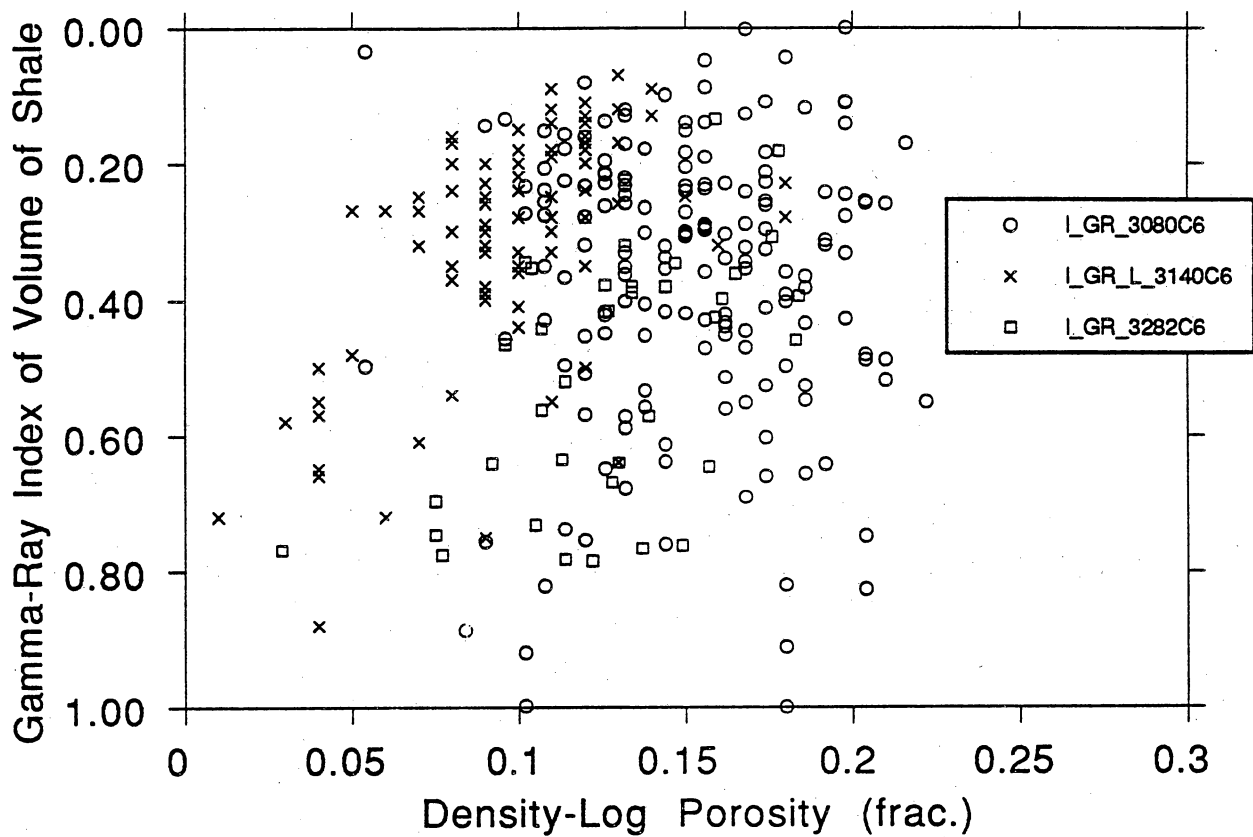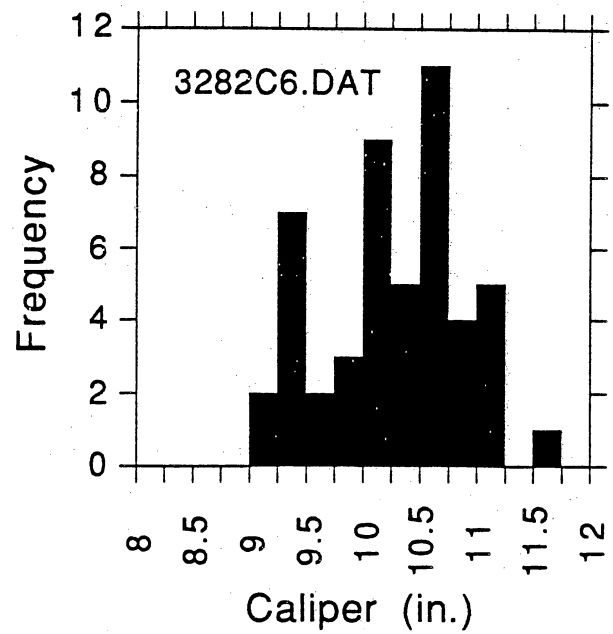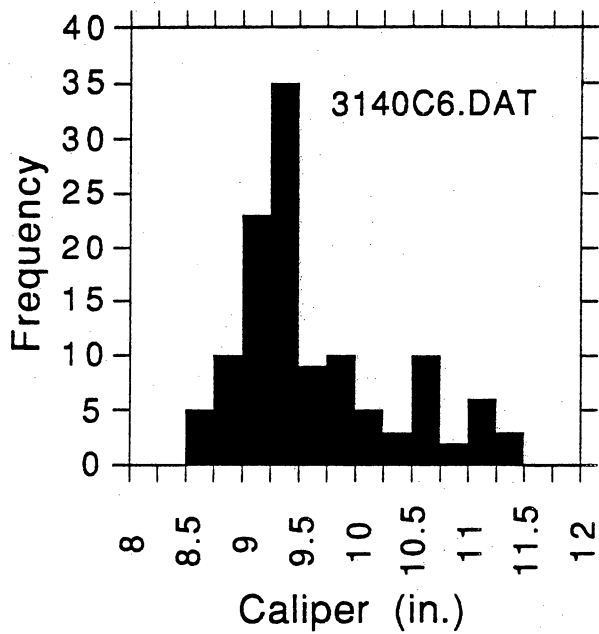
Figure 164. Gamma-ray index versus density porosity of the C-6-X Member.

Figure 165. Gamma-ray index versus density porosity of the C-7-X Member.
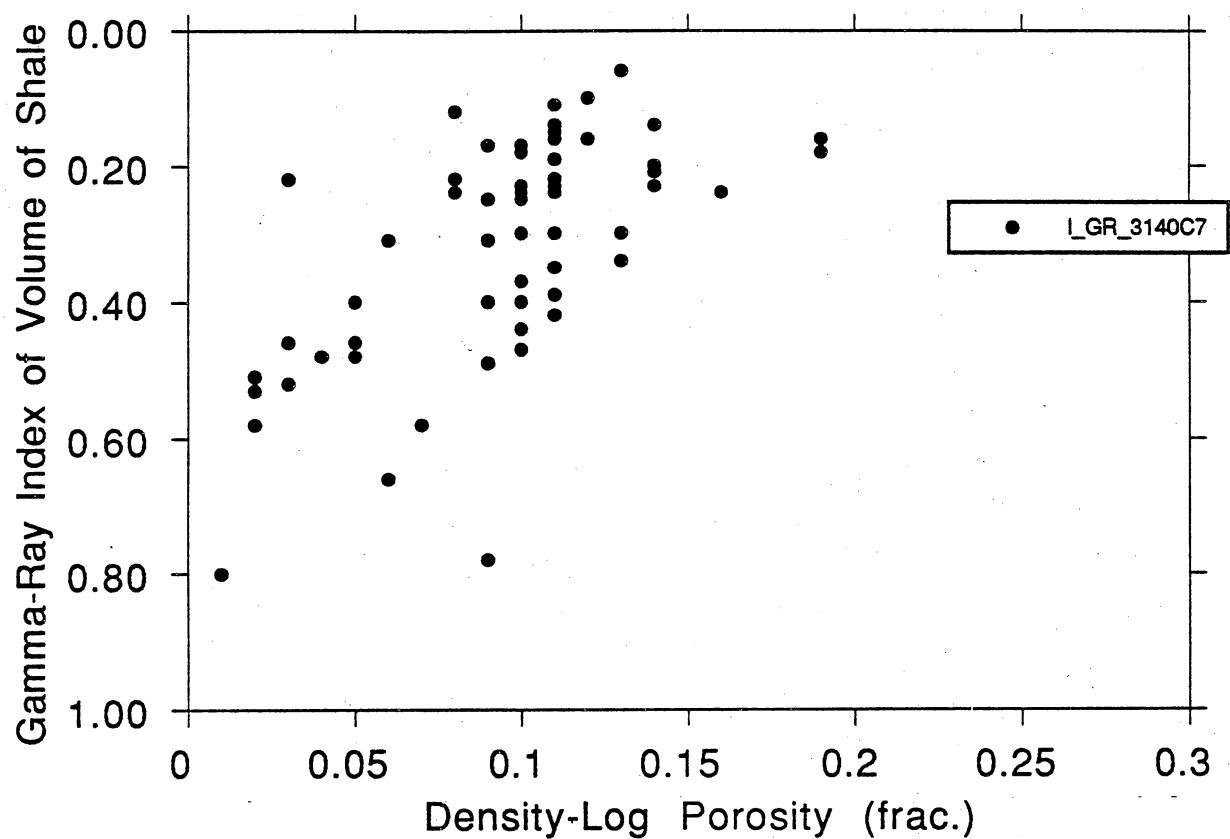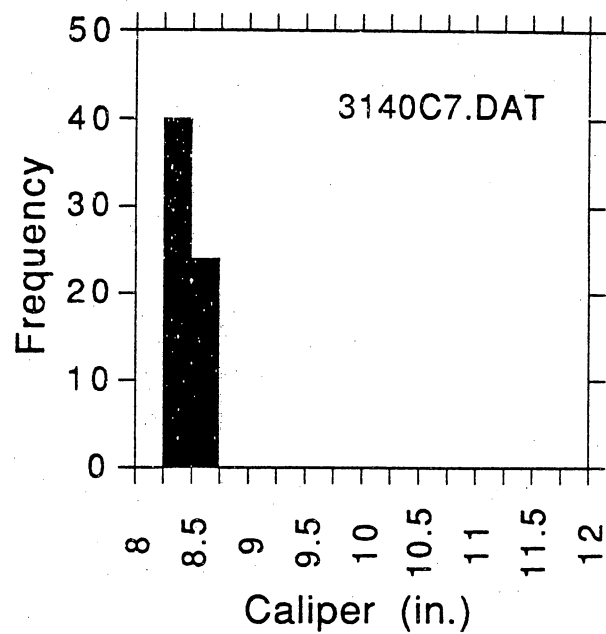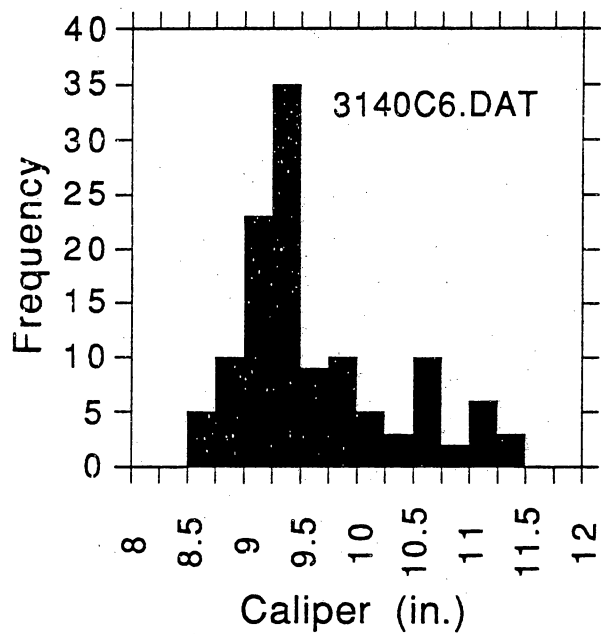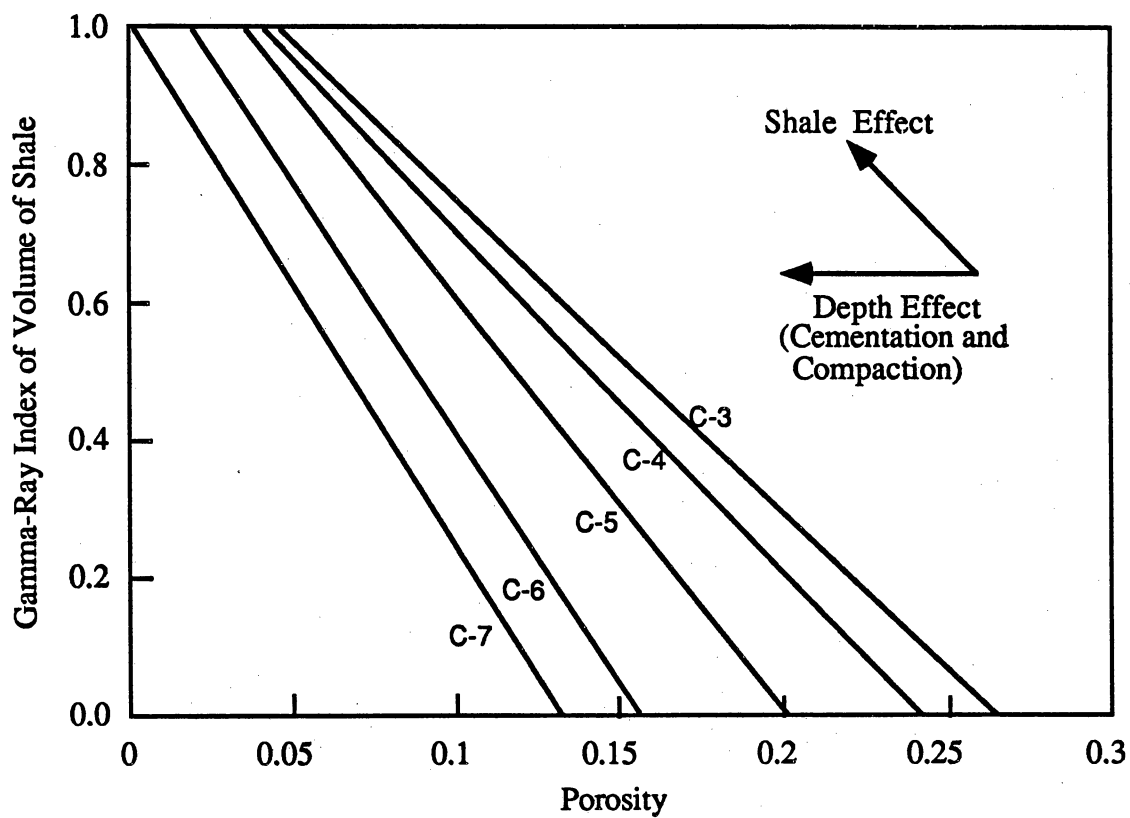
Figure 166. Relationship between gamma-ray index of shale volume and porosity for the C members.

for the C-4-X Member,

$$\phi = \frac{1.211 - V_{sh}}{6} \tag{4}$$

for the C-5-X Member,

$$\phi = \frac{1.17 - V_{sh}}{7.5} \tag{5}$$

for the C-6-X Member, and

$$\phi = \frac{1.02 - V_{sh}}{7.57} \tag{6}$$

for the C-7-X Member. The shale porosity (microporosity) decreases with depth from 4.5 percent in the C-3-X Member to 2 percent in the C-6-X Member. This decrease of microporosity with depth was also seen in the petrographic study.

As shown in track 3 of figure 167 in the LL-2850 well (7,285 to 7,315 ft) and in figure 168 for the LL-3080 well (9,057-9,070 ft) in zones of good density-log response, porosity derived from the GR log with V_{sh}-porosity transforms matches both density and core porosity within about two porosity units, whereas in washed-out intervals (9,000 to 9,056 ft and 9,071 to 9,200 ft), porosity derived from the GR log from V_{sh}-porosity transforms matches core porosity within two porosity units. These transforms work well for all members in track 4 (app. C). The shaded areas are washed-out intervals. Water saturation and permeability were calculated from porosity estimates. Another merit of V_{sh}-porosity transforms is that V_{sh} could be calculated from other logs such as SP or resistivity. Although density-log data were not reconstructed, they can be calculated from porosity values derived from V_{sh}-porosity transforms.

Permeability Model (Permeability-Porosity Transforms)

Permeability of shaly sandstones is a function of porosity, pore type, particle size, sorting, clay type and distribution, and degree of cementation. However, only porosity can be derived from conventional logs, and permeability is then calculated by permeability-porosity transforms obtained from core data. The ranges of scatter in permeability and porosity crossplots were of two to three orders of magnitude. This wide scatter was caused by factors other than porosity. Much effort has been placed on studies to determine the effect of each factor on permeability (Beard and Weyl, 1973; Neasham, 1977; Herron, 1987; Panda and Lake, 1992). Neasham (1977) showed that pore-bridging clays reduce permeability more effectively than pore-filling and pore-lining clays by an order of magnitude. The recent development of geochemical logs, which provide foot-by-foot information about cement and clay types, is designed to improve permeability estimates (Herron, 1987).

Average permeability values differ greatly between the C-3-X and C-4-X Members and the C-5-X, C-6-X, and C-7-X Members (fig. 89). The average permeabilities are 30 md in the C-3-X and C-4-X Members and only 1 md in the C-5-X, C-6-X, and C-7-X Members. These differences suggest depth control on permeability. Permeability varies greatly by member because of decrease in average porosity with depth.

Porosity-permeability correlation of each C member in each well is always very good. However, when all porosity-permeability data are combined (fig. 169), the range of scatter in data points is significantly increased by two orders of magnitude. The range of scatter is significantly reduced when these data are grouped by C member. The scatter is caused by differences in degree of cementation. However, the effects of other factors cannot be differentiated. The scatter can be reduced slightly by grouping porosity-permeability data by facies (fig. 89b) because many factors such as particle size, degree of sorting, and clay fraction and distribution can be better differentiated by facies than by members.

For the same porosity, permeability increases with depth (fig. 170). A similar trend exists in the Wilcox Formation (Eocene) in the Gulf of Mexico (Archie, 1950). For a given porosity value, the degree of quartz

304
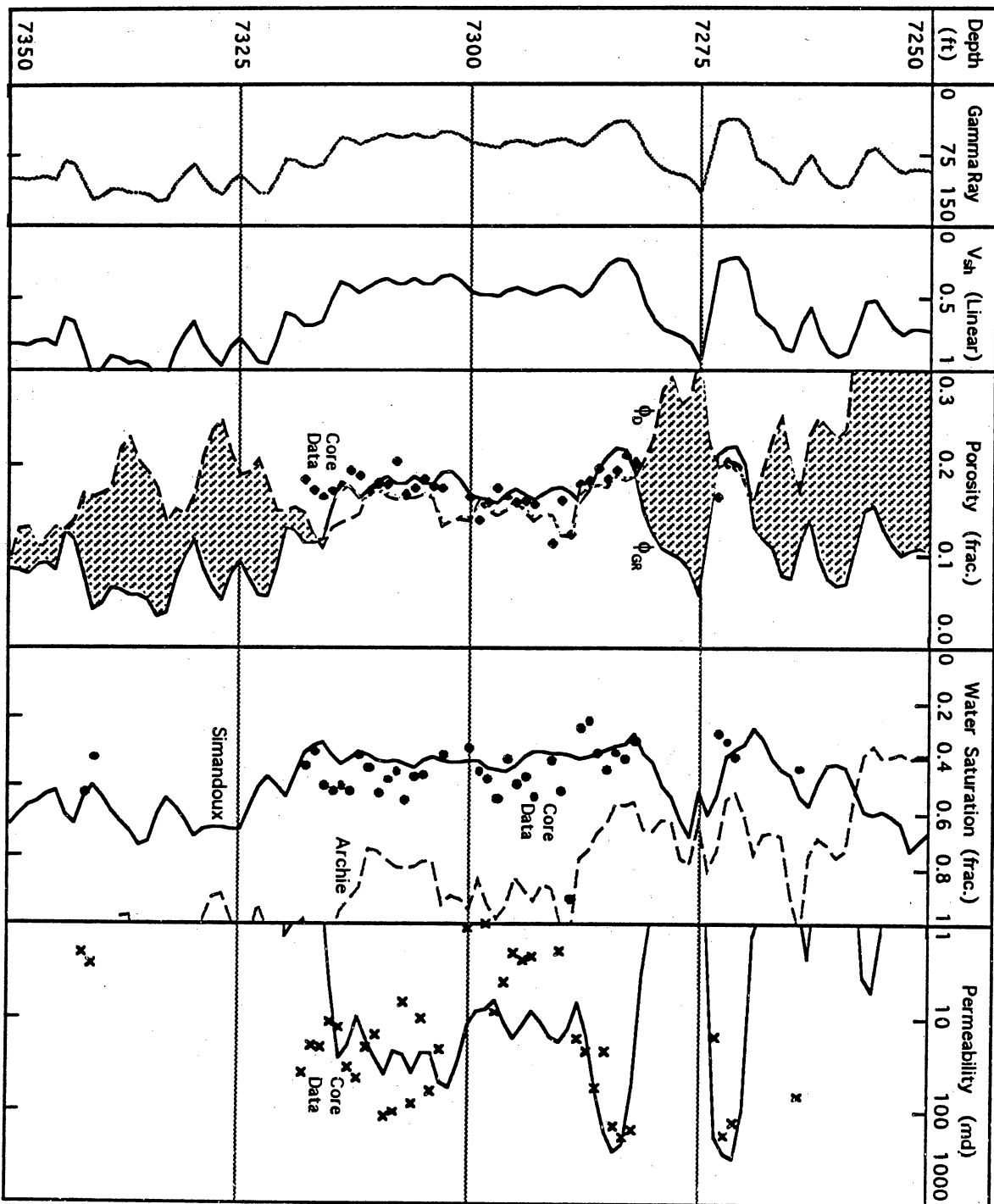
Figure 167. Comparison of petrophysical properties between core data and those calculated with porosity values derived from V_{sh}-porosity transforms in the C-3-X Member in the LL-2850 well.
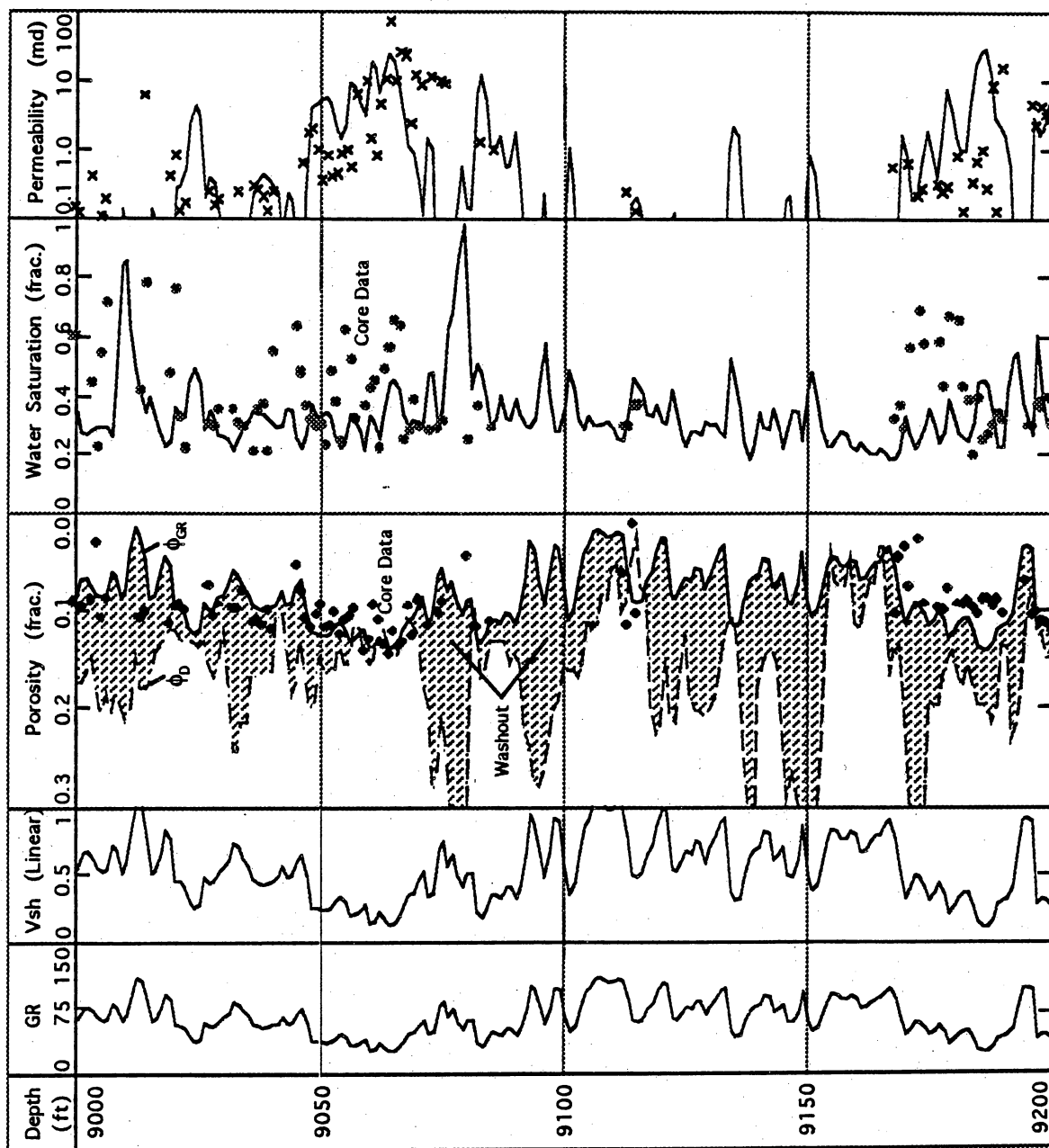
Figure 168. Comparison of petrophysical properties between core data and those calculated with porosity values derived from V_{sh}-porosity transforms in the C-6-X Member in the LL-3080 well.
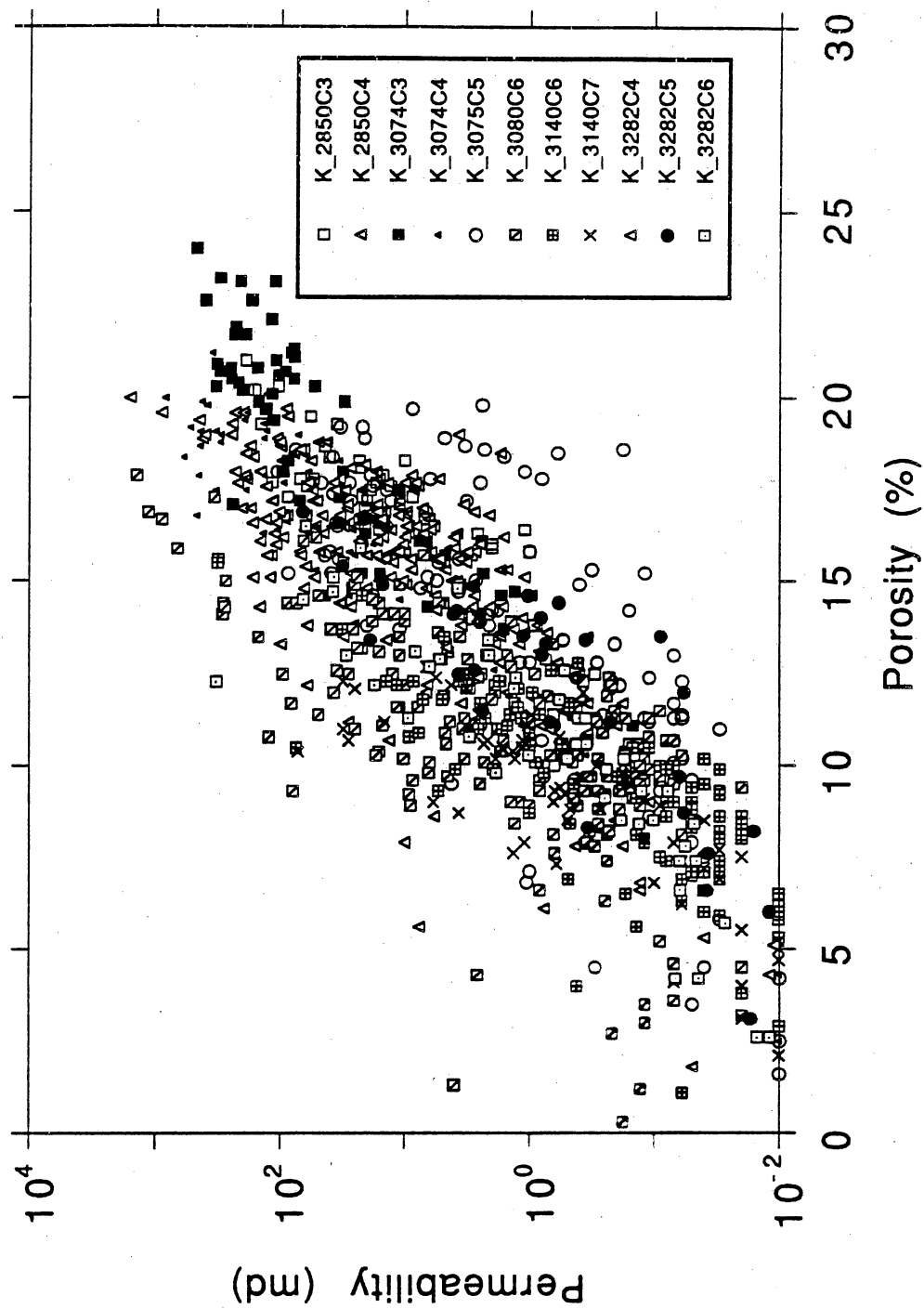
Figure 169. Core permeability versus core porosity of the C-3-X to C-6-X Members from key wells.
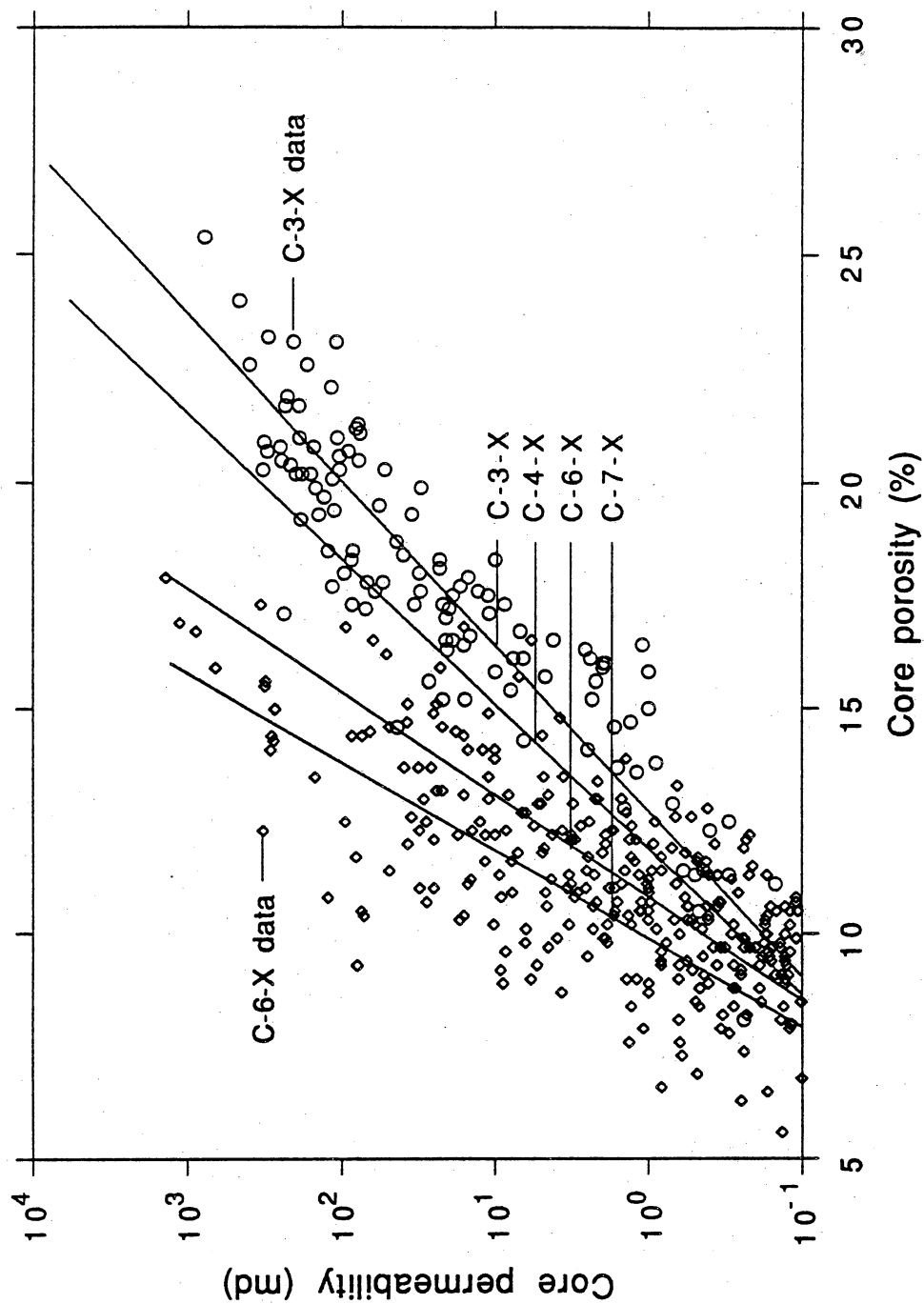
Figure 170. Relationships between permeability and porosity for the C-3-X, C-4-X, C-6-X, and C-7-X Members and data derived from cores in the C-3-X and C-6-X Members.

cementation increases with depth, whereas shale volume decreases with depth. Clean quartz-cement-lined pores, prominent at depth, have a higher permeability than shallow, mud-rich sediments with clay-lined pores. Pore-bridging clays can reduce permeability by an order of magnitude more than pore-filling cement. The equations for the porosity-permeability transforms are obtained by Reduced-Major-Axes (RMA) fit as:

$$k = 10^{-3.473+27.3\phi} \tag{7}$$

for the C-1-X to C-3-X Members,

$$k = 10^{-3.696+31.1\phi} \tag{8}$$

for the C-4-X Member,

$$k = 10^{-4.05+31.4\phi} \tag{9}$$

for the C-5-X Member,

$$k = 10^{-4.736+43.8\phi} \tag{10}$$

for the C-6-X Member, and

$$k = 10^{-5.048+51.0\phi} \tag{11}$$

for the C-7-X Member, where k (permeability) is in millidarcys and $\emptyset$ (porosity) is in fraction. Equation 9 for the C-5-X Member tends to underestimate permeability because core data in this member are limited.

The comparisons between permeability, calculated by these transforms, and core permeability are shown in track 5 in figures 167 and 168. The permeability values are consistent in most intervals. The transforms for the C-5-X, C-6-X, and C-7-X Members tend to underestimate the high permeability in core data. The gamma-ray curve does not adequately record thin sandstones; consequently, permeability is underestimated. Detailed comparisons between calculated and measured core permeabilities of the key wells are shown in app. C.

Water-Saturation Model

Water saturation is difficult to determine in shaly sandstones because they are dependent on shaly-sand models. The comprehensive study on the effect of shaly-sandstone models on water saturation calculations is beyond the scope of this study. However the parameters (1) water salinity, (2) V_{sh}, and (3) clay type were incorporated into the water-saturation model.

Formation Water Salinity and R_w Determination

Water salinity was selected from the frequency histogram (fig. 171) that shows ranges in salinity from laboratory water analysis. The variation in water salinity in the C members is not significant. For example, some wells have slightly higher salinity in the C-4-X Member than in the C-5-X Member. The water-salinity value used in the water-saturation model was 11,000 ppm NaCl, which corresponds to 0.50 ohm-m at 77° F.

Cementation and Saturation Exponents

The predominant clays in the C members are kaolinite, chlorite, and illite. The effect of clays is to increase conductivity and in turn to reduce cementation exponent (m) and saturation exponent (n). Overburden pressure affects both cementation and saturation exponents slightly. Data from special core analysis of the LL-3282 well (fig. 172) indicate that m increases from about 1.80 without overburden pressure to 1.90 with
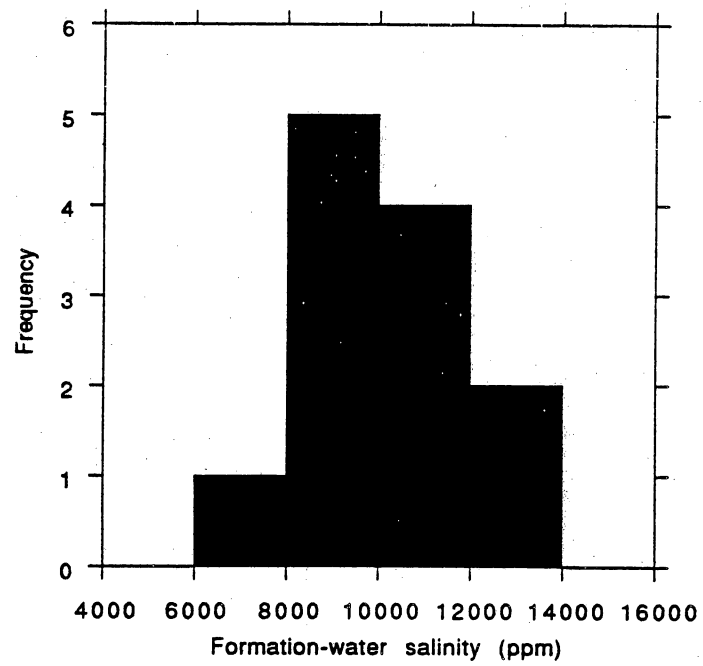
Figure 171. Histogram of formation-water salinity.
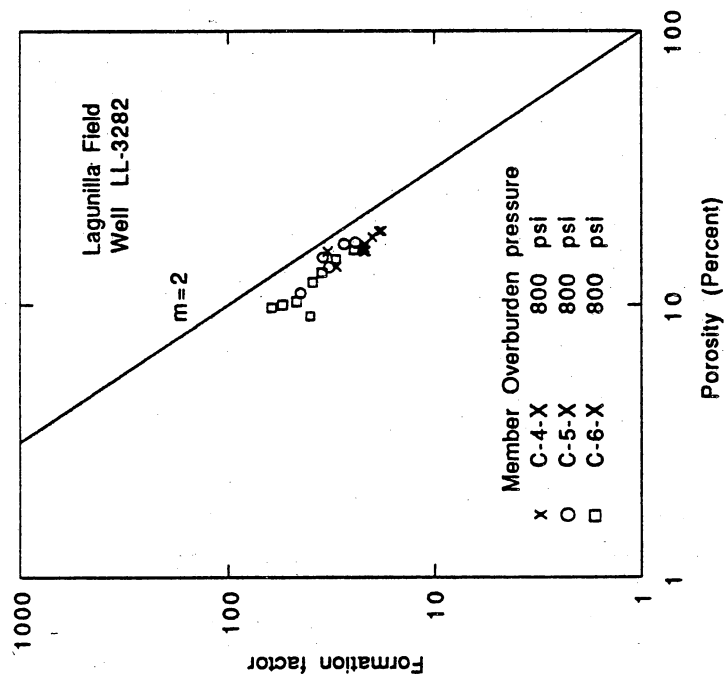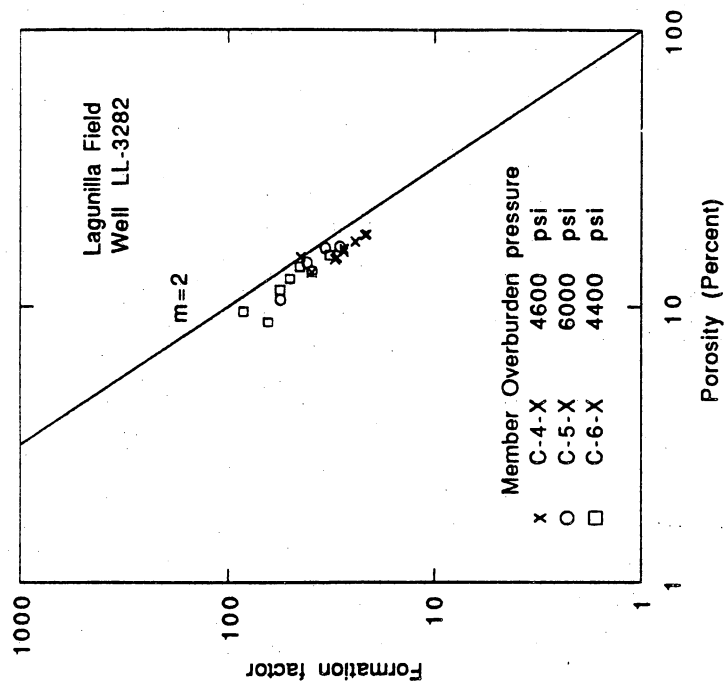
Figure 172. Overburden effect on cementation exponent (m).

4,600 or 6,000 psi overburden pressure. Similarly, n increases from about 1.48 without overburden pressure to 1.70 with 4,600 psi overburden pressure. After correcting the shaliness using the Waxman-Smit equation, both m and n were adjusted to 2.00 (fig. 173), which are the values used in the well log analysis.

Water Saturation Model Selection

Petrophysical parameters used in log analysis, listed in table 50, were used to calculate water saturation in each key well from the Archie, Simandoux, Indonesia, and Waxman-Smits models. As shown in track 4 in figure 167, the Archie equation always calculates too high water saturation and the Simandoux model matches water saturations measured from cores well. On track 2 of figure 174, Indonesian, Simandoux, and Waxman and Smit models are compared. The Waxman and Smit equation tends to calculate too high water saturation, whereas the Simandoux and Indonesian equations match the correlation well. The Simandoux model related resistivity to the total (laminated and dispersed) volume of shale:

$$S_w = \frac{0.5R_w}{\phi^2} \left(\sqrt{(\frac{4\phi^2}{R_w R_t} + \left(\frac{V_{sh}}{R_{sh}}\right)^2} - \frac{V_{sh}}{R_{sh}} \right) \qquad (12)$$

where R_w, R_{sh}, and R_t are the resistivities of water, shale, and formation, respectively, $\emptyset$ is the porosity, and V_{sh} is the volume of shale.

Finally, the petrophysical model was used to evaluate C members in the six key wells. Water saturations calculated by the Simandoux equation were matched to water saturations from core (figs. 167, 168, and app. C). Data obtained from core and from well logs show a general trend of water saturation decreasing with depth. As listed in table 51, the average water saturation is about 40 percent in the C-3-X and C-4-X Members and about 30 percent for the C-5-X, C-6-X, and C-7-X Members. This difference may result because the shale effect is more pronounced in the C-3-X and C-4-X Members, whereas the quartz cement effect is more pronounced in the C-5-X, C-6-X, and C-7-X Members. Microporosity associated with shale causes high capillary-trapped water saturation and high apparent water saturation. The water saturation in sandstone is actually much lower than the apparent water saturation. This may explain why there was a negligible amount of water produced from most wells in the C-3-X and C-4-X Members with high apparent water saturations.

At water salinity of about 11,000 ppm, the water saturation values calculated by equation using n values of 2, 2.02, and 2.04 are compared with those from core at 9,000 to 9,200 ft in the C-6-X Member, in the LL-3080 well. The n values of 2, 2.02, and 2.04 are within the limit of measurement error. However, the calculated water saturation varies by more than 20 percent in many intervals. Especially, at 9,090-9,170 ft, water saturations calculated using n = 2 indicate that these intervals are highly oil saturated, whereas those calculated using n = 2.02 and n = 2.04 indicate that these intervals are wet (fig. 175). Because porosity values are lower than 8 percent, high water saturations are expected. The low water saturations calculated using n = 2 are most likely incorrect. This is clearly one of the drawbacks in the Simandoux equation at low salinity and porosity. However, this discrepancy can be eliminated by careful selections of cutoff values for porosity and V_{sh}.

Fieldwide Formation Evaluation and Validation by Mapping

After these petrophysical models were developed from data from 6 key wells, we applied them to analyzing 65 control wells with GR logs and 39 wells without GR logs using the procedures listed in
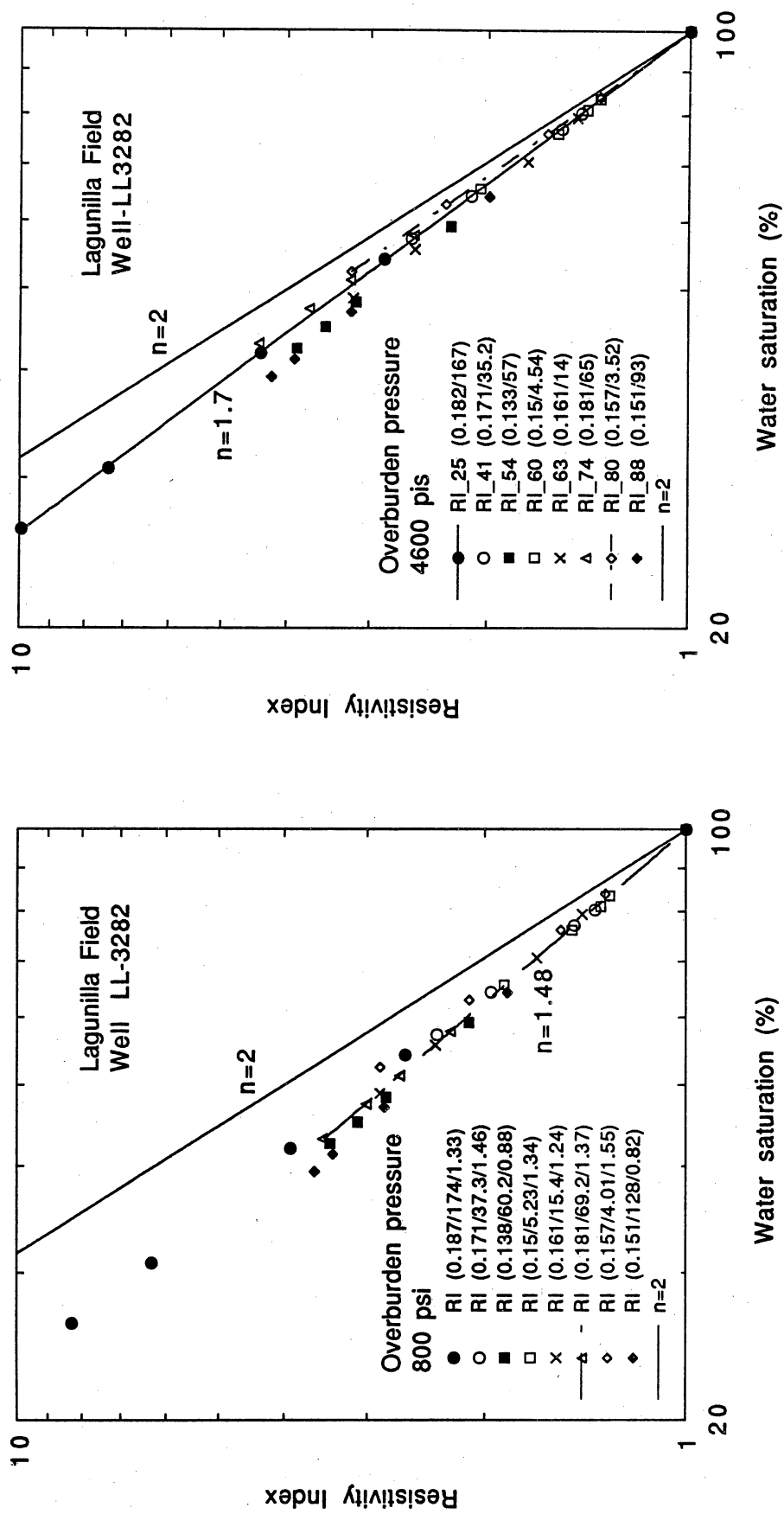
Figure 173. Overburden effect on saturation exponent (n).

313

Table 50. Petrophysical parameters used in fieldwide formation evaluation.

Formation-water salinity (ppm)	11,000
Water resistivity (ohm-m)	0.50
Cementation exponent (m)	2.0
Saturation exponent (n)	2.0
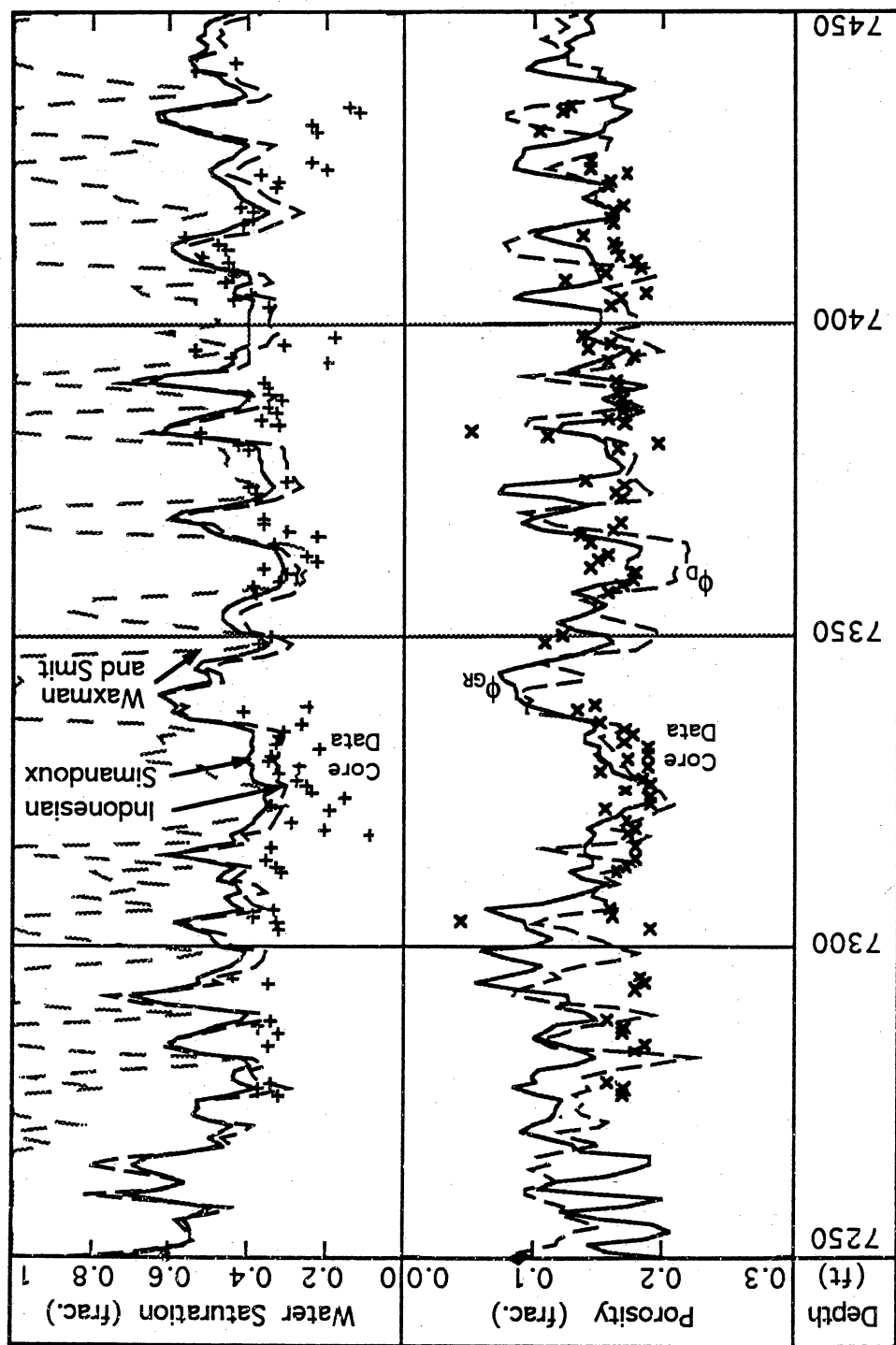
Figure 174. Comparison of water-saturation values calculated by Archie, Poupon, Simandoux, and Waxman and Smits models. Data are from the C-3-X Member in the LL-3282 well.

Table 51. Average water saturation of C Submembers from log analysis.

WELL	C1	C2U	C2L	C3U	C3M	C3L	C4U	C4M	C4L	C5U	C5UM	C5LM	C5L	C6UU	C6LU	C6M	C6UL	C6LL	C7
652		0.31		0.29	0.28	0.30	0.28	0.28	0.27	0.45	0.47								
827		0.52		0.52	0.37	0.48	0.43	0.24			0.49								
846		0.45		0.24	0.24	0.24	0.24				0.41								
847		0.50	0.50		0.31	0.48	0.34	0.37	0.46	0.40	0.37	0.29		0.19	0.23				
851				0.46	0.29	0.32	0.32				0.50	0.36							
862				0.48	0.38	0.47	0.42	0.42			0.42								
866				0.45	0.41	0.41	0.31	0.47											
895	0.52	0.51		0.44	0.41	0.48	0.46												
900	0.41	0.46		0.32	0.29	0.45	0.44												
917		0.35		0.11		0.36	0.35	0.32	0.36		0.24			0.37	0.34	0.33			
946	0.48	0.35		0.48	0.10		0.26	0.34			0.31			0.15	0.18				
971	0.39	0.47	0.49	0.52	0.37	0.45	0.43												
976		0.46		0.51	0.50														
1010		0.53	0.53	0.52	0.47	0.50	0.55	0.53	0.54	0.53									
1022		0.50		0.51	0.47														
1060											0.41								
1061											0.42								
1089		0.34		0.37	0.37	0.36	0.34	0.32	0.32		0.39			0.36	0.37	0.35	0.29	0.27	0.29
1095					0.10	0.22	0.26	0.26	0.26		0.33								
1106					0.42	0.50	0.33				0.46								
1129	0.50	0.53		0.52	0.35	0.45	0.47	0.41	0.47										
1130	0.46	0.52	0.47	0.54	0.42	0.49	0.44	0.44	0.51		0.10								
1162		0.50	0.48	0.46	0.39	0.44	0.40	0.43	0.45										
1172		0.45		0.43	0.42	0.45		0.39	0.47		0.42	0.42	0.32	0.45	0.42				
1176	0.53	0.53	0.52	0.48	0.43	0.47	0.44	0.44	0.52		0.42	0.44							
1198	0.46	0.44	0.46	0.50	0.47	0.46	0.38	0.46	0.45	0.46									
1218				0.30		0.44	0.38	0.37	0.46		0.45								
1245				0.43	0.40	0.32	0.44	0.44	0.49		0.37								
1276	0.34	0.48		0.52	0.40	0.46	0.34				0.43	0.42		0.39	0.44	0.42	0.38		
1293		0.41	0.46	0.42	0.33	0.40	0.40	0.37	0.34	0.34	0.35	0.45							
1303			0.49	0.42	0.35	0.45	0.40	0.39	0.43	0.50	0.33								
1307				0.42	0.37	0.37		0.45	0.49		0.36								
1310				0.31	0.21	0.31	0.28												
1312		0.47	0.48	0.46	0.43	0.45	0.43	0.50	0.49		0.43	0.43	0.31						
1316			0.48	0.37	0.38	0.40	0.31	0.33	0.38										
1679		0.54					0.53	0.49			0.37		0.41			0.37	0.41	0.39	
1695	0.49	0.39	0.38	0.37	0.39	0.39													
1748	0.40	0.43	0.49	0.40	0.37		0.33												
1782				0.30							0.47								
1799							0.41												
1803	0.45	0.47	0.52	0.49	0.40	0.53	0.49	0.38		0.47									
1876	0.47	0.53		0.39	0.41	0.35	0.33	0.55	0.47		0.29								
1985		0.44		0.45	0.30	0.46	0.41	0.42											
1986		0.45			0.32	0.42	0.39	0.41											
1987	0.52	0.51	0.52		0.49	0.49	0.50												
2010	0.42	0.50		0.35	0.38	0.44	0.40	0.38	0.41										
2038	0.52	0.51	0.48	0.45			0.42	0.47	0.49										
2089				0.36	0.38	0.43	0.36				0.40								
2094		0.54	0.50	0.48	0.39	0.47	0.48	0.53			0.43								

316

Table 51. Continued.

ID	1	2	3	4	5	6	7	8	9	10	11	12	13	14	15	16	17	18	19
2187																			-
2191	0.53																		
2197																			
2280																			
2542																			
2547																			
2729			0.48																
2850																			
2896																			
2901		0.38	0.47	0.49	0.35	0.48													
2938		0.46	0.49	0.46	0.29														
2942		0.41	0.55	0.47	0.44	0.42	0.44	0.46		0.47	0.42	0.33		0.42	0.38	0.40	0.34	0.32	0.24
2947		0.47	0.47	0.26	0.25	0.31	0.43				0.44	0.34			0.44	0.33	0.28	0.37	0.38
2981			0.50	0.45	0.33	0.39	0.43	0.43	0.25		0.40			0.38					0.32
3055	0.40		0.48	0.43	0.48	0.45	0.45	0.45	0.43	0.48	0.26								
3059			0.37	0.39	0.38	0.28	0.43		0.35	0.21	0.29								
3074	0.44		0.36	0.43	0.45	0.45	0.48	0.49	0.43	0.48	0.39	0.47		0.43					
3075	0.39	0.51	0.43	0.49	0.49	0.47	0.48	0.49	0.48		0.38	0.48		0.39	0.43	0.39	0.35	0.33	0.39
3080																			
3097			0.53	0.44	0.37	0.47	0.49	0.35		0.36	0.35		0.19						
3138		0.50										0.34							
3139			0.48	0.42	0.36	0.38	0.39	0.49		0.41									
3140		0.40	0.42	0.47	0.43	0.45	0.46	0.48	0.40	0.44	0.44	0.44	0.19	0.42	0.42				
3144		0.46	0.50	0.38	0.38	0.44	0.39	0.33	0.37										
3149		0.50	0.40	0.47	0.34	0.48	0.44	0.35	0.45			0.45		0.40	0.40	0.24	0.29		
3155	0.51		0.40	0.31	0.43	0.39				0.21	0.35		0.27						
3156	0.54	0.53	0.46	0.42	0.47	0.52	0.52		0.38		0.38								
3169	0.49		0.45	0.39	0.35	0.43													
3173	0.42	0.35	0.38	0.31	0.35	0.31	0.35												
3195		0.42	0.47	0.40	0.42	0.40	0.42	0.44	0.42	0.42	0.38	0.32							
3204		0.42	0.43	0.40	0.42	0.34	0.37	0.35		0.38	0.24								
3235		0.52	0.47	0.48	0.52	0.48		0.38											
3260	0.53	0.46	0.33	0.39	0.41	0.51	0.43		0.31	0.30	0.23	0.45	0.19						
3261	0.45	0.51	0.32	0.40	0.40	0.40	0.36	0.33	0.38	0.26	0.27								
3263	0.36	0.36	0.42	0.42	0.31	0.39	0.31		0.29										
3266			0.47	0.45	0.42	0.46													
3267	0.39	0.46	0.42	0.39	0.41	0.43	0.40	0.35	0.46	0.41	0.43	0.45	0.33	0.41	0.32	0.34	0.27	0.23	0.28
3273	0.51		0.47	0.45	0.41	0.35	0.43		0.43	0.25	0.33	0.40							
3274	0.52																		
3279	0.53			0.49	0.46			0.46		0.37									
3282			0.43	0.38	0.42	0.38	0.37	0.38	0.40	0.32	0.33	0.45	0.33	0.36	0.32	0.29	0.27	0.36	0.44
3286	0.37	0.50	0.36	0.36	0.45	0.34	0.36	0.40	0.36	0.45									
3306		0.50	0.46	0.46	0.51														
AVERAGE	0.46	0.46	0.48	0.43	0.37	0.42	0.39	0.41	0.42	0.46	0.38	0.38	0.28	0.35	0.36	0.32	0.31	0.30	0.35

Figure 175. Effect of saturation exponent (n) on water-saturation values calculated by Simandoux equation. Data from the C-6-X Member in the LL-3080 well.

figure 176. V_{sh} was derived from SP or resistivity logs in 34 other wells without GR and density logs. The V_{sh} calculated from SP logs is given by

$$V_{sh} = \frac{SP - SP_{min}}{SP_{max} - SP_{min}}$$ (13)

where SP is log value, SP_{min} is SP of clean sand, and SP_{max} is SP of shale. Base line shifting and selection of clean sand value were the major problems in using SP logs to calculate V_{sh}. Calculations were done by section whenever baseline was shifted. If SP logs could not be used, resistivity logs were used to estimate V_{sh} as

$$V_{sh} = \left(\frac{R_{sh}}{R_t}\right)\left(\frac{R_{max} - R_t}{R_{max} - R_{sh}}\right)^{\frac{1}{b}}$$ (14)

where R_{sh} is resistivity of adjacent shale, R_t the measured resistivity, R_{max} is the maximum resistivity of clean pay zone, and b is an empirical exponent (Terra Science, 1993). The uncertainties in V_{sh} calculated by resistivity were much higher than those calculated by GR or SP. The R_{max} and b were selected by trial and error. The V_{sh} is very sensitive to the value of the b exponent, which ranged from 2 to 3.5 and normally increased with the mean porosity of each member (depth). When this method is used and b values are carefully selected, the porosity calculated from resistivity logs agrees well with those calculated from density and GR logs (figure 177).

Results of all wells were mapped and these maps iteratively checked against facies maps. Anomalies in maps indicate problems in input parameters used in these models. These wells were reevaluated using new input parameters.

Net-Pay Determinations

Net-pay thickness values were determined with cutoff values of V_{sh}, water saturation, and porosity. Only the V_{sh} cutoff values were used for calculating net-sandstone thickness. The relationship of V_{sh} to net-sandstone thickness for each member was determined from net-sandstone thickness counted from cores.

Net-pay thickness was determined with cutoff values for V_{sh}, S_w, and porosity. S_w cutoff was determined from resistivity logs. For the C-1-X to C-4-X Members, the resistivity cutoff was determined to be 10 ohm-m; for the C-5-X Member, 12 ohm-m; and for the C-6-X Member, 14 ohm-m. For the C-7-X Member, porosity and permeability are too low for this interval to be productive, but it is still considered prospective in sandstones with resistivity greater than 25 ohm-m and porosity greater than 8 percent.

Production data were also used to validate the results of the petrophysical evaluation and cutoff values. Twelve production logs from the LL-1001, LL-1156, LL-1876, LL-2010, LL-2089, LL-2187, LL-2938, LL-3062, LL-3074, LL-3075, LL-3155, and LL-3156 wells were used. Open intervals with less than 8 percent porosity and more than 55 percent water saturation were considered nonproductive (see figs. 148 and 149). Cutoff values of V_{sh} and S_w (table 52) for net-sandstone and net-pay thicknesses were further modified during mapping. They were determined to be 55 percent for the C-1-X to C-4-X Members and 50 percent for the C-5-X to C-7-X Members. The higher cutoff in water saturation for the C-3-X and C-4-X Members reflected a shale effect that is more pronounced in the C-3-X and C-4-X Members and a cement effect that is more pronounced in the C-5-X, C-6-X, and C-7-X Members. Results of net-sandstone thickness, net pay, S_w, porosity, permeability, kh, and Øh by member and submember in each well are summarized in tables 51 and 53 to 58.

- Select GR_{min} or SP_{min} or R_{max} for clean sand
- Select GR_{max} or SP_{max} for shale
  from log

⬇

- Calculate V_{sh} using from GR or SP using linear model
  or from resistivity using updated input values

⬇

- Calculate porosity for each member
  using V_{sh} -Porosity Transforms

⬇

- Calculate permeability for each member
  using Permeability-Porosity Transforms

⬇

- Calculate water saturation for each member
  using Simandoux equation

Figure 176. Flow chart of procedures used in fieldwide formation evaluation.
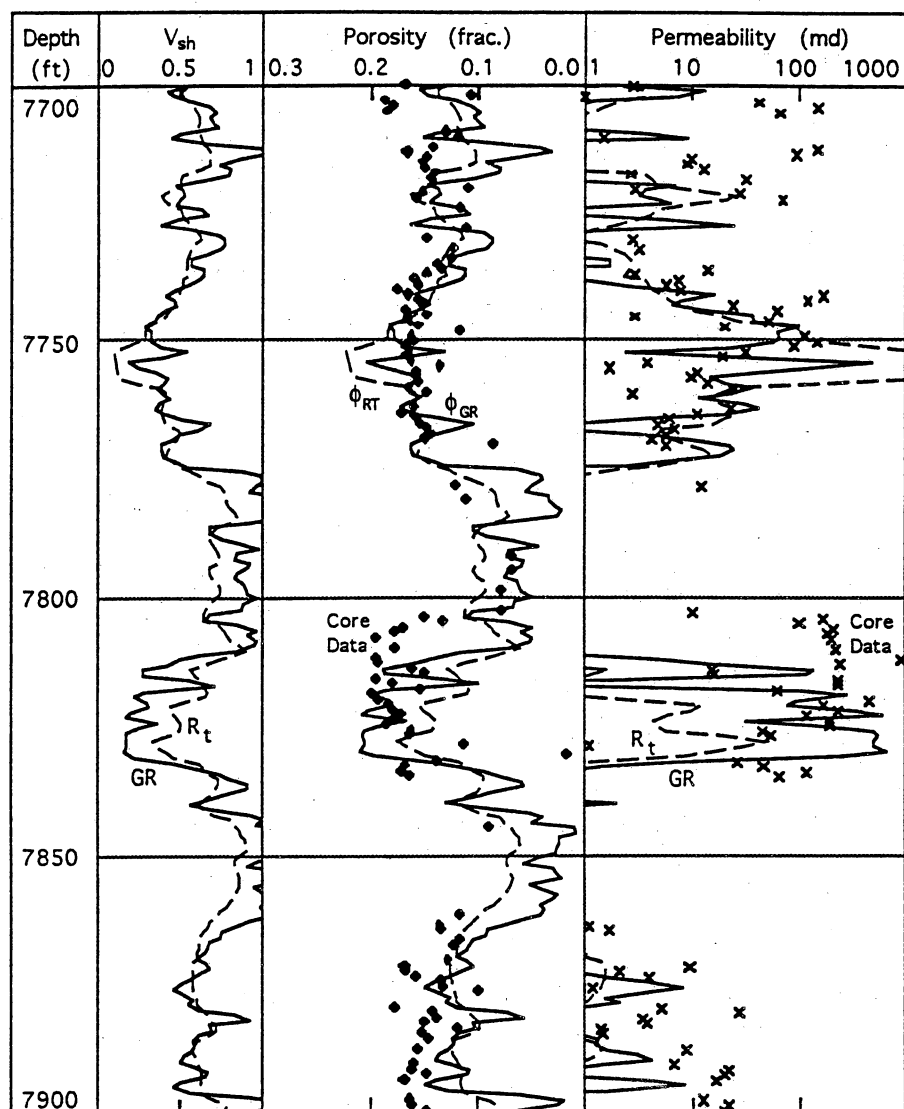
Figure 177. Comparison of V_{sh}, porosity, and permeability derived from gamma-ray and resistivity logs.

Table 52. Cutoff values of V_{sh}, water saturation and porosity.

Member	Volume of Shale	Water Saturation	Porosity
C-1-X	0.55	0.55	0.08
C-2-X	0.55	0.55	0.08
C-3-X	0.55	0.55	0.08
C-4-X	0.55	0.55	0.08
C-5-X	0.50	0.50	0.08
C-6-X	0.50	0.50	0.08
C-7-X	0.50	0.50	0.08

Table 53. Net-sandstone thickness of C Submembers from log analysis.

WELL	C1	C2U	C2L	C3U	C3M	C3L	C4U	C4M	C4L	C5U	C5UM	C5LM	C5L	C6UU	C6LU	C6M	C6UL	C6LL	C7
652		31.00	0.00	30.00	19.00	133.00	147.00	61.00	61.00	15.00	61.00	0.00	0.00						
827		90.00	6.00	60.00	35.00	58.00	94.00	0.00			57.00	0.00							
846		0.00	0.00	30.00	30.00	90.00	0.00	10.00			22.00								
847	0.00	0.00	51.00	6.00	24.00	99.00	85.00	36.00							4.00				
851	8.00	86.00	10.00	0.00	0.00	85.00	65.00			4.00					4.00				0.00
852		0.00	0.00	2.00	37.00	55.00	20.00	0.00	0.00	22.00	29.00								
866	38.00	28.00	0.00	16.00	22.00	21.00	93.00	34.00			33.00								
895	25.00	58.00	0.00	10.00	68.00	188.00	146.00	43.00			68.00								
900	4.00	0.00	0.00	50.00	33.00	26.00	54.00												
917	12.00	12.00	0.00	5.00	27.00	5.00	35.00	51.00		18.00	30.00	0.00	0.00	2.00	45.00	105.00		0.00	
946		113.00	0.00	33.00	18.00	0.00	64.00	12.00		0.00	24.00	0.00	18.00		71.00				
971	21.00	31.00	18.00	62.00	73.00	189.00	152.00	0.00		38.00	68.00		0.00						
975	18.00	3.00	2.00																
997	40.00	66.00	6.00	51.00	33.00	30.00	91.00	38.00			68.00		0.00						
1010		81.00	12.00			91.00													
1022	18.00	58.00	7.00																
1060	0.00	0.00	0.00	46.00	78.00	4.00	49.00	0.00	0.00	60.00	60.00	3.00	0.00	0.00	0.00	4.00	15.00	0.00	
1061		7.00	4.00																
1089	0.00	65.00	1.00	9.00	12.00	76.00	201.00	132.00	11.00	0.00	30.00	0.00			6.00	22.00	37.00	52.00	132.00
1095		0.00	128.00	0.00	23.00	17.00	190.00	50.00	82.00	0.00	14.00	0.00							
1106	0.00	0.00	45.00	151.00	62.00	195.00	150.00	0.00	0.00	0.00									
1129	15.00	42.00	0.00	83.00	72.00	348.00	164.00	164.00	241.00		28.00	80.00				89.00	123.00		
1130	19.00	28.00	3.00	15.00	64.00	190.00	49.00	49.00	90.00		23.00	80.00							
1162	3.00	9.00	3.00	17.00	55.00	55.00	78.00	43.00	38.00										
1172		34.00	4.00	12.00	30.00	45.00	112.00	41.00	22.00		0.00	20.00	59.00		31.00	65.00	3.00		
1176	2.00	43.00	4.00	39.00	43.00	50.00	46.00	46.00	20.00	15.00	0.00	11.00							
1198	16.00	25.00	0.00	4.00	21.00	55.00	67.00	40.00	31.00	16.00	67.00								
1218		1.00	4.00	42.00	33.00	86.00	79.00	134.00	40.00										
1245		0.00	0.00	9.00	16.00	13.00	48.00	8.00	3.00		30.00	34.00	112.00						
1276		0.00	0.00	33.00	33.00	105.00	164.00	0.00	1.00	3.00	12.00	14.00			32.00	83.00	123.00	60.00	118.00
1293	3.00	11.00	0.00	11.00	36.00	103.00	69.00	40.00	74.00	19.00	33.00	0.00							56.00
1303		91.00	77.00	146.00	69.00	60.00	60.00	13.00	72.00		36.00								
1307		0.00	2.00	9.00	12.00	60.00	35.00		36.00		36.00	31.00							
1310		0.00	1.00	3.00	30.00	9.00	6.00		31.00		31.00								
1312		13.00	0.00	16.00	33.00	72.00	94.00	68.00	34.00	13.00	34.00	23.00	103.00						
1316	45.00	45.00	15.00	28.00	33.00	86.00	184.00	39.00	34.00										
1679	50.00	27.00	4.00	48.00	27.00	161.00	166.00	54.00	68.00	50.00	12.00	20.00							
1695	50.00	42.00	2.00	19.00	30.00														
1748	22.00	25.00	9.00	0.00	35.00	14.00	75.00	16.00	0.00	68.00	17.00	5.00			5.00	39.00	40.00	51.00	92.00
1782		17.00	33.00	17.00	12.00	6.00	72.00	31.00			35.00	13.00							
1799	0.00	0.00	0.00	0.00			0.00	0.00	0.00	0.00			51.00	0.00	5.00	39.00	40.00	51.00	92.00
1803	15.00	4.00	1.00	36.00	46.00	22.00	136.00	25.00	12.00	12.00	35.00	13.00	0.00		0.00	35.00	46.00	48.00	86.00
1876	47.00	45.00	7.00	20.00	36.00	96.00	103.00	43.00											78.00
1985	1.00	5.00	0.00	3.00	37.00	79.00	76.00	76.00			27.00								
1986	13.00	9.00	1.00	13.00	57.00	47.00	68.00	68.00		13.00									
1987	114.00	58.00	21.00	6.00	6.00	113.00	150.00	28.00											
2010	9.00	7.00	2.00	17.00	23.00	57.00	92.00	11.00			36.00	33.00							
2038	22.00	44.00	32.00	57.00		23.00	111.00	42.00	33.00		36.00								
2089	5.00	24.00	0.00	19.00	40.00	50.00	113.00	31.00	13.00		33.00	13.00							

Table 53. Continued.

2094	5.00	22.00	6.00	10.00	51.00	72.00	115.00	45.00		6.00	51.00								
2187	0.00	0.00	3.00	13.00	38.00	49.00	118.00	50.00		36.00	23.00								
2191	231.00			179.00	68.00	165.00	109.00	48.00		8.00	28.00	18.00							
2197	0.00	0.00	1.00	11.00	32.00	28.00	83.00	10.00		8.00	23.00								
2280	6.00	13.00	10.00	8.00	28.00	30.00	79.00	17.00		0.00									
2542	0.00	0.00	0.00	4.00	37.00	76.00	73.00	36.00	0.00	9.00									
2547		0.00	3.00	27.00	30.00	30.00	47.00	0.00	0.00	0.00									
2729	94.00	56.00	20.00	34.00	40.00	109.00			102.00	94.00									
2850										0.00									
2896		52.00	11.00	24.00	41.00	46.00	80.00	26.00		46.00	30.00	8.00							
2901		46.00	8.00	30.00	38.00	112.00	118.00	39.00		32.00	38.00	18.00							
2938		9.00	0.00	16.00	36.00	72.00	108.00	49.00	286.00	24.00	68.00	32.00							
2942		16.00	10.00	11.00	22.00	39.00	99.00	28.00		38.00	30.00	52.00							
2947		69.00	14.00	28.00	30.00	106.00	102.00	43.00		54.00			70.00	21.00	35.00	97.00	59.00	110.00	104.00
2981	141.00	88.00	36.00	36.00	24.00	110.00	127.00	38.00	141.00	124.00	16.00	44.00		62.00	105.00	116.00	112.00	49.00	202.00
3055		91.00	23.00	58.00	43.00	180.00	122.00	94.00		66.00	24.00	5.00		20.00	28.00	77.00	70.00	69.00	142.00
3059	12.00		0.00	35.00	49.00	173.00	146.00	48.00	114.00	6.00	69.00	7.00	0.00	42.00	0.00				
3074		68.00	35.00	17.00	28.00	24.00	90.00	36.00	204.00	28.00	49.00	17.00		28.00	43.00	107.00	125.00		
3075		41.00	6.00	28.00	31.00	18.00	75.00	9.00		36.00	55.00	10.00		20.00	43.00	66.00	70.00	86.00	143.00
3080		27.00	4.00	12.00	30.00	42.00	86.00	25.00			36.00	10.00							90.00
3097		13.00	9.00	12.00	25.00	61.00	100.00	27.00			17.00								
3138		53.00	6.00	24.00	29.00	37.00	70.00	6.00		23.00			126.00	0.00					
3139		59.00	49.00	21.00	24.00	122.00	139.00	36.00		15.00	27.00	8.00	48.00	16.00	54.00	107.00	103.00	91.00	
3140		40.00	4.00	22.00	17.00	52.00	101.00	20.00		41.00	40.00	12.00							37.00
3144		22.00	6.00	33.00	34.00	88.00	115.00	39.00		68.00		22.00							
3149		43.00	12.00	10.00	41.00	81.00	118.00	63.00	5.00		24.00	10.00		4.00					
3155		35.00	13.00	25.00	24.00	80.00	55.00				30.00				34.00		126.00		
3156		49.00	15.00	27.00	34.00	109.00		41.00		35.00				42.00	35.00	6.00			
3169	104.00	23.00	1.00	34.00	24.00	57.00	78.00	42.00	0.00	231.00	34.00								
3173		24.00	10.00	23.00	60.00	68.00	101.00	42.00		25.00	24.00	16.00							
3195		25.00	5.00	10.00	32.00	66.00	124.00	42.00		52.00	41.00	86.00							
3204	18.00	0.00	60.00	22.00	25.00	59.00	95.00	40.00	18.00										
3235	68.00	58.00	17.00	31.00	27.00	90.00	159.00	42.00	0.00	28.00	38.00	6.00	52.00	69.00	0.00				
3260		66.00	12.00	60.00	62.00	165.00	130.00	118.00		6.00	32.00	10.00	69.00						
3261		17.00	3.00	29.00	14.00	41.00	68.00	18.00		74.00	25.00	16.00	48.00						
3263		35.00	11.00	19.00	22.00	49.00	124.00	47.00		20.00	37.00								
3265		46.00	6.00	17.00	31.00	166.00	90.00	56.00		29.00	56.00	2.00		47.00	0.00				
3267		37.00	13.00	50.00	32.00	82.00	130.00	56.00		117.00	22.00	27.00		24.00	32.00	67.00	69.00	110.00	
3273	204.00	45.00	12.00	15.00	38.00	79.00	158.00	50.00	3.00		43.00	29.00	125.00						116.00
3274	86.00	29.00	1003.00	51.00	17.00	144.00		77.00	3.00										
3279		31.00	14.00	31.00	52.00	119.00	136.00	77.00	12.00	26.00	28.00	12.00		13.00	29.00	47.00	48.00	60.00	
3282	0.00	0.00	0.00	37.00	36.00	69.00	126.00	38.00			31.00	12.00		18.00	0.00				36.00
3286		28.00	3.00	1.00	36.00	44.00	126.00	53.00	86.00	54.00	32.00	11.00							
3306		47.00	8.00	23.00	28.00	31.00		52.00											
AVERAGE	42.97	39.04	28.75	29.38	35.43	77.36	104.92	44.10	66.86	42.00	35.40	22.08	77.75	27.86	48.68	65.50	72.00	91.18	93.82

323

Table 54. Net-pay thickness of C Submembers from log analysis.

WELL	C1	C2U	C2L	C3U	C3M	C3L	C4U	C4M	C4L	C5U	C5UM	C5LM	C5L	C6UU	C6LU	C6M	C6UL	C6LL	C7
652		31.00	0.00	30.00	19.00	133.00	147.00	61.00	61.00	15.00	53.00	0.00	0.00						
827		40.00	0.00	20.00	25.00	58.00	94.00	0.00			39.00								
846	0.00	0.00	0.00	3.00	30.00	35.00	99.00	10.00			22.00								
847		20.00	0.00	0.00	24.00	15.00	85.00	35.00	4.00	22.00	26.00	19.00		4.00	4.00	0.00			
851	0.00	13.00	4.00	0.00	0.00	55.00	65.00		0.00		5.00	17.00							
852		0.00	0.00	8.00	37.00	13.00	18.00	0.00	0.00		66.00								
868	0.00	0.00	0.00	7.00	22.00	15.00	93.00	3.00	0.00										
895	20.00	56.00	0.00	46.00	64.00	160.00	135.00	24.00											
900	4.00	5.00	0.00	33.00	30.00	26.00	54.00				30.00								
917		12.00	0.00	5.00	27.00	5.00	35.00	51.00	8.00	0.00	30.00	0.00	0.00	2.00	43.00	105.00	0.00		
946		81.00	0.00	33.00	18.00	0.00	63.00	12.00	0.00	0.00	24.00	0.00	0.00	18.00	71.00				
971	21.00	31.00	18.00	62.00	73.00	189.00	152.00	0.00	0.00	0.00	64.00		0.00						
975	18.00	3.00	0.00																
997	0.00	0.00	0.00	26.00	5.00	0.00	14.00												
1010		33.00	3.00								64.00								
1022	0.00	25.00	0.00	46.00	78.00														
1060	0.00		0.00	0.00	0.00	4.00	22.00	132.00	0.00	0.00	58.00	0.00		0.00	0.00	4.00	15.00	0.00	
1061		0.00	0.00	9.00	12.00	76.00	201.00	50.00	11.00		30.00								
1089	0.00	65.00	1.00	0.00	23.00	17.00	181.00	50.00	82.00	0.00	13.00	0.00		6.00	22.00	37.00	52.00	132.00	27.00
1095		0.00	0.00	1.00	40.00	25.00	117.00	0.00	0.00					12.00	52.00				
1106	0.00	4.00	0.00	12.00	57.00	139.00	140.00	42.00	30.00		20.00	50.00							
1129	0.00	19.00	0.00	15.00	64.00	190.00	78.00	46.00	64.00		23.00	52.00							
1130	15.00	9.00	3.00	17.00	55.00	55.00	140.00	43.00	38.00		20.00	20.00	53.00	16.00	43.00	0.00			
1162	3.00	34.00	3.00	12.00	30.00	45.00	78.00	41.00	22.00	0.00	0.00	5.00							
1172		43.00	4.00	39.00	43.00	55.00	112.00	44.00	17.00	0.00	62.00		89.00						
1176	2.00	25.00	0.00	4.00	21.00	50.00	86.00	40.00	30.00	16.00	27.00	5.00		7.00	13.00	47.00	40.00	86.00	17.00
1198	16.00	0.00	4.00	42.00		33.00	67.00	134.00	38.00		12.00	3.00							
1218		0.00	0.00	9.00	16.00	13.00	79.00	8.00	3.00		33.00	5.00							
1245		0.00	0.00	3.00	15.00	23.00	16.00	0.00	0.00	2.00	57.00	3.00	89.00						
1276	2.00	6.00	0.00	9.00	36.00	102.00	145.00	33.00	37.00	15.00	36.00	0.00							
1293		35.00	3.00	43.00	43.00	31.00	64.00	25.00	19.00		21.00	21.00							
1303		0.00	2.00	9.00	12.00	60.00	35.00	13.00	6.00		28.00	28.00	89.00						
1307		0.00	1.00	3.00	30.00	9.00	94.00	32.00	68.00		12.00	20.00							
1310	0.00	13.00	0.00	16.00	33.00	72.00	154.00	34.00	34.00	0.00	25.00			5.00	39.00	40.00	51.00	92.00	
1312		0.00	8.00	13.00	28.00	66.00	166.00	54.00	68.00	6.00				0.00	24.00	42.00	48.00	86.00	73.00
1316	0.00	5.00		44.00	27.00	161.00		16.00	0.00	0.00	12.00		51.00						
1879	6.00	0.00	2.00	19.00	30.00	14.00	75.00	16.00	0.00	0.00	0.00	5.00	51.00						
1695	22.00	25.00	3.00	0.00	35.00	3.00	13.00	0.00	0.00	0.00	0.00	3.00	0.00						
1748		17.00	3.00	14.00	12.00	22.00	134.00	25.00	12.00	0.00	25.00	13.00							
1782	0.00	0.00	1.00	36.00	36.00	42.00	78.00	3.00											
1799	15.00	2.00	2.00	7.00	35.00	77.00	137.00	48.00			27.00								
1803	3.00	8.00	0.00	3.00	37.00	42.00	61.00	28.00	6.00		21.00								
1876	0.00	5.00	0.00	7.00	39.00	50.00	122.00	1.00		0.00									
1985	0.00	2.00	0.00	0.00	21.00	44.00	80.00	27.00	24.00		27.00								
1986	25.00	42.00	9.00	0.00			111.00	42.00	13.00		35.00								
1987	5.00	3.00	0.00	15.00					24.00										
2010	22.00	44.00	32.00	57.00					13.00		15.00								
2038	0.00	0.00	0.00	15.00	39.00	34.00	93.00	0.00		0.00									
2089																			

324

Table 54. Continued.

ID																		
2094	0.00	2.00	0.00	8.00	42.00	51.00	76.00	2.00	6.00	0.00	42.00							
2187	0.00	0.00	0.00	13.00	38.00	49.00	117.00	50.00	9.00									
2191	2.00	0.00	0.00	80.00	66.00	160.00	109.00	48.00	0.00		21.00							
2197	0.00	0.00	0.00	8.00	32.00	22.00	81.00	9.00	0.00									
2280	0.00	0.00	0.00	6.00	28.00	17.00	71.00	13.00	0.00									
2542	0.00	0.00	0.00	0.00	28.00	33.00	47.00	29.00	7.00	0.00	28.00							
2547				11.00	24.00	11.00	9.00	0.00			38.00							
2729	1.00	0.00	6.00	17.00	40.00	109.00			1.00		28.00	22.00						
2850				5.00	39.00	36.00	72.00	19.00	89.00		35.00							
2896				18.00	32.00	92.00	95.00	29.00	0.00		24.00							
2901		38.00	0.00	6.00	34.00	37.00	91.00	36.00	37.00		32.00	5.00						
2938		5.00	0.00	5.00	22.00	30.00	83.00	13.00	17.00	0.00	53.00	16.00						
2942		4.00	2.00	18.00	27.00	51.00	82.00	34.00	11.00		30.00	24.00	67.00	9.00	74.00	53.00	101.00	88.00
2947	0.00	18.00	7.00	34.00	22.00	103.00	125.00	37.00	14.00		21.00	49.00						
2981		0.00	4.00	19.00	30.00	125.00	107.00	79.00	54.00	0.00	16.00	15.00		38.00	86.00	89.00	20.00	0.00
3055		36.00	1.00	5.00	39.00	46.00	93.00	30.00	75.00		22.00	0.00		5.00	73.00	67.00	64.00	53.00
3059	0.00			12.00	26.00	21.00	87.00	31.00	34.00	25.00	43.00	4.00	0.00	42.00				
3074				12.00	21.00	4.00	47.00	4.00	5.00	0.00	39.00							
3075		34.00	0.00	7.00	27.00	23.00	62.00	15.00	21.00		55.00	5.00		20.00	75.00	109.00	77.00	41.00
3080		25.00	0.00	0.00	18.00	20.00	65.00	7.00	10.00		36.00	3.00		1.00	50.00	67.00		50.00
3097		0.00	2.00	16.00	26.00	13.00	24.00	0.00	0.00									
3138		1.00	1.00	18.00	24.00	112.00	137.00	36.00	23.00		15.00		124.00					
3139		30.00	10.00	20.00	17.00	49.00	97.00	13.00	12.00				48.00	0.00	94.00	89.00	85.00	36.00
3140		39.00	0.00	16.00	28.00	54.00	88.00	19.00	20.00		22.00	6.00		5.00	28.00			
3144		13.00	2.00	5.00	39.00	49.00	103.00	57.00	50.00		40.00	2.00		15.00				
3149		8.00	3.00	21.00	24.00	76.00	44.00				24.00	15.00		2.00	27.00	124.00		
3155		9.00	6.00	21.00	34.00	104.00		38.00	28.00	0.00	30.00	10.00		40.00	30.00			
3156		2.00	2.00	26.00	20.00	36.00	14.00											
3169	7.00	17.00	0.00	18.00	58.00	56.00	88.00	35.00										
3173		20.00	3.00	8.00	27.00	56.00	122.00	40.00	0.00	2.00	34.00	16.00						
3195		20.00	4.00	18.00	21.00	47.00	92.00	36.00	20.00		20.00	86.00						
3204	0.00			14.00	22.00	74.00	148.00	39.00	43.00	0.00	39.00							
3235	0.00			11.00	47.00	24.00	5.00	1.00										
3260		8.00	7.00	27.00	13.00	39.00	64.00	11.00	22.00	0.00	36.00	6.00	52.00	66.00				
3261		12.00	2.00	16.00	22.00	45.00	123.00	43.00	5.00		27.00	9.00	69.00	9.00				
3263		34.00	8.00	12.00	31.00	165.00		56.00	73.00		21.00	16.00	43.00					
3266		1.00	0.00	15.00	18.00	17.00	60.00	22.00	0.00		37.00	0.00		35.00				
3267	0.00	32.00	9.00	11.00	36.00	70.00	125.00	41.00	24.00		22.00	26.00		23.00	67.00	69.00	110.00	97.00
3273	0.00	10.00	0.00	42.00	15.00	142.00	158.00	50.00	82.00	3.00	30.00	10.00	109.00					
3274		8.00	771.00															
3279	0.00	3.00	0.00	1.00	33.00	62.00	98.00	12.00	26.00	0.00	26.00	1.00		1.00				
3282	0.00	0.00	0.00	25.00	36.00	63.00	125.00	49.00	24.00		31.00		67.00	3.00	45.00	43.00	53.00	16.00
3286		27.00	3.00	0.00	34.00	27.00	119.00	49.00	45.00	0.00	18.00	3.00		16.00				
3306		1.00	2.00	16.00	20.00	10.00												
AVERAGE	11.00	20.22	23.00	18.34	31.34	56.46	89.34	33.65	31.18	10.70	31.11	17.06	71.75	17.05	56.27	65.43	82.36	49.80

Table 55. Average porosity of C Submembers from log analysis.

WELL	C1	C2U	C2L	C3U	C3M	C3L	C4U	C4M	C4L	C5U	C5UM	C5LM	C5L	C6UU	C6LU	C6M	C6UL	C6LL	C7
652		0.16		0.17	0.17	0.16	0.16	0.16	0.16	0.14	0.20								
827		0.18		0.18	0.19	0.15	0.16	0.14			0.19								
846				0.15	0.17	0.16	0.15				0.17								
847		0.19			0.18	0.16	0.17	0.16	0.14		0.20	0.14		0.09	0.09				
851		0.24	0.17			0.18	0.18	0.16	0.16	0.15	0.21	0.15							
852						0.15	0.14												
866						0.16	0.18												
895	0.16	0.16		0.17	0.18	0.17	0.16	0.14											
900	0.17	0.15		0.16	0.17	0.15	0.14	0.16											
917		0.15		0.18	0.20	0.15	0.14	0.16	0.14		0.17			0.09	0.10	0.11			
946	0.16	0.20		0.16	0.18		0.14	0.14			0.18			0.10	0.12				
971	0.19	0.16	0.15	0.16	0.15		0.16												
975		0.15		0.16	0.19	0.17					0.20								
1010		0.19	0.19	0.20	0.21														
1022		0.19					0.17												
1060																	0.10		
1061				0.16	0.17		0.17									0.09			
1089		0.16		0.15	0.15	0.15	0.16	0.15	0.15		0.20			0.09	0.10	0.10	0.11		
1095					0.16	0.15	0.14	0.15	0.15		0.16							0.11	0.08
1106					0.20	0.16	0.19				0.19								
1129	0.16	0.15		0.15	0.16	0.17	0.16	0.16	0.15		0.18	0.14							
1130	0.16	0.16		0.15	0.19	0.16	0.15	0.17	0.15		0.16	0.14		0.10	0.11				
1162		0.15	0.16	0.16	0.18	0.16	0.16	0.15	0.15										
1172		0.16	0.15	0.17	0.17	0.16		0.16	0.14				0.11	0.10	0.11				
1176	0.15	0.15	0.15	0.16	0.18	0.17	0.16	0.17	0.14			0.14							
1198	0.17	0.18		0.15	0.16	0.16	0.16	0.15	0.16	0.17	0.21	0.15							
1218				0.20		0.21	0.17	0.17	0.14										
1245			0.15	0.17	0.18	0.19	0.18	0.15	0.14		0.18		0.12						
1276	0.16			0.19	0.18	0.17	0.16				0.15			0.11		0.11	0.11	0.12	0.10
1293		0.16		0.16	0.19	0.18	0.16	0.16	0.16	0.16	0.18	0.16				0.11	0.11		
1303		0.18	0.16	0.17	0.19	0.17		0.16	0.15	0.16	0.16	0.13							
1307			0.15	0.17	0.19	0.18		0.14			0.18								
1310				0.15	0.20	0.15	0.15		0.16		0.20								
1312		0.17		0.17	0.18	0.17	0.17	0.14	0.15		0.17	0.15	0.12		0.12				
1316				0.17	0.16	0.18	0.18	0.16	0.15										
1679		0.17	0.19																
1695	0.16	0.16	0.16	0.17	0.19	0.17	0.17	0.16	0.17	0.16	0.16	0.14		0.10					
1748	0.15	0.16	0.15	0.18	0.16	0.15	0.15						0.11				0.11	0.11	0.09
1782					0.17		0.16	0.15				0.12			0.11	0.10	0.11		
1799					0.16										0.10	0.10	0.11		
1803	0.14	0.18		0.17	0.19	0.17	0.16	0.15	0.15		0.19		0.11		0.10				
1876	0.17	0.16	0.16	0.16	0.17	0.18	0.17	0.19				0.13			0.10				
1985		0.15		0.17	0.17	0.16	0.16	0.17											
1986	0.18	0.15		0.16	0.19	0.17	0.18	0.18			0.19								
1987		0.18	0.18		0.17	0.19		0.17			0.19								
2010	0.15	0.17		0.17	0.17	0.17	0.16	0.15	0.16		0.17								
2038	0.15	0.15	0.16	0.17	0.20		0.17	0.15	0.15		0.18								
2089				0.19	0.17	0.17	0.17												
2094		0.16	0.15	0.16	0.20	0.17	0.17	0.16											

Table 55. Continued.

ID	1	2	3	4	5	6	7	8	9	10	11	12	13	14	15	16	17	18	19	20
2187			0.16	0.20	0.17	0.17	0.16	0.16	0.16		0.20									
2191	0.20			0.20	0.18	0.17	0.16	0.15	0.15		0.17									
2197				0.19	0.17	0.17	0.15	0.14												
2280				0.21	0.18	0.16	0.16	0.15												
2542				0.17	0.17	0.17	0.15		0.15		0.21	0.13								
2547				0.19	0.17		0.14				0.20									
2729			0.18	0.19	0.19	0.17		0.16	0.16		0.17	0.13								
2850				0.18	0.17	0.18	0.16				0.17									
2896				0.18	0.19	0.17	0.17				0.19									
2901		0.19		0.19	0.18	0.17	0.16	0.16			0.18	0.14		0.11	0.11	0.11	0.11	0.11	0.12	0.10
2938		0.17		0.17	0.18	0.17	0.17	0.17			0.21	0.15		0.11	0.11	0.11	0.11	0.11	0.12	
2942		0.18	0.17	0.18	0.17	0.16	0.16	0.15			0.16	0.16		0.10	0.11	0.11	0.12	0.12	0.12	
2947		0.16	0.17	0.17	0.17	0.18	0.18	0.16			0.18	0.14	0.11	0.11	0.11	0.11	0.11	0.12	0.12	
2981			0.17	0.17	0.17	0.16	0.17	0.17			0.16	0.15								0.09
3055		0.20		0.20	0.19	0.18	0.16	0.16	0.18		0.19									
3059				0.17	0.17	0.17	0.17	0.17			0.20	0.13								
3074				0.21	0.18	0.16	0.16	0.15			0.20									
3075		0.18	0.18	0.20	0.17	0.17	0.16	0.15			0.18	0.13		0.11	0.10	0.10	0.11	0.11		0.09
3080		0.18		0.19	0.18	0.16	0.17	0.17			0.18	0.12		0.11	0.11	0.11	0.11	0.12		0.10
3097			0.18	0.20	0.18	0.17	0.16				0.16		0.13							
3138		0.17		0.17	0.18	0.18	0.18	0.17					0.11							
3139		0.18		0.17	0.18	0.17	0.18	0.16			0.17	0.14		0.10	0.11	0.11	0.12	0.13	0.10	
3140		0.16	0.17	0.16	0.18	0.17	0.16	0.16			0.19	0.11		0.11	0.11					
3144		0.15	0.15	0.18	0.17	0.17	0.18	0.17			0.18	0.13								
3149		0.17	0.16	0.20	0.18	0.18		0.17	0.20		0.20	0.14		0.11	0.10	0.10	0.10	0.13		
3155		0.16	0.15	0.19	0.17															
3156		0.16		0.20	0.16	0.15	0.15				0.18									
3169	0.17	0.17		0.20	0.18	0.16	0.16	0.17			0.20									
3173		0.16		0.18	0.18	0.18	0.17				0.18	0.15	0.13							
3195			0.18	0.19	0.18	0.17	0.16	0.16			0.19	0.15	0.11							
3204			0.17	0.17	0.17	0.16	0.17	0.14			0.19									
3235				0.20	0.19	0.18														
3260		0.15	0.17	0.19	0.18	0.17	0.15	0.15			0.17	0.15	0.11	0.10			0.11			
3261		0.16	0.15	0.17	0.17	0.16	0.15	0.15			0.18	0.17	0.11							
3263		0.17	0.18	0.19	0.18	0.16	0.16	0.16			0.19	0.15	0.11							
3265				0.19	0.19	0.18	0.18				0.18			0.11						
3267		0.17	0.17	0.17	0.18	0.16	0.16	0.16	0.16		0.17	0.15		0.12	0.10	0.11	0.11	0.11	0.12	0.12
3273		0.18	0.17	0.18	0.18	0.16	0.18	0.17			0.17	0.14	0.11							
3274		0.17			0.16	0.18	0.16													
3279		0.18	0.13		0.17	0.18	0.17				0.18									
3282				0.18	0.18	0.18	0.18	0.16	0.15		0.19		0.11	0.10	0.10	0.10	0.11	0.13	0.12	0.10
3286		0.17	0.19	0.18	0.18	0.17	0.17	0.15			0.19			0.11						
3306			0.16	0.18	0.18	0.18	0.16	0.16				0.13								
AVERAGE	0.16	0.17	0.16	0.17	0.17	0.18	0.17	0.16	0.15	0.16	0.18	0.14	0.11	0.10	0.11	0.11	0.11	0.12	0.12	0.10

327

Table 56. Average permeability of C Submembers from log analysis.

WELL	C1	C2U	C2L	C3U	C3M	C3L	C4U	C4M	C4L	C5U	C5UM	C5LM	C5L	C6UU	C6LU	C6M	C6UL	C6LL	C7
652		6.93		16.82	25.70	10.56	44.10	114.19	43.85	2.08	94.19								
827		39.83		33.78	176.64	5.95	117.55				57.80								
846				5.50	54.21	8.61	17.57				72.67								
847		496.49			54.72	7.46	86.32	4.70			195.03	3.64		0.20	0.17				
851		1909.63	28.40			68.20	88.78	58.01	3.57	5.15	459.16	6.76							
852				17.51	63.73	4.73	5.30	3.50			226.18								
866	6.70			10.24	19.20	10.28	144.92	31.23											
895	24.05	7.98		82.84	298.99	15.96	38.39												
900		4.24		7.64	106.31	4.97	5.54												
917		5.06		10.33	82.98	3.72	6.98	51.14	3.41		54.21			0.16	1.44	1.82			
946		328.92		7.19	4.52		8.62	6.72			54.72			0.61	5.12				
971	13.26	11.76	5.63	9.33	233.36	22.11	23.44												
975	191.28	4.10																	
1010		61.36	46.55	155.70	459.16		47.77				298.99								
1022		58.20																	
1060																			
1061				5.96	15.02												0.79		
1089		6.59		3.33	3.31	3.68	152.78	22.44	8.48		269.52			0.19	0.74	0.21			
1095					7.23	3.92	8.77	15.98	15.22		7.59	3.05				0.51	3.34	1.64	0.18
1106					173.36	23.34	94.45				117.05								
1129	10.37	4.48		4.58	9.97	13.35	22.74	26.10	12.48		121.81	1.80		0.39	1.10				
1130	7.97	6.26		4.04	259.47	13.02	21.30	93.61	9.48		7.23	3.05							
1162		4.29	6.44	8.37	49.49	14.59	86.35	22.97	12.94										
1172		12.20	5.17	23.63	26.58	14.12		99.48	6.69			2.60	2.14	1.16	2.98				
1176	3.70	3.90		18.12	120.88	17.21	91.37	213.14	4.77			5.74							
1198	10.70	46.12		8.78	13.13	15.50	58.69	37.40	23.58	16.70	578.09								
1218			6.68	326.76	129.88	8.88		109.18	5.86										
1245				11.88	94.02	400.14	129.33	9.35	4.07		67.07		5.23						
1276	7.94	7.00		43.76	70.28	115.11	211.43		86.91		3.31	12.69		2.83	2.36	2.49	10.92	8.04	2.45
1293			10.14	9.22	53.88	98.01	56.25	45.15		7.94	108.14	1.36							
1303		33.26	3.56	48.03	268.51	28.69	86.93	35.26	11.85	10.37	9.97								
1307				23.51	162.03	97.21		6.57			53.88								
1310				4.47	144.98	4.82	33.47		27.06		284.25								
1312		17.55		25.37	108.14	46.65	224.27	8.60	48.75		32.07	5.75	8.23						
1316			95.82	44.58	9.75	118.47	187.69	30.49	7.36										
1679		24.59	28.99		274.51	45.04	154.42	52.53	99.99										
1695	9.58	6.86	7.34	31.31	7.59	5.08	12.65	15.61		9.58	6.61	2.64		0.34	0.92	0.35	3.81	3.44	
1748	5.15	8.56	2.99	132.31	21.79	6.40	78.17												
1782												0.67	3.81						
1799				27.55	6.61														
1803	2.08	27.28		35.00		28.91	72.79	11.99	13.14		176.64	0.96							
1876	28.52	7.28	7.25	9.80	173.35	138.80	173.11	131.79							1.13	0.74	2.45	2.86	0.89
1985		4.02		18.23	23.29	18.22	69.94	88.72											
1986		4.28		11.10	39.13	21.82	56.74	177.98			274.51								
1987	28.82	29.84	28.99		57.80	100.93	161.19												
2010	4.13	10.84	11.45	16.96	19.09	17.13	53.52	16.94	52.60		23.29								
2038	5.01	6.11		105.23		133.51	133.51	22.89	7.68		70.26								
2089				86.05	19.94	27.51	109.88												
2094		7.69	4.44	7.33	156.24	65.64	75.06	16.80											

Table 56. Continued.

ID	1	2	3	4	5	6	7	8	9	10	11	12	13	14	15	16	17	18	19
2187				35.67	169.22	27.73	120.70	48.39	23.95		156.24								
2191	112.31			293.52	226.18	47.81	108.42	71.08	9.59		19.09								
2197				7.47	91.20	16.14	22.16	5.05											
2280				25.79	215.22	38.25	120.32	27.00											
2542				42.81	26.29	20.41	29.52	11.39	6.92		215.22								
2547					216.69	19.86	4.51				169.22								
2729				24.92	81.29	248.65			36.11		26.29	2.41							
2850		39.81		44.25	57.79	24.12	38.19	220.42			21.79								
2896				70.86	78.69	79.12	155.22	114.72	42.55		216.69	2.89							
2901		162.84		23.36	70.71	99.96	252.19	114.21	163.60		78.69								
2938		17.57		15.04	72.67	20.32	25.69	21.06	12.11		311.37	4.81							
2942		154.39	16.21	118.73	67.07	33.12	295.79	209.73	88.08		25.58	21.64	3.32	1.93	2.22	2.47	2.14	6.72	3.89
2947		11.03	16.74	29.52	103.74	75.30	118.88	84.52	65.95		13.13	6.67		2.72	2.51	3.65	5.23	7.93	
2981		319.18	21.19	60.74	27.23	247.21	183.31	166.81	137.50		94.02	11.01		0.41	1.22	1.58	3.32	4.45	0.98
3055				78.30	152.48	59.62	341.66	36.79	126.58		103.74	0.95		2.18					
3059				26.01	90.83	14.74	73.44	52.35	18.10	28.82	268.51								
3074				209.06	284.25	54.16	46.72	18.42			152.48								
3075		50.33		277.56	69.48	17.25	71.57	11.80	30.84		49.49	1.59		1.42	0.62	1.13	5.53		0.78
3080		46.92			98.50	84.34	136.53	14.85	61.15		73.09	0.71			3.33	2.24	3.40	8.65	2.58
3097		31.84		539.43	195.03	19.54	38.84												
3138		30.98		23.05	43.10	68.70	221.20	89.75	67.75		9.59		23.95						
3139		72.13	41.22	43.78	369.51	107.00	127.06	153.97	11.05			5.89	2.45						
3140		11.26	11.45	88.81	32.07	92.72	131.78	33.53	55.78		26.22	0.23		0.80	3.60	5.16	8.23	16.26	2.94
3144		4.86	3.57	8.03	124.79	54.75	255.69	119.65	133.89		81.29	1.54							
3149		18.81	10.50	76.96	296.43	54.03	99.56				43.10			0.51	0.79	0.55	23.95		
3155		7.44	4.11	32.67	143.88	193.23		94.77	191.53		144.98	2.80		1.75	2.82				
3156		9.42		187.77	214.13	55.49	14.73	52.84											
3169	29.54			26.38	269.52	27.60	45.88	79.12		112.31									
3173		70.96	50.65	9.64	38.49	49.29	140.38	123.22	27.73		143.88	9.16							
3195		10.61	15.86	31.79	192.13	76.29	189.78	39.56	5.89		214.13	4.48							
3204			9.00	129.12	26.22	134.28	136.10				124.79								
3235				50.72	213.04	78.96	29.64												
3260		5.44	56.18	133.25	117.05	84.32	88.47	72.12	32.63		29.39	7.12	3.34	1.04					
3261		10.89	6.40	181.35	35.12	28.82	152.01	85.18	12.92		38.49	43.69	3.25						
3263		37.62	48.10	18.58	177.46	163.75		56.28	116.13		192.13	4.35	3.78						
3265				41.44	159.78	197.19	205.64	220.54			63.73			1.86					
3267		27.00	17.44	27.27	29.39	52.83	187.32	102.02	99.98	7.97	35.12	6.76	5.53	9.06	1.54	1.28	3.25	6.37	8.07
3273		48.11		32.23	9.59	62.29	114.06	154.78	119.23		27.23	6.30							
3274		18.64	27.37																
3279		32.19			73.99	76.49	211.77	55.88			90.83								
3282		38.77		32.09	73.09	78.75	113.86	202.51	26.33		177.46		3.40	0.73	0.93	1.42	3.78	9.52	1.48
3286			63.87	63.29	74.08	24.44	141.20	31.42	125.55		159.78	0.78		5.07					
3305					121.81	103.45													
AVERAGE	28.17	77.72	21.52	59.77	110.92	57.75	102.09	69.34	46.78	22.32	120.02	5.86	5.70	1.68	1.87	1.71	5.72	6.90	2.42

Table 57. Average kh of C Submembers from log analysis.

WELL	C1	C2U	C2L	C3U	C3M	C3L	C4U	C4M	C4L	C5U	C5UM	C5LM	C5L	C6LU	C6U	C6M	C6UL	C6LL	C7
652		214.90		504.58	488.24	1403.91	6482.42	6965.76	2675.06	31.24	4991.85								
827		1593.01		675.88	4415.99	344.82	11049.54				2254.32								
846				16.49	1626.20	301.17	1799.80	46.95			1598.74								
847		9929.75			1313.35	111.84	7337.42	2030.45	14.28		5070.80	69.23		0.80					
851		24825.18	113.61			3751.14	5770.84			113.20	2295.78	114.83			0.67				
852				140.08	2357.92	61.42	13477.33	10.49			14927.81								
866	134.07			71.88	422.31	154.21	95.44												
895	96.20	447.09		3810.78	19135.19	2553.05	5182.65												
900		21.20		262.05	3189.30	129.17	298.86	749.39											
917		60.66		51.64	2240.56	18.60	244.20	2608.17	27.31		1626.20			0.32	61.90	190.90			
946		26642.65		237.41	81.27		542.80	80.62			1313.35			11.03	363.45				
971	278.39	364.58	101.32	578.24	17035.04	4178.88	3562.54												
975	3443.12	12.29									19135.19								
1010		2025.00	139.64	4048.18	2295.78		668.75												
1022		1455.01																	
1060		428.46																	
1089				274.27	1171.52	298.01	1762.57	2962.40	93.26		227.81			1.16	16.17	18.94	173.61	216.06	4.72
1095				29.94	39.72	103.71	4261.39	798.98	1247.95		1521.59								
1106					6934.21	583.46	11050.98												
1129		17.85		54.90	568.43	1856.08	3183.81	1096.18	374.40		2436.29	90.05		4.70	57.19				
1130	155.53	118.84	19.32	60.59	16606.17	2473.41	1661.41	4305.86	606.81		166.36	158.75							
1162	23.91	38.57	15.52	142.21	2721.97	802.60	9671.43	987.81	491.53										
1172	7.39	414.70		282.39	767.27	635.51	7858.00	4077.84	147.10			52.04	113.47	18.53	127.93				
1176		187.62	18.31	628.60	5584.81	946.44	3925.63	9378.34	81.10			28.72							
1198	267.17	1127.89		23.16	275.74	775.03	10216.78	1496.16	707.52										
1218			22.74	13472.57		293.16			222.35										
1245				106.74	1504.25	5201.87	3382.83	14629.78	12.20	267.17	35841.31		465.19						
1276				131.24	1053.91	2647.63	8155.65	74.76			1810.75	63.44		19.77	30.66	117.14	436.90	690.98	41.67
1293	15.87	42.00	30.42	82.95	1939.55	9997.38	5583.38	1489.79	2475.55	15.87	3568.59	4.07							
1303		1163.88	7.13	2065.34	11546.01	889.34		881.54	225.15	155.53	568.43								
1307				211.57	1944.33	5832.65		85.35			1939.55								
1310				13.40	4349.37	43.40	1171.30		162.36		5969.18								
1312		228.10		405.91	3568.59	3358.92	21081.56	275.21	3315.26		897.99	120.75	732.72						
1316			766.55	579.55	272.97	7818.69	28904.56	1036.74	250.07										
1679	57.47	122.97								57.47	79.29	52.74							
1695	113.20	171.44	14.88	1377.48	7411.85	7251.74	25634.17	2836.37	6799.18										
1748		145.52	8.97	2513.84	227.81	71.14	948.65	249.68				3.36	194.47	1.70	35.69	13.79	194.47	316.32	
1782				385.76	762.78	19.19	1016.22												
1799					79.29														
1803	31.24	54.57		1260.04		636.03	9754.32	299.66	157.71		4415.99	12.51			27.03	31.05	117.53	245.56	64.97
1876	86.57	58.23	14.49	68.61	6240.49	5829.61	13502.71	395.36											
1985		20.10		54.69	815.11	1403.09	9581.56	4258.47											
1986		8.55		77.71	1447.75	916.60	3461.41	4983.31			7411.85								
1987	720.43	1253.26	260.89		2254.32	5046.48	19665.00												
2010	20.66	32.51		254.33	400.93	753.75	4281.49	457.29	1262.50		815.11								
2038	110.30	268.75	366.42	5997.98			14819.05	961.33	99.89		1053.91								
2089				1290.79	777.66	935.16	10218.94												
2094		15.37	13.32	58.61	6562.17	3347.76	5704.70	33.59											
2187				463.76	6430.33	1358.89	14121.67	2419.37	143.71		6562.17								

Table 57. Continued.

ID																			
2191	224.61		23481.72	14927.81	7649.16	11817.50		3411.67	86.34		400.93								
2197			59.75	2918.38	355.06	1795.21		45.44											
2280			154.72	6026.13	650.24	8542.93		351.03											
2542				736.20	673.46	1387.27		330.44	48.42		6026.13								
2547			470.87	5200.57	218.47	40.58					6430.33								
2729	238.88		423.63	3251.71	27102.47				3213.59		736.20	53.01							
2850			221.22	2253.69	868.14	2749.38		762.78			762.78								
2896			1275.43	2518.12	7278.56	14745.67		4187.97	1574.48		5200.57								
2901	6188.00		140.17	2403.98	3698.59	22949.05		3326.99	2781.18		2518.12	14.46							
2938	87.85		75.19	1598.74	609.58	2131.96		4111.45	133.17		16502.37	76.90							
2942	617.55	32.41	2137.18	1810.76	1689.13	24254.45		273.79	7130.72		767.27	519.48	17.40	39.90		113.47		678.43	342.45
2947	198.55	117.19	1003.50	2282.27	7755.61	14860.12		3127.14	1233.16		275.74	326.96	103.44	145.27		313.43		158.53	
2981	84.78		1154.03	816.86	30901.81	19614.03		13177.58	3561.49		1504.25	165.19	2.03	19.45		115.58		285.09	52.13
3055	11490.53		391.51	5946.75	2742.30	31774.63		1103.75	10312.60		2282.27		91.56						
3059			312.17	2361.64	309.51	6389.21		1622.87	4303.73		11546.01	3.81							
3074			2508.76	5969.18	216.63	2196.03		73.68	90.48	720.43	5946.75								
3075	1711.34		1942.91	1876.01	396.78	4437.25		176.94	647.68		2721.97	9.54	28.43	10.49		84.98		602.85	32.10
3080	1173.02			1773.00	1686.83	8874.43		103.93	611.53		2631.35	2.14		96.57		111.89		228.00	129.14
3097		63.68	8630.81	5070.80	254.05	932.13													
3138	929.48		368.85	1034.41	7694.05	30304.71		3231.00	1558.22		143.84				2969.52		2969.52		
3139	2813.03	412.19	875.58	6281.70	5243.16	12324.46		2001.64	132.57			35.34	4.02	100.70		732.72	117.53	1382.09	105.93
3140	146.34		1421.02	897.99	5007.09	11596.32		636.98	1115.56		576.82	0.46							
3144	38.87	22.91	40.15	4866.77	2682.67	26335.54		6819.84	8033.41		3251.71	23.17							
3149	169.31	10.72	1616.13	7114.42	4106.40	4380.45			1034.41			1.02	21.24		2969.52				
3155	14.89	62.98	686.04	4891.92	20095.36			3601.10	4349.37			27.95	69.87	84.63		2.73			
3156	160.06	8.22	4881.95	4282.51	1997.81	206.23													
3169	206.77		474.91	15632.31	1645.43	4037.55		1849.40		224.61									
3173	1419.24	151.96	77.10	1039.18	2760.24	17126.21		3164.69	554.59		4891.92	146.63							
3195	212.18	63.46	508.70	4034.74	3685.44	15561.88		4312.54	253.29		4282.51	385.30							
3204		36.99	1007.66	676.82	9936.81	20143.24		1542.72			4866.77								
3235			667.97	10013.06	1986.07	149.20													
3260	43.55	393.27	367.71	1621.88	3200.66	5601.87		793.33	717.66		1058.06	42.69	68.58			173.61			
3261	130.67	12.90	2901.96	772.71	1296.73	10697.13		3662.66	64.56		1039.18	393.22				223.95			
3263	1278.99	304.79	222.98	5601.31	27019.23			3151.56	8477.52		4034.74	89.63				162.65			
3265			621.61	2076.97	3962.28	12338.45		4851.82			2357.92		65.01						
3267	863.92	156.96	299.98	1058.08	3698.34	23415.28		4190.14	2399.47		772.71	175.87	208.42	43.20		223.95		700.80	782.27
3273	461.13		1363.64	143.84	8844.99	18022.05		7739.02	9776.43	23.91	816.86	62.95		85.45					
3274	149.08	21098.13																	
3279	96.57		2441.69	4742.28	20753.79			670.53			2361.64								
3282			2631.35	4961.50	14232.14			9922.75	631.94		5501.31	228.00	2.20	25.16		63.73		504.64	23.64
3286	1048.88	191.62	2518.69	659.84	16802.90			1539.41	5649.61		2875.97	81.12				162.65			
3306		17.47	1012.60	2436.29	1034.54							2.35							
Average	332.88	707.60	1841.25	1445.03	3630.56	3727.30	9776.84	2715.14	1898.36	178.83	3983.48	517.18	100.23	38.15	68.80	129.81	511.00	531.35	157.90

331

Table 58. Average Øh of C Submembers from log analysis.

WELL	C1	C2U	C2L	C3U	C3M	C3L	C4U	C4M	C4L	C5U	C5UM	C5LM	C5L	C6UU	C6LU	C6M	C6UL	C6LL	C7
652		4.85		5.00	3.20	21.30	23.06	9.72	9.80	2.06	10.46								
827		7.30		3.57	4.81	8.96	14.80	1.39			7.30								
846				0.46	4.94	5.51	14.89				3.82								
847		3.89			4.30	2.36	13.98	5.68	0.54		5.18	2.72		0.37					
851		3.09	0.68			9.85	11.37			3.35	1.05	2.62			0.36				
852				1.35	6.60	1.97	2.54	0.41			13.11								
866				1.14	3.68	2.41	16.30	3.84											
895	3.13	8.93		8.25	12.83	26.67	22.11							0.18	4.35				
900	0.70	0.75		5.13	5.48	3.95	7.63							1.84	8.52				
917		1.83		0.81	4.96	0.74	4.95	7.97	1.08		4.94					11.28			
946		16.49		5.15	2.72		9.09	1.72			4.30								
971	3.34	4.95	2.76	9.72	14.13	31.26	23.92												
975	3.43	0.45									12.83								
1010		6.31	0.56	5.10	1.05														
1022		4.77					2.42												
1060				7.13															
1061					12.91						11.61					0.37	1.54		
1089		10.15		1.32	1.76	0.59	3.58	20.22	1.63		4.70			0.55	2.21				
1095					3.61	11.30	28.89	7.62	12.37		2.43					3.66	5.64	14.41	2.26
1106					7.82	2.63	28.07							1.18					
1129	2.43	0.60		1.81	9.15	4.31	22.59	6.64	4.50		3.67	6.79							
1130	0.48	2.97		2.23	12.22	22.01	22.10	7.75	9.31		3.61	7.41							
1162		1.35	0.47	2.69	9.80	30.77	11.86	6.63	5.66			2.72	5.67	1.64	4.69				
1172		5.51	0.46	2.01	5.09	9.00	18.10	6.73	3.14			0.74							
1176	0.30	6.39	0.61	6.34	7.82	7.19		7.39	2.37										
1198	2.69	4.37		0.61	3.43	9.06		6.18	4.68										
1218			0.61	8.52		8.17		22.07	5.35	2.69	13.05								
1245				1.49	2.80	5.20	13.73	1.19	0.41		4.88		10.36						
1276				0.56	2.73	2.66	10.86				1.76	0.78		0.76					
1293	0.32	0.94		1.44	6.34	4.28	2.82	5.33	5.97	0.32	5.96	0.39			1.46	5.05	4.47	10.17	1.70
1303		6.13	0.49	7.48	8.06	18.15	22.92	4.06	2.81	2.43	9.15								
1307			0.30	1.51	2.22	5.40	10.31	1.86			6.34								
1310				0.45	5.89	10.94	5.18		0.94		4.27								
1312		2.17		2.71	5.96	1.38	15.93	4.60	9.96		4.86	3.08	10.82						
1316			1.50	2.23	4.48	12.37		5.42	4.98										
1679	0.97	0.87		7.47	5.06	12.02	27.24	8.68	11.23	0.97	1.87	2.71							
1695	3.35			3.45	4.70	28.09	28.18												
1748		3.90	0.32		5.91		11.20							0.49		3.86	5.66	10.22	
1782		2.72	0.43	2.44	1.87	2.13		2.41				0.62	5.66		4.11				
1799						0.47	2.12												
1803	2.06	0.35		6.12	6.87	3.72	21.80	3.72	1.76		4.81	1.65			2.41				6.82
1876	0.52	1.25	0.31	1.13	6.02	7.70	13.37	0.56								4.28	5.38	9.77	
1985		0.75		0.50	6.40	12.65	22.52	8.02											
1986		0.30		1.14	7.30	7.08	9.71	5.03			5.06								
1987	4.42	7.52	1.60			9.32	21.84	3.97											
2010	0.75	0.50		2.51	3.52	7.37	12.75	6.37	3.87		6.02								
2038	3.34	6.78	5.18	9.89			18.97		1.89		2.73								
2089				2.78	6.57	5.78	15.84												
2094		0.32	0.45	1.25	8.25	8.70	12.74	0.32											

332

Table 58. Continued.

ID	C1	C2	C3	C4	C5	C6	C7	C8	C9	C10	C11	C12	C13	C14	C15	C16	C17	C18	C19
2187				2.13	7.49	8.34	19.95	7.85	0.93			8.25							
2191	0.40			15.31	13.11	28.18	18.37	7.84	1.33			3.52							
2197				1.26	6.16	3.63	12.46	1.26											
2280				1.04	5.77	2.98	11.58	2.09	1.01										
2542					4.77	5.49	7.41	4.33											
2547				1.99	4.62	1.89	1.23		13.99			5.77							
2729				2.89	7.39	20.48						7.49							
2850			1.09	0.91	7.00	6.08	11.22	3.33		2.90		4.77							
2896				3.25	5.88	16.50	17.73	4.80	5.79			5.91							
2901		7.20		0.99	6.38	6.74	16.22	5.93	2.91			4.62							
2938		0.85		0.83	3.82	5.11	13.16	2.04	1.62		0.71	5.88							
2942		0.73	0.34	3.40	4.88	8.65	14.87	5.92	2.35		2.34	11.02		0.98	1.93	8.06	5.67	12.00	8.98
2947		2.91	1.17	5.89	4.13	17.76	20.86	5.90	8.83		3.86	5.09	7.48	4.24	6.40	9.43	10.36	2.43	
2981			0.68	3.43	5.19	23.23	18.42	13.92	12.89		7.08	3.43		0.49	1.73	7.79	7.48	7.37	4.96
3055		7.14		0.96	7.60	8.22	17.52	4.80	5.77		2.30	2.80							
3059				2.00	4.78	3.45	14.84	5.14	0.77	4.42		4.13		4.74					
3074				2.48	4.27	0.73	7.29	0.62			0.51	8.06							
3075		6.07		1.38	5.03	3.81	9.99	2.21	3.24		0.80	7.60		2.11	1.68	7.61	11.96		3.84
3080		4.58			3.39	3.57	10.90	1.07	1.66		0.37	9.80			3.30	5.30	7.38	8.98	5.06
3097			0.36	3.15	5.18	2.16	3.87		3.87			6.61							
3138		5.05		2.70	4.22	19.95	24.23	5.88	1.75		0.84	2.40	16.12						
3139		6.97	1.66	3.41	3.13	8.57	16.70	2.36	3.14		0.22	3.65	5.38						
3140		2.12		2.82	4.86	9.69	14.77	3.09	10.30		1.96	7.39		0.51	3.19	10.75	10.82	10.70	3.60
3144		1.21	0.33	0.79	7.30	8.39	18.49	9.96				4.22							
3149		1.49	0.44	3.84	4.73	13.38	7.87	6.39	4.62		1.39	5.89		0.20	2.75		16.12		
3155		0.32	0.95	3.62	6.42	17.91						6.42			3.19	0.50			
3158	1.16		0.30	4.73	4.02	6.31	2.14			0.40		4.02		4.35					
3169		2.69		2.99	11.61	9.45	14.14	5.80	3.09			7.30							
3173		3.42	0.54	1.29	4.80	9.79	21.38	6.45	6.17		2.43	6.27							
3195		3.23	0.67	2.73	3.92	8.40	14.64	5.92	3.39		12.48	4.80							
3204			0.64	2.68	3.65	13.50	25.33	6.17	0.74			3.92							
3235				1.98	9.26	4.45	0.80		11.76										
3260		1.22	1.22	4.96	2.43	6.97	10.90	1.87			0.90	6.60	5.64	6.83					
3261		1.94	0.31	3.07	3.71	7.50	20.78	7.06	3.88		1.51	3.71	7.56						
3263		5.76	1.42	1.97	5.72	29.42		9.17	14.19		2.34		4.77						
3265				2.75	3.41	3.29		3.93		0.48				3.95					
3267		5.48	1.51	1.92	6.27	12.36	10.79	6.72			3.82	5.19		2.77	2.90	7.05	7.56	13.18	11.93
3273		1.83		7.30	2.40	25.05	22.49	8.53			1.44		11.96						
3274		1.33	98.95				25.98												
3279		0.53			5.92	11.16	17.23	1.95				4.78							
3282				4.19	6.61	11.09	20.89	8.33	3.61			5.72	7.38	0.30	2.77	4.67	4.77	6.44	1.57
3286		4.63	0.57	2.86	5.99	4.59	20.34	7.75	7.37		0.38	3.41		1.79					
3306			0.32		3.67	1.84													
AVERAGE	1.88	3.65	3.62	3.26	5.71	9.70	14.85	5.60	4.90	1.90	2.51	5.74	8.23	1.92	3.34	5.98	7.49	9.61	5.07

333

X. VOLUMETRICS

Calculation of OOIP and Remaining Oil Volumes

The first step in the procedure of calculating OOIP and remaining oil volumes was to prepare computer-generated maps of net pay, S_w, $\emptyset$, k, kh, and $S_o\emptyset h$ for each reservoir submember. These maps were then hand-contoured to reflect trends in net-sandstone thickness and log-facies maps and were later digitized for volumetric calculation. The digitized maps were converted to grids with Zycor's PCMS mapping software (PC mapping system) on 328-ft (100-m) spacing to preserve geological information such as faults, compartment boundaries, and net-sandstone-thickness trends.

Hydrocarbon pore volume ($S_o\emptyset h$) maps were constructed by multiplying oil saturation (S_o), porosity ($\emptyset$), and net-pay (h) values at each grid point. Original oil in place (OOIP) was calculated for each submember and structural compartment by integrating the gridded $S_o\emptyset h$ data with area.

Values and spatial distribution of remaining oil volume were determined in a three-step process. First, OOIP per 80-acre well spacing was calculated by scaling up the 328-ft (100-m) grids to 1,968-ft (600-m) grids. Second, well-by-well production at the submember level, apportioned from kh, was partitioned among adjacent grids by the reverse-distance weighting method. Third, maps of remaining oil in place for individual submembers were prepared by subtracting oil production from oil-in-place values for each 80-acre spacing grid.

The volumetrics analysis has resulted in an increase in the original-oil-in-place resource base of 867 MMbbl (60 percent) to 2,318.2 MMbbl (table 59). This increase was mainly in the C-3-X and C-4-X Members by documenting additional reservoir areas and by using more appropriate and carefully validated petrophysical parameters. For example, the official porosity value used to calculate OOIP for these members was 14 percent, but this study determined a more appropriate value of 17 percent. In contrast, the OOIP estimate in the C-6-X Member was decreased by 31 percent (table 59) as a result of adjusting the average porosity value of 13.2 percent to 11 percent.

This study applied a recovery factor of 20.2 percent for reservoirs in the C members, the same value also previously used by Lagoven. Based on this recovery factor and the volumetric analysis, the estimated ultimate recovery (EUR) of oil at current technology is 468 MMbbl, an increase of 175 MMbbl (60 percent) (table 60). Additionally, the estimated amount of reserves increased by 137 percent (175 MMbbl) from 127.5 to 302.5 MMbbl (table 60).

Net Oil Sandstone

Net-oil-sandstone (net-pay) maps of the C members and submembers (figs. 178 to 185 and app. E) exhibit northeast-trending patterns, reflecting depositional influence on reservoir geometry. Net-pay contours extend across the field in most members and submembers, although in some intervals (for example, the Lower Upper C-6-X Submember, C-5-X Member, Lower C-5-X Submember, combined Middle and Upper Middle C-5-X Submembers, and C-2-X Member), net-pay thickness decreases northeastward, reflecting seaward (northeastward) pinchout of delta-front sandstones. Structural influences are indicated by abrupt changes in net-pay values across faults, particularly in the southwestern and northeastern parts of the field. Net-pay contours are closely spaced and bounded by zero values due to oil-water contacts on the southern and southeastern limbs of the field. Net-pay distribution varies greatly across the field for each member and submember but tends to be greater in the northern part of the field due to steeply dipping strata.

Table 59. Comparison of previous and current estimates of OOIP in the C Members.

Member	Official (Lagoven)	BEG/ Lagoven Study	Incremental	Percent Change
C-1-X	18.8	22.5	3.7	+20
C-2-X	15.9	20.9	5.0	+31
C-3-X-C-4-X	624.8	1,555.8	931.0	+150
C-5-X	220.8	296.1	75.3	+34
C-6-X	571.3	394.5	-176.8	-31
C-7-X	-	28.4	28.4	100
TOTAL	1,451.6	2,318.2	866.6	+60

Table 60. Comparison of previous and current estimates of OOIP, EUR, CP, and reserves in the C Members.

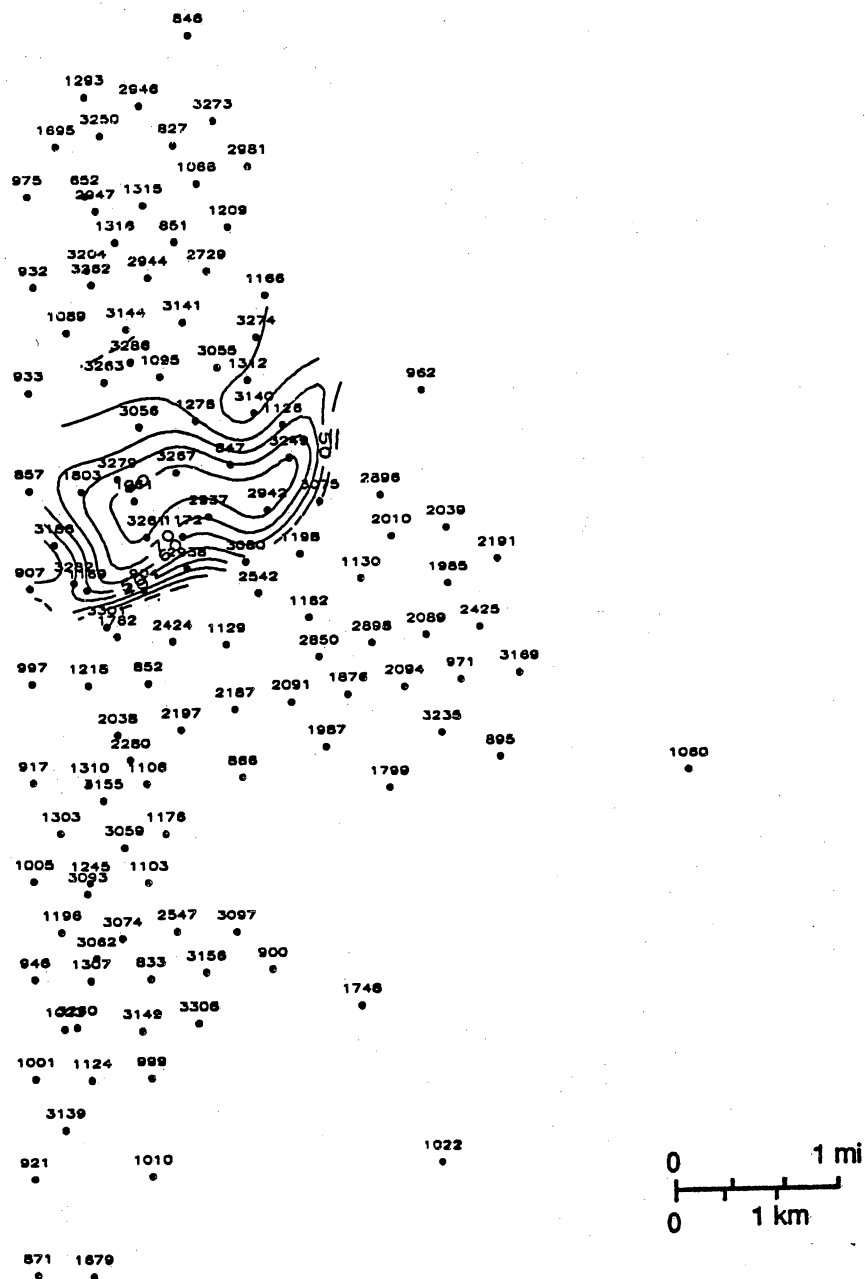|	Official (Lagoven)	BEG/ Lagoven Study	Incremental	Percent Change
OOIP	1,451.6	2,318.2	866.6	+60
EUR	293	468	175.0	+60
CP	165.5	165.5	-	-
Reserves	127.5	302.5	175.0	+137

Figure 178. Net-pay map of the C-7-X Member in the LL-652 area. Contour interval is 10 ft (3 m).
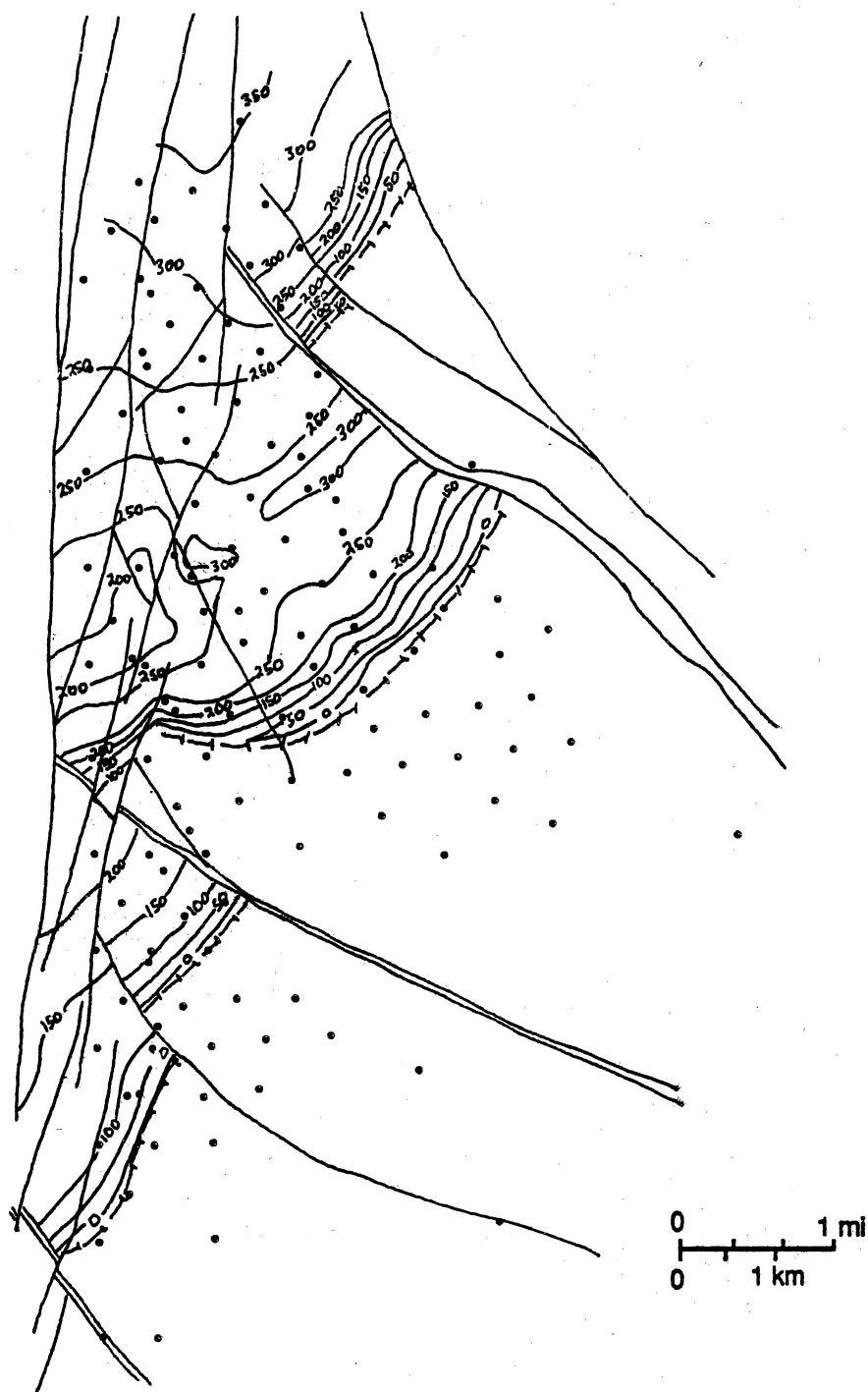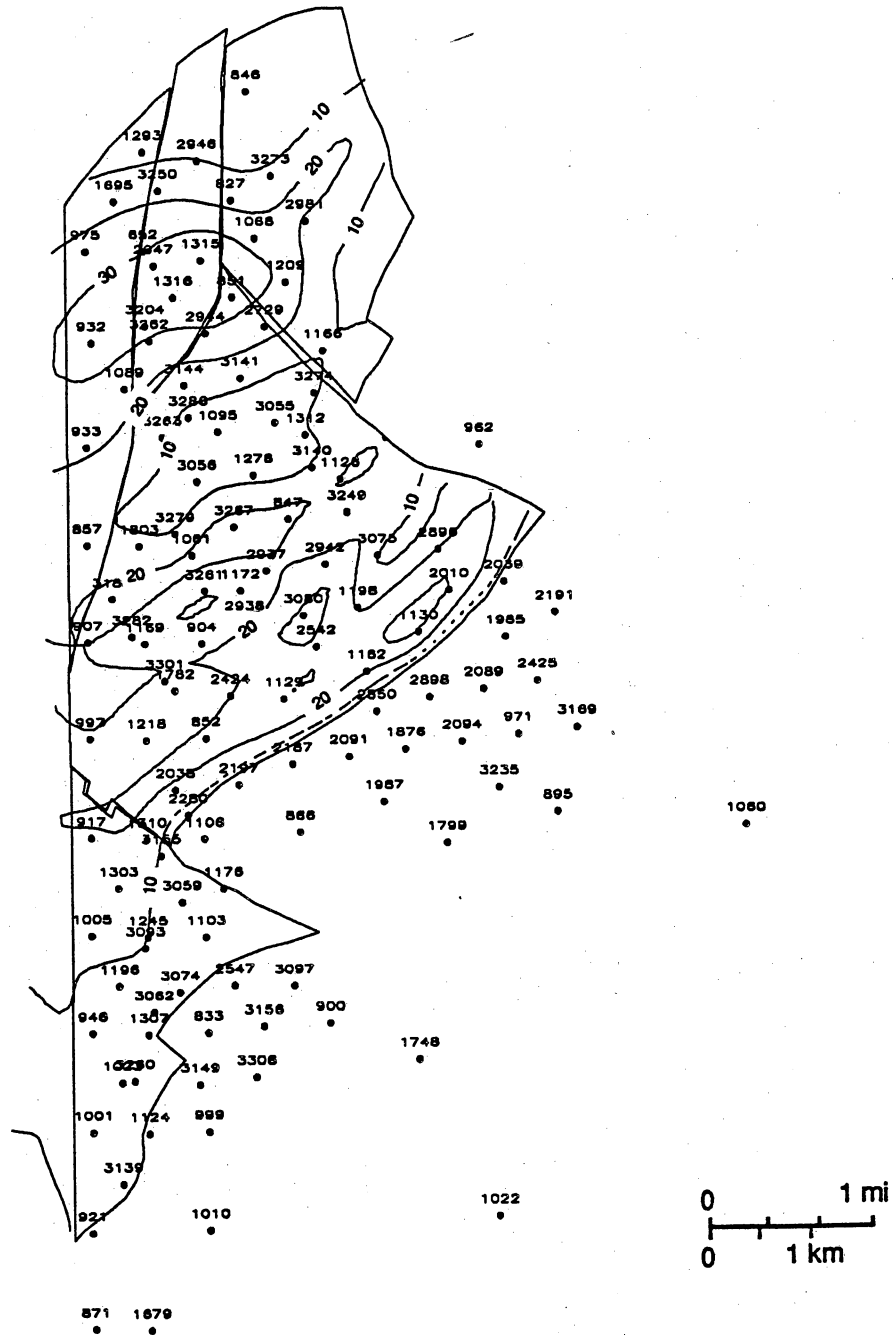
Figure 179. Net-pay map of the C-6-X Member in the LL-652 area. Contour interval is 50 ft (15.2 m).

Figure 180. Net-pay map of the C-5-X Member in the LL-652 area. Contour interval is 50 ft (15.2 m).

Figure 181. Net-pay map of the Lower Middle C-5-X Submember in the LL-652 area. Contour interval is 10 ft (3 m).

Figure 182. Net-pay map of the C-4-X Member in the LL-652 area. Contour interval is 50 ft (15.2 m).

Figure 183. Net-pay map of the Upper C-4-X Submember in the LL-652 area. Contour interval is 20 ft (6 m).

342

Figure 184. Net-pay map of the C-3-X Member in the LL-652 area. Contour interval is 50 ft (15.2 m).
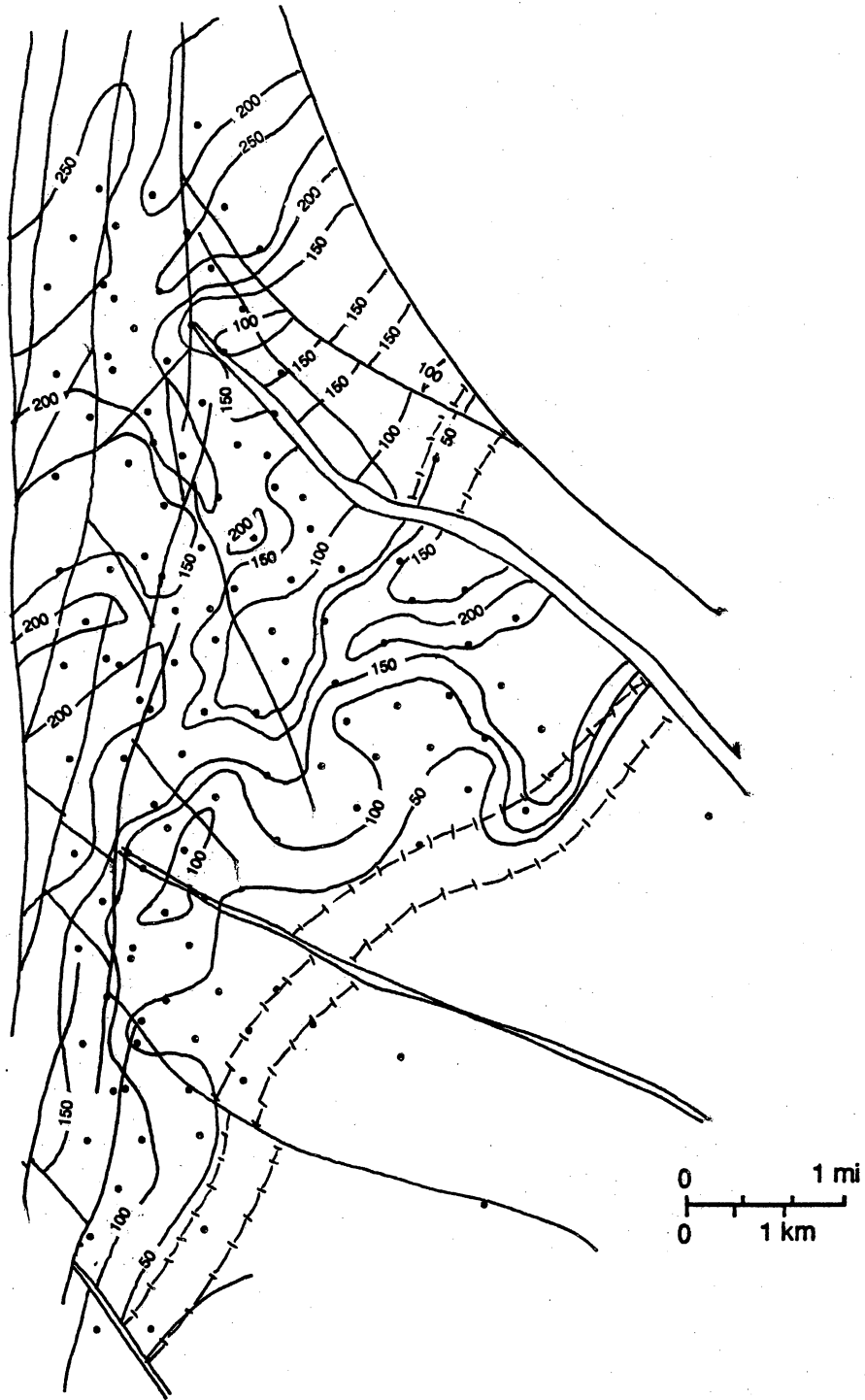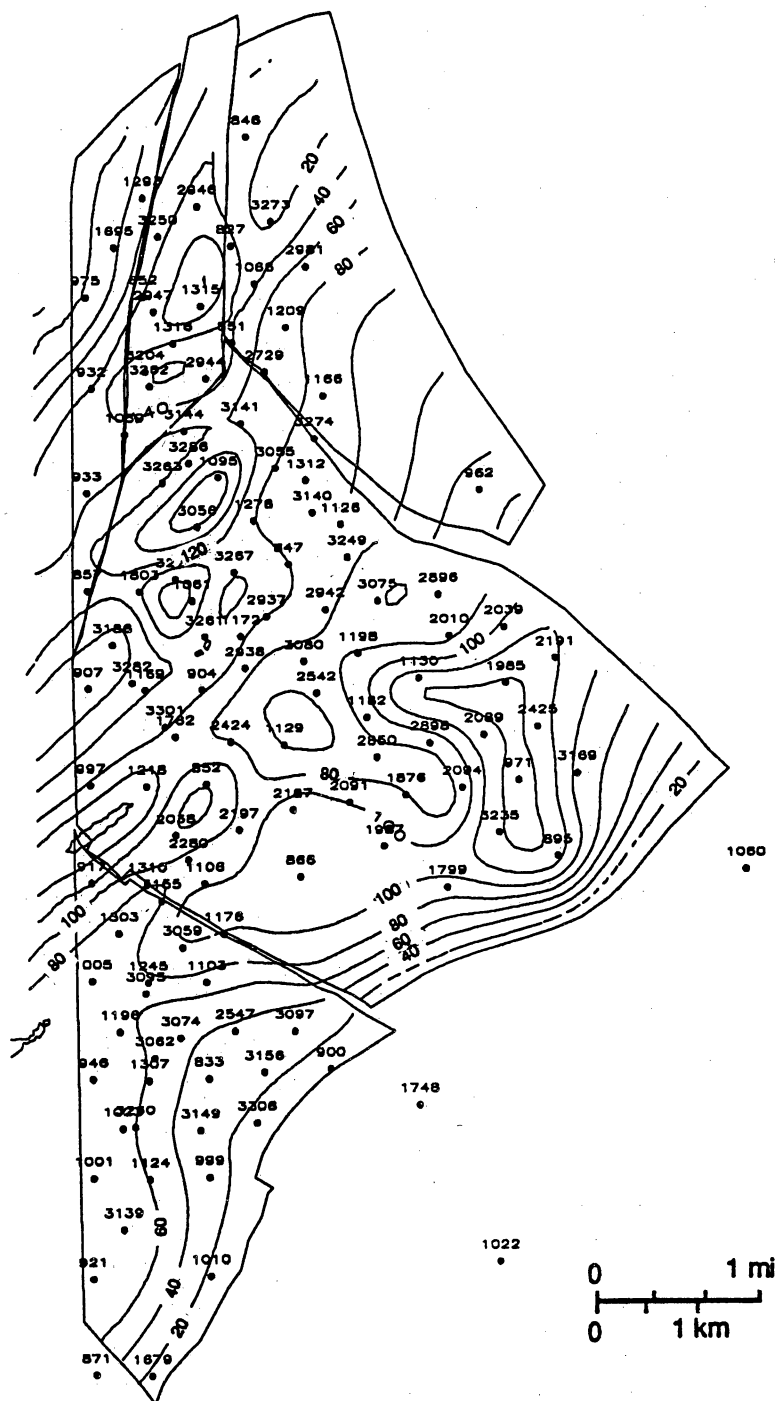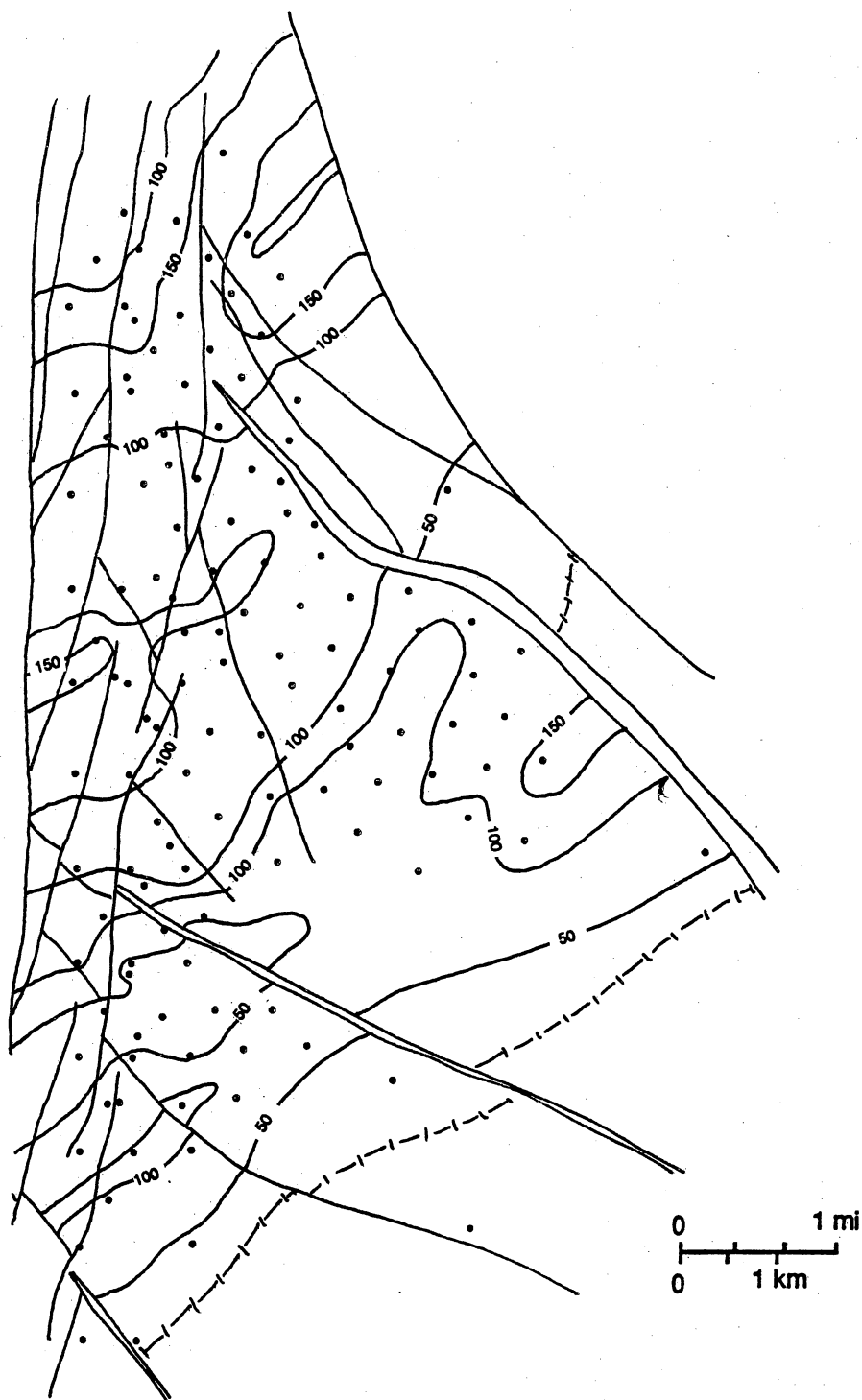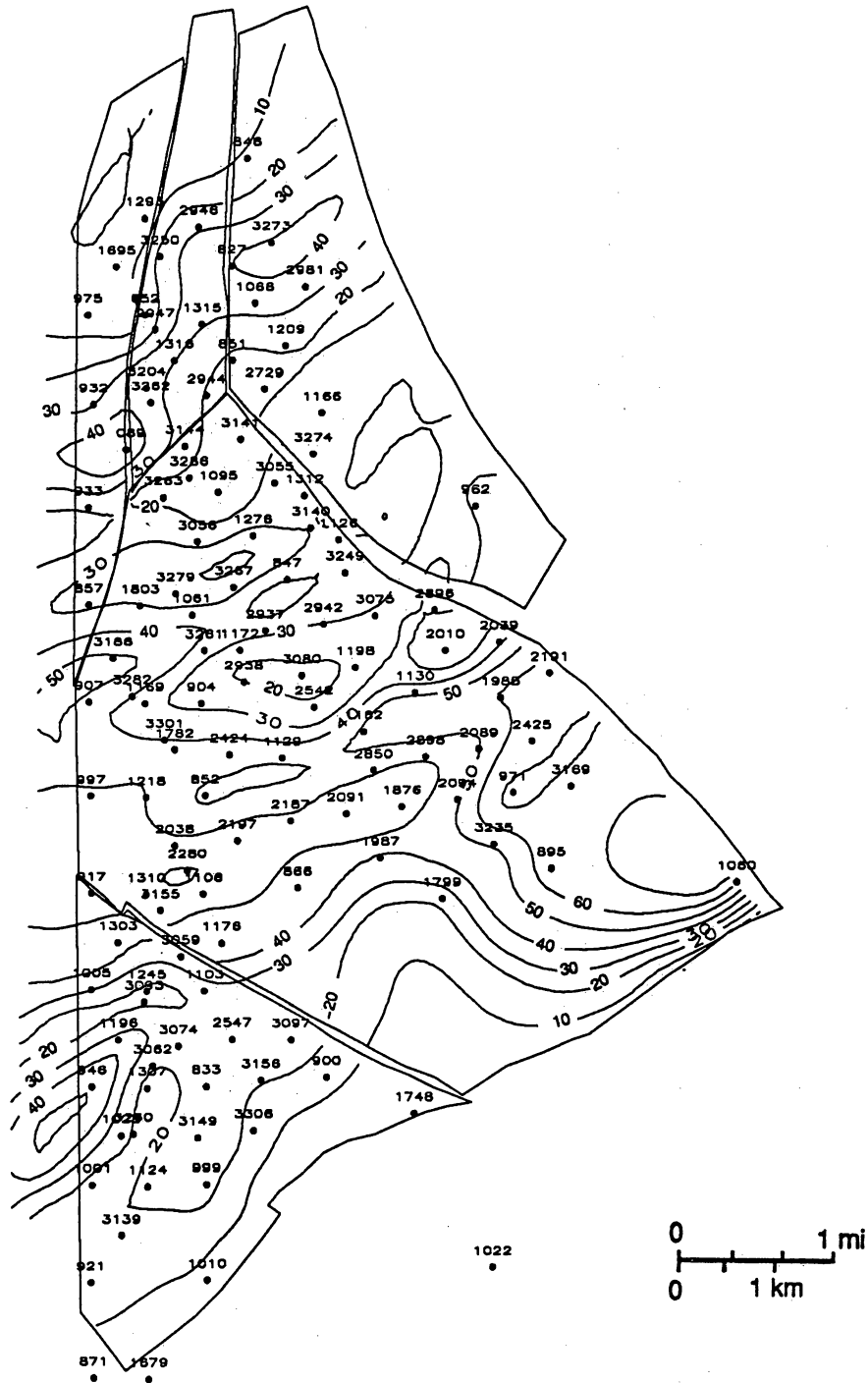
Figure 185. Net-pay map of the Middle C-3-X Submember in the LL-652 area. Contour interval is 10 ft (3 m).

C-7-X Member

The C-7-X Member is nonproductive due to high (>55%) water saturation. However, the net-pay map indicates a theoretical net-pay maximum of more than 60 ft (18 m) in an irregular, northeast-trending band that includes the LL-2942 and LL-3173 wells (fig. 178). These theoretically high values may reflect high net-sandstone thickness values in a deltaic depocenter. A structurally complex, prospective area exists northward where no wells have yet penetrated the C-7-X Member.

C-6-X Member

The C-6-X Member contains up to 350 ft (106.7 m) of net pay in the northern and central parts of the field (fig. 179). In contrast, the extreme southwestern part of the field commonly contains less than 200 ft (61 m) of net pay. The area of more than 250 ft (76.2 m) of net pay in the central part of the field is northeast-trending, whereas there is no apparent trend in the northern part of the field.

C-5-X Member and Lower Middle C-5-X Submember

The C-5-X Member contains the lowest net pay of the C-3-X through C-6-X Members. The net-pay thickness map of the C-5-X Member exhibits four bands of more than 100 ft (30.5 m), of which only one band centered on the LL-1782 and LL-1130 wells extends across the field (fig. 180). The low net-pay thickness of the C-5-X Member is partially controlled by the sandstone-poor, distal-deltaic nature of the Lower and Upper C-5-X Submembers (figs. 114 and 122), reflected by pinchout of net-pay patterns (fig. 180).

Net-pay in the Lower Middle C-5-X Submember exists as parallel, narrow (commonly less than 2,000 ft [610 m]) belts of 20 ft (6 m) or more in the central part of the field, corresponding to dip-parallel, delta-front sandstones (fig. 181). Because of the heterogeneous pay distribution, multiple infill well opportunities exist in the Lower Middle C-5-X Submember in this part of the field, particularly where relatively thick net-pay trends intersect the zone of sealing and partly sealing reverse faults.

C-4-X Member and Upper C-4-X Submember

Net pay in the C-4-X Member is strongly dip-oriented and is greatest (up to 280 ft [85.4 m]) in the northern part of the field (fig. 182). The Upper C-4-X Submember contains the greatest pay of the three submembers in the C-4-X Member, with up to 200 ft (61 m) of net pay in the northern part of the field (fig. 183). There is good correspondence between net-pay thickness and net-sandstone thickness in the Upper C-4-X Submember (fig. 126), suggesting a strong depositional control on reservoir geometry. However, high net-pay thickness in the northern part of the field is partly controlled by steeply dipping strata in a structurally complex area.

C-3-X Member and Middle C-3-X Submember

The C-3-X Member contains less net pay (fig. 184) than the C-4-X Member because most of the C-3-X Member is sandstone-poor, except for the Middle C-3-X Submember, in which net pay is distributed in multiple bands of more than 40 ft (12 m) of varying width that mostly extend across the field (fig. 185). The majority of the thicker net-pay bands correspond to depositional axes of more than 50 percent sandstone (fig. 130), although the band of thick net pay that includes the LL-866 and LL-1176 wells is slightly north of the corresponding zone of more than 50 percent sandstone. Multiple infill targets exist in the Middle C-3-X Submember because this interval is sandstone-rich and also internally heterogeneous, reflected in great net-pay contrast that ranges from 20 to 60 ft (6 to 18 m) (fig. 185).

C-1-X and C-2-X Members

The C-1-X and C-2-X Members are relatively unimportant targets for additional development because they each contain relatively thin net pay (commonly less than 20 and 40 ft [6 and 12 m], respectively) distributed in small, discrete areas in the field (app. E). These discontinuous areas of net pay may represent thin, shaly delta-front or inner-shelf sandstones with moderate to poor reservoir quality.

Porosity

As with net pay, porosity in the C members and submembers is distributed in narrow (commonly less than 3,000 ft [915 m] wide), northeast-trending belts (figs. 186 to 189 and app. E). However, there is a consistent decrease in maximum porosity from the C-3-X Member to the C-6-X Member (20 to 12 percent) related to burial diagenesis rather than to depositional control.

C-6-X and C-7-X Members

Porosity in the C-6-X and C-7-X Members is typically distributed in 2,000- to 3,000-ft (610- to 915-m) wide bands of 12 percent or more, bounded laterally by wide (more than 6,000-ft [1,829-m]) areas of 9 to 11 percent porosity (app. E). The Lower Lower C-6-X Submember is representative of these stratigraphic intervals and contains one northeast-trending band of more than 12 percent porosity (fig. 186) that coincides with the zone of deep incision inferred to be thick (90 to 130 ft [27.4 to 39.6 m]) fluvial-estuarine sandstones (fig. 106).

C-5-X Member and Lower Middle C-5-X Submember

Porosity in the C-5-X Member ranges from 11 to 17 percent (app. E), with maximum porosity confined to discontinuous, northeast-trending pods of more than 16 percent that occur within multiple belts of 14 to 16 percent porosity, 1,000 to 4,000 ft (305 to 1,220 m) wide. In the shalier submembers (for example, the Lower and Upper C-5-X Submembers), these belts of 14 to 16 percent porosity pinch out downdip (northeastward). The sandstone-rich Lower Middle C-5-X Submember contains four belts of 14 to 16 percent porosity that extend across the field (fig. 187). The dip-parallel nature of these high-porosity belts reflects a system of dip-elongate tidal-ridge sandstones that correspond to multiple parallel belts of 20 ft (6 m) or more of net pay (fig. 181).

C-4-X Member and Upper C-4-X Submember

Porosity in the C-4-X Member ranges from 13 to 19 percent and is distributed in multiple northeast-trending belts (app. E and fig. 188). The Upper C-4-X Submember contains the highest porosity in the C-4-X Member, which occurs in dip-elongate pods in the southwestern and northwestern parts of the field (fig. 188). The great variability and spatial complexity in porosity in the Upper C-4-X Submember impart a high degree of heterogeneity to this submember, making it an excellent candidate for infield development. Remaining oil may be stratigraphically trapped in isolated, high-porosity (more than 18-percent) pods in the central part of the field and may also be structurally trapped in the north-northeast-trending zone of reverse faults.

C-3-X Member and Middle C-3-X Submember

Porosity in the C-3-X Member is up to 20 percent (app. E) and highest in the Middle C-3-X Submember (fig. 189). The porosity distribution in each submember strongly reflects the net-sandstone and net-pay distribution. For example, in the Lower C-3-X Submember there are numerous, northeast-trending and

Figure 186. Porosity map of the Lower Lower C-6-X Submember in the LL-652 area. Contour interval is 1 percent.
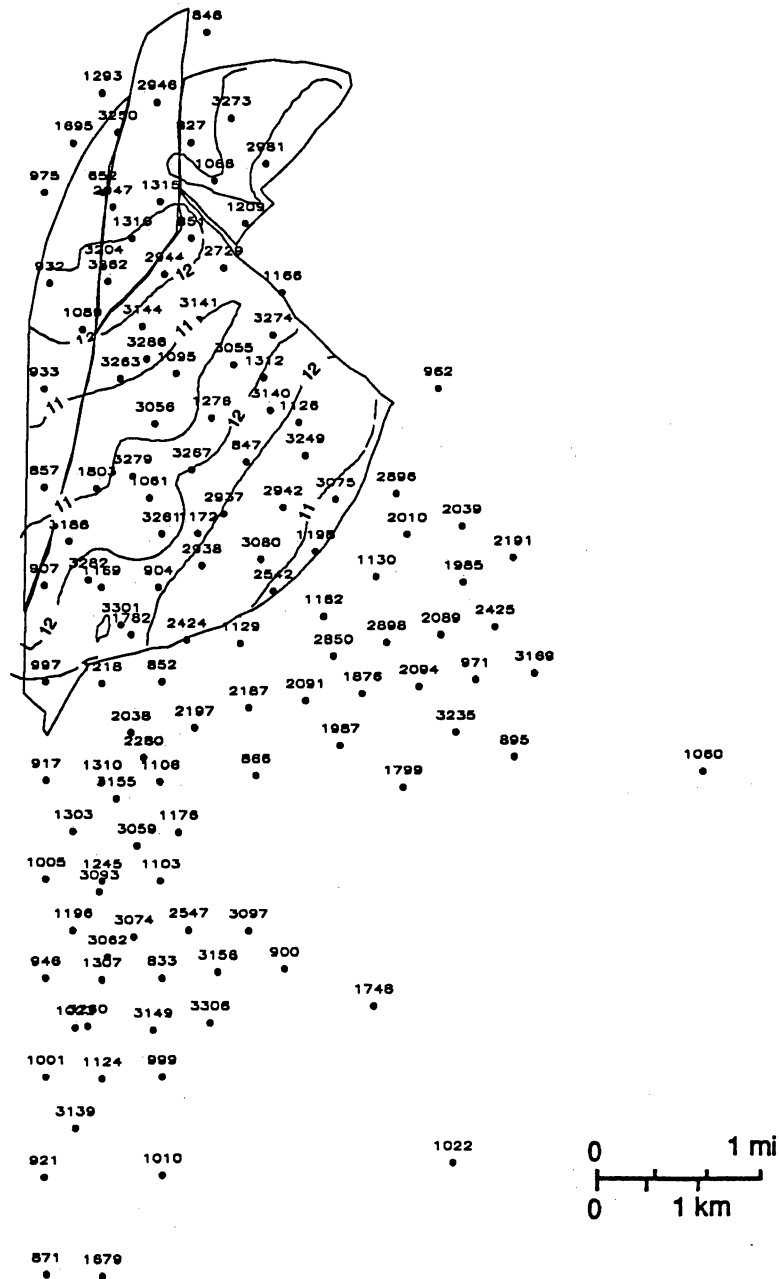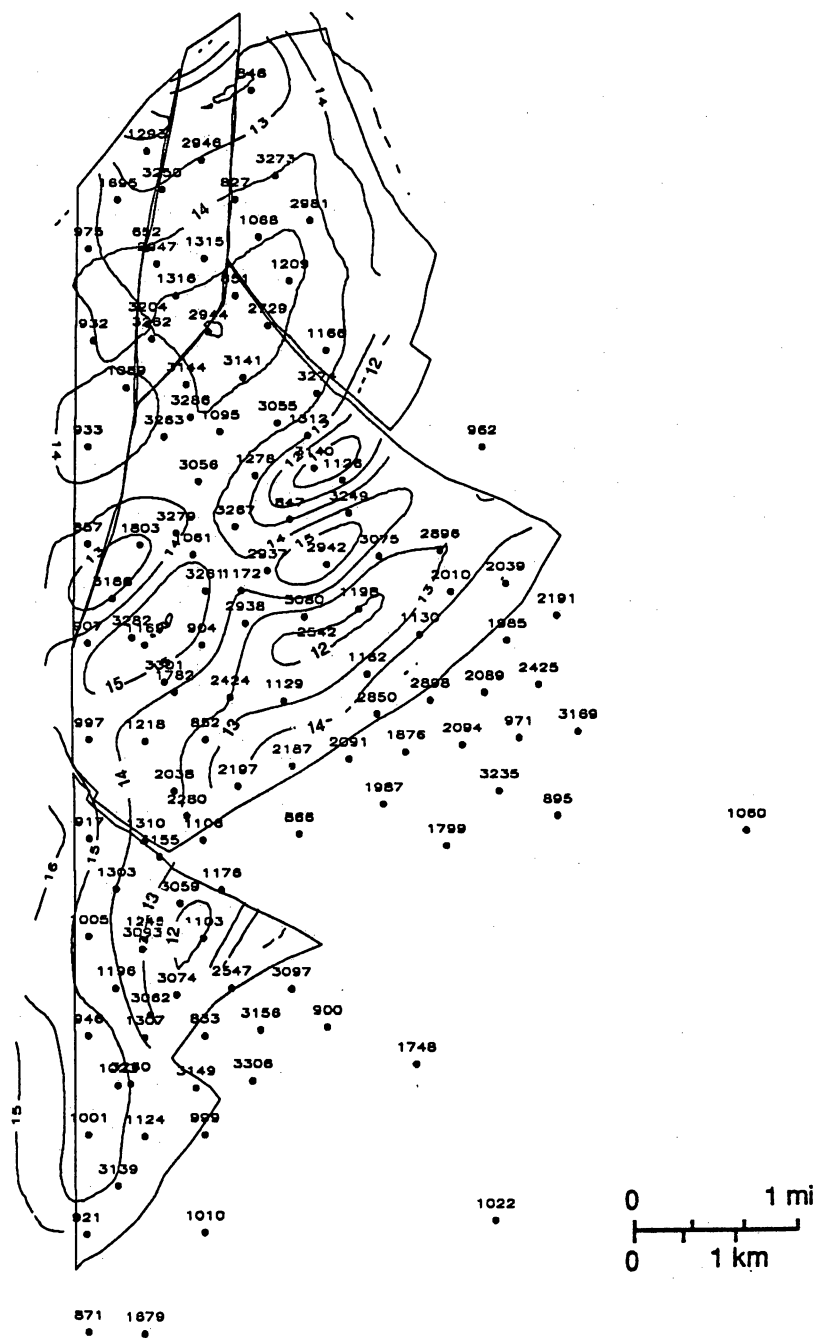
Figure 187. Porosity map of the Lower Middle C-5-X Submember in the LL-652 area. Contour interval is 1 percent.
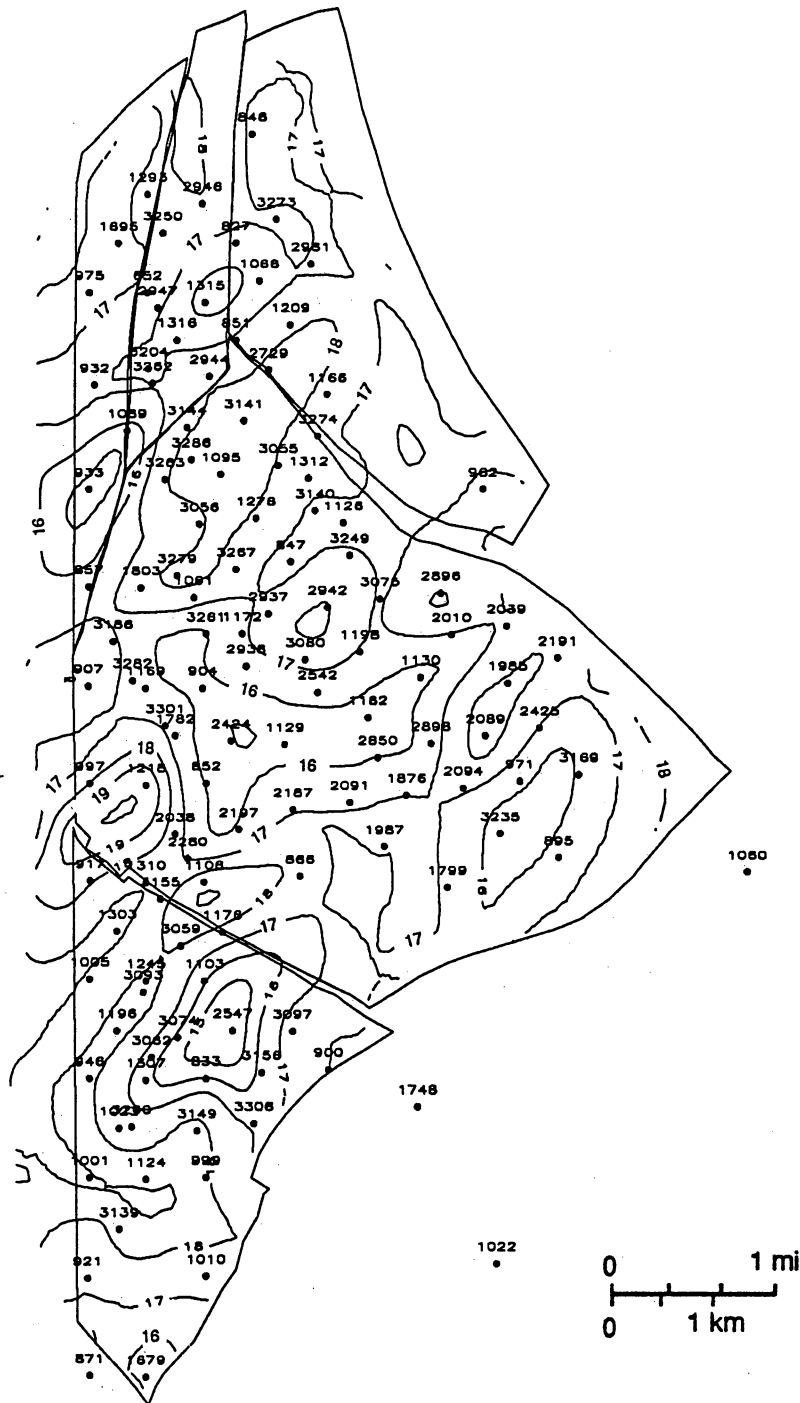
Figure 188. Porosity map of the Upper C-4-X Member in the LL-652 area. Contour interval is
1 percent.

Figure 189. Porosity map of the Middle C-3-X Submember in the LL-652 area. Contour interval is 1 percent.

narrow (commonly less than 1,200 [366 m] wide) belts of 18 to 20 percent porosity that correspond to tidal-ridge sandstones (app. E), whereas in the Middle C-3-X Submember the relatively wide belts of high porosity are related to thick (more than 40-ft [12-m]) multilateral distributary-channel sandstone bodies (fig. 189). Additionally, the east- and southeast-trending belts of high porosity in the Upper C-3-X Submember are controlled by the east- and southeast-trending depositional fabric of fluvial-dominated, distributary-channel sandstones.

Permeability

Average permeability in the C-3-X to C-7-X Members ranges from more than 200 md in the C-3-X Member to less than 10 md in the C-7-X Members (figs. 190 to 194 and app. E). Average permeability trends are similar to those of net pay and porosity and consist of northeast-trending belts that extend over large distances (typically over 4 mi [6.4 km]) across the field.

C-7-X and C-6-X Members

Greatest average permeability in the C-7-X Member occurs in a single northeast-trending belt centered on the LL-2940 well. This belt contains 4 md or more of average permeability and ranges from 2,000 to 4,000 ft (610 to 1,220 m) wide (fig. 190). Average permeability in the C-6-X Member is low and reaches a maximum only 16 md in the Lower Lower and Lower Upper Submembers (app. E). Permeability trends in the C-6-X Member are mostly simple dip-parallel or bifurcating belts, reflecting the dominance of delta-front facies (app. E).

C-5-X Member and Lower Middle C-5-X Submember

Average permeability in the C-5-X Member is equally low as in the C-6-X Member and is commonly less than 8 md (app. E). The Lower Middle C-5-X Submember has the greatest average permeability in the C-5-X Member, distributed in four belts of more than 6 md (fig. 191). These belts are 1,600 to 4,000 ft (488 to 1,220 m) wide with the central two bifurcating and pinching out northeastward.

C-4-X Member and Upper C-4-X Submember

Average permeability in the C-4-X Member (app. E) is significantly higher than in the C-5-X, C-6-X, and C-7-X Members and reaches a maximum of over 250 md in the Upper C-4-X Submembers, which contains three continuous and two discontinuous belts of more than 150 md permeability, 1,600 to 3,200 ft (488 to 976 m) wide (fig. 192). Average permeability in the Upper C-4-X Submember is highest in the central and north-central parts of the field, where the belts of high permeability are more continuous. Permeability contrast in the Upper C-4-X Submember is also higher than in the other C-4-X Submembers, which may indicate a higher average potential for unswept mobile oil in areas of abrupt change in permeability.

C-3-X Member and Middle C-3-X Submember

The C-3-X Member contains the greatest differences in permeability trends between individual submembers than in any other member in the LL-652 area (app. E and fig. 193). Highest average permeability in the Lower C-3-X Submember occurs in two discontinuous, northeast-trending belts of more than 150 md in widely separated areas (app. E), whereas the Middle C-3-X Submember contains a major, continuous northeast-trending belt of more than 200 md in the southern part of the field, as well as scattered pods of more than 150 md elsewhere (fig. 193). In contrast, average permeability distribution in the Upper C-3-X Submember occurs in discontinuous and narrow (less than 2,000 ft [610 m] wide) southeast-trending pods of more than 100 md (app. E).

Figure 190. Permeability map of the C-7-X Member in the LL-652 area. Contour interval is 2 md.

Figure 191. Permeability map of the Lower Middle C-5-X Submember in the LL-652 area. Contour interval is 2 md.
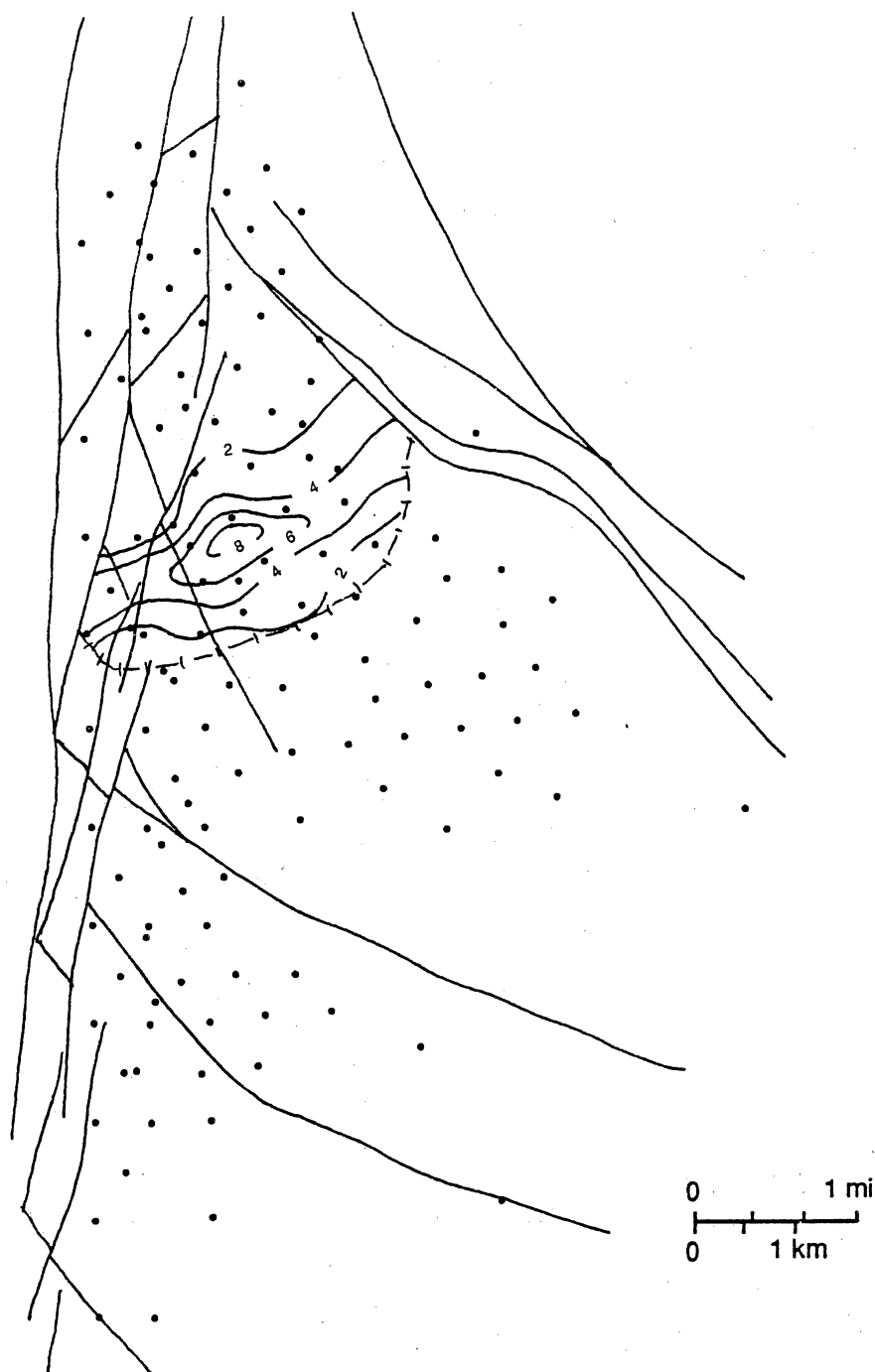
353

Figure 192. Permeability map of the Upper C-4-X Submember in the LL-652 area. Contour interval is 50 md.
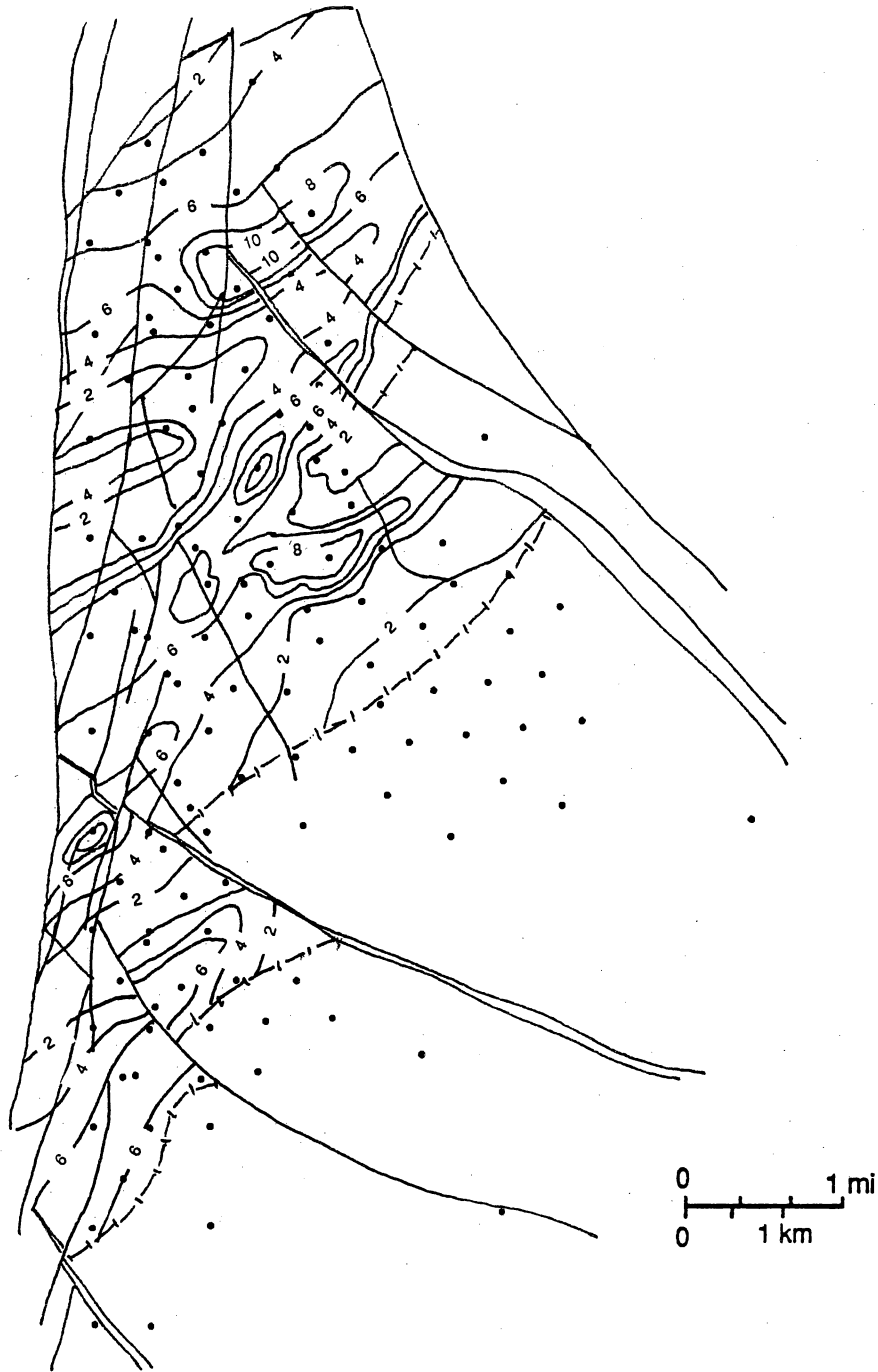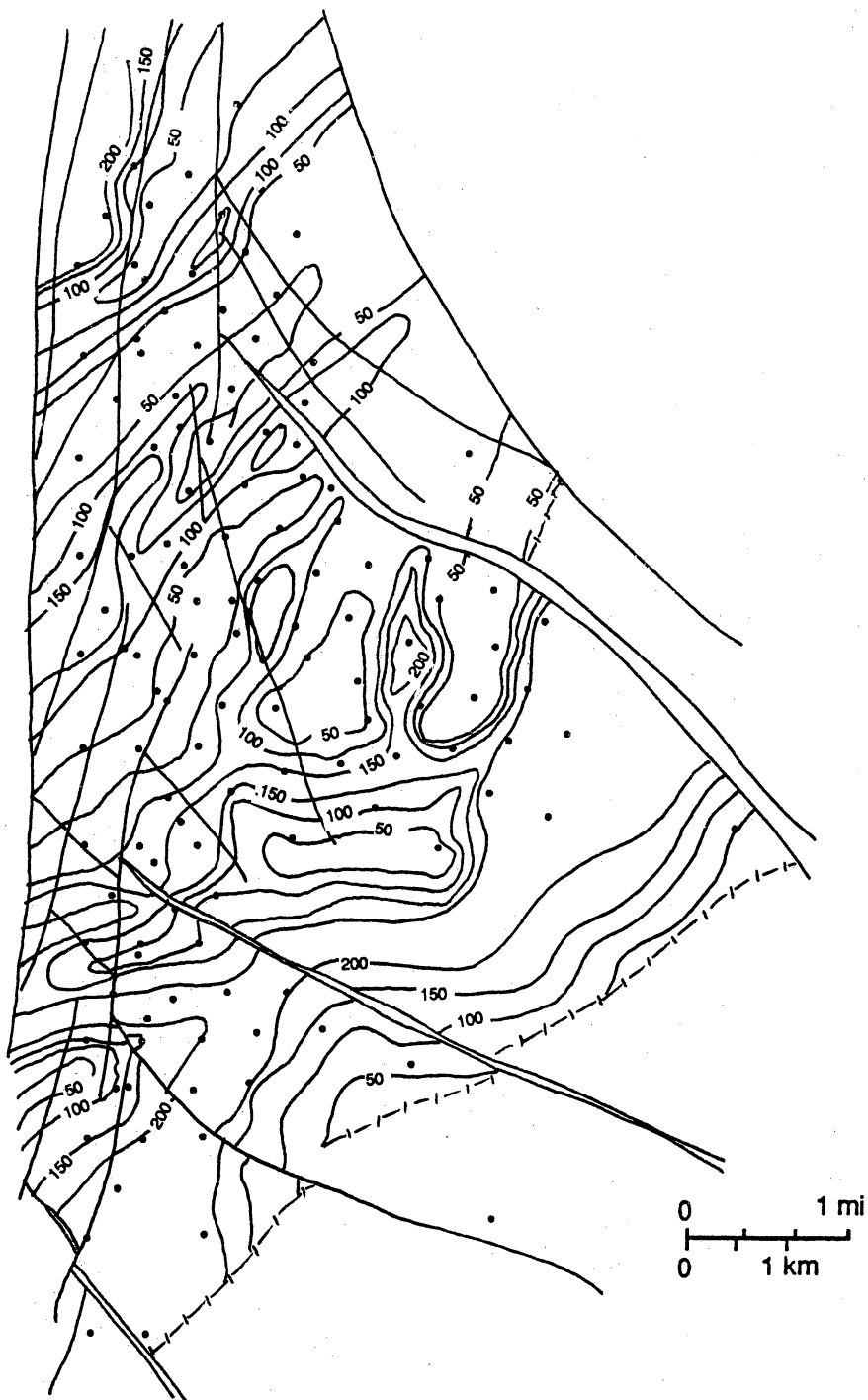
Figure 193. Permeability map of the Middle C-3-X Submember in the LL-652 area. Contour interval is 50 md.

Figure 194. Permeability map of the Upper C-2-X Submember in the LL-652 area. Contour interval is 20 md.

356

C-2-X Member

Average permeability in the C-2-X Member is significantly lower than in either the C-3-X and C-4-X Members. Greatest permeability occurs in isolated patches of more than 60 md (fig. 194). The low average permeability of the C-2-X Member is controlled by low net-sandstone content.

Water Saturation

Water saturation in the C-1-X to C-6-X Members ranges from approximately 25 to 55 percent inside the reservoir limits (app. E). Because the productive limit for the C members is 55 percent or less water saturation, the C-1-X to C-6-X interval produces oil (fig. 5). Water-saturation trends reflect structural control, although some members and submembers contain anomalous trends that may reflect depositional control.

C-6-X Member

Minimum water saturation (approximately 25 percent) in the C-6-X Member is present on the western edge of the LL-652 area in the Lower Lower and Upper Lower C-6-X Submembers (app. E). This area corresponds to 35 percent water saturation in the other C-6-X Submembers (app. E). Water-saturation trends in most C-6-X Submembers are structurally controlled. However, the lower C-6-X Submembers in the northern part of the field exhibit contours that are southward-deflected and oriented orthogonally to the main anticlinal structure.

C-5-X Member

Water-saturation values in the C-5-X Member are lowest (25 percent or less) in the Lower and Lower Middle C-5-X Submembers in the northwestern part of the LL-652 area (app. E). In the Upper and combined Middle and Upper Middle C-5-X Submembers, these areas correspond to 30 and 40 percent water saturation, respectively (app. E). Although the southern limb of the reservoir contains structurally controlled water-saturation contours, the central part of the field, particularly in the Upper and combined Middle and Upper Middle C-5-X Submembers, has podlike, northeast-trending contours that correspond to the depositional fabric (see also figs. 119, 120, 121, and 122). These contours cut across structurally high areas, and exhibit northeastward pinchouts consistent with net-sandstone-thickness trends.

C-4-X Member

Water-saturation values in the C-4-X Member are lowest (less than 40 percent) in the northern and western parts of the field (app. E). However, the Upper C-4-X Submember contains two northeast-trending belts of less than 40 percent water saturation that are 3,000 to 6,000 ft (915 to 1,820 m) wide and that extend across the field (fig. 195). These belts are depositionally influenced and correspond to sandstone-rich, distributary-channel and delta-front depositional axes (fig. 126).

C-3-X Member

Average water saturation in the C-3-X Member is higher than in the C-4-X to C-7-X Members and is typically 40 to 45 percent throughout most of the field (app. E and fig. 196). Trends of water saturation in the C-3-X Submembers are poorly related to net-sandstone thickness trends, except in the Middle C-3-X Submember where there are northeast-trending bands of low water saturation (less than 40 percent) that mimic net-sandstone thickness (fig. 130). In contrast, most water-saturation trends in the shaly Lower and Upper C-3-X Submembers are nearly at right angles to net-sandstone-thickness trends, suggesting that
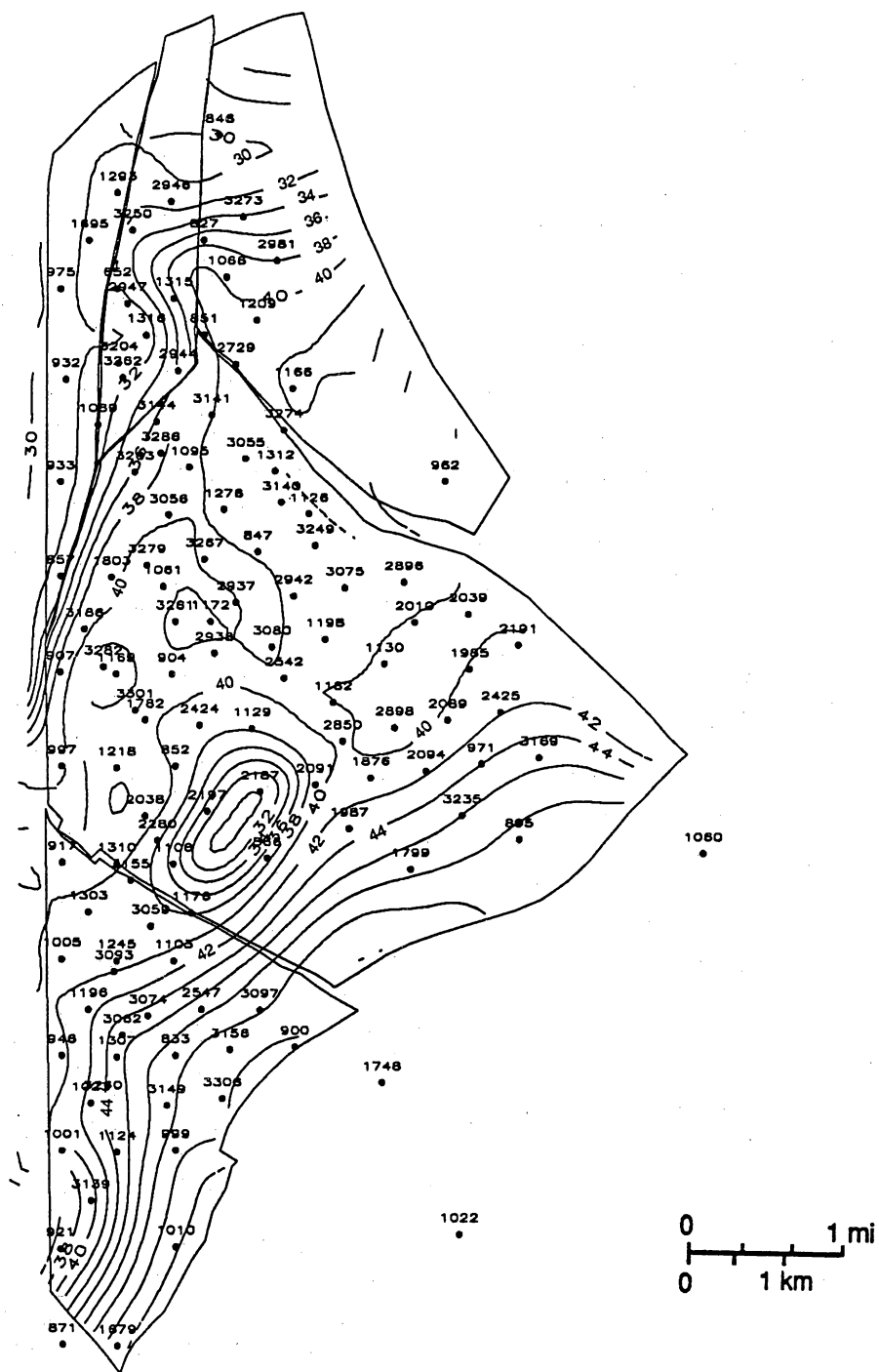
Figure 195. Water-saturation map of the Upper C-4-X Submember in the LL-652 area. Contour interval is 2 percent.
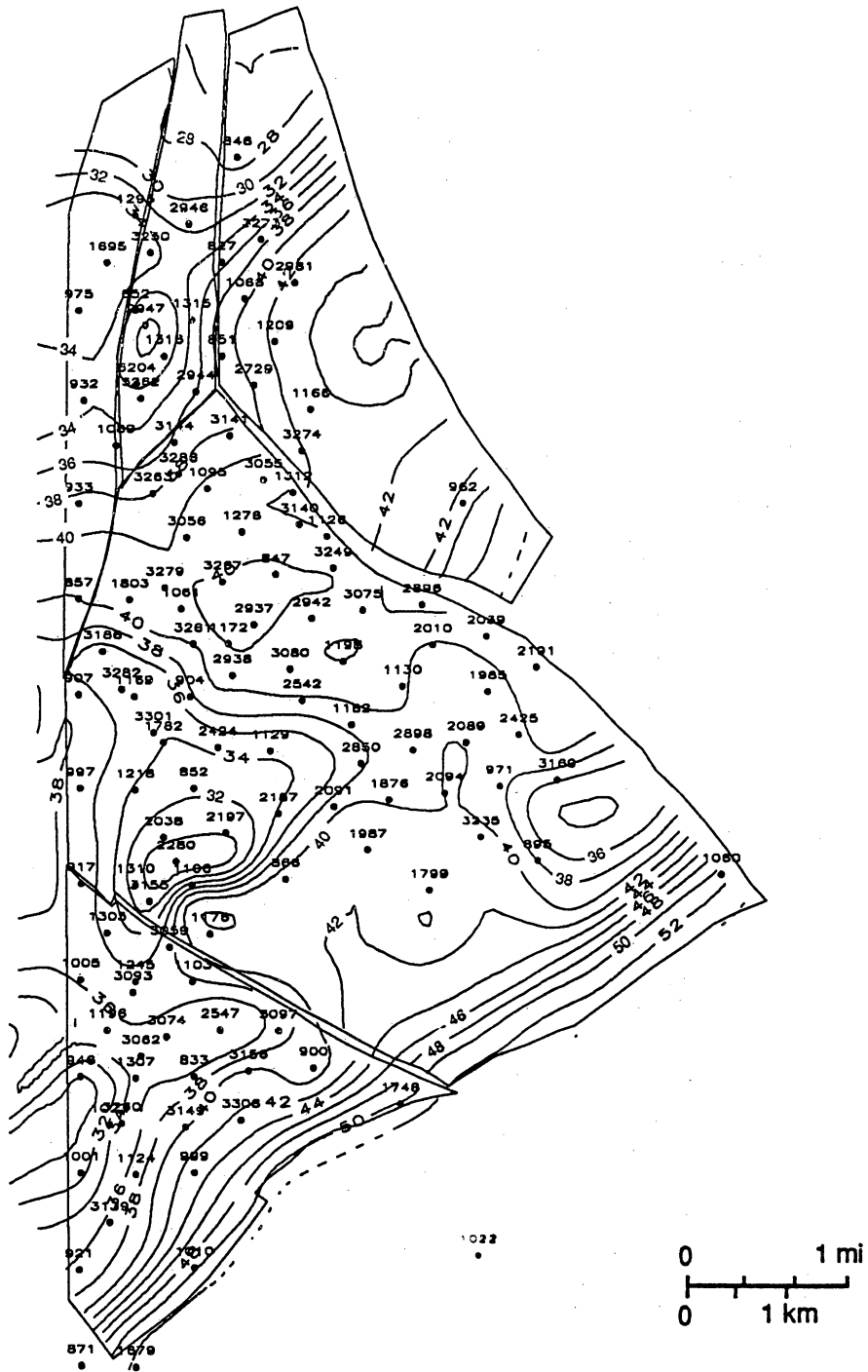
Figure 196. Water-saturation map of the Middle C-3-X Submember in the LL-652 area. Contour interval is 2 percent.

the shaly nature and numerous but thin sandstones in these submembers (individually commonly less than 5 ft [1.5 m]) are not sufficient to control water saturation except only on a local scale.

C-2-X and C-1-X Members

Water saturation in the C-2-X and C-1-X Members is high, with values commonly greater than 45 percent (app. E). There are few distinctive water-saturation trends in these members, except for small scattered pods of anomalously high or low values of water saturation in the C-2-X Member in the northern part of the field (app. E).

Porous Hydrocarbon Volume

Porous hydrocarbon volume ($S_o\varnothing h$), measured in feet, is distributed in five structural compartments in the LL-652 area (figs. 197 to 204). Northeast trends of $S_o\varnothing h$ in the LL-652 area strongly reflect net-pay distribution, which in turn is dominated by the northeast-trending depositional fabric. The greatest $S_o\varnothing h$ values in the C members occur in the sandstone-rich Upper C-4-X and Middle C-3-X Submembers.

C-7-X Member

Porous hydrocarbon volume ($S_o\varnothing h$) in the C-7-X Member reaches a maximum of 5.48 ft (1.67 m) (fig. 197). Greatest values of $S_o\varnothing h$ are northeast-trending and correspond to maximum net-pay thickness (fig. 178).

C-6-X Member

The Lower Lower C-6-X Submember contains the greatest value of $S_o\varnothing h$ (9.54 ft [2.91 m]) of all submembers in the C-6-X Member, with a northeast-trending band of more than 7 ft (2.1 m) centered on the LL-1172 and LL-1126 wells (fig. 198). This band of high $S_o\varnothing h$ values is controlled by the belt of thick (more than 90-ft [27.4-m]) fluvial-estuarine sandstone in a zone of relatively deep incision of the C-6-X Member into the C-7-X Member (figs. 106 and 107).

All other submembers in the C-6-X Member exhibit strong northeast-trending $S_o\varnothing h$ patterns (app. E), reflecting the predominant northeast-trending grain of net-sandstone thickness. Consistently higher $S_o\varnothing h$ values in the northern structural compartments reflect dipping strata.

C-5-X Member

The Lower C-5-X and combined Middle and Upper Middle C-5-X Submembers contain the greatest $S_o\varnothing h$ values (up to 9.60 ft [2.93 m] [fig. 199] and 8.57 ft [2.61 m] [fig. 200], respectively) in the C-5-X Member. High $S_o\varnothing h$ values in the Lower C-5-X Submember are controlled by the relatively great thickness (approximately 250 ft [76 m]) of this submember (fig. 5), which is sandstone-poor (fig. 114). In contrast, high $S_o\varnothing h$ values in the combined Middle and Upper Middle C-5-X Submembers are primarily controlled by thick distributary-channel and proximal delta-front sandstones (figs. 120 and 121), particularly in the central and southern structural compartments (fig. 200).

C-4-X Member

Submembers in the C-4-X Member contain the greatest $S_o\varnothing h$ values in the entire lower Eocene section, particularly in the Upper C-4-X Submember, where $S_o\varnothing h$ values reach a maximum of 26.6 ft (8.1 m)
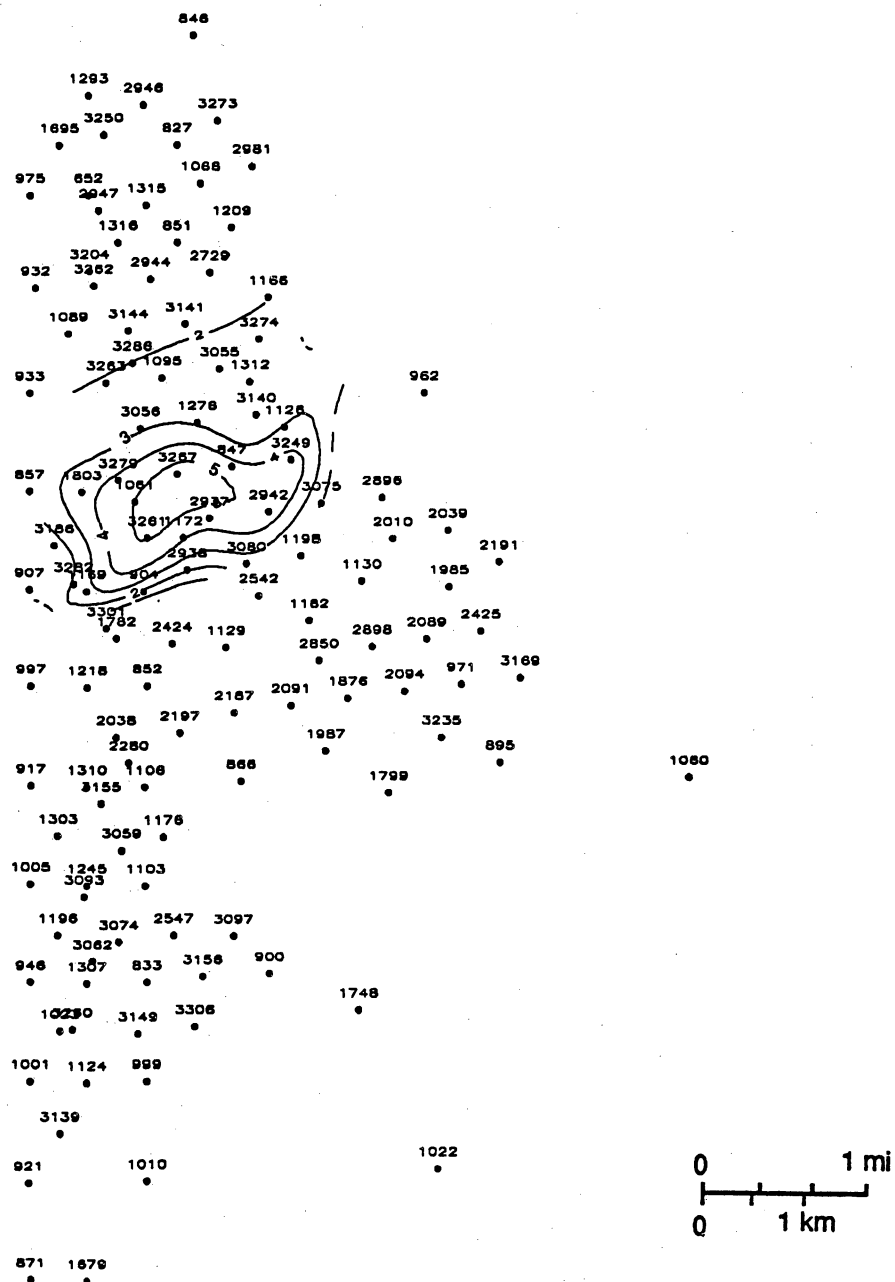
Figure 197. $S_O \emptyset h$ map of the C-7-X Member in the LL-652 area. Contour interval is 1 ft (0.3 m).
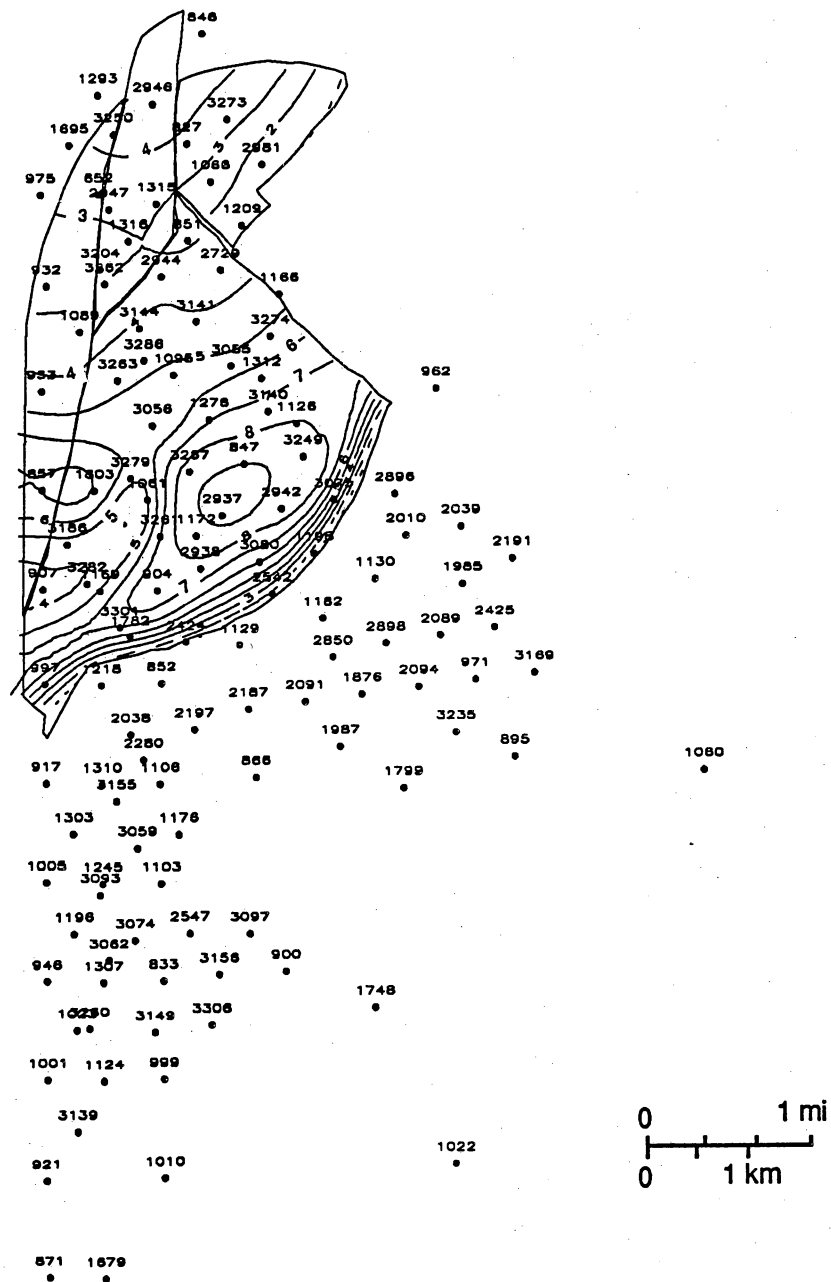
Figure 198. S$_o$Øh map of the Lower Lower C-6-X Submember in the LL-652 area. Contour interval is 1 ft (0.3 m).

Figure 199. S$_o$Øh map of the Lower C-5-X Submember in the LL-652 area. Contour interval is 1 ft (0.3 m).

Figure 200. $S_o\varnothing h$ map of the combined Middle and Upper C-5-X Submembers in the LL-652 area. Contour interval is 1 ft (0.3 m).

Figure 201. S₀Øh map of the Upper C-4-X Submember in the LL-652 area. Contour interval is 1 ft (0.3 m).

Figure 202. $S_O\emptyset h$ map of the Middle C-4-X Submember in the LL-652 area. Contour interval is 1 ft (0.3 m).

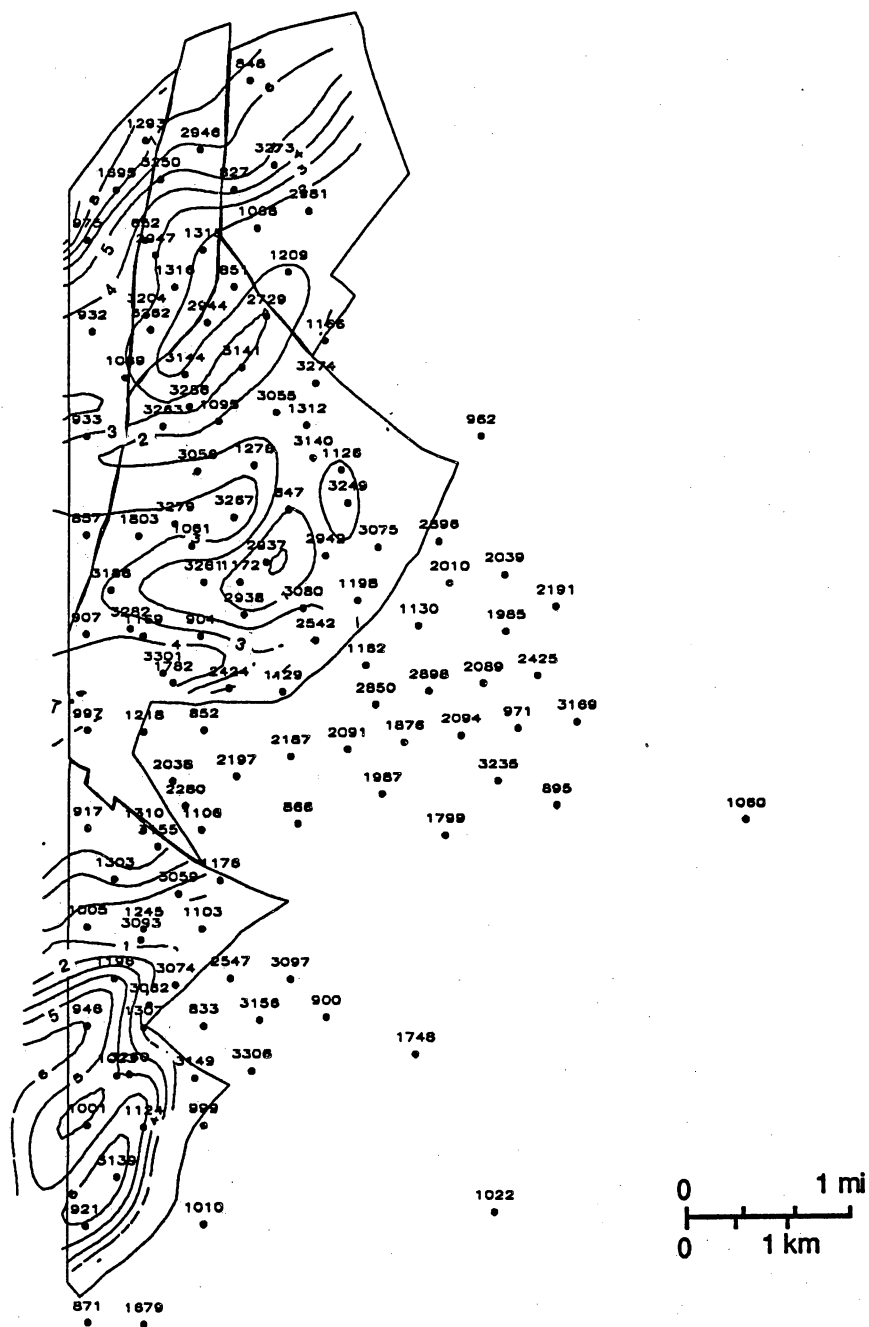Figure 203. $S_o\emptyset h$ map of the Lower C-3-X Submember in the LL-652 area. Contour interval is 1 ft (0.3 m).
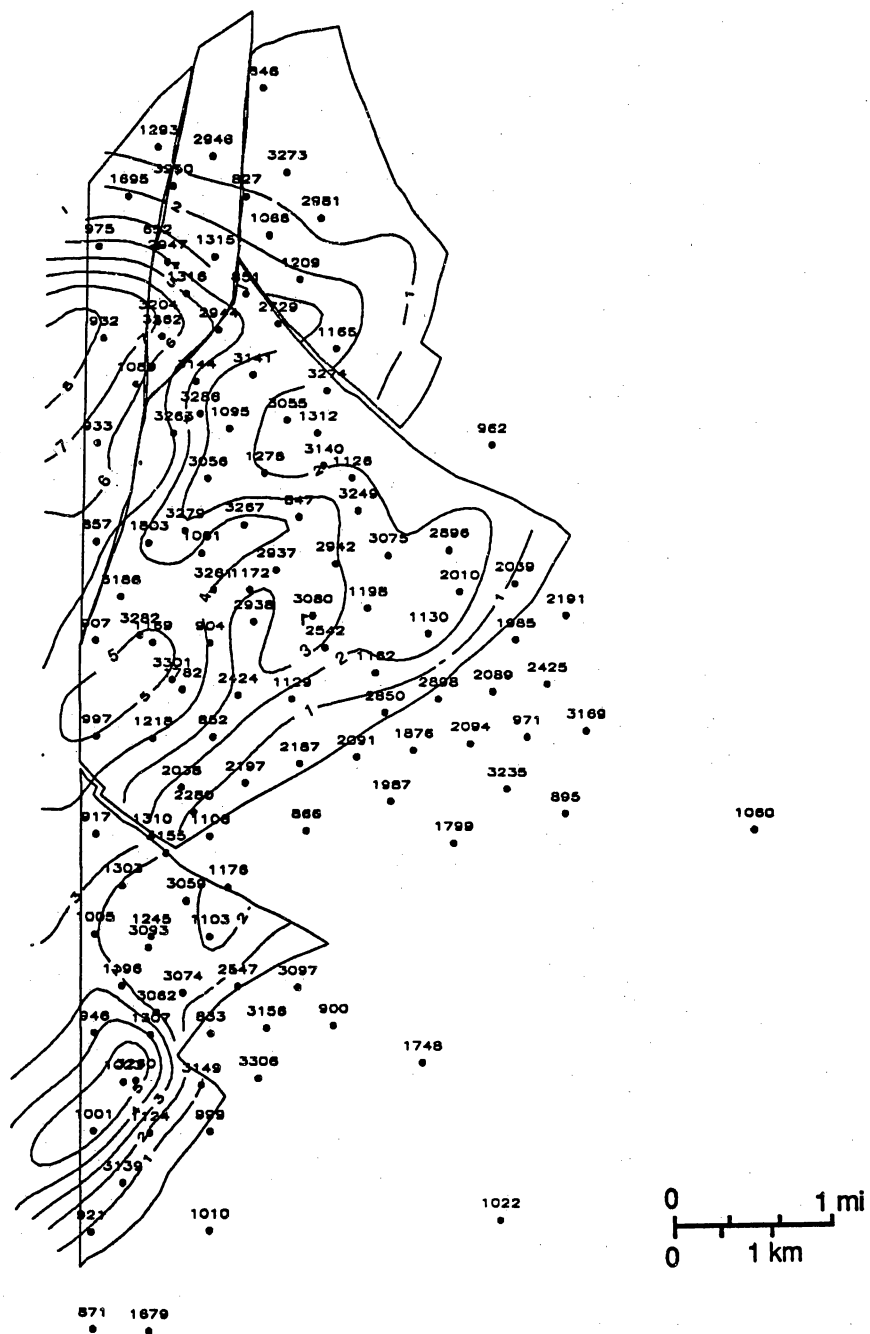
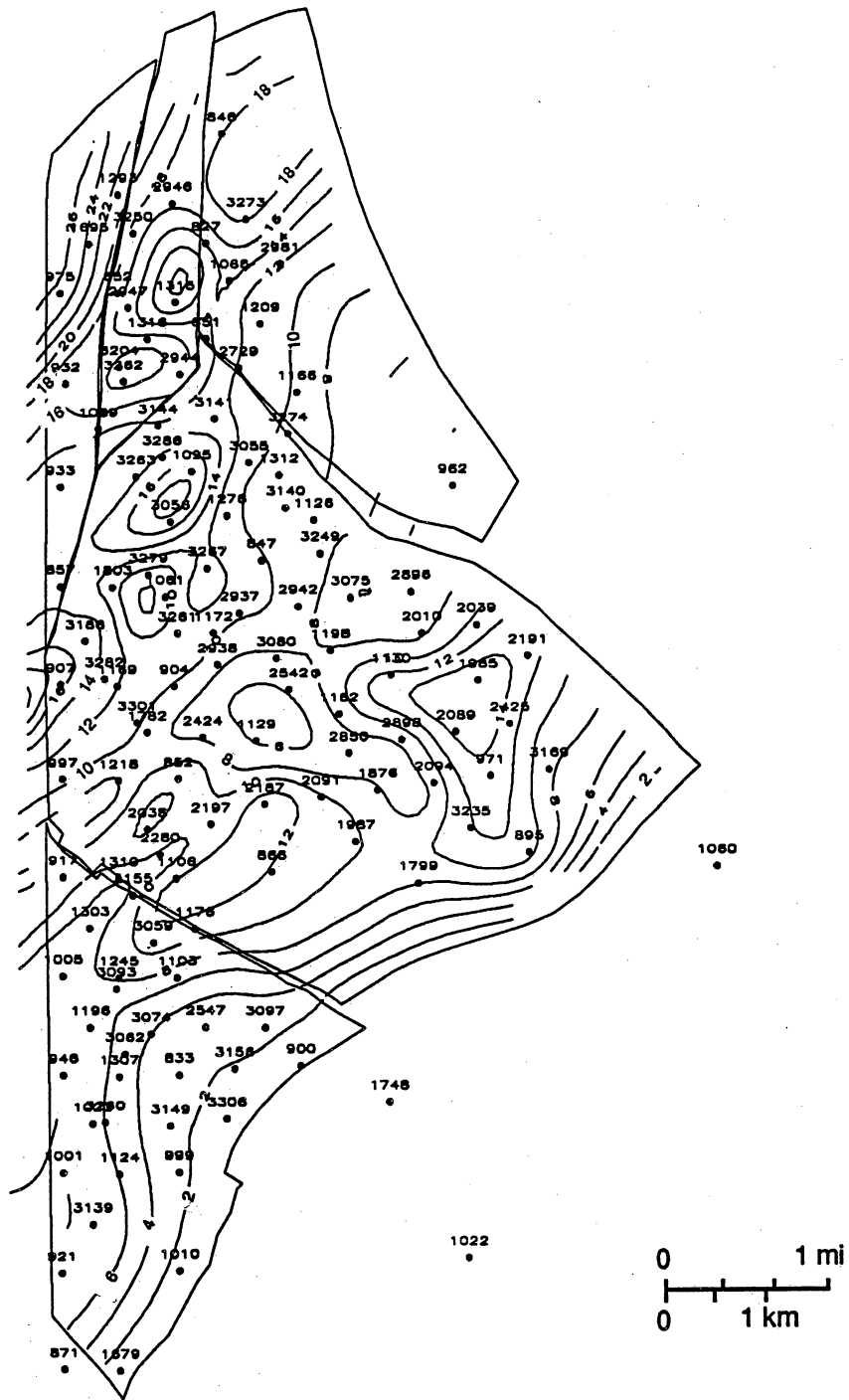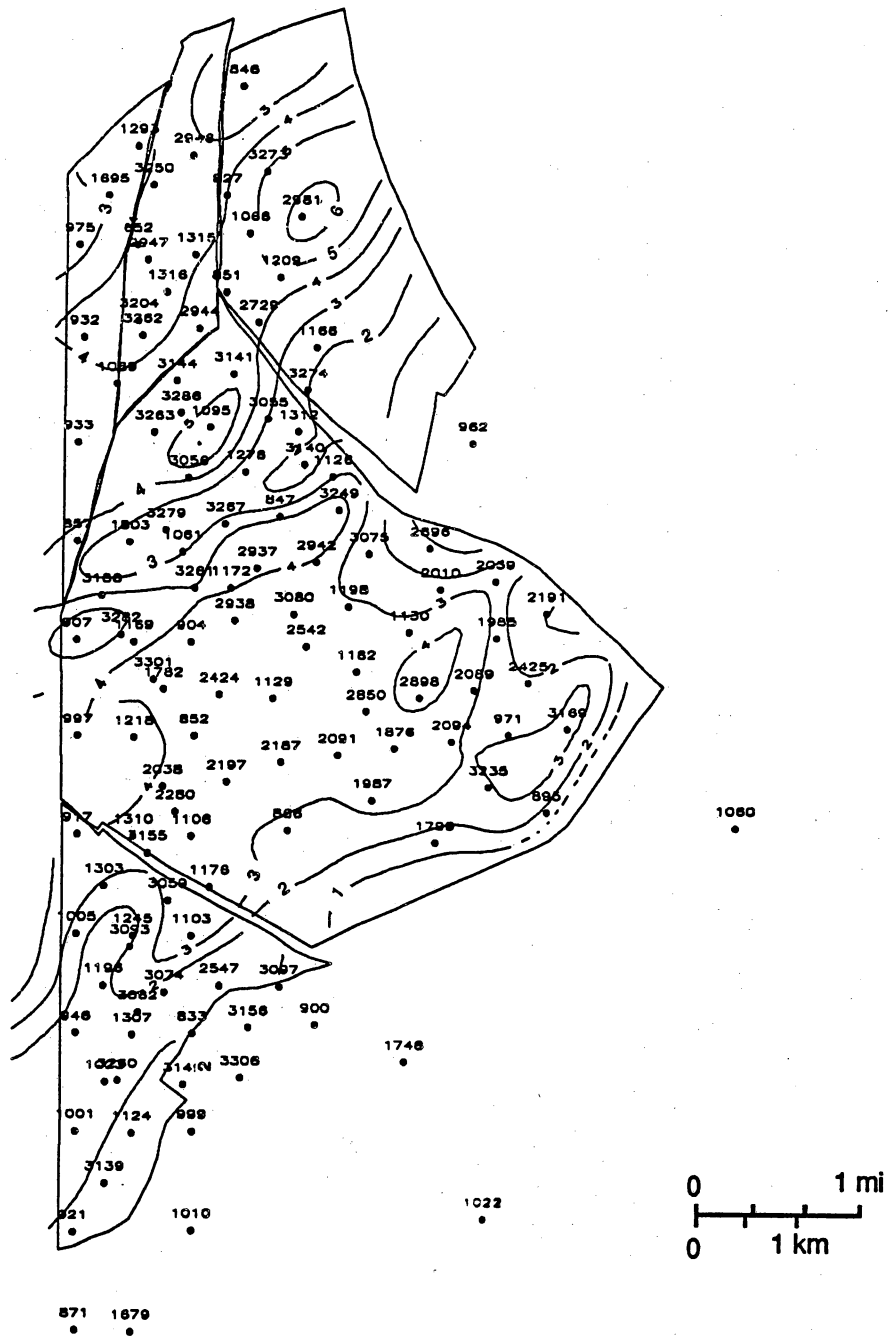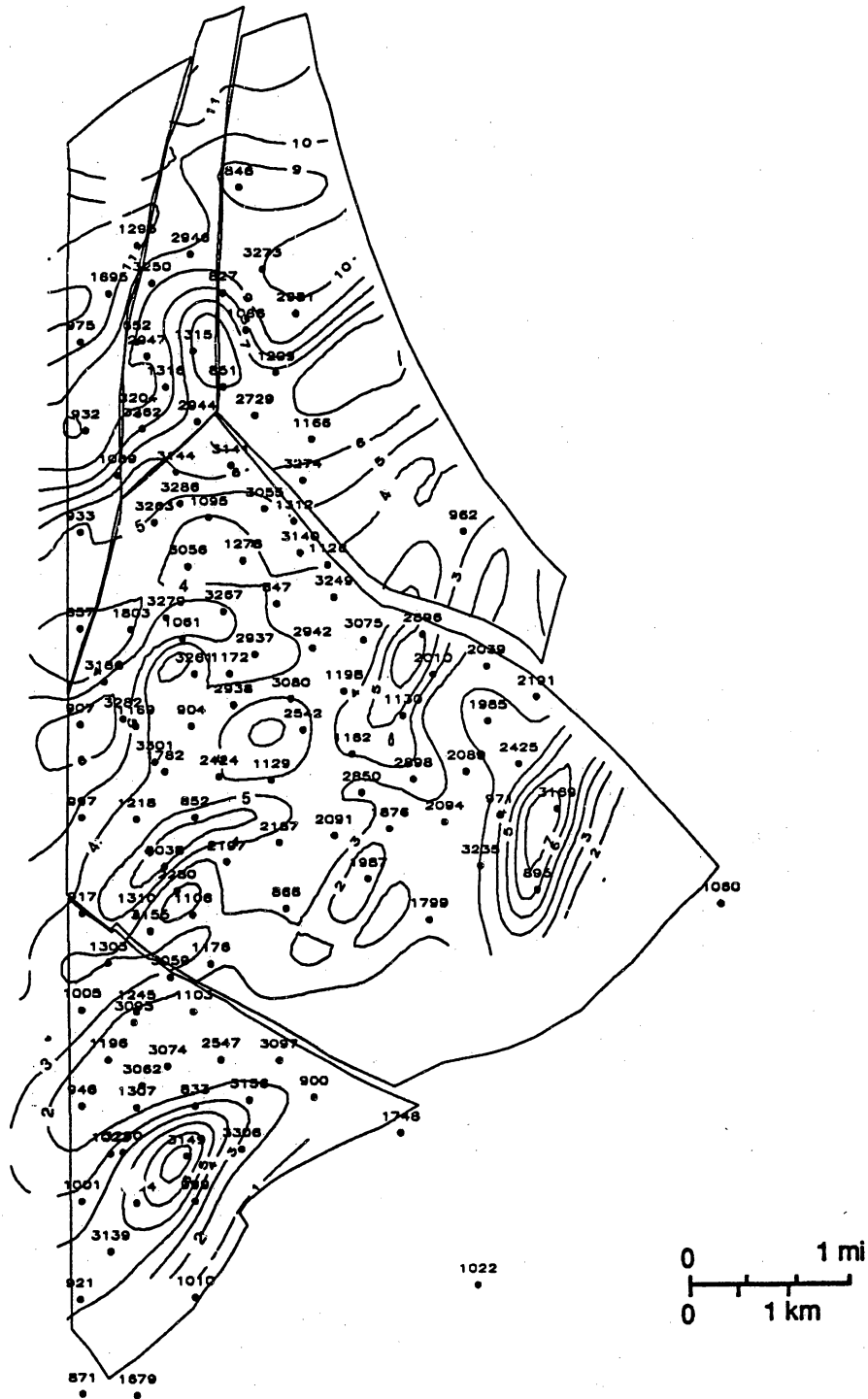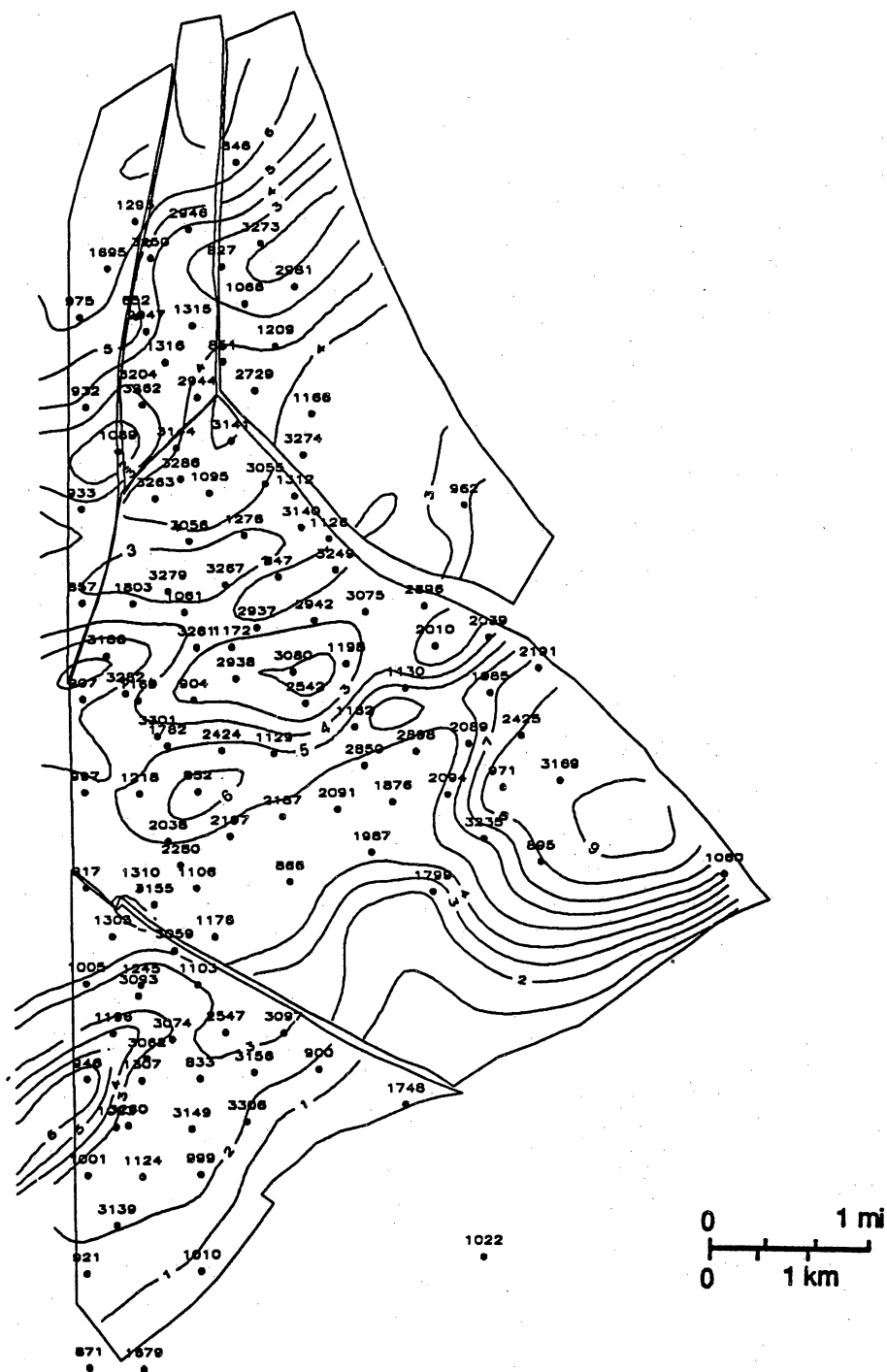Figure 204. S$_o$Øh map of the Middle C-3-X Submember in the LL-652 area. Contour interval is 1 ft (0.3 m).

368

(fig. 201). These high $S_O\varnothing h$ values primarily reflect thick net-pay values (fig. 183) associated with a major sandstone-rich, progradational deltaic wedge (figs. 5 and 126). Greatest $S_O\varnothing h$ values (more than 10 ft [3 m]) correspond to thick depositional axes of more than 100 ft (30.5 m) of net sandstone (fig. 126), particularly in the area of the LL-2089 and LL-3186 wells in the central structural compartment and the LL-3262 well in the north-central structural block (fig. 201).

The Lower and Middle C-4-X Submembers both feature prominent northeast-trending $S_O\varnothing h$ patterns (app. E). In contrast to the Upper C-4-X Submember, the Middle C-4-X Submember contains highest $S_O\varnothing h$ values (more than 5 ft [1.5 m]) in one 2,000-ft (610-m) wide, northeast-trending band in the north-central part of the field (fig. 202).

C-3-X Member

Greatest $S_O\varnothing h$ values in the Lower and Middle C-3-X Submembers are similarly high (12.44 ft [3.79 m] [fig. 203] and 9.62 ft [2.93 m] [fig. 204] respectively). The reason why these greatest $S_O\varnothing h$ values are similar is that even though the Lower C-3-X Submember is thicker than the Middle C-3-X Submember (fig. 5) it is much shalier than the Middle C-3-X Submember (figs. 129 and 130). Additionally, whereas high $S_O\varnothing h$ values are widely distributed across the field in the Middle C-3-X Submember (fig. 204), they are confined to narrow (less than 1,500-ft [457-m]) belts in the Lower C-3-X Submember (fig. 203). The difference in the $S_O\varnothing h$ geometry between these submembers is controlled by the different depositional systems and sandstone architecture: the Lower C-3-X Submember in the LL-652 area consists of narrow, distal delta-front, tidal-ridge sandstones (fig. 129) whereas the Middle C-3-X Submember is composed of sandstone-rich, distributary-channel and proximal delta-front sandstones (fig. 130).

Original Oil in Place

Original oil in place (OOIP) in the C Members in the LL-652 area is controlled by net-pay and net-sandstone thickness, commonly distributed in northeast-trending patterns. The Upper C-4-X and Middle C-3-X Submembers contain the greatest volumes of OOIP, with locally up to 16 MMbbl and 6.2 MMbbl per 80 acres, respectively. As a result of the volumetric analysis and use of improved petrophysical parameters, the net value of OOIP has been greatly increased for the C Members in the LL-652 area (table 59).

C-6-X Member

All submembers in the C-6-X Members have prominent, northeast-trending OOIP patterns (fig. 205 and app. E). The Lower Lower C-6-X Submember contains the greatest OOIP values (up to 8 MMbbl per 80 acres) in an area of northeast-trending contours centered on the LL-1172 and LL-847 wells (fig. 205), which corresponds to thick (more than 90-ft [27.4-m]) fluvial-estuarine deposits (figs. 106 and 107).

C-5-X Member

The Lower and combined Middle and Upper Middle C-5-X Submembers contain the greatest values of OOIP (locally more than 5 MMbbl per 80 acres [figs. 206 and 207, respectively]). Due to sparse well control, OOIP contours are poorly defined in the Lower C-5-X Submember in the southern structural compartment (fig. 206). However, contours are well-defined in the central structural compartment, and they consist of east- and northeast-trending pods of more than 1 MMbbl per 80 acres, corresponding to narrow (less than 2,000 ft [620 m]) distal delta-front, tidal sand-ridge deposits encased in inner-shelf mudstone (fig. 114). In contrast, OOIP contours in the combined Middle and Upper Middle C-5-X Submember in the central structural compartment consist of wide (more than 3,000 ft [915 m]), eastward-

Figure 205. OOIP map of the Lower Lower C-6-X Submember in the LL-652 area. Contour interval is 0.5 MMbbl.

Figure 206. OOIP map of the Lower C-5-X Submember in the LL-652 area. Contour interval is 0.5 MMbbl.
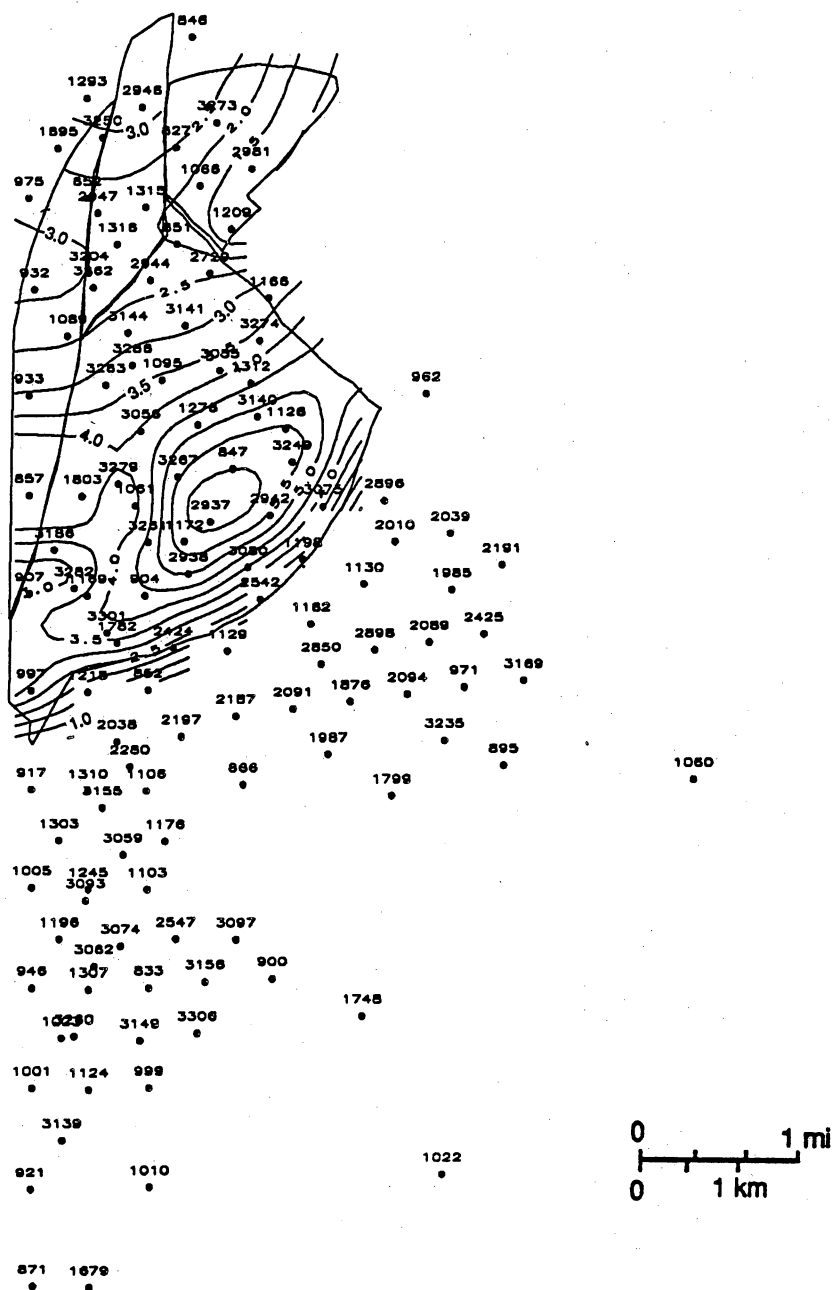
Figure 207. OOIP map of the combined Middle and Upper C-5-X Submembers in the LL-652 area. Contour interval is 0.5 MMbbl.

and northeastward-bifurcating pods that reflect the depositional geometry of distributary-channel sandstones in the Middle Middle C-5-X Submember (fig. 120).

C-4-X Member

The Lower and Middle C-4-X Submembers contain moderate volumes of OOIP (locally more than 4 MMbbl per 80 acres [app. E]), whereas the Upper C-4-X Submember contains high volumes of OOIP (commonly more than 6 MMbbl per 80 acres in the central and more than 10 MMbbl per 80 acres in the northern structural blocks [fig. 208]). Thick pods of more than 7 MMbbl per 80 acres of OOIP approximately correspond to thick (more than 80-ft [24.4-m]) distributary-channel and proximal delta-front sandstones (fig. 126) in the central structural block (fig. 208). The northern structural compartments commonly contain more than 10 MMbbl per 80 acres of OOIP coinciding with dipping strata in a northern deltaic depocenter of more than 100 ft (30.5 m) of net-sandstone thickness (fig. 126).

C-3-X Member

Greatest values of OOIP (more than 6 MMbbl per 80 acres) in the C-3-X Member occur in northern structural compartments in the Lower C-3-X Submember (fig. 209) and in the eastern part of the central structural compartment in the Middle C-3-X Submember (fig. 210). These high values of OOIP in the eastern part of the central structural compartment approximately correspond to thick (more than 50-ft [15.2-m]) distributary-channel sandstones (figs. 130 and 131). Although the Lower C-3-X Submember locally contains higher OOIP values than the Middle C-3-X Submember, average OOIP values in the Middle C-3-X Submember in the central structural compartment are higher than average OOIP values in the Lower C-3-X Submember (figs. 210 and 209, respectively), reflecting sandstone-rich, distributary-channel and proximal delta-front deposits in the Middle C-3-X Submember (fig. 130) as contrasted against muddy, distal delta-front deposits in the Lower C-3-X Submember (fig. 129).

Remaining Oil

Trends of remaining oil in the C submembers (figs. 211 to 217) are similar to identical to trends of original oil in place (figs. 205 to 210). Sites for each submember where values of remaining oil are identical or nearly identical to those of original oil in place indicate areas of undrained or poorly drained reservoir compartments that can be targeted for additional oil recovery.

C-6-X Member

The Lower Lower C-6-X and the Upper Lower C-6-X Submembers contain the greatest volumes of remaining oil in the C-6-X Member (up to 6 MMbbl and 4.4 MMbbl per 80 acres [figs. 211 and 212], respectively). These volumes of remaining oil are depositionally controlled. As with $S_o\emptyset h$ (fig. 198), greatest volumes of remaining oil in the Lower Lower C-6-X Submember occur in a northeast-trending band of more than 4 MMbbl per 80 acres, centered on the LL-1172 and LL-847 wells (fig. 211). This band also corresponds to the belt of thick (more than 90-ft [27.4-m]) fluvial-estuarine sandstones in the zone of relatively deep incision of the C-6-X Member into the C-7-X Member (figs. 106 and 107). Greatest volumes of remaining oil (more than 3.60 MMbbl per 80 acres) in the Upper Lower C-6-X Submember also occur in a northeast-trending band that corresponds to a northeast-trending belt of more than 70 ft (21.3 m) of fluvial-estuarine sandstones (fig. 108).

Remaining oil in other C-6-X Submembers is also distributed in northeast-trending patterns, reflecting the depositional fabric of distributary-channel and delta-front sandstones (app. E). Volumes of remaining oil in the Middle and Upper C-6-X Submembers are less than in the Lower C-6-X Submembers because they were deposited in sandstone-poor, retrogradational sequences (fig. 5).
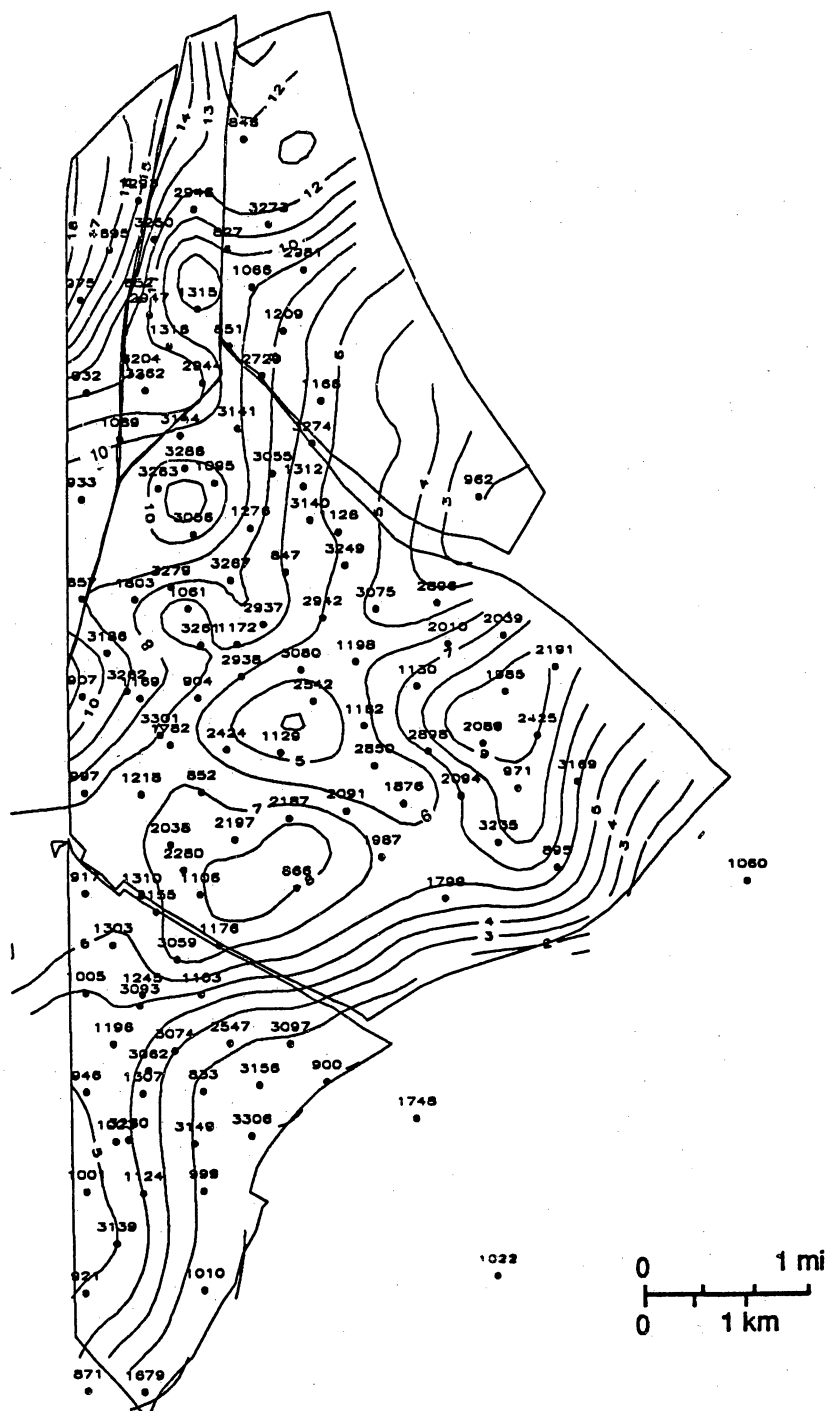
Figure 208. OOIP map of the Upper C-4-X Submember in the LL-652 area. Contour interval is 1 MMbbl.

Figure 209. OOIP map of the Lower C-3-X Submember in the LL-652 area. Contour interval is 0.5 MMbbl.

Figure 210. OOIP map of the Middle C-3-X Submember in the LL-652 area. Contour interval is 1 MMbbl.

Figure 211. Map of remaining oil in the Lower Lower C-6-X Submember in the LL-652 area. Contour interval is 0.5 MMbbl.

Figure 212. Map of remaining oil in the Upper Lower C-6-X Submember in the LL-652 area. Contour interval is 0.5 Mmbbl.

Figure 213. Map of remaining oil in the Lower C-5-X Submember in the LL-652 area. Contour interval is 0.5 MMbbl.

Figure 214. Map of remaining oil in the combined Middle and Upper Middle C-5-X Submembers in the LL-652 area. Contour interval is 0.5 MMbbl.

Figure 215. Map of remaining oil in the Upper C-4-X Submember in the LL-652 area. Contour interval is 1 MMbbl.
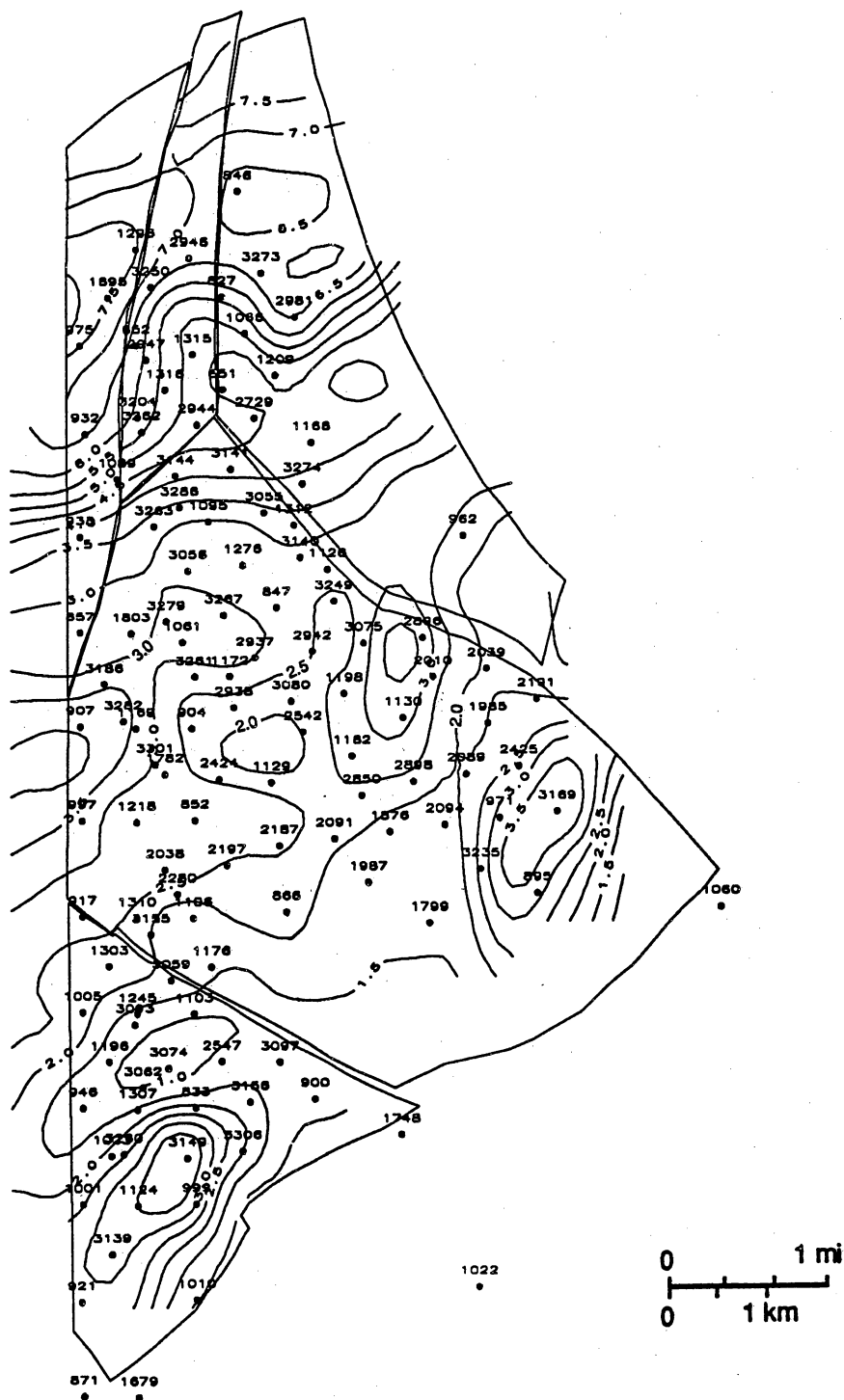
381
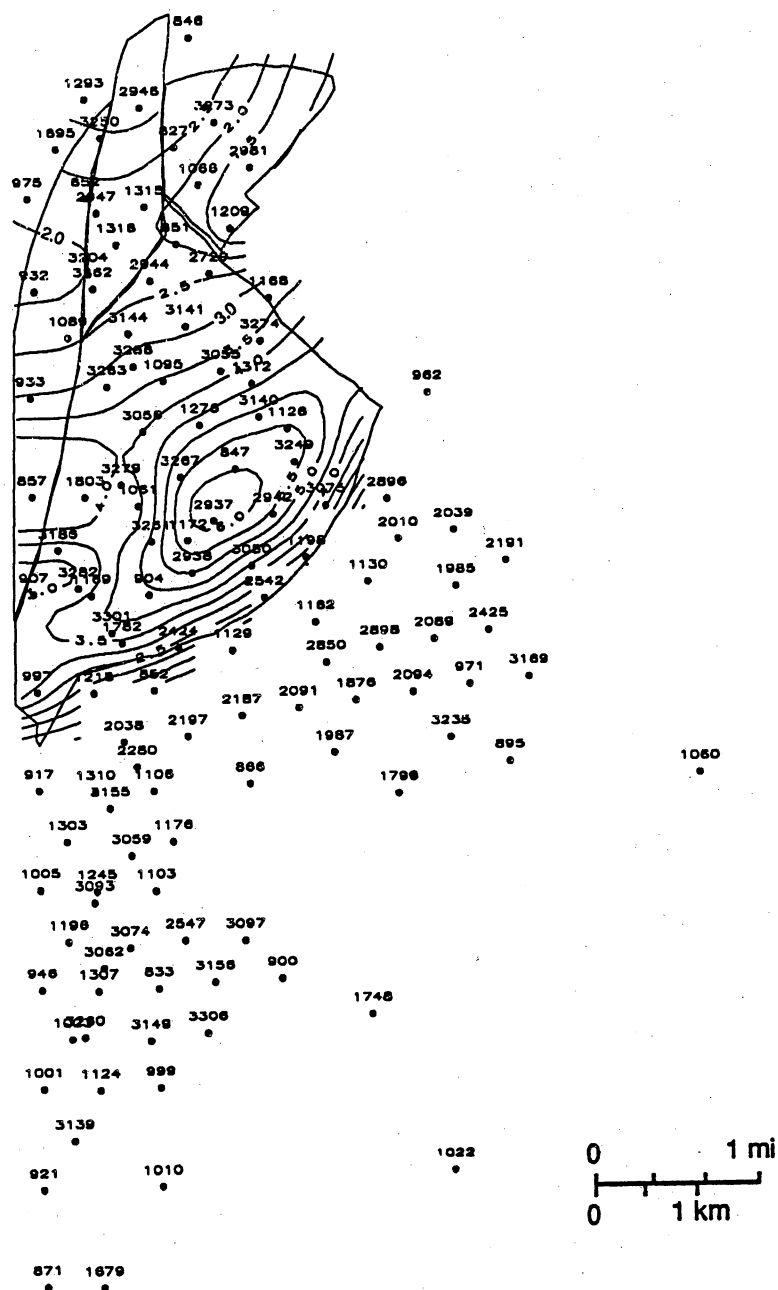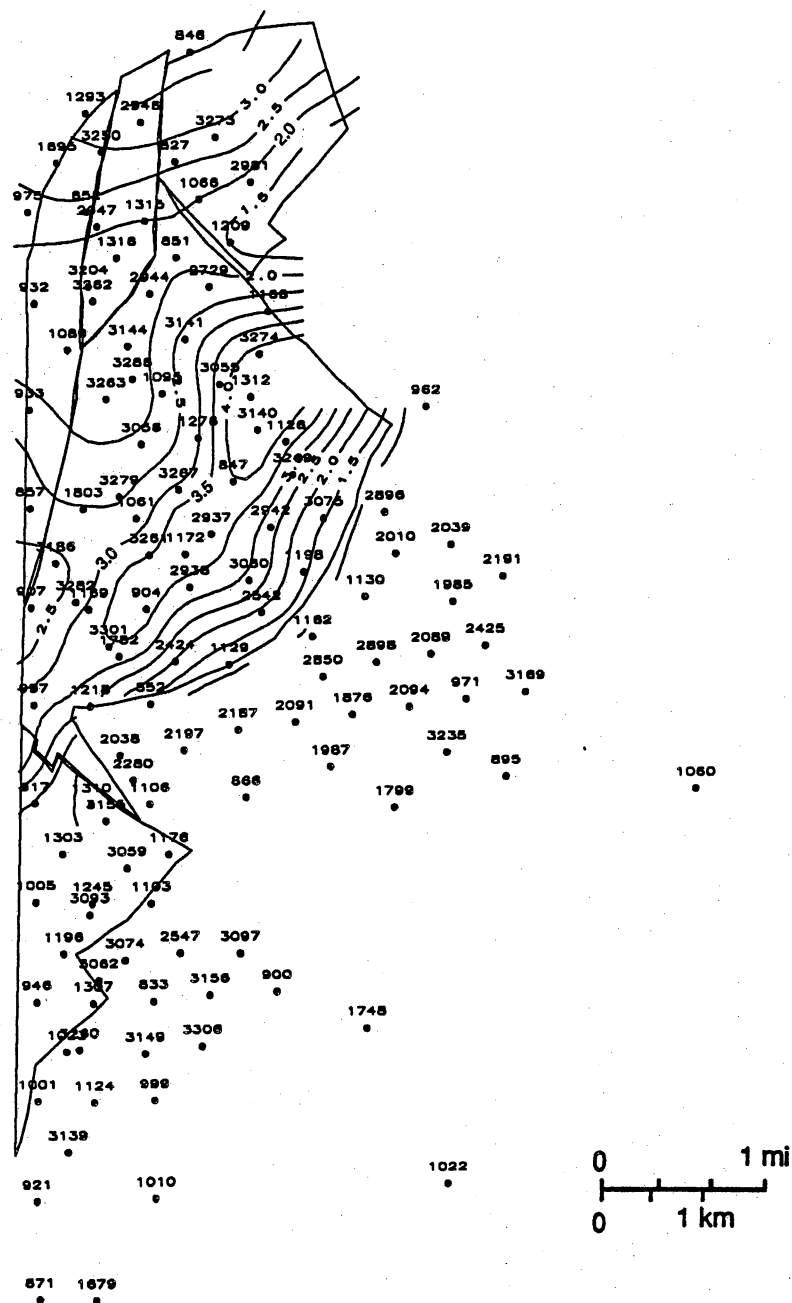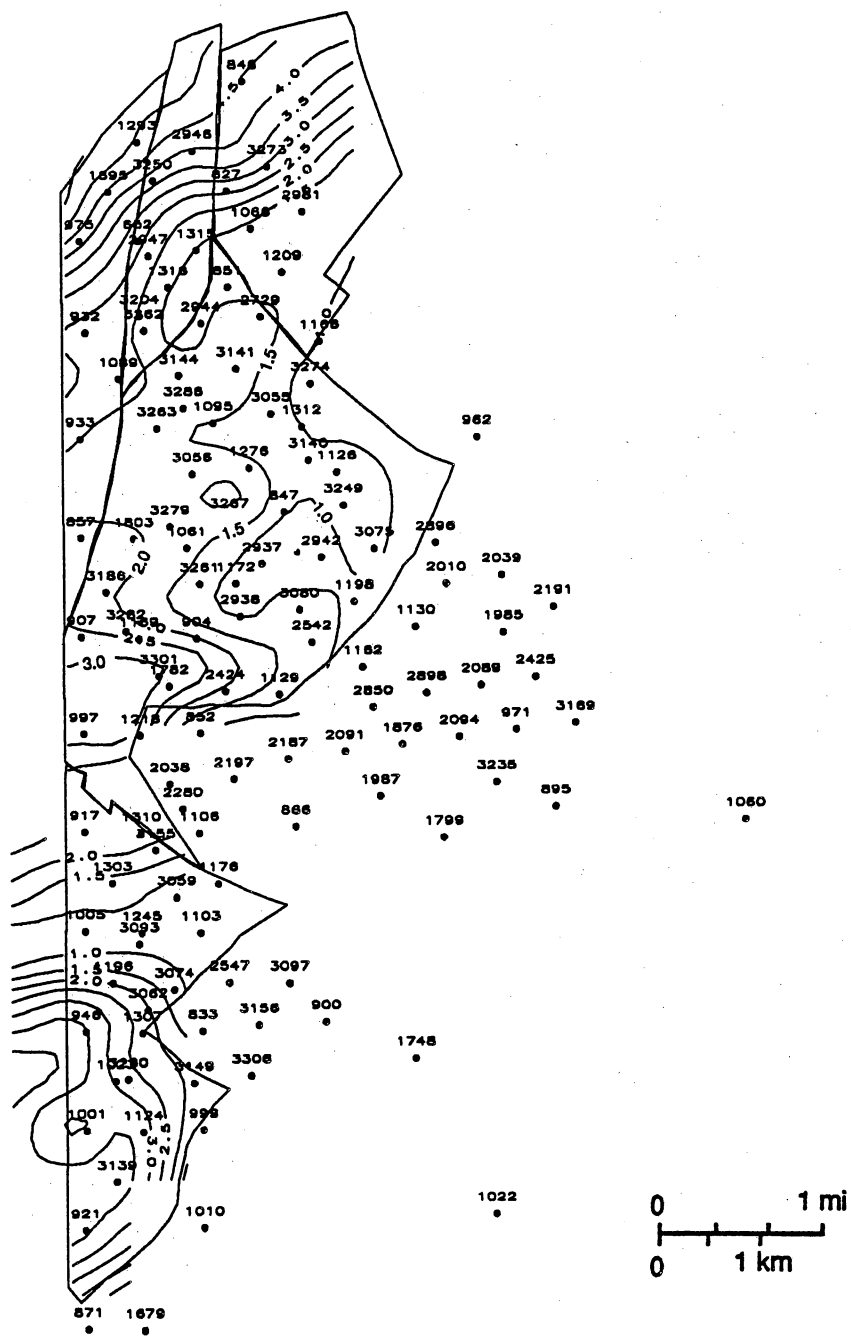
Figure 216. Map of remaining oil in the Lower C-3-X Submember in the LL-652 area. Contour interval is 1 MMbbl.

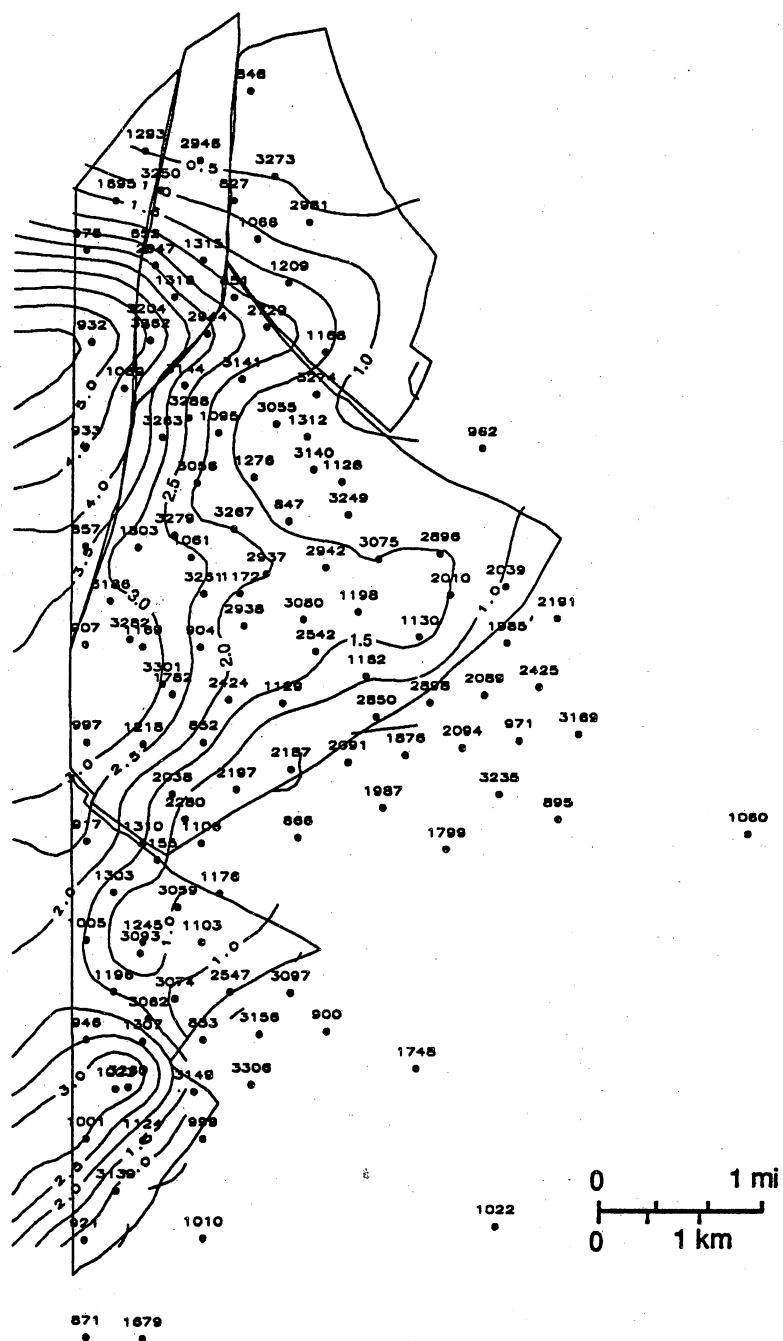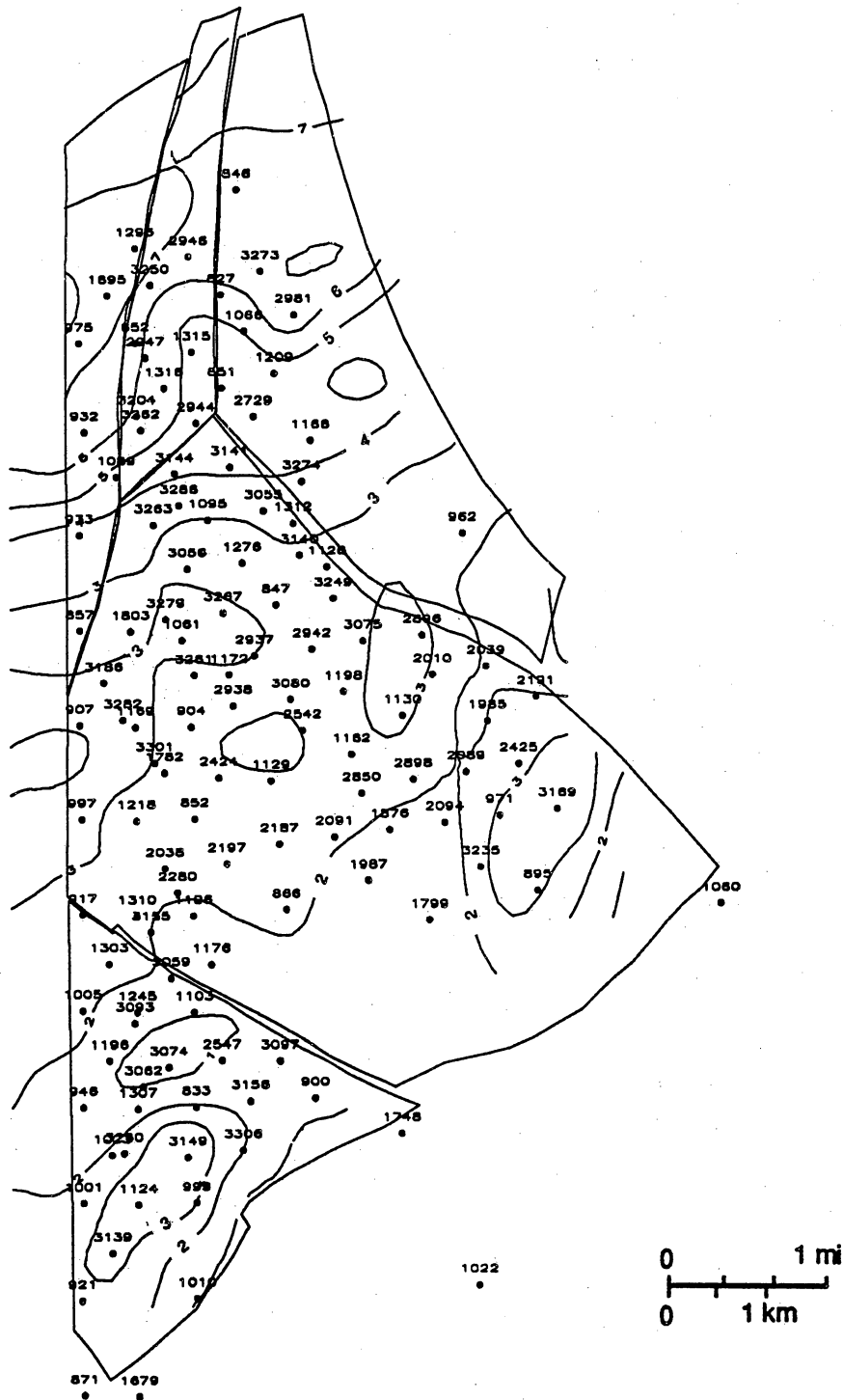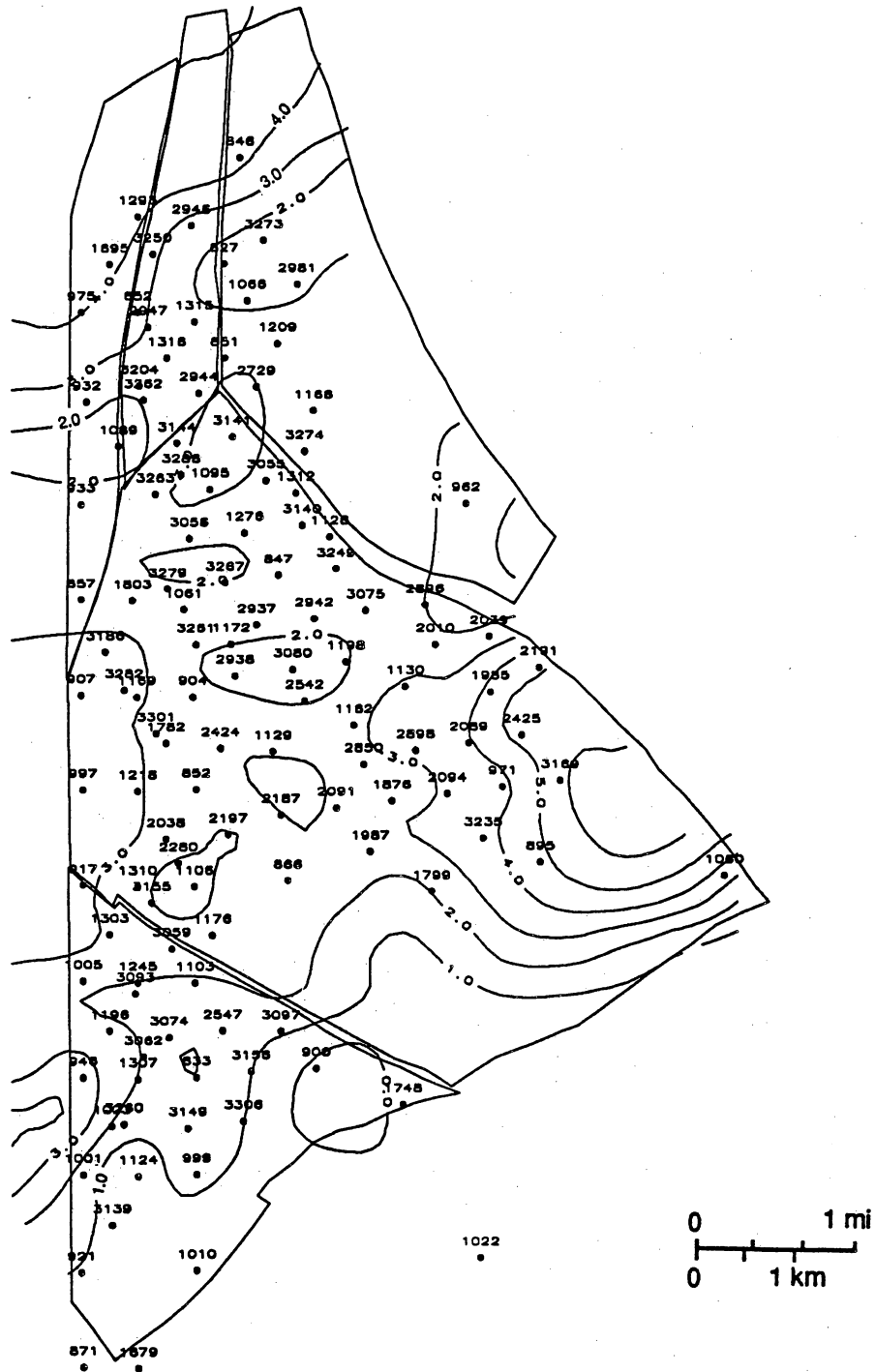Figure 217. Map of remaining oil in the Middle C-3-X Submember in the LL-652 area. Contour interval is 1 MMbbl.

C-5-X Member

The Lower and combined Middle and Upper Middle C-5-X Submembers contain the largest volumes of remaining oil in the C-5-X Member (figs. 213 and 214). The Lower C-5-X Submember contains high volumes of remaining oil per unit area in the southern and northern structural compartments (locally more than 3.6 MMbbl per 80 acres) but relatively less per unit area (typically 1 to 2 MMbbl per 80 acres) in the central structural compartment (fig. 213), reflecting the combined effects of sandstone thickness (fig. 114) and dipping strata in the structurally complex, northern part of the LL-652 area.

In contrast to the Lower C-5-X Submember, the combined Middle and Upper Middle Submembers features eastward- and northeastward-trending lobate trends of remaining oil (more than 1.8 MMbbl per 80 acres), reflecting depositional control by distributary-channel and channel-mouth-bar deposits in the Upper Middle C-5-X Submember (fig. 121).

C-4-X Member

The Upper C-4-X Submember (fig. 215) contains more remaining oil than the Lower and Middle C-4-X Submembers combined (app. E). Many areas, particularly in the northern part of the field, contain nearly as much remaining oil as original oil in place (cf. fig. 208), indicating that the Upper C-4-X Submember has a high potential for secondary oil recovery. Other areas with great volumes of remaining oil are in the western, northern, and eastern parts of the central structural compartment (more than 8 MMbbl per 80 acres) that coincide with thick (more than 80-ft [24.4-m]) delta-front and distributary-channel sandstones (fig. 126).

C-3-X Member

High volumes of remaining oil in the Lower C-3-X Submember (more than 4 MMbbl per 80 acres) occur in the northern part of the field (fig. 216), coincident with high values of original oil in place (fig. 209). High volumes of remaining oil in the Middle C-3-X Submember also occur in the eastern part of the central structural compartment (more than 4 MMbbl per 80 acres) and in the northern part of the three northern structural compartments (more than 3 MMbbl per 80 acres) (fig. 217). Volumes of remaining oil in the Middle C-3-X Submember are quite similar to those of original oil in place (fig. 210), indicating that this submember has an excellent potential for secondary oil recovery.

Reservoir Boundaries

Criteria for analyzing reservoir boundaries were mainly based on the degree of communication between faulted blocks and the architecture of individual sandstones, extremely important in the LL-652 area where the structural style and stratigraphic complexity combine to produce reservoir heterogeneity. Reservoir boundaries were determined by analyzing vertical and horizontal communication by assessing RFT data used in the fault-seal analysis and permeability data from special core analysis from six wells and integrating these data with petrophysical parameters and stratigraphy.

Vertical Communication

Vertical communication was estimated from RFT data in seven wells (table 5). This tool can resolve a pressure difference of 50 psi between two overlying sandstones, sufficient to indicate poor reservoir communication. In the LL-652 area there is poor or no communication between members and submembers because almost 98 percent of the pressure data (figs. 57, 58, and 59) indicate an average pressure difference of more than 50 psi. For example, the LL-3195 well (fig. 57) has a 625-psi difference between the C-3-X (2,200 psi) and C-4-X (1,575 psi) Members, and a 190-psi difference (fig. 58) between

the C-4-X (1,575 psi) and C-5-X (1,760 psi) Members. The LL-3186 well (fig. 58) has a 500-psi difference between the C-3-X (2,513 psi) and C-4-X (2,010 psi) Members. The LL-3141 well (fig. 59) has 1,950 psi in the Upper C-4-X Submember and an average of 2,480 psi in the Middle C-4-X Submember, a 530-psi difference. Also, the LL-3195 well (fig. 61) has a 255-psi difference between the Upper C-5-X (1,767 psi) and Upper Middle C-5-X (2,022 psi) Submembers. Finally, most of the RFT tests showed that between individual sandstones in submembers, there is poor or restricted vertical communication. For example, the LL-3173 well (fig. 57) has a 155-psi difference between the upper sandstone (1,720 psi) and lower sandstones (1,875 psi) in the Upper C-4-X Submember.

Permeability data from the LL-2850, LL-3074, LL-3075, LL-3080, LL-3140, and LL-3282 were used to verify vertical communication between overlying sandstones. Permeability is a measurement of the ability of the filling fluid to move through the pore space and reflects the interconnectivity of pores in the rock. The low-quality reservoirs in the LL-652 area have a correlation line on the porosity-permeability crossplot (fig. 169) that plots lower along the permeability axis with respect to that of good-quality reservoirs. In particular, the LL-652 reservoirs are low-permeability more than they are low-porosity. The vertical variation of permeability from core was also a good indicator of interbedded, complexly stratified reservoirs. For example, the horizontal versus vertical permeabilities for the LL-2850 well, shown in figure 218, indicate that horizontal permeabilities are higher than vertical permeabilities for the same depth. For average samples, horizontal permeabilities are approximately 400 times higher than vertical permeabilities.

Horizontal Communication

RFT and pressure data indicate strong stratigraphic controls on pressure values in conjunction with complex fault patterns. Boundaries of reservoir compartments are inferred from pressure analysis. By using fault-seal-probability data (table 6) we recognized four faults that form reservoir boundaries. The Master fault, located in the Maraven area, represents the western limit of the LL-652 area and should be considered a geological boundary for engineering models. The main fault and the northeast reverse fault (#11) combine to isolate compartment I (fig. 12), located on the downthrown side of these faults. The main fault separates other reservoirs (C-4-X.01, C-5-X.02, and C-6-X.01) that are located on the upthrown block of these two faults. The south fault forms the southern limit of the C-4-X.03, C-5-X.08, and C-6-X.16 reservoirs. The central fault bounds the C-4-X.01, C-5-X.02, and C-6-X.01 reservoirs from the C-4-X.03, C-5-X.08, and C-6-X.16 reservoirs.

Another reservoir boundary is formed by the northwest reverse fault, but due to the small area west of this fault in the high-dip zone, we recommend that reserves in this area be assigned to the C-4-X.01 and C-05-X.02 reservoirs. The southeastward boundary is defined by an aquifer (individual oil-water contacts by submembers) previously described in the production-analysis section. The northern limit is unknown due to the sparse well control, but it was defined for each of the C-3-X, C-4-X, C-5-X, and C-6-X Members for the structurally lowest, oil-saturated sandstone interpreted by petrophysical analysis and was estimated with the equivalent structural depth of the oil-water contact from the southeastern flank of the field.

Production

Cumulative production, apportioned by kh in each C submember, varies greatly across the LL-652 area. Reasons for this variability include (1) differences in age of producing well, in which old wells have had time to produce larger quantities of oil than young wells, (2) greater-than-average production in areas of repeat section and inferred great fracture-permeability in zones of reverse faults, (3) greater-than-average production in areas of thick net pay and net sandstone along deltaic depositional axes, and (4) differences in net thickness of intervals perforated in each submember.
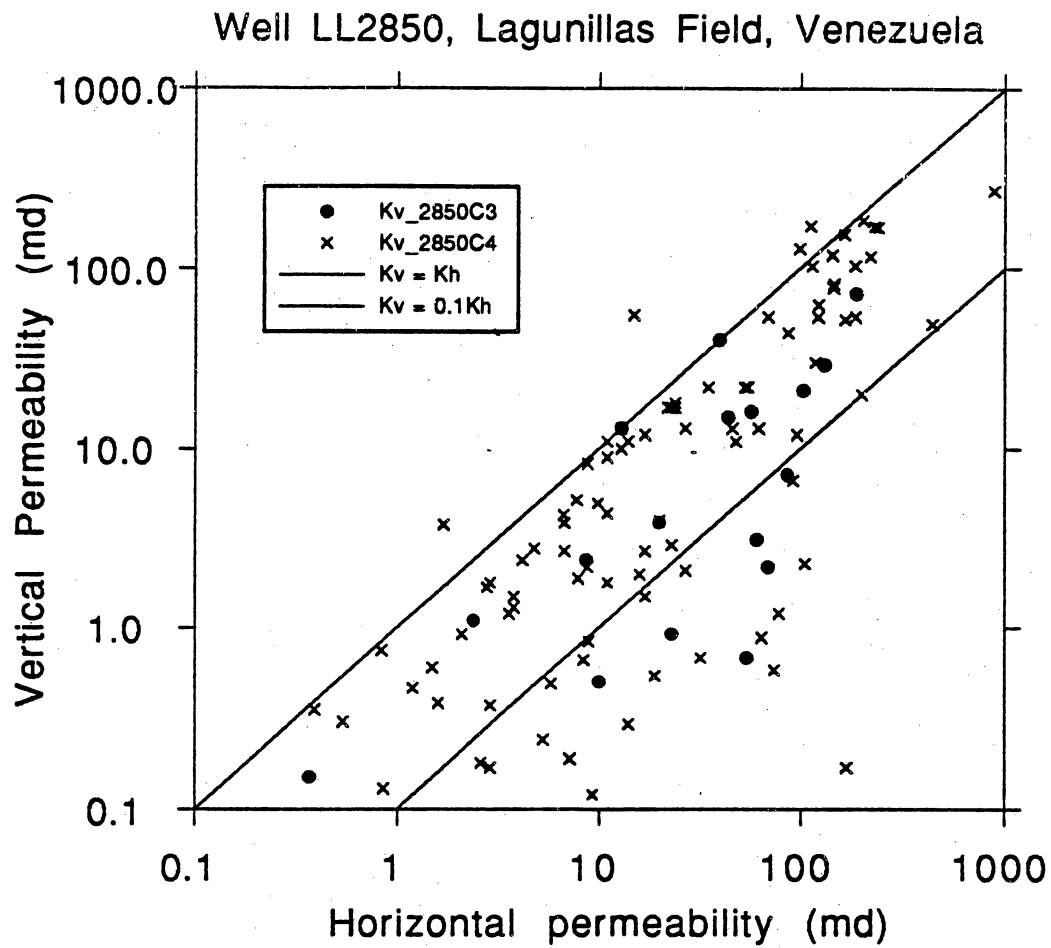
Figure 218. Horizontal versus vertical permeability in the LL-2850 well.

General areas of opportunity for optimizing oil recovery were determined by comparing maps of cumulative production (see figs. 219 to 226) with maps of $S_O\emptyset h$ and remaining oil (see figs. 197 to 204 and figs. 211 to 217). Numerous areas exist for infill wells, particularly in the sparsely developed northern part of the LL-652 area. These areas have little or no cumulative production and are inferred to contain great volumes of OOIP and remaining oil.

C-6-X Member

Lower Lower C-6-X Submember

Production from the Lower Lower C-6-X Submember is sparse, with greatest cumulative production (85,216 bbl) in the LL-3056 well and 76,806 bbl in the LL-1276 well (fig. 219a). However, none of these wells have contacted the northeast-trending zone of greatest remaining oil (more than 5 MMbbl per 80 acres) (fig. 211) that coincides with thick (more than 90-ft [27.4-m]) fluvial-estuarine sandstones (figs. 106 and 107). Additionally, there is no production from the northern part of the LL-652 area, where remaining oil values are up to 3 MMbbl per 80 acres (fig. 211).

Upper Lower C-6-X Submember

Most production from the Upper Lower C-6-X Submember is from the LL-1061 well (961,228 bbl), the LL-1095 well (475,249 bbl), and the LL-3056 well (204,519 bbl) (fig. 219b). Other production is from seven wells to the south and east. However, none of these wells have contacted the northeast-trending band of highest remaining oil (more than 3.6 MMbbl per 80 acres) (fig. 212) that corresponds to thick (more than 70-ft [21.3-m]) fluvial-estuarine sandstones (fig. 108).

Lower Upper C-6-X Submember

Nineteen wells have produced from the Lower Upper C-6-X Submember (fig. 220). Of the six wells that have produced more than 100,000 bbl, four intersect the zone of reverse faults. Areas of high potential for incremental oil recovery are in the north, where there is only one producing well in which remaining oil exceeds 2 MMbbl per 80 acres (app. E). Additionally, the area of the LL-2424 well contains relatively thick (more than 40-ft [12-m]) distributary-channel and delta-front sandstones, has not been produced, and has more than 1.6 MMbbl per 80 acres. Other promising sites exist along the zone of reverse faults in areas distant from the previously producing wells.

C-5-X Member

Lower C-5-X Submember

The Lower C-5-X Submember has been produced from 21 wells, of which 4 (LL-904, LL-1001, LL-1005, and LL-1111) have each produced more than 800,000 bbl (fig. 221). The LL-1001 and LL-1005 wells are located in the zone of reverse faults, whereas the LL-904 and LL-1111 wells occur in a northeast-trending band of more than 70 ft (21.3 m) of net sandstone (fig. 114). Additionally, the LL-904 well is in an area of approximately 1.6 MMbbl of remaining oil per 80 acres (fig. 213) and is expected to produce large volumes of additional oil. The west-central belt of high net-pay thickness (app. E) controls productive wells in the center of the field. Also, the northern area has been untapped in the Lower C-5-X Submember, where there are alternating bands of high and low net-sandstone thickness (fig. 114) and $S_O\emptyset h$ (fig. 199).

387

Figure 219. (a) Cumulative production map of the Lower Lower C-6-X Submember in the LL-652 area. Values are in Mbbl.

Figure 219. (b) Cumulative production map of the Upper Lower C-6-X Submember in the LL-652 area. Values are in Mbbl.

Figure 220. Cumulative production map of the Lower Upper C-6-X Submember in the LL-652 area. Values are in Mbbl.

Figure 221. Cumulative production map of the Lower C-5-X Submember in the LL-652 area. Values are in Mbbl.

Figure 222. Cumulative production map of the combined Middle and Upper Middle C-5-X Submember in the LL-652 area. Values are in Mbbl.

Figure 223. Cumulative production map of the Middle C-4-X Submember in the LL-652 area. Values are in Mbbl.

Figure 224. Cumulative production map of the Upper C-4-X Submember in the LL-652 area. Values are in Mbbl.

394
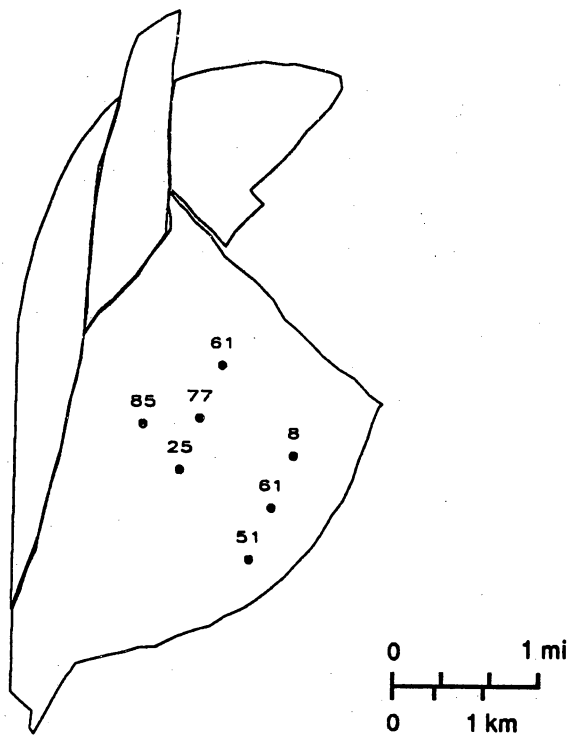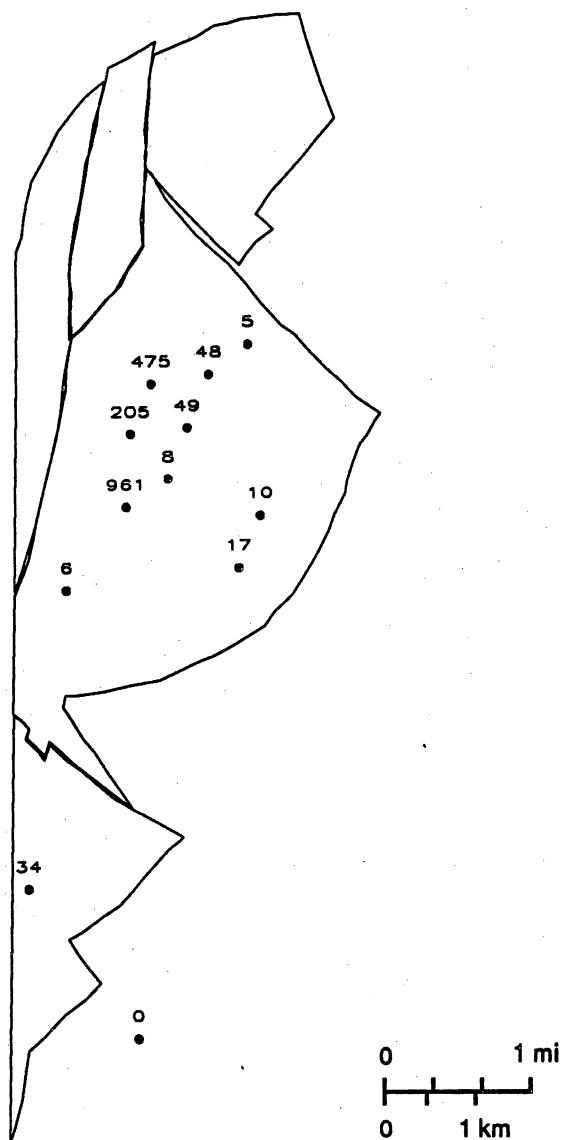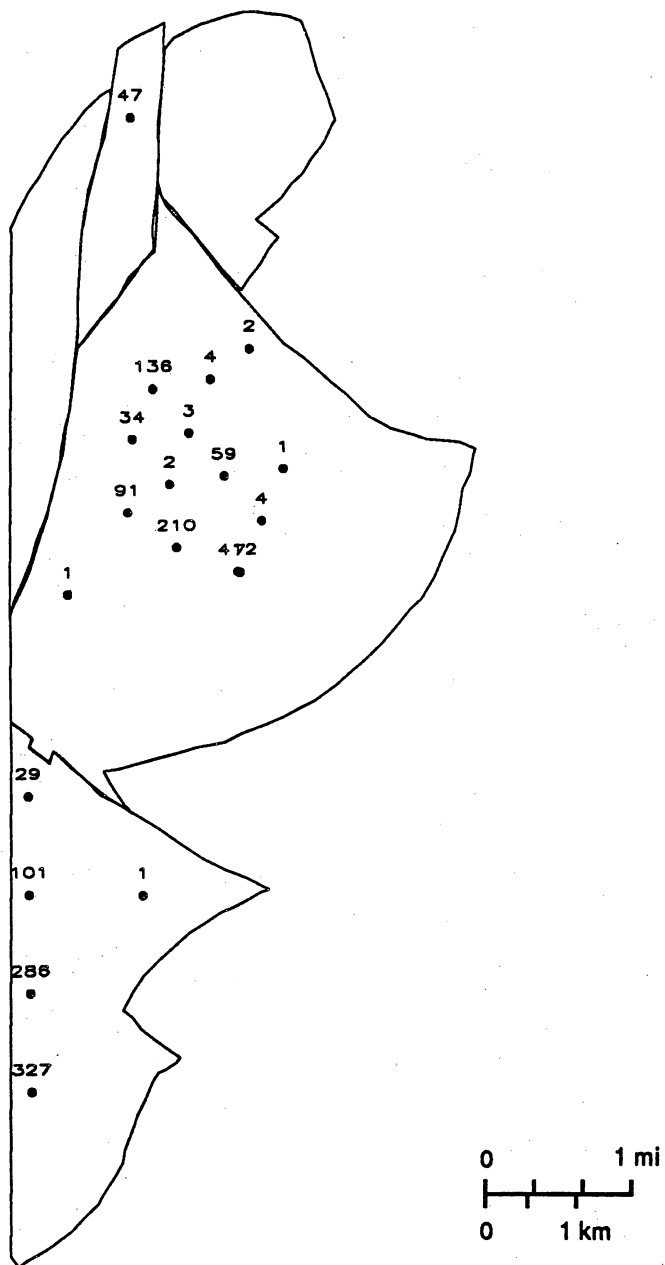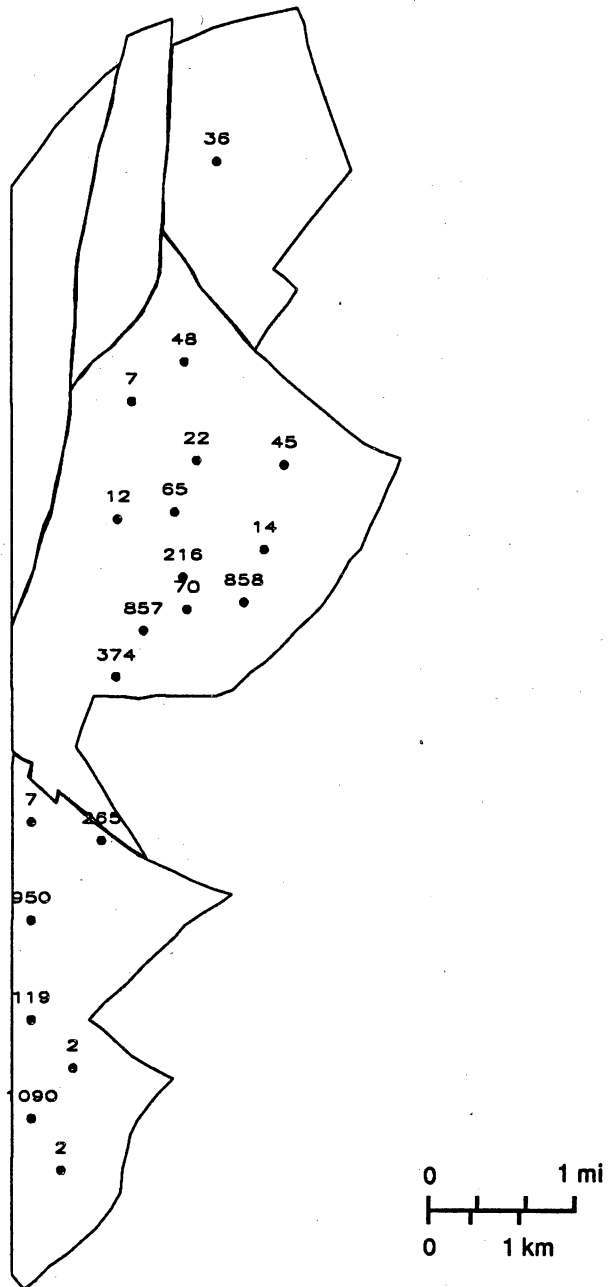
Figure 225. Cumulative production map of the Lower C-3-X Submember in the LL-652 area. Values are in Mbbl.

Figure 226. Cumulative production map of the Middle C-3-X Submember in the LL-652 area. Values are in Mbbl.
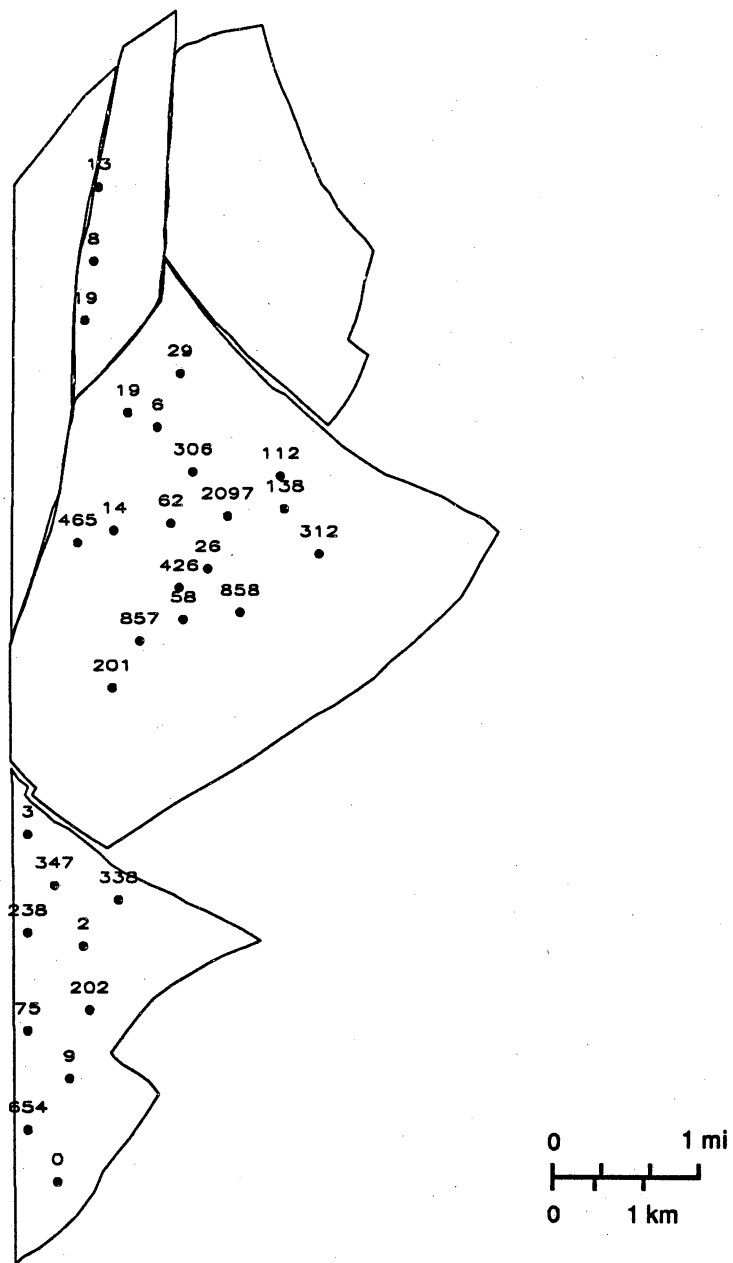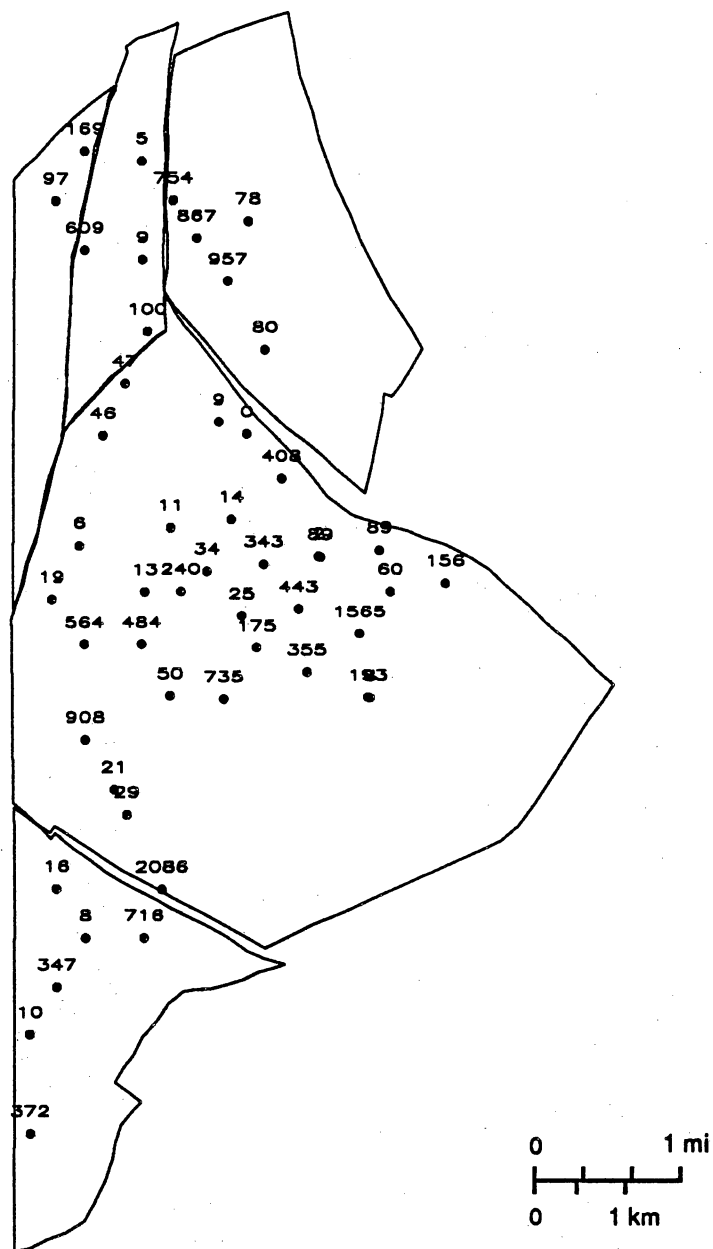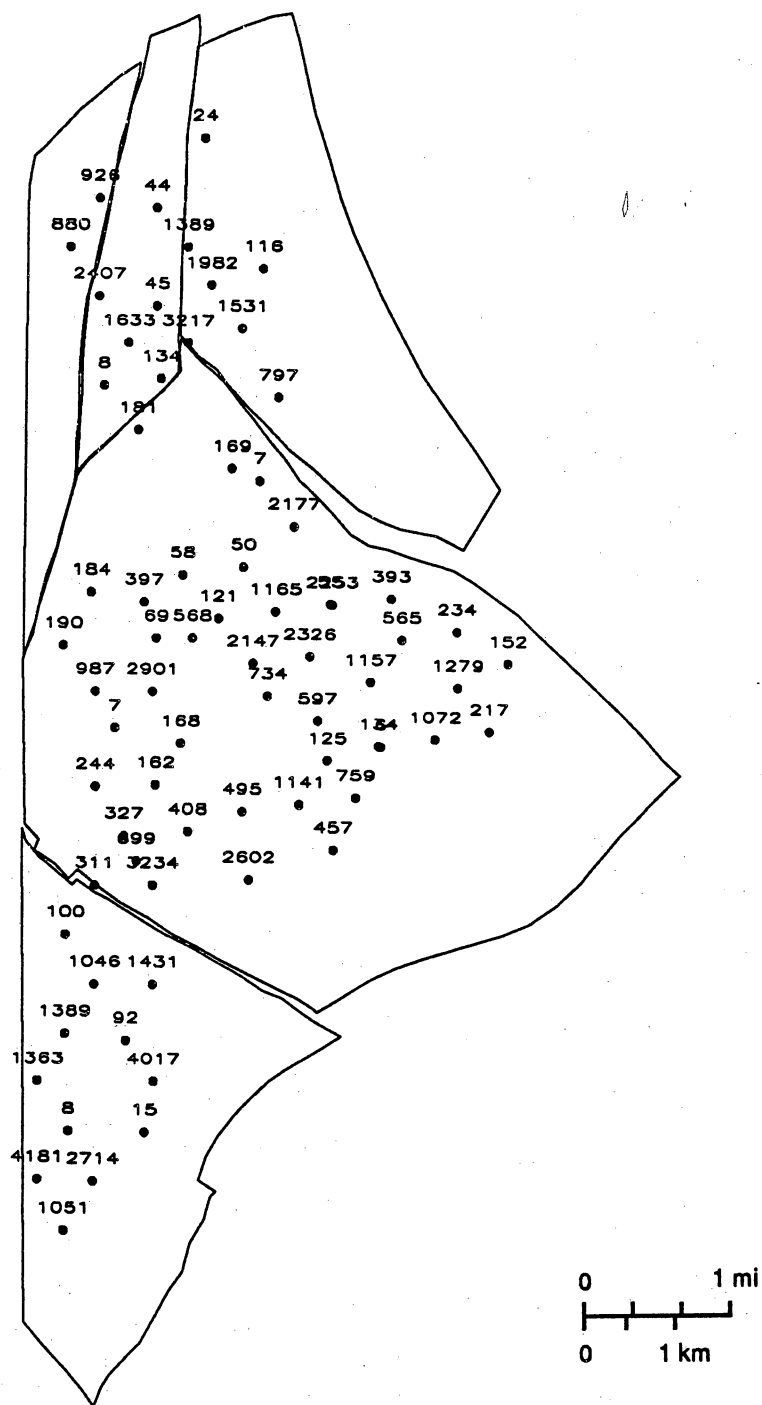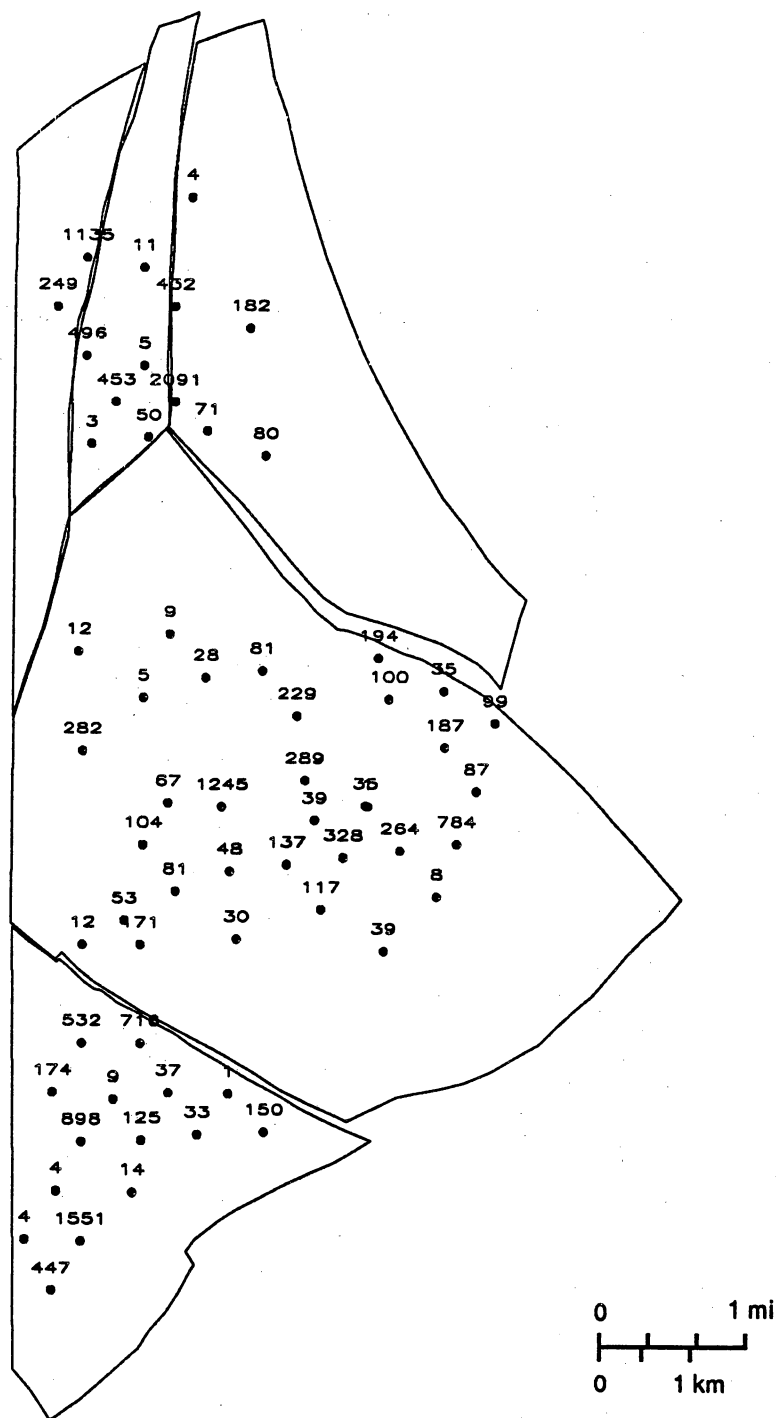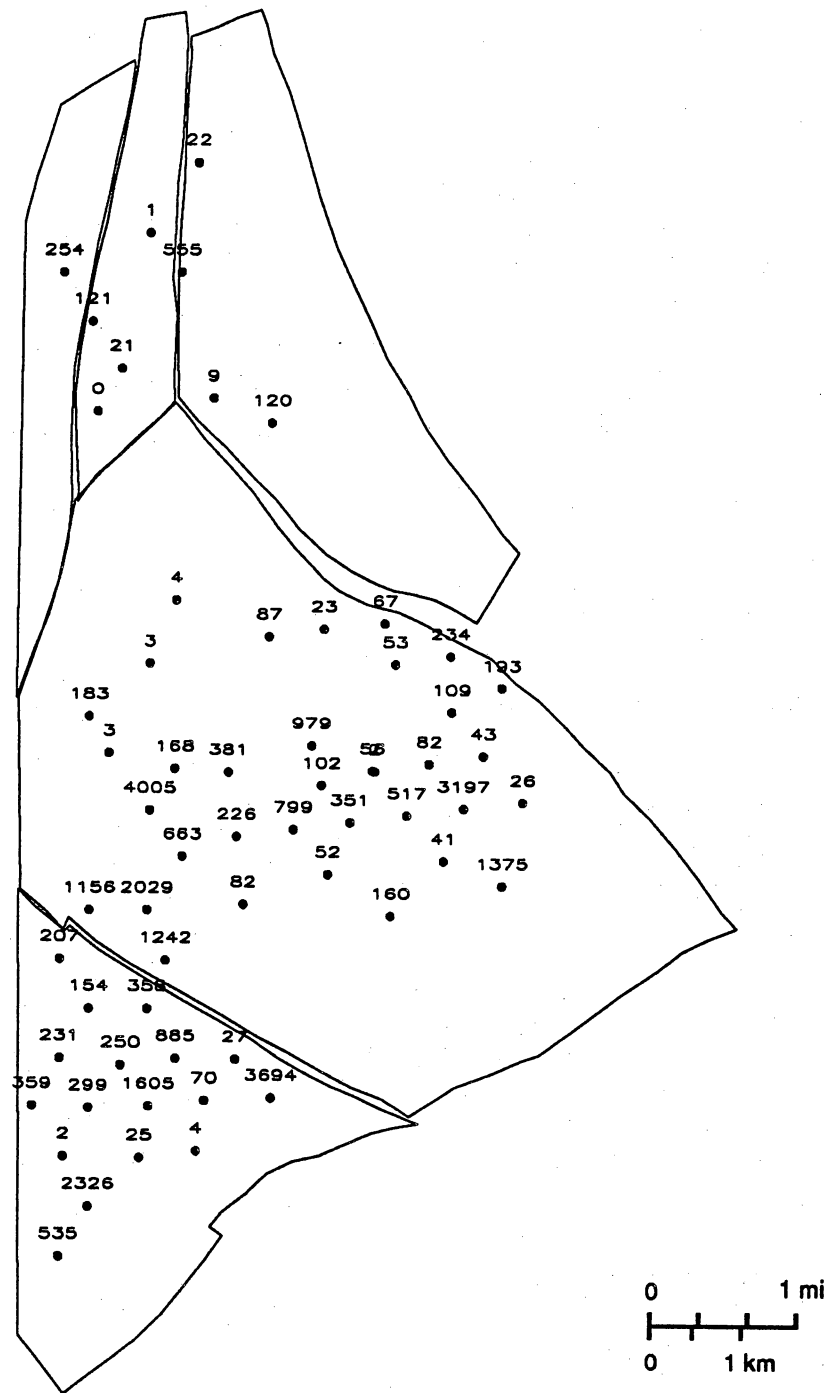
Combined Middle and Upper Middle C-5-X Submember

Twenty-eight wells have produced from the combined Middle and Upper Middle C-5-X Submember (fig. 222). The best producer, the LL-847 well, accounts for more than 4 MMbbl near a zone of high net pay (app. E) that also corresponds to intermediate $S_0\emptyset h$ values (app. E). Two of the three northern structural compartments contain high net-pay values, have not been developed, and, therefore, should be targeted for oil recovery.

C-4-X Member

Middle C-4-X Submember

The Middle C-4-X Submember has produced from 51 wells (fig. 223). However, only one well (the LL-1130) has produced more than 1 MMbbl. A group of superior wells in the central part of the field correspond to axes of high net pay (more than 30 ft [9 m]), whereas poorer wells are in low-net-pay zones (app. E). Additionally, there is a belt of three wells, each with more than 750,000 bbl (LL-827, LL-1066, LL-1209) of cumulative oil production, in the northern part of the field. Development opportunities exist in the southeastern part of the field area near the LL-1387 and LL-2094 wells where there are moderate $S_0\emptyset h$ values (fig. 202) and high net-pay values (app. E). Also, there is a linear, high-$S_0\emptyset h$ belt (fig. 202) that cuts across the area of the LL-1095 and LL-3056 wells that has not yet been produced (fig. 223).

Upper C-4-X Submember

The Upper C-4-X Submember is the most productive interval in the C members and has produced from 14 wells, each with cumulative production more than 1.5 MMbbl, and 11 wells, each with 1.0 to 1.5 MMbbl (fig. 224). Despite high production in the Upper C-4-X Submember, there are numerous sites in the LL-652 area where high volumes of remaining oil coincide with little or no production. For example, high values of remaining oil (more than 10 MMbbl per 80 acres) (fig. 215) occur in the area of the LL-1095 and LL-3263 wells, where there has been no previous production. In addition, the extreme northern part of the field is projected to have high values of remaining oil where there has been no production. There are also areas of more than 7 MMbbl of remaining oil in the western part of the central structural block that coincide with no production (LL-997 well) or limited production (LL-1803 and LL-3186 wells) (fig. 224). High values of net pay (more than 180 ft [54.9 m]) (fig. 183) occur in the extreme northern, non-produced part of the field. Also, high values of net pay (more than 120 ft [39.6 m]) occur in the area of the LL-1095 and LL-3056 wells where there is no production (fig. 224).

A final consideration in infield development of the Upper C-4-X Submember is locating infill wells in the northeast-trending zone of reverse faults. Some wells in this fault zone (LL-852, LL-946, LL-1001, and LL-1196) have each produced more than 1 MMbbl. However, there are numerous segments of other reverse faults in the Upper C-4-X Submember that have not been contacted, particularly in the western part of the LL-652 area.

C-3-X Member

Lower C-3-X Submember

Eight wells have each produced more than 500,000 bbl in the Lower C-3-X Submember (fig. 225). The leading two wells (LL-851 and LL-1124) have produced approximately 2.09 and 1.55 MMbbl of oil, respectively.

Although the Lower C-3-X Submember is composed of multiple thin sandstones with limited lateral extend (table 38 and fig. 129), it still has good potential for incremental oil recovery because it is a thick (more than 250-ft [76-m]) interval (fig. 5) that locally contains more than 60 ft (18 m) of net pay (app. E) and 4 MMbbl of remaining oil per 80 acres (fig. 209). There are several areas in the field where there has been no or limited production that coincide with high volumes of remaining oil. For example, high volumes (more than 6 MMbbl per 80 acres) of remaining oil may exist in the extreme northern part of the field, beyond areas of previous production. Additionally, a broad (more than 4,000 ft [1,200 m] wide) east-trending swath of no production cuts across the north-central part of the field and is centered on the LL-1095 well (fig. 225). This area coincides with values of remaining oil that range from 2.8 to 4.2 MMbbl per 80 acres (fig. 209).

The north-northeast-trending zone of reverse faults also contains numerous sites where either recompletions or infill wells can tap additional remaining oil resources. Virtually no wells have been perforated in the Lower C-3-X Submember along these faults, where as a result of repeat section and fractures, kh values and permeability are inferred to be significantly higher.

Finally, as a result of the extremely limited lateral extent of distal delta-front, tidal-ridge sandstones that comprise most of the Lower C-3-X Submember (fig. 129), opportunities for infill wells exist even in the extensively developed central structural block. For example, up to 3.6 MMbbl per 80 acres of remaining oil exists in narrow (less than 2,000 ft [620 m] wide) uncontacted tidal-ridge sandstones between the LL-1198 and LL-2896 wells that are separated by 3,000 ft (915 m) (fig. 209).

Middle C-3-X Submember

The Middle C-3-X Submember has produced oil from 60 wells (fig. 226). Seventeen of these wells have each produced more than 500,000 bbl. Most production is from southern and central areas, with limited production in the north. Although the Middle C-3-X Submember is sandstone-rich throughout the entire LL-652 area (fig. 130), there are broad areas in the western, extreme northern, and north-central part of the field that have no production (fig. 226). Each of these three unexploited areas contains large volumes (typically 3 MMbbl per 80 acres) of remaining oil (fig. 217). In addition, the eastern part of the central structural compartment still contains large volumes of remaining oil (more than 3 MMbbl per 80 acres) (fig. 217) in permeable (fig. 193) distributary-channel and proximal delta-front sandstones (fig. 130), despite the presence of six wells, each with more than 500,000 bbl of cumulative production (fig. 226).

The Middle C-3-X Submember has also been poorly developed along the north-northeast-trending zone of reverse faults (fig. 226). Several opportunities exist for infill wells or recompletion in this fault zone, especially in areas of high volumes of remaining oil. Examples include the area of the LL-857, LL-997, LL-1218, and LL-1782 wells in the western part of the central structural compartment and the area of the LL-1061 to LL-3140 wells in the northern part of the central structural compartment (figs. 217 and 226).

XI. OPPORTUNITIES AND STRATEGIES FOR RECOVERY OPTIMIZATION AND RESERVE GROWTH

The potential for oil field reserve additions is a function of the oil volumes originally in place, level of development of the reservoir, and importantly, the degree of internal geologic complexity of the field. Reservoirs in the C members in LL-652 area contain a high degree of depositional and structural variability. The product of this combined structural and depositional complexity is reservoirs that have a high degree of geologic heterogeneity, considerable variation in reservoir quality, and hence, relatively low recovery efficiency. The poor recovery efficiency is a function of the weak solution-gas drive mechanism and well spacing that is greater than the size of the reservoir compartments that collectively compose the main reservoir sandstones.

In addition to relatively low permeabilities, detailed well-log correlations indicate that considerable between-well variability is also responsible for the low recovery efficiency of the LL-652 area. Wells from the same reservoir yield widely varying amounts of oil, further demonstrating even smaller scale heterogeneity. These reservoirs have a current well spacing of 80 acres and a primary recovery efficiency of 20 percent (468 MMSTB). The 923 MMSTB of unrecovered oil (fig. 227) compose a major target for reserve additions and increased production.

Reservoir rock-quality analysis focused on petrophysical and diagenetic factors (e.g., pore scale distribution and clay mineralogy) that currently influence oil production and that could be critical in future advanced oil recovery projects. Together with stratigraphic and structural complexity, rock-property variation emphasizes the fact that targeted strategies must be defined for increasing ultimate recovery. Maps of porous hydrocarbon volume $(S_o\varnothing h)$ and remaining oil were indispensable in planning strategies for additional recovery and reserve growth. These maps were interpreted in the planning of optimum new well location, continued conventional development, targeted off-pattern infill-drilling, well-recompletion programs, and a pilot waterflood.

The maps of remaining oil in the LL-652 area represent the integration of geological, petrophysical, and production studies and showed that most of the remaining oil occurs in areas with high cumulative production. These areas have the highest permeability-ft (kh) and the greatest original oil in place. Infill-drilling, new locations, and recompletion strategies were based on comparison of the mutual occurrence of remaining resources, kh values, and current production.

New Extended-Development Locations

New development well locations were primarily directed toward the recovery of proved hydrocarbon resources that could not be recovered by existing wells. In some cases, development wells were proposed as alternate wells or to accelerate production. Well-location maps (figs. 228 to 223) show 97 recommended new well locations in addition to 14 horizontal and 23 inclined wells shown in figures 228 and 229. In the C-3-X and C-4-X Members, most of the new locations for extended development are in the sparsely drilled northern and northeastern parts of the LL-652 area (figs. 228 and 229). However, other locations are targeted for the reverse fault in the eastern part of the central structural compartment, as well as the southern limb of the field in the southern structural compartment. The eastern and south-central parts of the central structural compartment contain areas where delta-front and distributary-channel sandstones of the C-3-X and C-4-X Members have been incompletely contacted. The majority (more than 20) of extended-development locations in the C-5-X Member are in the northern and central structural blocks, whereas only six are targeted in the southern structural block, principally along the zone of reverse faults (figs. 230 and 231). In contrast, virtually all of the extended-development locations in the C-6-X Member are in the central structural block and target relatively high volumes of remaining oil in delta-front sandstones (figs. 232 and 233).

399

Pie chart labels:
- Cumulative production (166 MMbbl, 7%)
- Residual (927 MMbbl, 40%)
- Reserves (302 MMbbl, 13%)
- Unrecovered mobile oil (923 MMbbl, 40%)
- EUR (468 MMbbl, 20%)
- Targeted infill drilling and secondary recovery projects (460 MMbbl, 20% of OOIP).

QAa5270c
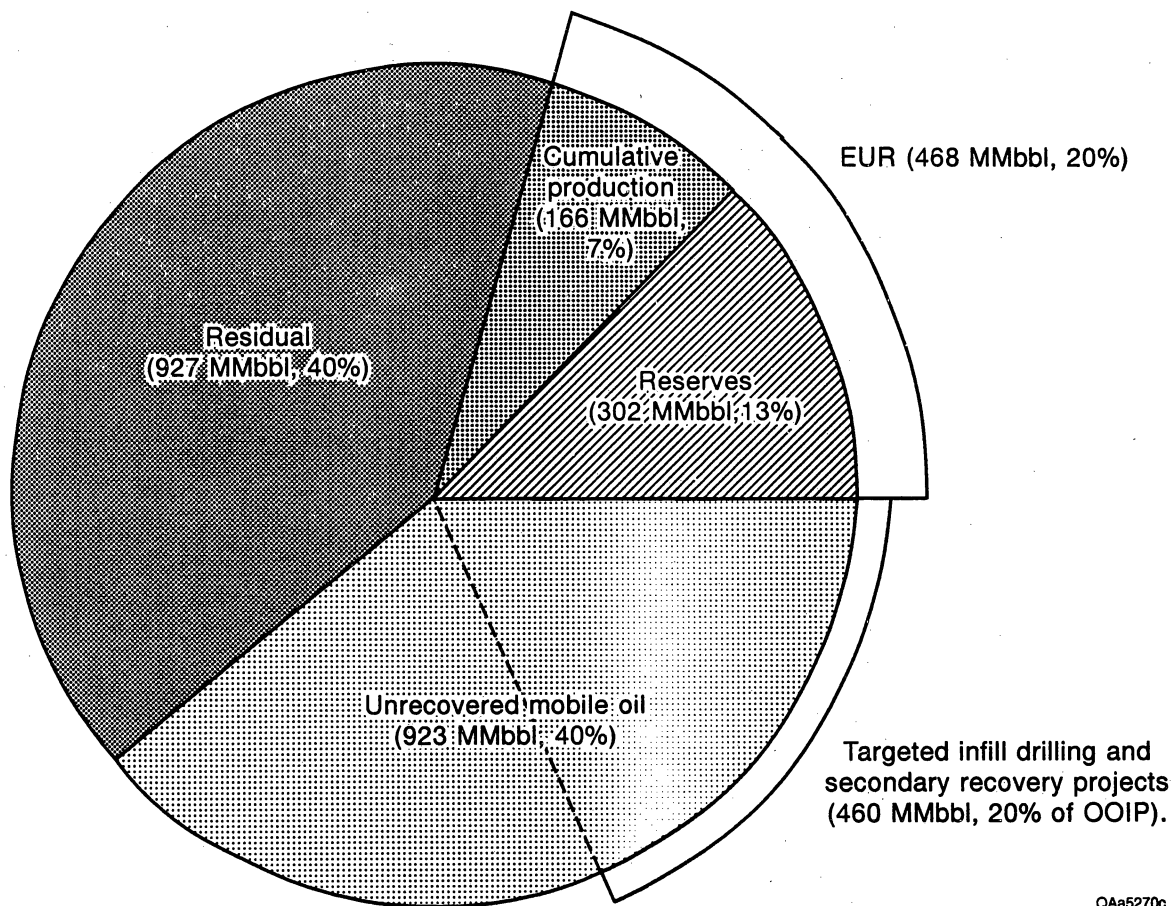
Figure 227. Reservoir volumetrics of the C members in the LL-652 area.
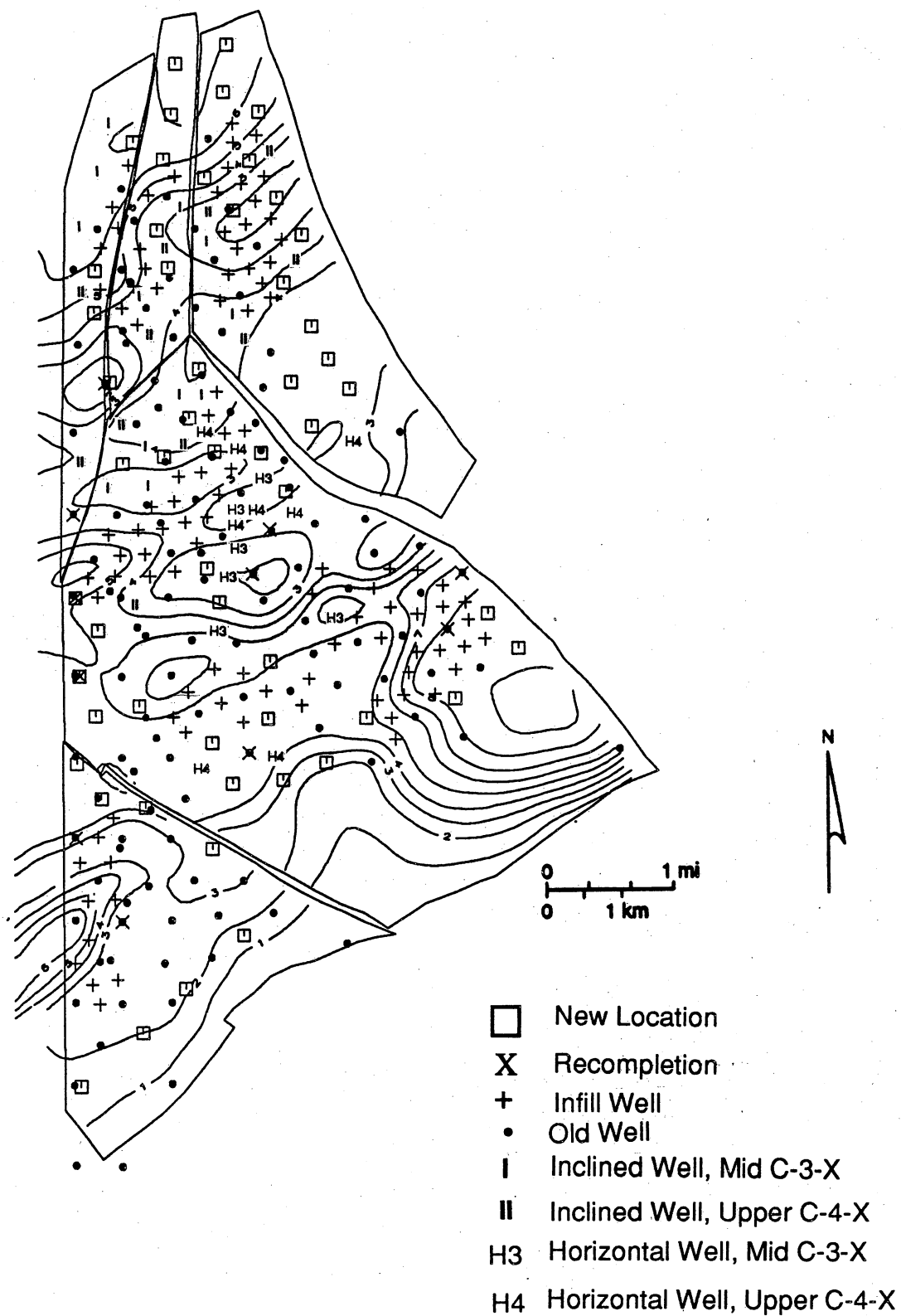
Figure 228. Porous hydrocarbon volume in the Middle C-3-X Submember.

Legend:

☐ New Location
X Recompletion
+ Infill Well
• Old Well
I Inclined Well, Mid C-3-X
II Inclined Well, Upper C-4-X
H3 Horizontal Well, Mid C-3-X
H4 Horizontal Well, Upper C-4-X

New Location
X **Recompletion**
+ **Infill Well**
• **Old Well**

I Inclined Well, Mid C-3-X

II Inclined Well, Upper C-4-X

H3 Horizontal Well, Mid C-3-X

H4 Horizontal Well, Upper C-4-X
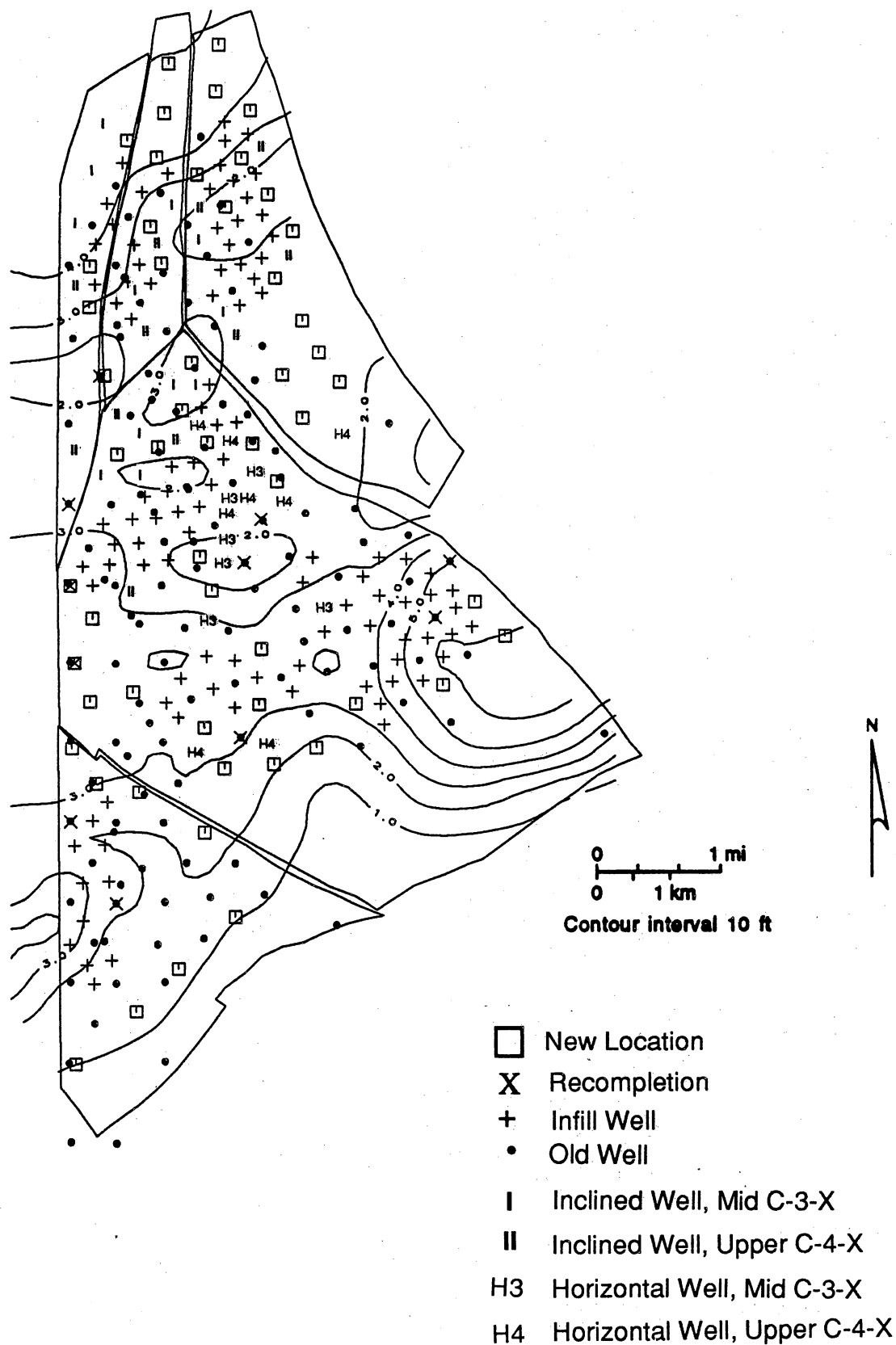
Figure 229. Map of remaining oil in the Middle C-3-X Submember showing new locations, recompletions, redrilled wells, deepened wells, infill wells, horizontal, and inclined wells for the C-3-X and C-4-X Members.

402
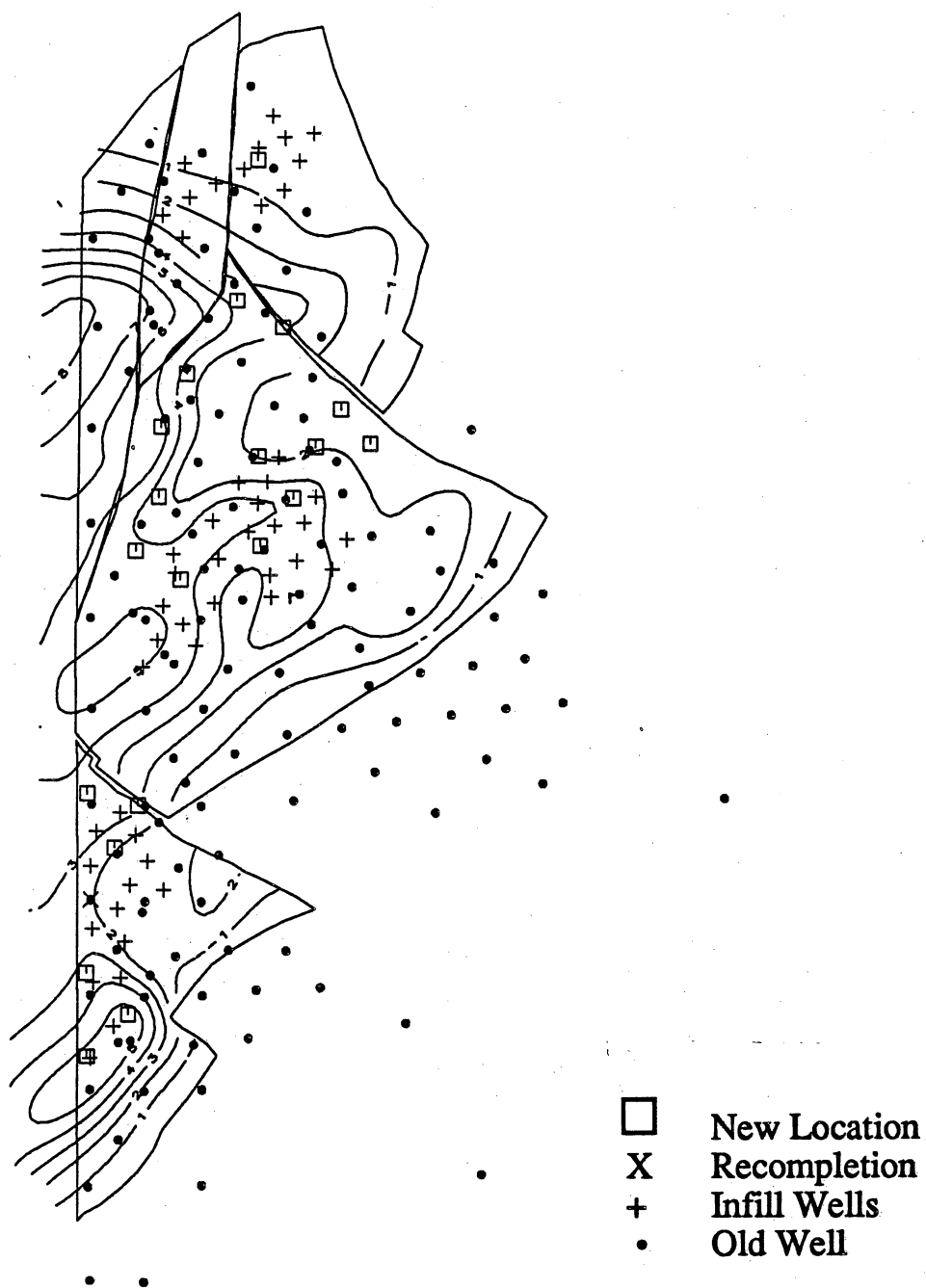
Figure 230. Porous hydrocarbon volume in the combined Middle and Upper Middle C-5-X Submembers with new locations and infill wells for the C-5-X Member.

New Location — □
Recompletion — X
Infill Wells — +
Old Well — •
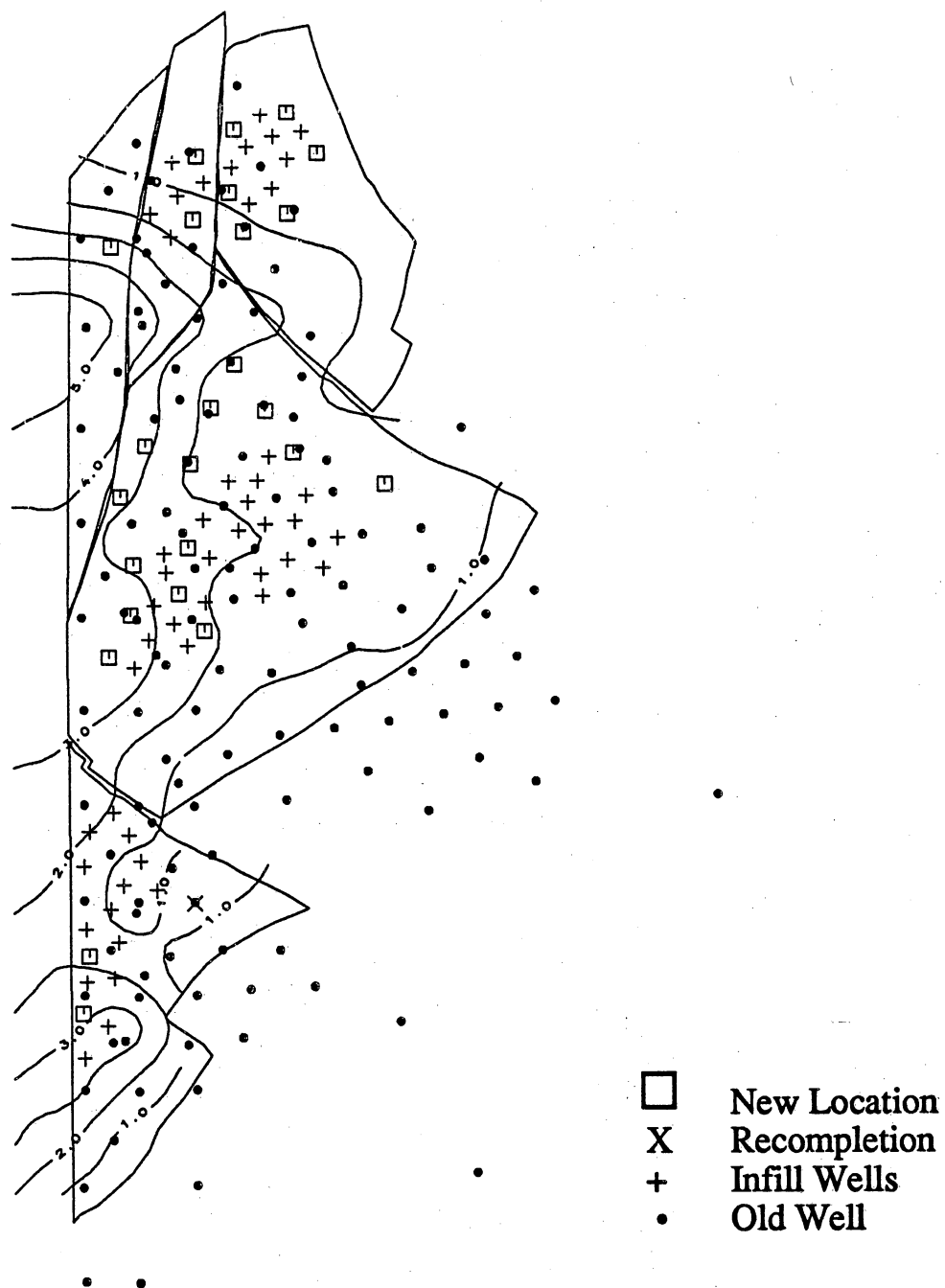
Figure 231. Map of remaining oil in the combined Middle and Upper C-5-X Submembers with new locations and infill wells for the C-5-X Member.

New Location ☐
Recompletion X
Infill Wells +
Old Well ●

404
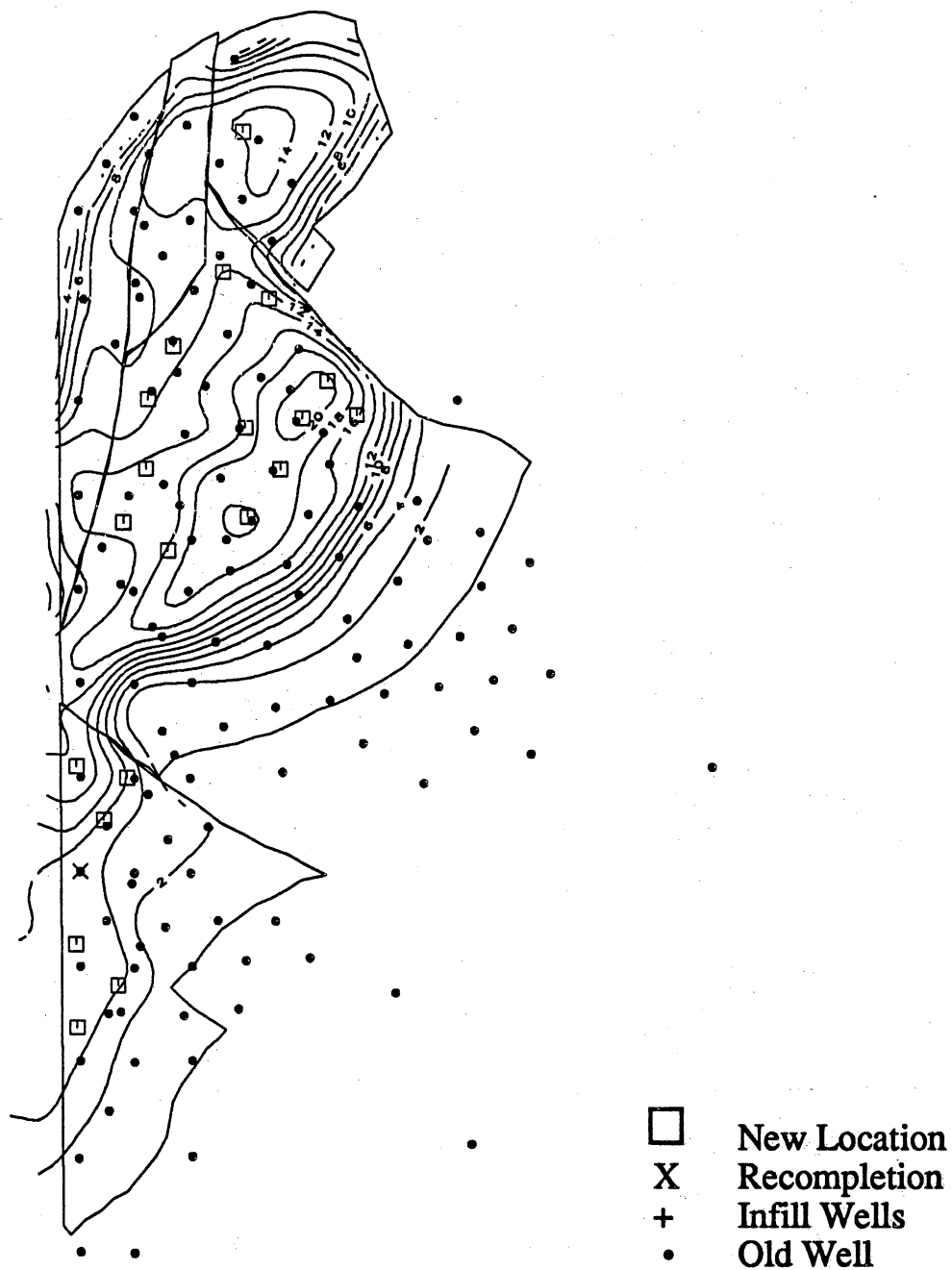
Figure 232. Porous hydrocarbon volume in the Upper Upper C-6-X Submember with new locations for the C-6-X Member.

Legend:
- ☐ New Location
- X Recompletion
- + Infill Wells
- • Old Well
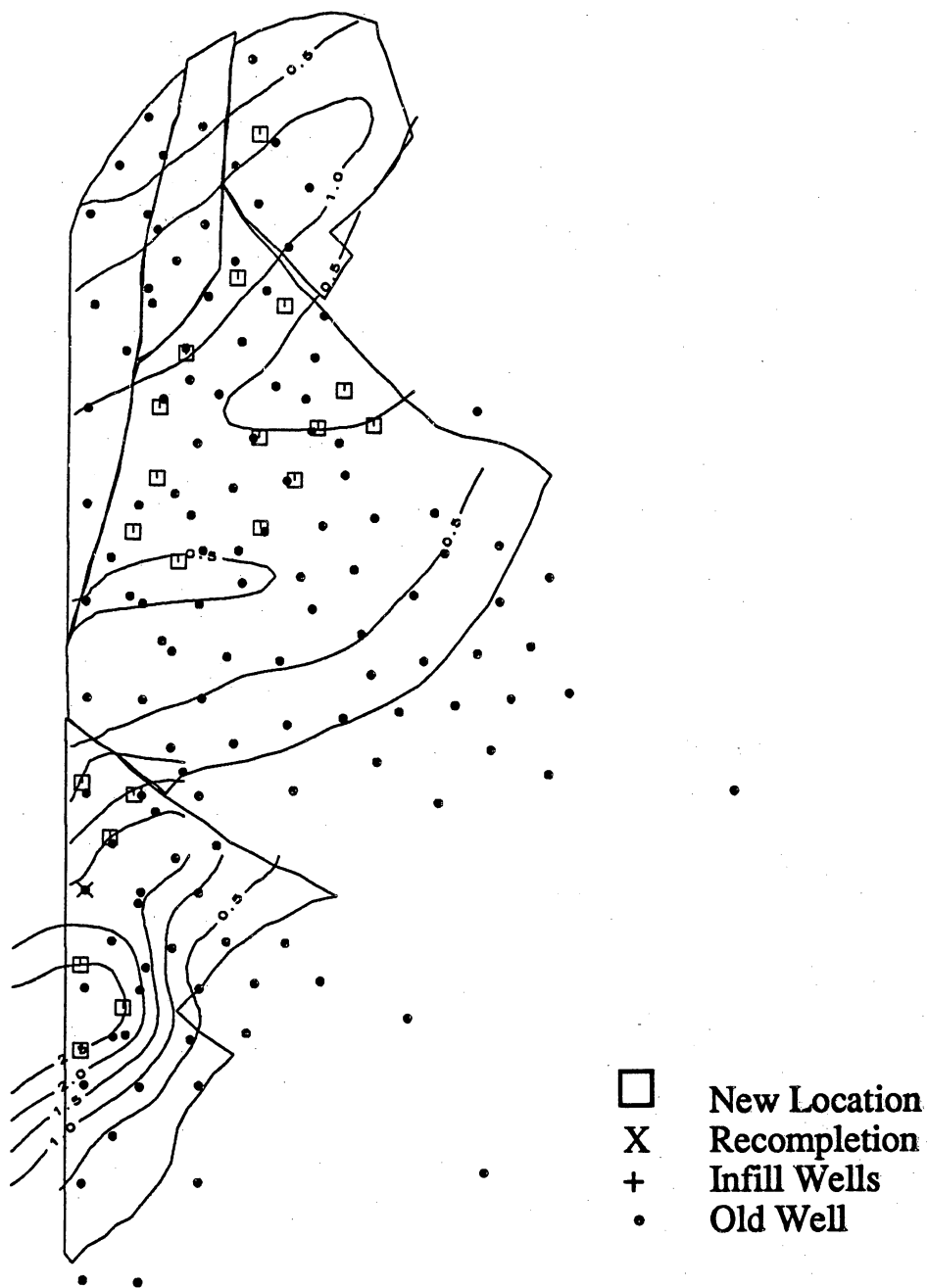
Figure 233. Map of remaining oil in the Upper Upper C-6-X Submember with new well locations for the C-6-X Member. Contour interval is 0.5 MMbbl.

406

Table 61 shows the total number of well locations by reservoir and potential (high >250 BOPD, moderate 150 to 250 BOPD, and low <150 BOPD) for each reservoir, and table 62 shows names of these new well locations. The C-4-X.01 reservoir has the highest number (30) of locations of conventional vertical wells in the area and the C-4-X.New has the highest number (8) of high-potential locations. From 97 new locations of conventional wells in 9 reservoirs, 34 have high preliminary potential, 55 have moderate, and 8 have low preliminary potential. These wells are projected to have an average recovery of 1.5 MMSTB of oil in C-3-X and C-4-X Members, and 1.0 MMSTB of oil in C-5-X and C-6-X Members. In total, we project an additional 123 MMSTB of oil from the conventional wells.

Deepened, Recompleted, and Redrilled Wells

Twelve wells are recommended for evaluation of mechanical condition (table 63) in order to propose deepening, recompletion, or redrilling. The mechanical condition of each well will determine the type of workover required. Wells with poor mechanical conditions require a new (twinned) well location.

Resource-Targeted Infill Wells

Resource-targeted, or strategic infill, drilling is required to tap remaining mobile oil in uncontacted compartments of heterogeneous reservoirs. The LL-652 area is structurally and stratigraphically complex and has a high potential for drilling successful, off-spacing infill wells. Experience has shown (Tyler and others, 1986; Bebout and others, 1987) that strategic infill-well locations in mature fields are often located in parts of the reservoir with superior reservoir quality. Typically, these are the most productive areas of conventional primary production as delineated by early development wells. Clearly, optimum advanced recovery through deployment of targeted infill drilling in the LL-652 area should focus on areas of superior reservoir quality and high productivity.

Depositional trends govern the location of areas of the reservoir with high remaining mobile oil. The sandstone trends are strongly linear and consistently oriented northeastward, reflecting deposition in dip-elongate, distributary-channel, and tidal sand-ridge facies tracts. Though partially drained by existing wells, these sandstone-rich trends offer numerous sites for strategic infill wells. Volumes of the remaining oil resource and its residency (as displayed by $S_o\emptyset h$ and remaining oil maps) have been addressed in the previous chapter. We estimate that deployment of infill wells will increase recovery efficiency by an incremental 5 percent of the OOIP.

In the C-3-X and C-4-X Members 102 infill well locations have been targeted to contact remaining mobile oil (figs. 228 and 229), and 50 locations have been targeted in the C-5-X Member (figs. 230 and 231). These infill well locations target large volumes of remaining mobile oil and are projected to recover an average of 830,000 STB of oil in the C-3-X and C-4-X Members and 500,000 STB of oil in the C-5-X Member. In total, these wells are projected to add 110 MMSTB of oil produced from the C-3-X, C-4-X, and C-5-X Members to the LL-652 reserve base.

Secondary Recovery

A pilot waterflood is recommended for structurally uncomplicated parts of the LL-652 area. These complexly stratified C member reservoirs have large vertical and lateral variations in permeability that result in great volumes of unswept mobile oil locally occurring in poorly drained reservoir compartments. Because reservoirs in the C members are so complexly stratified, more detailed geologic modeling and pilot waterflood simulations are required to predict fluid-flow pathways to most effectively sweep remaining mobile oil.

The Upper C-4-X Submember in the central structural compartment was chosen for the pilot waterflood (fig. 234). The pilot area covers about 4.6 mi^2 (12 km^2), includes 18 wells, and was selected because

Table 61. Summary of new well locations.

Reservoir	Total per Reservoir	Preliminary Potential (BOPD)		
		High (>250)	Moderate (250 to 150)	Low (<150)
C-4-X.01	30	6	22	2
C-4-X New	14	8	4	2
C-4-X.03	8	3	5	-
C-5-X.02	17	3	13	1
C-5-X.16	2	2	-	-
C-5-X.New	6	4	2	-
C-6-X.01	13	4	7	2
C-6-X.New	1	-	-	-
C-6-X.08	6	4	2	-
Total area	97	34	55	8

Table 62. Names of new well locations.

Reservoir	Well Location	Preliminary Potential (BOPD)	Reservoir	Well Location	Preliminary Potential (BOPD)
C-4-X.01	LL-AD-13C5	M	C-5-X.02	LL-AE-09	M
C-4-X.01	LL-AD-12R10	M	C-5-X.02	LL-AF-8	H
C-4-X.01	LL-AF-14R9	M	C-5-X.02	LL-AF-7	H
C-4-X.01	LL-AH-14C5	M	C-5-X.02	LL-AF-6	M
C-4-X.01	LL-AI-15R11	M	C-5-X.02	LL-AG-07	M
C-4-X.01	LL-AJ-16R2	L	C-5-X.02	LL-AH-08	M
C-4-X.01	LL-AK-16R2	L	C-5-X.02	LL-AH-7R8	M
C-4-X.01	LL-AKAL-315	M	C-5-X.02	LL-AI-9R10	H
C-4-X.01	LL-ZAJ-134	M	C-5-X.02	LL-AI-8C3	M
C-4-X.01	LL-AI-13R4	M	C-5-X.02	LL-ZAJ-310	M
C-4-X.01	LL-AL-13R10	M	C-5-X.02	LL-AJ-10R9	M
C-4-X.01	LL-AMAN-314	M	C-5-X.02	LL-AJ-11R10	M
C-4-X.01	LL-AL-12	M	C-5-X.02	LL-AK-11	M
C-4-X.01	LL-AI-11C6	M	C-5-X.02	LL-AL-12	M
C-4-X.01	LL-AI-10R9	M	C-5-X.02	LL-AE-3	M
C-4-X.01	LL-AF-9	M	C-5-X.02	LL-AF-3R6	L
C-4-X.01	LL-AF-8	M	C-5-X.02	LL-ZAD-301	M
C-4-X.01	LL-AG-8	H	C-5-X.16	LL-AP-18R1	H
C-4-X.01	LL-AH-8	M	C-5-X.16	LL-AQ-19R3	M
C-4-X.01	LL-AI-8	M	C-5-X New	LL-AD-03	M
C-4-X.01	LL-AG-07	H	C-5-X New	LL-AC-03	M
C-4-X.01	LL-AF-06	H	C-5-X New	LL-ZAD-302	H
C-4-X.01	LL-AG-04R4	M	C-5-X New	LL-AB-2	H
C-4-X.01	LL-AFAG-303	M	C-5-X New	LL-AB-1	H
C-4-X.01	LL-AE-03	M	C-5-X New	LL-AC-1	H
C-4-X.01	LL-AD-02R6	H	C-6-X.01	LL-AE-8	M
C-4-X.01	LL-AA-1CR6 [1]	M	C-6-X.01	LL-AE-7	M
C-4-X.01	LL-ZACAD-301a	M	C-6-X.01	LL-AF-8	M
C-4-X.01	LL-AD-1a	L	C-6-X.01	LL-AG-8	H
C-4-X.01	LL-AB-1bR8 [2]	M	C-6-X.01	LL-AG-9	H
C-4-X New	LL-AD-7R8	L	C-6-X.01	LL-AH-10	M
C-4-X New	LL-ZADAE-306	M	C-6-X.01	LL-ZAJ-310	L
C-4-X New	LL-ACAD-307	L	C-6-X.01	LL-AJ-9C6	L
C-4-X New	LL-ACAD-306	M	C-6-X.01	LL-AI-8C6	H
C-4-X New	LL-AC-5	M	C-6-X.01	LL-AH-7C2	H
C-4-X New	LL-AC-4	H	C-6-X.01	LL-AG-6	M
C-4-X New	LL-AB-3	H	C-6-X.01	LL-ZAE-305	M
C-4-X New	LL-AB-2	H	C-6-X.01	LL-AE-4C6	M
C-4-X New	LL-AB-1	H	C-6-X New	LL-AC-1R10	L
C-4-X New	LL-AC-1	H	C-6-X.08	LL-AQ-20C4	H
C-4-X New	LL-AC-2	H	C-6-X.08	LL-AP-19R5	M
C-4-X New	LL-AA-1bC5	H	C-6-X.08	LL-AP-18R5	H
C-4-X New	LL-AAAB-301b	H	C-6-X.08	LL-ANAO-316	H
C-4-X New	LL-ZAA-301c [3]	M	C-6-X.08	LL-AMAN-315	M
C-4-X.03	LL-ASAT-323	M	C-6-X.08	LL-AN-14R10	H
C-4-X.03	LL-AP-21	M			
C-4-X.03	LL-AQ-21R10	M			
C-4-X.03	LL-AN-20	M			
C-4-X.03	LL-ZAM-317	M			
C-4-X.03	LL-AM-16R8	H			
C-4-X.03	LL-ANAO-316	H			
C-4-X.03	LL-ANAO-315	H			

(1) and (3) advanced locations, depending on results at the LL-AB-1bR8 and LL-AAAB-301b locations. (2) Depending on results at the LL-ZACAD-301a location.

Table 63. Redrilled wells, recompletions, and deepened wells targeted in the
C-4-X.01, C-4-X.03, and C-5-X.16 reservoirs.

Target (Reservoir)	Well	(Job)	Preliminary Potential	Comments
C-4-X.03	LL-1307	Red	H	
C-4-X.03	LL-995	D	H	
C-4-X.01	LL-2425	Red	M	
C-4-X.01	LL-2191	Red	M	
C-4-X.01	LL-3080	Rec	H	Producing 90% water from C-6-X.01 reservoir
C-4-X.01	LL-2942	Rec	H	Producing 80% water from C-6-X.01 reservoir
C-4-X.01	LL-997	D	M	
C-4-X.01	LL-907	D	H	
C-4-X.01	LL-857	Rec	M	
C-4-X.01	LL-1089	Rec	M	
C-4-X.01	LL-866	Red	M	
C-5-X.16	LL-992	Rec	M	Hw in C-6-X.08 reservoir
Total	12			

H=high   D=Deepening
M=moderate   Red=Redrill
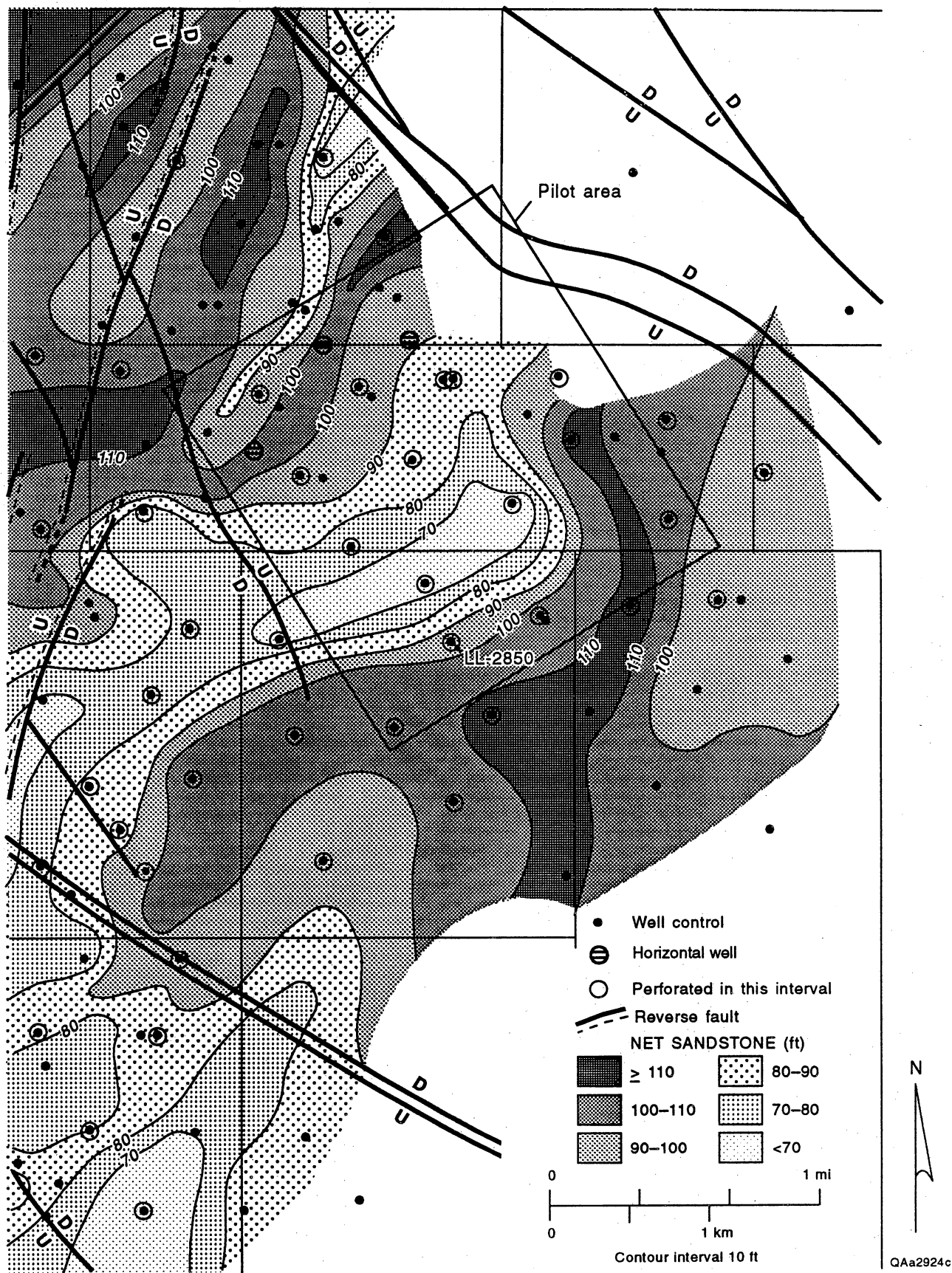L=low   Hw=high water
Rec=Recompletion

Figure 234. Net-sandstone thickness map of the Upper C-4-X Submember in the area of the pilot waterflood area, with recommended sites for horizontal wells.

411

(1) initial geologic studies suggest lateral discontinuities in the pilot area, (2) the reservoir pressure in the pilot area is declining faster than in other reservoirs, and (3) it is in a structurally simple area. For example, in well LL-3195 (located in fig. 6), repeat formation test results indicate an average reservoir pressure in the Upper C-4-X Submember of 1,600 psi and an average reservoir pressure in the Middle C-3-X Submember of 2,200 psi.

Geologic and engineering assessment of the pilot waterflood should include three overlapping and integrated tasks. Task 1 would construct a detailed, high-resolution geologic framework showing the three-dimensional distribution of the complexly stratified reservoir sandstones of the Upper C-4-X Submember. Task 2 would quantify this framework petrophysically using available core data, wireline logs, pressure data, and production history and geostatistical techniques to interpolate petrophysical data between wells. Task 3 would simulate recovery in a three-dimensional numerical simulator to test various water-injection patterns to evaluate production performance. Methods of scaling up reservoir parameters should be investigated in preparation for simulation studies of larger areas.

Sandstones in the Upper C-4-X Submember were deposited in northeast-trending deltaic progradational wedges in a net retrogradational sequence, resulting in the lower part of the sequence containing thick (commonly more than 30-ft [9-m]) distributary-channel and lower-delta-plain sandstones and the upper part containing numerous but thin (commonly 5- to 15-ft [1.5- to 4.5-m]) delta-front and prodelta sandstones (fig. 125). As a result of strong tidal processes, the deltaic sands were reworked into narrow (600- to 1,500-ft [183- to 457-m]), northeast-trending, dip-parallel belts (fig. 126) that may control anisotropic reservoir drainage patterns.

The pilot study area is located in a 4.6-mi^2 (12-km^2) structurally simple area between a major northwest-trending, sealing normal fault and a minor non-sealing normal fault to the southwest (fig. 45). This pilot study area is on the northern limb of a rapidly north- to northwest-advancing zone of water encroachment that may be halted or slowed by a relatively shaly area defined by a northeast-trending band of less than 70 ft (21.3 m) of net sandstone that bisects the pilot study area (fig. 234). The project could be expanded beyond the pilot area to include the entire fault block, providing a larger area in which different water-injection patterns could be tested.

All sandstones and shales in the Upper C-4-X Submember would be correlated in the study area to document the geometry of the reservoirs and to predict the pathways of injected water in each zone. Additionally, vertical connectivity of sandstones should be documented to construct a three-dimensional model of the Upper C-4-X Submember. The detailed geologic model will then be integrated with petrophysical data to more accurately simulate the projected waterflood.

Simulation studies must critically evaluate the effectiveness of waterflooding in the Upper C-4-X Submember. The important parameters to be addressed are (1) geometry of lithofacies, (2) injection patterns, (3) hysteresis effect on gas flow, (4) vertical communication, (5) gascap-pressure maintenance, and (6) methods of scaling up reservoir parameters for fieldwide simulation. Water channeling through the lower thick sandstone and oil flowing into the gas cap will be the most serious problems for waterflooding. Optimizing injection patterns and strategies to minimize these problems must be critically assessed.

The potential of secondary recovery to add to the LL-652 reserve base will be quantified through this detailed simulation exercise. However, an indication of the volume of reserves that may be added can be gained by comparison with analogous reservoirs in Texas. Fluvial-deltaic reservoirs under secondary recovery in Texas have recovery efficiencies that average 40 percent. These reservoirs are typically more densely drilled that the LL-652 area with 20- to 4-acre well spacings as compared to the 80-acre spacing in the LL-652 area. Styles of reservoir architecture also differ. However, by comparison with maturely drilled U.S. fields, there is potential to add as much as 20 percent of the OOIP to the LL-652 reserve base by deployment of secondary recovery technology (fig. 227). Over 460 MMbbl of oil is the possible reward for application of waterflooding throughout the LL-652 area.

412

Horizontal Drilling

Opportunities exist for contacting remaining oil in the high-permeability Middle C-3-X and Upper C-4-X Submembers with 14 horizontal wells (figs. 228 and 229). In contrast to conventional vertical wells (new locations or infill wells), horizontal wells in these submembers target reservoir areas that have (1) high permeability, (2) high volumes of remaining oil, (3) high $S_o\emptyset h$ values, and (4) low water saturation, and that are (5) poorly developed by previous wells and occur (6) in structurally simple parts of the field. Because reservoir sandstones in the Middle C-3-X and Upper C-4-X Submembers occur in northeast-trending belts of distributary-channel and delta-front deposits, horizontal wells should be oriented northeast-southwest to intersect zones of maximum permeability, $S_o\emptyset h$, and remaining oil. Additionally, horizontal wells can contact bypassed oil in internally heterogeneous reservoirs such as the Upper C-4-X Submember that consists of multiple sandstones interbedded with low-permeability mudstones (fig. 125). Complexly stratified reservoirs such as the Upper C-4-X Submember contain numerous vertical flow baffles and boundaries associated with facies changes; multiple compartments in this type of reservoir can be drained simultaneously by a single horizontal borehole (Finley and others, 1990).

Middle C-3-X Submember

Recommended sites for horizontal wells in the Middle C-3-X Submember (figs. 228 and 229) are located in areas of (1) average permeability of more than 100 md (fig. 193), (2) remaining oil greater than 2 MMbbl per 80 acres (fig. 217), (3) $S_o\emptyset h$ greater than 4 ft (1.2 m) (fig. 204), and (4) S_w less than 40 percent (fig. 196). In addition, the areas are far away from previous producing wells (fig. 226) and are structurally simple (fig. 44). These areas coincide in the north-central part of the central structural compartment (figs. 228 and 229). Unfortunately, many of these sites occur along the north-northeast-trending zone of reverse faults (fig. 44) and, therefore, are inappropriate for horizontal wells. However, these sites can be targeted for inclined wells (see following section).

Upper C-4-X Submember

Locations for horizontal wells in the Upper C-4-X Submember (figs. 228 and 229) occur in areas of (1) average permeability of more than 150 md (fig. 192), (2) remaining oil greater than 7 MMbbl per 80 acres (fig. 215), (3) $S_o\emptyset h$ greater than 12 ft (3.7 m) (fig. 201), and (4) S_w less than 40 percent (fig. 195). These areas are distant from previous producing wells (fig. 224) and are structurally simple (fig. 45). Most locations that satisfy these criteria occur in the central structural compartment, east and southeast of the north-northeast-trending reverse faults (figs. 228 and 229). In particular, three locations for horizontal wells in the Upper C-4-X Submember occur in the northern part of the proposed waterflood pilot area (fig. 234), where there is more than 90 ft (27.4 m) of net-sandstone thickness in a northeast-trending belt that corresponds to a belt of more than 150 md of average permeability (fig. 192).

Inclined Wells

Twenty-three inclined wells are recommended to target the Middle C-3-X and Upper C-4-X Submembers in areas of steeply dipping strata in the northern part of the LL-652 area (figs. 228 and 229). In addition, these inclined wells are projected to contact areas of (1) high permeability, (2) high volumes of remaining oil, (3) high $S_o\emptyset h$ values, (4) low water saturation, and (5) poor development.

In contrast to horizontal wells, inclined wells are not limited by structural complexity. Because strata adjacent to the reverse faults commonly dip at high angles (fig. 40), inclined wells will be necessary to contact remaining oil (figs. 228 and 229). Additionally, there are 15 recommended inclined wells in the three northern structural compartments. Seven of these wells are targeted for the Middle C-3-X Submember and eight are selected for the Upper C-4-X Submember. Because $S_o\emptyset h$ and net-pay values are uniformly high and water-saturation values are pervasively low in the northern part the LL-652 area,

the main criteria used in selecting inclined-well locations were areas of steeply dipping strata with high permeability values at relatively great distances from previously producing wells.

XII. CONCLUSIONS

The LL-652 resource base has been substantially increased as a result of this study. Rigorously established field limits, together with careful petrophysical analysis have documented the OOIP resource to be 2.3 BSTB. Extended development through continued pattern infill can increase reserves from 127 to 302 MMSTB (fig. 227). Substantial volumes of oil (923 MMSTB) will remain in the LL-652 area following recovery of proved and extended-development reserves. This mobile oil is targeted through deployment of geologically optimized infill wells that are projected to recover 116 MMSTB of oil and a pilot waterflood that could recover almost 70 MMSTB. Expansion of waterflood operations to the entire field could increase recovery by as much as 20 percent of the OOIP. Other significant results include the following:

- A 137-percent increase in oil resources (175 MMSTB) and a 60-percent increase in OOIP have been estimated for the LL-652 area from volumetric analysis of the C members.

- 97 new well locations to continue the field development have been identified in the LL-652 area to contact additional remaining oil.

- There is a 60-percent increase in expected ultimate recovery (175 MMSTB) in the C members in the LL-652 area. Most of the remaining mobile oil exists in the combined C-3-X and C-4-X Members.

- The primary control on reservoir quality in the C members is diagenetic: porosity loss is controlled by increasing quartz cement with increasing depth.

- A 4.6-mi^2 (12-km^2) area has been selected in the eastern part of the LL-652 area for a pilot waterflood simulation in the prolific Upper C-4-X Submember to maximize secondary oil recovery by predicting between-well, fluid-flow pathways.

- 102 geologically targeted infill well locations have been selected to contact remaining oil in the C-3-X and C-4-X Members, and 50 locations have been selected for the C-5-X Member.

- An additional 14 geologically targeted horizontal and 23 inclined wells are projected to contact nondeveloped areas of projected high permeability in structurally simple areas in the C-3-X and C-4-X Submembers.

Poorly drained or undrained reservoir compartments in the LL-652 area are defined by a combination of structure and depositional-facies geometry. The complex, multistage tectonic history of Lake Maracaibo has created many structural compartments between faults of different ages. Sandbody trends, as a result of the tide-dominated deltaic depositional system, are linear, parallel, and consistently oriented northeastward, imparting a preferred pathway for reservoir drainage. Because the sandbodies are narrow, typically less than the distance between wells (1,968 ft [600 m]), and are bounded laterally by low-permeability mudstones, they contain uncontacted oil that can be produced with cost-effective, geologically targeted recovery strategies.

The structure of the LL-652 area is a north-northeast-trending, elongate anticline with a steeply dipping (25°–45°) western and northwestern limb and a relatively gently dipping (5°–10°) east and southeast limb. Multiple tectonic events generated three trends of normal faults and one trend of younger reverse faults, representing the local scale of five major structural trends in the Maracaibo Basin (Lugo, 1991). The principal reservoir areas (C-4-X.01, C-5-X.02, and C-6-X.01) are separated from the C-4-X.03, C-5-X.08, and C-6-X.16 reservoir areas by a major northwest-trending normal fault in the northeast part of the LL-652 area. Other northwest-trending normal faults bound the reservoirs. A north-northeast-trending zone of partly sealing reverse faults with repeat section ranging from 60 to 150 ft (18 to 45.7 m) internally divides the principal reservoirs and provides additional compartments for remaining oil.

A net-thickness map of the interval between the Eocene unconformity and the top of the C-3-X Member indicates anomalies along the Maraven boundary as well as areas in the northern, northeastern, and southern parts of the field. The most complex structural area is the northern part of the field. A grid of 22 structural cross sections shows that young reverse faults offset the unconformity and truncate oldest normal faults. All normal faults except the master fault terminate below the unconformity. Minor block rotation is associated with reverse faults. Strata are locally tilted up to 54° along faults, as indicated by dipmeter logs.

The net-thickness map of the C-3-X Submember shows different trends on either side of the master fault that may be due to either syntectonic growth faulting or strike-slip fault movement. Erosion associated with the Eocene unconformity, controlled by normal faults in the LL-652 area, increases from north to south. However, in the Maraven area normal faults do not control degree of erosion.

Tectonic features such as microfaults, fault breccia, fractures, and faulted zones are common in cores in the LL-652 area. The best example of a faulted zone in core is from the LL-3282 well that contains a 45-ft (13.7-m) faulted zone with vertically tilted beds and anomalous resistivity and GR log responses.

Fault-seal analysis indicates that there are at least seven compartments in the LL-652 area bounded by faults varying in degree of sealing probability from 28 to 90 percent. Four compartments are in the C-4-X.01, C-5-X.02, and C-6-X.01 reservoirs, and two are in the C-4-X.03, C-5-X.08, and C-6-X.16 reservoirs. One compartment is isolated from other compartments by the zone of north-northeast-trending reverse faults.

The lower Eocene in the LL-652 area is approximately 4,000 ft (1,220 m) thick and contains multiple regressive-transgressive cycles in a net-retrogradational sequence. Individual deltaic cycles are 50 to 80 ft (15.2 to 24.4 m) thick. The C-7-X Member is a major progradational wedge truncated by an unconformity inferred to have been caused by fall in sea level. Lower C-6-X progradational deposits above this unconformity are overlain by muddy Upper C-6-X retrogradational deposits. The C-5-X Member and the Lower C-4-X Submembers contain minor progradational cycles, whereas the Upper C-4-X Submember, although a net retrogradational sequence, contains deltaic wedges that offlapped northeast of the LL-652 area. Sandstones in the Upper C-4-X Submember consistently exhibit excellent gamma-ray and resistivity responses, reflecting good reservoir quality and high oil saturation. A major retrogradational phase commenced with deposition of the C-3-X Member. The sandstone-rich Middle C-3-X Submember represents a brief period of deltaic offlap, but the majority of sequences in the C-3-X, C-2-X, and C-1-X Members are sandstone-poor, highstand systems tracts that contain only minor volumes of hydrocarbons.

The C members contain three major seismic stratigraphic units (lower, middle, and upper) that correspond approximately to the C-7-X to C-5-X, C-4-X to C-3-X, and C-2-X to C-1-X Members, respectively. The lower seismic unit is a 0.1- to 0.3-s zone of low- to moderate-amplitude reflectors that are irregular, wavy, and discontinuous. These reflectors represent multiple regressive/transgressive couplets. The middle seismic unit encompasses a 0.15- to 0.20-s zone bounded below by a pair of moderate-amplitude, semicontinuous reflectors and above by a pair of high-amplitude, continuous and parallel reflectors that corresponds to a zone of high-velocity contrast between the shaly C-3-X Member and the sandy Upper C-4-X Submember. This boundary is an onlapping, marine-flooding surface that marks the onset of a major retrogradational sequence in the Upper C Members. The upper seismic unit represents a major retrogradational highstand systems tract that onlaps southwestward over the regressive, progradational cycles of the C-4-X Member. The upper seismic unit consists of multiple, moderate-amplitude reflectors in a 0.20- to 0.25-s zone that is bounded above by the Eocene unconformity, represented by a continuous, high-amplitude pair of parallel reflectors that merge with and are inferred to truncate underlying reflectors westward and southwestward.

The tide-dominated deltaic depositional model of the C members in the LL-652 area contains a system of dip-elongate distributary- and tidal-channel sandstones that merge northeastward with extensive, dip-parallel delta-front sandstones. The distributary-channel and delta-front facies comprise most of the reservoir sandstones and therefore contain most of the remaining oil. Minor facies are tidal-channel, tidal-

flat, channel-mouth-bar, transgressive sand-shoal, shelf, and fluvial-estuarine channel. The dominant reservoir geometry consists of narrow (commonly less than 2,000 ft [610 m] wide), northeast-trending sandstones, reflecting strong inferred tidal processes that redeposited channel-mouth-bar and proximal delta-front deposits into linear tidal sand ridges.

Thickest sandstones in progradational sequences in the LL-652 area occur in delta-front, channel-mouth-bar, and distributary-channel facies. In contrast, thickest sandstones in retrogradational sequences occur in distributary-channel facies, whereas the delta-front facies is relatively muddy. In sequences with base-level fall and extreme offlap northeast of the LL-652 area, thickest sandstones occur locally in thick fluvial belts bounded by wide, muddy areas.

Permeability in the C members in the LL-652 area is mainly a function of depth and is similar for major facies. However, there are significant permeability contrasts (up to three orders of magnitude) locally between distributary-channel and tidal-flat, fluvial-estuarine channel and distal delta-front, and distributary-channel and delta-front facies where the base of the distributary-channel facies contains clay clasts that may retard vertical fluid flow.

Diagenesis, not depositional environment, is the main control on porosity and permeability distribution in the C members. In particular, the volume of quartz cement is the main influence on reservoir quality, and because the volume of quartz cement increases significantly with depth, reservoir quality decreases with depth. Quartz, plagioclase, and metamorphic and sedimentary rock fragments are the most abundant detrital grains. Quartz overgrowths, siderite, calcite, illite, and kaolinite are the major cements in the sandstones. An average of 5 percent primary porosity remains in these sandstones even after compaction and cementation. Porosity is enhanced by dissolution of feldspar, rock fragments, and calcite cement to form secondary pores.

Cumulative production to March 1993 in 130 active wells in the LL-652 area was 165.5 MMbbl of oil, mainly 37° API, and 8.3 MMbbl of water. Eighty-two percent (135.8 MMbbl) of the oil production comes from the C-3-X and C-4-X Members, and the C-5-X Member accounts for only 12 percent (20.5 MMbbl). The C-6-X Member has 5 percent (8.4 MMbbl), and the C-2-X Member has only 1 percent (0.8 MMbbl) of cumulative oil production. The central structural compartment is the largest production area in the field and includes 76 wells with a cumulative production of 85.8 MMbbl. Seventy-seven percent (66.1 MMbbl) of this production comes from the C-4-X.01 reservoir compartment.

Multiple oil-water contacts exist in each reservoir because of the high degree of sandstone and mudstone interbedding. Irregular production and lateral stratigraphic changes introduce barriers to the normal movement of the oil-water contacts not parallel with structural contours, particularly in the C-3-X and C-4-X Members.

V_{sh}-porosity and permeability-porosity transforms were developed for each C member rather than for each facies, in recognition of depth control on reservoir quality. The Simandoux model of water saturation best matches water-saturation values measured from cores. There is a general trend of decreasing water saturation with increasing depth in the C members in the LL-652 area. Net-pay thickness values were determined with cutoff values of V_{sh}, water saturation, and porosity. For the C-1-X to C-4-X Members, the resistivity cutoff is 10 ohm-m; for the C-5-X Member it is 12 ohm-m; and for the C-6-X Member it is 14 ohm-m. Cutoff values of water saturation, further modified during mapping, were determined to be 55 percent for the C-1-X to C-4-X Members and 50 percent for the C-5-X to C-7-X Members.

As a result of volumetric analysis, the original-oil-in-place resource base was increased by 867 MMbbl (60 percent) to 2,318.2 MMbbl. This increase was mainly from the C-3-X and C-4-X Members by documenting additional reservoir areas and by using improved petrophysical parameters. For example, the official porosity value used to calculate OOIP for the C-3-X and C-4-X Members was 14 percent, but this study determined a value of 17 percent. In contrast, the OOIP value for the C-6-X Member was decreased by 31 percent as a result of adjusting the average porosity value of 13.2 percent to 11 percent.

Maps of net pay, porosity, permeability, $S_0\varnothing h$, OOIP, and remaining oil in the C members and submembers exhibit northeast-trending patterns, reflecting depositional influence on reservoir geometry. Values of these volumetric parameters commonly decrease downdip (northeastward) and are commonly controlled by pinchout of delta-front sandstones. Structural influences are indicated by abrupt changes in values across faults, particularly in the southwestern and northeastern parts of the LL-652 area. Net-pay, $S_0\varnothing h$, OOIP, and remaining-oil contours are closely spaced and bounded by zero values due to oil-water contacts on the southern and southeastern limbs of the field and tend to be greater toward the north due to steeply dipping strata. In contrast, water-saturation trends reflect structural control, although some members and submembers contain anomalous trends that may reflect depositional control.

Maps of remaining oil in the C members have similar to nearly identical trends to maps of OOIP, indicating that the reservoirs contain areas of undrained or poorly drained compartments that can be targeted for advanced oil recovery. The Lower Lower C-6-X and Upper Lower C-6-X Submembers contain the greatest volumes of remaining oil in the C-6-X Member (locally up to 6 MMbbl and 4.4 MMbbl per 80 acres, respectively). In the C-5-X Member, the Lower and combined Middle and Upper Middle C-5-X Submembers contain the greatest volumes of remaining oil (up to 3.6 MMbbl per 80 acres). The Upper C-4-X Submember contains more remaining oil than the Lower and Middle C-4-X Submembers combined. Areas of more than 8 MMbbl per 80 acres of remaining oil in the Upper C-4-X Submember coincide with thick (more than 80-ft [24.4-m]) delta-front and distributary-channel sandstones as well as steeply dipping strata. High volumes of remaining oil in the Lower C-3-X Member (locally more than 4 MMbbl per 80 acres) principally occur in the northern part of the field, and in the Middle C-3-X Member areas of more than 4 MMbbl per 80 acres occur in the eastern part of the central structural compartment.

Vertical communication between C reservoir sandstones is poor. RFT data indicate average pressure differences of more than 50 psi between subjacent sandstones. However, horizontal communication in sandstones is better than vertical communication, except in faulted areas such as the master fault and the zone of reverse faults.

Cumulative production, apportioned by kh in each C submember, varies greatly across the LL-652 area. Reasons for this variability include (1) differences in age of producing well, (2) greater-than-average production in areas of repeat section and inferred great fracture permeability in zones of reverse faults, and (3) differences in net thickness of intervals perforated in each submember.

In the Lower Lower and Upper Lower C-6-X Submembers, few wells have been perforated in thick fluvial-estuarine sandstones in the north-central part of the field. These sandstones locally contain up to 3 MMbbl of remaining oil per 80 acres that could be contacted through recompletions.

The Lower and combined Middle and Upper Middle C-5-X Submembers contain numerous areas that have not been produced, particularly in the northeast-trending zone of reverse faults and in narrow, elongate delta-front and distributary-channel sandstones. In the combined Middle and Upper Middle C-5-X Submember, two of the three northern structural blocks with high net-pay values have not been developed and therefore can be targeted for secondary oil recovery.

There are substantially more producing wells in the C-4-X Member than in the C-5-X Member. For example, the Middle C-4-X Submember has been produced from 51 wells, whereas the combined Middle and Upper Middle C-5-X Submember has produced from only 28 wells. The Upper C-4-X Submember is the most productive interval in the C members: 14 wells in the Upper C-4-X Submember have each produced more than 1.5 MMbbl and 11 wells have each produced between 1.0 and 1.5 MMbbl. However, there are numerous sites in the LL-652 area in the Upper C-4-X Submember where high volumes of remaining oil (more than 6 MMbbl per 80 acres) coincide with little or no production, especially in the north-central and extreme northern parts of the field.

The most productive submember in the C-3-X Member is the Middle C-3-X Submember, which has produced from 60 wells. Seventeen wells have each produced more than 0.5 MMbbl. Most of the

production is from southern and eastern areas, with limited production in the north. Despite the intense level of development, there are areas in the Middle C-3-X Submember that have no production, particularly in the zone of reverse faults and in thicker segments of distributary-channel and proximal delta-front sandstones in the central structural compartment.

XIII. ACKNOWLEDGMENTS

XIV. REFERENCES

Allan, U. S. , 1989, Model for hydrocarbon migration and entrapment within faulted structures: American Association of Petroleum Geologists Bulletin, v. 73, no. 7, p. 803–811.

Allen, G. P., and Posamentier, H. W., 1993, Sequence stratigraphy and facies model of an incised valley fill: the Gironde Estuary, France: Journal of Sedimentary Petrology, v. 63, no. 3, p. 378–391.

Añez, M. E., 1989, Estrategias de explotación para el área LL-652 (segregaciones: Liviano y condensado): Lagoven, S.A., Internal Report, 34 p.

Añez, M. E., 1990a, Estrategias de explotación en zonas poco desarrolladas del área LL-652: Lagoven, S.A., Internal Report, 20 p.

_____ 1990b, Resultados de la estrategia de explotación de yacimiento C-4-X.01: Lagoven, S.A., Internal Report, 22 p.

Archie, G. E., 1950, Introduction to petrophysics of reservoir rocks: American Association of Petroleum Geologists Bulletin, v. 34, p. 943–961.

Asquith, George, 1985, Log evaluation of shaly sandstone reservoirs: a practical guide: American Association of Petroleum Geologists, Methods in Exploration Series, No. X, 59 p.

Atkins, J. E., and McBride, E. F., 1992, Porosity and packing of Holocene river, dune, and beach sands: American Association of Petroleum Geologists Bulletin, v. 76, p. 339–355.

Beard, D. C., and Weyl, P. K., 1973, Influence of texture on porosity and permeability of unconsolidated sand: American Association of Petroleum Geologists Bulletin, v. 57, p. 349–369.

Bebout, D. G., Lucia, F. J., Hocott, C. R., Fogg, G. E., and Vander Stoep, G. W., 1987, Characterization of the Grayburg reservoir, University Lands Dune field, Crane County, Texas: The University of Texas at Austin, Bureau of Economic Geology Report of Investigations No. 168, 68 p.

Bloch, S., 1991, Empirical prediction of porosity and permeability in sandstones: American Association of Petroleum Geologists Bulletin, v. 75, p. 1145–1160.

Bjoraker, R., 1980, A geological study of the C-4-X.01 reservoir: Lagoven, S.A., Internal Report, 15 p.

Bot, P., and Perdomo, J. L., 1987, Analisis sismoestratigrafico del Eoceno y evolucion tectonica en la Cuenca del Lago de Maracaibo: Lagoven, S.A., Caracas, Internal Report, 98 p.

Bouvier, J. D., Kaars-Sijpesteijn, C. H., and others, 1989, Three-dimensional seismic interpretation and fault sealing investigation Nun River field, Nigeria: American Association of Petroleum Geologists Bulletin, v. 73, no. 11, p. 1397–1414.

Burley, S. D., and Kantorowicz, J. D., 1986, Thin section and S.E.M. textural criteria for the recognition of cement-dissolution porosity in sandstones: Sedimentology, v. 33, p. 587–604.

Clifton, H. E., 1982, Estuarine deposits, in Scholle, P. A., and Spearing, Darwin, eds., Sandstone depositional environments: American Association of Petroleum Geologists Memoir 31, p. 179–189.

Coleman, J. M., and Prior, D. B., 1982, Deltaic environments of deposition, in Scholle, P. A., and Spearing, Darwin, eds., Sandstone depositional environments: American Association of Petroleum Geologists Memoir 31, p. 139–178.

Core Laboratories, 1984a, Análisis convencionales de núcleos en el pozo LL-2850: preparado para Lagoven, S.A., Internal Report, 51 p.

_____ 1984b, Análisis especiales de núcleos en el pozo LL-2850: preparado para Lagoven, S.A., Internal Report, 70 p.

_____ 1989a, Análisis convencionales de núcleos en el pozo LL-3074: preparado para Lagoven, S.A., Internal Report, 46 p.

_____ 1989b, Análisis especiales del núcleos en el pozo LL-3074: preparado para Lagoven, S.A., Internal Report, 65 p.

_____ 1991a, Análisis convencionales de núcleos en el pozo LL-3140: preparado para Lagoven, S.A., Internal Report, 46 p.

_____ 1991b, Propiedades avanzado de la roca en el pozo LL-3140: preparado para Lagoven, S.A., Internal Report, 100 p.

_____ 1992a, Propiedades avanzada de la roca en el pozo LL-3282: preparado para Lagoven, S.A., Internal Report, 90 p.

_____ 1992b, Propiedades basicas soterramiento de la roca en el pozo LL-3282: preparado para Lagoven, S.A., Internal Report, 96 p.

Dalrymple, R. W., Zaitlin, B. A., and Boyd, Ron, 1992, Estuarine facies models: conceptual basis and stratigraphic implications: Journal of Sedimentary Petrology, v. 62, no. 6, p. 1130–1146.

Delgado, I., 1985, Estudio geológico de los miembros C-2, C-3 y C-4 Pilar norte, Bloque I: Maraven, S.A., Caracas, Internal Report, 75 p.

De Mowbray, Tessa, and Visser, M. J., 1984, Reactivation surfaces in subtidal channel deposits, Oosterschelde, southwest Netherlands: Journal of Sedimentary Petrology, v. 54, no. 3, p. 811–824.

Downey, M. W., 1984, Evaluating seals for hydrocarbon accumulations: American Association of Petroleum Geologists Bulletin, v. 68, no. 11, p. 1752–1763.

Dutton, S. P., 1993, Influence of provenance and burial history on diagenesis of Lower Cretaceous Frontier Formation sandstones, Green River Basin, Wyoming: Journal of Sedimentary Petrology, v. 63, no. 4, p. 665–677.

Dutton, S. P., and Diggs, T. N., 1990, History of quartz cementation in the Lower Cretaceous Travis Peak Formation: Journal of Sedimentary Petrology, v. 60, no. 2, p. 191–202.

Egep-Consultores, S. A., 1985, Evaluación para la explotación futura del yacimiento C-4-X.01: preparado para Lagoven, S.A., Internal Report, 8 volumes of 120 p. each.

Eschard, R., Ravenne, C., Hovel, P., and Knox, R., 1991, Three-dimensional reservoir architecture of a valley-fill sequence and a deltaic aggradational sequence: influences of minor relative sea-level variations, in Miall, A. D., and Tyler, Noel, eds., The three-dimensional facies architecture of terrigenous clastic sediments, and its implications for hydrocarbon discovery and recovery: Society of Economic Paleontologists and Mineralogists (Society for Sedimentary Geology), v. 3, Concepts in Sedimentology and Paleontology, p. 233–244.

Finley, R. J., Laubach, S. E., Tyler, Noel, and Holtz, M. H., 1990, Opportunities for horizontal drilling in Texas: The University of Texas at Austin, Bureau of Economic Geology Geological Circular 90-2, 32 p.

Fisher, W. L., 1987, Can the U.S. oil and gas resource base support sustained production?: Science, v. 236, p. 1631–1636.

Fisher, W. L., Brown, L. F., Jr., Scott, A. J., and McGowen, J. H., 1969, Delta systems in the exploration for oil and gas: The University of Texas at Austin, Bureau of Economic Geology Special Publication, 78 p.

FLSTP, 1989a, Análisis convencionales, pozo LL-3075: preparado para Lagoven, S.A., Internal Report, 25 p.

_____ 1989b, Análisis convencionales, pozo LL-3080: preparado para Lagoven, S.A., Internal Report, 54 p.

_____ 1989c, Análisis especiales, pozo LL-3080: preparado para Lagoven, S.A., Internal Report, 133 p.

_____ 1990, Analisis especiales, pozo LL-3075: preparado para Lagoven, S.A., Internal Report, 101 p.

Folk, R. L, 1974, Petrology of sedimentary rocks: Austin, Texas, Hemphill, 182 p.

Galloway, W. E., Ewing, T. E., Garrett, C. M., Jr., Tyler, Noel, and Bebout, D. G., 1983, Atlas of major Texas oil reservoirs: The University of Texas at Austin, Bureau of Economic Geology Special Publication, 139 p.

Ghosh, Santos, Di Croce, Juan, Isea, Andreina, and Gonzalez, Cesar, 1988a, Control estratigrafico—diagenetico: relacion entre los ambientes de sedimentacion, diagenesis y profundidad de soterramiento en areniscas del Eoceno, Cuenca de Maracaibo: Lagoven, S.A., Internal Report, 227 p.

_____ 1988b, Relación entre los ambientes de sedimentacion, diagénesis y profundidad de en areniscas del Eoceneo, Cuenca de Maracaibo: Intevep, S.A., Los Teques, Internal Report, 376 p.

Gómez, M. E., 1987, Comportamiento de producción del yacimiento C-4-X.03 area LL-652: Lagoven, S.A., Maracaibo, Internal Report, 29 p.

Gómez, M. E., and Guzmán, T., 1984, Distribución de fluídos remanentes en el yacimiento C-4-X.01 (Area LL-652): Lagoven, S.A., Internal Report, 34 p.

Gonzalez de Juana, C., Iturraide, J., and Picard, X., 1980, Geologia de Venezuela y sus cuencas petroliferas: Caracas, Foninves, 1031 p.

González, G., 1985, Estudio geologico del miembros C-5 (Eoceno Inferior)-Pilar norte Bloque I: Maraven, S.A., Caracas, Internal Report, 70 p.

González, M., Ochoa, E., and Sampson, E., 1983, Estudio geológico de las anenas "C" Formacion Misoa area LL-652, Lago de Maracaibo: Lagoven, S.A., Internal Report, 28 p.

Graves, G. R., Adams, G. E., Guzman, J. I., Seijas, F., Petzal, C. de, Furrer, M., and Meyer, R., 1987, Estudio del Eoceno del Lago de Maracaibo, parte norte y este: Lagoven, S. A., Caracas, Internal Report, 197 p.

Harding, T. P., 1985, Seismic characteristic and indentification of negative flower structures, positive flower structures, and positive structural inversion: American Association of Petroleum Geologists Bulletin, v. 69, no. 4, p. 582–600.

_____ 1990, Identification of wrench faults using subsurface structural data: criteria and pitfalls: American Association of Petroleum Geologists Bulletin, v. 74, no. 10, p. 1590–1609.

Harding, T. P., and Lowell, J. D., 1979, Structural styles, their plate-tectonic habits, and hydrocarbon traps in petroleum provinces: American Association of Petroleum Geologists Bulletin, v. 63, no. 7, p. 1016–1058.

Harding, T. P., and Tuminas, A. C., 1989, Structural interpretation of hydrocarbon traps sealed by basement normal block faults at stable flank of foredeep basins and at rift basins: American Association of Petroleum Geologists Bulletin, v. 73, no. 7, p. 812–840.

Herron, M. M., 1987, Estimating the intrinsic permeability of clastic sediments from geochemical data: Transactions, Society of Professional Well Log Analysts, 28th Annual Logging Symposium, paper HH.

Hilchie, D. W., 1989, Advanced well log interpretation: Boulder, Co., D. W. Hilchie Inc., 496 p.

Houseknecht, D. W., 1987, Assessing the relative importance of compactional processes and cementation to the reduction of porosity in sandstones: American Association of Petroleum Geologists Bulletin, v. 71, p. 633–642.

Johnson, W. L., and Linke, W. A. 1978, Some practical applications to improve formation evaluation of sandstones in Mackenzie Delta: Transactions, Society of Professional Well Log Analysts, 19th Annual Logging Symposium, paper C.

Klein, G. de V., 1970, Depositional and dispersal dynamics of intertidal sand bars: Journal of Sedimentary Petrology, v. 40, p. 1095–1127.

Knott, S. D., 1993, Fault seal analysis in the North Sea: American Association of Petroleum Geologists Bulletin, v. 77 no. 5, p. 778–792.

Kreisa, R. D, and Moiola, R. J., 1986, Sigmoidal tidal bundles and other tide-generated sedimentary structures of the Curtis Formation, Utah: Geological Society of America Bulletin, v. 97, p. 381–387.

Levey, R. A., 1991, Infield gas reserve growth potential: Gulf Coast sandstone reservoirs (Frio, Vicksburg, Wilcox): The University of Texas at Austin, Bureau of Economic Geology, short course prepared for the Gas Research Institute under contract no. 5088-212-1718, unpaginated.

Lugo, J., 1991, Cretaceous to Neogene tectonic control on sedimentation: Maracaibo Basin, Venezuela: Ph.D. dissertation, The University of Texas at Austin, 219 p.

Maguregui, J. A., 1990, Evolution and reservoir properties of middle Eocene tide-dominated deltaic sandstones in eastern Lagunillas field, Maracaibo Basin, Venezuela: The University of Texas at Austin, Master's thesis, 171 p.

Maguregui, Jesus, 1993, Facies architecture and diagenetic control on middle Eocene tide-dominated deltaic sandstones in Lagunillas field, Maracaibo Basin, Venezuela (abs.): American Association of Petroleum Geologists Bulletin 1993 Annual Convention Program, p. 143.

Maguregui, J. A., and Tyler, Noel, 1991, Evolution of middle Eocene tide-dominated deltaic sandstones, Lagunillas field, Maracaibo Basin, western Venezuela, in Miall, A. D., and Tyler, Noel, eds., The three-dimensional facies architecture of terrigenous clastic sediments, and its implications for hydrocarbon discovery and recovery: Society of Economic Paleontologists and Mineralogists (Society for Sedimentary Geology), v. 3, Concepts in Sedimentology and Paleontology, p. 233–244.

Meckel, L. D., 1975, Holocene sand bodies in the Colorado delta area, northern Gulf of California, in Broussard, M. L., ed., Deltas: models for exploration: Houston Geological Society, p. 239–265.

Neasham, J. W., 1977, The morphology of dispersed clay in sandstone reservoirs and its effect on sandstone shaliness, pore space and fluid flow properties: SPE paper 6858 presented at the 52nd Annual Technical Conference, Denver, Colorado.

Off, Theodore, 1963, Rhythmic linear sand bodies caused by tidal currents: American Association of Petroleum Geologists Bulletin, v. 47, no. 2, p. 324–341.

Panda, M. N., and Lake, L. W., 1992, Estimation of single-phase permeability from parameters of particle-size distribution: presented at annual meeting of the American Association of Petroleum Geologists, Calgary, Canada.

Pittman, E. D., 1979, Porosity, diagenesis, and productive capability of sandstone reservoirs, *in* Scholle, P. A., and Schluger, P. R., eds., Aspects of diagenesis: Society of Economic Paleontologists and Mineralogists Special Publication No. 26, p. 159–173.

Pryor, W. A., 1973, Permeability-porosity patterns and variations in some Holocene sand bodies: American Association of Petroleum Geologists Bulletin, v. 57, p. 162–189.

Reineck, H. E., and Singh, I. B., 1973, Depositional sedimentary environments: Berlin, Springer-Verlag, 439 p.

Reineck, H. E., and Wunderlich, F., 1968, Classification and origin of flaser and lenticular bedding: Sedimentology, v. 11, p. 99–104.

Smith, D. A., 1980, Sealing and nonsealing faults in Louisiana gulf coast salt basin: American Association of Petroleum Geologists Bulletin, v. 64, no. 2, p. 145–172.

Tearpock, D. J., and Bischke, R. E., 1991, Applied subsurface geological mapping: Tamore, Venezuela, Unpublished course notes prepared for CEPET, 610 p.

Terra Science, 1993, Manual for TerraStation v. 5.4: Denver, Co., Terra Science Inc.

Tye, R. S., and Coleman, J. M., 1989, Depositional processes and stratigraphy of fluvially dominated lacustrine deltas: Mississippi delta plain: Journal of Sedimentary Petrology, v. 59, no. 6, p. 973–996.

Tyler, Noel, 1988, New oil from old fields: Geotimes, v. 33, p. 8–10.

Tyler, Noel, Galloway, W. E., Garrett, C. M., Jr., and Ewing, T. E., 1984, Oil accumulation, production characteristics, and targets for additional recovery in major oil reservoirs of Texas: The University of Texas at Austin, Bureau of Economic Geology Geological Circular No. 84-2, 31 p.

Tyler, Noel, Gholston, J. C., and Ambrose, W. A., 1986, Genetic stratigraphy and oil recovery in an Upper Cretaceous wave-dominated deltaic reservoir, Big Wells (San Miguel) field, South Texas: The University of Texas at Austin, Bureau of Economic Geology Report of Investigations No. 153, 38 p.

Walton, W. M., 1967, The informal units of the subsurface Eocene: Asociacion Venezolana de Geologia, Mineria y Petroleo Boletin, v. 10, no. 1, p. 21–30.

Wilson, M. D., and Pittman, E. D., 1977, Authigenic clays in sandstones: recognition and influence on reservoir properties and paleoenvironmental analysis: Journal of Sedimentary Petrology, v. 47, p. 3–31.

Worthington, P. E., 1985, The evolution of shaly-sand concepts in reservoir evaluation: The Log Analyst, v. 25, no. 1, p. 23–40.

Zambrano, E., Vasquez, E., Duval, B., Latreille, M., and Confineres, B., 1972, Paleogeographic and petroleum synthesis of Western Venezuela: 27, Rue Ginoux, Paris 15e, Editions Technip, 62 p.